# DAMAGING EFFECT OF MOVING TANK LOADS ON FLEXIBLE PAVEMENT

Dr. Saud Abdulaziz Sultan
Department of Highways and Transportation, College of Engineering,
Al- Mustansirya University, Baghdad, Iraq

**ABSTRACT**

Presented in this paper is a new study of the damaging effect of the tank loads on flexible pavements. The equivalent load was developed on the basis of mechanistic - empirical approach. It was found that the damaging effect of the studied tank loads is 0.898 to 2.356 times the damaging effect of the standard 18 kips (80 kN) axle load. It was found that the damaging effect of tank braking forces is 2.375 times the damaging effect of tank weight only in terms of tensile stain (fatigue cracking). It was found that the damaging effect of tank turning maneuver is 1.216 times the damaging effect of tank weight only in terms of tensile stain (fatigue cracking). These loads have also severe damaging effects on the functional serviceability of the surface of asphalt layer.

**KEY WORDS: Tanks, AASHTO, Equivalency Factors, Braking Forces, Turning Maneuver, Flexible Pavement, and Damaging Effect.**

# التأثير التخريبي لأحمال ألدبابات المتحركة على التبليط ألإسفلتي

د.سعود عبدالعزيز سلطان
قسم هندسة الطرق والنقل، كلية الهندسة، الجامعة المستنصرية, بغداد. العراق

**الخلاصة**

دراسة جديدة للتأثير التخريبي لأحمال الدبابات المتحركة على التبليط الإسفلتي من خلال أبجاد معاملات آشتو المكافئة لها ولأول مرة وباستخدام طريقة الحل الميكانيكي – التجريبي. لقد وجد إن تأثير الأحمال التخريبية للدبابة التي تمت درستها يتراوح بين 0.898– 2.356 مرة تأثير حمل آشتو القياسي. ولقد وجد إن التأثير التخريبي لقوى التوقف للدبابة التي تمت درستها هو 2.375مرة بقدر التأثير التخريبي لوزن الدبابة و إن التأثير التخريبي لمناورة الدوران للدبابة التي تمت درستها هو 1.216 مرة بقدر التأثير التخريبي لوزن الدبابة إضافة إلى التأثيرات التخريبية الأخرى على الخواص الوظيفية لطبقة الإسفلت السطحية.

**الكلمات الرئيسية: دبابات, آشتو, معاملات مكافئة, قوى الاحتكاك, مناورة الدوران, التبليط المرن, و التأثير التخريبي.**

## - INTRODUCTION

**- Static Analysis**

Road projects are considered the most important and expensive part of the civil infrastructure and the progress backbone of any nation's economy all over the world. The planning, design, construction, and maintenance of roads attracted and attracting more importance. The effect of the traffic using these roads should be focused upon carefully from the standpoint of pavement structural design. Yoder and Witczak (1975) reported that this effect includes among other considerations, the expected vehicle type and the corresponding number of repetitions of each type during the design life of the pavement. The effect of various types of vehicles (and axles distribution) on the structural design of road pavement is considered by means of the approach of axle load equivalency factor. In this approach, a standard axle load is usually used as a reference and the damaging effect of all other axle loads (corresponding to various types of axles) is expressed in terms of number of repetitions of the standard axle.

The AASHTO standard axle is the 18 kips (80 kN) single axle with dual tires on each side (2). Thus, the AASHTO equivalency factor defines the number of repetitions of the 18 kips (80 kN) standard axle load which causes the same damage on pavement as caused by one pass of the axle in question moving on the same pavement under the same conditions.

The AASHTO equivalency factor depends on the axle type (single, tandem, or triple), axle load magnitude, structural number (SN), and the terminal level of serviceability (pt). The effect of structural number (SN) and the terminal level of serviceability (pt) are rather small; however, the effect of axle type and load magnitude is pronounced (Razouki and Hussain, 1985).

There are types of vehicle loads that not included in the AASHTO road test such as the heavy military tanks that move on paved roads occasionally during peace times and frequently during war times. **The effect of these tank loads on flexible pavements is not known, and not mentioned in the literature up to the capacity of the author's knowledge**. Therefore, this research was carried out to find the equivalency factors based on AASHTO method and the damaging effect of T family of military tanks. There are two main approaches used by researchers to determine the equivalency factors, the experimental and the mechanistic (theoretical) approach. A combination of two approaches was also used by Wang and Anderson (1979). In the mechanistic approach, some researchers adopted the fatigue concept analysis for determining the destructive effect (Havens, 1979), while others adopted the equivalent single wheel load procedure for such purposes (Kamaludeen, 1987). The mechanistic empirical approach is used in this research depending on fatigue concept.

Following Yoder and Witczak (1975), the equivalent wheel load factor defines the damage per pass caused to a specific pavement by the vehicle in question relative to the damage per pass of an arbitrarily selected standard vehicle moving on the same pavement system:

$$\mathbf{EWLF = F_j = \left(\frac{d_j}{d_s}\right) = \left(\frac{N_{fs}}{N_{fj}}\right)} \qquad \mathbf{(1)}$$

where, **EWLF** = $\mathbf{F_j}$ = equivalent wheel load factor, $\mathbf{d_j}$ = (1/ $\mathbf{N_{fj}}$), $\mathbf{d_s}$ = (1/ $\mathbf{N_{fs}}$), $\mathbf{d_j}$ & $\mathbf{d_s}$ = damage per pass for the **j**th vehicle and the standard vehicle respectively, and **Nfj** & $\mathbf{N_{fs}}$ = number of repetitions to failure for the **j**th vehicle and the standard vehicle respectively.
AASHTO (1986) design method recommended the use of 18 kips (80 kN) standard axle with dual tires on each side, thus, the AASHTO equivalency factor $\mathbf{F_j}$ becomes:

$$\mathbf{F_j = \left(\frac{d_j}{\phantom{d}}\right) = \left(\frac{N_{18}}{\phantom{N}}\right)} \qquad \mathbf{(2)}$$

$d_s$ $N_{fj}$

where, $N_{18}$ & $N_{fj}$ = number of repetitions to failure for the 18 kips standard single axle and the **j**th axle respectively.

Following Yoder and Witczak (1975) fatigue results of asphalt concrete have shown that the number of repetitions to failure can be related to the tensile strain in the form of:

$$N_f = k_q \left(\frac{1}{\varepsilon_q}\right)^c \tag{3}$$

where, $\varepsilon$ = the maximum principal tensile strain, **k** and **c** represent regression constants, and the subscript **q** is the test or pavement temperature (modulus).
Using this equation, the $F_j$ in equation (2) above for any vehicle can be expressed by:

$$F_j = \left(\frac{\varepsilon_j}{\varepsilon_s}\right)^c \tag{4}$$

Yoder and Witczak (1975) reported that both laboratory tests and field studies have indicated that the constant **c** ranges between 3 and 6 with common values of 4 to 5.

Van Til et. al. (1972) and AASHTO (1986) recommended two fatigue criteria for the determination of AASHTO equivalency factors namely, the tensile strain at the bottom fiber of asphalt concrete and the vertical strain on sub-grade surface. AASHTO (1986) reported a summary of calculations for tensile strain at the bottom fiber of asphalt concrete (as fatigue criterion) due to the application of 18 kips standard axle load on flexible pavement structures similar to that of original AASHTO road test pavements. Also, AASHTO (1986) reported a summary of calculations for vertical compressive strain on sub-grade surface (as rutting criterion) due to the application of 18 kips standard axle load on flexible pavement structures similar to that of original AASHTO road test pavements. The AASHTO (1986) calculated strains are function of the structural number (**SN**), the dynamic modulus of asphalt concrete, the resilient modulus of the base materials, the resilient modulus of roadbed soil, and the thickness of pavement layers. These reported AASHTO (1986) strains which represent ($\varepsilon_s$) in equation (4) above in addition to Van Til et. al. (1972) & Huang (1993) reported experimental values for the constant c in equation (4) above for different pavement structures. Huang (1993) reported that in fatigue analysis, the horizontal minor principal strain is used instead of the overall minor principal strain. This strain is called minor because tensile strain is considered negative. Horizontal principal tensile strain is used because it is the strain that causes the crack to initiate at the bottom of asphalt layer. The horizontal principal tensile strain is determined from:

$$\varepsilon_r = \frac{\varepsilon_x + \varepsilon_y}{2} - \sqrt{\left(\frac{\varepsilon_x - \varepsilon_y}{2}\right)^2 + (\gamma_{xy})^2} \tag{5}$$

where, $\varepsilon_r$ = the horizontal principal tensile strain at the bottom of asphalt layer, $\varepsilon_x$ = the strain in the x direction, $\varepsilon_y$ = the strain in the y direction, $\gamma_{xy}$ = the shear strain on the plane x in the y direction.
Therefore, ($\varepsilon_r$) of equation (5) represents ($\varepsilon_j$) of equation (4) and will be used in fatigue analysis in this research. These two criteria were used in this research to determine the AASHTO equivalency

factors of T family of military tanks. The tensile strains at the bottom fiber of asphalt concrete and vertical compressive strains on sub-grade surface of similar pavement structures to that of AASHTO road test as reported by AASHTO (1986) were calculated under T-72 military tank in this research. Also, a comparison was made between different calculated three-direction strains under T-72 military tank at the surface of flexible pavement and that of AASHTO 18 kips standard axle to study the damaging effect of these tanks on the functional features of the asphalt layer. KENLAYER computer program (DOS version by Huang, 1993) was used to calculate the required strains and stresses in this research at 400 points each time in three dimensions at different locations within AASHTO reported pavement structures under T-72 military tank.

## - Dynamic Analysis

### Moving Load and Braking Forces

AASHTO (1986) equivalency factors are determined based on static vehicle loads. Huang (1993) found in his simplified closed form solution of moving loads on flexible pavement that the effect of moving load on flexible pavement is less than the effect of static load because the maximum value of the moving load is equal to the value of static load at a certain point of time (haversine function).Therefore, the maximum damaging effect of moving load on flexible pavement is less than the damaging effect of the same load in static condition. Garber and Hoel (2002) reported that the maximum braking force (**F**) of a vehicle moving on a level road is equal to the maximum frictional force, which equals to the product of the weight of the vehicle (**W**) times the coefficient of friction (**f** ):

$$\mathbf{F} = \mathbf{W} \times \mathbf{f} \qquad (6)$$

where, **F** = maximum braking force, W= weight of vehicle, and **f** = coefficient of friction. They reported that AASHTO represents the friction coefficient as (**a**/**g**), where **a** = vehicle deceleration and **g** = acceleration of gravity 9.81 m/sec$^2$ (32.2 ft/sec$^2$) to ensure that the pavement will have and maintain the coefficient of friction (**f**).

$$\mathbf{F} = \mathbf{W} \times (\mathbf{a}/\mathbf{g}) \qquad (7)$$

They reported that AASHTO recommended that a comfortable deceleration rate of 3.41 m/sec$^2$ (11.2 ft/sec$^2$) should be used. Also, they reported that many studies have shown that when most drivers need to stop in an emergency the deceleration rate is greater than 4.51 m/sec$^2$ (14.8 ft/sec$^2$). Substituting the value of deceleration rate of 3.41 m/sec$^2$ (11.2 ft/sec$^2$) in equation (7) gives a value of 0.348**W** for the allowed braking force (**F**) by AASHTO. In the same way, a maximum value of braking force can be found to be 0.46**W** for an emergency stop.

Therefore, the maximum damaging effect of a moving vehicle trying to stop equals to the damaging effect of its static vertical weight plus an additional value of a static horizontal force of 0.496**W** at a certain point of time during braking process. These braking forces are tangential stresses in addition to the normal weight of the tank. Poulos and Davis (1974) reported closed form solution for uniform horizontal stresses applied on a circular area placed on two layers pavement structure. This closed form solution will be used in this study to evaluate the damaging effect of tank braking forces on the asphalt pavement in terms of AASHTO equivalency factors as mentioned in section 1 above. For the purpose of the analysis of braking force the modulus of the sub-grade layer will be chosen to be similar to the modulus of the base layer in order to use the two layer pavement structure as mentioned in section 1 above.
**The damaging effect of braking force on the flexible pavement structure is not mentioned in the literature up to the capacity of the authors knowledge**, therefore the damaging effect of

braking force will be studied to determine the value of this damage in comparison with the damage caused by weight only.

**Turning Maneuver of a Tank**

It was noticed that when a tank or any tracked vehicle tries to carry out a turning maneuver tangential stresses are applied to the surface of asphalt pavement. These stresses are generated by the relative movement of one side of the track while the other is not in movement (locked). These stresses are tangential stresses in addition to the normal weight of the tank. These stresses can be simulated by two opposite directions.

Poulos and Davis (1974) presented closed form solution for uniform horizontal stresses applied on a circular area placed on two layers pavement structure. This closed form solution will be used in this study to evaluate the damaging effect of tank turning maneuver on the asphalt pavement as mentioned in section 1 above. For the purpose of the analysis of turning movement the modulus of the sub-grade layer will be chosen to be similar to the modulus of the base layer in order to use the two layer pavement structure as mentioned in section 1 above. **The damaging effect of the tank turning movement on the flexible pavement structure is not mentioned in the literature up to the capacity of the authors,** therefore the damaging effect of turning movement forces will be studied to determine the value of this damage in comparison with the damage caused by tank weight only.

**- CHARACTERISTICS OF T FAMILY OF MILITARY TANKS**

The characteristics of T family of military tanks which required in this research are their three dimensions (height, length, and width) in addition to weight. The width and length of the tank track in contact with the surface of flexible pavement are required, also. These features were obtained from the brochure of the manufacturing company (Uralvagonzavod, 2009) and the website (Fas, 2009). The width and the length of the track in contact with the surface of asphalt pavement were measured from the available tank markings on the surface of asphalt concrete pavements at different locations. Figure (1) and Figure (2) were prepared to show the obtained characteristics of T family of military tanks. The combat weight of this tank of 41 tons was taken for the purpose of analysis as the gross tank load (Fas, 2009).

**Figure (1): T-72 military tank (Uralvagonzavod, 2009).**

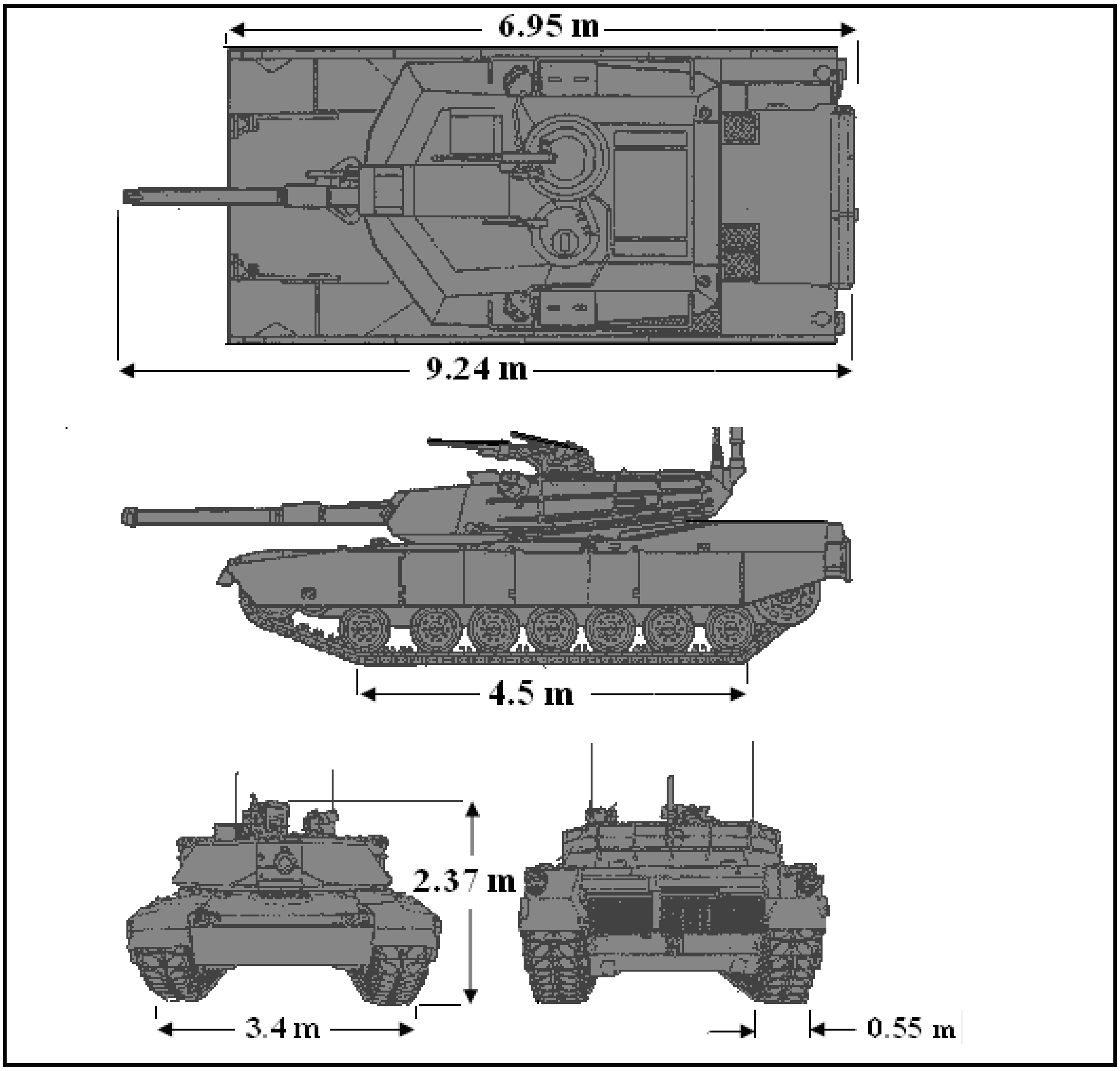


**Figure (2): Dimensions of T-72 military tank (Fas, 2009).**

## - ANALYSIS METHODOLOGY

### <u>The simulation of T-72 military tank loads</u>

T-72 military tank was used to represent T family of military tanks (main combat tank (Fas, 2009)) that is widely used. The length of the track of the tank that in direct contact with the ground was taken as 4.50 m as shown in Figure (2) above.

This length value was obtained from the brochure of the manufacturing company (Uralvagonzavod, 2009) and the website (Fas, 2009) in addition to that this width value was found to be almost equal to that measured from markings left on the surface of asphalt layer at different locations. The value for the width of the track of 0.55 m was taken in the analysis.

The simulation of tank loads in this analysis was taken as shown in Figure (3) which represents the (0.55 m x 4.50 m) track on each side of the tank. This track area was simulated by 9 circular areas on each side of the tank with a radius of (0.240 m) each to take the maximum contact width of the track into consideration and to keep the same tank load without change.

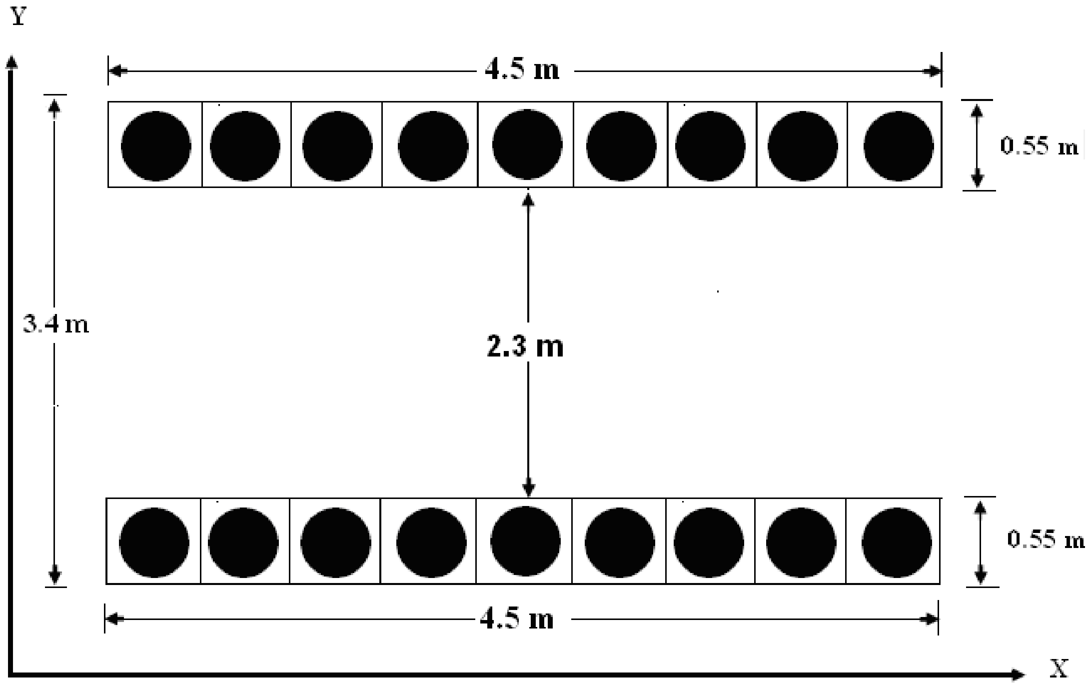


**Figure (3): Simulation of the distribution of tank loads on the surface of flexible pavement for analysis purposes.**

## AASHTO equivalency factors of T-72 military tank loads

Three-layer pavement structure was taken as mentioned in the introduction above to simulate AASHTO original road test pavements as shown in Figure (4).

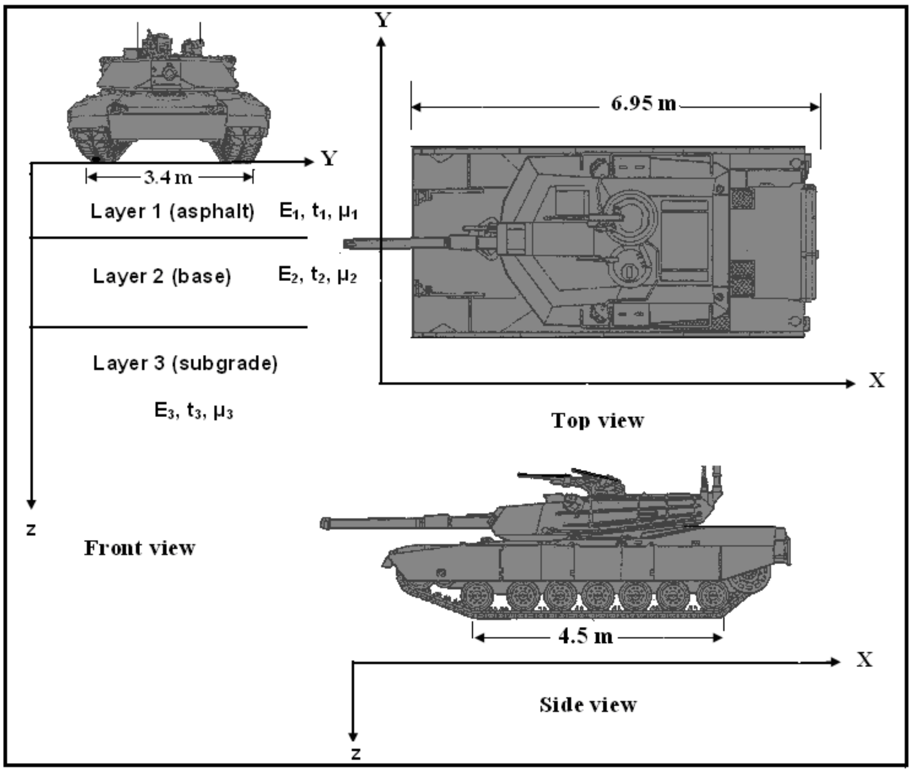


**Figure (4): The layout of the tank on the pavement for analysis purposes.**

Only one set of values for the modulus of asphalt layer ($E_{1}$=1035.5 MPa), the base layer ($E_{2}$=103.5 MPa), and the sub-grade modulus ($E_{3}$=51.7 MPa) was taken from the original AASHTO road test because it is similar to the modulus values of local materials in practice (Kamaludeen, 1987). AASHTO Poisson's ratio (**$\mu_1$**) = 0.4 for asphalt layer, (**$\mu_2$**) = 0.35 for base layer, and (**$\mu_3$**) = 0.4 for sub-grade layer were taken for the purpose of this analysis (Yoder and Witczak, 1975).

Figure (5), Figure (6), and Figure (7) were prepared to show the calculated tensile strains in the direction of x, y, and r at the bottom fiber of asphalt concrete layer respectively under the T-72 military tank. These calculated strains were for the AASHTO pavement structure shown in Figure (4) and for the simulation shown in Figure (3) above for the layout of T-72 tank loads. These strains were obtained for 400 calculating points for each one of these Figures using KENLAYER computer program (DOS version by Huang, 1993). Figure (8) was prepared to show the calculated vertical compressive strains on the surface of sub-grade layer of AASHTO pavement structure shown in Figure (4) under T-72 military tank. These strains were obtained for 400 calculating points using KENLAYER computer program (DOS version by Huang, 1993). It was found that the calculated vertical compressive strains on the surface of sub-grade layer under T-72 military tank are much more conservative than calculated tensile strains in the direction of x, y, and r at the bottom fiber of asphalt concrete layer in comparison with their similar type of strains reported by AASHTO (1986), as shown in Figure (5) to Figure (8). Therefore, the rutting criterion governed and was used to calculate the AASHTO equivalency factors of T-72 military tank.

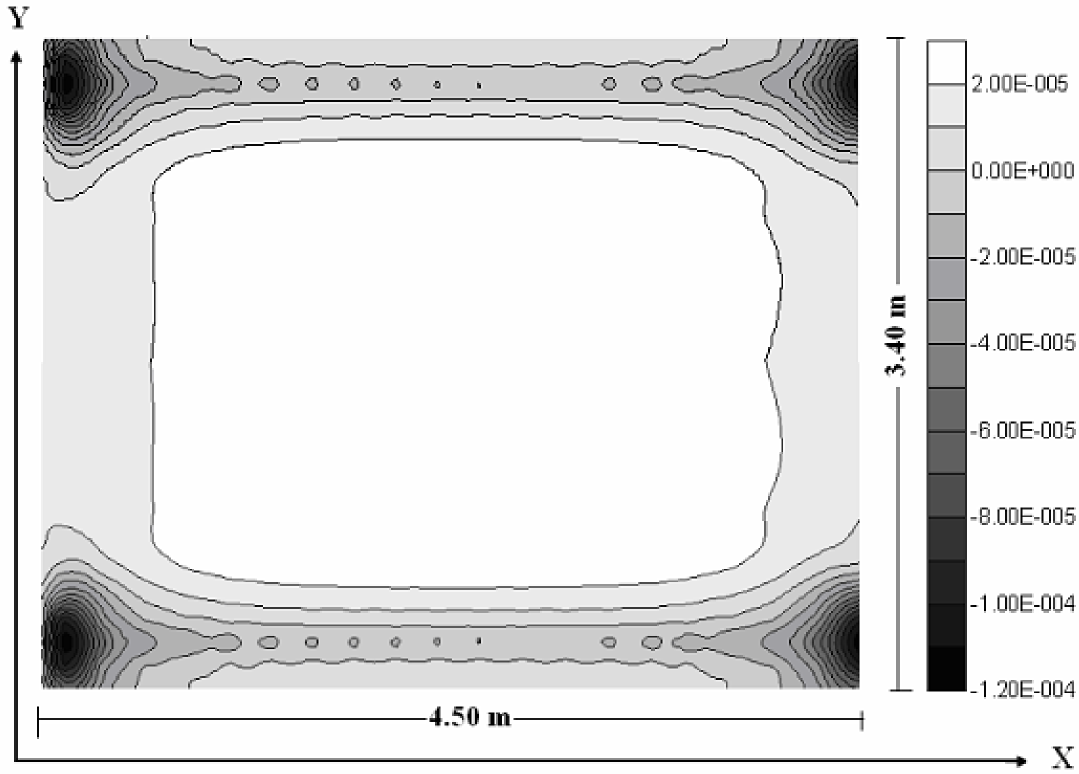


**Figure (5): Tensile strain in the x direction ($\varepsilon_x$) at the bottom fiber of asphalt layer ($t_1$=7.6 cm and $t_2$=56.6 cm).**

The maximum calculated vertical compressive strains on the surface of sub-grade layer under T-72 military tank for the AASHTO (1986) pavement structures are summarized in Table (1). The AASHTO (1986) reported maximum vertical compressive strains on the surface of sub-grade layer for the AASHTO pavement structures under the standard 18 kips (80 kN) are shown also in Table (1). The values for the constant c of equation (4) for each one of AASHTO (1986) pavement structures were obtained from Van Til et. al. (1972). The AASHTO equivalency factors of T-72 military tank were calculated using equation (4) are shown in Table (1).

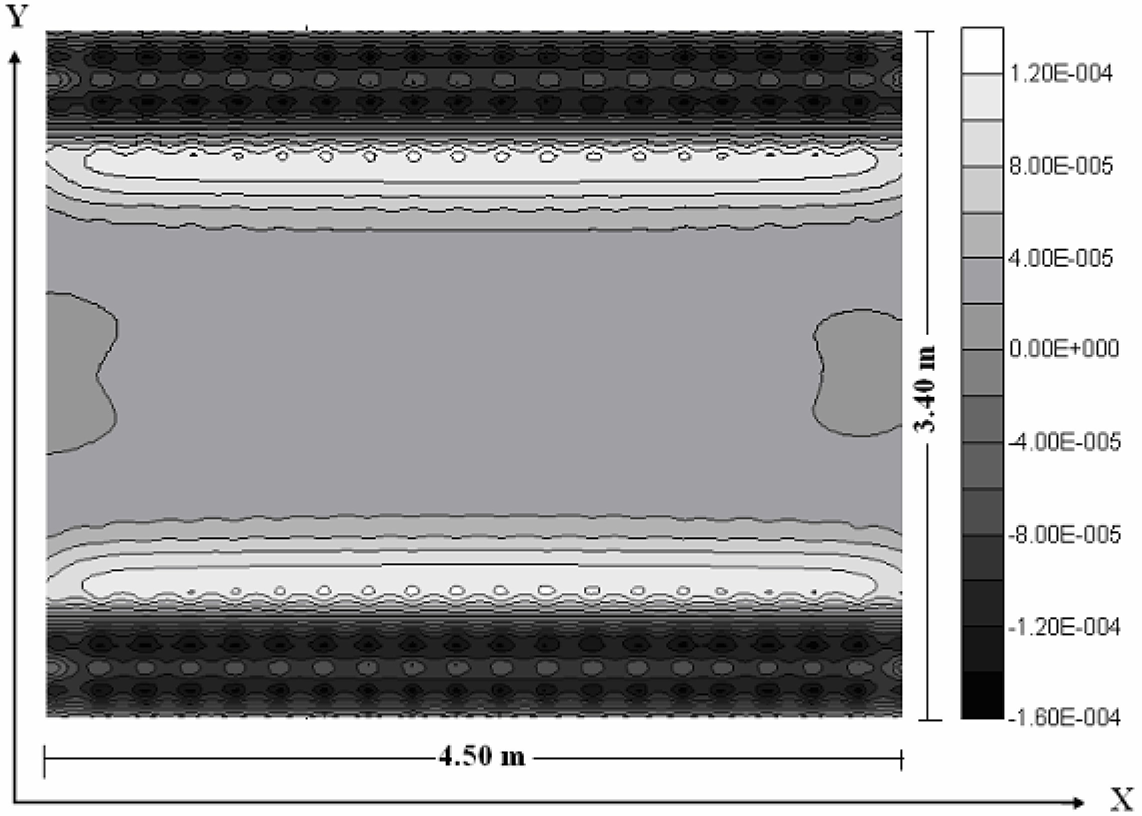


**Figure (6): Tensile strain in the y direction $(\varepsilon_y)$ at the bottom fiber of asphalt layer ($t_1$=7.6 cm and $t_2$=56.6 cm).**

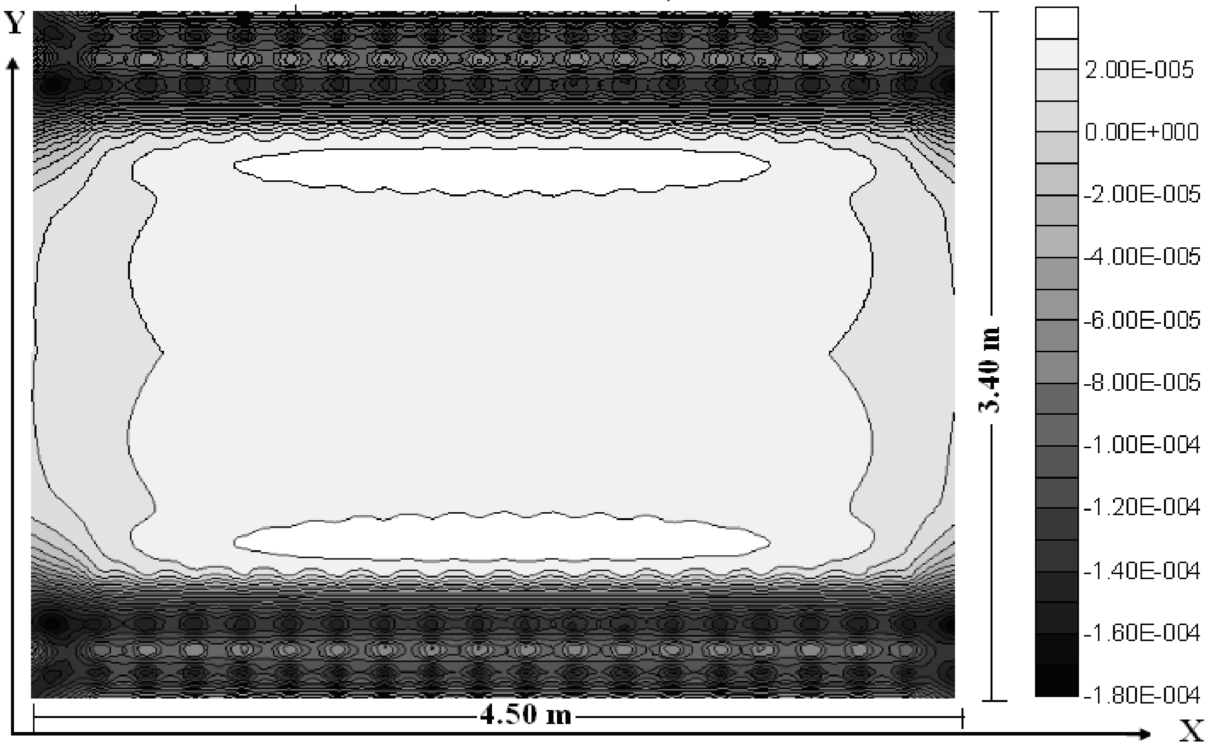


**Figure (7): Horizontal principal tensile strain at the bottom of asphalt layer $(\varepsilon_r)$ ($t_1$=7.6 cm and $t_2$=56.6 cm).**

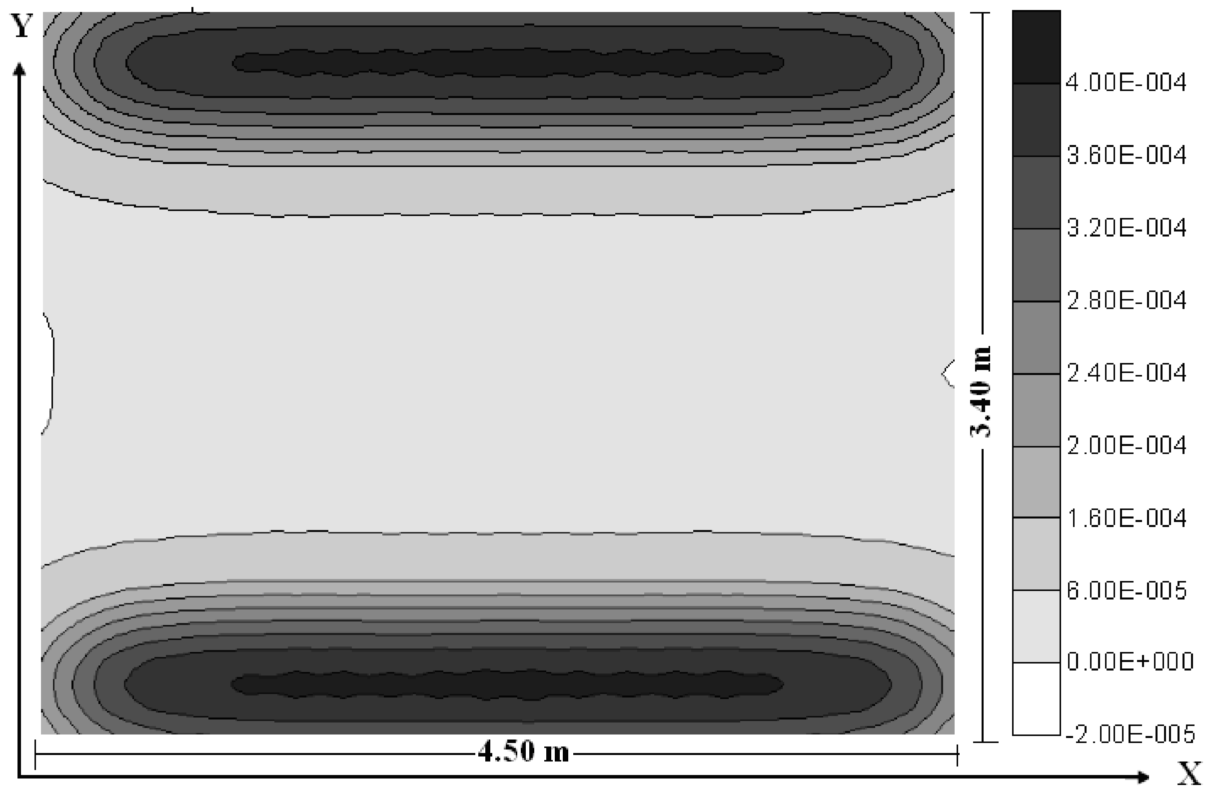


**Figure (8): Vertical strain in the z direction ($\varepsilon_z$) on the surface of sub-grade layer ($t_1$=7.6 cm and $t_2$=56.6 cm).**

**Table (1): AASHTO equivalency factors of T-72 tank using rutting criterion and for tank load simulation (Figure (3)).**

| **Modulus Layer 1 = 1035.5 MPa, $\mu_1$ = 0.40** | | | | | | |
|---|---|---|---|---|---|---|
| **Modulus Layer 2 = 103.5 MPa, $\mu_2$ = 0.35** | | | | | | |
| **Modulus Layer 3 = 51.7 MPa, $\mu_3$ = 0.40** | | | | | | |
| **Thickness Layer 1 cm** | **Thickness Layer 2 cm** | **Source of Data** | **Vertical strain ($\varepsilon_z$) on sub-grade** | **SN** | **c** | **Tank AASHTO Equivalency Factor** |
| **7.62** | **56.64** | **AASHTO**(1) | **0.0004330** | **4** | **3.54** | 0.898 |
| **7.62** | **56.64** | Calculated(2) | 0.0004200 | **4** | **3.54** | 0.898 |
| **10.16** | **47.50** | **AASHTO**(1) | **0.0005280** | **4** | **3.43** | 0.600 |
| **10.16** | **47.50** | Calculated(2) | 0.0004550 | **4** | **3.43** | 0.600 |
| **12.70** | **59.18** | **AASHTO**(1) | **0.0003420** | **5** | **3.43** | 1.397 |
| **12.70** | **59.18** | Calculated(2) | 0.0003770 | **5** | **3.43** | 1.397 |
| **15.24** | **50.04** | **AASHTO**(1) | **0.0003740** | **5** | **3.43** | 1.280 |
| **15.24** | **50.04** | Calculated(2) | 0.0004020 | **5** | **3.43** | 1.280 |
| **20.32** | **52.58** | **AASHTO**(1) | **0.0002940** | **6** | **4.29** | 2.356 |
| **20.32** | **52.58** | Calculated(2) | 0.0003590 | **6** | **4.29** | 2.356 |

**(1) AASHTO (1986) maximum vertical strain ($\varepsilon_z$) on the sub-grade surface under the standard 18 kips (80 kN) axle load for terminal of serviceability (Pt) of 2.0.**
**(2) Calculated maximum vertical strain ($\varepsilon_z$) on the sub-grade surface under the T-72 military tank for simulated layout of tank loads as shown in Figure (3) above.**

**Damaging Effect of Braking Forces**

It was mentioned in section 1-2-1 above that closed form solution of uniformly distributed horizontal load on a circular area on the two layers pavement structure [10] will be used to study the effect of braking force of the tank on asphalt pavement structure. Figure (9) was prepared to simulate the distribution of tank braking force on pavement structure. Three-layer pavement structure was taken as mentioned in the introduction above to simulate AASHTO original road test pavements as shown in Figure (4).

Only one set of values for the modulus of asphalt layer ($\mathbf{E_1}$=1035.5 MPa), the base layer ($\mathbf{E_2}$=103.5 MPa), and the sub-grade modulus ($\mathbf{E_3}$=103.5 MPa) was taken from the original AASHTO road test because it is similar to the modulus values of local materials in practice (Kamaludeen, 1987) and allows the use of two layers closed form solution because $E_2 = E_3$. AASHTO Poisson's ratio of 0.5 was taken for asphalt layer, base layer, and for sub-grade layer for the purpose of this analysis (the effect of Poisson's ratio is very small on analysis results, Huang, 1993).

Figure (10) was prepared to show the horizontal principal tensile ($\boldsymbol{\varepsilon_r}$) under the tank due to horizontal braking forces combined with tank weight. Figure (11) was prepared to show the maximum vertical strain ($\varepsilon_v$) under the tank due to horizontal braking forces combined with tank weight. Table (2) was prepared to the results of braking force analysis.

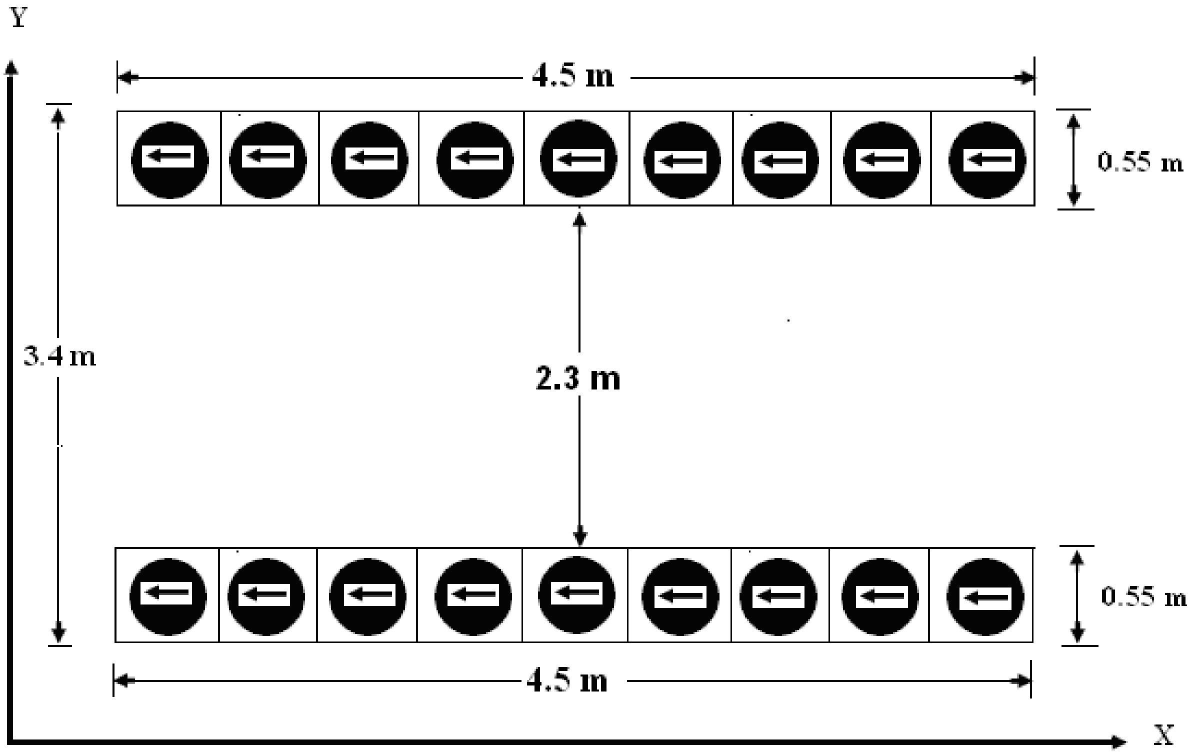


**Figure (9): Simulation of tank braking forces distribution for analysis purposes.**

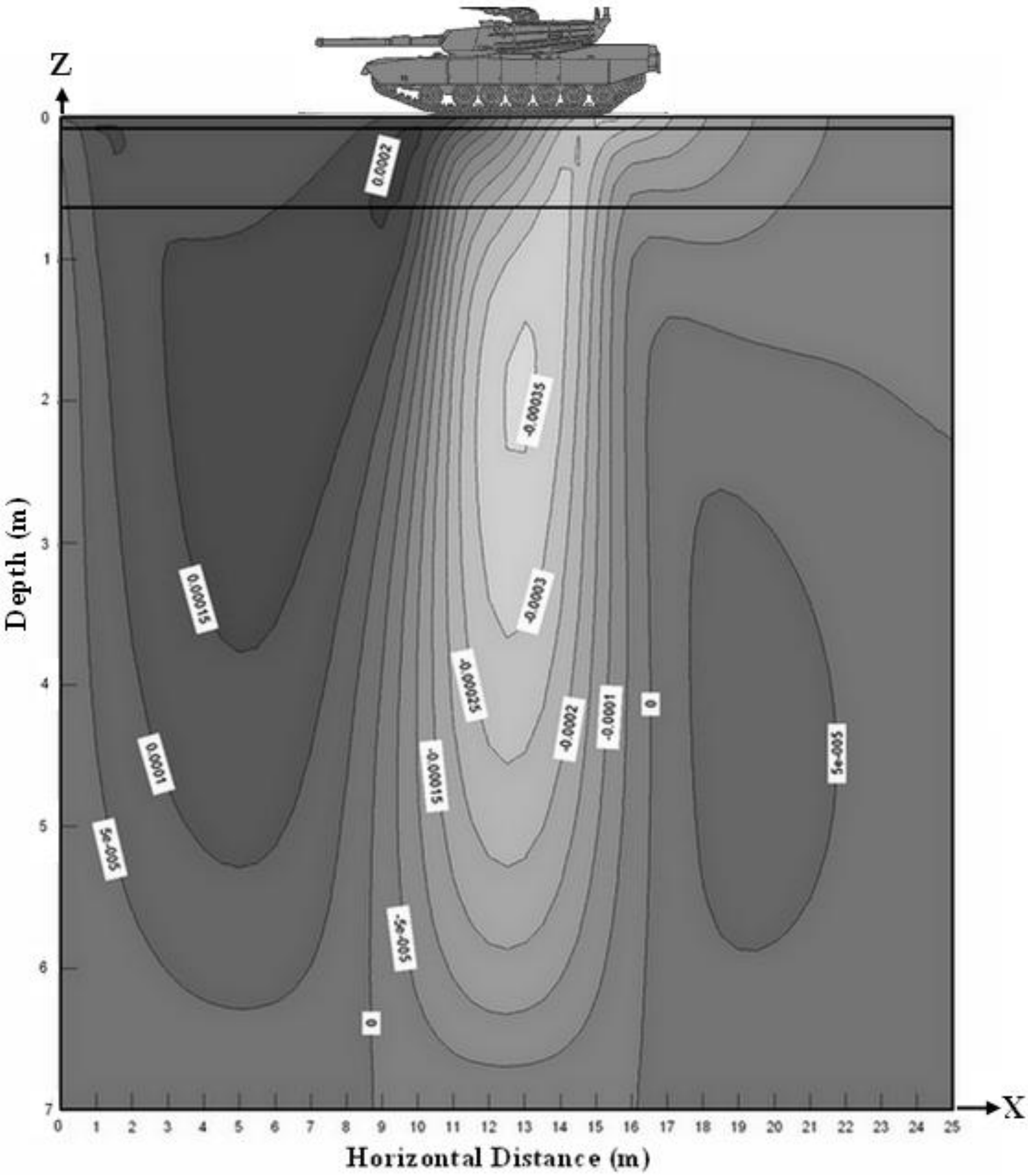


**Figure (10): Horizontal principal tensile strain ($\varepsilon_r$) due to braking force combined with tank weight as shown in figure (9),($t_1$=7.6 cm and $t_2$=56.6 cm).**

**Damaging Effect of Tank Turning Maneuver**

It was mentioned in section 1-2-1 above that closed form solution of uniformly distributed horizontal load on a circular area on the two layers pavement structure [10] will be used to study the effect of tank turning maneuver on asphalt pavement structure. Figure (12) was prepared to simulate the distribution of tank turning maneuver force on pavement structure. Three-layer pavement structure was taken as mentioned in the introduction above to simulate AASHTO original road test pavements as shown in Figure (4).

**Table (2): Effect of tank braking force.**

| Type of Tank Load | Max Horizontal Strain $(\varepsilon_r)$ | Max Vertical Strain $(\varepsilon_v)$ |
|---|---|---|
| **weight only** | 0.0000940 | 0.0002898 |
| **weight +Braking** | 0.0003000 | 0.0003379 |
| **Braking only** | 0.0002233 | 0.0001243 |

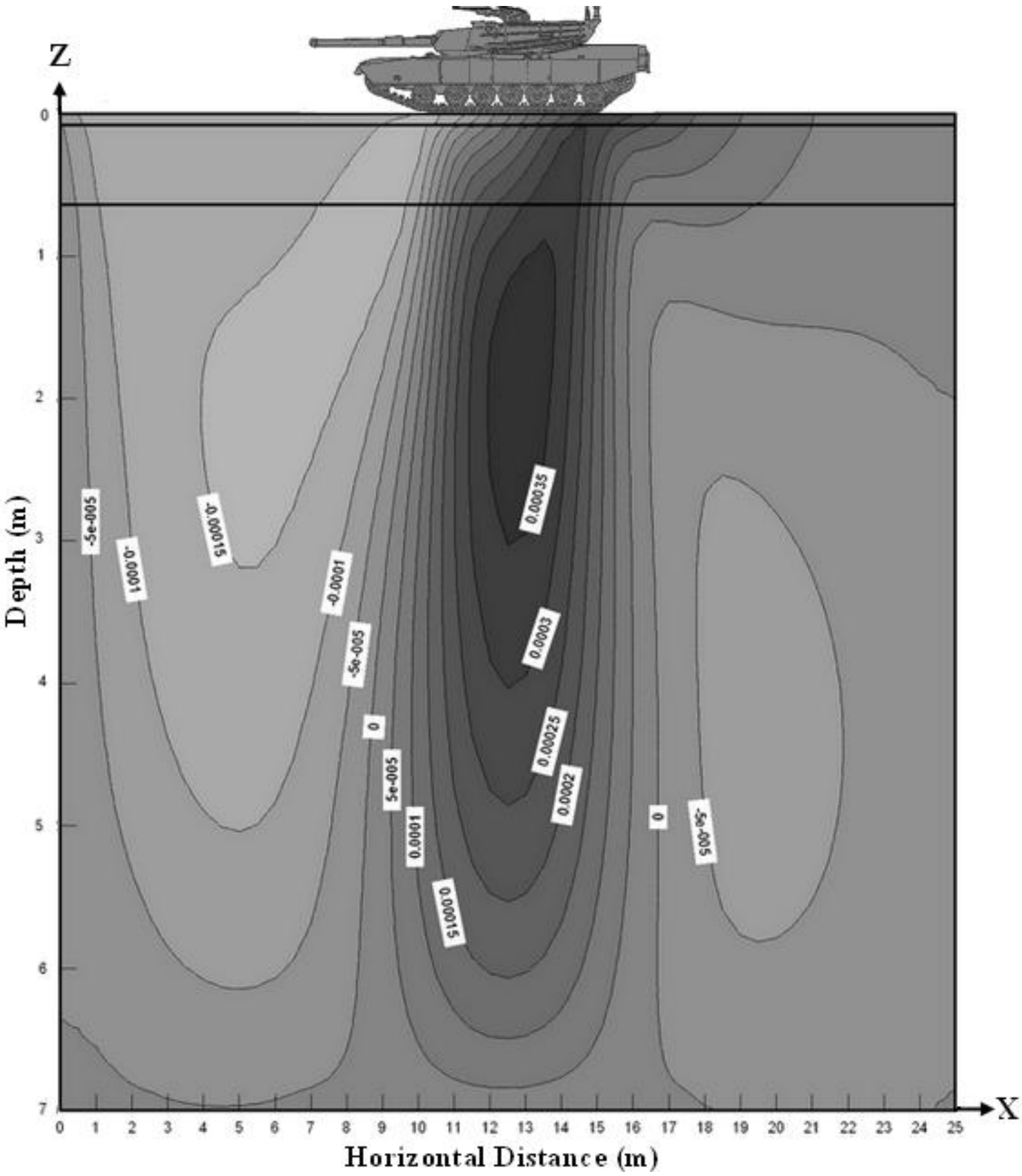


**Figure (11): Vertical strain $(\varepsilon_v)$ due to braking force combined with tank weight as shown in figure (9), ($t_1$=7.6 cm and $t_2$=56.6 cm).**

**<u>Damaging Effect of Tank Turning Maneuver</u>**

It was mentioned in section 1-2-1 above that closed form solution of uniformly distributed horizontal load on a circular area on the two layers pavement structure [10] will be used to study the effect of tank turning maneuver on asphalt pavement structure. Figure (12) was prepared to simulate the distribution of tank turning maneuver force on pavement structure. Three-layer pavement structure was taken as mentioned in the introduction above to simulate AASHTO original road test pavements as shown in Figure (4). Only one set of values for the modulus of asphalt layer (**$E_1$**=1035.5 MPa), the base layer (**$E_2$**=103.5 MPa), and the sub-grade modulus (**$E_3$**=103.5 MPa) was taken from the original AASHTO road test because it is similar to the modulus values of local materials in practice (Kamaludeen, 1987) and allow the use of two layers closed form solution because **$E_2$** = **$E_3$**. AASHTO Poisson's ratio of 0.5 was taken for asphalt layer, base layer, and for sub-grade layer for the purpose of this analysis (the effect of Poisson's ratio is very small on analysis results, Huang (1993)). Table (3) was prepared to show the results of the damaging effect of the tank turning movement.

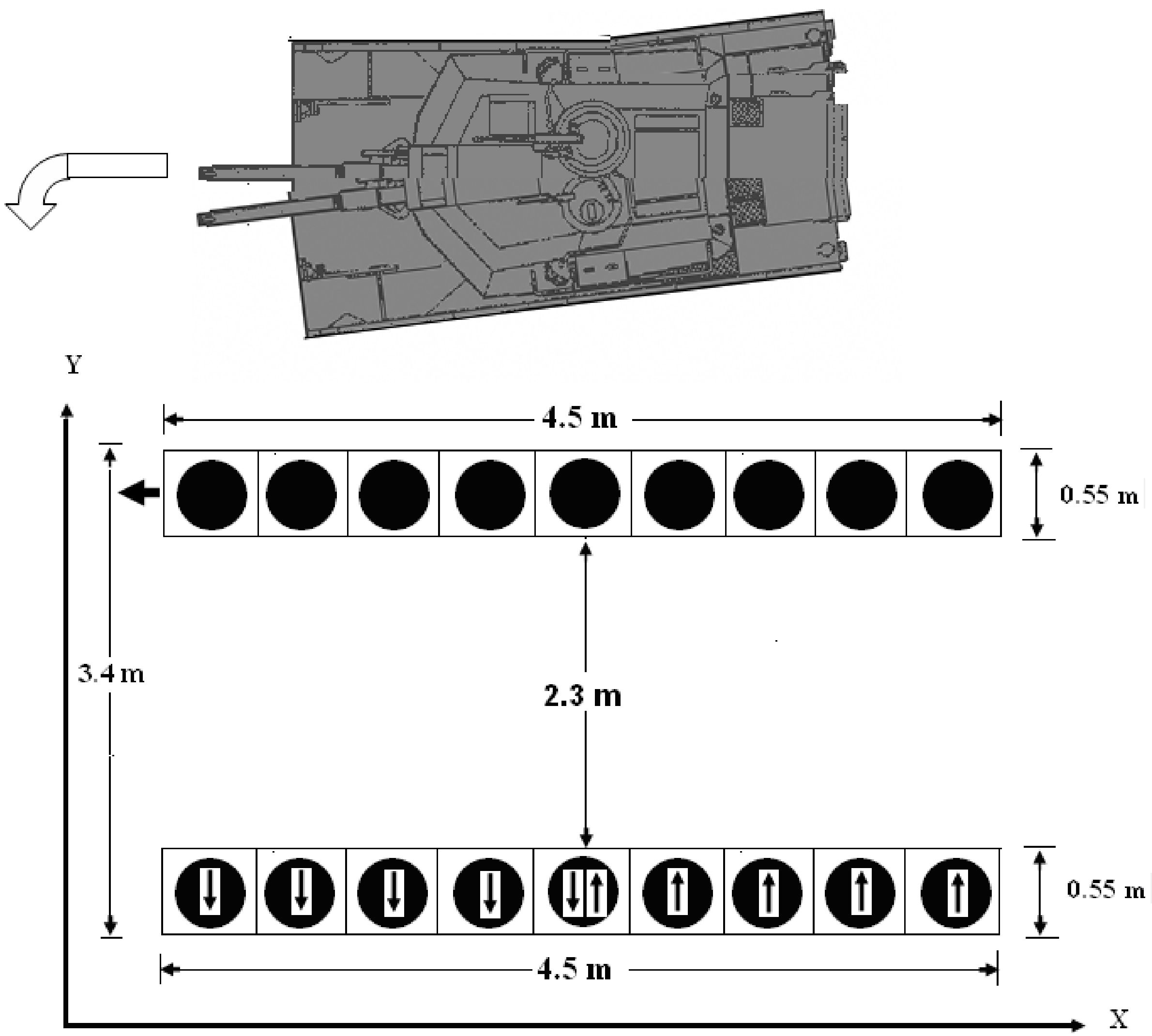


**Figure (12): Simulation of tank turning maneuver loads distribution for analysis purposes.**

**Table (3): Effect of tank turning maneuver forces**

| Type of Tank Load | Max Horizontal Strain ($\varepsilon_r$) | Max Vertical Strain ($\varepsilon_v$) |
|---|---|---|
| **weight only** | 0.00002996 | 0.00009719 |
| **weight +Turning** | 0.00004142 | 0.00009906 |
| **Turning only** | 0.00003643 | 0.00001636 |

## - COMPARISON OF T-72 TANK LOADS WITH OTHER MILITARY TANKS

In order to compare the damaging effect of T-72 military tank loads with other types of military tanks in the world, two families of tanks were considered. The first was the American family of Abrams M1 military tanks and the British family of Challenger military tanks. The most important features of the military tanks that affect on the magnitude of the AASHTO equivalency factors of any tank are the weight of the tank and the area of contact with the surface of pavement, in other words, the contact pressure. Table (4) was prepared to compare the weight, contact area of one side of tank track, and the contact pressure of different types of military tanks around the world (Fas, 2009). The contact pressure of T-72 military tank is the lowest and the damaging effect of its loads is the lowest too.

**Table (4): Comparison between features of different tanks (Fas, 2009).**

| Tank Property | Type of Tank | | | | |
|---|---|---|---|---|---|
| | Abrams M1A1 | Challenger 1 | Challenger 2 | T-72 | T-90 |
| **Track Length In contact** (m) | 5.35 | 6.13 | 5.20 | 4.5 | 4.3 |
| **Track Width In contact** (m) | 0.61 | 0.61 | 0.61 | 0.55 | 0.55 |
| **Combat Weight** (ton) | 69 | 62.5 | 62.5 | 41 | 46 |
| **Contact Pressure** (MPa) | 0.104 | 0.082 | 0.097 | 0.081 | 0.095 |

## - DISCUSSION OF RESULTS AND CONCLUSION

It was found that T-72 military tank has a pronounced damaging effect on flexible pavements in terms of AASHTO equivalency factors. The AASHTO equivalency factors of T-72 military tank were found to be from 0.83 to 2.36 based on rutting criterion. Increasing the thickness of the asphalt layer pavement increases the AASHTO equivalency factors of T-72 military tank. This means that the structural damaging effect of T-72 military tank on flexible pavements of major highways and main principal roads is much more than its damaging effect on the flexible pavement of local and secondary roads.

It was found that the damaging effect of tank braking forces is 2.375 times the damaging effect of tank weight only in terms of tensile stain (fatigue cracking) as shown in table (2). It was found that the damaging effect of tank turning maneuver forces is 1.216 times the damaging effect of tank weight only in terms of tensile stain (fatigue cracking) as shown in table (3).It was found also, that T-72 military tank has a severe damaging effect on the functional serviceability of surface of asphalt layer in terms of deformation and strains due to the effect of metal track.

## - RECOMMENDATIONS

- 1-Based on the results of this study, an economic evaluation for the cost of damage that had been caused by the frequent movement of T family of military tanks on the national road network is required.

- 2-Another study is necessary to determine the damaging effect of military tanks on the national road network during summer seasons.

## - REFERENCES


- AASHTO, " AASHTO guide for the design pavement structures 1986", The American Association of State Highway and Transportation Officials, Washington D.C., 1986.

- Fas, Military Analysis Network, www.fas.org., Feb. 3rd, 2009.

- Garber, N. J., and Hoel, L. A. " Traffic & Highway Engineering", Int. Student Ed., Thomson Corporation, United States, 2002.

- Havens, J. H., Southgate, H.F., and Deen, R, C, "Fatigue damage to flexible pavements under heavy loads", TRB record 725, 1979.

- Huang, Yang H., "Pavement analysis and design", 1st. edition, Prentice Hall, Inc., New Jersey, USA, 1993.

- Kamaludeen, N. M., "Damaging effect of triple axle loads on flexible pavements", M.Sc. thesis, College of Engineering, University of Baghdad, Baghdad, 1987.

- Poulos, H. G., and Davis, E. H., "Elastic Solutions for Soil and Rock Mechanics", John Wiley and Sons, Inc., New York, 1974.

- Razouki, S. S., and Hussain, S. F., "Equivalency factors for floating tandem axle loads on flexible pavements", Proceedings, Iraqi Conference on Engineering, ICE 85, College of Engineering, University of Baghdad, vol. 1, Baghdad, 1985.

- Uralvagonzavod Co.,"T-72 brochure", Russian Federation, http://www.army-guide.com, Feb. 3rd, 2009.

- Van Til , C. J., McCullough, B. F., Vallerga, B. A., and Hicks, R. G., "Evaluation of AASHTO interim guides for design of pavement structures", Highway Research Board, NCHRP report 128, Washington D.C., 1972.

- Wang, M.C., and Anderson, R. P., "Load equivalency factors for triaxial loading for flexible pavements", TRB record 725, 1979.

- Yoder, E. J., and Witczak, M. W., "Principles of pavement design ", 2nd edition, John Wiley and Sons, Inc., New York, 1975.

**- SYMBOLS**

**AASHTO:** American Association of State Highway and Transportation Officials**.**
**a : ** Vehicle deceleration**.**
**c : ** Regression constant**.**
**$d_j$ :** Damage per pass for the jth vehicle.
**$d_s$ :** Damage per pass for standard vehicle**.**
**F :** Maximum braking force.
**$E_1$ :** The modulus of asphalt layer**.**
**$E_2$ :** The modulus of base layer.
**$E_3$ :** The modulus of subgrade layer**.**

**$F_j$ :** Factor of equivalent wheel load..
**f :** Coefficient of friction.
**g :** Acceleration of gravity 9.81 m/sec$^2$.
**$k_q$ :** Regression constant.
**$N_{18}$:** Number of repetitions to failure for the 18 kips standard single axle.
**$N_{fj}$ :** Number of repetitions to failure for the jth axle.
**$N_{fs}$ :** Number of repetitions to failure for the jth standard vehicle.
**SN :** Structural number .
**$t_1$ :** Thickness of asphalt layer.
**$t_2$ :** Thickness of base layer.
**$t_3$** : Thickness of subgrade layer.
**Pt :** Terminal of serviceability.
W **:** Weight of vehicle.
**ε :** The maximum principal tensile strain.
**$\varepsilon_j$ :** The strain for the jth vehicle.
**$\varepsilon_r$ :** Maximum horizontal strain.
**$\varepsilon_s$ :** The strain for standard vehicle.
**$\varepsilon_v$** : Maximum vertical strain.
**$\varepsilon_x$ :** The strain in the x direction.
**$\varepsilon_y$ :** The strain in the y direction.
**$\mu_1$ :** Poisson's ratio of asphalt layer.
**$\mu_2$ :** Poisson's ratio of base layer.
**$\mu_3$ :** Poisson's ratio of subgrade layer.
**$\gamma_{xy}$ :** The shear strain on the plane x in the y direction.

Number 3 Volume 16 September 2010 Journal of Engineering

# INVESTIGATION ON THE USE OF MICROPILES FOR SUBSTITUTION OF DEFECTED PILES BY THE FINITE ELEMENT METHOD

Dr. Mohammed Y. Fattah
Assistant Professor, Building and Construction Engineering Department, University of Technology.

Dr. Yousif J. Al –Shakarchi
Professor, Civil Engineering Department, University of Baghdad.

Yasser M. Kadhim
Formerly graduate student, Civil Engineering Department, University of Baghdad.

## ABSTRACT

Micropiles are small diameter, cast in – place or grouted piles with steel pipes of (50 to 300 mm) diameters and driven by boring machine. Despite their small wall thickness, high bearing capacity of micropiles provides both axial and pullout resistance.

This paper is directed to study the behavior of micropiles under static and dynamic loading conditions using the finite element method.

The program OpenSees is used in the analysis, it is open – source program, provides information about the software architecture, access to the source code, and the development process. The program is based on the basic commands, which are written in Tcl (pronounced, "tickle"; tool command language).

A model for groups of laterally loaded pipe piles in sand was adopted to study the effect of defects on their lateral performance. The geometric arrangement consisted of group series of 2, 4 and 6 equally spaced piles. Eight node brick elements are used to model the pile and the surrounding soil.

It was concluded that the deflection of laterally loaded piles decreases when inserting steel micropiles beside the defect pile at two opposite directions. The increase in the group deflection is greater when the defected pile is modeled in the front row.

## تحري عن استعمال الركائز المصغرة كبديل عن الركائز المتضررة بطريقة العناصر المحددة

الخلاصة:

الركائز المصغرة, هي ركائز تكون باقطار صغيرة , اما ان تصب موقعيا او بواسطة ادخال انابيب حديدية بقطر (50-300) ملم ويتم ادخال هذه الانابيب بواسطة آلة ثقب. على الرغم من ان الركائز المصغرة ذات سمك قليل الا ان التحمل العالي للركائز المصغرة يعطي مقاومة للاحمال المحورية ومقاومة لقوى السحب.

ان هذه البحث موجه نحو دراسة تصرف الركائز المصغرة تحت تأثير الاحمال الساكنة والاحمال الديناميكية وباستخدام طريقة التحليل بالعناصر المحددة

تم اعتماد البرنامج (OpenSees) في التحليل, وهو برنامج عام يقوم بتزويد معلومات الكترونية عن المنشأ ويكون خاضعاً لمجموعة قوانين محددة وكذلك يعتمد على طبيعة تطور المعالجة. ان هذا البرنامج يعتمد على اوامر لغة الحاسوب والتي تكتب بلغة (Tcl) و وهي مختصر لما يسمى بلغة ادوات الاوامر (Tool Command Language).

تم تبني دراسة نموذج من مجموعة من الركائز المحملة جانبيا في تربة رملية لغرض دراسة تاثير الخلل في الركائز على فعالية السلوك الجانبي للركائز. الركائز تتألف في هيئتها من مجاميع مكونة من 2, 4 و 6 ركائز موزعة على مسافات متساوية فيما بينها. تم استخدام عناصر محددة طابوقية ذات ثمانية عقد (Eight-node brick elements) لتمثيل الركيزة والتربة التي تحيط بها.

و قد تم التوصل الى ان الانحراف الجانبي لمجموعة الركائز المحملة جانبياً يقل عند غرس ركائز مصغرة بجانب الركيزة المتضررة من اتجاهين متقابلين. ان الزيادة في الانحراف للمجموعة يكون اكبر عندما تكون الركيزة المتضررة ممثلة في السطر الامامي للمجموعة .

## INTRODUCTION

Micropiles are often used to improve the bearing capacity of the foundation against applied loading. In many cases, steel pipes of 50 to 200 mm diameters are used as micropiles. The strengthened ground acts as coherent mass and behaves remarkably well, capable of sustaining high compressive loads at defined settlement or alternatively defined loads at reduced movement. Lizzi (1982) and Plumelle (1984) showed that micropiles create an in-situ coherent composite reinforced soil system and the engineering behavior of micropile-reinforced soil is highly dependent on the group and network effects that influence the overall resistance and shear strength of composite soil- micropile system. Juran et al. (1999) presented a state of art review, covering all the studies and contributions, on the state of practice using micropiles. Considerable information on single micropile design, evaluation of load bearing capacity, movement estimation models as well as effect of group and network effect have been covered in considerable detail. They also reviewed geotechnical design guidelines in different countries for axial, lateral load capacities and approach for movement estimation.

The use of small-diameter piles and micropiles in seismic retrofitting or in new construction in seismic zones requires a thorough analysis of the seismic induced response for groups of flexible piles with inclined elements. As a matter of fact, as the stiffness and resistance of vertical flexible piles to lateral loading is generally small, the use of inclined small-diameter piles presents a potential alternative to withstand inertial forces and to ensure stability of the foundations system under seismic loading.

As reported by Gazetas and Mylonakis (1998), in recent years evidence has been accumulating that inclined piles may, in certain cases, be beneficial rather than detrimental both for the structure they support and the piles themselves. One supporting evidence to this issue was noted during the Kobe earthquake. It was noted that one of the few quay-walls that survived the disaster in Kobe harbor was a composite wall relying on inclined piles, conversely, the near wall, supported on vertical piles, was completely devastated.

## ADVANTAGES OF MICROPILES:

Micropiles are installed by drilling mainly to increase the vertical bearing capacity of the soil. The advantages of micropiles are that high capacity piles would require fewer elements for support than standard H-pile foundations, and the micropiles could also be constructed from underneath an existing super-structure with low headroom constraints. Additionally, as the design progressed, the micropiles could be installed around the utilities in a confined space. Therefore, the pier construction could be completed without interfering with rail traffic and any movement of the existing piers during foundation installation would be minimized by utilizing the micropile foundations, with low noise, and vibration during installation process. It can be used for any type of soil, but with conditions for rock soil, regardless of the kind of soil or the presence of water table; or its accessibility, (Hronek, et al., 2007).

Notably, micropiles require small area of footing when they are utilized as foundation piles, they also promise easy construction of batter and staggered piles. Similar to other conventional piles, micropiles can be used both individually as bearing piles and in groups for soil strengthening. The typical illustration of a high capacity micropile system is presented in Figure (1).

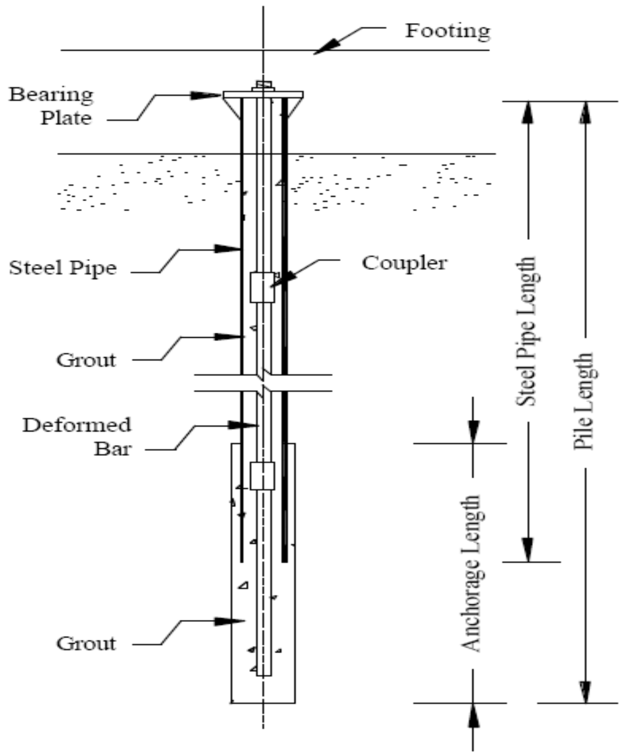


**Figure (1): Details of Micropiles System (Kalkan, 2003).**

## COMPUTER PROGRAM USED:

OpenSees has advanced capabilities for modeling and analyzing the nonlinear response of systems using a wide range of material models, elements, and solution algorithms. The program is designed for parallel computing to allow simulations on high-end computers or for parameter studies. The program interpreter is an extension of the Tcl (pronounced "tickle"). Tcl comes from "Tool Command Language" is a non-typed language, that means an expression can always be seen as a numeric value, a string or another value, conversions are done on-the-fly. All types are implemented as string, even lists are strings with embedded separating spaces) language for use with OpenSees. The Tcl scripting language was chosen to support the OpenSees commands, which are used to define the problem geometry, loading, formulation and solution, (Silvia et al., 2005).

### OpenSees Analysis Capabilities:

Linear equation solvers, time integration schemes, and solution algorithms are the core of the OpenSees computational framework. The components of a solution strategy are interchangeable, allowing analysts to find sets suited to their particular problem. Outlined here are the available solution strategies. New parts of the solution strategy may be seamlessly plugged into the existing framework (Silvia et al., 2005).

## BRICK UP ELEMENT:

It is an 8-node hexahedral linear isoparametric element. Each node has 4 degrees of freedom (DOF): DOFs 1 to 3 for solid displacement (u) and DOF 4 for fluid pressure (p). This element is implemented for simulating dynamic response of solid-fluid fully coupled material, based on Biot's theory of porous medium.

This element is used in this paper to model the pile and the surrounding soil.

## USE OF MICROPILES FOR SUBSTITUTION OF DEFECTED PILES:

A model for groups of laterally loaded hollow pipe piles in sand was made by Ata, and El-Kilany, (2006). Tests were performed to study the effect of anomalies (defects) on their lateral performance. The geometric arrangement consisted of a group series of 2, 4 and 6 equally spaced piles. The defect pile was introduced as 50% necking or reduction in the thickness of the pipe pile at selected depths. It is attempted here that two steel micropiles are inserted in the model surrounding the defect pile in two opposite sides with diameter of (6 mm) in order to study the effect of the micropile on the load-deflection relationship as shown in Table (1). Each geometric series contained only one defective pile and the location of the defective pile was varied within the rows of the group. Each pile consisted of a hollow steel pipe of 16 mm inside diameter, 3 mm wall thickness and a length of 650 mm. Model pile groups of 2, 4 and 6 piles spaced at 3 times the diameter (in both directions) were assembled in place at the center. Pile caps were modeled using 25-mm thick steel plate. The load was applied incrementally by 100 N and up to the maximum total load of 2000 N. All series of pile groups were laterally loaded under similar conditions with no constraint on the pile heads as shown in Figure (2) which shows the finite element mesh for the pile cap while the mesh of elements around the piles is not shown in order to clarify the pile locations. The bottom of the mesh was restrained against horizontal movement in x- and z- directions while the side boundaries of the mesh are restrained against vertical movement in y- direction. In order to prevent concentration of stresses on small zone, the lateral loads were applied on the pile cap as distributed loads within an area of 3D (three pile diameters) as shown in Figure (2).

**Table (1): Cases Due To Presence of Defected Piles with Proposed Micropile.**

| Group Configuration | Depth of Defect ($\alpha L$) | | 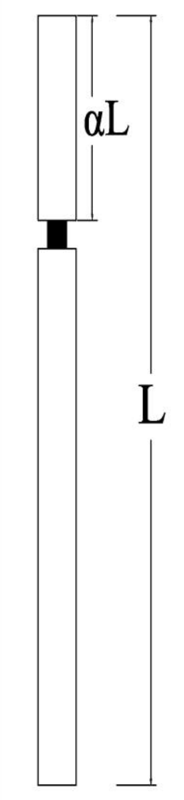 |
|---|---|---|---|
| 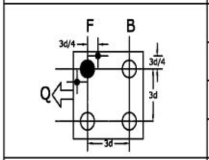 | Case 1 | 0.2L | |
| | Case 2 | 0.3L | |
| | Case 3 | 0.4L | |
| | Case 4 | 0.5L | |
| 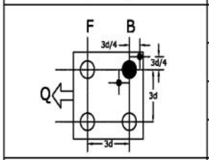 | Case 1 | 0.2L | |
| | Case 2 | 0.3L | |
| | Case 3 | 0.4L | |
| | Case 4 | 0.5L | |
| 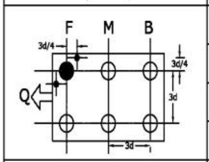 | Case 1 | 0.2L | |
| | Case 2 | 0.3L | |
| | Case 3 | 0.4L | |
| | Case 4 | 0.5L | |
| 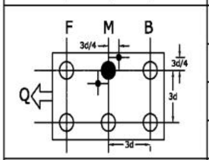 | Case 1 | 0.2L | |
| | Case 2 | 0.3L | |
| | Case 3 | 0.4L | |
| | Case 4 | 0.5L | |
| 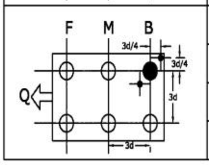 | Case 1 | 0.2L | |
| | Case 2 | 0.3L | |
| | Case 3 | 0.4L | |
| | Case 4 | 0.5L | |

○ non-defective pile.

● defective pile.

The lateral deflection of the group was calculated at the head of the piles. The defected piles were prepared by assuming 50% off the wall thickness of the pipes to model a necking anomaly and extending for a length of 3 mm. The location of the defect was set at four different locations below the pile head represented by a fraction $\alpha$ of the total length L, where the value of $\alpha$ was 0.2, 0.3, 0.4 and 0.5 as shown in Table (1). The properties of the soil – micropile –structure are shown in Tables (2), (3), and (4).

It is intended in this study to model the micropiles that are used as a substitute to the defected piles. The micropiles used have the properties listed in Table (5). The load–deflection curve for this condition will be compared with other cases.

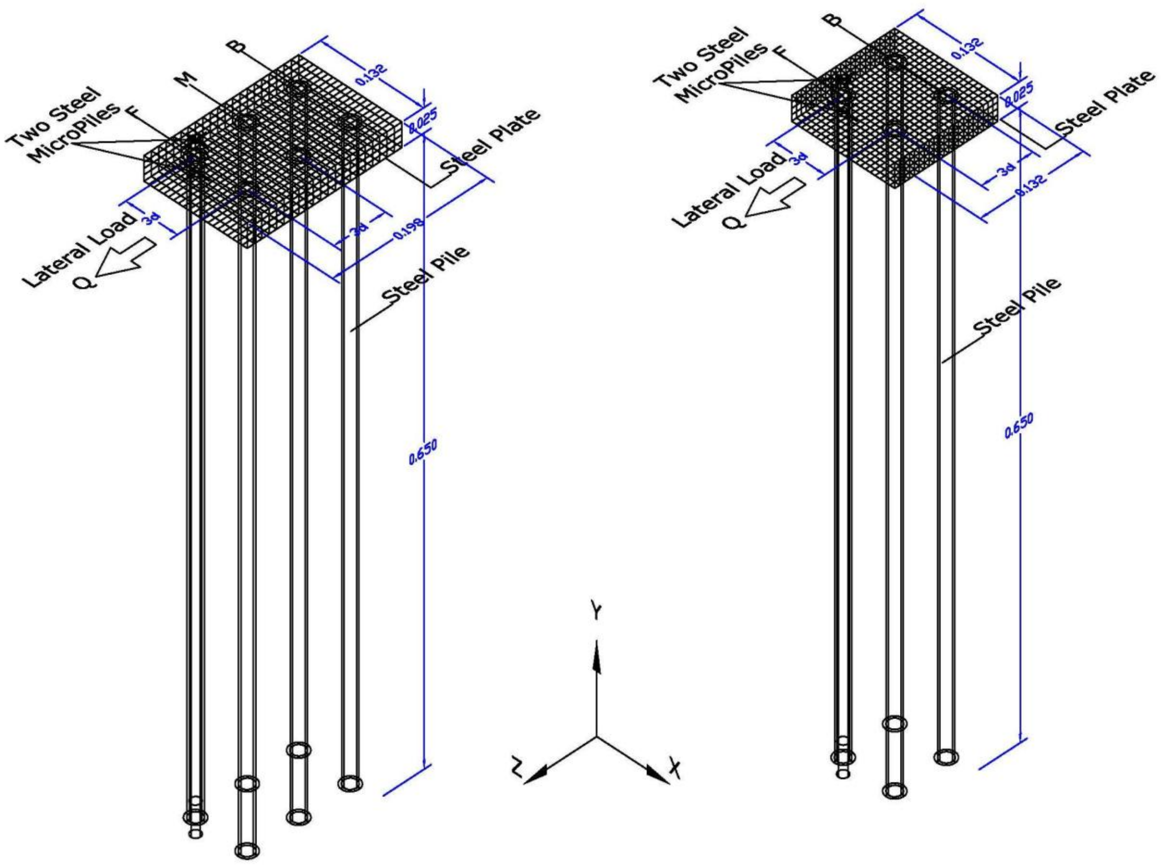


**Figure (2): Finite Element Mesh Used for Modeling 4-Pile Group and 6-Pile Group for Different Cases in the Program OpenSees.**

**Table(2):Properties of the Soil, (Ata, and El-Kilany, 2006).**

| *Type of Soil* | *Unit Weight* $\gamma_t$ *(kN/m$^3$)* | *Modulus of Elasticity E (kPa)* | *Poisson's Ratio* (ν) | *Internal Friction* ϕ (degrees) |
|---|---|---|---|---|
| *Sandy Soil* | *17.20* | *8000* | *0.45* | *39* |

**Table (3): Properties of piles (steel pipe), (Ata, and El-Kilany, 2006).**

| Unit Weight $\gamma_t$ ($kN/m^3$) | | | Modulus of Elasticity E (MPa) | | Poisson's Ratio ($\nu$) | | |
|---|---|---|---|---|---|---|---|
| 78.33 | | | 205000 | | 0.3 | | |
| $A_x$ ($mm^2$) | $I_z$ ($mm^4$) | $I_y$ ($mm^4$) | $I_p$ ($mm^4$) | Outer Diameter (mm) | Inner Diameter (mm) | Wall thickness t(mm) | Length (mm) |
| 179.1 | 8280 | 8280 | 16560 | 22 | 16 | 3 | 650 |

**Table (4): Properties of Pile Cap, (Ata, and El-Kilany, 2006).**

| Type | Unit Weight $\gamma_t$ ($kN/m^3$) | Modulus of Elasticity E (MPa) | Poisson's Ratio($\nu$) |
|---|---|---|---|
| Steel Plate | 78.33 | 205000 | 0.3 |

**Table (5): Properties of Micropiles.**

| Type | Unit Weight $\gamma_t$ ($kN/m^3$) | Modulus of Elasticity E (MPa) | Poisson's Ratio($\nu$) | Outer Diameter (mm) | Wall thickness t(mm) | Length (mm) |
|---|---|---|---|---|---|---|
| Steel Pipe | 78.33 | 205000 | 0.3 | 6 | 0.82 | 650 |

**FOUR-PILE GROUP:**

The results of the total group load versus top deflection for the 4-pile group are presented in Figures (3) through Figure (6). The figures show results of four series of analysis with defects introduced at depths of 0.2L, 0.3L, 0.4L and 0.5L as considered from the top of the piles. For each analysis, three relationships are shown:

a) no defective piles or reference case,
b) one defective pile at back row.
c) one defective pile at front row.
d) one defective pile at back row surrounded by two proposed steel micropiles.
e) one defective pile at front row surrounded by two proposed steel micropiles.

It should be noted that in each group, only one defected pile was modeled either in the back row or the front row. The results show that the deflection of the piles increases when a defect is present in one of the piles. The increase in the group lateral deflection is greater when the defected pile is modeled in the front row. The results also indicate that the deflection of the piles decreases as the depth ratio ($\alpha$L) of the anomaly increases from 0.2L to 0.5L. The results also indicate that the deflection of the piles decreases when inserting the steel micropiles beside the defect pile at two opposite directions as shown in the figures.

Figures (7) and (8) present the variation of the pore water pressure as predicted at top of the pile with the lateral load for different conditions of the piles. It can be noticed that the shape of this relationship is similar to load- deflection relation and the maximum values of pore water pressure are generated at the top of the piles where maximum deflection is expected.

## SIX-PILE GROUP:

Figures (9) through (13) present the results for the 6-pile group model. Six series of model are shown with defects introduced at depths of 0.2L, 0.3L, 0.4L and 0.5L considered from the top of the piles. For each series, four relationships are shown:

a) no defective piles or reference case.
b) one defective pile at back row.
c) one defective pile at middle row .
d) one defective pile at front row.
e) one defective pile at back row surrounded by two proposed steel micropiles.
f) one defective pile at middle row surrounded by two proposed steel micropiles.
g) one defective pile at front row surrounded by two of steel micropiles.

Again, only one defect was modeled in one pile, which was placed alternatively in three rows. The results show that the pile head deflection increases as the defective pile is moved from the back row to the middle row and then to the front row. Similar to the cases of the 4-pile groups, the results indicate that the deflection of the piles decreases as the depth ratio (αL) of the defect increases from 0.2L to 0.5L. The results also indicate that the deflection of the piles decreases when inserting the steel micropile beside the defect pile at two opposite directions as shown in the figures.

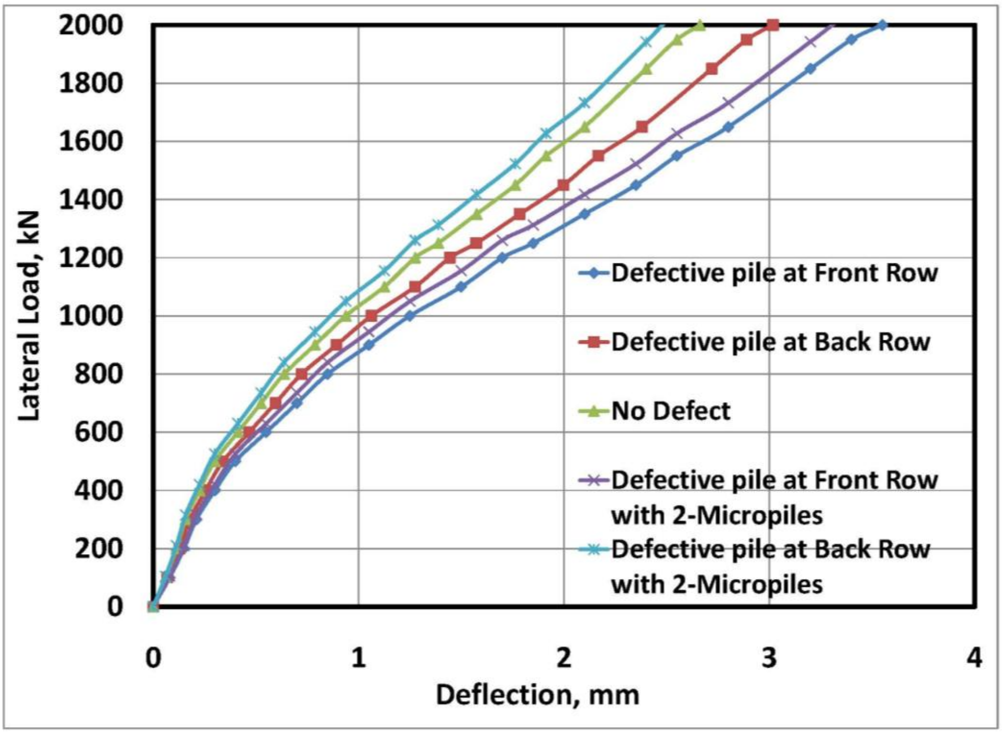


**Figure (3): Load-Deflection Curves for 4-Pile Group with Defect at Depth Ratio (0.2L) Using the Program OpenSees.**

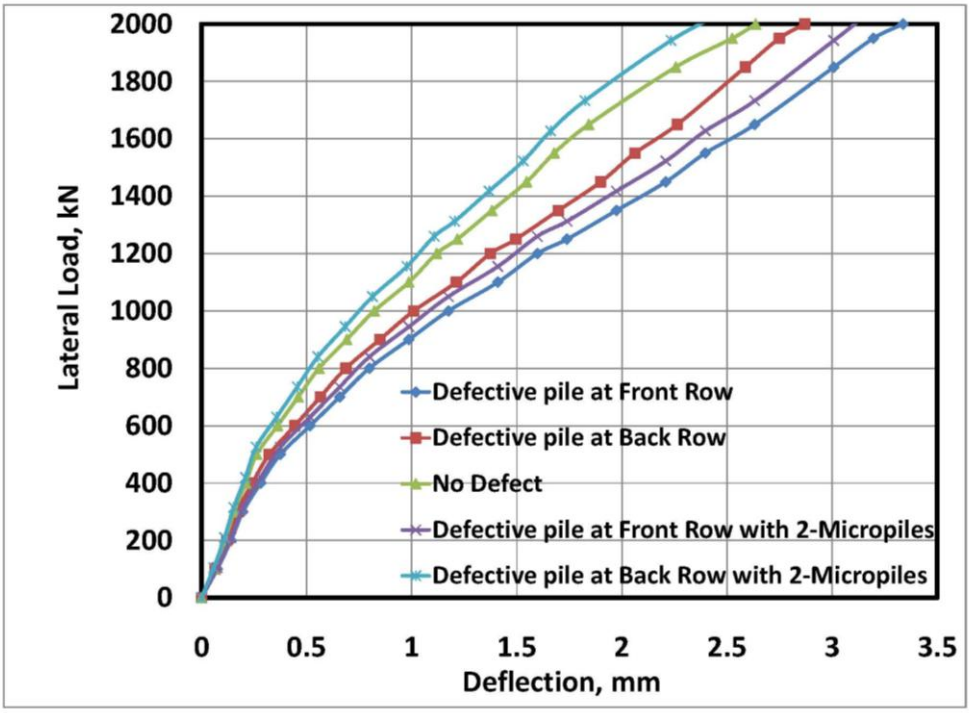


**Figure (4): Load-Deflection Curves for 4-Pile Group with Defect at Depth Ratio (0.3L) Using the Program OpenSees.**

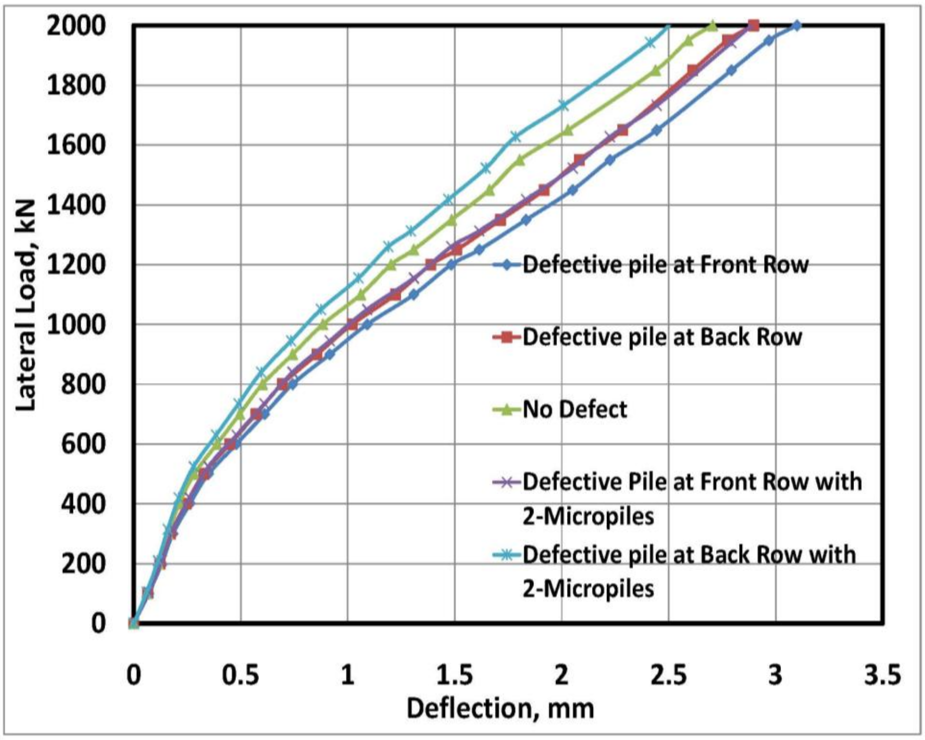


**Figure (5): Load-Deflection Curves for 4-Pile Group with Defect at Depth Ratio (0.4L) Using the Program OpenSees.**

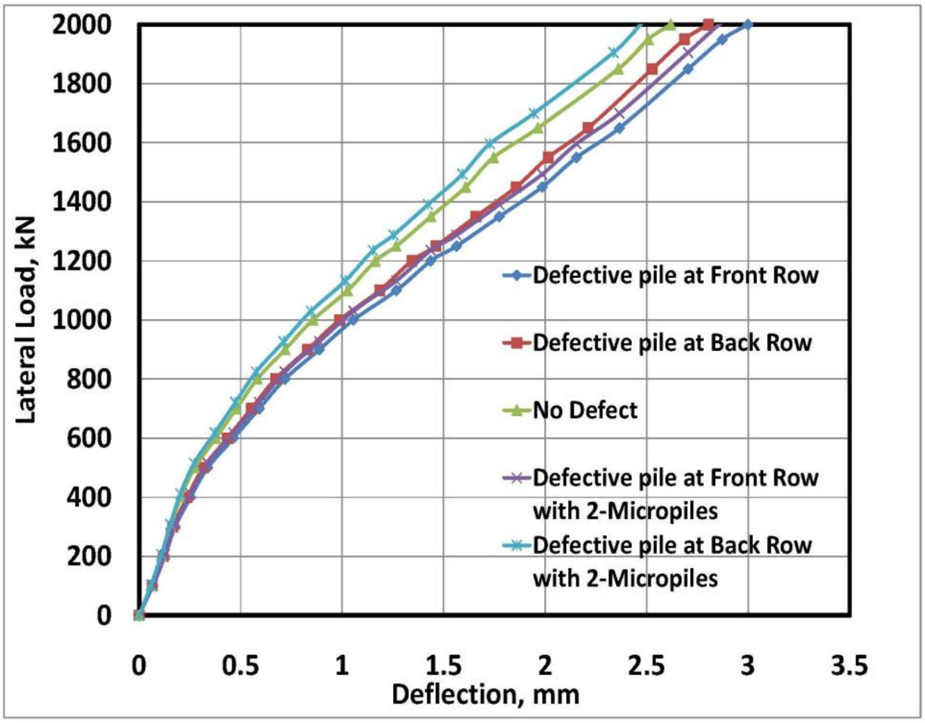


**Figure (6): Load-Deflection Curves for 4-Pile Group with Defect at Depth Ratio (0.5L) Using the Program OpenSees.**

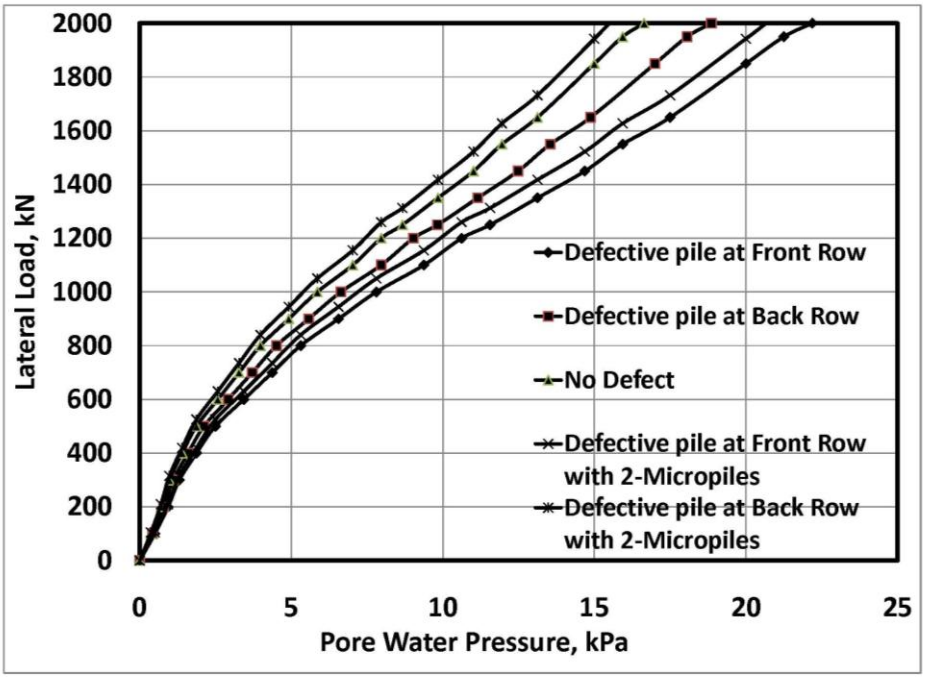


**Figure (7): Max.Variation of Pore Water Pressure with Lateral Load for 4-Pile Group with Defect at Depth Ratio (0.2L) Using the Program OpenSees.**

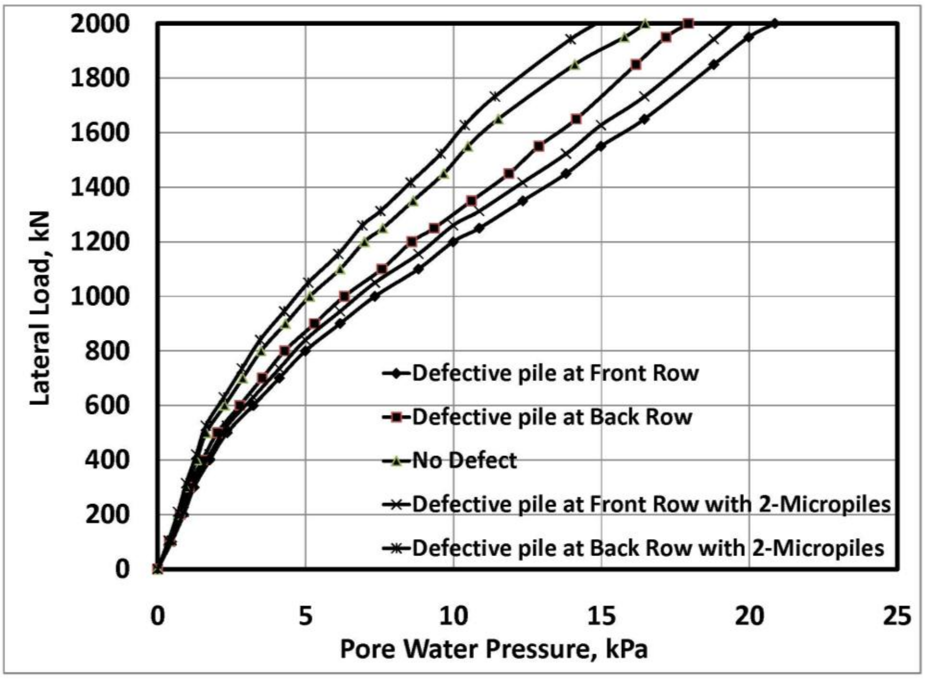


**Figure (8): Max.Variation of Pore Water Pressure with Lateral Load for 4-Pile Group with Defect at Depth Ratio (0.3L) Using the Program OpenSees.**

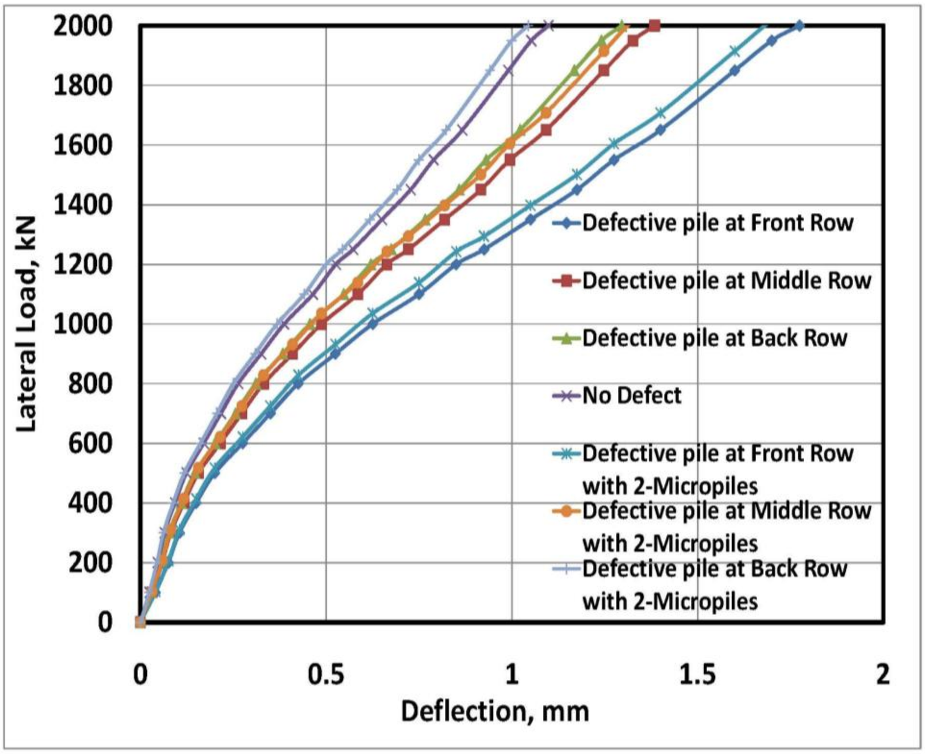


**Figure (9): Load-Deflection Curves for 6-Pile Groupwith Defect at Depth Ratio (0.2L) Using the Program OpenSees.**

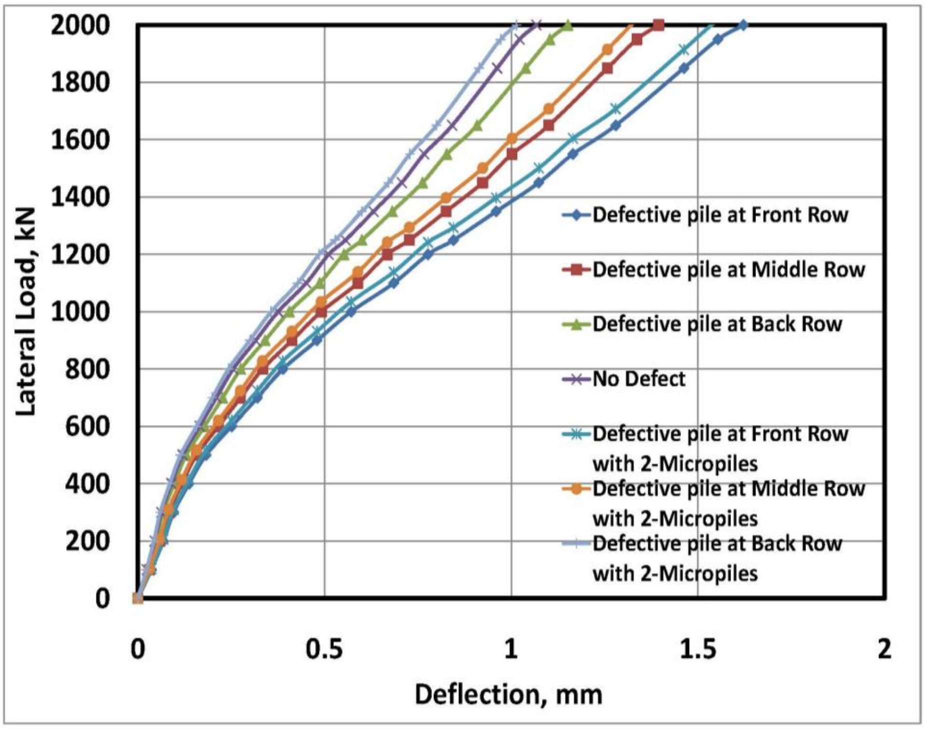


**Figure (10): Load-Deflection Curves for 6-Pile Groupwith Defect at Depth Ratio (0.3L) Using the Program OpenSees.**

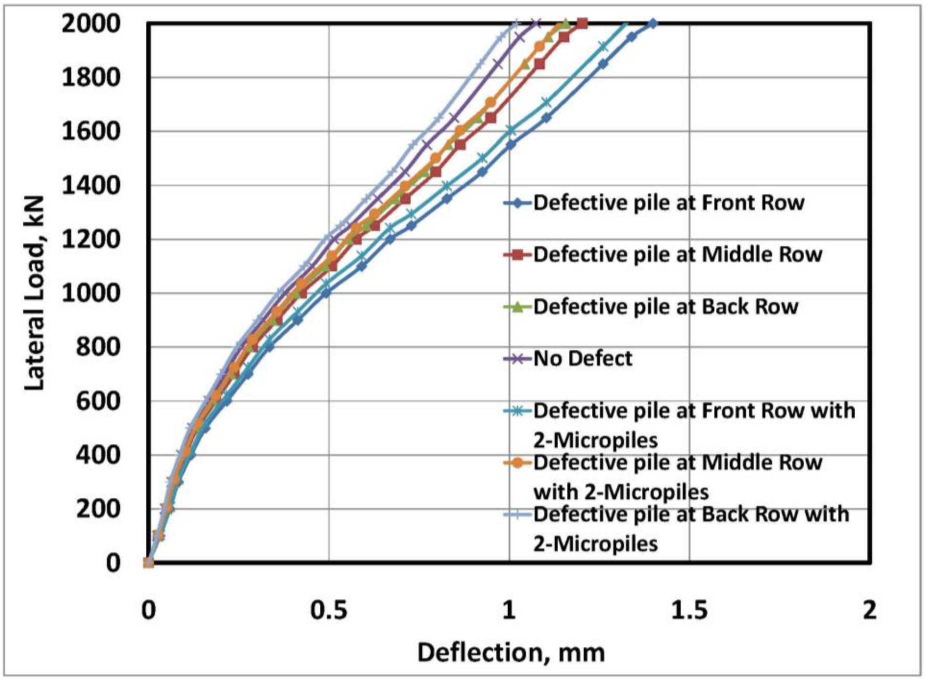


**Figure (11): Load-Deflection Curves for 6-Pile Groupwith Defect at Depth Ratio (0.4L) Using the Program OpenSees.**

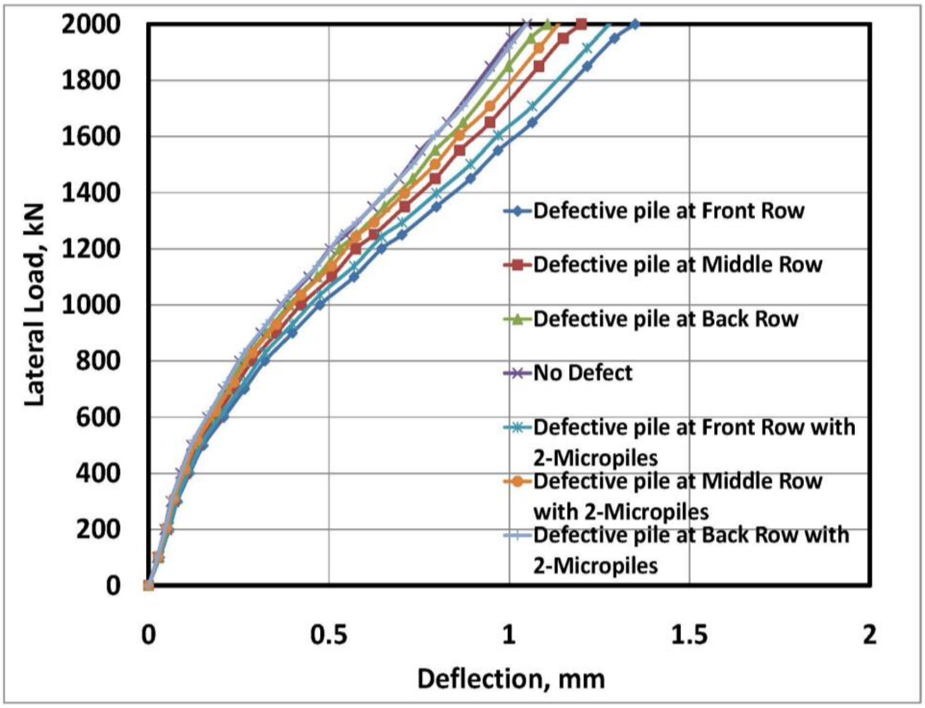


**Figure (12): Load-Deflection Curves for 6-Pile Group with Defect at Depth Ratio (0.5L) Using the Program OpenSees.**

## PROPOSED AMPLIFICATION FACTORS:

A simplified method is proposed for quantifying the effect of presence of a defect in one defective pile within a group of piles spaced center-to-center by the distances of 3d x 3d. In this method, an amplification factor is calculated by dividing the top deflection of the group containing the defective piles by the deflection of the same group arrangement without defects. In addition, another amplification factor is evaluated by dividing the top deflection of the group containing the defective piles by the deflection of the group treated by adding two micropiles, (Kadhim, 2008)

The results of the calculated amplification factors for the cases of 4-pile and 6-pile groups are presented in Figures (13) and (14). The data indicate that for the case of 4-pile group, the amplification factor ranges between 1.06 and 1.34 while for the case of 6-pile group, the amplification factor ranges between 1.02 and 1.65, depending on the position of the defective pile within the group.

These values for the case of 4-pile group become 1.03 and 1.31 while for the case of 6-pile group they become 1.00 and 1.61 when micropiles are inserted. This means that using micropiles for substituting defected piles leads to a decrease in the amplification factor of lateral deflection. In all cases, the decrease is in the order of 2-4%.

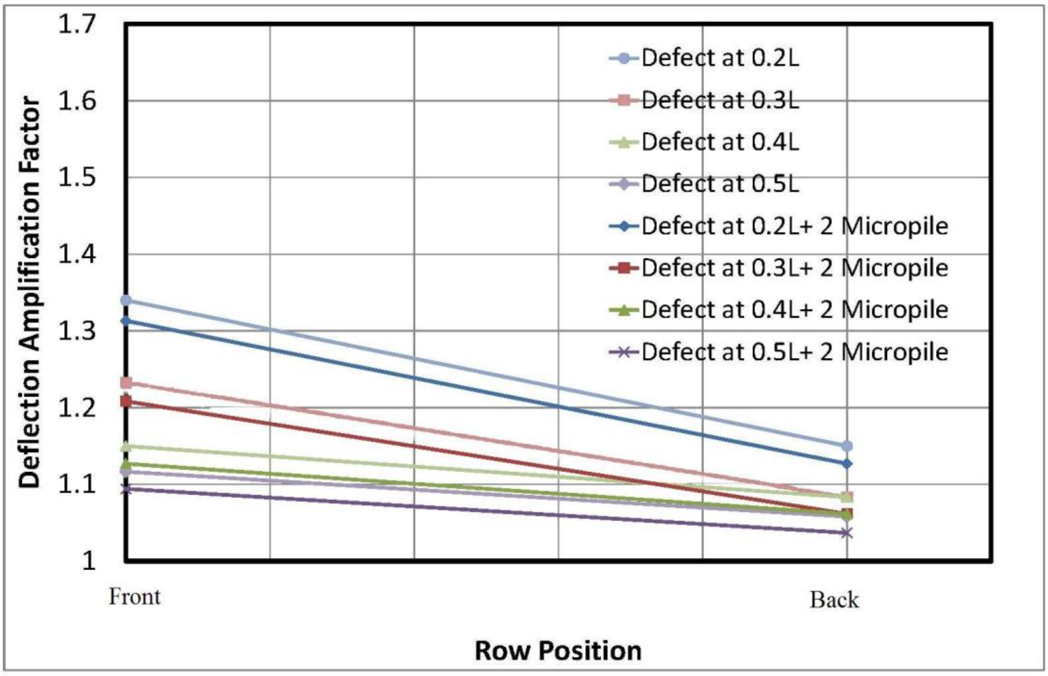


**Figure (13): Effect of Defect Location withRespect to Pile Depth and Row Position for 4-Pile Group.**

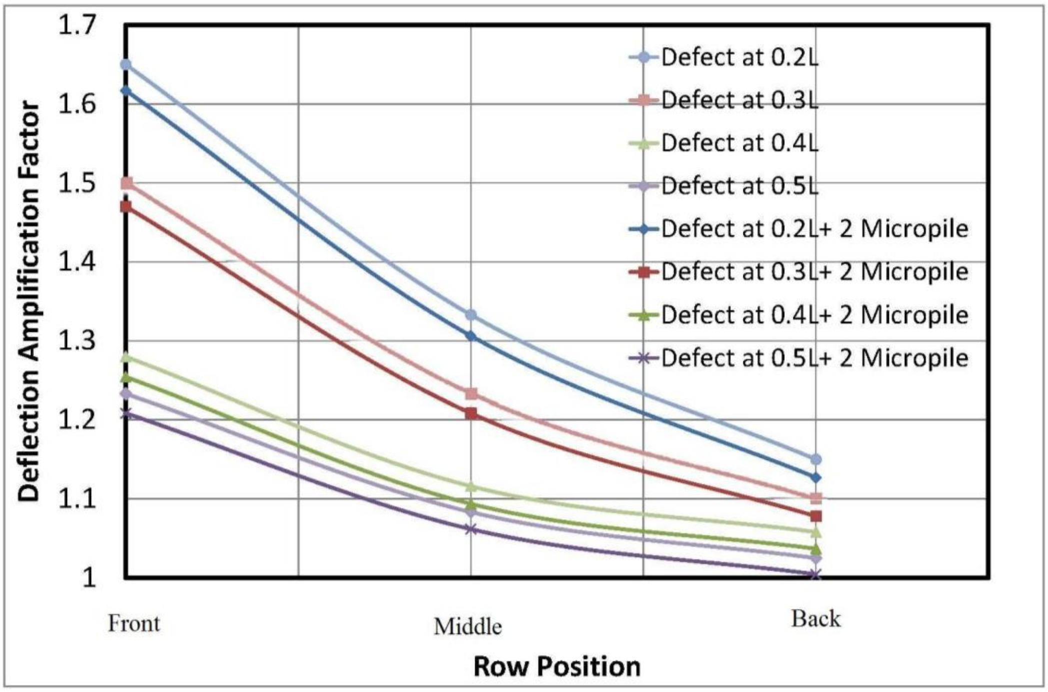


**Figure (14): Effect of Defect Location with Respect to Pile Depth and Row Position for 6-Pile Group.**

## CONCLUSIONS:

- The increase in the group deflection is greater when the defected pile is modeled in the front row. The deflection of the piles decreases as the depth ratio (αL) of the defect increases from 0.2L to 0.5L. The deflection of the piles decreases when inserting two steel micropiles beside the defected pile at two opposite directions.
- The pile head deflection increases as the defective pile is moved from the back row to the middle row and then to the front row. Similar to the cases of the 4-pile groups, the deflection of the piles of the 6-pile group decreases as the depth ratio (αL) of the defect increases from 0.2L to 0.5L. The lateral deflection of the piles decreases when inserting two steel micropiles beside the defected pile at two opposite directions.
- The amplification factor (the top deflection of the group containing the defective piles divided by the deflection of the same group arrangement without defects) for the case of 4-pile group ranges between 1.06 and 1.34 while for the case of 6-pile group the amplification factor ranges between 1.02 and 1.65, depending on the position of the defective pile within the group. These values for the case of 4-pile group become 1.03 and 1.31 while for the case of 6-pile group they become 1.00 and 1.61 when micropiles are inserted. This means that using micropiles for substituting defected piles leads to a decrease in the amplification factor of lateral deflection. In all cases, the decrease is in the order of (2-4) %.

## REFERENCES:


- Armour, T.P.E., Paul, G. P.E., James, K. P.E. and Sunil S. P.E., (2000), " **Micropile Design and Construction Guidelines "**, U.S. Department of Transportation, Federal Highway Administration, Priority Technologies Program.
- Ata, A. and El-Kilany, M. (2006), **"Effect of Anomalies on the Behavior of Laterally Loaded Pile Groups"**, Proceedings of the 4th Jordanian Civil Engineering Conference, 10-13April 2006, Amman – Jordan.
- Hronek, J.W. Madlyn, P.E., and Guarino, G., (2007), **"Developing Foundation Support for the Reconstruction of Bridge Over Como Avenue, Minneapolis, MN"**, Report from Internet.
- Juran, I., Bruce, D.A., Dimillio, A., and Benslimane, A., (1999), **"Micropiles: The State of Practice. Part II:** Design **of Single Micropiles and Groups and Networks of Micropiles"**. Ground Improvement, Vol. 3, pp. 89-110.
- Kadhim Y.M., (2008), **"Investigation on the Use of Micropiles as Foundation Support Elements"**, Ph.D. Thesis, College of Engineering, University of Baghdad, Iraq.
- Kalkan E., (2003), **"Nonlinear Modeling of Micropile Foundation Systems "**, University of California, Davis, U.S.A., Report from Internet.
- Lizzi, F., (1982), **"The Pali Radice (Root Piles),"** Symposium on Soil and Rock Improvement Techniques including Geotextiles, Reinforced Earth and Modern Piling Methods, Bangkok, December, Paper $D_1$ , ( as Cited by Armour, et al., 2000).
- Plumelle, C., (1984), **"Improvement of the Bearing Capacity of Soil by Inserts of Group and Reticulated Micropiles"**, International Symposium on In-situ Reinforcement of Soils and Rocks, Paris, ENPC Press, pp. 83-89.
- Silvia M., Frank M., and Gregory L. F., (2005), **"OpenSees Command Language Manual"**, OpenSees v. 1.6, Printed on 31 January.

Number 3 Volume 16 September 2010 Journal of Engineering

# FINITE ELEMENT ANALYSIS OF A FRICTION PENDULUM BEARING BASE ISOLATION SYSTEM FOR EARTHQUAKE LOADS

Asst.Lect. Zuhair Abd Hacheem
Highway & Transportation Eng. Dep.
College of engineering
AL-Mustansiriya University

Asst. Lect. Israa Khudhair AL-Shimmari
Highway & Transportation Eng. Dep.
College of engineering
AL-Mustansiriya University

**ABSTRACT**

Base isolation systems have become a significant element of a structural system to enhance reliability during an earthquake. One type of base isolation system is Friction Pendulum Bearing in which the superstructure is isolated from the foundation using specially designed concave surface and bearing to allow sway under its own natural period during the seismic events. This study presents the finite element analysis of Friction Pendulum System (FPS) of a multi-story building and without base isolation, subjected to two real different earthquakes (El Centro & Loma Prieta) by use engineering program (ETABS Nonlinear version 9.5). Comparing with the available experimental data, the application of the current model gives close prediction. It has been shown that as a result of isolation, base shear acting are reduced considerably.

A parametric study dealing with the coefficient of friction μ (0.08,0.15 and 0.25) and radius of concave surface R (40 in, 80 in and 400 in) to study the base shear and the displacement of Friction Pendulum System. Overall the base isolated system showed a significant improvement in dynamic response of the model structure by reducing the base shear and increasing the damping of the system

**التحليل بالعناصر المحددة لنظام العزل بقاعدة بندول الاحتكاك للأحمال الزلزالية**

**الخلاصة**

أصبحت أنظمة العزل القاعدي من العناصر الهامة في تعزيز فاعلية المباني إثناء الهزات الأرضية. واحد هذه الأنظمة هو نظام العزل بقاعدة بندول الاحتكاك الذي يقوم بعزل المبنى عن أساسة ويستخدم تصميم خاص لتقعر سطح قاعدة الاستناد ويسمح بالتأرجح بفترة طبيعية أثناء حدوث الزلزال.

تقدم هذه الدراسة تحليل العناصر المحددة للمبنى متعدد الطوابق غير معزول و معزول بنظام العزل بقاعدة بندول الاحتكاك معرض لزلزالان حقيقيان مختلفين (El Centro & Loma Prieta) باستخدام برنامج هندسي (ETABS Nonlinear version 9.5) وقورنت مع النتائج العملية المتوفرة حيث أعطا النظام المستخدم نتائج متقاربة و كما لوحظ كنتيجة للعزل, انخفاض كبير بقوة قص القاعدة.

وتم أخذ ثلاث قيم مختلفة لكل من معمل الاحتكاك (0.08, 0.15 & 0.25) μ و نصف قطر التقعر(R( 40 in, 80 in & 400 in لدراسة القص القاعدي وإزاحة نظام بندول الاحتكاك.

وقد أظهرت النتائج إن لنظام بندول الاحتكاك تحسين هام عنده الاستجابة الحركية لنموذج المبنـى بتقليل القص القاعدي وزيادة إخماد المبنى .

**KEY WORD**

**Base-isolated, friction pendulum, finite element, earthquake, seismic isolation bearings**

## INTRODUCTION

In recent years, the Friction Pendulum System (FPS) has become a widely accepted device for seismic isolation of structures. The concept is to isolate the structure from ground shaking during strong earthquake. Seismic isolation systems like the FPS are designed to lengthen the structural period far from the dominant frequency of the ground motion and to dissipate vibration energy during an earthquake. The FPS consists of a spherical stainless steel surface and a slider, covered by a Teflon-based composite material. During severe ground motion, the slider moves on the spherical surface lifting the structure and dissipating energy by friction between the spherical surface and the slider.

The period of the Friction Pendulum System (FPS) is selected simply by choosing the radius of curvature of the concave surface. It is independent of the mass of the supported structure. The damping is selected by choosing the friction coefficient. Torsion motion of the structure are minimized because the center of stiffness of the bearing automatically coincides with the center of mass of the supported structure. The bearing's period, vertical load capacity, damping, displacement capacity, and tension capacity, can all be selected independently.

## BASE ISOLATION TYPES

Base isolation systems are divided into two main groups of systems with a recentering (Restoring) mechanism and systems without this mechanism. The recentering mechanism is responsible to push the structure back to its original place to minimize the permanent displacement of the structure in its base. Regarding isolation mechanisms, base isolated systems can be divided into three main groups: elastomeric-based systems, sliding-based types, and spring type systems

1. Elastomeric-based systems
   1.1 BLow-damping rubber systems
   1.2 BHigh-damping rubber systems
2 . BSliding-based systems
   2.1 BElectricite-de-France system
   2.2 BEERC system
   2.3 BResilient-Friction based isolation system (R-FBI)
   2.4 Fiction pendulum systems
      2.4.1 Bearing F.P.S
      2.4.2 Tension F.P.S

3. Spring-type systems

(a)

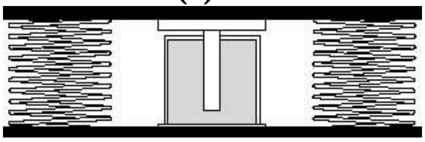

(b)

(c)

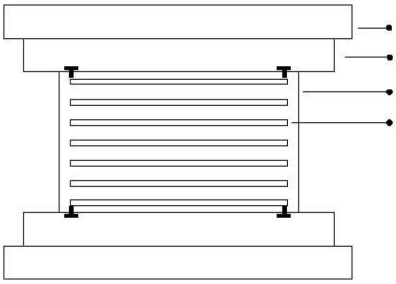

(d)

**Fig.1 Most popular building isolation devices: (a)Spring-based isolator,(b) Tension F.P.S,(c) BElectricite-de-France system,(d) Bearing F.P.S**

## CONCEPT OF FRICTION PEMDULUM SYSTEM

Friction Pendulum Bearings work on the same principle as a simple pendulum. When activated during an earthquake, the articulated slider moves along the concave surface causing the structure to move in small simple harmonic motions, as illustrated in Fig.2 & 3 Similar to a simple pendulum, the bearings increase the structures natural period by causing the building to slide along the concave inner surface of the bearing. The bearings filter out the imparting earthquake forces through the frictional interface. This frictional interface also generates a dynamic friction force that acts as a damping system in the event of an earthquake. This lateral displacement greatly reduces the forces transmitted to the structure even during strong magnitude eight earthquakes. This type of system also possesses a re-centering capability, which allows the structure to center itself, if any displacement is occurred during a seismic event due to the concave surface of the bearings and gravity.

**Fig.2 Pendulum motion**

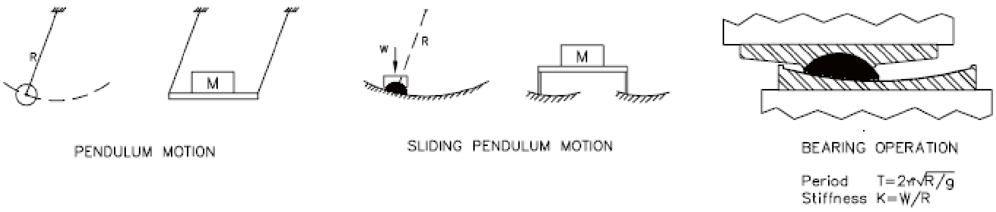


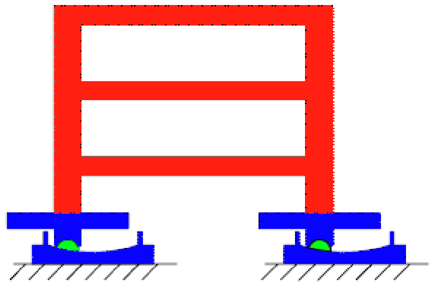

**Fig.3 Basic Principles of the Friction Pendulum Bearing**

## EXPERIMENT STUDY OF NIKOLAG KRAVCHUK, RYAN COLQUHOUN, AND ALI PORBAHA

This model (Fig. 4) was tested by [Nikolag Kravchuk, Ryan Colquhoun, and Ali Porbaha California State University, Sacramento] to simulate the pendulum motion of a single Friction Pendulum Bearing. The springs acted as the force that centered the system when it was displaced in any direction. The preliminary model was modified slightly to improve the response of the system. The new design had four actual bearings machined to reduce the friction and better represent the response of an actual pendulum system.

Both model structures (with and without isolation system) were made from the same flexible material and mounted on the same shake table to allow comparison of the responses of the two structures during lateral loading.

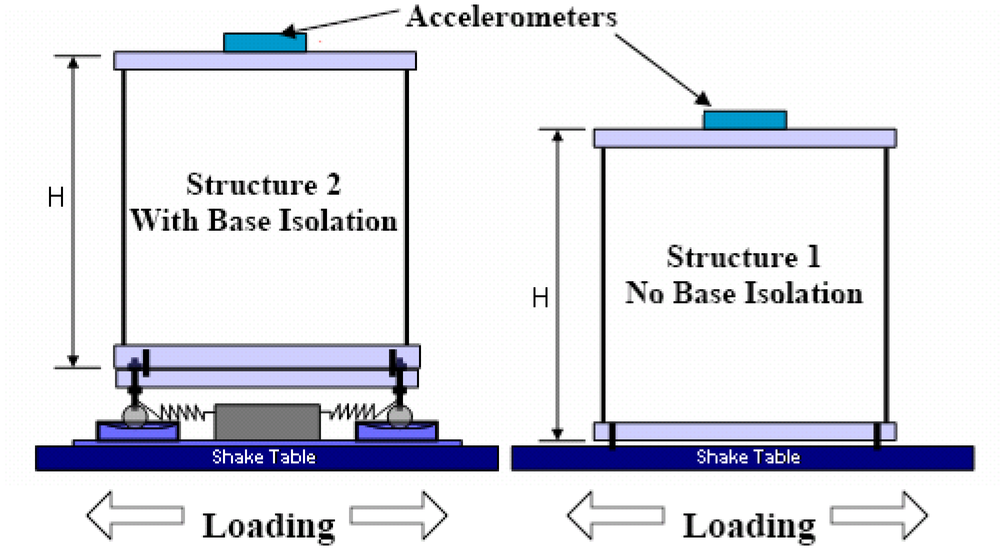


**Fig.4 Experimental Setup of Nikolag Kravchuk, Ryan Colquhoun, and Ail Porbaha**

## TESTING AND RESULTS OF NIKOLAG KRAVCHUK, RYAN COLQUHOUN, AND ALI PORBAHA

### Free Vibration

The first sequence in the experiment testing was to get the response of the structures under free vibration. An equal drift was applied to the top of both structures with and without base isolation system. The force was released and the structures allowed to oscillate until the natural damping of the structures brought the system to stop. The accelerometers recorded the acceleration that each structure experienced until they stopped oscillating. Fig. 5 shows the responses of these two structures.

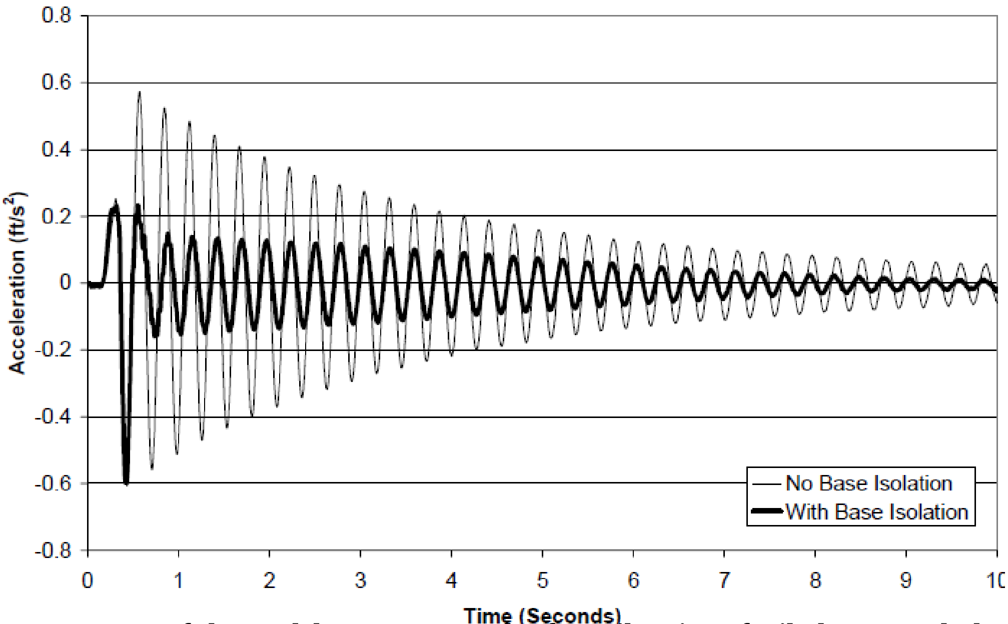


**Fig.5 Responses of the model structures under free vibration of Nikolag Kravchuk, Ryan Colquhoun, and Ali Porbaha.**

**Forced Vibration**

The second sequence of experiment was the forced vibration of the structures. The shake table was loaded with an increasing acceleration (sweep) for a period of 10 seconds. The acceleration of each structure was recorded and the responses of both structures were recorded, as shown in Fig 6.

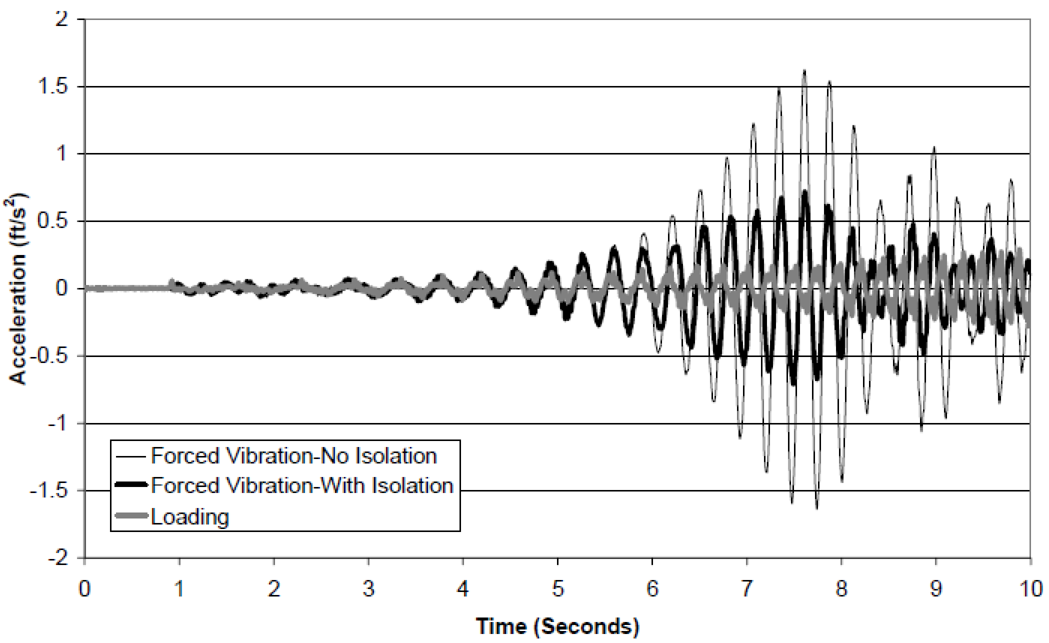


**Fig.6 Responses of the model structures under forced vibration of Nikolag Kravchuk, Ryan Colquhoun, and Ali Porbaha.**

**Table1. Results of the shake table tests**

| | **Free Vibration** | | **Forced Vibration** | |
|---|---|---|---|---|
| | **With Base Isolation** | **Without Base Isolation** | **With Base Isolation** | **Without Base Isolation** |
| Maximum acceleration | 0.23 | 0.57 | 0.72 | 1.63 |
| Damping ratio | 0.085 | 0.016 | - | - |

**USING OF FRICTION PENDULUM SYSTEM**

Friction Pendulum may be used between components of the structures (Friction pendulum gap - element) or between structure and foundation (Friction pendulum base isolation)

**San Francisco Airport International Terminal** was designed by Skidmore, Owings and Merrill with Dr. Anoop Mokha as project Eng. The seismic design used friction pendulum seismic isolation to resist a magnitude 8 earthquake occurring on the San Andreas Fault, with no structural damage.

**Benicia-Martinez Bridge** is one of the largest bridges to date to undertake a seismic isolation retrofit, and uses the largest seismic isolation bearings ever manufactured. [Dr. Victor Zayas. Earthquake Protection Systems, Inc. 2801 Giant Hwy . Blodg. A Richmond, California 94806 . (510)232-5993. Fax 232-6577].


San Francisco Airport International Terminal


SF Airport Terminal Installed Bearing

**Friction pendulum system bearing base isolation between column and separate footing**


Hayward City Hall

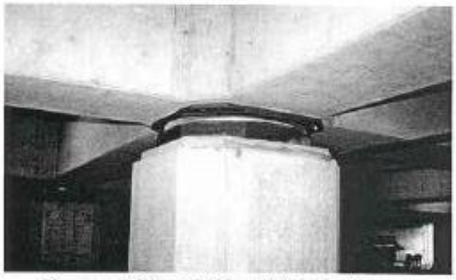
Hayward City Hall Installed Bearing

**Friction pendulum gap - element between beam and column**


Benicia-Martinez Toll Bridge


Concave for Benicia-Martinez Bridge Bearing

**Friction pendulum system bearing base isolation between pier and foundation**

**Fig.7 Using of Friction pendulum system [Dr. Victor Zayas. Earthquake Protection Systems, Inc. 2801 Giant Hwy . Blodg. A Richmond, California. www.earthquakeprotection.com].**

## FINITE ELEMENT ANALYSIS OF FRICTION PENDULUM SYSTEM (FPS)

The differential equation governing an FPS isolated structure is [Almazan and Llera, 2002and 2003]:

$$M\ddot{q}+C\dot{q}+Kq+Q=-ML_wW \qquad (1)$$

where $\boldsymbol{q}$ is the vector of the system degrees of freedom. $\boldsymbol{M}$, $\boldsymbol{C}$, and $\boldsymbol{K}$ are mass, damping, and stiffness matrices, respectively. $\boldsymbol{W}$ is the 3-D excitation input vector, $\boldsymbol{L}_W$ the input influence matrix, and $\boldsymbol{Q}$ the vector of non-linear restoring force generated by isolators with respect to the degree-of-freedom $\boldsymbol{q}$ of the structure. To keep track of the axial force in bearings a friction pendulum element has been incorporated in the set Fig.8. The sliding displacement of the isolator is:

$$\delta_k = \overline{O_k S_k} = \{\delta_{xk}\delta_{yk}\delta_{zk}\}^T \qquad (2)$$

By imposing the kinetic constraint, i.e. spherical surface of the isolator, the three components of the deformation $\boldsymbol{\delta_k}$ and its velocity $\dot{\delta}_k$ are implicitly expressed in terms of each other as:

$$\delta_{xk}^2 + \delta_{yk}^2 + (\delta_{zk} - R_k)^2 = R_k^2 \qquad (3)$$

$$\delta_{xk}\,\dot{\delta}_{xk} + \delta_{yk}\,\dot{\delta}_{yk} + \dot{\delta}_{zk}(\delta_{zk} - R_k) = 0 \qquad (4)$$

where $R_k$ is the radius of curvature of the spherical surface of the $k^{th}$ isolator.

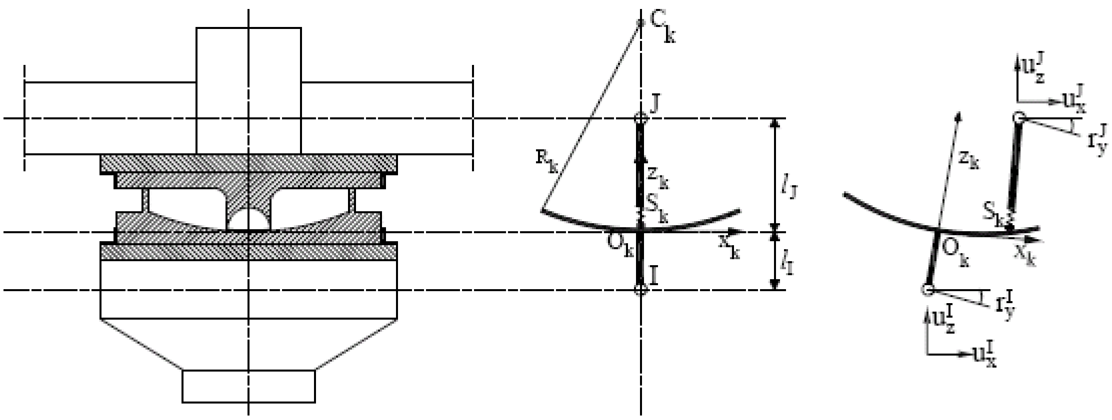


**Fig.8 Friction pendulum element in downward position [Almazan and Llera, 2002and 2003]**

The element demonstrated in fig. 8 has 2 nodes, *I* and *J*, and 12 degrees of freedom, which are linearly related to the global degrees-of-freedom ($\boldsymbol{q}$):

$$u_k = \{u_k^J; u_k^I\} = P_k q \qquad (5)$$

where $P_k$ is the nodal kinetic transformation matrix of the $k^{th}$ isolator. $u_k^J$ and $u_k^I$ are nodal deformation vectors of the lower and upper element nodes.
Assuming small node rotations, it is possible to relate deformation and velocity in the isolator, $\delta_k$ and $\dot{\delta}_k$, with nodal deformations, $u_k$ as:

$$\delta_k = \bar{S}(u_k)u_k \tag{6}$$

$$\dot{\delta} = \hat{S}(u_k)\dot{u}_k \tag{7}$$

In which

$$\bar{S}(u_k) = \begin{bmatrix} 1 & 0 & 0 & 0 & -l_j & 0 & -1 & 0 & 0 & 0 & \Delta u_z + l_I & \Delta u_y \\ 0 & 1 & 0 & -l_j & 0 & 0 & 0 & -1 & 0 & \Delta u_z + l_I & 0 & -\Delta u_x \\ 0 & 0 & 1 & 0 & 0 & 0 & 0 & 0 & -1 & \Delta u_y & \Delta u_x & 0 \end{bmatrix}$$

(8)

$$\hat{S}(u_k) = \begin{bmatrix} 1 & r_z^I & -r_y^I & 0 & -l_j & 0 & -1 & -r_z^I & r_y^I & 0 & -(\Delta u_z + l_I) & \Delta u_y \\ -r_z^I & 1 & r_x^I & l_j & 0 & 0 & r_z^I & -1 & -r_x^I & \Delta u_z + l_I & 0 & -\Delta u_x \\ r_y^I & -r_x^I & 1 & 0 & 0 & 0 & -r_y^I & r_x^I & -1 & -\Delta u_y & \Delta u_x & 0 \end{bmatrix}$$

(9)

Where $\Delta u_i = u_i^J - u_i^I$ for $i = x, y, z$ and $l_J$ and $l_I$ are vertical distances between nodes $J$ and $I$ and origin $O_k$ in the original configuration of the fraction pendulum system, corresponding Fig. 8
In the next step the non-linear restoring force vector $\boldsymbol{Q}$ must be determined. The restoring force in an isolator of this type is composed of the two main terms of the pendulum effect, *fp*, and the frictional part, $f\mu$:

$$f_k = fp + f\mu$$

$$f_k = N_k \hat{n}_k + \bar{\eta}_k \mu_k N_k \hat{s}_k$$

$$f_k = N_k(\hat{n}_k + \bar{\eta}_k \mu_k \hat{s}_k) = N_k r_k \tag{10}$$

Where $N_k$ is the magnitude of the normal force $\hat{n}_k$ and $\hat{s}_k$ are unit vectors in the outward normal direction and tangential to the trajectory of the isolator, respectively. $\mu_k$ is the friction coefficient. $\bar{\eta}_k$ is a positive non-dimensional variable with value one during sliding phases and less than one during sticking phases [Wen, 1976] and [Park, 1986].
In sticking phases, it is not possible to determine the magnitude and direction of the friction force, as regarding equation 10, the sliding velocity vanishes. To overcome this problem, instead of the Coulomb friction law an equivalent hysteretic model is applied.
To compute the restoring force in the global coordinate system, the restoring force computed in equation 10 is transformed as Fig.9.

$$Q_k = L_k^T f_k \tag{11}$$

Where
$Q_k$ is local vector of non-linear restoring force for fraction pendulum element and

$$L_k = \hat{S}_k P_k \tag{12}$$

Finally adding restoring forces of all isolators in the system:

$$Q = \sum_k Q_k = \sum_k L_k^T f_k = L^T F \tag{13}$$

Where

$Q$ the global vector of non-linear restoring force from fiction pendulum systems [Almazan and Llera, 2003]

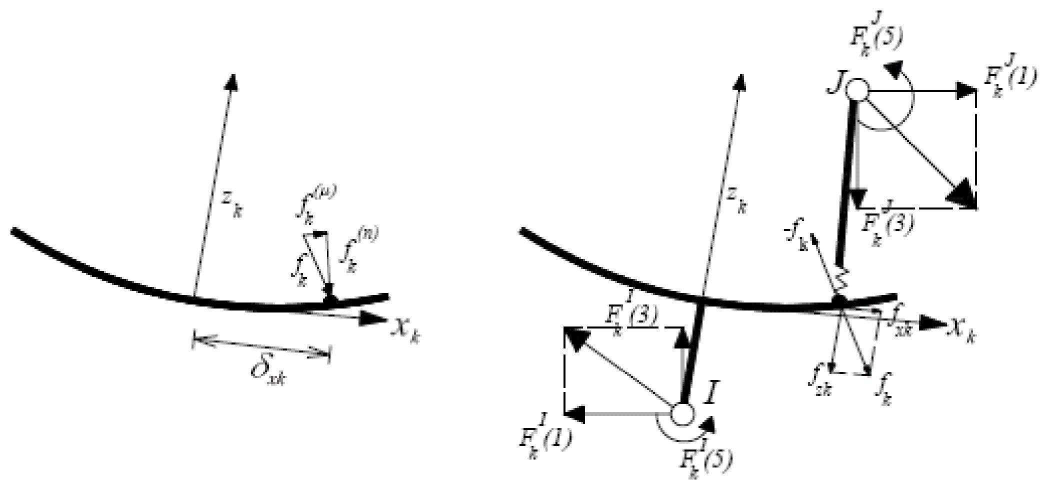

**Fig.9 Forces acting on an FPS bearing (left) in local coordinates, (right)in global coordinates system [Almazan and Llera, 2002and 2003]**

## CASE STUDIES

The finite element mesh model of a three-story structure with two bays on the two direction by engineering programs (ETABS Nonlinear version 9.5). The columns (24 in x 24in) , beams (36 in x 24 in) and slab thickness (8 in) Fig.11. The material properties of structure (Table 3 & 4) and the linear and nonlinear properties of friction pendulum in table (Table 5 & 6). The response of the aforementioned system has been subjected to two strong earthquakes are studied. El Centro earthquake has 500 increment and 0.02 time step and Loma Prieta earthquake has 2000 increment and 0.02 time step (Table 2) and fig.10.

Two type of supports have been taken (fixed support and base isolation of friction pendulum) as a result of finite element analysis has been found that the friction pendulum show a significant improvement in dynamic response of structure by reducing the base shear fig. 12 & 13.

As a comparison with model of [Nikolay Kravchuk, Ryan Colquhoun, and Ali Porbaha 2008] fig. 5 & 6 there is a good agreement in the general behavior.

The numerical analysis show that the input energy from earthquakes (El Centro & Loma Prieta) and efficiency the FPS on dissipation of the vibration energy to keep the structure from failure fig. 14 & 15.

**Table 2 Earthquake motion used in the analysis.**

| Excitation | Record | Duration [s] | Magnitude |
|---|---|---|---|
| El Centro | USA, Imperial Valley, May 18, 1940 | 10 | 6.7 |
| Loma Prieta | USA, Santa Cruz, California October 17, 1989 | 40 | 7.1 |

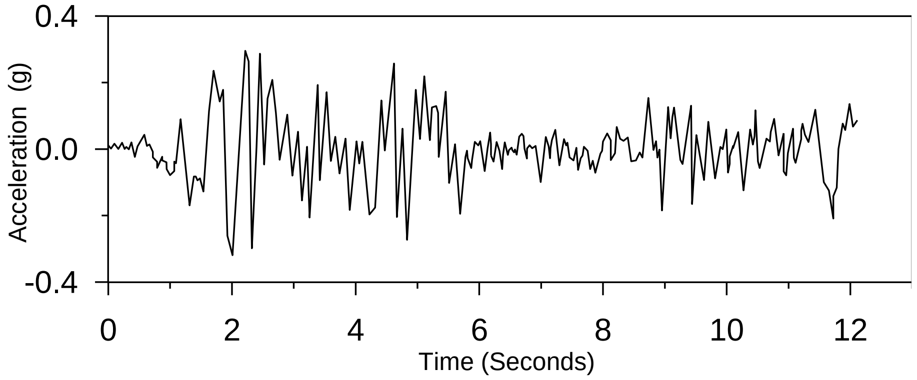


**(a) El Centro earthquake, 1940**

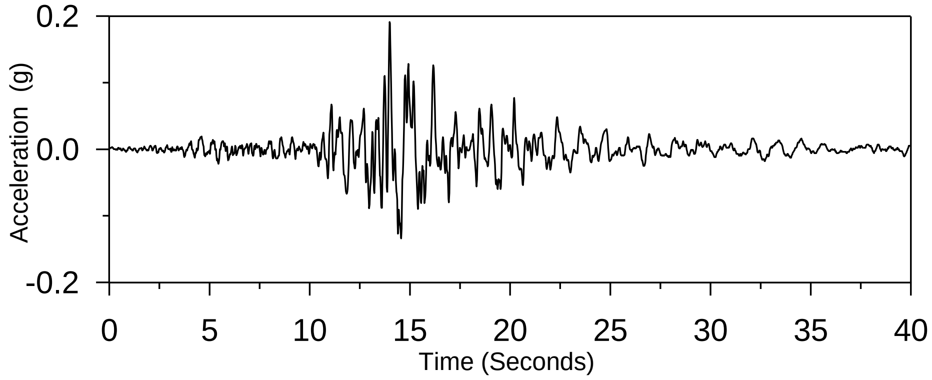


**(b) Loma Prieta earthquake, 1989**

**Fig.10 Earthquake Loads used in analysis**

**Table 3 Analysis Property Data.**

| | |
|---|---|
| Modulus of elasticity , (Kip-in) | 3600 |
| Mass per unit volume, (Kip-in) | 2.246E-7 |
| weight per unit volume, (Kip-in) | 8.841E-5 |
| Poisson's ratio , ν | 0.2 |
| Coefficient of thermal expansion, (Kip-in) | 5.5E-6 |
| Shear Modules, (Kip-in) | 1500 |

**Table 4 Design Property Data.**

| | |
|---|---|
| Reinforcing Yield Stress, (Kip-in) | 60 |
| Compressive strength, (Kip-in) | 4 |
| Shear Steel Yield Stress, (Kip-in) | 40 |
| Concrete Shear Strength, (Kip-in) | 4 |

**Table 5 Linear Properties of FPS.**

| Direction | Effective Stiffness, (Kip-in) | Effective Damping |
|---|---|---|
| $U_1$ | 1000 | o |
| $U_2$ | 4 | o |
| $U_3$ | 4 | o |

**Table 6 Non Linear Properties of FPS.**

| Direction | Stiffness, (Kip-in) | Rate parameter | μ | R (in) |
|---|---|---|---|---|
| $U_1$ | 1000 | ------- | ------ | ------ |
| U2 | 100 | 20 | 0.08 | 40 |
| | | | 0.15 | 80 |
| | | | 0.25 | 400 |
| U3 | 100 | 20 | 0.08 | 40 |
| | | | 0.15 | 80 |
| | | | 0.25 | 400 |

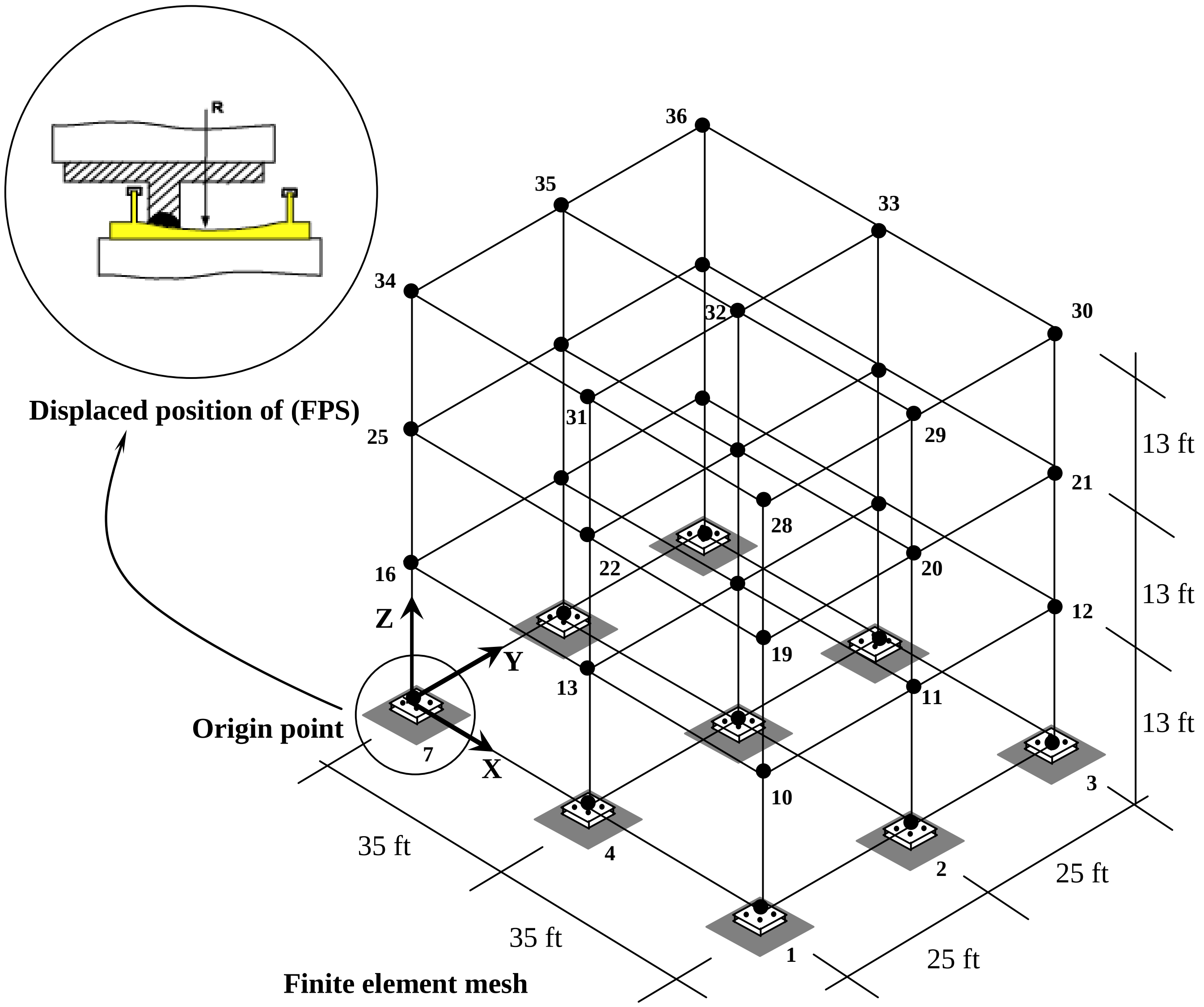


**Fig.11 Finite element mesh of three-story building with friction pendulum system**

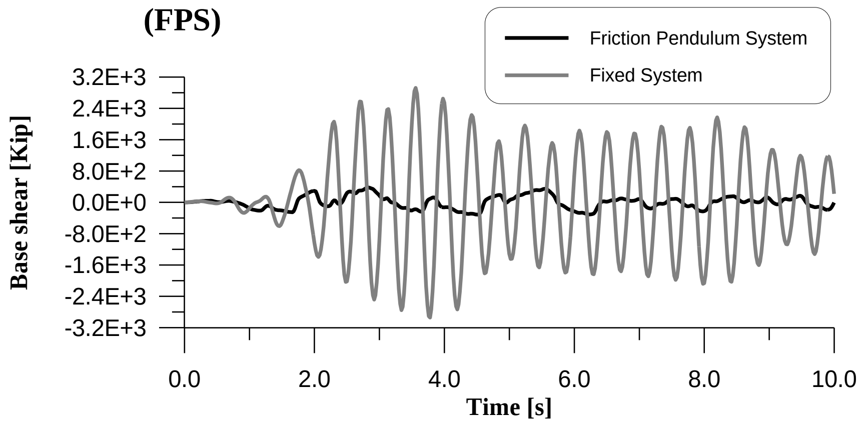


**Fig.12 Comparison of the base shear in an isolated system with the one in a fixed-base structure to El Centro, R=40 in , μ =0.08**

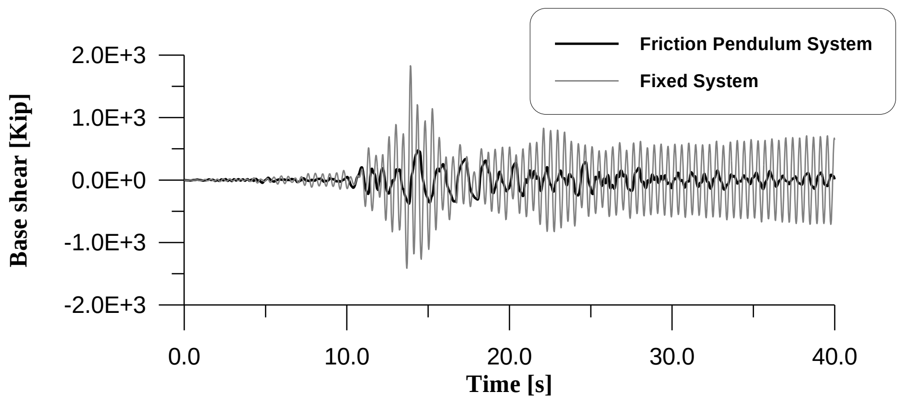


**Fig.13 Comparison of the base shear in an isolated system with the one in a fixed-base structure to Loma Prieta, R=40 in , μ =0.08**

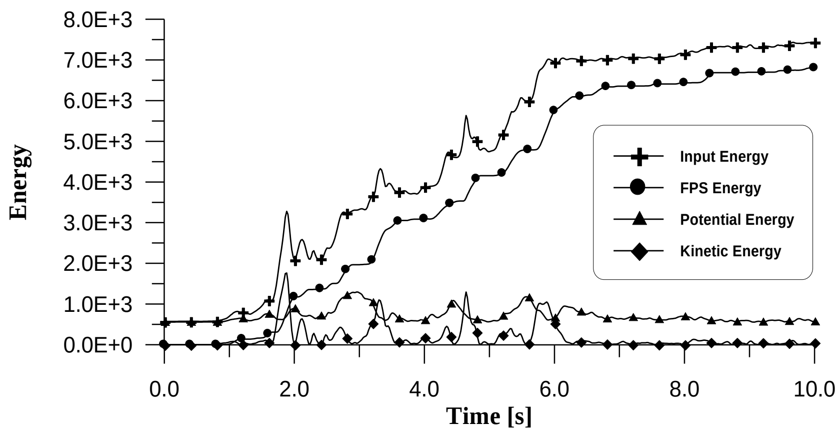


**Fig.14 Energy with time in an isolated system to El Centro, R=40 in , μ =0.08**

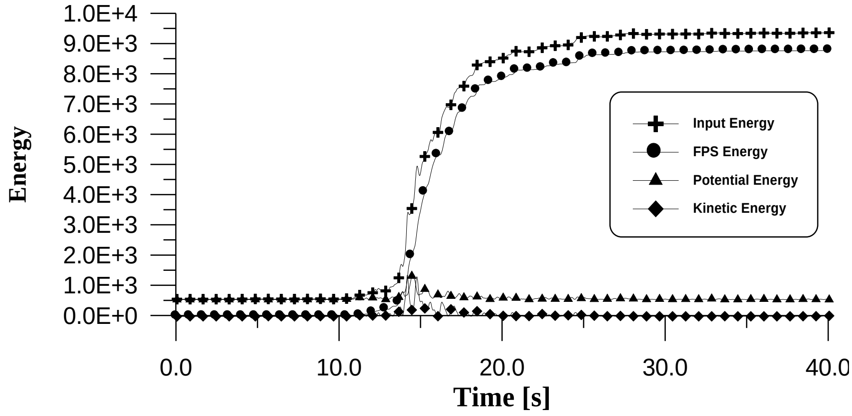


**Fig.15 Energy with time in an isolated system to Loma Prieta, R=40 in , μ =0.08**

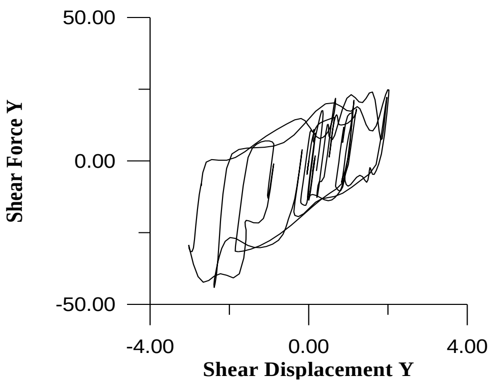


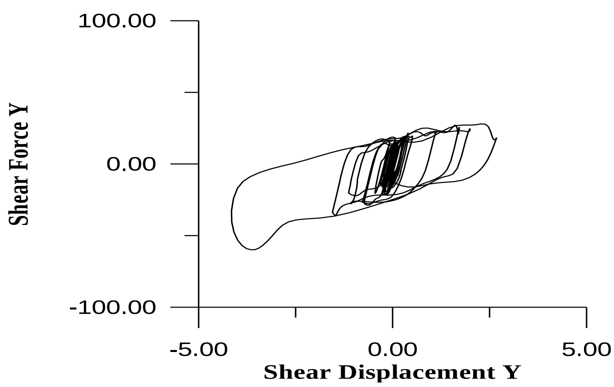


**Fig.16 Shear force with displacement in Y direction to El Centro & Loma Prieta earthquake respectively ,R=40 in , μ =0.08**

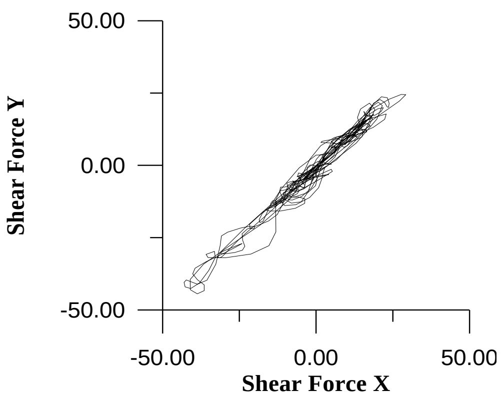


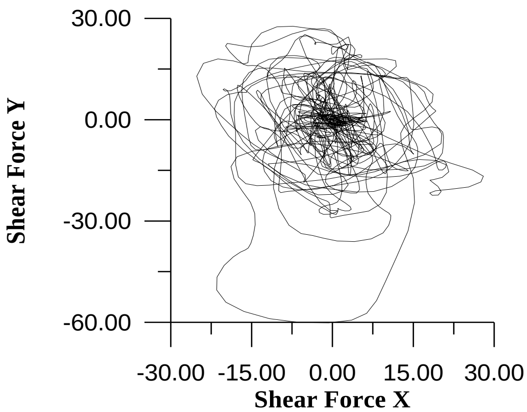


**Fig.17 Shear force in Y direction. With Shear force in Y direction. To El Centro & Loma Prieta earthquake respectively ,R=40 in , μ =0.08**

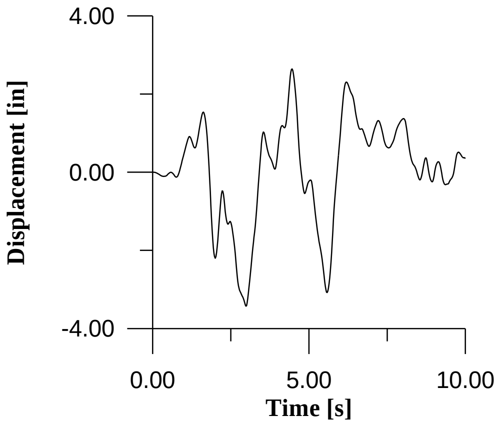


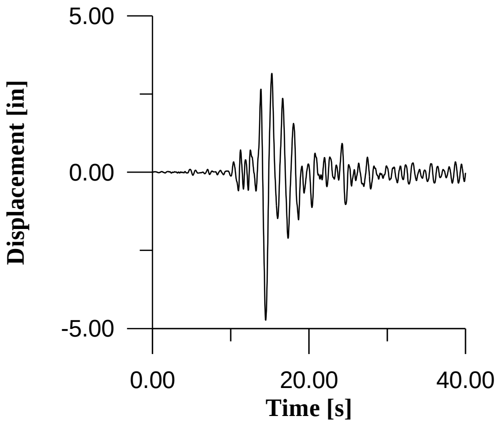


**Fig.18 Drift at the top the structure (third floor) to El Centro & Loma Prieta earthquake respectively ,R=40 in , μ =0.08**

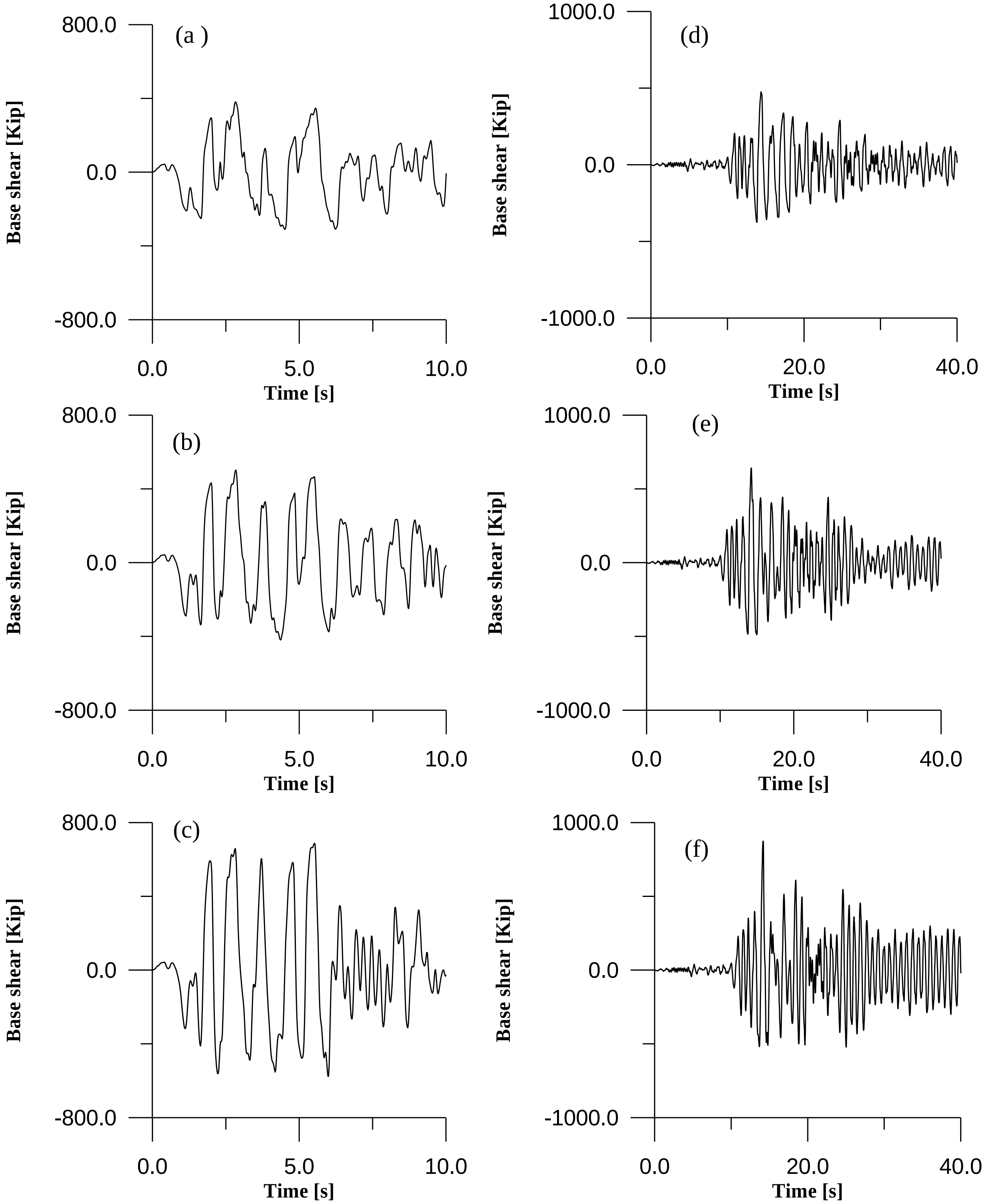


**Fig.19 Base shear Y for 3 story building isolated by FPS with deferent coefficient of friction (a) 0.08 (b) 0.15 (c) 0.25 El centro and (d) 0.08 (e) 0.15 (f) 0.25 Loma Prieta**

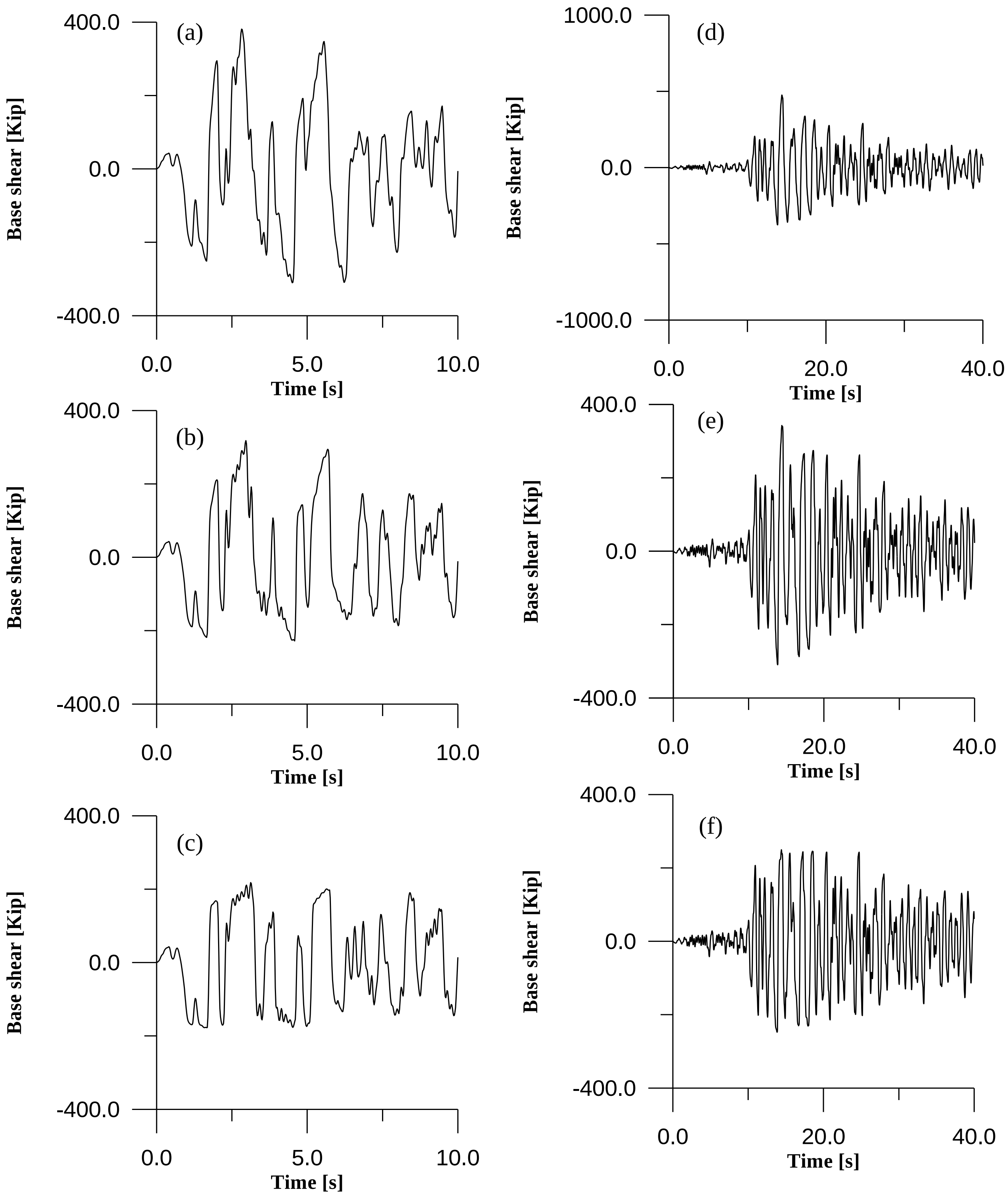


**Fig. 20 Base shear Y for 3 story building isolated by FPS with deferent radiuses of concave surface (a) 40 in (b) 80 in (c) 400 in El centro and (d) 40 in (e) 80 in (f) 400 in Loma Prieta**

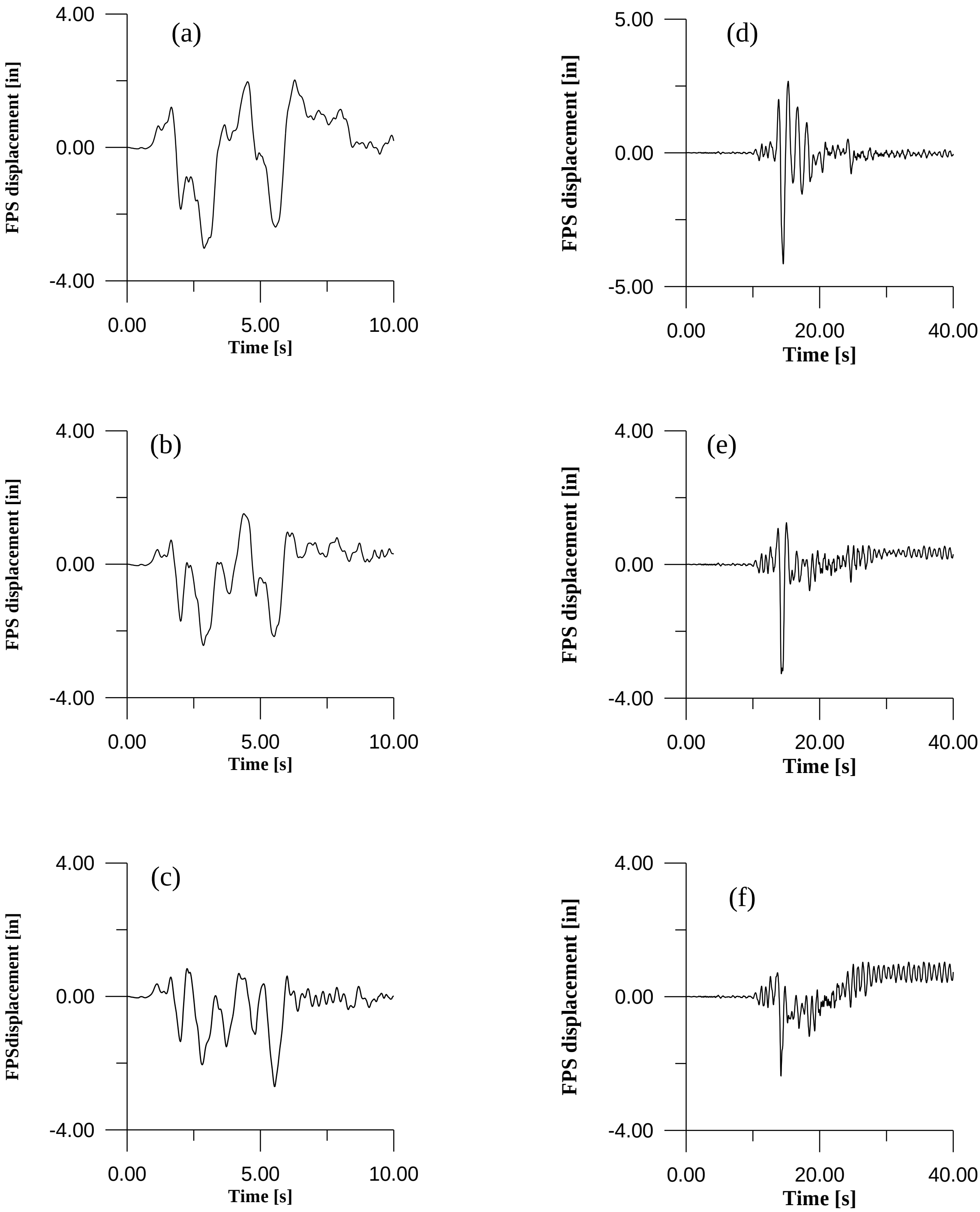


**Fig. 21 FPS displacement Y (in) with deferent coefficient of friction (a) 0.08 (b) 0.15 (c) 0.25 El centro and (d) 0.08 (e) 0.15 (f) 0.25 Loma Prieta**

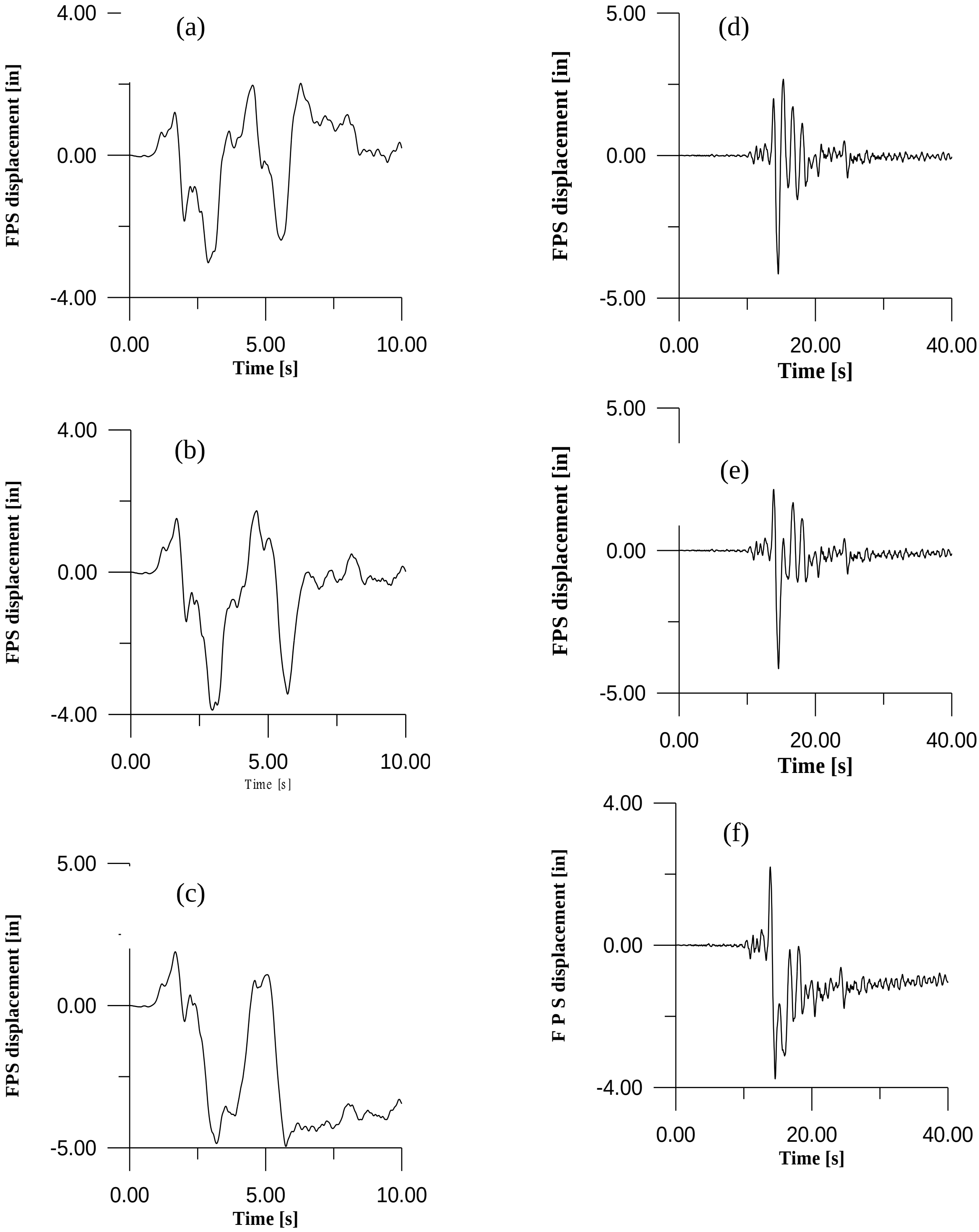


**Fig. 22 FPS displacement Y (in) with deferent radiuses of concave surface (a) 40 in (b) 80 in (c) 400 in El centro and (d) 40 in (e) 80 in (f) 400 in Loma Prieta**

## PARAMETRIC STUDY

### The Effect of Coefficients of Friction

In order to study this effect a three different coefficient of friction (0.08), (0.15) and (0.25) have been carried out with radius of concave 40 in for each type of earthquake. As a result of comparison between curves, it has been shown that the larger the friction coefficient the later the isolation mechanism is activated. In an extreme cases the base shear force does not overcome the friction force. In such a case, an isolated system responds the same as a classical fixed-base system. Fig.19

The displacement of friction pendulum system decreases with the increase in the coefficient of friction due to increased the damping of the system. Fig. 21

### The Effect of the Radius of Concave Surface

To study this effect, the same model as before with a friction coefficient of 0.08 is analyzed for three different radius of concave (40 in), (80 in) and (400 in) for each type of earthquake fig 20 & 22. The base shear decreases with the increase in the radius In such a case, when the radius approach to infinity an isolated system responds the same as a classical roller support. a more concaved sliding surface with accordingly larger geometrical stiffness, reduces the permanent displacement of the bearing.

## CONCLUSIONS

It has been shown that base shear in a sliding-based isolated system is 88.2 % for El Centro earthquake & 73.7 % for Loma Prieta smaller than the one in a fixed-base structure. This can be achieved at the cost of a sliding displacement in bearings.

As the magnitude of an earthquake increases, the sliding displacement becomes larger. For near source cases, to restrict the maximum sliding displacement, a higher amount of friction coefficient or an extra damping source is required. The sliding displacement anticipated by simulation matches the result reported by the experiment very well.

As a result of concavity of sliding plates in all investigated cases, bearings return back to their original configurations with a good degree of precision. This complies with results of shaking table tests done by [Nikolay Kravchuk, Ryan Colquhoun, and Ali Porbaha 2008].

Permitting a structure sliding over its foundation distracts earthquake-induced forces from the structural system. In this way, drift in isolated systems is much smaller in comparison with the classical fixed-base systems.

**REFERENCES**


- AL-Hussaini TM, Zayas VA, Constantinou MC.(1994),"Seismic isolation of multi-storey frame structures using spherical sliding isolation system". Technical Report No. NCEER-0007, National Center for Earthquake Eng. Research, State University of New York at Buffalo, New York.

- Almazan, J. L., Llera, J. C. (2002),’’Analytical model of structures with frictional pendulum isolators’’, Earthquake engineering and structural dynamics, 31, 305-322.

- Almazan, J. L., Llera, J. C. (2003), ’’Physical model for dynamic analysis of structures
- isolated with FPS isolators’’, Earthquake engineering and structural dynamics, 32, 1157-1184.

- Derjaguin, B.V. and Toporov, Y.P. (1982), "Influence of Adhesion on the Sliding and Rolling Friction," in Microscopic Aspects of Adhesion and Lubrication, edited by J.M. Georges, Tribology Series 7, Elsevier Scientific Publishing Co.

- Kelly JM.(1986),"A seismic base isolation: review and bibliography. Soil Dynamics and Earthquake Eng."

- Naeim, F., Kelly, J. M. (1999), "Design of Seismic Isolated Structures from Theory to Practice", John Wiley & Sons, New York.

- Nikolay Kravchuk, Ryan Colquhoun, and Ali Porbaha California State University, Sacramento (2008), "Development of a Friction Pendulum Bearing Base Isolation System for Earthquake Eng. Education", proceedings of the 2008 American Society for Eng. Education.

- Roussis, P. C., Constantinou, M. C. (2006), ’’Uplift-restraining friction pendulum seismic isolation system’’, Earthquake engineering and structural dynamics, 35, 577-594.

- Zayas, V.A., Low, S.S., and Mahin S.A.,(1989),"Shake Table Testing of a Friction Pendulum Seismic Isolation System." Seismic Engineering: Research and Practice, The American Society of Civil Engineering, Structural Congress, San Francisco.

- Zayas, V., Piepenbrock, T. and Al-Hussaini, T.(1993),"Summary of Testing of the Friction Pendulum Seismic Isolation System: 1986-1993", Proc., ATC-17-1 Seminar on Seismic Isolation, Passive Energy Dissipation and Active Control, Applied Technology Council, San Francisco.

- Charles K. Erdey (2007) "Earthquake Engineering Application to Design" book, published by John Wiley & Sons, Inc., Hoboken, New Jersey.

- M. A. Crisfield (1997)"Non-liner Finite Element Analysis of Solids and Structures " book, published by John Wiley & Sons, Inc., Hoboken, New Jersey.

- Earthquake protection systems (EPS) "Friction pendulum seismic isolation bearing " www.earthquakeprotection.com last accessed December 1, 2007.

# SEISMIC DESIGN OF SINGLE SPAN STEEL GIRDER BRIDGES AND BRIDGES IN SEISMIC PERFORMANCE CATEGORY A

Asst. Prof. Dr. Abdul Muttalib I. Said
University of Baghdad
College of Engineering
Department of Civil Engineering

Esraa Mubder Edaan
University of Baghdad
College of Engineering
Department of Civil Engineering

**ABSTRUCT**

This paper studies the validity and accuracy of the seismic design force recommended by AASHTO for single span bridges. A parametric study for single steel girder bridges is presented, included the effect of span length and elastomeric bearing and lateral bracing (cross-frame) stiffness. The results of simplified AASHTO method are compared with response spectrum and time history analysis. Also studying the seismic design reqiurements for continuous steel girder bridges in seismic performance category (A), included the effect of span length, seismic zone, effect of elastomeric bearing and cross-frame stiffness and bridge skew on their seismic responses. It is concluded that the AASHTO simplified analysis method for single span bridges underestimates the seismically induced forces at supports and the proposed seismic design force of (2.5 multiplied by acceleration coefficient multiplied by tributary weight w(x)) has been recommended for single span bridges for seismic zone 3 and 4 and for soil type II. Also it is observed that the seismic design force for two span continuous bridges in performance category A is safe and conservative method to predict the shear forces transferred by connection elements to the substructures.

**الخلاصة**

يدرس هذا البحث صلاحية ودقة قوى التصميم الزلزالية الموصاة من قبل (AASHTO) للجسور ذات الفضاء الواحد. تم عمل دراسة مقارنة للجسور ذات العوارض الفولاذية بفضاء واحد متضمنة تأثير طول الفضاء و صلابة الوسائد المطاطية وانظمة التثبيت الجانبي. تم مقارنة نتائج طريقة ال AASHTOالمبسطة مع طريقة طيف الاستجابة والتحليل الزمني. أيضاً تم دراسة متطلبات التصميم الزلزالي لجسور العارضة الفولاذية المستمرة في صنف الأداءِ الزلزالي (A)، متضمنة تأثير طول الفضاء، المنطقة الزلزالية، تأثير صلابة الوسائد المطاطية وانظمة التثبيت الجانبي وإنحراف الجسر على استجاباتهم الزلزالية. تم التوصل الى ان طريقة ال ( AASHTO) المبسطة لتصميم الجسور ذات فضاء واحد تقلل من مقدار القوى عند المساند وان القوى التصميمية المقترحة من (2.5 ) مضروبة في معامل التعجيل (A) مضروبة في و زن منتظم W(X) ينصح بها لتصميم الجسور ذات الفضاء الواحد للمناطق الزلزالية 3 ,4 و لنوع التربة II. وايضاًاظهرت الدراسة ان قوة التصميم الزلزالية (20%من وزن المنشأ) الموصى بها من قبل ال (AASHTO) للجسور الواقعة في صنف الاداء الزلزالي (A) أمينة ومحافظة للتنبأ بمقدار قوى القص المنتقلة عبر عناصر الربط الى الهيكل السفلي.

**KEYWORDS: Seismic; Design; Steel girder; Bridge; Elastomeric bearing; Cross frame**

## SEISMIC DESIGN OF SINGLE SPAN STEEL GIRDER BRIDGES

## INTRODUCTION

The recent edition of AASHTO specification ***(AASHTO, 2002)*** does not required any seismic analysis, regardless of seismic zone for single span bridges. However, AASHTO required that the connection between the superstructure to substructure shall be designed to resist a force equal to design acceleration coefficient (A) multiplied by the site coefficient (S) multiplied by the tributary weight at the abutment.

To study the validity and accuracy of the seismic design force recommended by AASHTO for single span bridges, a parametric study for single span steel-girder bridges is presented in this paper included the effect of span length and support stiffness (bearing and cross-frame stiffness) on seismic response of these bridges.

## DESCRIPTION OF BRIDGES

A steel-girder bridge consisting of (0.24m) reinforced concrete slab built integrally with rolled steel beams spaced at (2 m) is studied. The carriage way is (10 m) and the slab has a (1 m) overhang on both sides of the deck. The span lengths of these bridges range between 20 and 60 m with increment of (10 m). The end of steel beam is placed on elastomeric bearing in the longitudinal direction and the steel girders are connected together by cross-frames as shown in Fig. (1). The bridges are designed according to the AASHTO requirements and the bearings are designed according to Iraqi loading. The properties of bridges are summarized in tables (1) and (2).

The slab is modeled with (2×2 m) shell elements and the girders are modeled by frame elements connected to the shell elements at each joint. The end of each girder is attached to a spring representing the elastomer's lateral stiffness in longitudinal direction and in transverse direction it is attached to a spring representing the lateral stiffness of end cross-frame. The value of stiffness for both elastomeric bearing and lateral bracing system is determined as explained in the following sections. The finite element model of the bridges is shown in Fig. (2). Modeling of the superstructure is consistent with recommendations of ***(Tarhini and Frederick, 1989)*** and ***( Mabsout, et. al., 1997)***. SAP 2000 finite element program is used for analysis (***Computer and Structures, SAP 2000, 1998***).

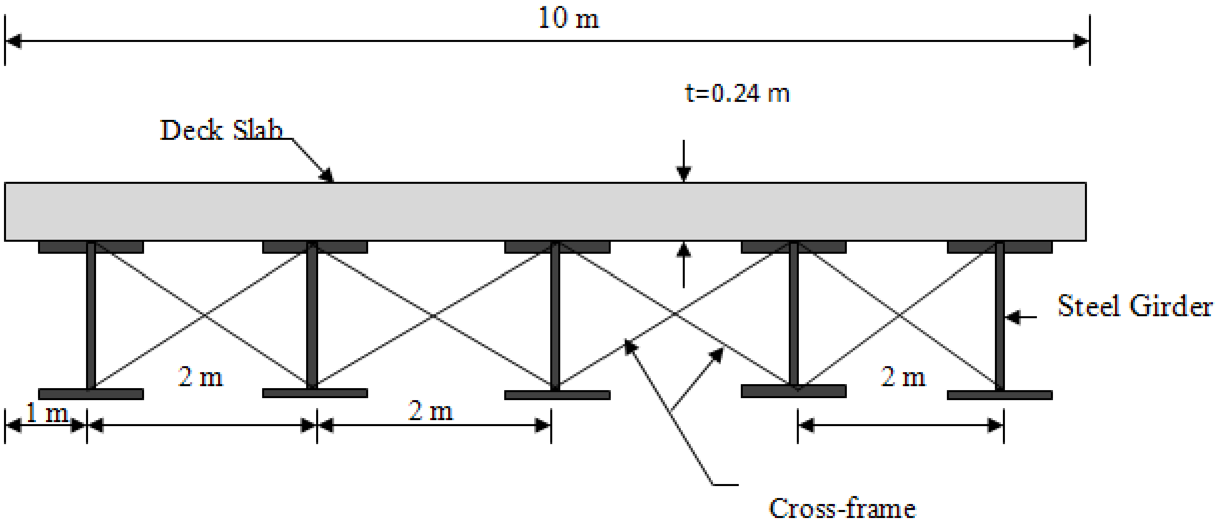


**Fig. (1) Cross section of the bridge**

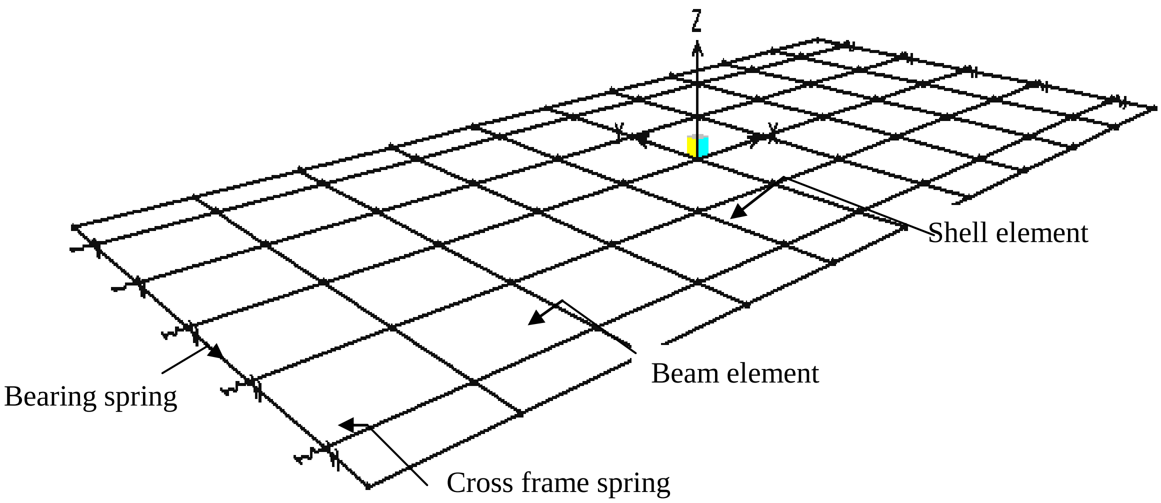


**Fig. (2) Finite element model of the bridge**

**Table (1) Properties of the bridges used in the analysis**

| L (m) | $t_s$ (m) | Girder properties | | | | | | | | |
|---|---|---|---|---|---|---|---|---|---|---|
| | | h (m) | $b_{fb}$ (m) | $b_{ft}$ (m) | $t_{fb}$ (m) | $t_{ft}$ (m) | $t_w$ (m) | A ($m^2$) | $I_y$ ($m^4$) | $I_Z$ ($m^4$) |
| 20 | 0.24 | 1.0 | 0.58 | 0.5 | 0.055 | 0.025 | 0.008 | 0.05176 | 0.00910 | 0.00116 |
| 30 | 0.24 | 1.4 | 0.58 | 0.5 | 0.055 | 0.025 | 0.011 | 0.05892 | 0.01977 | 0.00116 |
| 40 | 0.24 | 1.7 | 0.58 | 0.5 | 0.055 | 0.025 | 0.014 | 0.06708 | 0.03177 | 0.00116 |
| 50 | 0.24 | 2.0 | 0.65 | 0.6 | 0.060 | 0.030 | 0.015 | 0.08565 | 0.05840 | 0.00191 |
| 60 | 0.24 | 2.4 | 1.00 | 0.8 | 0.080 | 0.040 | 0.018 | 0.15304 | 0.15080 | 0.00800 |

**Table (2) Properties of elastomeric bearing and lateral bracing systems**

| Span (m) | Elastomeric bearing size(mm) [DIN 4141] | Cross-frame size (mm) | Bearing stiffener size (mm) | $K_e$ (kN/m) | $K_b$ (kN/m) | |
|---|---|---|---|---|---|---|
| | | | | | In. beam | Ex. beam |
| 20 | 200 × 300 ×52 | L120 × 10 | 2PL.130 × 10 × 920 | 1622 | 417237 | 233892 |
| 30 | 200 × 400 × 52 | L160 × 10 | 2PL.150 × 14 × 1320 | 2162 | 309669 | 173148 |
| 40 | 300 × 400 × 74 | L180 × 12 | 2PL.150 × 14 × 1620 | 2264 | 262602 | 141496 |
| 50 | 300 × 400 × 74 | L180 × 14 | 2PL.180 × 16 × 1910 | 2264 | 273469 | 148843 |
| 60 | 350 × 450 × 69 | L200 × 15 | 2PL.200 × 18 × 2280 | 3214 | 197475 | 104898 |

## STIFFNESS OF LATERAL BRACING SYSTEM

Diaphragms provide an important load path for the seismically induced load acting on slab steel-girder bridges. ***Zahrai and Bruneau*** *(1998)* have shown that the intermediate cross-frames do not affect the seismic response of straight slab on girder bridges, in either the elastic or inelastic range also proposed a simplified model for bridge with only end cross-frames as shown in Fig. (3).

The stiffness of lateral bracing system ($k_b$) at one end depends on the geometry of the bridge and the properties of the bearing stiffeners and diaphragm braces. $K_b$ can be calculated by the following equation (***Zahrai and Bruneau, 1998***):

$$k_b = \sum_1^{ng} \frac{12EI_s}{h_w^3} + \sum_1^{ng-1} \frac{2EA_b\cos^2\theta}{L_b} \tag{1}$$

The $k_b$ for each interior steel beam can be determined from the following formula:

$$k_b = \frac{12EI_s}{h_w^3} + \frac{2EA_b\cos^2\theta}{L_b} \tag{2}$$

The $k_b$ for exterior steel beam can be determined from the following formula:

$$k_b = \frac{12EI_s}{h_w^3} + \frac{EA_b\cos^2\theta}{L_b} \tag{3}$$

where:
$I_S$ : moment of inertia of the bearing web stiffener about the longitudinal axis of girder.
ng : the number of girders.
$h_w$ : the web height between top and bottom flanges.
$A_b$ : cross sectional area of the brace.
$L_b$ : length of brace.
$\theta$ : slope angle of brace.

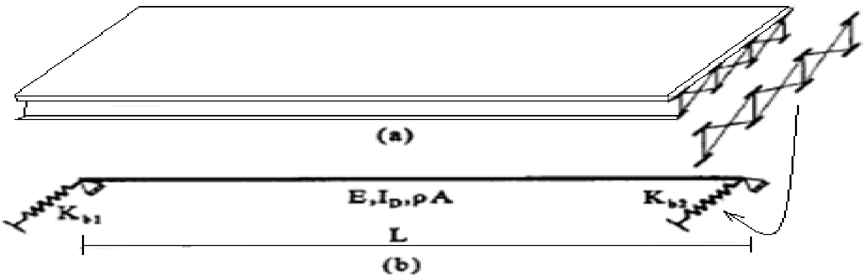


**Fig. (3) Schematical simplified model for bridges with end diaphragms**
(***Zahrai and Bruneau, 1998***)

### Elastomeric Bearings Stiffness

The elastomeric bearings transmit the force from the superstructure to substructure. Spring is used to model the stiffness of elastomeric bearing ($k_e$) in the longitudinal direction. The value of bearing stiffness can be determined from the following equation (***Mast et. al., 1996***):

$$k_e = \frac{G\,A}{T} \tag{4}$$

where:
G : shear modulus of elastomer.
A : area of bearing.
T : total thickness of rubber layers.

## SEISMIC DESIGN FORCE FOR BRIDGE

The bridges are assumed to be located in Iraq (Baghdad city). The contour map in AASHTO is for United State. Depending on UBC code (Uniform Building Code), Baghdad is located in zone 3 and the AASHTO divided the region into contour lines with (A) range (A>0.29), therefore (A) for Baghdad is assumed to equal (0.3).
To study the validity and accuracy of seismic design force recommended by AASHTO for single span bridge, the bridge models are analyzed for three loading cases:

- Multi mode response spectrum analysis ***(MMRS method)***: using the AASHTO'S design response spectrum curve for seismic zone of acceleration coefficient (A) equal to (0.3) and soil profile type II (Site coefficient (S)=1.2).
- Simplified AASHTO method ***(AASHTO method)*** in this method the bridge models are subjected to load of ($S \times A = 1.2 \times 0.3w(x) = 0.36w(x)$) in two orthogonal directions.
- Time history analysis ***(TH method)*** in this method the bridges are assumed to excite by a real earthquake time history accelerogram. El Centro earthquake accelerogram of May 18, 1940 is used for time history analysis. The El Centro horizontal component (north-south component) is applied in the two horizontal directions (X, Y) and the ground acceleration data includes 1559 data points of equal time intervals of (0.02 sec) (***Chopra, 1996***). The numerical values of the data are in units of the gravitational acceleration (g).

The response spectrum for El Centro ground motion with scale ratio of (3/4) and 5% damping ratio agrees well with the AASHTO design response spectrum for acceleration coefficient (A=0.3) and soil type II (S=1.2) as shown in Fig. (4), therefore, the (3/4) scaled El Centro accelerogram with 5% damping ratio is used for linear time history analysis. The response spectrum of El Centro ground motion is obtained and drawing by using SAP Nonlinear program.

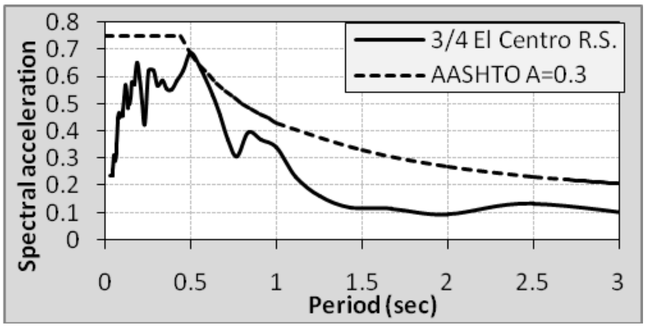


**Fig. (4) Comparison of El Centro spectrum with AASHTO design spectrum for A=0.3**

To investigate the effect of support stiffness, the bridge models are analyzed with four cases of support conditions which are:

- Case (1) **spring support**: springs ($k_e$) and ($k_b$) attached at end of each girder in longitudinal and transverse directions, respectively.
- Case (2) **pin-y:** spring ($k_e$) in longitudinal direction and ($k_b$) is replaced with pin support in transverse direction.
- Case (3) **pin-x:** one end is pin support and another is free in the longitudinal direction, while spring ($k_b$) in transverse direction.
- Case (4) **pin x-y:** one end is pinned and another is free in the longitudinal direction and pin support in the transverse direction.

Fig. (5) shows that the AASHTO design response spectrum have a constant acceleration of (2.5A) for soil type I and II for periods below than (0.43715 sec). The single span bridges which are studied have periods less than (0.43715 sec) of transverse vibration for all support stiffness and of longitudinal vibration with pin-x and pin x-y cases. The bridges are analyzed for seismic force of 2.5 A multiplied by tributary weight.

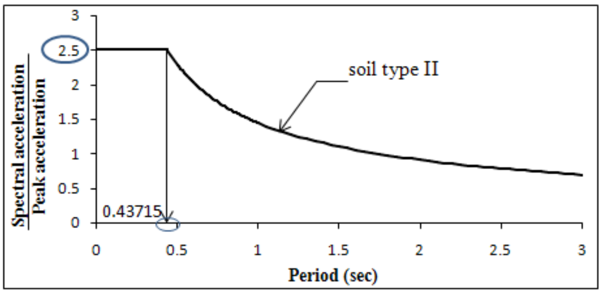


**Fig. (5) Normalized response spectra**

The variation of longitudinal periods against the span length for bridge models with different support conditions is shown in Fig. (6). Whereas, The longitudinal period decreases severely when the elastomeric bearing stiffness reached infinity (pin-x support). However, the periods of spring and pin-y condition coincide. This means that longitudinal vibration is unaffected by the lateral bracing stiffness (cross-frame stiffness). The longitudinal period for all cases increase as the span length increases. Fig. (7) shows the variation of transverse periods against span length for different support conditions. Comparing the transverse period for spring support and pin-y support condition, it can be concluded that the period decrease as the stiffness of cross-frame increases toward infinity (pin-y). The transverse period for pin-x support is closed to period for elastic support for span length upon (30 m) that means the increasing of elastomeric bearing to infinity for span length upon (30 m) does not affect the transverse period significantly.

Maximum longitudinal and transverse deck displacements due to MMRS method versus span length are plotted in Figs. (8) and (9), respectively. It is shown that the displacement increases as span length increases. The longitudinal displacement for bridges which are supported on elastomers is much higher that for bridges with pin-x support, because that the bridges with elastomers support are more flexible and have vibration periods higher than for pin-x support bridges by several times.

Fig. (10) shows the variation of longitudinal shear forces against span length for the three loading cases. In the longitudinal, the simplified AASHTO and time history forces are very close for all support conditions, but the MMRS method is yielding a higher force than (AASHTO) and (TH) methods.

Fig. (11) shows the variation of transverse shear forces versus span length with different support conditions for the three loading cases. In transverse direction, the simplified AASHTO method yields a higher force than time history force at 20m span length, but for span length beyond 20 m, the simplified AASHTO method yields a lower force demand for all support conditions and it become unsafe. While the MMRS method is yielding higher forces than (AASHTO) and (TH) methods.

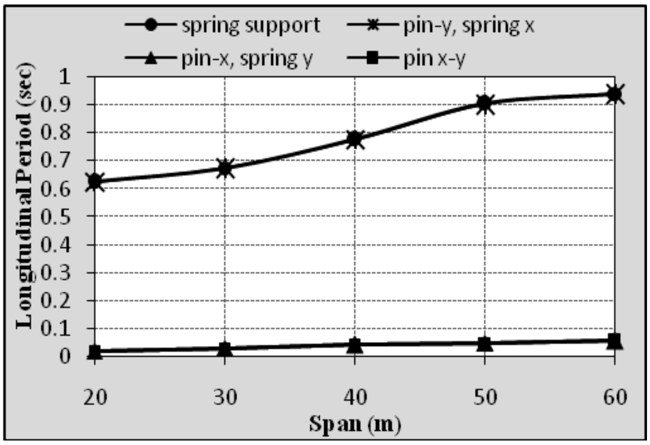


**Fig. (6) Longitudinal period variation versus span length for a single span bridge with different support conditions.**

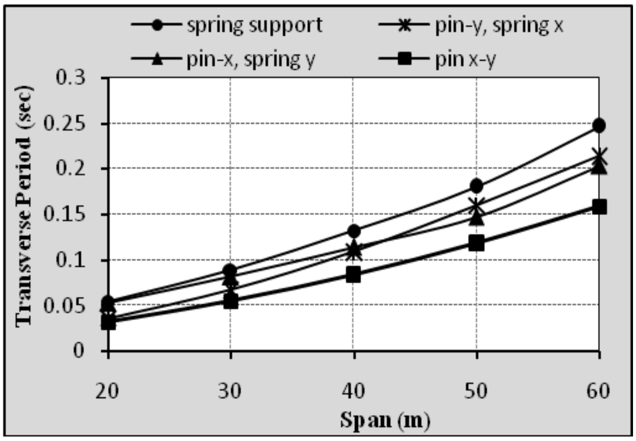


**Fig. (7) Transverse period variation versus span length for a single span bridge with different support conditions**

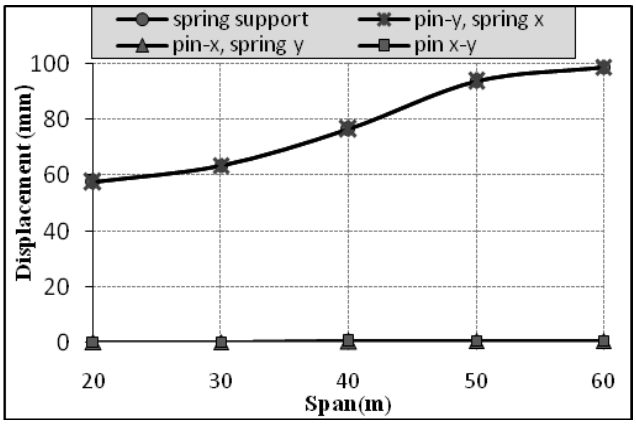


**Fig. (8) Longitudinal displacement due to MMRS method versus span length.**

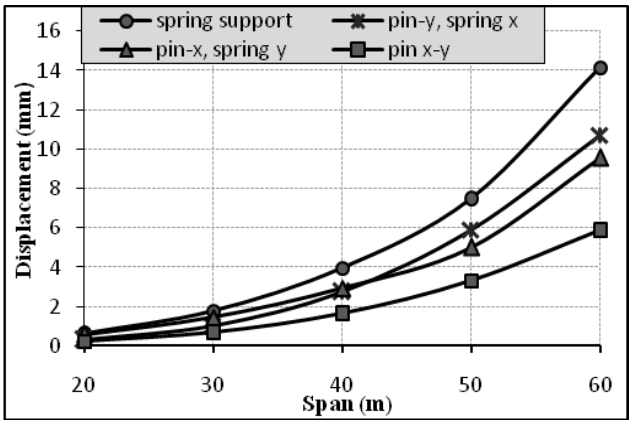


**Fig. (9) Maximum transverse displacement due to MMRS method versus span length.**

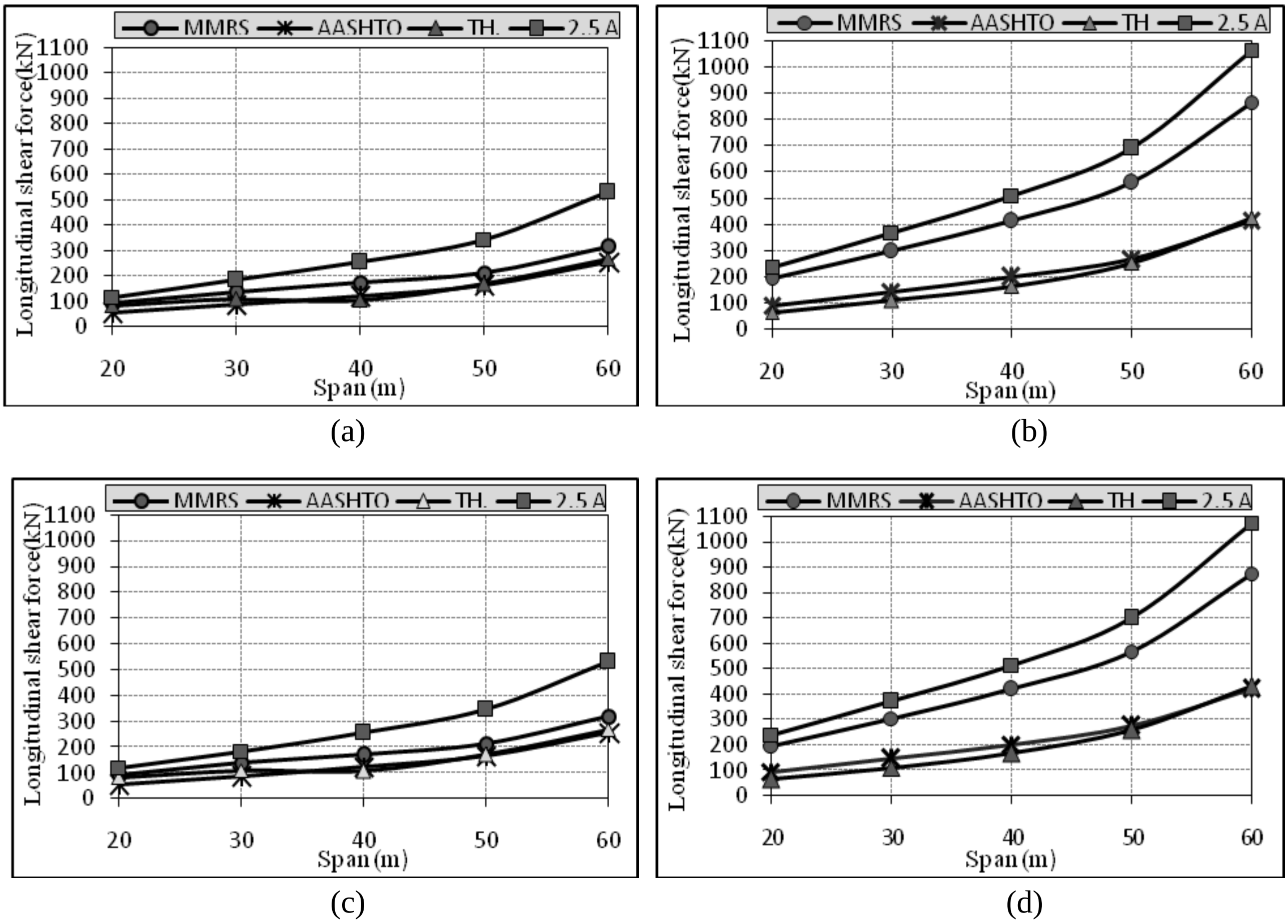


**Fig. (10) Longitudinal shear force versus span length (a) spring support (b) pin-x (c) pin-y (d) pin x-y**

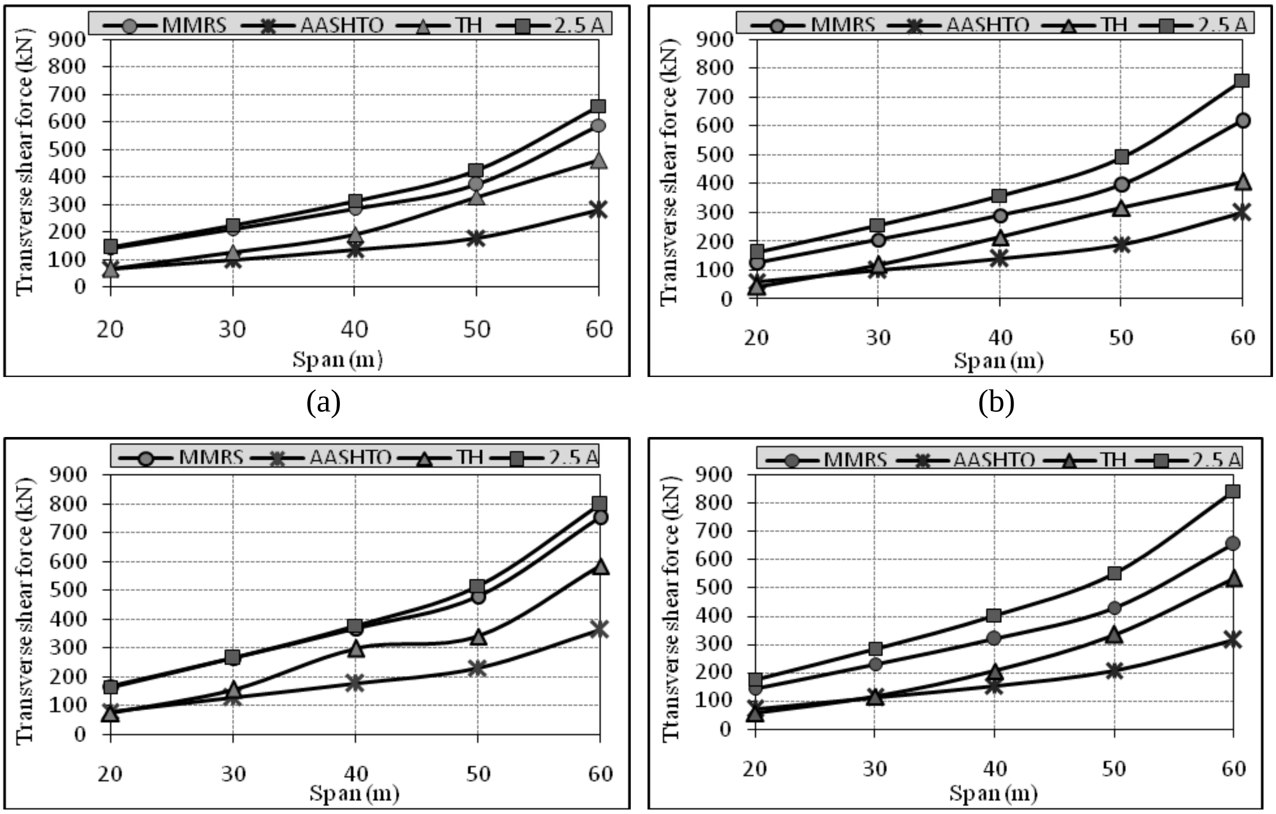


(a) (b) (c) (d)

**Fig. (11) Transverse shear force versus span length (a) spring support (b) pin-y (c) pin-x (d) pin x-y**

## SEISMIC DESIGN OF BRIDGES IN SPC (A)

## INTRODUCTION

AASHTO specification does not consider seismic forces for design of structural components for bridges in low seismic zones such as SPC (A) [A<= 0.09] except for the connection between superstructures to substructures. AASHTO requires that the minimum connection force that must be transferred from superstructure to its supporting through the bearings is 20% of the weight that is effective in the restrained direction.

## CASES STUDIED

Two span continuous steel girder bridges are studied. The same cross section properties that were used for single span bridges are adopted here. The span length of these bridges range between 20 and 60 m with increment of 10 m. The straight and skewed bridges with skew angles varying from 0 to 60 degrees are considered. The bridge is supported on elastomeric bearings in the longitudinal direction and cross-frames in the direction parallel to skew of the deck. The values of stiffness for both elastomeric bearings and cross-frames are determined as explained above. The elastomeric bearing and lateral bracing are designed due to Iraqi loading. The properties of elastomeric bearing and lateral bracing system for end support are summarized in table (3) and for central support are the twice of these for end support. Springs are used to model the elastomeric bearing stiffness and cross-frame stiffness. For skewed bridge, the spring in the direction parallel to the skew that simulates the stiffness of cross-frame is modeling using the nonlinear link element of SAP2000. This is only way one can model skewed spring with this program. However, the nonlinear portion of the spring is not activated. The finite element model of the bridge is shown in Fig. (12).

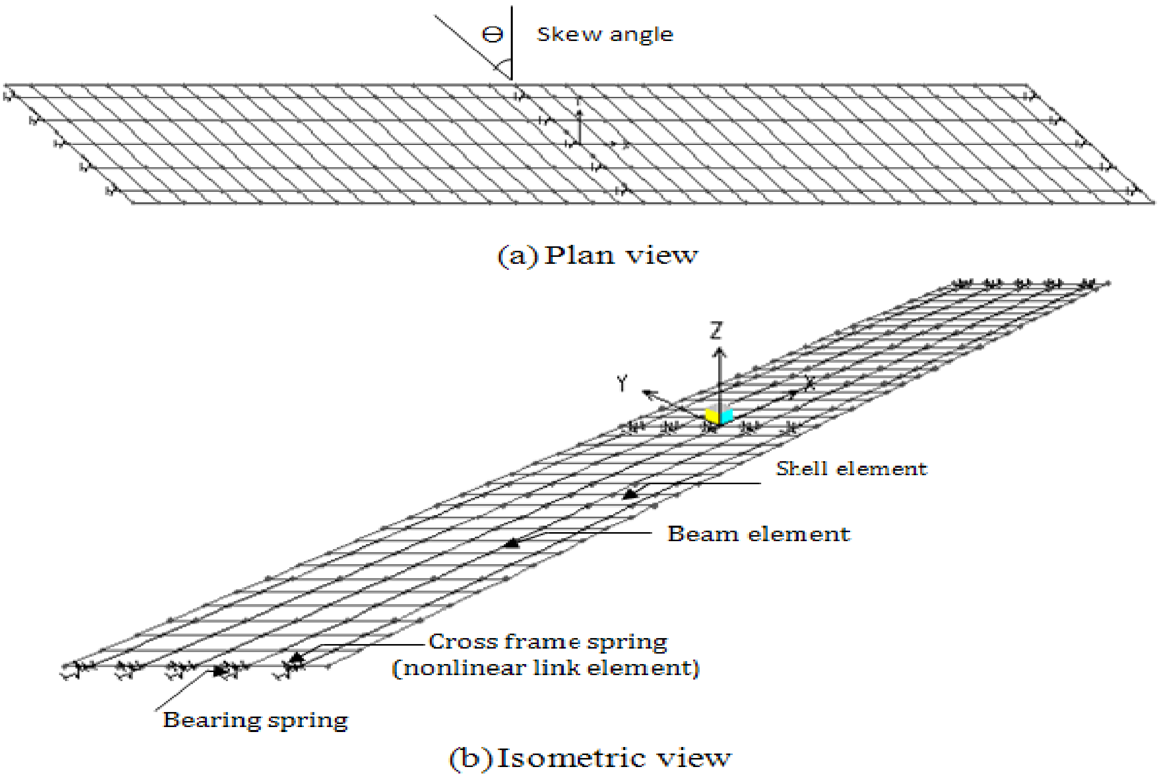


**Fig. (12) Finite element model of two span continuous bridge**

**Table (3) Properties of elastomeric bearing and lateral bracing system**

| L (m) | Elastomeric bearing size (mm) [DIN 4141] | Cross-frame size (mm) | Bearing stiffener size (mm) | $K_e$ (kN/m) | $K_b$ (kN/m) | |
|---|---|---|---|---|---|---|
| | | | | | In. beam | Ex. beam |
| 40 | 200 × 250 × 52 | L120 × 10 | 2PL.130 × 10 × 920 | 1352 | 417237 | 233892 |
| 60 | 200 × 400 × 52 | L130 × 12 | 2PL.150 × 14 × 1320 | 2162 | 298871 | 167750 |
| 80 | 250 × 400 × 74 | L140 × 14 | 2PL.150 × 14 × 1620 | 1887 | 236362 | 141496 |
| 100 | 250 × 400 × 85 | L180 × 14 | 2PL.180 × 16 × 1910 | 1640 | 217565 | 120891 |
| 120 | 300 × 400 × 96 | L200 × 16 | 2PL.200 × 18 × 2280 | 1740 | 181415 | 101798 |

## Analysis of the Bridge Models

A parametric study is performed to study the validity of seismic design force recommended by AASHTO for bridges in SPC (A). The bridge models are analyzed by two methods:

- Response spectrum analysis (dynamic analysis) using the AASHTO's design response spectrum curve with acceleration coefficient (A) equals to (0.05 & 0.09) and soil profile type II (site coefficient(S)=1.2) which are applied in two horizontal orthogonal directions X and Y.
- Simplified AASHTO method (static analysis): according to his method a static load of [0.2 w(x)] is applied uniformly on the bridge model in two horizontal orthogonal directions X and Y.

The vibration modes and corresponding mass ratio of the bridge models are summarized in table (4). The variation of the maximum value of individual elastomer shear forces and bracing forces at end and center support against span length when the base excitation in X and Y directions are summarized in Figs. (13), (14), (15) and (16).

It is noticed that the elastomer and bracing shear forces increase as the bridge length increases. In addition the elastomer shear forces at end and center support and bracing forces at end support decrease for all skew angles ranging from 0 to 45 degrees, but remained much closed and for skew angle over 45 degrees the shear forces increase with increasing skew angles, while bracing forces at center support decrease with increasing skew angle from 0 to 60. It is also observed that bridge with 45 degrees skew angle or higher, the max. responses reverses its direction, for example the max. elastomer shear force is obtained by applying the base excitation in opposite direction (Y).

For all cases, the simplified AASHTO method has yield a higher force than response spectrum method with (A=0.05 & 0.09) except for straight and 15 skewed bridges, whereas AASHTO method underestimates the bracing forces at center support by ratio of (3.025 to 12.262%).

**Table (4) Vibration modes and corresponding mass ratio of the bridge models**

| Skew angle | | 0 | | | 15 | | | 30 | | | 45 | | | 60 | | |
|---|---|---|---|---|---|---|---|---|---|---|---|---|---|---|---|---|
| L (m) | mode | T (sec) | (x) mass% | (y) mass% | T (sec) | (x) mass% | (y) mass% | T (sec) | (x) mass% | (y) mass% | T (sec) | (x) mass% | (y) mass% | T (sec) | (x) mass% | (y) mass% |
| 40 | 1 | 0.6829 | 100.00 | - | 0.7902 | 93.24 | 6.76 | 0.7913 | 74.82 | 25.18 | 0.9697 | 49.77 | 50.23 | 1.3719 | 24.84 | 75.16 |
| | 2 | 0.0521 | - | 96.07 | 0.0517 | 6.45 | 89.38 | 0.0505 | 23.89 | 70.95 | 0.0494 | 44.88 | 44.45 | 0.0538 | 25.21 | 8.31 |
| | 3 | 00268 | - | 1.23 | 0.0276 | 0.10 | 1.35 | 0.0302 | 0.61 | 1.83 | 0.0353 | 3.89 | 3.87 | 0.0426 | 47.09 | 15.58 |
| 60 | 1 | 0.6749 | 100.00 | - | 0.6990 | 93.14 | 6.86 | 0.7804 | 74.55 | 25.50 | 0.9569 | 49.45 | 50.55 | 1.3546 | 24.63 | 75.37 |
| | 2 | 0.0817 | - | 94.89 | 0.8084 | 6.51 | 88.19 | 0.0785 | 23.89 | 69.88 | 0.0759 | 44.95 | 43.90 | 0.0802 | 26.89 | 8.73 |
| | 3 | 0.0233 | - | 4.16 | 0.0237 | 0.28 | 3.90 | 0.0466 | 0.47 | 1.39 | 0.0544 | 3.35 | 3.32 | 0.0652 | 44.19 | 14.48 |
| 80 | 1 | 0.8502 | 100.00 | - | 0.8806 | 93.09 | 6.90 | 0.9834 | 74.44 | 25.56 | 1.2061 | 49.34 | 50.66 | 1.7075 | 24.56 | 75.44 |
| | 2 | 0.1157 | - | 93.64 | 0.1142 | 6.46 | 87.00 | 0.1102 | 23.74 | 69.00 | 0.1051 | 45.00 | 43.71 | 0.1094 | 25.86 | 8.35 |
| | 3 | 0.0333 | - | 5.85 | 0.0338 | 0.40 | 5.53 | 0.0353 | 1.53 | 4.56 | 0.0751 | 2.44 | 2.41 | 0.0901 | 44.03 | 14.38 |
| 100 | 1 | 1.0618 | 100.00 | - | 1.0998 | 93.08 | 6.92 | 1.2283 | 74.40 | 25.60 | 1.5064 | 49.31 | 50.69 | 2.1322 | 24.56 | 75.43 |
| | 2 | 0.1521 | - | 91.78 | 0.1497 | 6.36 | 85.24 | 0.1431 | 23.33 | 67.60 | 0.1344 | 44.70 | 43.36 | 0.1364 | 26.01 | 8.40 |
| | 3 | 0.0436 | - | 7.81 | 0.0442 | 0.54 | 7.45 | 0.0463 | 2.13 | 6.36 | 0.0948 | 1.26 | 1.24 | 0.1143 | 41.43 | 13.52 |
| 120 | 1 | 1.2787 | 100.00 | - | 1.3248 | 93.01 | 6.98 | 1.4802 | 74.23 | 25.77 | 1.8160 | 49.12 | 50.88 | 2.5710 | 24.45 | 75.55 |
| | 2 | 0.2048 | - | 92.12 | 0.2016 | 6.45 | 85.52 | 0.1925 | 23.62 | 67.79 | 0.1801 | 45.37 | 43.66 | 0.1801 | 28.58 | 9.17 |
| | 3 | 0.0583 | - | 7.49 | 0.0591 | 0.52 | 7.13 | 0.0616 | 2.02 | 6.04 | 0.1264 | 1.11 | 1.09 | 0.1525 | 40.17 | 13.03 |

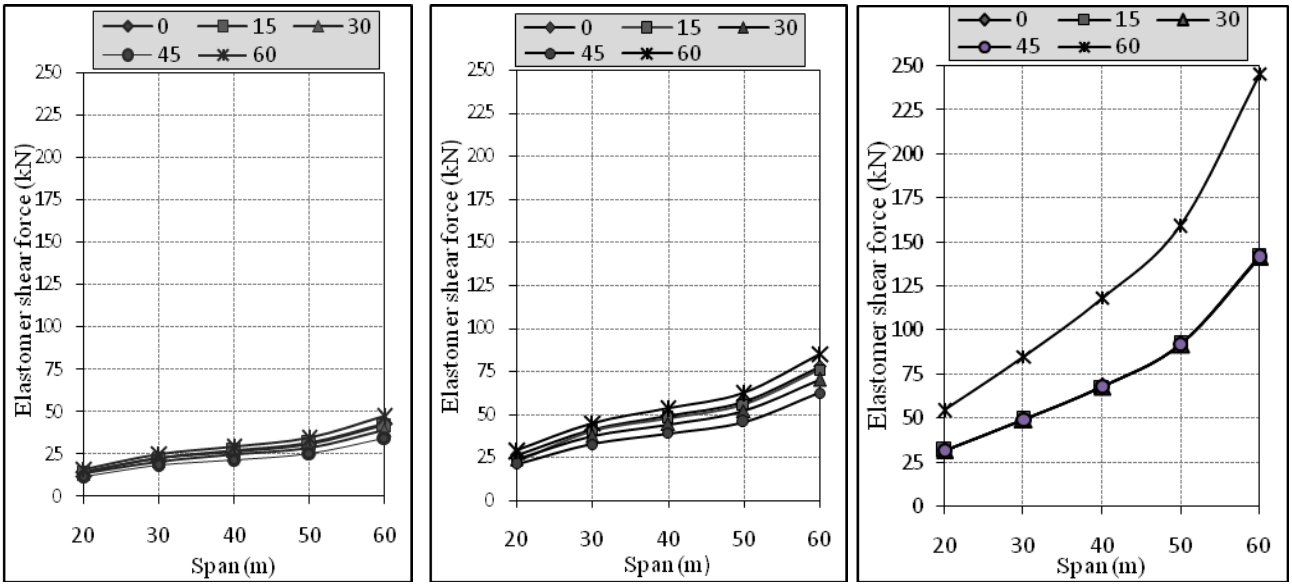


(a) (b) (c)

**Fig. (13) Elastomer shear forces at end support due to (a) response spectrum with A=0.05 (b) response spectrum with A=0.09 (c) AASHTO methods.**

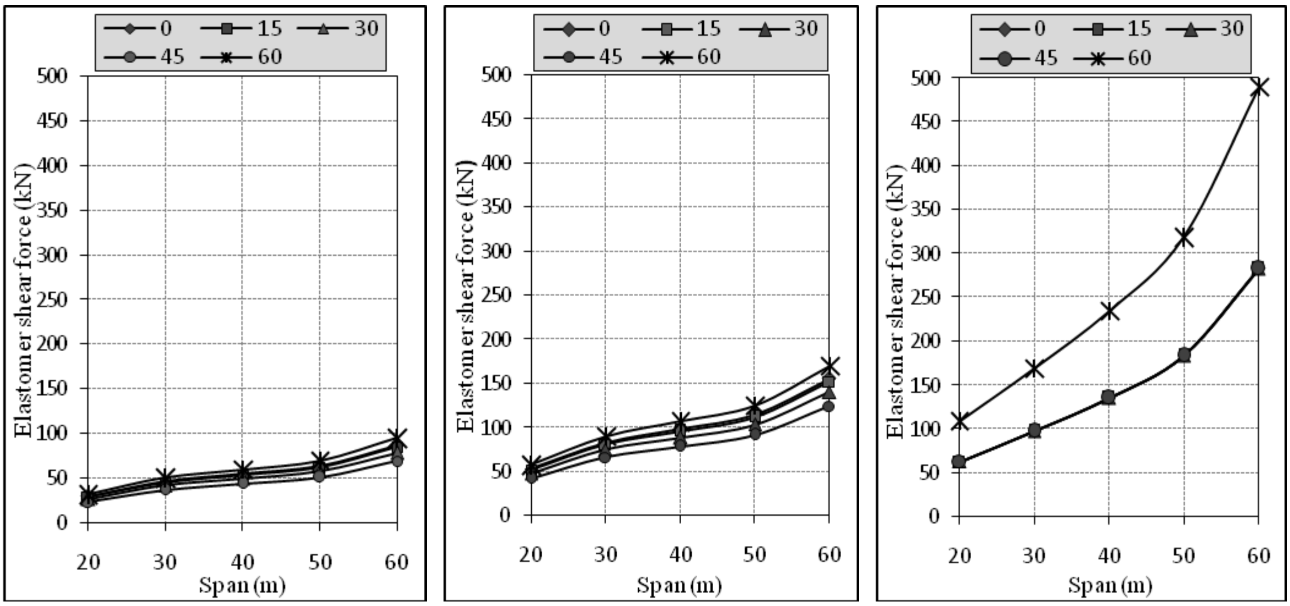


(a) (b) (c)

**Fig. (14) Elastomer shear force at center support due to (a) response spectrum with A=0.05 (b) response spectrum with A=0.09 (C) AASHTO method**

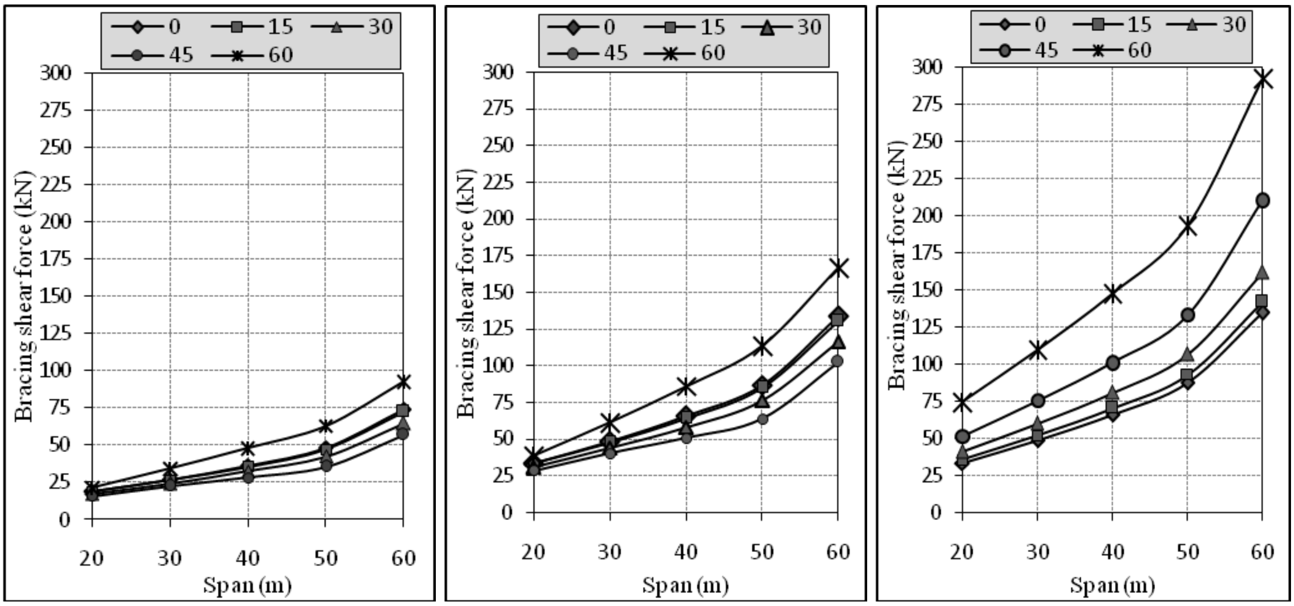


(a) (b) (c)

**Fig. (15) Bracing shear force at end support due to (a) response spectrum with A=0.05 (b) response spectrum with A =0.09 (c) AASHTO method.**

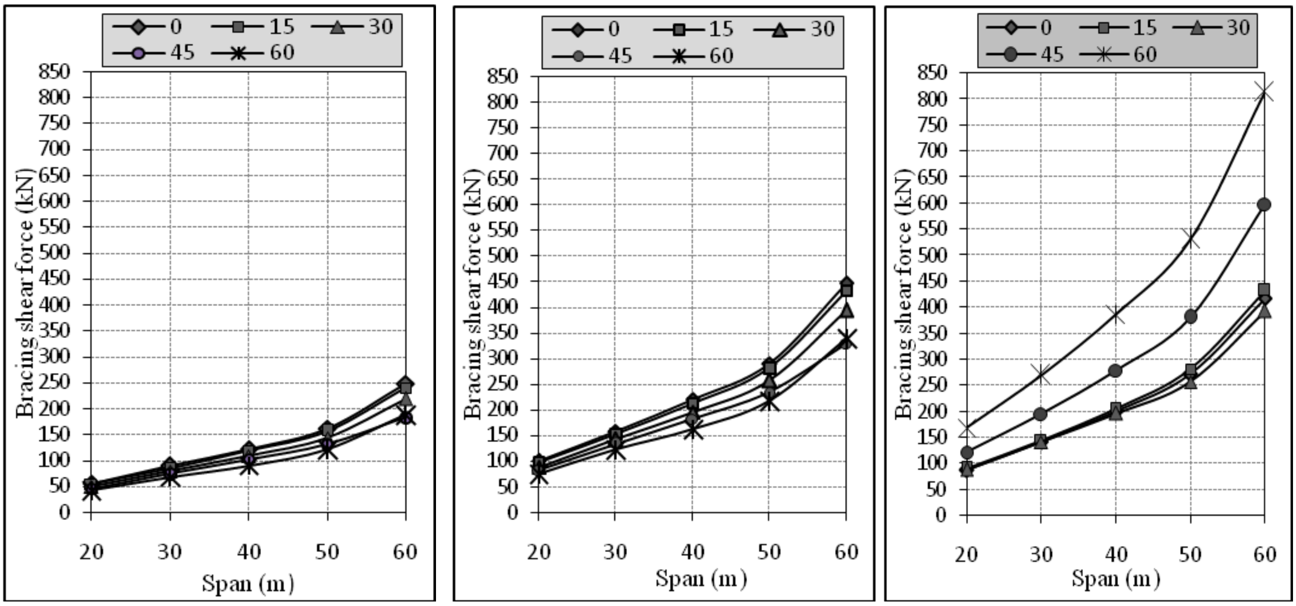


(a) (b) (c)

**Fig. (16) Bracing shear force at center support due to (a) response spectrum with A=0.05 (b) response spectrum with A=0.09 (c) AASHTO method.**

## CONCLUSIONS

- For the case studies considered, the results indicate that the simplified AASHTO method for single span bridges when compared with MMRS method can underestimate the seismically induced transverse shear forces (cross- frame forces) with different support conditions by as much as 52%. The same trend for the longitudinal shear forces (elastomeric bearing forces) for bridges with supports that restrained in the longitudinal direction X (pin-x) and with supports that restrained in the longitudinal and transverse directions (X and Y) (pin x-y) supports. The underestimate ratio range between (19.98–39.05%) for the longitudinal shear force (elastomeric bearing forces) of bridges with spring support and with supports that restrained in transverse direction (Y); therefore, the simplified AASHTO method can become unsafe for zone 3 and 4 and soil type II.

- The results shows that the proposed seismic design force of (2.5 multiplied by acceleration coefficient multiplied by tributary weight w(x)) is suitable and safety method for all cases and can be recommended for single span bridges in lieu the simplified AASHTO method for seismic zone 3 and 4 and for soil type II.

- A parametric study on seismic design force for two span continuous bridges in performance category A (SPC A) shows that the seismic design force [0.2 w(x)] which is recommended by AASHTO is safe and conservative method to predict the shear forces transferred by connection elements to substructures for practical bridge systems in SPC (A).

## REFERENCES

- ***American Association of State Highway and Transportation Officials (AASHTO)***, ″Standard Specification for Highway Bridges″, 17th Edition, 2002.

- ***Chopra, A. K.***, "Dynamics of Structures: Theory and Applications to Earthquake Engineering", Prentice-Hall of India, New Delhi, 1996.

- ***Computer and Structures, Inc. SAP2000, Version 7.4*** "Integrated Structural Analysis and Design", Analysis Reference Volume I, Berkely, CA, 1998.

- ***Mabsout, M. E., Tarhini, K. M. and Frederick, G. R.***, "Finite-Element Analysis of Steel Highway Bridges", Journal of Bridge Engineering, ASCE, Vol. 2, No. 3, pp. 83-87, 1997.

- ***Mast, R., Marsh, L., Spry, C. and Johnson, S.***, "Seismic Bridge Design Application-Part Two", NHI Course No. 13063, Report No. FHWA-SA-97-018, Federal Highway Administration, Washington, 1996.

- ***Tarhini, K. M. and Frederick, G. R.***, "Load Distribution on Highway Bridges Using ICES-STRUDL Finite Element Analysis", Journal of Computers and Structures, Vol. 32, No.6, pp.1419-1428, 1989.

- ***Zahrai, S. M. and Bruneau, M.***, "Impact of Diaphragms on Seismic Response of Straight Slab-on-Girder Steel Bridges", Journal of Structural Engineering, ASCE, Vol. 124, No. 8, pp. 938-947, 1998.

## ABBREVIATIONS

| | |
|---|---|
| AASHTO | American Association of State Highway and Transportation Officials |
| ASCE | American Society of Civil Engineers |
| Ex. | Exterior |
| In. | Interior |
| MMRS | Multi mode response spectrum method |
| SAP 2000 | Structural Analysis Program |
| UBC | Uniform Building Code |

## SYMBOLS

| | |
|---|---|
| $A$ | Cross sectional area of steel beam |
| $b_{fb}$ | Bottom flange width of steel beam |
| $b_{ft}$ | Top flange width of steel beam |
| $h$ | Depth of steel beam |
| $I_y$, $I_z$ | Second moment of area about y and z axes respectively |
| $k_b$ | Lateral bracing stiffness |
| $k_e$ | Elastomeric bearing stiffness |
| $L$ | Bridge length |
| $t_{fb}$ | Bottom flange thickness of steel beam |
| $t_{ft}$ | Top flange thickness of steel beam |
| $t_s$ | Deck slab thickness |
| $t_w$ | Web thickness of steel beam |

Number 3 Volume 16 September 2010 Journal of Engineering

# EFFECT OF MINERAL FILLER TYPE AND CONTENT ON PROPERTIES OF ASPHALT CONCRETE MIXES

Eng.Noor M. Asmael
(Assis.Lecturer / HWY and
Transportation Department
Al-Mustansiriyah University )

**ABSTRACT**
Some of the newly constructed highway pavements in Iraq have shown premature failures with consequential negative impacts on both roadway safety and economy. Major types of these failures are permanent deformation (rutting) and cracking. Fillers were suspected to be a major contributor to these failures. The objective of this study is to evaluate the influence of new different fillers extracted from different local sources on the performance of asphalt mixtures. The effect of filler type and content on the failures potential of asphalt concrete as well as other mixes properties was investigated. A detailed laboratory study is carried out by preparing asphalt mixtures specimens using aggregate from Al-Taji quarry, (40-50) grade asphalt from dourah refinery and three different types of fillers (Portland cement, Silica fume, and Fly ash) were tested in the laboratory. Marshal Mix design was made using all types of fillers and different ratios to evaluate the performance of different types and filler quantities in the asphalt mixture. The mechanical properties of mixes were studied using indirect tensile strength, creep and marshal tests. Three different tests temperature (15,30,45C°) were employed in the indirect tensile test to investigate the susceptibility of these mixes to change in temperature. Results of this study indicate that replacement of Portland cement by 9.8% of silica fume aggravates resistance of the mixes to rutting and cracking. Furthermore, coal fly ash cannot be used as mineral filler in hot mix asphalt paving applications.

**الخلاصة**

البعض مِنْ أرصفةِ الطرق المَبْنيةِ حديثاً في العراق تحدث بها حالاتَ فشل لها تأثيراتِ سلبيةِ على كل من الأمان واقتصاد الطرق. النوع الرئيسي لحالاتِ الفشل هذه الأخاديد والشقوق. المواد المالئة تُعتبر من العوامل المساهمة في حدوث مثل حالاتِ الفشل هذه. إنّ هدفَ هذه الدراسةِ هو تُقييّمَ تأثيرَ المواد المالئة المختلفِة الجديدِة المستخرجة مِنْ المصادرِ المحليّةِ المختلفةِ على أداءِ الخلطاتِ الإسفلتية. إن تأثير النوعِ ومحتوى المواد المالئة على إمكانيةِ حدوث حالاتَ فشل الخرسانةِ الإسفلتية بالإضافة إلى خواص الخلطات الأخرى قد تم التحُقّق منها. تم عمل دراسة مفصلة بتحضير نماذج خلطات إسفلتية باستعمال ركام من مقلع التاجي و إسفلت (40−50) من مصفاة الدورة و ثلاثة أنواعِ من المواد المالئة (الاسمنت البورتلندي، دخان السيليكا، رماد الفحم) قد تم اختبارها في المختبر. تم عمل تصميم مارشال باستعمال مختلف أنواع المواد المالئة والنِسَبِ المختلفةِ لتَقييم أداءِ الأنواعِ المختلفةِ وكمياتِ المادة

المالئة في الخَلِيْطِ الإسفلتي. تم دراسة الخواص الميكانيكية للخلطات باستعمال فحص الشدِّ الغير مباشر، فحص الزحف وخواص مارشال. ثلاثة من درجات الحرارة المختلفةِ (15,30,45C°) قد إستخدمتْ في فحص الشدِّ الغير مباشرِ لتَحرّي سهولةِ تأثّر هذه الخلطات بالتغير بدرجةِ الحرارة. نَتائِج هذه الدراسةِ تُشيرُ بان استبدالِ الإسمنتِ البورتلندي ب الـ9.8 % مِنْ دخانِ السيليكا يحسن مقاومةَ المزيجِ إلى الزحف والشقوق. علاوة على ذلك، إن رماد الفحم لايمكن استعماله كمالئ معدني في تطبيقات خلطات التبليط الاسفلتي .

**KEY WORD:** Mineral Filler, Silica Fume, Fly Ash.

## INTRODUCTION

Pavement systems in Iraq are exposed to a multitude of severe environmental factors, mainly the heavy axle load applied on the road, the high traffic and the excessive high temperature. Road usually show excessive failures at an early stage of the pavement life. A major step in the improvement of the existing performance of roads starts with modification of mix design. The filler plays a major role in the properties and behavior of bituminous paving mixtures *(Ilan Ishai, et al, 1980*). The mechanical properties of bituminous road pavement depend decisively upon the properties of its filler-bitumen (*S.Huschek,et al,1980*). For modification of asphalt paving materials, the high quality additives are quit expensive for the mass production of bituminous mixtures, a solution to this problem can be obtained by considering the influence of natural mixture ingredients, such as filler (*Ilan Ishai, Joseph Craus, 1980*). Mineral fillers were originally added to dense-graded HMA paving mixtures to fill the voids in the aggregate skeleton and to reduce the voids in the mixture (*Brian D. Prowell, et al, 2005*). Filler used in the asphalt mixture are known to affect the mix design, specially the optimum asphalt content. The term (filler) is often used loosely to designate a material with a particle size distribution smaller than #200 sieve. The filler theory assumes that "the filler serves to fill voids in the mineral aggregate and thereby create dense mix", (*I.Abdulwahhab, 1981*). Filler particle are beneficial because of increased resistance to displacement resulting from the large area of contact between particles. It was found that fillers increase compactive effects required to compact specimens to the same volume or air void content. This effect becomes more pronounced with increasing concentration of fillers. An early study made by Clifford Richardson, concluded that the role of the filler was more than void filling, implying that some sort of physical – chemical interaction occurred. Increasing amount in excess of upper limits produced pavements that cracked and checked while being rolled. In warm weather traffic tests, the pavement with excessive filler showed more cracking and checking under load. The cold weather tests showed no detrimental effects resulting from the excessive filler (*Ervin L. Dukatz, et al, 1980*). It is believed that the filler had a dual role: a) a portion participates in the particle to particle contact, and b) the rest floats in the asphalt, forming a high consisting binder. High filler concentration introduced non_newtonian flow behavior.(*Ervin L. Dukatz, et al, 1980*). The addition of filler to the mixture can improve adhesion and cohesion substantially. The effect of the addition of filler is directly related to their characteristics and the degree of concentration of the filler in the bitumen-filler system. The addition of filler might benefit the reduction of hardening by age and improve the property of flow at low temperature. The function of mineral filler is essentially to stiffen the binder. A higher percentage of very fine filler may stiffen the mixture excessively, making it difficult to work with and resulting in a crack susceptible mixture. According to various studies, the properties of mineral filler especially the material passing 0.075mm (No. 200) sieve (generally called P200 material) have a significant effect on the performance of asphalt paving mixtures in terms of permanent deformation, fatigue cracking, and moisture susceptibility. ( *Kandhal, et al ,1998*)

## OBJECTIVE OF THE STUDY

- To determine the effect of filler type and content on the mechanical properties of asphalt concrete paving mixture.
- To study the effect of new material of mineral filler on the properties of asphalt mixtures and compared it with traditional filler (Portland cement)

## MATERIALS

The Materials used in this study are locally available and selected from the currently used materials in road construction in Iraq.

### Asphalt Cement

One type of asphalt cement with penetration graded of (40-50) was used in this study; it is obtained from Dourah refinery. The physical properties of this type of asphalt cement are shown in Table (1).

**Table (1): Physical Properties of Asphalt Cement.**

| Test | Unit | ASTM | Results D ( 40-50 ) |
|---|---|---|---|
| Penetration 25°C,100 gm , 5 sec. | 1/10 mm | D5 | 43 |
| Absolute Viscosity at 60°C (*) | Poise | D2171 | 2070 |
| Kinematics' Viscosity at 135C (*) | C St. | D2170 | 370 |
| Ductility (25°C, 5 cm/min.) | Cm. | D 113 | >100 |
| Softening Point ( Ring & Ball ) | C° | D 36 | 50 |
| Specific Gravity at 25°C (*) | ……. | D 70 | 1.04 |
| Flash Point | C° | D 92 | 332 |

(*) The test was conducted in Dourah refinery

### Aggregate

One type of crushed aggregate was used in this study, which was brought from Mix plant of Amanat Baghdad. The source of this type of aggregate is Al-Taji quarry. The physical properties of the aggregate are shown in Table (2). One nominal maximum size (12.5) was selected with two selected aggregate gradations; these two gradations were selected to compare the effect of restricted zone on the mix performance. Where G2 gradation is passing through the Superpave limitation control points and restricted zone, while, the gradation G1 is located out of the Superpave restricted zone requirement. Mixes design were prepared for heavy traffic level using the traditional Marshall methodology. These gradations are shown in Figure (1) and presented in Table (3). Three Selected Combined Gradations of Aggregate and Filler are shown in Table (4).

**Table (2): Physical Properties of Al-Taji Quarry Aggregate.**

| Property | Coarse Aggregate | | Fine Aggregate | |
|---|---|---|---|---|
| | G1 | G2 | G1 | G2 |
| Bulk specific gravity ASTM C 128 | 2.52 | 2.53 | 2.6 | 2.61 |
| Apparent specific gravity ASTM C127 and C128 | 2.525 | 2.528 | 2.632 | 2.651 |
| Percent water absorption ASTM C 127 and C 128 | 0.54 | 0.55 | 0.62 | 0.933 |

**Table (3): Job Mix Formula's for Wearing Course of the Selected Gradation.**

| Sieve opening ( mm ) | Percent Passing Gradation Shape | |
|---|---|---|
| | G1 | G2 |
| 19 | 100 | 100 |
| 12.5 | 94 | 91 |
| 9.5 | 85 | 79 |
| 4.74 | 70 | 57 |
| 2.75 | 42 | 43.4 |
| 1.18 | 29 | 34 |
| 0.6 | 20.2 | 27 |
| 0.3 | 14.4 | 16 |
| 0.15 | 11.6 | 12.2 |
| 0.075 | 9.8 | 9.8 |

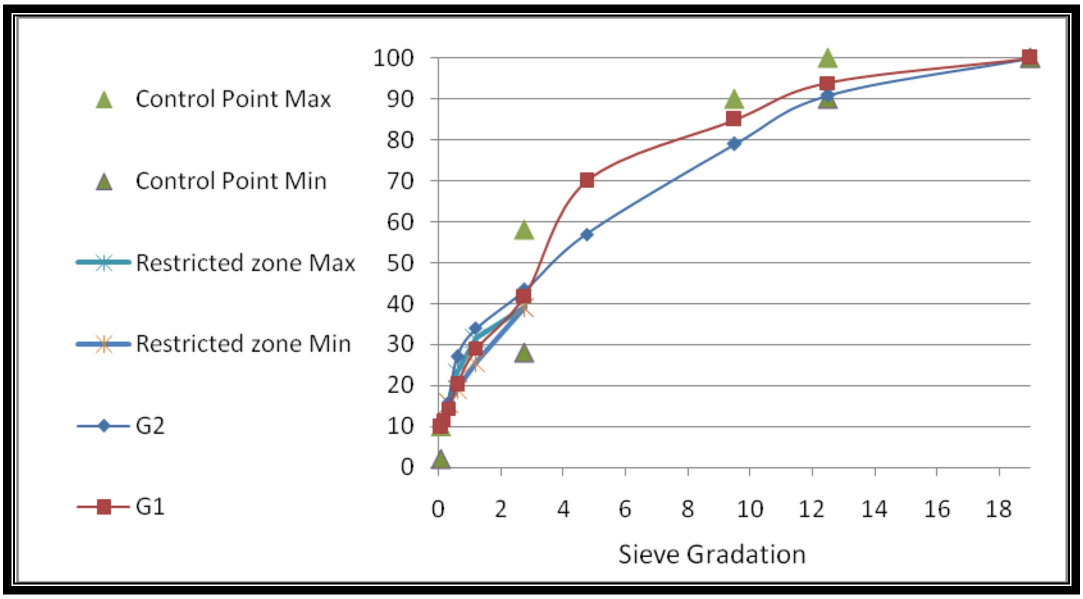


**Figure (1) Gradation of Wearing Course for two selected gradation.**

**Table (4) Selected Combined Gradations of Aggregate and Filler**

| Sieve Size (mm) | Percent Filler | | | | | |
|---|---|---|---|---|---|---|
| | 5.8% (C) | | 7.8% (B) | | 9.8% (A) | |
| | Percent Passing | | | | | |
| | Gradation Shape | | | | | |
| | G1 | G2 | G1 | G2 | G1 | G2 |
| **19** | 100 | 100 | 100 | 100 | 100 | 100 |
| **12.5** | 94 | 91 | 94 | 91 | 94 | 91 |
| **9.5** | 85 | 79 | 85 | 79 | 85 | 79 |
| **4.74** | 70 | 57 | 70 | 57 | 70 | 57 |
| **2.75** | 42 | 43.4 | 42 | 43.4 | 42 | 43.4 |
| **1.18** | 29 | 34 | 29 | 34 | 29 | 34 |
| **0.6** | 20.2 | 27 | 20.2 | 27 | 20.2 | 27 |
| **0.3** | 14.4 | 16 | 14.4 | 16 | 14.4 | 16 |
| **0.15** | 11.6 | 12.2 | 11.6 | 12.2 | 11.6 | 12.2 |
| **0.075** | 5.8 | 5.8 | 7.8 | 7.8 | 9.8 | 9.8 |
| **Mix Composition** | | | | | | |
| **Asphalt** | 4.75% | 4.55% | 4.75% | 4.55% | 4.75% | 4.55% |
| Gmm of Mix when Silica Fume is used | | | | | | |
| **Gmm** | 2.4082 | 2.4044 | 2.406 | 2.4023 | 2.404 | 2.4 |
| Gmm of Mix when Fly Ash is used | | | | | | |
| **Gmm** | 2.314 | 2.3105 | 2.28 | 2.278 | 2.2498 | 2.2462 |
| Gmm of Mix when Portland Cement is used | | | | | | |
| **Gmm** | 2.4339 | 2.4301 | 2.4409 | 2.437 | 2.449 | 2.445 |

## Mineral Filler

It has long been recognized that the filler plays a major role in behavior of the asphalt mixtures. The importance of fillers in asphalt mixtures has been studied extensively. In this study three types of fillers (Portland cement, silica fume, and fly ash) has been used, which is obtained from the different local sources. The physical properties of different fillers are shown in Table (5).

Table (5): Physical Properties of Mineral Fillers.

| Property | Portland cement | Silica fume | Fly Ash |
|---|---|---|---|
| Specific Gravity | 3.12 | 2.5 | 1.41 |
| % Passing sieve No.200 ASTM C117 | 90 | 90 | 90 |

## Characterization of the Mineral Filler

Fillers fill voids between coarse aggregates in the mixture and alter properties of the binder, (*Yong-Rak Kim et al ,2003*). Mineral filler increase the stiffness of the asphalt mortar matrix, improving the rutting resistance of pavements. Mineral filler also help reduce the amount of asphalt drain down in the mix during construction which improve durability of the mix by maintain the amount of asphalt initially used in the mix. The addition of fillers is known to stiffen asphalt. The degree of stiffening is a function of several filler and asphalt properties, which are not well understood (*Naga Shashidhar[1], Pedro Romero[1] 1998*). The fillers used in this study are:

**Portland cement**

Portland cement is essentially a calcium silicate cement, which is produced by firing to partial fusion, at a temperature of approximately 1500C°,(*John Newman, Ban Seng Choo, 2003*).

***Fly Ash***

Since the first edition of Fly Ash Facts for Highway Engineers is in 1986. Fly ash is the finely divided residue that results from the combustion of pulverized coal. It can be used as cost-effective mineral filler in hot mix asphalt (HMA) paving applications. Where available locally, fly ash may cost less than other mineral fillers. Also, due to the lower specific gravity of fly ash, similar performance is obtained using less material by weight, further reducing the material cost of HMA.,(*American coal ash association, 2003*).

***Silica Fume***

Silica fume is a by-product resulting from the reduction of high purity quartz with coal in electric arc furnaces in the manufacture of silicon and ferrosilicon alloys.

Silica fume is an ultra-fine powder consisting of nearly spherical particles around 100 times smaller than a grain of cement. A size distribution of silica fume, relative to portland cement and fly ash, is shown in the following Figure(2), (*Prof.Zongjin Li,2007*).

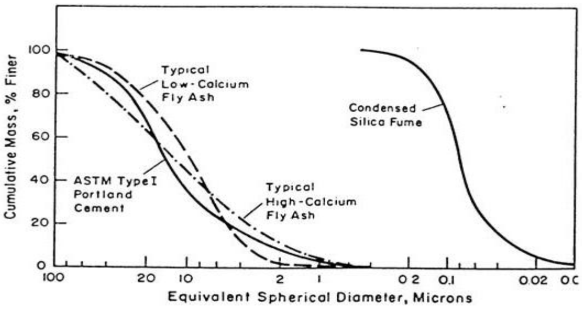


**Figure** Comparison of particle size distributions of portland cement, fly ashes, and condensed silica fume.

**Figure(2), Size Distribution of Silica Fume, Fly Ash, and Portland Cement.**

**Preparation of Mix Design**

In the work reported in this paper a series of minus No. 200 (75 m) mineral fillers were used to prepare and characterize hot-mix asphalt concrete. The same mix design methods that are commonly used for hot mix asphalt paving mixtures are also applicable to mixes in which different filler is used. The percentage of filler to be incorporated into the design mix is the three percentage (5.8%, 7.8%, 9.8%), denoted as C, B, A respectively, to determine which percentage satisfy all the required design criteria. The mix proportions and aggregate gradation for the asphalt mixtures tested are shown in Table( 3) and Table (4). During the mixing in the laboratory, it is noticed that the mixtures with fly ash became so stiff that it could not be mixed by hand, and silica fume shows good dispersion throughout the mixture.

**Testing Procedures**

**Indirect Tensile (IDT) Strength Test**

The indirect tensile test was developed to determine the tensile properties of cylindrical concrete and asphalt concrete specimens through the application of a compression load along a diametrical plane through two opposite loading heads. This type of loading produces a relatively uniform stress acting perpendicular to the applied load plane, causing the specimen to fail by splitting along the loaded plane, (*Ahmed, et al , 2006*). Test specimens 2.5 inches thick and 4 inches diameter were compacted and then tested using curved steel loading strips 0.5 inch wide. The maximum load carried by the specimen was found, and the indirect tensile stress at failure was determined and presented.

***Static Creep Test***

The Static Creep test method is used to determine the resistance to permanent deformation of HMA at temperatures and loads similar to those experienced in the field. Measured creep properties include strain_time relationship and stiffness. According to TxDOT, the main disadvantage of this test is that the results do not seem to be repeatable. The main advantage of this test is that it can be performed within a day and test results reasonably predict the field performance (*Rajpal Sugandh, et al, 2007*).

**Test Result and Discussion**

**Effect of Mineral Fillers on the Volumetric Properties of HMA**

The HMA specimens were prepared in the laboratory; it were tested in the laboratory to determine the properties of asphalt concrete mixtures, such as, Marshall properties (bulk density, air voids, voids filled with asphalt, voids in mineral aggregate), to evaluate their effect on the HMA behavior. Figures (3,4,5) shows that the relations between filler content and Marshall properties is typical to common trend in asphalt content mixes. It can be seen from Figures, that these volumetric properties are checked against the requirements. For silica fume and Portland cement, all the requirements are satisfied. For the silica fume, increasing the filler content increased the air voids. This abnormal effect may be due to the stiffening of the mixture by silica fume. It can be seen from Figures, that the volumetric properties of fly ash filler shows, that VTM, VMA values are higher if compared with Marshall properties values and lower VFA values. The specific gravity of fly ash is low, therefore, a given weight percentage of fly ash will usually occupy a greater volume than that of a conventional filler material.

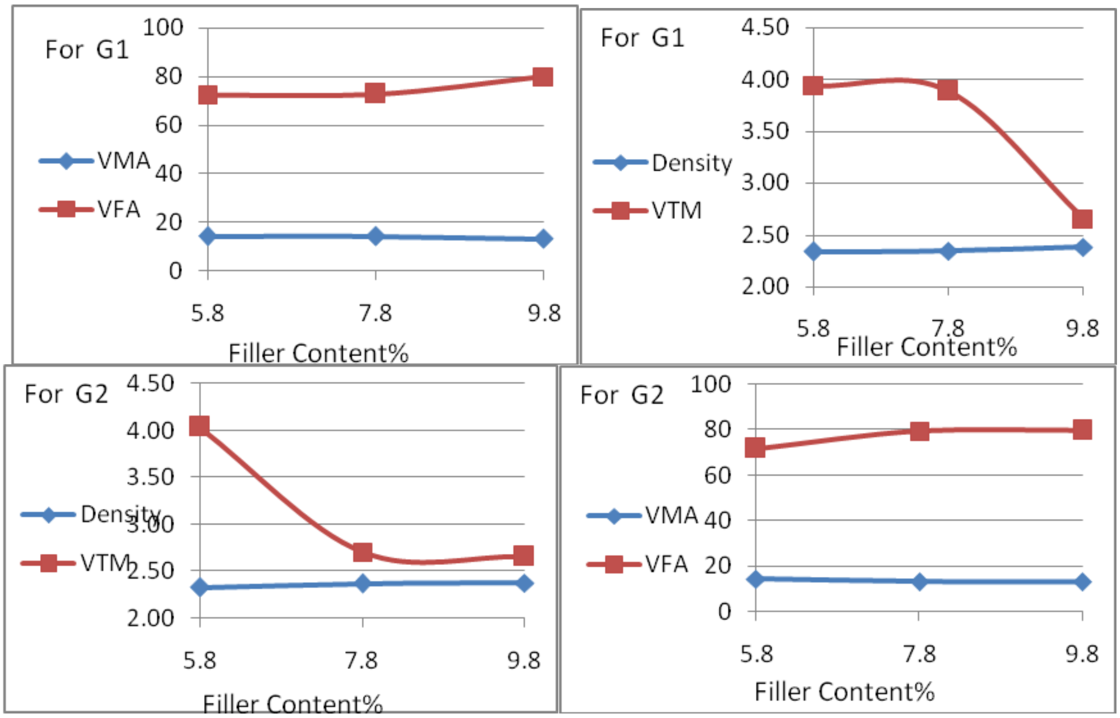


Figure (3) Effect of Portland Cement on volumetric properties.

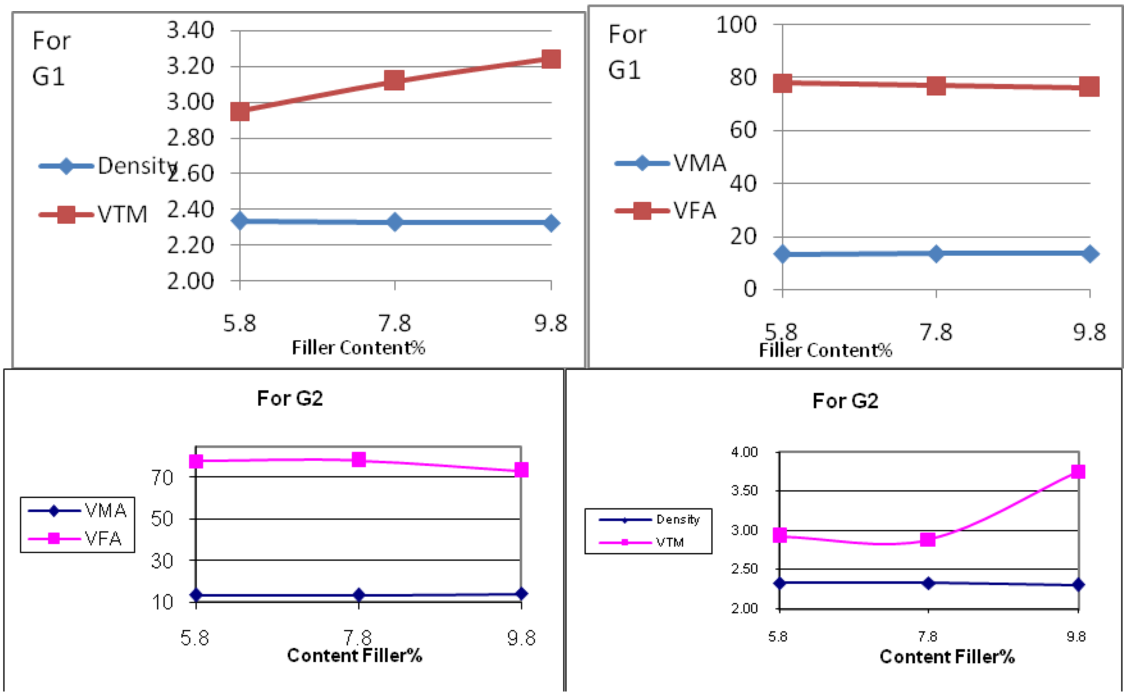


Figure (4) Effect of Silica Fume on volumetric properties.

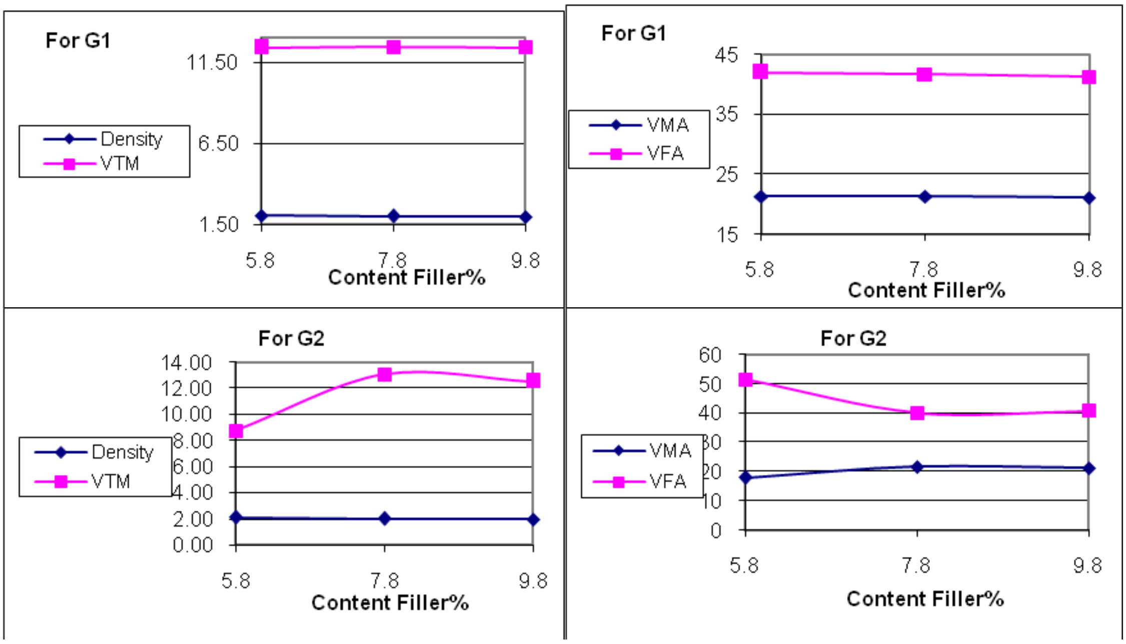


Figure (5) Effect of Fly Ash on volumetric properties.

## EFFECT OF MINERAL FILLERS ON THE PERFORMANCE OF HMA

Filler content have a considerable effect on the mixture making it act as a much stiffer, and thereby affect the HMA pavement performance including its fracture behavior. The indirect tensile strength has been used to evaluate the mixture resistance to cracking. To study the effect of varying test temperature on the quantity of mixture, three different temperatures (15, 30 and 45C°) are used in the indirect tensile strength test. Figures from (6) to (8) show the influence of mineral fillers on tensile strength at different test temperatures. For filler type, from figure (8) shows that mixture with silica fume has the highest tensile strength at all test temperatures. And it indicated higher value of temperature susceptibility than other fillers, indicating that silica fume can be expected to provide excellent resistance to stripping. Figure (7) shows that mixtures with fly ash have the lowest tensile strength. Amount in excess of filler content of fly ash produced pavements that cracked and checked while being rolled. The failure in the tensile strength is attributed to the many voids that weaken the cross-section. The success of Portland cement as a filler was believed to be caused partly by its high specific gravity.

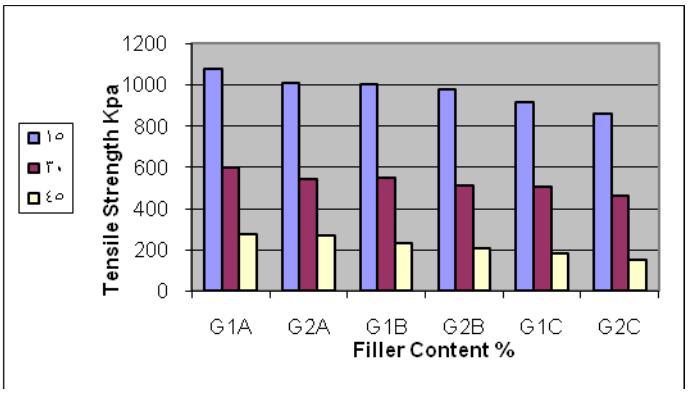


**Figure(6) Effect of Portland Cement on Tensile Strength for asphalt mixtures**

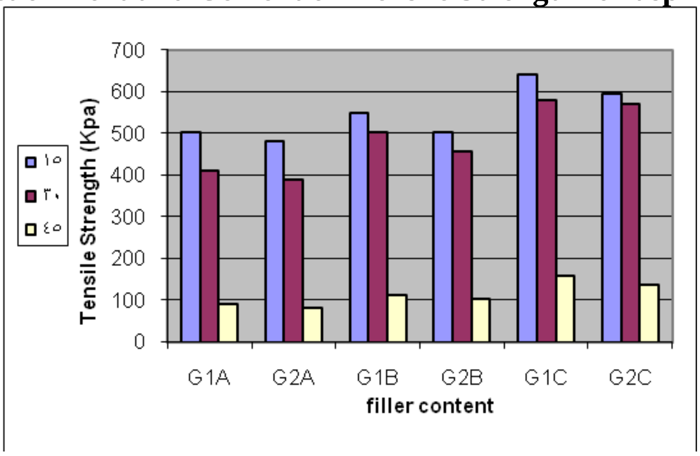


**Figure(7) Effect of Fly Ash on Tensile Strength for asphalt mixtures**

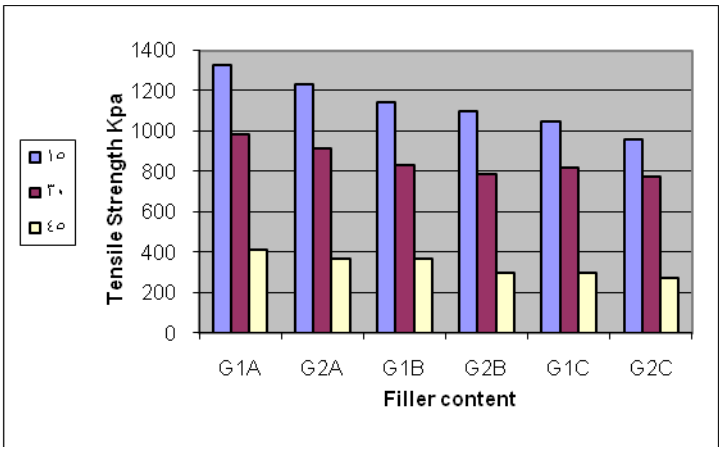


**Figure(8) Effect of Silica Fume on Tensile Strength for asphalt mixtures**

The rheological properties of the material resulting from the incorporation of mineral filler into mixture may differ substantially from those of the traditional mixture. The creep test results, reported in Figures (9,10,11) and presented in the form of strain_time curves for various mixes. From Figures, it can be conclude, that fly ash had a very significant effect on the creep properties of the asphalt concrete mixtures. At 5.8% and 7.8% percent, Portland cement have the less permanent strain when comparing with silica fume, but when the percent is increased to 9.8%, the silica fume has the lowest permanent strain.

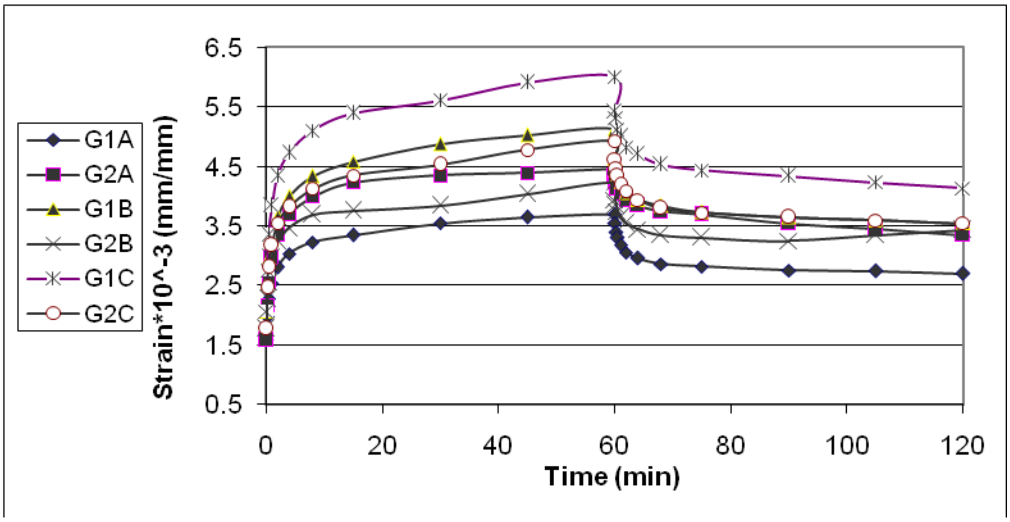


**Figure(9) Strain-Time relationship for Cement filler in asphalt mixtures.**

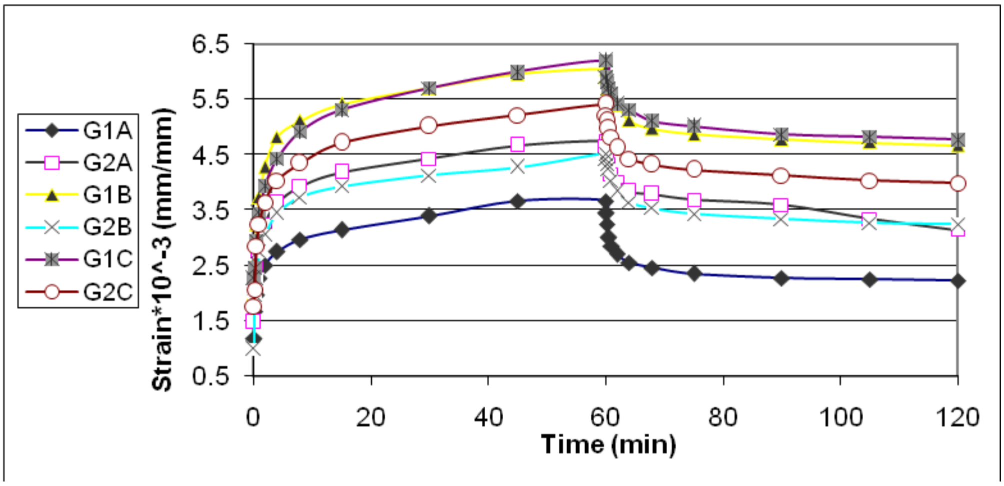


**Figure(10) Strain-Time relationship for Silica fume filler in asphalt mixtures.**

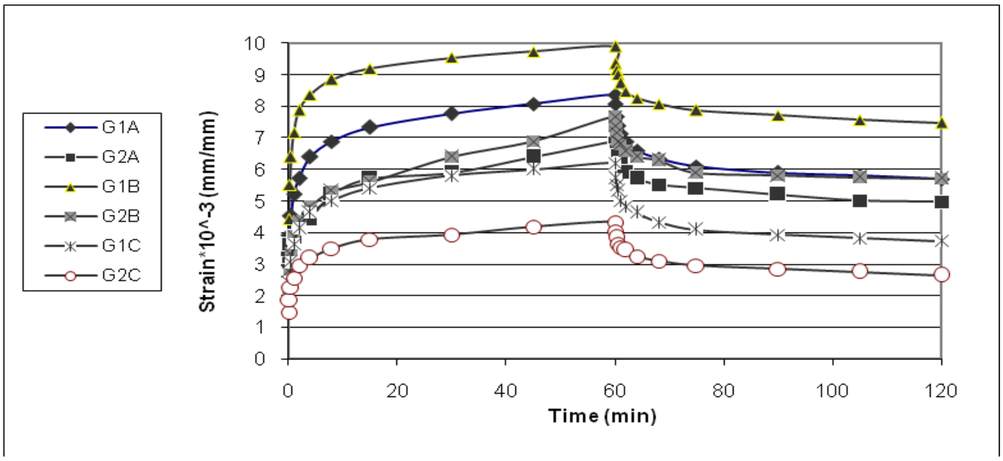


**Figure(11) Strain-Time relationship for Fly ash filler in asphalt mixtures.**

## CONCLUSIONS

Based on the experiment employed in this study, the following conclusions could be made.

- Fly ash has less workability and less tensile strength of asphalt concrete mixtures when compared to other asphalt concrete mixes.
- Silica fume and Portland cement have more workability and higher tensile strength in asphalt concrete mixes.
- The compaction effort required to achieve density increases as the concentration of filler in asphalt concrete mixtures is increased.
- The incorporation of fly ash filler in the mixture will always cause a significant reduction in mixtures mechanical properties.
- The percentage of fly ash filler to be incorporated into the mix design is the lowest percentage that will enable the mix to satisfy all the required design criteria.

## REFERENCES


- Ilan Ishai, Joseph Craus, and Arieh Sides, "A Model for Relating Filler Properties to Optimal Behavior of Bituminous Mixtures", AAPT, 1980, Vol.49.
- S.Huschek and CH.Angst, "Mechanical Properties of Filler-Bitumen Mixes at High and Low Service Temperatures", AAPT,1980,Vol.49.
- Ilan Ishai, and Joseph Craus , "Effect of the Filler on Aggregate-Bitumen Adhesion Properties in Bituminous Mixtures", AAPT, 1977, Vol.46.
- Brian D Prowell, Jingna Zhang, and E.Ray Brown," Aggregate Properties and the Performance of Superpave-Designed Hot Mix Asphalt", National Center for Asphalt Technology, 2005.
- Ervin L.Dukatz and David A.Anderson, ' The Effect of Various Filler on the Mechanical Behavior of Asphalt and Asphaltic Concrete",AAPT,1980,Vol.49.
- Prithvi S.Kandal, Cynthia Y.Lynn, Frazier Parker, " Characterization Tests for Mineral Fillers Related to Performance of Asphalt paving Mixtures", National Center for Asphalt Technology, 1998.
- Yong-Rak Kim and Dallas N.Little, Injun Song, "Mechanistic Evaluation of Mineral Filler on Fatigue Resistance and Fundamental Material Charateristics",2003.
- Naga Shashidhar[1], Pedro Romero، 1998 "Factors Affecting the Stiffening Potential of Mineral Fillers"
- American coal ash association, "Fly Ash Facts for Highway Engineers"2003.
- Lecture by Prof.Zongjin Li," Construction Material",2007
- Hassan Y. Ahmed, Ayman M. Othman and Afaf A. Mahmoud,2006 " Effect of Using Waste Cement Dust as A Mineral Filler on the Mechanical Properties of Hot Mix Asphalt"
- Rajpal Sugandh, MS, Manuel Zea, BS, Vivek Tandon, PhD, PE, Andre Smit, PhD, Jorge Prozzi, PhD"Performance Evaluation of HMA Consisting of Modified Asphalt Binder", 2007.
- Hamad I. Al-Abdulwahhab, "The Effects of Baghouse Fines and Mineral Fillers on Asphalt Mix Properties in the Eastern Province of Saudi Arabia", Thesis, 1981.

# MODELING AND SIMULATION OF A BUCK CONVERTER CONTROLLED A SENSORLESS DC SERIES MOTOR

Bassim M.H. Jassim & Tagreed M. Ali
University of Baghdad, college of Eng., electrical Eng. Dept.

**ABSTRACT**

This paper presents modeling and simulation of a speed sensorless control for dc series motor driven by a buck converter through computation of the motor speed from converter output voltage and current. The system model considers the nonlinearity of the series motor magnetization characteristics including the variation of the field inductance with the motor current.

**الخلاصه:**

يقدم البحث نمذجة ومحاكا ة محرك تيار مستمر متوالي الاثاره مغذى من محول تيار مستمر خافض للفولتيه ومسيطر على سرعته بدون استخدام متحسس سرعه. نمذجة المحرك تاخذ بنظر الاعتبار اللا خطيات للخواص المغناطيسيه للمحرك متضمنة تغير معامل الحث الذاتي لملفات الاثاره المتواليه مع تغير التيار.

**KEY WORDS:** DC series motor, speed control, sensorless.

**List of Symbols:**

$e_g$ : Motor generated voltage (or back emf).

$f_s$ : Converter switching frequency.

$i_a$ : Motor armature current.

$i_L$ : Converter inductor current.

$i_o$ : Converter output current.

$K_p$ : Controller proportional constant.

$n$ : Motor speed.

$n_o$ : Motor speed corresponding to that of $E_g$ versus $I_a$ curve.

$n_{ref}$ : Motor reference speed.

$T_d$ : Developed torque.

$v_a$ : Motor armature voltage.

$v_c$ : Converter capacitor voltage.

$v_o$ :Converter output voltage.
$B$ :Friction coefficient.
$C$ :Converter capacitance.
$D$ :Duty ratio.
$E_g$ :Average motor generated voltage.
$I_a$ :Average armature current.
$J$ :Moment of inertia.
$Ka.\Phi$ :Back emf and torque constant.
$L$ :Converter inductance.
$L_a$ :Motor armature circuit inductance.
$L_f$ :Series field inductance
$R_a$ :Motor armature circuit resistance.
$R_f$ :Series field resistance
$R_{esr}$ :Capacitor equivalent series resistance.
$R_l$ :Converter inductor internal resistance.
$T_d$ : Motor developed torque.
$T_i$ :Controller integral constant.
$T_l$ :Load torque.
$T_s$ : Switching time period
$V_a$ :Average motor armature voltage.
$V_c$ :Average capacitor voltage.
$V_o$ :Average converter output voltage.
$V_s$ :Converter input voltage.
$\Delta i_L$ :Converter inductor current ripple.
$\psi$ : Flux linkage in the field in Wb-turn.
$\Phi$ : Flux in Wb.

**INTRODUCTION**

DC series motor are extensively used in traction and application which required high starting torque[Seen].Its speed can be controlled by varying the armature voltage using dc-dc converter operated in high switching frequency to supply continuous armature current without significant torque and speed ripple. There are many articles study the modeling of the dc series motor, some of them like [Okoro 08] and [Soliman 95] ignores all the nonlinearity of the magnetization characteristics while [Samir 98] take its effect on the back emf and the developed torque, but consider the inductance of the series field is constant.

In much application the use of speed sensors like tachogenerator or shaft encoder will add a significant cost and weight to the drive system. In this work, these adverse effects can be avoided using a sensorless speed control. The first section of this work demonstrates the design, modeling and simulation of the buck converter, while section two explains the dc series motor modeling and simulatin.The speed computing unit , the PI controller will explained in section four and five respectively. The system performance is evaluated using Matlab Simulink toolbox through demonstrating the transient response of the motor speed and current due to step change in the desired speed, load torque, and the input voltage. The block diagram of the proposed system is shown in **Fig.1,** where the output voltage of the buck converter is applied to the dc series motor. The motor armature voltage and hence its speed is controlled by using a pulse width technique to control the power MOSFET. The reference speed signal which represents the required motor speed is compared with the actual speed which is computed from the measurement of the armature voltage and current. Any disturbance in the motor load torque or converter input voltage or change in the reference speed causes the PI controller to produce an adequate control signal which is then compared with a constant frequency sawtooth waveform to adjust the duty ratio of the gate control pulses to maintain the motor actual speed equal to the reference speed.

## -The buck converter design, modeling and simulation:

The buck converter steady state output voltage depends linearly on the duty ratio D which is defined as the ratio of the on duration to the switching time period. The converter output voltage is given by:

$$V_a = D.V_s \qquad 0 \leq D \leq 1 \qquad (1)$$

The buck converter modes of operation are explained in details by [Mohan 03].
The converter switching frequency is 20 KHz, and the input voltage is 240V.

## Inductor design:

The inductor value depends on the admissible current ripple $\Delta iL$ which is given by the following relation [Mohan 03]:

$$\Delta i_L \equiv \frac{1}{L}(V_s - V_a).\frac{D}{f_s} \qquad (2)$$

The continuous conduction mode of the converter is ensured by making the minimum output current equal to the minimum permissible motor current which is taken to be 1A according to the specifications of the used motor in this work. Therefore $\Delta i_L = 2A$ is the maximum admissible value. Solving eq. (2) for $L$ yields:

$$L = \frac{(V_s - V_a).D.T_s}{\Delta i_L} \qquad (3)$$

Where: $T_s = \dfrac{1}{f_s}$

Substitute eq.(1) in eq.(3), gives:

$$L = \frac{V_s(1-D)D.T_s}{\Delta i_L} \qquad (4)$$

Clearly the maximum value of the right hand side of eq. (4) occurs at $D = 0.5$, thus the value of the inductor becomes:

$$L = \frac{V_s . T_s}{4 \Delta i_L} \tag{5}$$

Taking $\Delta i_L = 2A$ , the value of the inductor will be $1.5\,mH$ .

**<u>Capacitor Design:</u>**

The output voltage ripple can be minimized by making the corner frequency $f_c$ of the output LC filter such that $f_c << f_s$, also a rule of thumb of $300\mu f \,/\, A$ minimum at $20KHz$ is more realistic when electrolytic capacitors are used[Chyrysis 89]; accordingly for the 8.2A rated armature current, the capacitor selected to be 3300 $\mu f$ .

**<u>Converter Model:</u>**

The averaged state space equations for the buck converter are [Chrip 07]:

$$\frac{\partial i_L}{\partial t} = \frac{1}{L}(d.v_s - i_L R_l - v_o) \tag{6}$$

$$\frac{\partial v_c}{\partial t} = \frac{1}{C}(i_L - i_o) \tag{7}$$

$$v_o = v_c + R_{esr}(i_L - i_o) \tag{8}$$

Where:

$d = 1$ When the switch is on.

$d = 0$ When the switch is off.

The converter matlab-simulink is shown in **Fig.2** where the converter is controlled using pulse width modulation technique which its matlab-simulink is simply shown in **Fig.3.**

**<u>III-DC motor Modeling and Simulation:</u>**

The dc series motor is modeled by the equations below:

$$v_a = e_g + (R_a + R_f).i_a + L_a . \frac{\partial i_a}{\partial t} + L_f . \frac{\partial i_a}{\partial t} \tag{10}$$

Where:

$$e_g = Ka.\Phi(i_a)..n$$

$$L_f = \frac{\partial \Psi}{\partial i_a} \approx \frac{\Psi(i_a + \Delta i_a) - \Psi(i_a)}{\Delta i_a} \quad \text{Where } \Delta i_a \approx 0$$

The torque balance equation is:

$$T_d = T_l + B.n + J.\frac{\partial n}{\partial t} \tag{11}$$

Where:

$$T_d = Ka.\Phi(i_a).i_a$$

$E_g$ Versus $I_a$ and $\Psi_f$ versus $I_a$ for the used motor are shown in **table (1)** [Sailendra 87].These curves are interpolated with piecewise linear interpolation using the one dimension lookup tables of the matlab simulink library. These curves and motor parameters shown in the appendix are used in the matlab- simulink of the dc series motor as in **Fig.4.**

**Table 1. Flux linkage ($\Psi_f$) and emf ($E_g$) as a function of armature current**

| $I_a$ in $A$ | $\Psi_f$ in $Wb-turn$ | $E_g$ in $V$ at $n_o$ =1600 $rpm$ |
|---|---|---|
| 0.0 | 0.0 | 5.0 |
| 1.0 | 0.115 | 22.25 |
| 2.0 | 0.28 | 35.0 |
| 3.0 | 0.415 | 52.5 |
| 4.0 | 0.54 | 67.0 |
| 5.0 | 0.665 | 79.0 |
| 6.0 | 0.76 | 88.5 |
| 7.0 | 0.82 | 95.5 |
| 8.0 | 0.88 | 102.0 |
| 9.0 | 0.94 | 106.5 |
| 10.0 | 0.99 | 108.5 |

**<u>IV- Speed Computing Unit, PI controller, and Current Limiter:</u>**

Using eq.(10) in terms of the average values, the motor speed can be computed as:

$$n = \frac{V_a - (R_a + R_f)I_a}{Ka.\Phi(I_a)} \tag{12}$$

$Ka.\Phi(I_a)$ is found from the one dimension lookup table ($E_g$ versus $I_a$) after division the back emf by the motor speed ($n_o$) at which the motor back emf is measured. The output of this unit is passed through a low pass filter to remove or reduce the noise. The simulink of this unit is built as shown in **Fig.5.**

Using transient performance specification [Basilio 02], P-I controller is designed and tuned such that its transfer function is given by:

$$K(S) = K_p (1 + \frac{1}{T_i . S}) \qquad (13)$$

Where: $K_p = 1.1$ and $T_i = 0.4 Sec.$

A current limiter is used to protect the system from the large starting and transient currents, which can be damage the converter and possibly the motor**.** **Fig.6** and **Fig.7** represent the simulink of the controller and the current limiter respectively.

## V-Simulation Results:

Based on the system model, the motor parameters, and the converter parameters shown in appendix, Simulink is used to simulate the system under consideration as shown in **Fig.8.** The dynamic performance of the drive system is evaluated through step disturbances in the desired speed, load torque, and converter input voltage.**Fig.9** shows the transient response of the motor speed and current due to step increase and decrease in the desired speed ( from 100 rad/sec to 200 rad/sec at t = 5 sec and from 200 rad/sec to 100 rad/sec at t =10sec), when the load torque is 2.5N.m at rated converter input voltage. The motor attained its reference speed in about 2.5 sec. **Fig.10** demonstrates the response due to step increase and decrease in the load torque (from 1.5 N.m to 3 N.m at t = 6sec and from 3 N.m to 1.5 N.m at t = 10sec), when the desired speed is 200 rad/sec at rated converter input voltage. The speed is restored to the reference value within 1.5 sec. Furthermore the system is tested by step decrease and increase in the converter input voltage as shown in **Fig.11** ( from 240V to 180V at t = 5sec and from 180V to 240V at t= 10 sec, when the load torque is 2.5N.m and motor speed is 200 rad/ Sec.).The motor retained its reference speed within 2 sec. The three figures clarify the soft start of the motor and the operation of the current limiter.

## VI-Conclusion:

A dc series motor fed from buck converter with sensorless speed control is simulated taking the nonlinearity of the dc series motor in consideration and this will lead, to expected good coherency between the simulation and practical results if the system is implemented. Speed computation unit is used based on the measurement of the converter output voltage and current. The system simulation shows the effectiveness of this speed unit with satisfactory operation of the PI controller since the speed response has small overshoot, accepted rise time with nearly zero steady state error.

## REFERENCES:


- Basilio J.C. and Matos S.R.,"Design of PI and PID controller with transient performancespecification,"IEEE- Trans. on education, Vol.45, No.4, Nov.2002

- Chrip, p. and Bunlaksananusorn, C,"Large signal average modeling and simulation of dc-dc converters with simulunk," IEEE- Power Conversion Conference-Nagoya, 2007.

- Chyrysis, C. George, High frequency switching power supplies, 2nd ed., McGraw-Hill, 1989.

- Mohan, N., Undland, T.M., and Robbin, W.P., Power electronics: converters application and design, 3rd ed., Wiley& Sons, 2003.

- Okoro, O.I, Ogbuka, C.U.and Agu, M.U,"Simulation of dc machines transient behaviors: teaching and research," Thee pacific journal of science and technology, Vol.9, NO.1, 2008.

- Sailendra N.Bhadra, Ajit K. Chattopadhyay, Nisit K. DE, and Prakas C. Basak,"Computer aided analysis of a multiphase chopper-driven dc series motor and test results on a microprocessor based three-phase chopper drive," IEEE Trans. on Industrial Applications. Vol.23, No.2, 1987.

- Samir Mehta, and John Chiasson,"Nonlinear control of a series dc motor: theory and experiment,"IEEE Trans.on Industrial Electronics, Vol.45, No.1, Feb., 1998.

- Sen, P.C., Principles of electric machines and power electronics, 2nd ed., John Wiley & Sons, 1997

- Soliman, Hussein, F, Mansour,M.M., Kandil, S.A., and Sharaf, A.M.,"A robust tunable fuzzy logic control scheme for speed regulation of dc series motor drives," Canadian Conference on Electrical & Computer Engineering, Vol.1, P296-299, 1995.


**APPENDIX:**

The dc series motor used has the following specifications:

DC series motor, 110V, 8.2-A, 2300 rpm, 0.9 Kw

$R_a + R_f = 2.32\Omega,\ L_a = 25mH,\ J = 0.025Kg - m^2,\ B = 0.001N.m.\sec/rad.$

The buck converter specifications are:

Input voltage $V_s = 240V$.

Output voltage $V_o = V_a$ is adjustable according to required speed and load.

Output current $I_o = I_a = 8.2\,A$.

$L = 1.5mH$, with internal resistance $R_l = 0.017\,\Omega$, $C = 3300\,\mu f$. with $R_{esr} = 0.05\,\Omega$, switching frequency $f_s = 20KHz.$

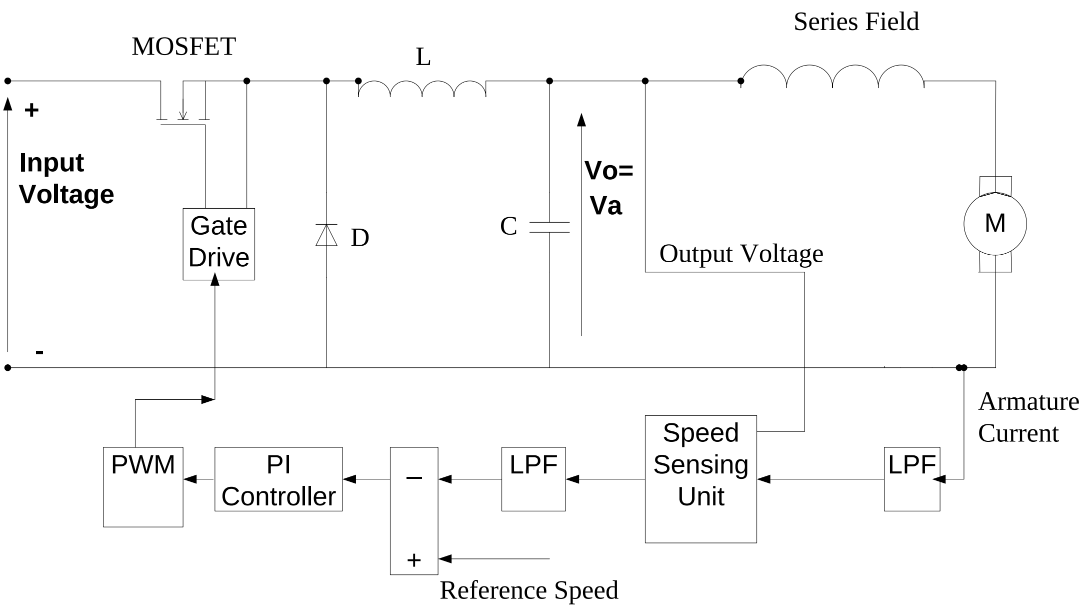


**Fig.1 Sensorless dc series drive system**

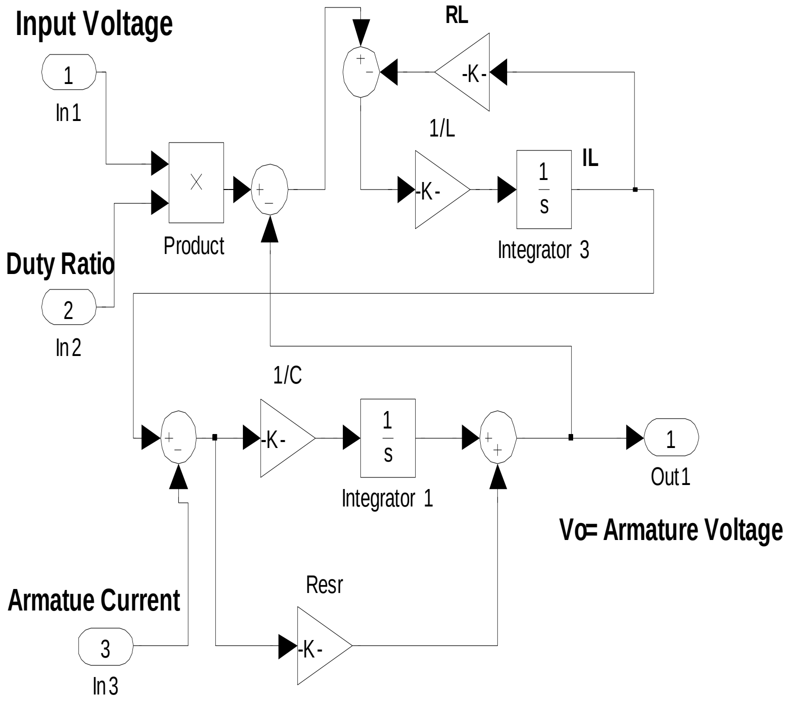


**Fig.2 Simulink of a buck converter**

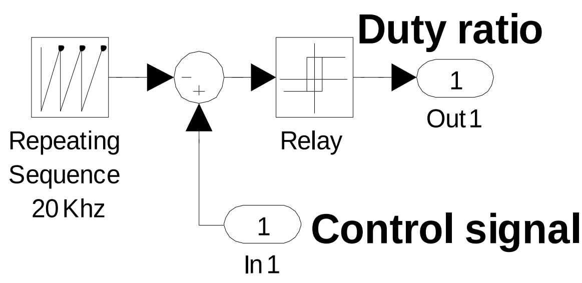


**Fig.3 Simulink of PWM**

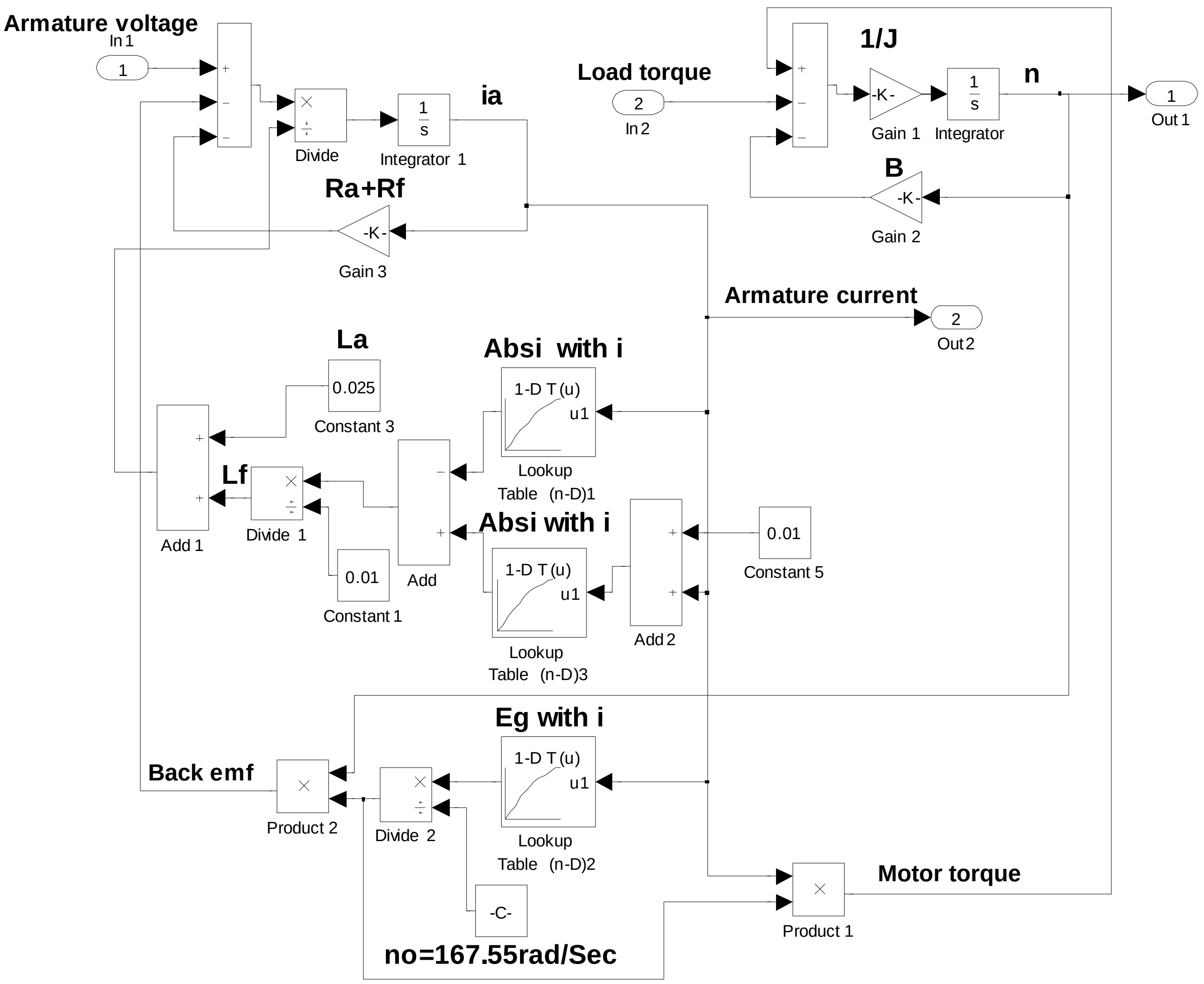


**Fig.4 Simulink of dc series motor**

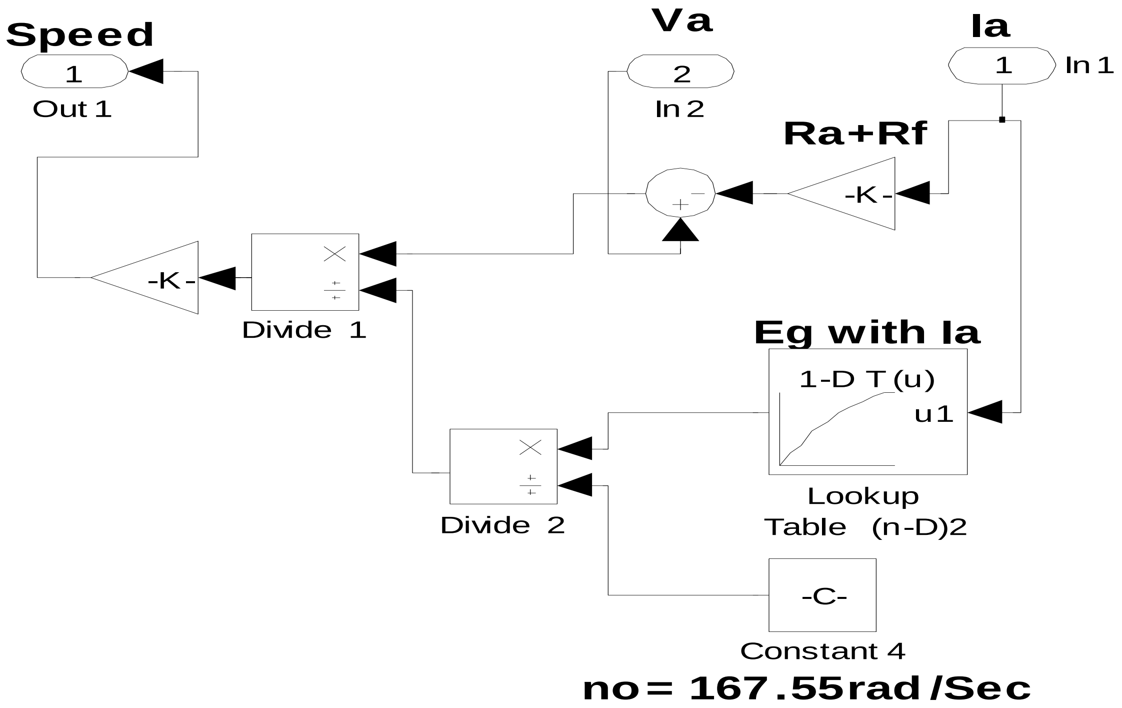


**Fig.5 Simulink of speed sensing unit**

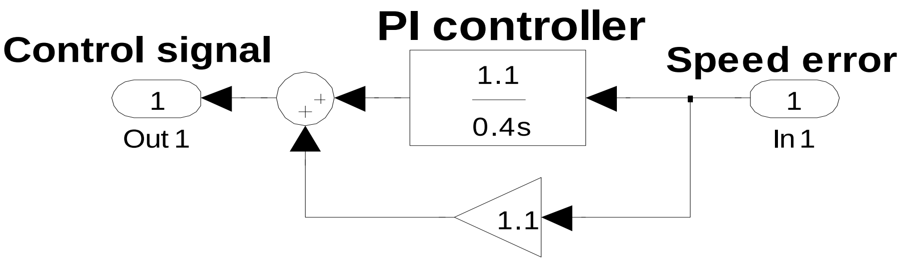


**Fig.6 Simulink of PI controller**

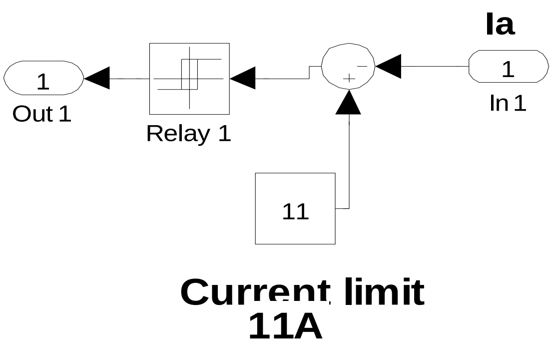


**Fig.7 Simulink of current limiter.**

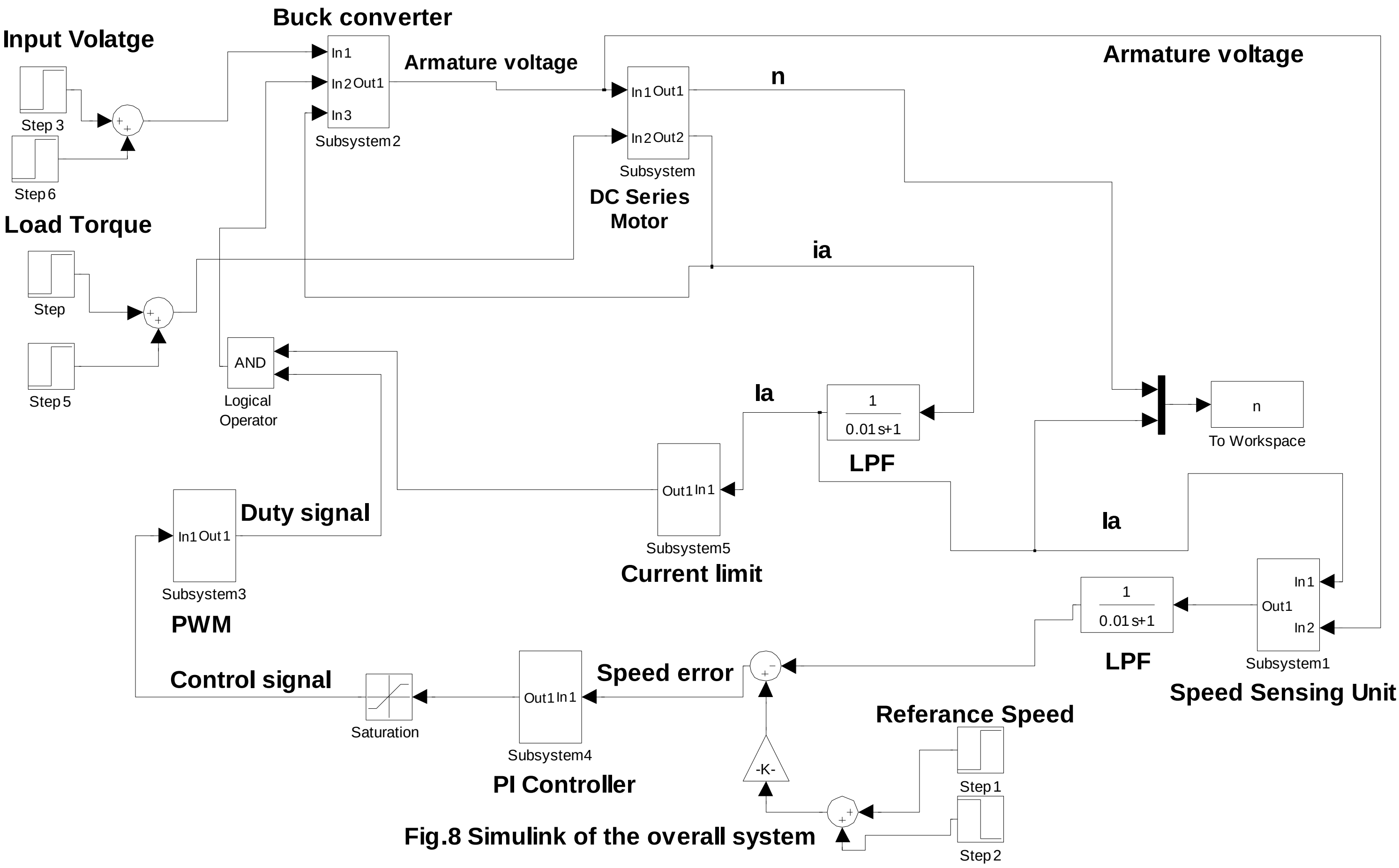


Fig.8 Simulink of the overall system

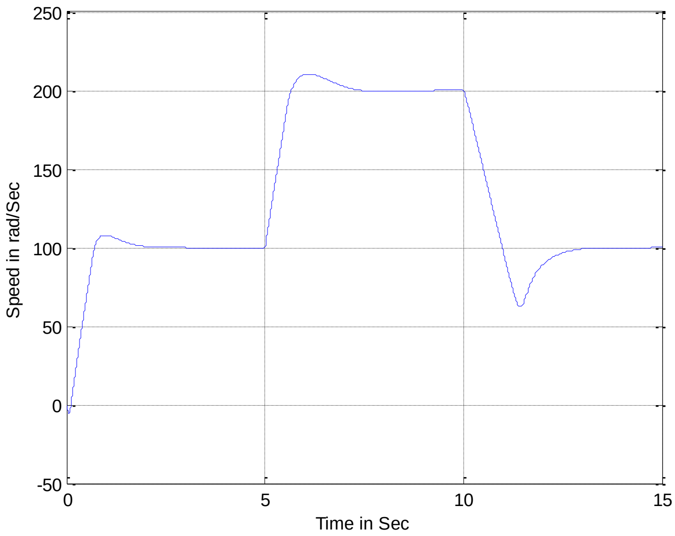


**(a)- Speed**

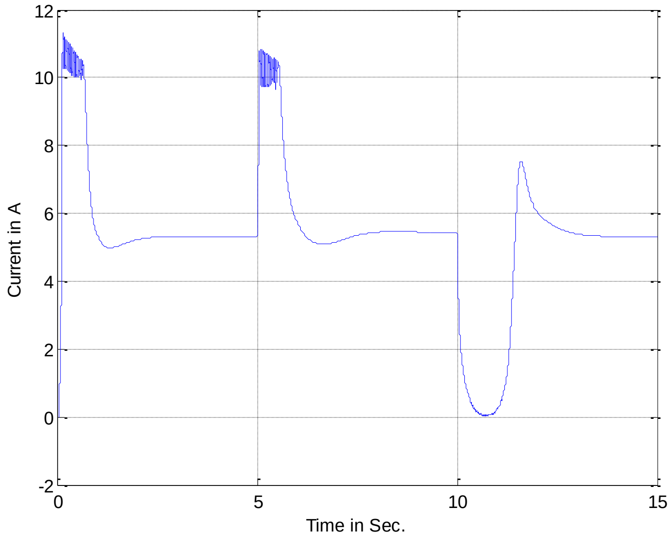


**(b)- Current**

**Fig.9 Transient response due to step increase and decrease in speed**

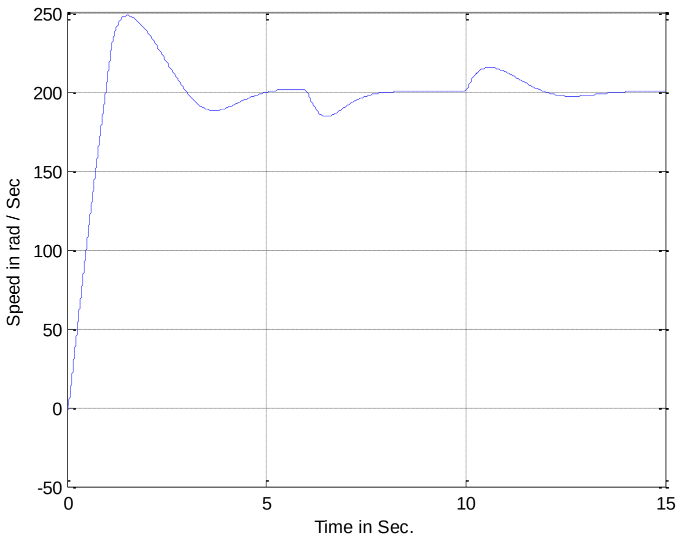


**(a)- Speed**

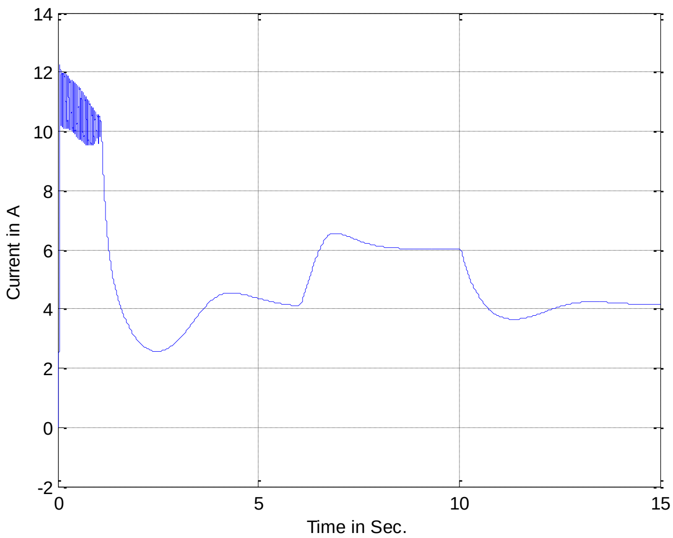


**(b)- Current**

**Fig.10 Transient response due to step increase and decrease in load torque**

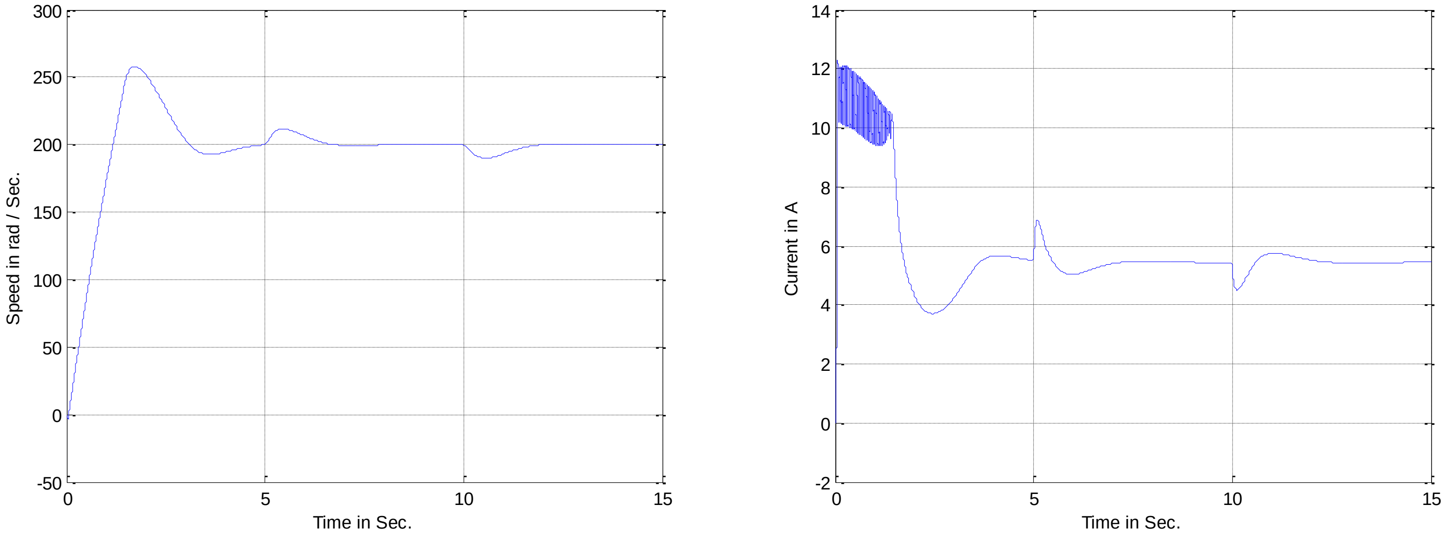


**(a)- Speed** **(b)- Current**

**Fig.11 Transient response due to step increase and decrease in the input voltage**

# DERIVATION OF THE LORENTZ-EINSTEIN TRANSFORMATION VIA ONE OBSERVER

O.M.AL-Kazalchi Faiz T. Omara
Electrical Department
College of Engineering
University of Baghdad

**ABSTRACT:**

Lorentz-Einstein transformation derived by Einstein in his theory of special relativity. Physical laws and principles are invariant in all Galilean reference frames under this transformation. The transformation in every day use in a host of contexts as in free solution of the Dirac equation in the modern field of heavy ion in atomic physics. Most books on theoretical physics and special theory of relativity and all research papers have derived the Eorentz-Einstein transformation using various propositions and employing two observers each located in Galilean system with relative motion receding the same events in the space-time manifold. This paper derives Lorentz-Einstein transformation by proposing just one observer using local coordinates of two Galilean system with relative motion following the track of a spherical pulse of light, which to our knowledge is not found in the literature.

**الخلاصة:**

انشتاين في نظريته النسبية الخاصة على تحويل يدعى الان تحويل لورانتز- انشتاين حيث تكون القوانين الفزيائية لازمة في جميع الانظمة الغاليلية في هذا التحويل. ان لهذا التحويل استخدامات متعددة كما هو الحال في معادلة ديراك في المجال الحديث للايون الثقيل في الفيزياء الذرية. يشتق تحويل لورانتز- انشتاين في معظم كتب الفيزياء النظرية وكتب النظرية النسبية وفي جميع البحوث بموجب فرضيات متباينة وبفرض وجود مشاهدين كل واحد منهما مستقر عند مرجع نظام غاليلي بينهما حركة نسبية ويحسب كل واحد منهما على انفراد نفس الحوادث في فضاء الثر مكان يهدف لأشتقاق تحويل لورانتز- انشتاين بفرض مشاهد واحد يستخدم احداثيات نظامين غاليليين بينهما حركة نسبية ويتبع المسار لنبضة ضوئية كروية.

**KEY WORDS:** Relativity theory, Lorentz-Einstein transformation.

## INTRODUCTION:

### - Four-Dimensional Manifold.

An observer observing the positions in three-dimensional Euclidean space of certain events records with reference to an orthogonal Cartesian system X of axes (x, y, z) or $(x^i)$ , i=l, 2, 3 the space coordinates. The observer using system of axes also measures by means of synchronized clocks stationary in the system, the time " t " at which the events occupying the observed positions thus an event is completely recorded by the $(x^i)$ , i=l, 2, 3, 4 where the $x^4$ denotes the variable time " t ", which is one-dimensional continuum " *The variable " t " is regarded to be independent not only of the space variables* $(x^i)$, *i=l, 2, 3 but also of the possible motion of the space reference system*" [1].

It is possible to think of $(x^i)$, i=l, 2, 3, 4 as a point in Four-dimensional manifold, which may be called the space -time manifold of four dimensions. The same observer who is observing the same events will similarly be able to record these events in terms of $(\bar{x}^i)$, i=l, 2, 3, 4 with reference to another orthogonal Cartesian system $\bar{X}$ of axes where $(\bar{x}^4)$, is the variable time t measured by clocks stationary in the system $\bar{X}$. Therefore, $(x^i)$ and $(\bar{x}^i)$, must be uniquely related to each other, since both record the same events in this four-dimensional manifold.

$(\bar{x}^1)$,

### - The Fundamental Laws of Newtanian Mechanics

The first fundamental laws of mechanics as stipulated by Newton (which is so-called the law of inertia) states that "*a material body continues to be in its state of rest or of uniform rectilinear motion unless it is acted by an external force*" [2].

This law holds only in a special reference frames, which are known as "Galilean system of reference (or inertial systems of reference)". All systems of reference are equivalent from point of view of mechanics, in any such system the three laws of Newtonian mechanics hold and are invariant, that is the laws of mechanics have the same form, which is called the "Galilean principle of relativity".

### - GALILEAN TRANSFORMATION

Consider a Galilean system of reference X, and a second system $\bar{X}$ which is moving with a constant velocity V with respect to the first system. Taking the space axes of the systems in such away that they are respectively parallel to one another and oriented so that the $x^1$ and $(\bar{x}^1)$, axes are parallel to the velocity V. The formulas for the change of axes are:

$$\left.\begin{aligned} \bar{x}^1 &= x^1 + Vx^4 \\ \bar{x}^2 &= x^2 \\ \bar{x}^3 &= x^3 \\ \bar{x}^4 &= x^4 \end{aligned}\right\} \quad \ldots(1)$$

$(\bar{x}^4)$,

Where the origins of the two systems coincide at = $x^4$ =0
The set of equations (1) is called a "Galilean transformation ". This leads to the invariance of Newton laws of mechanics in $\bar{X}$, thus the system $\bar{X}$ is a Galilean system too, therefore the laws of inertia valid in X if it is valid in $\bar{X}$
From (1)

$$\frac{d\bar{x}^1}{d\bar{x}^4} = \frac{dx^1}{dx^4} + V \qquad \dots (2)$$

Therefore the velocity of a particle is not invariant when transformed from X to $\bar{X}$ under Galilean transformation. Hence, certainly a statement of any law that depends on the velocity relative to two Galilean systems, it will not be formally invariance when transformed from one Galilean system to another Galilean system. In particular the fundamental laws of electromagnetic are not invariant with respect to Galilean transformation because these laws depend on the velocity of propagation of light. To achieve the invariance of the fundamental laws of electromagnetic as well as mechanics, it is necessary to abrogate the hypotheses that the time is the same for all observer using Galilean systems independent of their relative motion, that is the time " t " is not universal and each system has its own time.

## - LORENTZ-EINSTEIN TRANSFORMATION

To resolve this crises in physics, in 1905, Einstein proposed two propositions:-

- physical laws and principles have invariant form in all Galilean systems.
- The speed of light in free space has the same constant value in all Galilean systems. [3]

An observer employing the two reference frames X and $\bar{X}$ as defined above finds that a particle acted by no force, will describe a straight line in the X reference frame, this means that its space coordinates ($x^i$), i=l, 2, 3 referred to the X-system will be linearly expressed in terms of the time $x^4$. According to the first proposition of Einstein, the same observer finds that the particle will also describe a straight line in the $\bar{X}$-system, consequently the space-time coordinate of $\bar{X}$ are linear functions of the space-time coordinates of X. Thus:

$$\left.\begin{aligned} \bar{x}^i &= a^i_j x^j + a^i_4 x^4 \\ \bar{x}^4 &= a^4_j x^j + a^4_4 x^4 \end{aligned}\right\} \qquad \dots (3) \text{ (summation on j and I, j=1, 2, 3)}$$

Where the a's are functions of the constant velocity V.

Now, the event $x^i$=0, coincides with the event $(\bar{x}^i)$=0, i=l, 2, 3, 4.

Since the relative motion is parallel to $x^1$ , the planes $x^2=0$ and $x^3 = 0$ must be identical.
Therefore:
$a_1^2 = a_3^2 = a_4^2=0$
Because the $x^1$, $(\bar{x}^1)$, axes in the direction of the velocity V, $x^2$ and $x^3$ cannot be involved in the equations of $x_2$ and $x_4$, and therefore**,**
$a_2^4 = a_3^4=0$
$a_2^1 = a_3^1=0$
Thus,

$$\left.\begin{aligned} \bar{x}^1 &= a_1^1 x^1 + a_4^1 x^4 \\ \bar{x}^2 &= a_2^2 x^2 \\ \bar{x}^3 &= a_3^3 x^3 \\ \bar{x}^4 &= a_1^4 x^1 + a_4^4 x^4 \end{aligned}\right\} \qquad \ldots (4)$$

All directions normal to V are equivalent, hence $\bar{x}^2 = \alpha(v)x^2$
Where $\alpha$ is a function of v. But it is also true $\bar{x}^2 = \alpha(-v)\bar{x}^2$
Hence $\therefore \alpha(v)= \alpha(-v)$
For directions normal to V , the sign of V unimportant $\therefore \alpha(v)=1$
Therefore

$$\left.\begin{aligned} \bar{x}^1 &= a_1^1 x^1 + a_4^1 x^4 \\ \bar{x}^2 &= x^2 \\ \bar{x}^3 &= x^3 \\ \bar{x}^4 &= a_4^1 x^1 + a_4^4 x^4 \end{aligned}\right\} \qquad \ldots (5)$$

Put $a_1^1 = A, +a_4^1 = B, a_1^4 = E, a_4^4 = F$
Then (5) becomes

$$\left.\begin{aligned} \bar{x}^1 &= Ax^1 + Bx^4 \\ \bar{x}^4 &= Ex^1 + Fx^4 \end{aligned}\right\} \qquad \ldots (6)$$

Taking differentials to obtain

$$dx^1 = Adx^1 + Bdx^4$$
$$dx^4 = Edx^1 + Fdx^4$$

$$\therefore \frac{d\bar{x}^1}{d\bar{x}^4} = \frac{A\frac{dx^1}{dx^4} + B}{E\frac{dx^1}{dx^4} + F} \qquad \ldots (7)$$

Suppose that a spherical pulse of light sent out from the point $P(x^i)$, 1=1, 2, 3 of the system X at the time $x^4$. Light travels with constant velocity in all directions independent of the Galilean reference frame, [3, 4]. This means that:

$$\therefore \frac{dx^1}{dx^4} = C \quad \text{and} \quad \frac{d\bar{x}^1}{d\bar{x}^4} = C$$

Substituting in the above relationship, then

$$C = \frac{AC + B}{EC + F}$$

Or $EC^2+(F-A)C-B=0$ …(8)

Now for a particle not in motion in the X-system, it has the velocity V in the

$$\bar{X}-\ \text{system, hence}\ \frac{dx^1}{dx^4}=0,\qquad \frac{d\bar{x}^1}{d\bar{x}^4}=V$$

∴ Substituting in (7) then

$$V=\frac{B}{F}\quad \text{or}\ B=EF\qquad \dots(9)$$

For the same reasons

$$\frac{d\bar{x}^1}{d\bar{x}^4}=0,\qquad \frac{dx^1}{dx^4}=-V\qquad \text{then (7) gives}$$

$-AV+B=0 \quad \therefore B=AV \qquad \dots.(10)$

From equations 8, 9 and 10

$$F=A,\qquad E=\frac{AV}{C^2},$$

After substituting in (6), the result is

$$\left.\begin{aligned}\therefore \bar{x}^1 &= A(x^1+x^4)\\ \bar{x}^4 &= A(x^1\frac{V}{C^2}+x^4)\end{aligned}\right\}\qquad \dots(11)$$

But for the spherical pulse,

$$(dx^1)^2-C^2(dx^4)^2=(d\bar{x}^1)^2-C^2(d\bar{x}^4)^2\qquad \dots\ (12)$$

From (11) and (12), one may find that

$$A=\frac{1}{\sqrt{1-\frac{V^2}{C^2}}}$$

Hence (11) becomes

$$\left.\begin{aligned}\bar{x}^1 &= \frac{1}{\sqrt{1-\frac{V^2}{C^2}}}(x^1+Vx^4)\\ \bar{x}^4 &= \frac{1}{\sqrt{1-\frac{V^2}{C^2}}}(x^1+Vx^4)\end{aligned}\right\}\qquad \dots(13)$$

Equation (13) is what so called the Lorentz-Einstein transformation's, 6].

## CONCLUSIONS:

This paper presents a method for driving the Lorentz-Einstein transformation by proposing one observer following a track of a spherical pulse of light in two Galilean reference frames in relative motion.

## REFERENCES:


- Tensor Analysis
  - I.S. Sokolnikoff
  - New york. John Willy and sons 1 nc.
  - London 1951. pp
- The theory of relativity
  - R. K. Pathria
  - Pergamon press, Oxford 1 974.
- A. Einstein, The meaning of relativity. Second edition 1 956.
- O. M. AL- Kazalchi: An alternative approach to the second postulate of the special theory of relativity.
- مجلة الهندسة والتكنلوجيا الجامعة التكنلوجية العدد4 المجلد الثاني عشر 1993.
- W. Gresnier: (1997) Relativistic Quantum Mechanics, Wave equations
- springer
- Weirnstrock: Derivation of the Lorentz equations without a linearty
- assumption. Amer. J. Phy. 32 (1964). 260-264.
- G. Nadean: The Lorentz-Einstein transformation obtained by vector method.
- Amer. J. Phy. 30 (1962) 602-3.
- O. M. AL- Kazalchi: New method for derivation of Lorentz transformation.
- Journal of Eng., College of Engineering
- University of Baghdad No. 1 Vol.9 march 2002.
- Moller, C (1972): The theory of relativity. Oxford clarendon press.
- G. J. Whitrow: A derivation of the Lorentz formulas. Quant. J. math. 4(1933).

# HYDRODYNAMIC STUDIES OF BED EXPANSION IN LIQUID SOLID FLUIDIZED BED

Sawsan A. M. Mohammed
Chemical Engineering Department – College of Engineering – University of Baghdad – Iraq

**ABSTRACT**

Expanded bed behavior was modeled by using the Richardson-Zaki correlation between the superficial velocity of the feed stream and the void fraction of the bed at moderate Reynolds number. The terminal velocity expression was developed by introducing two empirical parameters, the effective diameter of the particles and an exponent for the $\left[(\rho_p - \rho_l)^2 / \rho_l \mu_l\right]$ term. The Richardson-Zaki exponent constant (n) was found to vary with the density ratio $(\rho_p - \rho_l)/\rho_l$ and diameter ratio $d_p/D$. It was noted that when the density ratio $(\rho_p - \rho_l)/\rho_l$ is less than one, there is no dense phase at the bottom of the test section. However, for density ratio $(\rho_p - \rho_l)/\rho_l$ greater than unity, there exists accelerating or dense regime at the bottom of the test section.

**الخلاصة:**

تم في هذا البحث تمثيل تصرف الاعمدة المتمددة باستخدام علاقة ريتشاردسن- زاكي بين السرعة الظاهرية للمجرى الداخل ونسبة الفراغ للعمود في حدود معتدلة من رقم رينولدز. تم استحداث علاقة جديدة للسرعة . النهائية وذلك بادخال مقدارين تجريبيين وهما القطر المؤثر لحبيبات الحشوة ومقداراسي للحد $\left[(\rho_p - \rho_l)^2 / \rho_l \mu_l\right]$

لقد وجد ان المقدار الاسي(n) لعلاقة ريتشاردسن – زاكي يتغير مع الحد $(\rho_p - \rho_l)/\rho_l$ والنسبة بين قطر الحبيبة وقطر العمود $d_p/D$ . كذلك تم ملاحظة انه عندما تكون نسبة الكثافة $(\rho_p - \rho_l)/\rho_l$ اقل من واحد لم يظهر طور كثيف في اسفل العمود بينما في حالة كون نسبة الكثافة اكبر من واحد ظهرطور كثيف متسارع في اسفل العمود.

**KEYWORDS: Liquid-solid fluidized bed, Bed expansion, Richardson-Zaki correlation.****دراسة هيدروديناميكية لتمدد الاعمدة المسالة المتكونة من الصلب والسائل**

## INTRODUCTION

Fluidized beds find extensive applications in chemical process industries as they provide large interfacial area, high degree of mixing, and temperature uniformity. In particular, liquid-solid fluidization beds are increasingly used in chemical processes such as fermentation, biological wastewater treatment, flow gas desulfurization, ore reduction etc. Although fluidization can be achieved either by liquid or gas as fluidizing medium, gas fluidized beds have gained more importance in scientific community due to its far more applications. This is in spite of the fact that possible uses of liquid fluidization in the mining industry were suggested as early as in 16$^{th}$ century as a means of separating solids of different sizes. Since the emergence of biosciences in the recent years and the adaptability of liquid fluidized bed for various applications, the importance of solid-liquid fluidized bed is receiving greater attention among scientists and researchers (Navaez et al., 1996, Yang and Renken, 2003, Bo and Yan, 2003). In recent years, the applications of liquid-solid fluidized beds are being extended for hydrometallurgy, food technology, biochemical processing, etc. Scientific research concerns with reference the hydrodynamic structure of liquid-particle, the equilibrium forces for fluid-particle interactions and heat or mass transfer properties in fluidized beds. Fluidization quality is closely related to the intrinsic properties of particles, e.g. particle density, particle size and size distribution, and also their surface characteristics. The expansion characteristic of solid particles in a liquid-solid fluidized bed is a function of superficial liquid velocity. A quantitative relationship linking the bed expansion with these parameters is necessary for a fundamental understanding of fluidization behavior and subsequent applications (Richardson and Jeronimo, 1979). The first important study of the forces acting on an immersed body moving relative to a viscous fluid was made in 1851 by Stokes who derived an equation for the viscous resistance to the motion of a single spherical particle in an infinite fluid.

$$F = 3\pi\,\mu_l V d_p \qquad (1)$$

The terminal falling velocity $V_t$ of the particle is obtained by equating the viscous drag as given by eq. (1), to the effective gravitational force.

$$3\pi\,\mu_l V_t d_p = \frac{\pi\, d_p^3}{6}\left(\rho_p - \rho_l\right)g$$

Hence

$$V_t = \frac{g\, d_p^2\left(\rho_p - \rho_l\right)}{18\mu_l} \qquad (2) \qquad \text{for } Re_p<0.4$$

In the flow region where $Re_p$ varies between 2 and 500, which has been called the intermediate law, Lewis et al., 1952 defined the terminal velocity by the equation:

$$V_t = \frac{0.153 g^{07} d_p^{1.14} \left(\rho_p - \rho_l\right)^{0.71}}{\rho^{0.29} \mu_l^{0.43}}$$

Wen and Yu, 1966 estimated the terminal velocity at moderate Reynolds number using the following equation:

$$V_t = \left[ \frac{4}{225} \frac{\left(\rho_p - \rho_l\right)^2 g^2}{\rho_l \mu_l} \right]^{1/3} d_p \qquad (3) \qquad \text{for } 0.4 < Re_p < 500$$

Expanded bed technology lacks understanding about its hydrodynamic behavior as has been available for the conventional packed column technology. Therefore a method to describe the behavior of the expanded bed incorporating the properties of particles and feed stream should be provided.

**MATHMATICAL APPROACH**

There are two methods to describe the expanded bed behavior. One is the dimensional analysis method, which has been successfully applied for the design of various fluid processing equipments. The other is the Richardson-Zaki equation, which predicts a linear correlation between logarithms of the superficial fluid velocity ($V_0$) and the void fraction of the bed ($(1-\phi_s$) for fluidized bed by

$$\log V_0 = n \log\left(1 - \phi_s\right) + \log V_t \qquad (4)$$

where $\phi_s$ and $V_t$ are the solid fraction of the expanded bed and the terminal settling velocity of the particle at infinite dilution $\left(\phi_s = 0\right)$, respectively (Richardson and Zaki, 1954, Davidson and Keaims, 1978).

The superficial velocity $V_0$ is determined by dividing the volumetric flow rate of the feed stream by the cross sectional area of the column.

The solid fraction $\phi_s$ of the expanded bed at height H can be obtained by

$$\phi_s = \phi_0 \frac{H_0}{H} \qquad (5)$$

where $\phi_0$, and $H_0$, are the solid fraction and height of the bed at zero flow stream, respectively. Combining eqs. (5) and (4) results

$$H/H_0 = \phi_0 \Big/ \left[1 - \left(V_0/V_t\right)^{1/n}\right] \qquad (6)$$

An attempt was made to correlate values of n and $V_t$ with the properties of particles and feed streams.

## EXPERIMENTAL WORK

The schematic representation of experimental set-up is shown in Fig.1; it consists of a glass column of 2.45 cm internal diameter and a height of 75 cm. The column was packed with glass beads (0.4 – 0.6) mm in diameter, to a height of 8 cm. The fluidizing particles are supported by a wire mesh fitted at the column bottom. The liquid from the storage tank was pumped through a rotameter connected on the line. In order to change the solution properties, tap water and glycerol solutions (10, 20 and 30 wt percent) were used as feed streams. The viscosity of each glycerol solution was obtained by using a Fann V-G meter and density was measured by a standard hydrometer. The height of the bed was measured over a certain range of feed velocities.

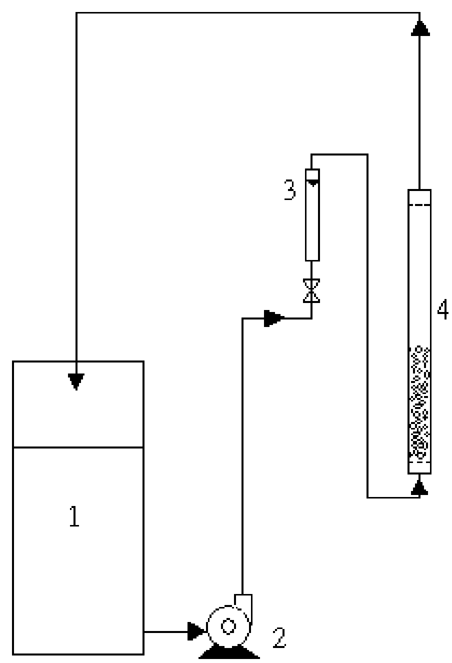


**Fig.1: Schematic diagram of the experimental set up (1.liquid reservoir, 2.pump, 3.flow meter, 4.test section)**

Another set of experiments were made using a variety of solid particles with tap water to estimate the effect of density ratio ($\left(\rho_p - \rho_l / \rho_l\right)$ and diameter ratio ($d_p / D$) on the Richadson-Zaki exponent constant (n). The solids used and therein characteristics are given in Table 1.

**Table 1: Solid particles used and their characteristics**

| Particles used | $d_p$, mm | $\rho_p$, kg/m$^3$ | $V_{mf}$, m/s |
|---|---|---|---|
| Glass beads | 0.4 -0.6 | 2250 | 0.0018 |
| Perspex beads | 0.5-2 | 1600 | 0.0051 |
| Porcelain | 1.3 | 2100 | 0.0094 |

| | | | |
|---|---|---|---|
| PVC beads | 2.1 | 1750 | 0.0137 |
| Activated carbon | 1.8 | 1350 | 0.0058 |
| Silica gel | 1.5-2 | 1900 | 0.0124 |
| Sand | 0.66 | 2600 | 0.0039 |

The minimum fluidized velocity for the solid materials ($V_{mf}$) had been estimated using the following equation (Ramaswamy, 2008):

$$V_{mf} = \frac{\mu_l}{d_p \rho_l}\left[\sqrt{(33.7)^2 + 0.0408\frac{d_p^3 \rho_l(\rho_p - \rho_l)g}{\mu_l^2}} - 33.7\right] \qquad (7)$$

**RESULTS AND DISCUSSION**

**Modification of the terminal velocity expression using the Richardson-Zaki correlation:**

The effects of superficial velocity ($V_0$) of the feed stream on the bed expansion ($H/H_0$) were measured. The bed expansion factor was limited below 3 as recommended by Reichent et al., 2001, for proper performance of expanded beds.

A dimensional analysis can be performed for the expansion of the bed. The bed expansion ($H/H_0$) can be expressed as a function of various operating conditions, such as the fluid velocity V, particle diameter $d_p$, solution viscosity $\mu_l$, and fluid density $\rho_l$, by the following equation

$$H/H_0 = f(V, d_p, \mu_l, \rho_l) \qquad (8)$$

Dimensional analysis of eq. (8) propose that the bed expansion may be represented by eq. (9) using the particle Reynolds number ($\mathrm{Re}_p = d_p V \rho_l / \mu_l$) as a single combined parameter incorporating various operating conditions.

$$H/H_0 = g(\mathrm{Re}_p) \qquad (9)$$

Fig.2 shows the bed expansion as a function of particle Reynolds number, the expansion of the bed becomes greater as the solution viscosity increases at a fixed flow rate of the feed stream. The average diameter of the particles was used to calculate $\mathrm{Re}_p$ values.

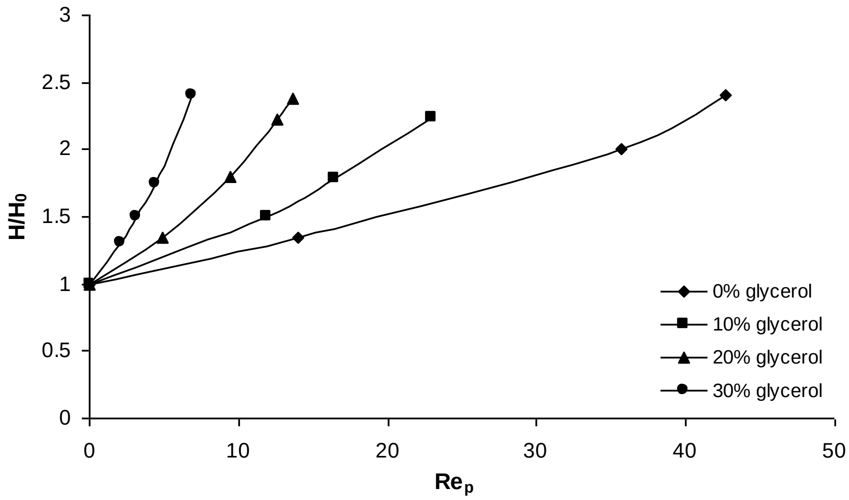


**Fig.2 Bed expansion of the bed as a function of Reynolds number.**

Although Coulson et al., 1991, provided $(\phi_s)_0$, values for spherical particles of various sizes, $(\phi_s)_0$ value for the bed was measured as follows. In the column the particles were settled in distilled water. The water contained inside the void fraction of the sedimented bed was drained off. The volume of the drained water was measured and divided by that of the total sedimented bed to determine the void fraction, $\varepsilon$ of the bed. Finally, $(\phi_s)_0$ value determined by 1-$\varepsilon$ was 0.85.

Fig. 3 shows the Richardson – Zaki plots for the experimental data in Fig.2. All the lines in Fig.3 have approximately the same slope (n) values with different intercepts. The average value of the slopes, $n_{av}$, was 1.66.

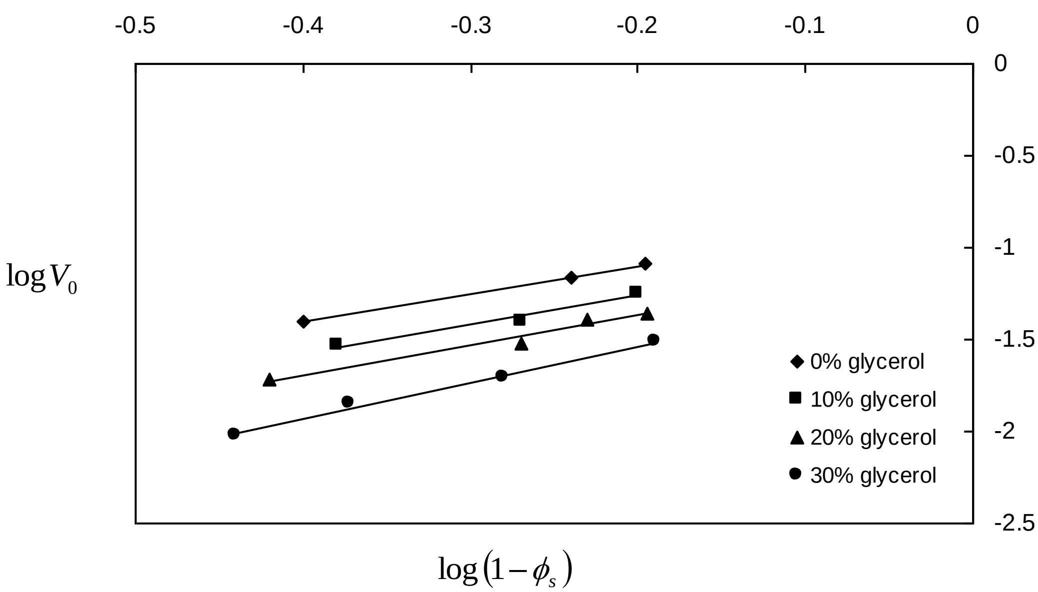


**Fig.3 Richardson-Zaki plots for the bed expansion**

The terminal velocity may be evaluated from bed expansion data by extrapolation at $\phi_s$ equals zero. Table 2 lists values of n and $V_t$ in glycerol solutions along with their density and viscosity values.

**Table 2. Physical properties of glycerol solutions at 20°C and the parameter values of Richardson-Zaki correlation.**

| Glycerol (wt %) | Density, kg/m$^3$ | Viscosity, mPa.s | n | $V_t$ , m/s |
|---|---|---|---|---|
| 0 | 1000.0 | 1.005 | 1.513 | 0.1675 |
| 10 | 1022.1 | 1.310 | 1.56 | 0.1265 |
| 20 | 1046.9 | 1.760 | 1.60 | 0.0925 |
| 30 | 1072.7 | 2.500 | 1.97 | 0.0721 |

Eq. (3) implies that $\log V_t$ values can be linearly correlated with $\log\left[(\rho_p - \rho_l)^2 / \rho_l \mu_l\right]$ values. Fig. 4 shows that this is true. A modified expression for the terminal velocity is developed from the linear correlation in Fig.4 as follows

$$\log V_t = 0.386 \log\left[\frac{(\rho_p - \rho_l)^2}{\rho_l \mu_l}\right] - 3.261 \qquad (10)$$

Comparing eqs. (10) and (3) enables the introduction of two empirical parameters, the effective particle diameter, $d_{pe}$ and an exponent, a, to modify the terminal velocity expression as in the following general equation

$$V_t = \left(\frac{4\,g^2}{225}\right)^{\frac{1}{3}} \left(\frac{(\rho_p - \rho_l)^2}{\rho_l \mu_l}\right)^{\frac{a}{3}} d_{pe} \qquad (11)$$

or

$$\log V_t = \log\left[\frac{4g^2}{225}\right]^{\frac{1}{3}} d_{pe} + \frac{a}{3} \log\left[\frac{(\rho_p - \rho_l)^2}{\rho_l \mu_l}\right] \qquad (12)$$

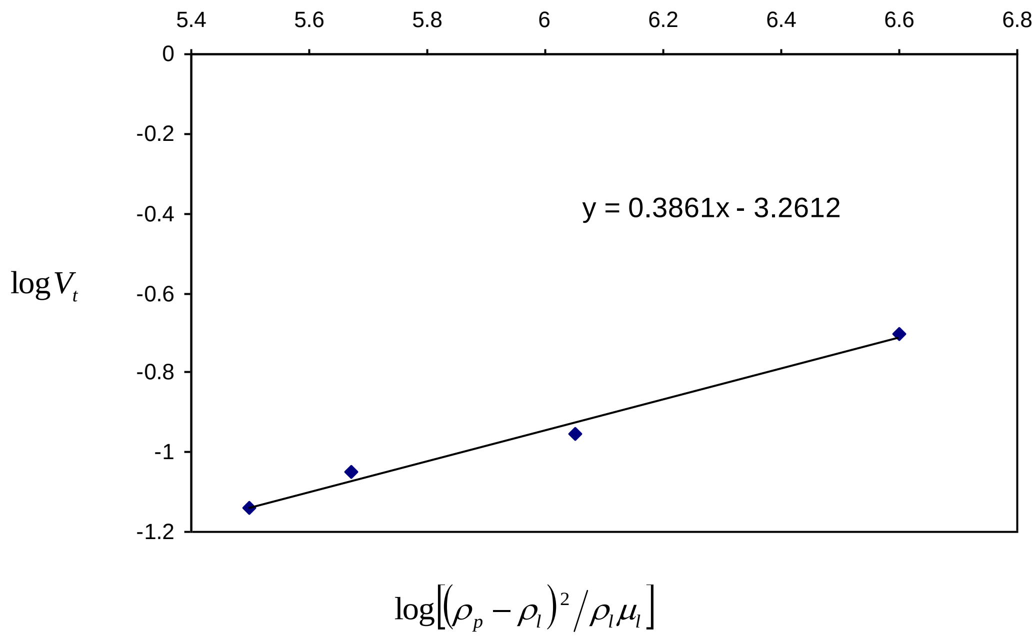


**Fig.4 Linear correlation between $\log V_t$ values determined from Richardson-Zaki plots with $\log\left[\left(\rho_p - \rho_l\right)^2 / \rho_l \mu_l\right]$ values.**

By comparing eqs. (10) and (12), values of $d_{pe}$ and a are calculated to be 0.458 mm and 1.158, respectively. It is very reasonable that the effective diameter is close to the diameter of the smallest particles used, since the smallest particles would be at the top of the expanded bed, and therefore should be used as a basis in modeling the behavior of the expanded bed.

Fig. 5 demonstrates that the calculated bed expansion, $(H/H_0)_{cal}$ using the modified expression eq. (10) and eq. (6) are in good agreement with experimentally measured values of the bed expansion $(H/H_0)_{exp}$. In this case the n values of eq. (6) are replaced by the average, $n_{av}$ of n values, the slopes of the linear plots in Fig. 3 for all glycerol solutions.

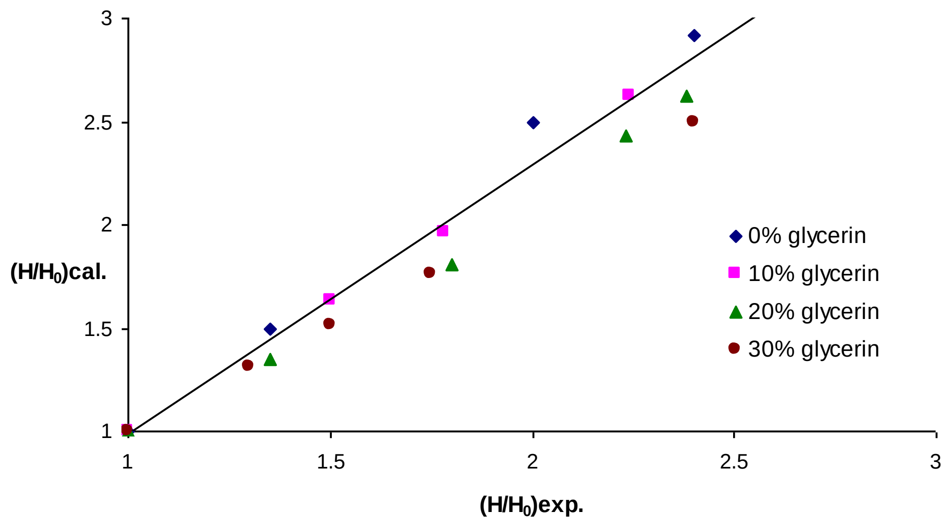


**Fig.5 Comparison of the bed expansion calculated using the modified terminal velocity expression, $(H/H_0)_{cal}$, with those of experimentally determined values, $(H/H_0)_{exp}$.**

## EFFECT OF DENSITY RATIO AND DIAMETER RATIO ON THE RICHARDSON- ZAKI EXPONENT CONSTANT (N):

The effect of density ratio on the values of n is shown in Fig. 6. The exponent n decreases with an increasing density ratio as long as the value of $(\rho_p - \rho_l)/\rho_l$ is less than unity. In the case the ratio is unity, the exponent value is also unity. For the case where $(\rho_p - \rho_l)/\rho_l$ is greater than unity, the decreasing trend in exponent value reverses i.e. increasing. In a similar manner, the variation of exponent n has been plotted against particle to column diameter ratio $(d_p/D)$ in Fig. 7. The exponent was found to decrease with increasing particle to column diameter ratio for both the cases when $(\rho_p - \rho_l)/\rho_l$ <1 and $(\rho_p - \rho_l)/\rho_l$ >1.

$$n = f\left[\left(\frac{\rho_p - \rho_l}{\rho_l}\right), \frac{d_p}{D}\right]$$

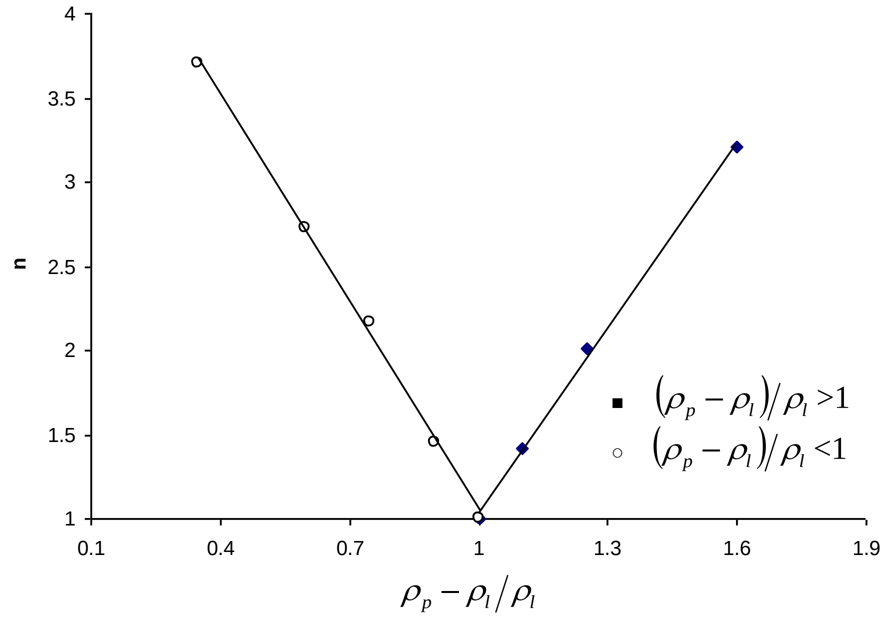


**Fig. 6 Exponent variation with relative density to fluid density ratio**

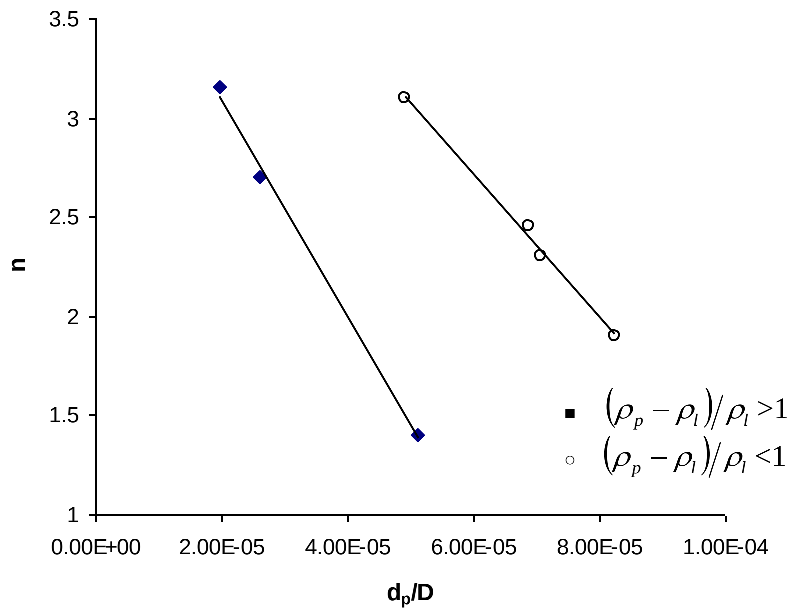


**Fig. 7 Exponent variation with particle to bed diameter ratio.**

It was noted that when the density ratio $\left(\rho_p - \rho_l\right)/\rho_l$ is less than one, there is no dense phase at the bottom of the test section. However, for density ratio $\left(\rho_p - \rho_l\right)/\rho_l$ greater than unity, there exists accelerating or dense regime at the bottom of the test section.

## CONCLUSION

- The expression of the Richardson- Zaki correlation in combination with the modified Wen and Yu expression for terminal velocity, developed in this study, can be successfully used to model the behavior of expanded beds at moderate Reynolds number.
- For beds composed of particles of mixed sizes it is observed that the smallest particles collect near the top. The same result was obtained by McCune and Wilhelm, 1949 and Lewis and Bowerman, 1952.
- The Richardson-Zaki exponent constant n varies with $(\rho_p - \rho_l)/\rho_l$ and $d_p/D$. These variations have been found to be of two types, namely, $(\rho_p - \rho_l)/\rho_l$ <1 and $(\rho_p - \rho_l)/\rho_l$ >1.
- It was observed that for the case of high density particles, there was a considerable height of dense phase at the bottom of the test section. In the case of lower density particles, no dense phase was noted at the bottom of the test section. The reason of this type of behavior can be explained as follows: for heavy solid particles, the gravitational force is more predominant and particles have to accelerate so as to reach the fully developed regime since the contribution of drag is obtained by the gravitational component on particles. For lesser density particles, the buoyancy force is more predominant as compared to the gravitational force, so, the particles soon reach the fully developed regime with smooth and homogeneous type of fluidization. The same behavior was observed by Rao, 2005.

## NOMENCLATURE

| | |
|---|---|
| $d_p$ | Particle diameter (m) |
| $d_{pe}$ | Effective particle diameter (m) |
| $D$ | Column diameter (m) |
| $F$ | Drag force (N) |
| $g$ | Acceleration due to gravity (m/s$^2$) |
| $H$ | Height of the expanded bed (m) |
| $H_0$ | Height of bed at zero flow stream (m) |
| $n$ | Richardson- Zaki exponent constant (−) |
| $\mathrm{Re}_p$ | Particle Reynolds number (−) |
| $V$ | Particle velocity (m/s) |
| $V_{mf}$ | Particle minimum fluidization velocity (m/s) |
| $V_0$ | Superficial velocity (m/s) |
| $V_t$ | Particle terminal velocity (m/s) |

***Greek letters***

$\rho_l$ Density of fluid ($kg/m^3$)

$\rho_p$ Density of particle ($kg/m^3$)

$\mu_l$ Dynamic viscosity of fluid (kg/m.s)

$\phi_s$ Solid fraction of the expanded bed (−)

$\phi_0$ Solid fraction of the bed at zero flow stream (−)

$\varepsilon$ Void fraction of the bed (−)

**REFRENCES**


- Bo, X., and Yan, S., 2003, "*Modeling of Sedimentation of Polydisperse Spherical Beads with a Broad Size Distribution"*, 58, pp 1531-1543.

- Coulson, J. M., Richardson, J. F., Backhurst, J. R. and Harker, J. H., 1991, *Chemical Engineering* Vol. 2, 4th Edn. Pergamon Press, Oxford.

- Davidson, J.F. and Keaims,D.L., 1978, *Fluidization*, Cambridge University Press.

- Lewis, E. W., and Bowerman, E. W., 1952, "*Fluidization of Solid Particles in Liquids* ", Chem. Engng. Progr., 48, pp 603-609.

- McCune, L. K., and Wilhelm, R. H., 1949, "*Mass and Momentum Transfer in Solid-Liquid System* ", Industr. Engng. Chem., 41, pp 1124-1134.

- Narvaes, I., Orio, A., Aznar, M.p. and Corella, J., 1996, "*Biomass Gasification with Air in an Atmospheric Bubbling Fluidized Bed. Effect of Six Operational Variables on the Quality of the Produced Raw Gas*", Ind. Eng.Chem. Res., 35, pp 2110-2120.

- Ramaswamy, E., Sirinivasakannan, C. and Balasubramaniam, N., 2008,"*Bed Expansion Characteristics of Liquid-Solid Fluidized Bed with Internals*", Modern Applied Science, 2(2), pp 84-92.

- Rao, V.V.B., 2005, "*Hydrodynamic Predictions in Liquid Solid Circulating Fluidized Bed*", IE Journal- CH, 85, pp 64-68.

- Reichent, U., Knieps, E., Slusarczyk, H., Kular, N. R. and Thommes, J., 2001, "*Isolation of a Recombinant Format Dehdrogenase by Pseudo- Affinity Expanded Bed Adsorption*", J. Biochem. Biophys. Methods, 49, pp 533.

- Richardson, J.F. and Zaki, W.N., 1954, "*Sedimentation and Fluidization. Part I*", Trans. Instn Chem. Engrs., 32, pp 35-53.

- Richardson, J.F., and Jeronimo, M.A.D.S., 1979, "Velocity-Voidage Relations for Sedimentation and Fluidization", Chem. Eng. Sci., 34, pp 1419-1422.

- Wen, C.Y. and Yu, Y.H., 1966, "*A Generalized Method for Predicting the Minimum Fluidization Velocity*", AICHEJ, 12, pp 610-612.

- Yang J. and Renken A., 2003, "*A Generalized Correlation for Equilibrium of Forces in Liquid – Solid Fluidized Beds*", Chem. Eng. J., 92(7), pp 7-14.

# REMOVAL OF COPPER IONS FROM WASTE WATER BY ADSORPTION WITH MODIFIED AND UNMODIFIED SUNFLOWER STALKS

Besma Ismael Hussein
Chemical Engineering Department, College of Engineering, University of Baghdad


## ABSTRACT

Unmodified and modified sunflower stalks were examined for adsorption as a replacement of expensive activated carbon which has been recognized as a highly effective adsorbent for the removal of heavy metal-ion.

Two modes of operation were used, batch mode and fixed bed mode. In batch experiment the effect of sunflower stalk doses (2,3,4,5 and 6g/L) with constant initial copper concentration of 100 mg/L and constant particle size less than1.18 mm was studied.

Batch kinetics experiments showed that the adsorption rate of copper ion by sunflower stalks was rapid and reached equilibrium within 60 min. Adsorption models Freundlich, Langmuir and Freundlich-Langmuir were fitted to experimental data and the goodness of their fit for adsorption was compared. In the fixed bed isothermal adsorption column, the effect of particle size (1.18-2.36, 2.36-4.75 and 4.75-9.00) mm, influent flow rate (2,4and 6) L/hr, bed depth (25, 30 and 35) cm and initial metal concentration (100 and 150) mg/L was studied. In addition, the modification of sunflower stalks could enhance their natural capacity. Sunflower stalks were modified by activation with nitric acid. The results of this study show that sunflower stalk, both modified and unmodified, is an efficient adsorbent for the removal of copper from waste water. Percent removal of copper reaches 100% when particle size (2.36-4.75)mm ,bed depth 35 cm and influent flow rate 4 L/hr.



## الخلاصة:

قد تم في هذا البحث دراسة امكانية جعل سيقان نبات عباد الشمس المعامل وغير المعامل كبديل لمادة الكاربون المنشط والتي تعد مادة فعالة جدا في امتزاز المعادن الثقيلة.

تم استخدام نمطين من التشغيل في هذا البحث وهي تجارب النمط الدفعي وتجارب النمط المستمر. تم اجراء تجارب دفعية لدراسة تأثير كمية عباد الشمس (2، 3، 4، 5 و6)غم/ لتر بثبوت التركيز الابتدائي لايون النحاس (100 ملغم/ لتر) وحجم ثابت لجسيمات المادة الممتزة الذي هو اقل من1.18 ملم، أظهرت النتائج ان نسبة ازالة المعدن تزداد بزيادة كمية سيقان عباد الشمس و الزمن. كذلك أظهرت النتائج ان الوصول الى حالة التعادل تستتغرق تقريباً (60) دقيقة، تم تحليل النتائج باستعمال موديلات (Langmuir, Freundlich and Langmuir-Freundlich) وأظهرت النتائج ان جميع الموديلات ذات تقارب جيد. كذلك اجريت تجارب النمط المستمر وتم دراسة تأثير تركيز المعدن الابتدائي (100 و150 ملغم/ لتر) وحجم جسيمات المادة الممتزة (1.18-2.36 و 2.36-4.75 و4.75-9.00ملم) بمعدل جريان الداخل (2 و4 و6 لتر/ ساعة) وارتفاع عمود الامتزاز (25، 30،35 سنتمتر) وبالاضافة الى ذلك تم دراسة تاثير معاملة سيقان عباد الشمس بحامض النتريك. لقد أظهرت النتائج ان سيقان عباد الشمس المعاملة وغير المعاملة هي فعالة في امتزاز المعادن من مياه الصرف وكانت نسبة ازالة النحاس تصل الى 100% عندما يكون حجم جسيمات المادة الممتزة (2.36-4.75) ملم ومعدل جريان الداخل 4 لتر/ساعة وارتفاع عمود الامتزاز 35 سنتمتر.

**KEY WORDS:**

**Wastewater, Adsorption, Sunflower stalks, heavy metals removal, copper, low cost adsorbent.**

## INTRODUCTION

The idea of using various agricultural products and byproducts for the removal of heavy metals from solution has been investigated by number of authors. Friedman and Waiss, (1972), Radalletal et al. (1974) and Henderson et al.(1977) have investigated the efficiency of number of different organic waste materials as sorbents for heavy metals. The obvious advantages of this method compared to other are lower cost involved when organic waste materials are used. Activated carbon adsorption appears to be a particularly competitive and effective process for the removal of heavy metals at trace quantities (Huang and Blankenship, 1984). However, the use of activated carbon is not suitable for developing countries because of its high cost (Panday et al., 1985).For that reason, the uses of low cost materials as possible media for metal removal from wastewater have been highlighted. These materials range from industrial products such rubber tyres (Knocke and Hempill (1981))., industrial wastes and some natural material including agricultural product and by-product as mentioned earlier.

Sunflower stalks have reasonable maximum adsorption capacities (Sun and Shi, 1998). Residues, which are mainly ligno-cellulosic materials, can inherently adsorb waste chemicals such as dyes and cations in water due to the Coulombic interaction between the two substrates and physical absorption. They are renewable agricultural wastes available abundantly at no or low cost. Disposal of the agricultural biomasses in California and many states is the major obstacle to the sustainable agriculture and environment utilization of the biomasses has been studied extensively and some alternatives have been developed. Among many new technologies, utilizing plant residues as adsorbents for the removal of toxic chemicals in waste water is a prominent technology (McKay et al.,1987; El-Geundi, 1991).which have proven relatively strong Coulombic adsorption to cations such as organic bases as well as intrinsic adsorption to other materials such as acidic and anionic compounds (Sun and Xu, 1997). Sunflower stalks have relatively large surface areas that can provide intrinsic adsorptive sites to many substrates. On the basis of the structural analysis of the sunflower stalks, it was expected that the adsorbents should be able to remove cationic metal ions as well

The adsorbents are usually used in the fixed bed process because of the ease of operation. To design and operate a fixed bed adsorption process successfully, the column dynamics must be understood, that is the breakthrough curves under specific operating conditions must be predictable (Markovska and Meshkoco, 2001). The location of the breakpoint and the shape of the breakthrough curve (degree of concavity) are influenced by many parameters pertaining to the nature of the adsorption equilibrium isotherm and the mass transfer rate (Basheer and Najjar, 1996).

This paper presents a study on adsorption of copper ions on sunflower stalks as adsorbent. Contact time and adsorbent surface area were identified preliminarily as the most important variables that affect the adsorption of copper ions.

## EXPERIMENTAL WORK

### Materials:

### Adsorbent

All of the used sun flower stalks were analytical grade, purchased and applied without further purification. The fibrous part was removed, crushed in a mill, washed with de-ionized water and air-dried. Then it was sieved to different sizes and activated with 2% (v/v) nitric acid for 24 hr and washed with deionized water. The air dried adsorbent was divided into two parts, one part was modified and the other left unmodified.

The Sunflower stalks were sieved to produce a particle size of 1.18-2.36, 2.36-4.75and 4.75-9.00 mm.

### Adsorbate

Copper sulfate ($CuSO_4.5H_2O$) solution was used as adsorbate.

## EXPERIMENTAL

### Batch Experiments

Batch experiments were used to obtain the equilibrium isotherm curves and then the equilibrium data. In batch mode the effect of sunflower stalks weight on adsorption process and equilibrium isotherm experiments were studied.

All experiments were carried out at $25C^o$ ±1 ,rpm 120 and PH 4.2 because It was found that the adsorption of copper remains almost unchanged regardless of any change in the temperature and the maximum adsorption start at pH 4.2 (Sun and Shi, 1998) . Five 1 L flasks were used for experiments conducted with an initial copper concentration of 100 mg/L, sun flower stalks dosage was used for 2, 3, 4, 5 and 6 g/L. Samples were collected and tested. A metal ion that was lost from the solution was assumed to be adsorbed onto the adsorbents. Data obtained from batch tests fitted to Freundlich, Langmuir and Freundlich-Langmuir adsorption isotherm equations as shown in figures.

### Fixed Bed Column Experiments

Column experiments were carried out for various particle sizes (dp), flow rates (Q), bed depths (H), initial metal concentrations ($C_o$) and the nature of the adsorbate to measure the breakthrough curves for the systems.

The fixed bed adsorber studies were carried out in Q.V.F. glass column of 8.75cm I.D. and 50 cm in height. The sun flower stalks was confined in the column by fine mesh at the bottom to avoid loss the adsorbent. The influent solution was introduced to the column through a small water distributor to ensure a uniform distribution of influent through the adsorbent, fixed at the top of the column.

The schematic representation of experimental equipment is shown in **Fig 1**.

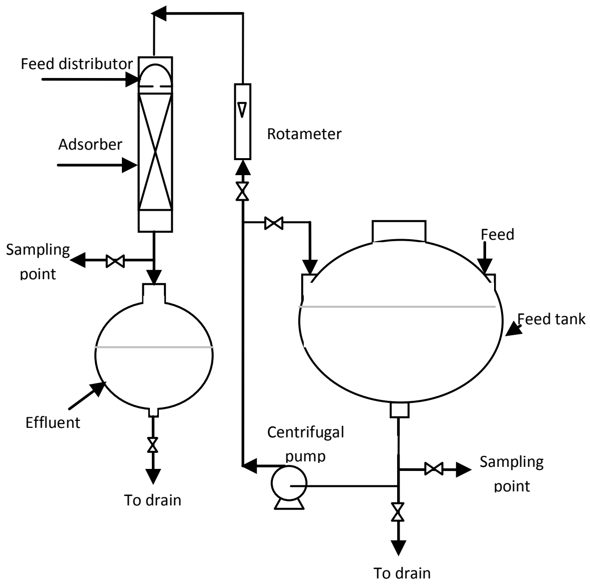


**Fig. 1, Schematic representation of experimental equipment**

## RESULTS AND DISCUTION:

### Batch Experiments:

### Adsorption Isotherms:

Adsorption isotherm studies were performed to obtain equilibrium isotherm curves and data required for the design and operation of fixed bed adsorber. The adsorption isotherm curves were obtained by plotting the weight of the solute adsorbed per unit weight of the adsorbent ($q_e$) against the equilibrium concentration of the solute ($c_e$). **Fig. 2** shows the adsorption isotherm curve for adsorption of copper on unmodified sun flower stalks at 25 C$^o$

The obtained data was correlated with Langmuir, Freundlich and Langmuir-Freundlich models. The Langmuir model describing adsorption showed in **eq. (1)**

$$\frac{x}{m} = \frac{abC_e}{1+aC_e} \tag{1}$$

**Eq. (2)** described the Freundlich adsorption model):

$$\frac{x}{m} = kC_e^{1/n} \tag{2}$$

Combination of Langmuir-Freundlich Isotherm Model, i.e. the Sips model for single component adsorption presented by **eq.(3)** (Sips, 1984) .

$$q_e = \frac{bq_mC_e^{1/n}}{1+b\,C_e^{1/n}} \tag{3}$$

The parameters for each model obtained from non-linear statistical fit of the equation to the experimental data. All parameters with their correlation coefficients are summarized in **Table 1**.

From the statistical analysis “Excel program” it was found that adsorption of metal by sun flower stalks could be well described by the three isotherm models. The correlation coefficients were in the range of (0.983 -0.999 %) for initial copper concentration 100 mg/l. The correlation coefficient value was higher for Langmuir-Freundlich than other correlations. This indicates that the Langmuir-Freundlich isotherm is clearly the better fitting isotherm to the experimental data.

**Effect of Mass of Unmodified Sunflower Stalks on the Adsorption Process:**

The effect of mass of unmodified sun flower stalks on adsorption of copper at constant adsorbate concentration was studied for the purpose of determining the best adsorbent mass that will bring a best removal. The results of the dependence of copper on the mass of unmodified sun flower stalks of size 1.18-2.35 mm at 25 $C^o$ is shown in **Figs. 3and4**. These figures represent the plotting concentration of copper with time and the percentage removal of copper against the mass of unmodified sunflower stalks.

The percent removal of copper increases with increasing weight of sunflower stalks up to a certain value, depending on adsorption sites. These figures can clearly show that the increase in the percent removal of copper is due to the greater availability of adsorption sites or surface area of adsorbent. An identical trend was observed by other investigations ((Sun and Xu, 1997; Maruf et al., 2006)

**Table 1, Isotherm Parameters for Copper Adsorption onto Unmodified Sun Flower Stalks with the Correlation Coefficient.**

| Model | Parameters | Values |
|---|---|---|
| Langmuir (1) | a, L/mg | 0.0077 |
| | b, mg/g | 142.8 |
| | Correlation coefficient ($R^2$) | 0.983 |
| Freundlich (2) | K, L/g | 1.6 |
| | n, | 1.2136 |
| | Correlation coefficient ($R^2$) | 0.99 |
| Combination of Langmuir-Freundlich (3) | $q_m$, mg/g | 196.79 |
| | b, mg/g | 0,0057 |
| | n, | 1.03 |
| | Correlation coefficient ($R^2$) | 0.999 |

**FIXED BED EXPERIMENTS:**

**Effect of Volumetric Flow Rate**

In a design of fixed bed adsorption column, the contact time is the most significant variable and therefore the bed depth and the metal solution flow rate are the major design parameters (Markovska, 2001). The effect of varying volumetric flow rate was investigated at constant concentration 100 ppm and particle size 2.35-4.75 mm and bed depth 30 cm and the breakthrough curves are presented in **Fig.5**. It is obvious that increasing the flow rate decreases the volume treated. This is due to decreasing contact time between the metal and the adsorbent at higher flow rate. Increasing the flow rate may be expected to make reduction of the surface film. Therefore, this will decrease the resistance to mass transfer and increase the mass transfer rate. But, according to **Fig.5**, the mass transfer rate decreases with increasing the flow rate .This is because the reduction in the surface film is due to the disturbance created when the film of the bed increased resulting of easy passage of the adsorbate molecules through the particles and entering easily to the voids. The easy entering of molecules decreased contact time between metal and sunflower stalks at high flow rate. These results agree with those obtained by Kim et al.(2003a)and Maruf et al.(2006).

**Effect of Bed Depth:**

The effect of bed depth was investigated for copper adsorption on sun flower stalks. The experimental breakthrough curves are presented in **Fig. 6.** The breakthrough curve was obtained for different bed depth of sun flower stalks at constant flow rate (4 l/h), constant particle size (2.35-4.75) mm and constant copper concentration (100 ppm). It is clear that the increase in bed depth increases the breakthrough time and the residence time of the solute in the column, due to the availability greater surface area (Malkoc and Nugoglu, 2006).

Thus, the residence time in the column is more important than fluid velocity in improving removal efficiency.

**Effect of Particle Size:**

In case of using an adsorbent particles of much smaller size, that will eliminate inter particle mass transfer resistance. This means that the rate determining step is diffusion through film around each particle. The experimental breakthrough curves are presented in **Fig. 7** were obtained for different particle size (1.18-2.36, 2.36-4.75 and 4.75-9.00 mm) at constant initial concentration of copper (100 ppm), bed depth of sun flower stalks (30 cm) and constant flow rate (4 l/h). The experimental results showed that fine particle sizes (1.18-2.36 mm) gave a higher metal removal than others particle sizes. This was due to large surface area of fine particles.

**Effect of initial copper concentration:**

The initial copper concentration of the influent is important since a given mass of adsorbent can only adsorb a fixed amount of metal. Therefore, the more concentrated an influent, the smaller is the volume of effluent that a fixed mass of adsorbent can purify. So, experiments were under taken to study the effect of varying the initial metal concentration on the rate of metal adsorption and they are presented in **Fig. 8**. The effect of the initial concentration in the inlet flow is one of the limitation factors and a main process parameter. Increasing the inlet concentration increases the slope of the breakthrough curve and makes it much steeper, reducing the volume of the effluent treated and reducing the throughput until breakthrough. This may be caused by saturation of adsorbent more quickly with high concentration, thereby decreasing the breakthrough time .Since the rate of diffusion is controlled by the concentration gradient, it takes a longer contact time to reach saturation for the case of low value of initial solute concentration. Wastewater treatment is limited by the breakthrough point or the dynamics of reaching that point. These systems have a small time delay with higher concentrations in the inlet, so the metal solutions have to be diluted before separation for better removal. The same conclusion was obtained by Markovska, 2001 and Maruf et.al, 2006.

**Effect of Modification of Adsorbate:**

Sunflower stalk is an environmental pollutant has been found to be a good adsorbent for the removal of Cu (II) ions from aqueous solutions. The modification of the adsorbent by nitric acid has been shown to enhance the adsorption capacity as illustrated in **Fig.9.**

The high binding capacities of cationic species on the adsorbents are mainly the results of columbic interactions (Weixing et al., 1998). Although sunflower stalks showed to be effective adsorbent for a wide range of solutes, particularly divalent metals cations, crop residues suffer from at least two major drawback: low exchange or sorption capacity, and poor physical stability (i.e. partial solubility) (Laszlo and Dintzis, 1994). In order to overcome these problems, chemical modification and/or activation of the raw adsorbents are required.

## CONCLUSIONS:

- Unmodified and modified Sun flower stalks were effective in adsorbing copper from wastewater.
- In batch experiment the percent removal of copper increases (70 -80 %) with increasing in sunflower stalks dose (2 - 6 g/l).
- Batch kinetics experiments showed that equilibrium time was about 60 min with mechanical mixing 120 rpm, initial concentration 100 ppm and adsorbent weight 4 gm/l.
- The isotherm models (Langmiur, Freundlich and Langmiur- Freundlich) gave good fitting for the adsorption capacity of sunflower stalks versus equilibrium concentration of copper ions. The correlation coefficients ($R^2$) obtained from Excel program for these models were in the range of 98.3- 99.9% but the Langmiur- Freundlich model gave the best fitting for adsorption capacity.
- In fixed bed experiment, the percent removal of copper increases with increasing contact time (reducing the flow rate), adsorbent surface area, and bed height.
- Modification of the sun flower stalks by nitric acid enhances the adsorption capacity to some extent.

## NOMENCLATURE:

| | |
|---|---|
| a | Langmiur constant (L/mg) |
| b | Langmiur constant (mg/g) |
| C | concentration of solute in solution at any time (mg/l) |
| $C_e$ | concentration of solute in solution at equilibrium (mg/l) |
| $C_0$ | initial concentration of adsorbate (mg/l) |
| $k$ | Freundlich equilibrium constant indicative of adsorption capacity |
| m | mass of solute adsorbent (g) |
| $n$ | Freundlich constant indicative of adsorption intensity |
| H | bed depth (m) |
| Q | flow rate (l/h) |
| $q_e$ | amount of metal ion adsorbed at equilibrium (mg/g) |
| $R^2$ | correlation coefficient |
| t | time (min) |
| x | mass of solute adsorbed (mg) |
| $d_p$ | particle size (mm) |
| qm | maximum amount of metal ion adsorbed at equilibrium (mg/g) |

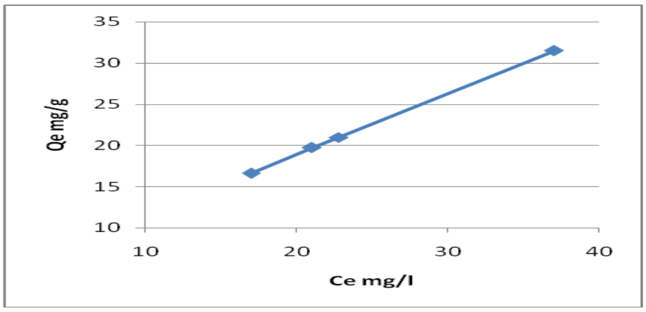


**Fig. 2, Adsorption isotherm for Copper onto Sunflower Stalks ($C_o$=100mg/L,Temp.=25C$^o$, particle size =1.18 mm)**

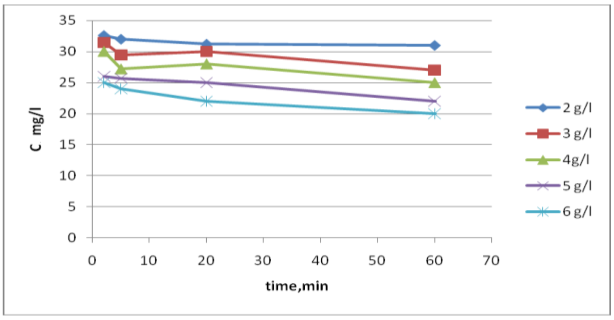


**Fig.3, Change in Copper Concentration with Time of Batch Tests ($C_o$=100mg/L, Temp. =25C$^o$,
particle size=1.18 mm)**

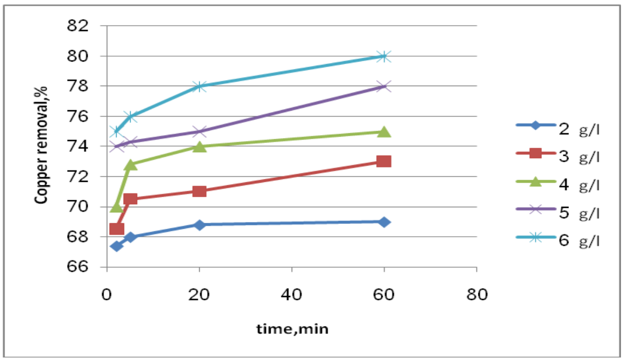


**Fig. 4, The Effect of Sunflower Stalks on Copper Removal of Batch Tests (Co=100mg/L, Temp. =25Co, particle size=1.18mm)**

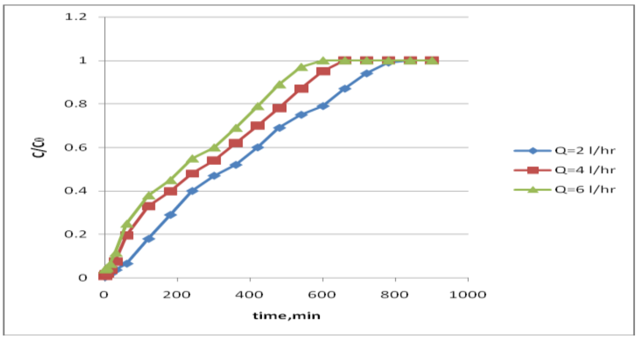


**Fig.5, Experimental Breakthrough Curves for Adsorption Copper on Unmodified Sunflower Stalks for Different Flow Rates (H=0.30 cm, $d_p$=0.35 cm,$C_0$=100 ppm)**

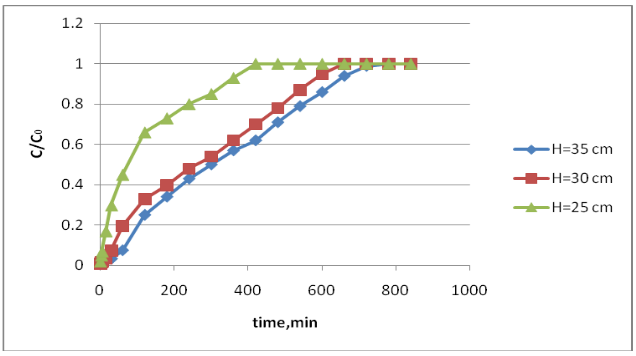


**Fig.6, Experimental Breakthrough Curves for Adsorption Copper on Unmodified Sunflower Stalks for Different Bed Depths (Q=4 l/hr, $d_p$=0.35 cm,$C_0$=100 ppm)**

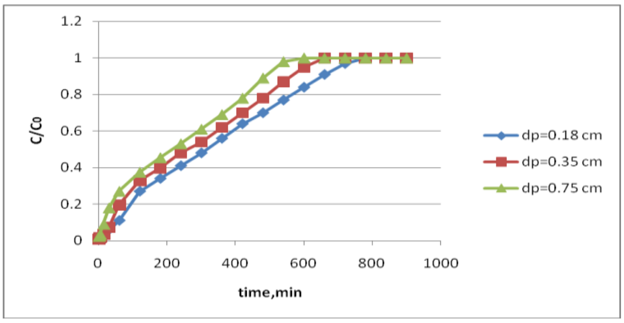


**Fig.7, Experimental Breakthrough Curves for Adsorption Copper on Unmodified Sunflower Stalks for Different Particle Sizes(Q=4 l/hr, H=30 cm,$C_0$=100 ppm)**

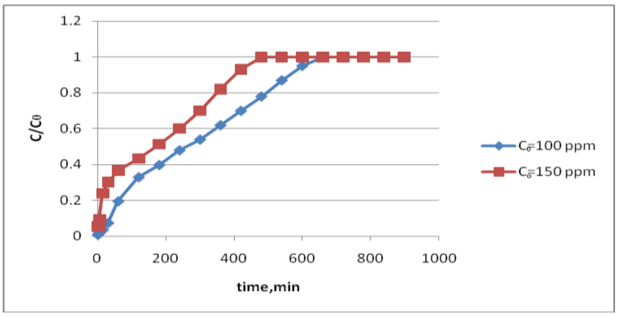


**Fig.8, Experimental Breakthrough Curves for Adsorption Copper on Unmodified Sun Flower Stalks for Different Initial Concentrations (Q=4 l/hr, H=30 cm ,$d_p$=0.35 cm)**

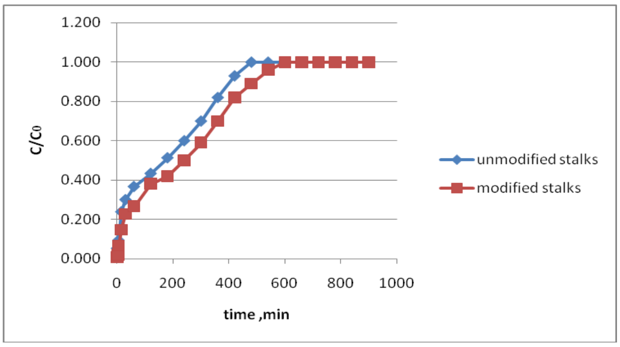


**Fig.9, Experimental Breakthrough Curves for Adsorption Copper on Modified and Unmodified Sun Flower Stalks (Q=4 l/hr, H=30 cm,dp=0.35 cm ,$C_0$=150 ppm)**

## REFERENCE


- Basheer, I. A. and Najjar, Y. M., (1996), "Predicting Dynamic Response of Adsorption Column with Neural Nets", J. Computing in Civil Engineering, 10 (1), pp 31-39.
- El-Geundi, M. S.( 1991), “Color Removal From Textile Effluents by Adsorption Techniques”. Water Res., 25, 271-273.
- Friedman M, Waiss AC Jr. (1972). “Mercury uptake by selected agricultural products and by-products”. Environ. Sci. Technol. 6: 457- 458
- Hendreson RW, Andrews DS, Lightsey GR, Poonawala NA (1977).” Reduction of mercury, copper, nickel, cadmium, and zinc levels in solution by competitive adsorption on to peanut hulls, and raw and aged bark”. Bull. Environ. Contam. Toxicol. 17, 355-359.
- Huang CP, Blankenship DW (1984). “The removal of mercury (II) from dilute aqueous solution by activated carbon”. Water Res. 18(1), 37- 46.
- Kim, J.G., Kim, J.H., Moon, H-S., Chon, C-M. and Ahn, J.S., 2003a, "Removal Capacity of Water Plant Alum Sludge for Phosphorus in Aqueous Solutions", Chemical Speciation and Bioavailability, 14, pp 67-73.

- Knocke WR, Hemphill LH (1981). “Mercury sorption by waste rubber” Water Res. 15: 275-282 Sips, R., (1984), J. Chem. Phys., 16, 490-495.

- Laszlo JA, Dintzis FR (1994). “Crop Residues as Ion-exchange Materials: Treatment of soybean hull and sugar beat fiber (pulp) with epichlorohydrin to improve cation-exchange capacity and physical stability”. J. Appl. Poly. Sci. 52: 531-538.

- Malkoc, E. and Nuhoglu, Y., (2006), "Fixed Bed Studies for the Sorption of Chromium (VI) onto Tea Factory Waste", Chemical Engineering Science, V.61, pp 4363-4372.

- Markovska, L. and Meshko, V., (2001), "Solid Diffusion Control of the Adsorption of Basic Dyes onto Granular Activated Carbon and Natural Zeolite in Fixed Bed Column", J. Serb. Chem. Soc., 66 (7), pp 463-475.

- Maruf Mortula, Meaghan Gibbons and Graham, A. Gagnon, (2006), "Phosphorus Adsorption by Naturally-Occurring Materials and Industrial by-Products", J. Environ. Eng. Sci., 6, pp 157-164

- McKay, G.; Geundi, M. El.; Nassar, M. M. (1987),” Equilibrium Studies during the Removal of Dyestuffs From Aqueous Solutions Using Bagasse Pith”. Water Res., 21, 1513-1520.

- Panday KK, Prased G, Singh VN (1985). “Copper (II) Removal from Aqueous Solution by Fly Ash”. Water Res. 19: 869-873.

- Randall JM, Bermann RL, Garrett Vand, Waiss AC Jr. (1974a). “Use of bark to remove heavy metal ions from waste solutions”. For. Prod. J. 24(9): 80-84.

- Sun, G.; Xu, X. (1997),”Sunflower Stalks as Adsorbents for Color Removal from Textile Wastewater”. Ind. Chem. Eng. Res., 36, 808- 812

- Sun G, and Shi W,( 1998)” Sunflower Stalks as Adsorbents for the Removal of Metal Ions from Wastewater” Ind. Eng. Chem. Res., 1998, 37 (4), 1324-1328

- Weixing S, Xiangjing X, Gang S (1998). “Chemically modified sunflower stalks as adsorbent for colour removal from textile wastewater”. J. of Appl. Poly. Sci. 71: 1841-1850.

# REMOVAL OF KEROSENE FROM WASTE WATER USING IRAQI BENTONITE

Abbas H. Sulaymon and Ziad T. Abd Ali
Environmental Engineering Department
College of Engineering -University of Baghdad


## ABSTRACT

The aim of the present research is to study the potentiality of Iraqi bentonite as adsorbent for removing of kerosene from wastewater. Also the capacity of bentonite for kerosene removal was compared to the activated carbon capacity. The sorption of kerosene onto bentonite and AC. were described by two well – known adsorption isotherm models namely Langmuir and Freundlich models. It was found that the Freundlich model can fit very well the equilibrium isotherm adsorption of kerosene onto bentonite and AC. Batch experiments were carried out to study the effect of adsorption of kerosene onto bentonite using various conditions such as initial concentrations of kerosene ( 100-500 ) mg/L, agitation speeds (125, 250, 500, 800) RPM, and weights of bentonite ( 0.05, 0.5,1.1 ) gm, particle sizes (0.5- 0.6) mm, and temperature 303 k . It was found that the best results for removing kerosene onto bentonite were obtained at $C_o$=500 mg/L, RPM =800. Activated carbon was used as powder and granular of particle sizes ranged (1-1.18) mm and (0.5-0.6) mm. The results indicated that the activated carbon was more active than bentonite for removing of kerosene from wastewater


**KEYWORDS:**
Bentonite; activated carbon; kerosene; adsorption


**الخلاصة**

الهدف من هذا البحث هو دراسة قدرة البنتونايت العراقي كمادة ممتزة (adsorbent) على ازالة الكيروسين من الماء. وكذلك مقارنة كفاءة ازالة الكيروسين بواسطة البنتونايت مع كفاءة ازالة الكيروسين بواسطة الكاربون المنشط.

ان عملية امتزاز الكيروسين على البنتونايت و الكاربون المنشط تم وصفها بمودلين معروفين(لا نكمير وفرندلش) والتي تعتبر من الموديلات الشائعة في مجال معالجة المياه الملوثة,وقد وجد بأن معادلة (فرندلش) هي اكثر تطابقا من معادلة (لانكمير) في عملية امتزاز الكيروسين على البنتونايت والكاربون المنشط عند حالة التوازن(Equilibrium Isotherm). تم اجراء تجارب النمط الدفعي (Batch Process) لدراسة تأثير : تغير التركيز الابتدائي للكيروسين ، سرعة الرج، تغير وزن البنتونايت مع الزمن. وقد تمت كل التجارب تحت نفس الظروف. وجد بان افضل النتائج لازالة الكيروسين على البنتونايت هي بتركيز ابتدائي = 500 ملغرام/ لتر ، سرعة الرج = 800 ، حجم حبيبي= (0.6- 0.5) ملمتر. وتم استخدام الكاربون المنشط باحجام مختلفة (1.18-1) ملمتر ، (0.6- 0.5) ملمتر ،(بودر) . لقد اشارت النتائج بأن الكاربون المنشط هو اكثر فعالية من البنتونايت في ازالة الكيروسين من الماء .

## INTRODUCTION:

Numerous standards and regulations were adopted for discharge of oily waste water into surface water or sewage systems. These regulations may vary from country to another, and even within a country itself. Environment Canada (1976b) established a discharge limit for oil and grease of 15 mg/L at federal establishment. In Iraq (Iraqi Specification 1967) the allowable oil and grease concentration for discharge into water is 10 mg/L

Oils that are found in contaminated water can be grouped into four categories (Patterson,1975): (1)light hydrocarbons including light fuels such as gasoline, kerosene and jet fuel; (2)heavy hydrocarbons; (3)lubricants and cutting fluid; and (4)fats that are found in both plants and animals. The aqueous effluents from industrial, municipal and petroleum refineries contain different pollutants including oil, furfural, phenolic compounds, sulfides, suspended solids, toxic metals, ammonia and biochemical oxygen demand. Methods of removal of those pollutants generally involve biological degradation, chemical oxidation, physical stripping and adsorption process (Prather, 1970). Adsorption techniques are widely used in the field of removing small quantities of pollutant present in the large volume of fluid, which can be carried out in batch wise or continuous manner of operation (Rao, 1994). Many factors may affect the decision of choosing an adsorbent for removal of oil from water, these are: (1) economical factor (cost of the adsorbent); (2) abundance and availability of the adsorbent, and (3) effectiveness of the adsorbent in removing a particular pollutant. The removal of organic material by adsorption using activated carbon or polymers is an effective treatment technique. Although, activated carbon is a preferred adsorbent, its wide spread uses are restricted due to its high cost and expends much of its capacity in removal of incidental constituents (Dentel et al.,1995). Therefore many studies are directed in finding an efficient and economical sorbent. Clay (bentonite) can be considered as an alternative adsorbent due to its effectiveness in removing certain organic compounds from water and its abundance, availability, and low cost (Baker & Luh, 1971).

Numerous quantitative empirical mathematical expressions, called isotherms, have been developed to describe sorption. The two most common sorption models are the Langmuir and Freundlich isotherms (Sulaymon, A. H. and Ahmed K. W., 2008).

The Langmuir model is based on the assumption that a single monolayer of sorbate accumulate at the solid surface. As the concentration of the sorbate is increased in the liquid phase, proportionately more of the sorbent surface is covered with the sorbate. The equation that describes Langmuir system is the

$$q_e = \frac{x}{m} = \frac{ab\ \mathrm{Ce}}{1 + \mathrm{bCe}} \qquad (1)$$

The Langmuir equation may be transformed to a linear expression by inverting Equation (1) and separating variables:

$$\frac{\mathrm{Ce}}{q_e} = \frac{1}{ab} + \frac{\mathrm{Ce}}{a} \qquad (2)$$

The empirical coefficients (a) and (b) may be obtained by plotting Ce/qe as a function of Ce. Using linear regression, the slope = 1/a and the y- intercept = 1/ (ab) can be obtained. (Richard, 1997).

The Freundlich model is characterized by sorption that continues as the concentration of sorbate increases in the aqueous phase. The mass of material sorbate is proportional to the aqueous phase concentration at low sorbed concentrations and decreases as the sorbate accumulates on the sorbent surface. Sorption then continues with increasing aqueous phase sorbate concentrations, but to a diminishing degree. The Freundlich isotherm is quantified by:

$$q_e = \frac{x}{m} = K_F C_e^{1/n} \qquad (3)$$

The coefficients "$K_F$" and "n" may be determined by plotting experimental data on log –log paper. Alternatively, Equation (3) can be transformed logarithmically:

$$\text{In } q_e = \text{In } K_F + \frac{1}{n} \text{ In } C_e \qquad (4)$$

Logarithmic transformations of experimental data may then be plotted on arithmetic paper as In $q_e$ as a function of In $C_e$; through linear regression, $K_F = 10^{\text{y-intercept}}$ and 1/n = slope can be found. ( Richard, 1997)

## EXPRIMENTAL PROCEDURES:

### Materials:

- **Adsorbate:**

Kerosene is obtained by atmospheric distillation of crude oil and consists mainly of normal and branched chain alkanes, cycloalkanes, alkyl benzenes and alkyl naphthalene's (Ellison et al., 1999). Aliphatic hydrocarbons are the primary components (80%) ranging from $C_9$ to $C_{16}$. Aromatic hydrocarbon makes up about 20% of the components and consists mainly of single- ring compounds such as alkyl benzene. The kerosene used in this study was supplied by "AL-Dora Refinery "; it was distilled at range (180-270) $^oC$.

- **Adsorbent:**

**Bentonite:**

bentonite used in this study was an Iraqi bentonite (Calcium base). It was supplied by "State Company of Geological Survey and Mining" as pecieses of rocks. These rocks were destructed by a crusher (type: Jaw Crusher – BBI Restch) to granules different sizes, and then sieved using sieves (type: Restch, Germany) to produce granules of sizes (0.5-0.6) mm. The granules were grained to powder (0.074-0.088) mm by graindер (type: National MK – 51N). The granules of bentonite were dried at 100 $^oC$ for 30 min before used.

**Activated carbon (AC.):**

Granulated activated carbon (GAC) was supplied by "Unicarbo, Italians". The physical properties were measured by Oil Research and Development Center-Ministry of Oil and were coincided with that supplied by the manufacture. The granulated activated carbon (GAC) was crushed, sieved into (0.5- 0.6) mm, (1-1.18) mm, and then grained to powder (0.074-0.088) mm by a graindеr (type: National MK – 51N). The require sieve fraction was removed and washed by distilled water to remove fines from the crushed GAC. The GAC was placed in a clean beaker filled with distilled water. Then it was stirred with a glass rod and allowed to settle. After allowing the GAC particles to settle for (5) minutes, the supernatant was poured off and new distilled water was added. This process was repeated until the supernatant was clear. The wet GAC was dried in an oven that was maintained at (100) $^oC$ for (24) hours, after which the GAC was kept in a desiccators for experimental use.

- **Solvent:**

  Iso-propyl alcohol $[CH_3)_2CHOH]$ was used as a solvent for kerosene in water. It's molecular weight is (60.1) g/g mol.

## Equilibrium isotherm experiment:

Batch studies were adopted to obtain the equilibrium data. Solutions were prepared containing the desired solute (kerosene) concentration of 100, 200, 300, 400, and 500 mg/L. 100 ml of each prepared solution were placed in nine bottles each of 250 ml volume. Adsorbent of 0.05, 0.1, 0.2, 0.3, 0.5, 0.75, 0.9, 1, and 1.1 gm were placed in nine individual bottles, each sample of them should be gathered with another sample containing the same quantity of adsorbent solution (adsorbent and distilled water) as a blank. The bottles were then placed on a shaker (Type: B.BRAUN) and agitated continuously for 30 hours at 30 $^oC$. Ten ml from each sample was taken and mixed with 10 ml of iso-propyl alcohol (extra pure) as co- solvent (Bastow et al., 1997) and the mixture was shaked by shaker (type: Stuart scientific, Auto vortex SA6, UK) for (1.5) min,and then filtered by filter paper (type: Whatman 542, England).

The equilibrium concentrations were measured by means of UV- spectrophotometer (Type: GENESYS$^{TM}$ 10 series spectrophotometers, thermo). At that point the concentration was in equilibrium. The adsorbed amount is calculated using the following equation:

$$qe = \frac{V_L (C_0 - Ce)}{m} \tag{5}$$

The adsorption isotherms curves were obtained by plotting the weight of solute adsorbed per unit weight of adsorbent (qe) against the equilibrium concentration of kerosene in the solution ($C_e$) (Crittenden& Weber, 1978). All batch experiments were conducted at constant temperature 30 $^oC$.

## Swelling test experiment:

The swelling of bentonite clay in water and kerosene was measured. One gm of powderd bentonite was gradually added in small portions to 50 ml of water and the same quantity of bentonite was added to 50 ml of kerosene contained in a 100 ml graduated cylinder, without stirring .

After (24) hours at room temperature, the volume of the column of clay was measured, after which the content was stirred with a glass rod and allowed to stand for another (24) hours. The swelling was then recorded in both water and kerosene.

## Analytical technique:

The UV – technique was used to measure the concentration of kerosene in a single system.

The optimal wavelength of kerosene was found to be 298 nm, using a Shemadzu model UV-160A ultraviolet / visible spectrophotometer, The concentration of the individual single component solute were determined using UV spectrophotometer directly from the calibration curve, figuer (1 ).

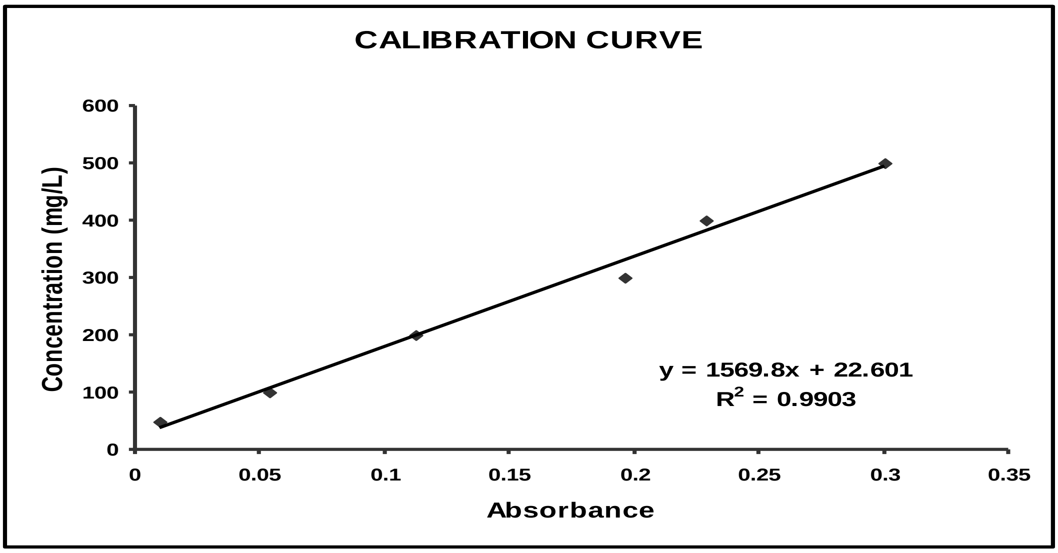


**Fig. (1) Calibration curve for kerosene system**

## RESULTS & DISCUSSION:

**Batch isotherm studies of bentonite:**

The data collected from adsorption isotherm experiments were subjected to non – linear estimation using the two well – known adsorption isotherms commonly adopted in the field of environmental engineering (Langmuir and Freundlich isotherm). The non – linear estimation was performed on a statistical package "AXCEL for Windows". The adsorption isotherms of kerosene onto bentonite of concentrations 100, 200, 300, 400, and 500 mg/L, agitation speed (RPM=250), and particle size 0.5- 0.6 mm at 30 $^oC$ are shown in figure (2).

Plotting Ce/qe versus Ce to obtain the value of constants in Langmuir model (a and b). These values were obtained from the slop and intercept of the lines, and tabulated in table (1).

Plotting ln qe versus ln Ce to obtain the value of constants of the Freundlich model ($K_F$ and 1/n). These values were obtained from the slop and intercept of the lines, and tabulated in table (1).

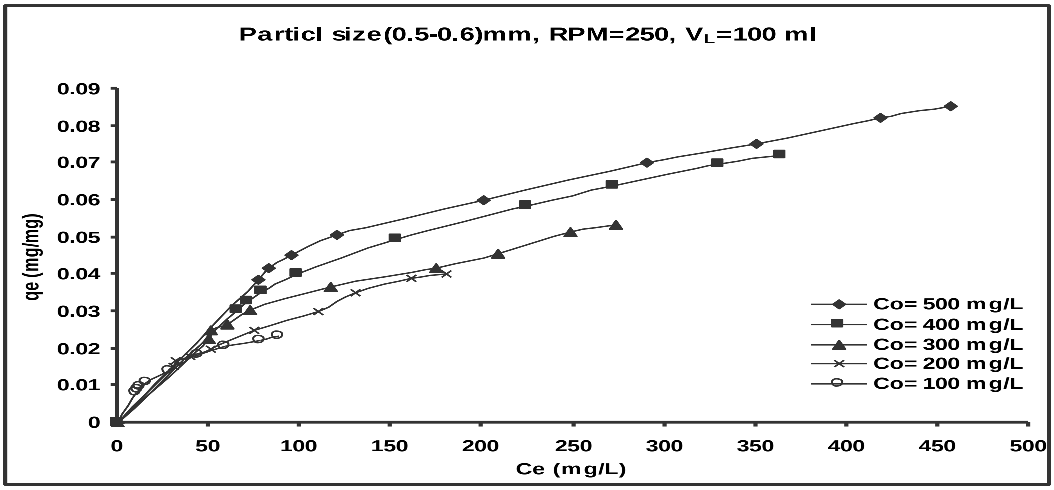


**Fig (2) Adsorption of kerosene onto bentonite at different initial Concentrations**

**Table (1) Regression equations of (Langmuir and Freundlich) isotherm models for various initial concentrations of kerosene and bentonite.**

| Initial Concentration | Isotherm model | Equation of regression | $R^2$ |
|---|---|---|---|
| $C_o$ = 500 mg/L | Langmuir | $\frac{x}{m}=\frac{(0.1084)(0.0070)Ce}{1+0.0070Ce}$ | 0.9921 |
| | Freundlich | $\frac{x}{m}=0.0065\ Ce^{1/2.3872}$ | 0.9936 |
| $C_o$ = 400 mg/L | Langmuir | $\frac{x}{m}=\frac{(0.1008)(0.0065)Ce}{1+0.0065Ce}$ | 0.9947 |
| | Freundlich | $\frac{x}{m}=0.0029\ Ce^{1/1.7439}$ | 0.9952 |
| $C_o$ = 300 mg/L | Langmuir | $\frac{x}{m}=\frac{(0.0714)(0.0094)Ce}{1+0.0094Ce}$ | 0.9858 |
| | Freundlich | $\frac{x}{m}=0.0040\ Ce^{1/2.0325}$ | 0.9895 |
| $C_o$ = 200 mg/L | Langmuir | $\frac{x}{m}=\frac{(0.0606)(0.0103)Ce}{1+0.0103Ce}$ | 0.9775 |
| | Freundlich | $\frac{x}{m}=0.0024\ Ce^{1/1.8480}$ | 0.9955 |
| $C_o$ = 100 mg/L | Langmuir | $\frac{x}{m}=\frac{(0.0305)(0.0357)Ce}{1+0.0357Ce}$ | 0.9933 |
| | Freundlich | $\frac{x}{m}=0.0028\ Ce^{1/2.1000}$ | 0.9935 |

It is clear from figure (2) and table (1) that:

- The equilibrium isotherm for each initial concentrations of kerosene is of favorable type (figure 1), for being convex upward and the amount adsorbed is proportional to the concentration in the fluid.
- The results of regression equations obtained for various initial concentrations of kerosene are presented in table (1). Higher values of correlation coefficient it were observed in Freundlich model for initial concentrations of 100, 200, 300, 400, and 500 mg/L.
- The sorption capacity of bentonite for various kerosene initial concentrations varied from (0.0082) to (0.0852) mg of kerosene per mg bentonite table (2). The average kerosene sorption capacity of bentonite was the highest for initial concentration of 500 mg/L and the lowest for initial concentration of 100 mg/L.

**Table (2) Experimental kerosene sorption capacity values (x/m) of bentonite for various kerosene initial concentrations, Co**

| Kerosene initial concentration | mg kerosene sorbed per mg bentonite, $\frac{x}{m}$ | |
|---|---|---|
| | Range | Mean |
| $C_o$ = 500 mg/L | 0.0384 - 0.0852 | 0.0608 |
| $C_o$ = 400 mg/L | 0.0304 - 0.0722 | 0.0503 |
| $C_o$ = 300 mg/L | 0.0227 - 0.0534 | 0.0369 |
| $C_o$ = 200 mg/L | 0.0153 - 0.0402 | 0.0265 |
| $C_o$ = 100 mg/L | 0.0082 - 0.0232 | 0.0152 |

**Batch kinetic studies of bentonite:**

The plots of kerosene concentrations versus time for kerosene emulsion ($C_o$ = 500 mg/L) used in this study and bentonite of 0.05, 0.5, and 1.1 gm are presented in figure (3). Based on this plot, an equilibrium time of 4 hours were chosen for kerosene, (based on 1.1 gm). It is notable that the kerosene concentrations decreased sharply at the beginning of adsorption indicating a rapid sorption rate(this is due to high surface area available for sorption at the beginning of the process), and then the decreased gradually, indicating a slow sorption rate.

,

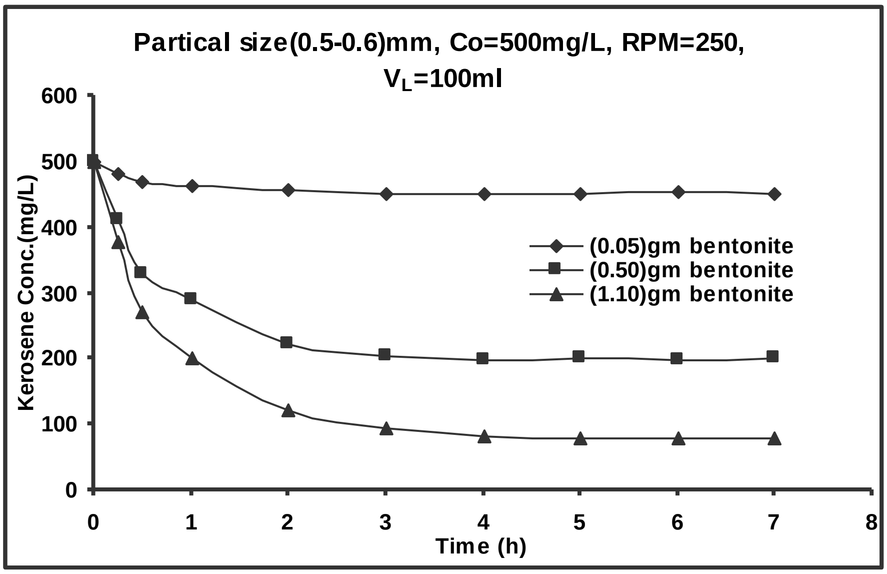


**Fig.(3)Equilibrium times for the sorption of kerosene by various quantities of bentonite**

The plots of kerosene concentrations at equilibrium Ce versus quantities of bentonite for various kerosene initial concentrations 0f 100, 200, 300, 400, 500 mg/L, RPM= 250 are presented in figure (4). As shown in this figure (4), when the quantity of bentonite is higher than 1.1 gm, the kerosene removal will not be increased due to reaching the equilibrium state.

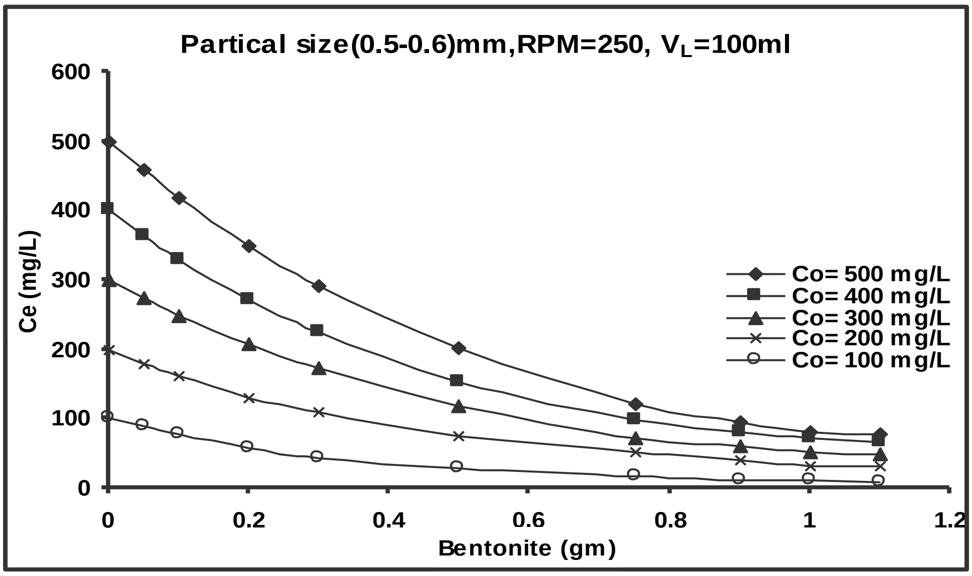


**Fig. (4) Kerosene removal by bentonite for various initial concentrations**

**Effect of agitation speeds of bentonite:**

The typical concentration decay curves of kerosene in batch experiments at different agitation speeds are shown in figure (5). It is observed that with increasing agitation speed, the kerosene concentration decreased.

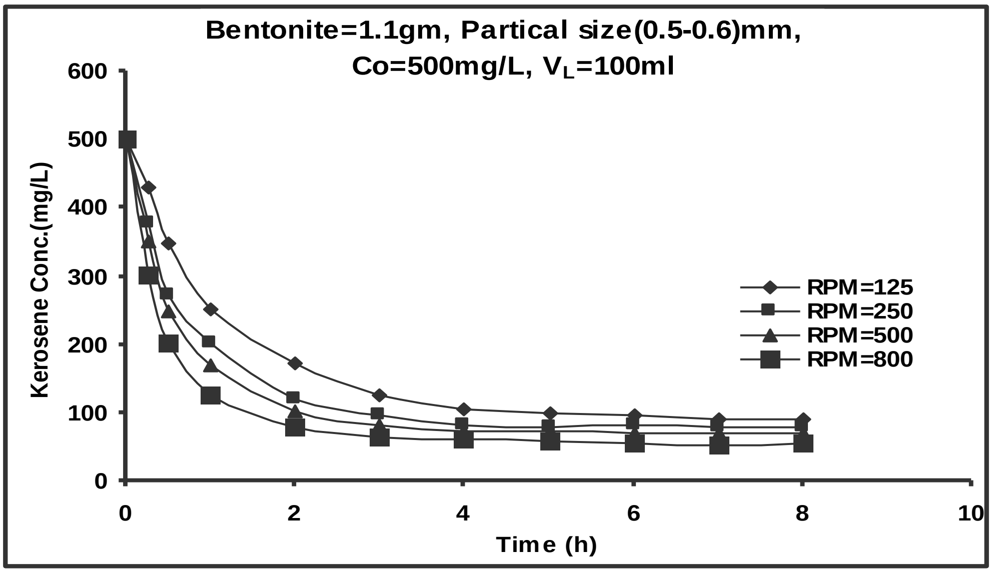


**Fig.(5) Concentration – time decay curves for kerosene onto bentonite in batch process at different agitation speeds**

**Swelling tests of bentonite:**

Figure (6) shows the swelling of the bentonite. The bentonite showed high swelling values in water with and without mixing (i.e. 4 and 6.5 ml/gm, respectively), and a low 1.5 ml/gm swelling value in kerosene (with and without mixing). No significant increase was found when the swelling was recorded after 48 hours and after mixing. This test emphasized that bentonite was posed hydrophilic nature more than organophilic nature.

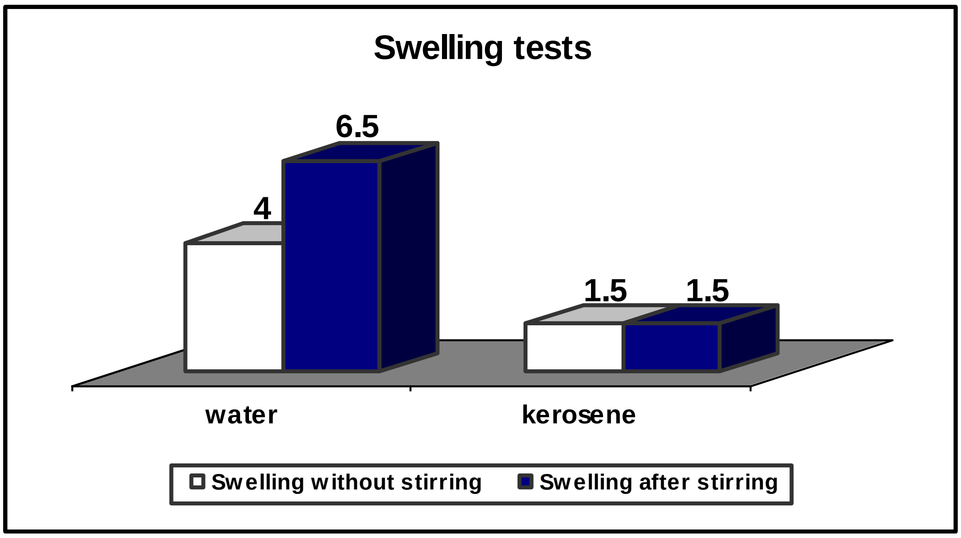


**Fig. (6) Swelling values with and without stirring**

**Batch isotherm studies of activated carbon:**

The adsorption isotherm of kerosene onto activated carbon of $C_o$= (500) mg/L, agitation speed RPM= 800, powdered and granular of size activated carbon (0.5-0.6) and (1-1.18) mm, at 30 $^oC$ is shown in figure (7).

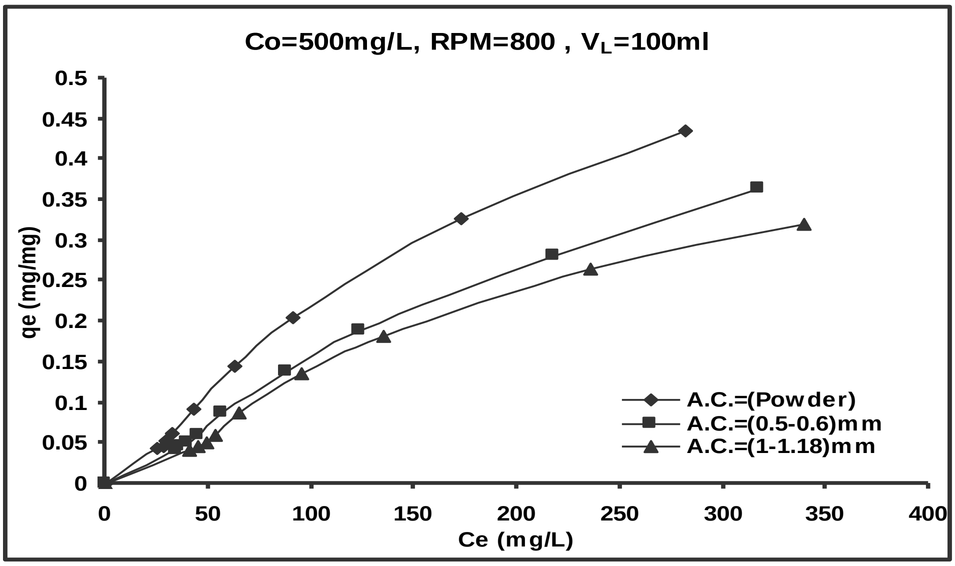


**Fig. (7) Adsorption of kerosene onto activated carbon at different particle sizes.**

The values of empirical constants for two models (Langmuir and Freundlich) were similarly as for bentonite, and are presented in table (3 ).

**Table (3) Regression equations of (Langmuir and Freundlich) isotherm model for various particle sizes of activated carbon.**

| Particle size (mm) | Isotherm model | Equation of regression | $R^2$ |
|---|---|---|---|
| (powder) | Langmuir | $\frac{x}{m}=\frac{(0.0940)(0.0006)Ce}{1+0.0006Ce}$ | 0. 1536 |
| | Freundlich | $\frac{x}{m}=0.0020\ Ce^{1/1.0146}$ | 0.9748 |
| (+0.5, -0.6) | Langmuir | $\frac{x}{m}=\frac{(3.0618)(0.0004)Ce}{1+0.0004Ce}$ | 0.1581 |
| | Freundlich | $\frac{x}{m}=0.0014\ Ce^{1/1.0183}$ | 0.9817 |
| (+1, -1.18) | Langmuir | $\frac{x}{m}=\frac{(3.3134)(0.0003)Ce}{1+0.0003Ce}$ | 0.0604 |
| | Freundlich | $\frac{x}{m}=0.0011\ Ce^{1/0.9983}$ | 0.9634 |

It is clear from above figures (7) and table (3) that:

- The equilibrium isotherm for various particle sizes of activated carbon is of favorable type, figure (7).
- The results of regression equations obtained for various particle sizes of activated carbon are presented in table (3). Higher value of correlation coefficient indicated that the Freundlich model was valid isotherm for all particle sizes.
- The sorption capacity of activated carbon for various particle sizes varied from (0.0417) to (0.4358) mg of kerosene per mg activated carbon, (table 4). The average kerosene sorption capacity of activated carbon was the highest for the powder and the lowest for particle size(1-1.18) mm. As shown in table (4), it is notable that as the particle size of activated carbon decreases, the sorption capacity increases due to the increase of surface area.

**Table (4) Experimental kerosene sorption capacity values (x/m) of activated carbon for various particle sizes.**

| Particle size(mm) | mg kerosene sorbed per mg activated carbon, x/m | |
|---|---|---|
| | Range | Mean |
| (1-1.18) | 0.0417 to 0.321 | 0.1318 |
| (0.5- 0.6) | 0.0423 to 0.3646 | 0.1401 |
| (powder) | 0.0431 to 0.4358 | 0.1566 |

- The results indicated that as the particle size of activated carbon decreased the kerosene removal efficiencies increased, at certain constant agitation speed and weight of adsorbent .The plot of kerosene concentration at equilibrium $C_e$ versus quantities of activated carbon for various particle sizes is presented in figure (8). It is of interest to note that the kerosene concentration at equilibrium Ce decreased very sharply at lower quantities of A.C. (up to 0.3 gm), and then the decrease became gradual.

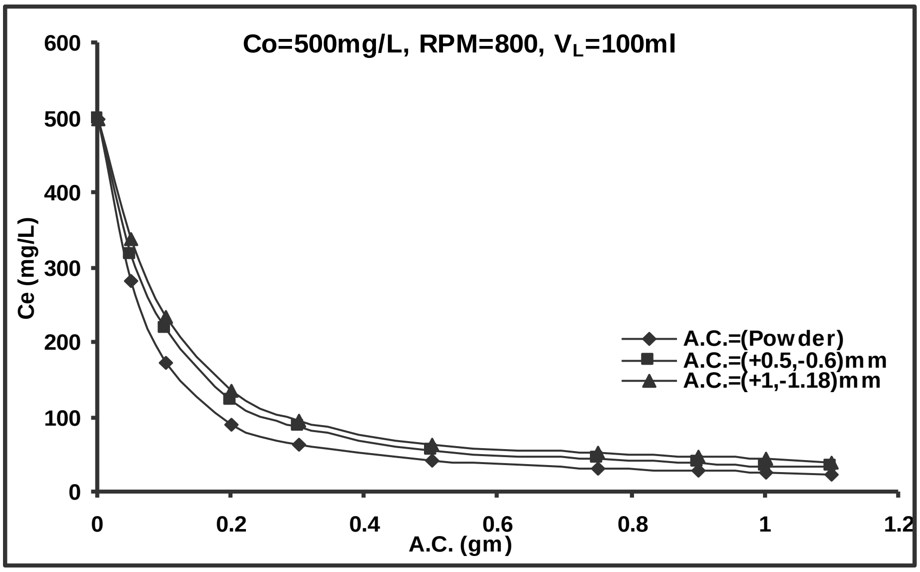


**Fig. (8) Kerosene removal by activated carbon for various Particle sizes**

**Batch isotherm studies of bentonite and activated carbon:**

The adsorption isotherm of kerosene onto bentonite and activated carbon of Co = (500) mg/L, agitation speed RPM = 800, particle size (0.5-0.6) mm at 30 $^oC$ is shown in figure (9).

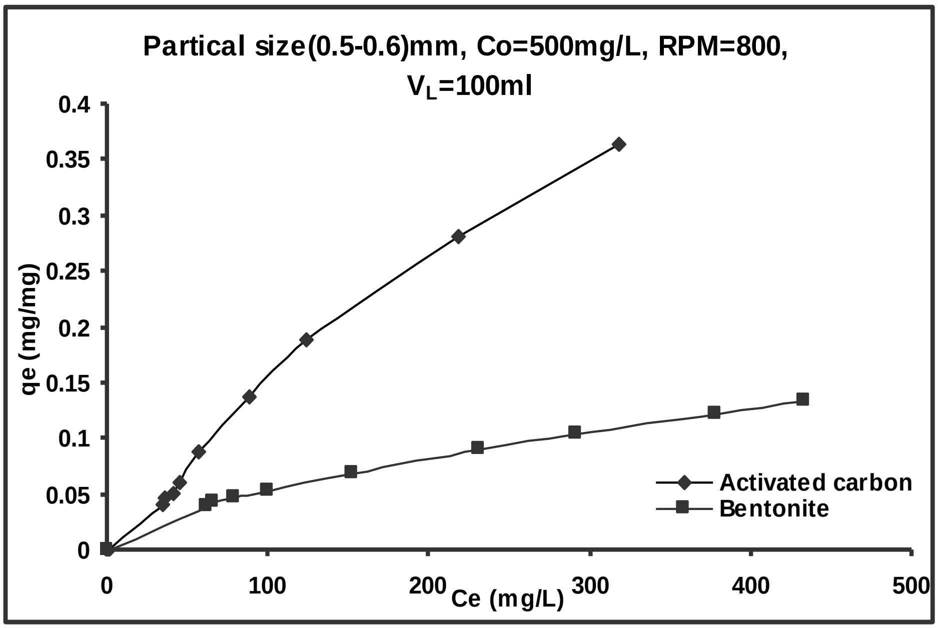


**Fig. (9) Adsorption of kerosene onto bentonite and activated carbon**

The values of empirical constants for two models (Langmuir and Freundlich) were calculated by the same previous manner, their values were tabulated in table (5).

**Table (5) Regression equation of (Langmuir and Freundlich) isotherm model for bentonite and activated carbon**

| Adsorbent | Isotherm model | Equation regression | $R^2$ |
|---|---|---|---|
| Bentonite | Langmuir | $\frac{x}{m}=\frac{(0.2128)(0.0034)C_e}{1+0.0034C_e}$ | 0.9737 |
| | Freundlich | $\frac{x}{m}=0.0033\ C_e^{1/1.6455}$ | 0.9987 |
| A.C. | Langmuir | $\frac{x}{m}=\frac{(3.0618)(0.0004)C_e}{1+0.0004C_e}$ | 0.1581 |
| | Freundlich | $\frac{x}{m}=0.0014\,C_e^{1/1.0183}$ | 0.9817 |

It is clear from above figure (9) and table (5) that:

- The equilibrium isotherm for bentonite and activated carbon are of favorable type and nearly follow the same behavior, figure (9).

- Freundlich model was the most valid isotherm for bentonite and activated carbon.
- The sorption capacity of bentonite varied from 0.0398 to 0.1334 mg of kerosene per mg bentonite, and sorption capacity of activated carbon varied from 0.0423 to 0.3646 mg of kerosene per mg activated carbon, table (6). The average kerosene sorption capacity of activated carbon was the highest and the lowest for bentonite.

**Table (6) Experimental kerosene sorption capacity values (x/m) of bentonite and activated carbon**

| Adsorbent | mg kerosene sorbed per mg (bentonite or A.C.), (x/m) | |
|---|---|---|
| | Rang | Mean |
| Bentonite | 0.0398 to 0.1334 | 0.0780 |
| A.C. | 0.0423 to 0.3646 | 0.1401 |

The kerosene removal efficiencies obtained at the equilibrium time (4 h) for bentonite and activated carbon are presented in table (7)

**Table (7) Kerosene removal efficiencies for bentonite and activated carbon**

| Adsorbent | Co (mg/L) | Ce (mg/L) | Kerosene removal % |
|---|---|---|---|
| Bentonite | 500 | 61.9 | 87.6 |
| A.C. | 500 | 34.1 | 93.1 |

The plot of kerosene concentration at equilibrium Ce versus quantities of adsorbent (bentonite or A.C.) is presented in figure (10). At the lower adsorbent mass (lower than 0.3 gm) the kerosene concentration decreased more sharply for activated carbon than bentonite, and then the decrease became gradual for both.

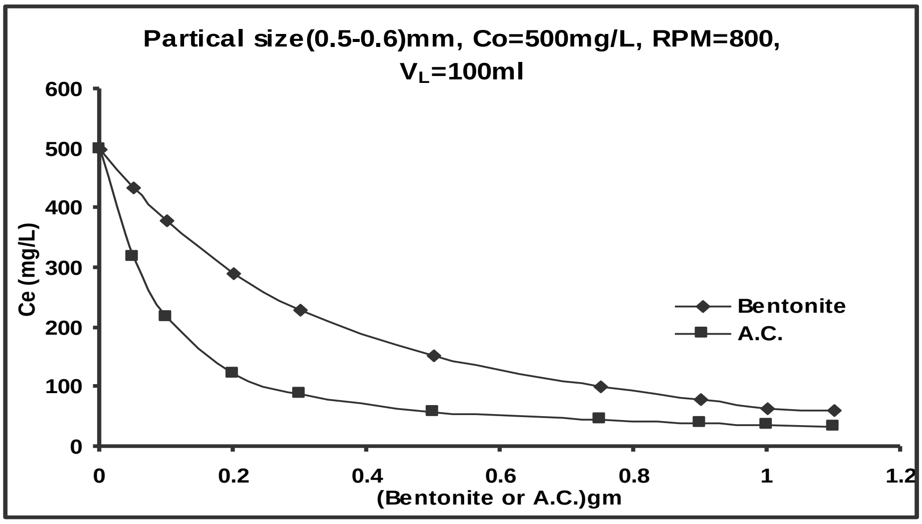


**Fig. (10) Kerosene removal by bentonite and activated carbon**

## CONCLUTIONS:

- The equilibrium isotherm for removal of kerosene onto bentonite at various initial concentrations was of favorable type. The correlation coefficient shows that Freundlich equation fits the experimental data more than Langmuir equation.
- The sorption rate of bentonite increased with increasing initial concentration of kerosene.
- The batch results of kinetic studies of bentonite showed that the equilibrium time was four hours.
- It was found that increasing the mass of bentonite will increase the percentage of kerosene removal until (1.1) gm of bentonite for the given conditions [particle size= (0.5-0.6) mm, Co=500mg/L, RPM=250, $V_L$=100ml] due to the system reaches equilibrium state.
- The percentage of kerosene removal increased with increasing the agitation speed. The best removal is 87.4% for RPM = 800.
- The swelling of bentonite in water was more than its swelling in kerosene, which insure that bentonite is a hydrophilic substance.
- The equilibrium isotherm for adsorption kerosene onto activated carbon for various particle sizes was of favorable type. The correlation coefficient shows that Freundlich equation fits the experimental data more than Langmuir equation.
- The sorption capacity of activated carbon increased with decreasing particle size, because of increasing the surface area with decreasing the particle sizes.
- For a given conditions the sorption capacity and efficiency of activated carbon were higher than sorption capacity and efficiency of bentonite, Which means that the activated carbon was more active for removal of kerosene from waste water than bentonite. The activated carbon is non- selective for this purpose because the oil can blind the pore space of activated carbon during operation as well as it is a costly material. Therefore bentonite can be considered as alternative adsorbent.
- At the beginning of adsorption, the kerosene concentration decreased more sharply for activated carbon than bentonite, and then the decrease became gradual, indicating a higher sorption rate for activated carbon than bentonite.

## REFERENCES


- Baker, R.A. and Luh, M., (1971), "Pyridine Sorption from Aqueous Solution by Montmorillonite and Kaolinite". Water Research, 5,839-848.

- Bastow T, Durnie W.H., Jefferson A., and Pang J., (1997), " Ultraviolet Spectroscopy for the Analysis of Oil – in Water Effluent Using Isopropanol as Co – Solvent, " Apple. Spectro Sc. 51, 318- 322

- Blokker, P.C.,(1971)," Prevention of Water Pollution from refineries", Water Pollution by Oil, P. Hepple(ed.), The Institute of Petroleum, London, 21-45.

- Crittenden, J. C. and Weber, I.R., (1978), " Predictive Model for Design of Fixed – Bed Adsorbers, Single Component ,Model Verification," Environmental Engineering Division, 104(EE3), June, pp433-443.

- Dentel, S.K., Bottero, J.Y., Khatib, K., Demougeot, H., Duguet, J.P. and Anselme, C., (1995), "Sorption of Tannic Acid, Phenol, and 2, 4, 5- Trichlorophenol on Organo clays". Water Research, 29(5), 1273 -1280.

- Ellison, R.J., Larnimaa, K. Margary, S.A., Mata, J.M., Muller, J.M., Peterson, D.R., Dmytrasz, B., Short, D., Simpson, B.J., (1999), "Exposure Profile: Kerosines / Jet Fuels". Report No. 99/ 5.2 Prepared for the CONCAWE Petroleum Products Management Group. 42pp.

- Environment Canada (1976b),"Guidelines for Effluent Quality and Wastewater Treatment at Federal Establishment", Report EPS-ES-76-1,Ottawa, Ontario, Canada

- Law No.25 ,(1967),"Maintenance of Rivers and Public Water from Pollutions"

- Patterson, J.W., (1975), "Waste water Treatment Technology". Ann Arbor Inc., U.S.A.

- Prather, B.V., (1970), "The Removal of Furfural from Water by Adsorption with Polymeric Resin". JWPCF, 42(4), PP596-603

- Rao, C.S., (1994), "Environmental Pollution Control Engineering", Wiley Eastern, India.

- Richard, J. W., (1997), "Hazardous Wastes, Sources, Pathways, Receptors", Department of Civil & Environmental Engineering, Washington State University.

- Sulaymon, A. H. and Ahmed K. W., (2008),"Competitive Adsorption of Furfural and Phenolic Compounds onto Activated Carbon in Fixed Column", Environment Science and Technology V42, No.2.


**NOMENCLATURE:**

$a$ Empirical constant (mg/mg)
$b$ Saturation coefficient (L/mg)
$C_e$ Concentration of contaminant remaining in solution at equilibrium (mg/L)
$K_F$ Freundlich equilibrium constant indicative of adsorptive capacity, (mg/mg)
$m$ Mass of sorbent (mg)
$n$ Freundlich constant indicative of adsorption intensity,(mg/L)
$q_e$ Contaminant concentration sorbed on the solid(mg/mg)
$x$ Mass of material sorbed on the solid phase (mg)

# SIMULATION OF SULFUR DIOXIDE REMOVAL FROM A GAS STREAM IN A FLUIDIZED-BED REACTOR

Nibras M. Abdulrasol Waleed M. S, Kadhem
Department of Environmental Engineering
College of Engineering,Baqhdad Universty

**ABSTRACT**

The object of this work is to model and simulate a fluidized bed desulfurization reactor by coupling a reactor kinetic model with a fluidized bed model based on two –phase theory(bubbling-bed model) proposed by **Kunni and Levenspiel(1968)**.This model is useful for analysis of a reaction involving gas and solid. It generates the conversion data with respect to reaction time of both reacting gas and solids in a continuous flow(for both gas and solids) in fluidized bed. The flue gas or stack gas from a combustor which normally contains sulfur dioxide mixed with excess air is used as the fluidizing gas with calcium oxide as the fluidized solids . Calcium oxide is quite capable of reacting with $SO_2$ to effect its removal from the gas phase according to the exothermic reaction :

$$CaO_{(s)} + SO_{2(g)} + \frac{1}{2}\,O_{2(g)} \longrightarrow CaSO_{4(s)} + Heat$$

The effects of the solid feed rate, $SO_2$ concentration in the flue gas, bed height, bed diameter, particle size, fluidizing velocity and operating temperature on the extent of conversion of both gas and solid were investigated, for a fixed feed rate of flue gas and $SO_2$concentration (50.000 $cm^3/sec$ ,3-5% by volume)at temperature range of (950-1000$^o$C)and pressure 1 *atm*.

الخلاصة

الهدف من الدراسة هو انموذج رياضي ومحاكاة ازالة غاز ثاني اوكسيد الكبريت في مفاعل الطبقة المميعة وذلك بدمج حركة التفاعل الكيمياوي وموديل مفاعل الطبقة المميعة اعتمادا على نظرية الطورين (طور الفقاعة وطور الاستحلاب). الغاز المستخدم هو غاز خارج من مدخنة او محرقة تحوي غاز ثاني اوكسيد الكبريت . الغاز المستخدم للتمييع يكون قابل للتفاعل مع المادة الصلبة المستخدمة(اوكسيد الكالسيوم) المتوفرة موقعيا و القادرة على ازالتة .

تم في البحث دراسة تاثير معدل جريان المادة الصلبة ,تركيز الغاز ,قطر الطبقة و ارتفاعها,معدل حجم الجزيئات للمادة الصلبة ,سرعة الغاز ,وحرارة الغاز داخل الطبقة بعد تثبيت معدل جريان الغاز ومعدل التركيز (50000 سم3/ثانية,5-3% نسبة حجمية)
النتائج النهائية لعملية المحاكاة اوضحت التصميم الامثل للمفاعل للحصول على اعلى تركيز لكل من الغاز والصلب ضمن الظروف السابقة.

## INTRODUCTION

Sulfur dioxide, $S0_2$ originating from many sources, is a pollutant can result from the burning of coal, oils, and gases; refining of petroleum; smelting of ores containing sulfur, manufacture of sulfuric acid[1,2],paper,and pulp mills. It is produced by volcanoes and in various industrial processes. During the manufacture of sulfuric acid by rather the old chamber process or the newer contact process, some sulfur dioxide is emitted to the atmosphere [3].

The amount of this pollutant depends upon the size, type of plant and the efficiency of conversion of sulfur dioxide to sulfur trioxide [2].

Almost every sulfur dioxide control system in operation or under construction for full-scale utility or industrial boilers involves systems that produce a "throwaway" or disposable waste form of sulfur rather than a recovered product for sale. Most of these throwaway systems used direct lime or limestone a few others involve sodium-based sulfur dioxide absorption[4].Oxidation of $SO_2$ usually in the presence of acatalyst such as ($VO_2$), form($H_2SO_4$),and thus acid rain.

Although a wide range of toxic gases and fumes can be released in accidents in chemical plants or stores, there are several gases and vapors which are commonaly encountered in many pollution situation, including contaminated land waste disposal and fuel combustion. It is interesting to note that the most hazardous of these, when judged by the concentration causing toxicity, is sulfur dioxide[5]. Sulfur dioxide has the following four adverse effects:

i. Toxicity to humans.
ii. Acidification of lakes and surface waters.
iii. Damage to trees and crops.
iv. Damage to buildings).

## Fluidization and Fluidized-Bed Reactors

The fluidized bed is one of the best known contacting methods used in the processing industry, for instance in oil refinery plants. Among its chief advantages are that the particles are well mixed leading to low temperature gradients, they are suitable for both small and large scale operations and they allow continuous processing. The fluid used to fluidize the solid particles can be either liquid or gas. Gas-solid fluidization is considered. A one-parameter model, termed the bubbling-bed model, is described by Kunii and Levenspiel (1991). It is used to calculate the hydrodynamic parameters. The one parameter is the size of bubbles. This model endeavors to account for different bubble velocities and the different flow patterns of fluid and solid that result.Compared with the two-region model, the Kunii-levenspiel (KL) model introduces two additional regions. The model establishes expressions for the distribution of the fluidized bed and of the solid particles in the various regions. These, together with expressions for coefficients for the exchange of gas between pairs of regions, form the hydrodynamic + mass transfer basis for a reactor model.

## Simulation Procedure

The following assumptions were made in the simulation :

- The reactor is under steady state operation.
- The lime particles are of uniform size and are completely mixed in the bed.
- 3.No elutriation of particles occurs.
- Following these assumptions,an iterative computational algorithm was set up.The calculation procedure is described below and to start the computation a set of input data is required .These are as follows:
    - Mean particles size(0.1,0.075,0.05,0.025 *cm*).
    - Bed diameter range(50,75,100,150,200,250,300 *cm*).
    - Bed height range(50,75,100,125 *cm*).
    - Temperature of flue gase entering reactor (750,850,950,1000 $^oC$) accordingly the viscosity as a function of temperature is determined (6)**,** a nomograph to determine absolute viscosity of gas as a function of temperature). Table (1) gives the viscosity as a function of temperature.

**Table (1) viscosity as a function of temperature**

| Temp. ($^oC$) | 750 | 800 | 850 | 900 | 950 | 1000 |
|---|---|---|---|---|---|---|
| Viscosity(gm/cm.sec) $\times 10^{-4}$ | 4.5 | 4.7 | 4.9 | 5 | 5.2 | 5.4 |

- $T_o$ (referans temperature) =273 *K*, P=1 *atm*, Mwt.*CaO* =56 *gm/mol* ,Mwt. of inlet gas mixture(fluidizing gas) =30.75 *gm/mol*
  consists mainly of $SO_2$=5% and air 95%(20%excess) as reactants..
- Mass flow rate of *CaO* (280,560, 840,1120 *gm/s*ec).
- Density of solid *CaO*(7) =2.8 $gm/cm^3$.

=0.5 $\varepsilon_{mf}$ =0.4, $\varepsilon_m$ *

* g=980 gm/$sec^2$,

- 9- Density of fluidizing gas = (M.wt. p)/(RT)

The sequence of steps of calculations are as follows:

- The minimum fluidization velocity, $u_{mf}$ , is evaluated by Ergun equation as:

$$u^2_{mf} + \frac{150(1-\varepsilon_{mf})\mu_g}{1.75\,\rho_g\,d_p} u_{mf} - \frac{g(\rho_s-\rho_g)\varepsilon^3{}_m d_p}{1.75\rho_g} = 0 \qquad (1)$$

- Determine $\mathrm{Re}_p$ and calculate $u_t$ through equations:

$$\mathrm{Re}_p = \frac{d_p \rho_g u_{mf}}{\mu_g} \qquad (2)$$

$$u_t = \frac{(\rho_s - \rho_g) g d_p^{\,2}}{18\mu_g} \quad \text{for} \quad \mathrm{Re}_p \ \langle \ 0.4 \tag{2.a}$$

$$u_t = \left[\frac{3 d_p\, g(\rho_s - \rho_g)}{\rho_g}\right]^{0.5} \quad \text{for } 0.4 < \ \mathrm{Re}_p < 500 \tag{2.b}$$

$$u_t = \left[\frac{3.1 g(\rho_s - \rho_g) d_p}{\rho_g}\right]^{\frac{1}{2}} \quad \text{for } 500 < \ \mathrm{Re}_p < 2\times 10^5 \tag{2.c}$$

- Predication of $u_o$ (i,e. $u_o = \ factor \times u_{mf}$),the factor is between (3-6).
- Calculate $d_p$ by equation (3):

$$d_b = 0.00376\times(u_o - u_{mf})^2 \tag{3}$$

- Substitute $d_p$ in equation (4) to calculate $u_{br}$.

$$u_{br} = 0.711\ (g\, d_b)^{1/2} \tag{4}$$

- Calculate $u_b$ by equation (5):

$$u_b = u_o - u_{mf} + u_{br} \tag{5}$$

- The bed fraction of bubble phase , $\delta$ , is determined by equation (6),
$\gamma_b = 0.0055$, $\alpha = 0.3$ , $D_O = 2.6\times 10^{-4}\ cm^2/sec$

$$\delta = (u_o - u_{mf}) \ / \ u_b \tag{6}$$

- Calculate $m_b$ by equation (7):

$$m_b = (\delta\, \gamma_b)/((1-\varepsilon_{mf})(1-\delta)) \tag{7 }$$

- Calculate $\gamma_c$ by equation (8).

$$\gamma_c = (1-\varepsilon\ \mathrm{mf}) \left(\frac{3u_{mf}/\varepsilon_{mf}}{u_{br} - u_{mf}/\varepsilon_{mf}} + \alpha\right) \tag{8}$$

- Calculate $m_c$ by equation (9).

$$m_c = (\delta\ \gamma_c)/((1-\varepsilon_{mf})\ (1\ldots-\delta)) \tag{9}$$

- Calculate $\gamma_e$ by equation (10).

$$\gamma_e = ((1-\varepsilon_{\ mf})\ (1-\delta))/\delta) + (\gamma_b + \gamma_c) \tag{10}$$

- Calculate $m_e$ by equation (11).

$$m_e = (\delta\ \gamma_e)/((1-\varepsilon_{mf})\ (1-\delta)) \tag{11}$$

- Checking for $m_b + m_c + m_e = 1$
- Calculate the diffusivity by equation (12), effective diffusivity by equation (13), and $D_s$ by equation (14).

$$D = D_O\left(\frac{T}{T_O}\right)^{1.83} \tag{12}$$

$$D_e = D\varepsilon_{mf} \qquad (SO_2 \text{ through flue gas}) \tag{13}$$

$$D_s = D0.15 \qquad (SO_2 \text{ through solid}) \tag{14}$$

- From equation (15) and (16) Calculate $K_{bc}$, $K_{ce}$.

$$K_{bc} = 4.5\left(\frac{u_{mf}}{d_b}\right) + 5.85\left(\frac{D^{\frac{1}{2}} g^{\frac{1}{4}}}{d_b^{\frac{5}{4}}}\right) \tag{15}$$

$$K_{ce} = 6.78\left(\frac{\varepsilon_{mf}\ D_e\ u_b}{d_b^{\ 3}}\right)^{1/2} \tag{16}$$

- Select values of $Kr$ between l and 1000 sec$^{-1}$ and for each value of $Kr$ :-
a. Calculate $Kf$ by equation ( 17) and substitute in to equation (18 ) to find $XA$.

$$Kf = (\gamma_b\ Kr) + \frac{1}{\dfrac{1}{K_{bc}} + \dfrac{1}{(\gamma_c Kr) + \dfrac{1}{\dfrac{1}{k_{ce}} + \dfrac{1}{\gamma_e kr}}}} \tag{17}$$

$$1 - XA = \frac{C_{Ao}}{C_{Ai}} = e^{-kf} \tag{18}$$

b. Calculate $\tau$ by equation (19 ).

$$\tau = \frac{\rho_B R}{bk_c C_A} = \frac{\rho_B d_p}{2bk_c C_A} \tag{19}$$

and

$\rho_B$ = molar density of $CaO$ particle(density of $CaO$ /M.wt. of $CaO$) , and $Kc$ fromAreniesequation(i.e $Kc = Ae^{\frac{-Ea}{RT}}$)
(19.a)

c. Calculate the over all rate constant( $K_m$ )by equation (20).

$$\frac{1}{K_m} = \frac{1}{kc} + \frac{d_p}{12D_s} \tag{20}$$

d. Determine $L_f$ from eq.(21) and $L_{mf}$ from the correlation between them (i.e. eqn 22).

$$L_f = -(\ln(1 - XA)u_b)/Kf \tag{21}$$

The bed height can be related as follows:

$$\frac{L_f}{L_{mf}} = \frac{1-\varepsilon_m}{1-\varepsilon_{mf}} \tag{22}$$

e. Determine the mean residence time of particles in the bed ( $\bar{t}$ ) by equation (23).

$$\bar{t} = \frac{W}{F_1} = \frac{A_t\, L_{mf}\left(1-\varepsilon_m\right)}{F_1} \tag{23}$$

Where

$W$=weight of bed(gm), $F_1$ = out flow rate of solid(gm/sec)

$A_t$ is the cross-sectional area of bed needed and obtained by mass balance.

$A_t$ = ((Fo*CAI)/mwts)/(((uo*(To./(To+T)))*(((0.21-0.1)/22400)+((CAI-(CAI*0.01))/22400)))

f. Substitute $\bar{t}$ and $\bar{\tau}$ in equation (24) to find $\overline{XB}$ .

$$\overline{XB} = 1\text{-}3\left(\frac{\bar{t}}{\tau}\right)+6\left(\frac{\bar{t}}{\tau}\right)^2 -6\left(\frac{\bar{t}}{\tau}\right)^3 \left[1-\exp(-\tau/\bar{t})\right] \tag{24}$$

g. Calculate $\phi$ and $\overline{CA}$ by equation (25) and ( 26)respectively.

$$\phi = \left[\frac{1}{1+y_e\,\frac{kr}{k_{ce}}}\right]\left[\frac{1}{y_c + \frac{1}{\frac{kr}{k_{ce}}+\frac{1}{y_e}}}\right] \tag{25}$$

$$\overline{C_A} = \frac{(1+m_c\gamma_e\,\frac{kr}{kce})C_{Ai}X_i\phi}{(L_{mf}\,kr/u_b)} \tag{26}$$

h. Calculate $XA$ by equation (27 ).

$$\frac{1}{b}\left(\frac{F_0}{M_b}\right)\overline{XB} = A_t\,u_o\,C_{Ai}\;XA \tag{27}$$

i . Compare $XA$ calculated from equations (18) with $XA$ calculated from equation ( 27).If they do not match, assign new trial value for $Kr$ and repeat steps a through i.

k . The calculation is terminated when the error criterion $\left|XA(18)-XA(27)\right|<10^{-3}$ is satisfied.

***Results and discussion***

The effects of the fluidizing velocity,solid feed rate,mean particle size of the solids,operating temperature,$SO_2$ concentration of feed gas and bed geometry on the conversion efficiency of both gas and solids are discussed separately. Fig.s(1)-(19) show these effects on plots as % conversion versus reaction time.It should be noted that in this study the feed gas flow rate is set within the range of 49580-51600 $cm^3/sec$ (average 50000 $cm^3/sec$) as a design parameter.

## Effect of Operating Temperature

The effect of temperature on the conversion efficiency of the gas and solids are presented in Fig.s (1) and (2) respectively. The temperature range covered in this study is 750 $^{o}$C-1000$^{o}$C.At relatively lower temperatures (<500$^{o}$C) calcium sulfite($CaSO_4$) an unstable product of the reaction can be formed and may react reversibly to give back $SO_2$.It is therefore important that temperatures higher than 650$^{o}$c should be used to avoid the formation of *CaSO3*. For this purpose, temperatures above 650 $^{o}$C were used in this investigation(8). As it is seen maximum conversions are obtained within the temperature range(950 $^{o}$C-1000 $^{o}$C) , shorter reaction times are obtained as the temperature is increased because the rate of reaction increases with temperature as well as the solute mass diffusivity (9) .From these plots led to the conclusion that the desirable range of temperature is 950 $^{o}$C-1000 $^{o}$C ,preferably 950 $^{o}$C .Consequently, the operation temperature chosen is 950$^{o}$C and used throughout the calculations of the simulation program.

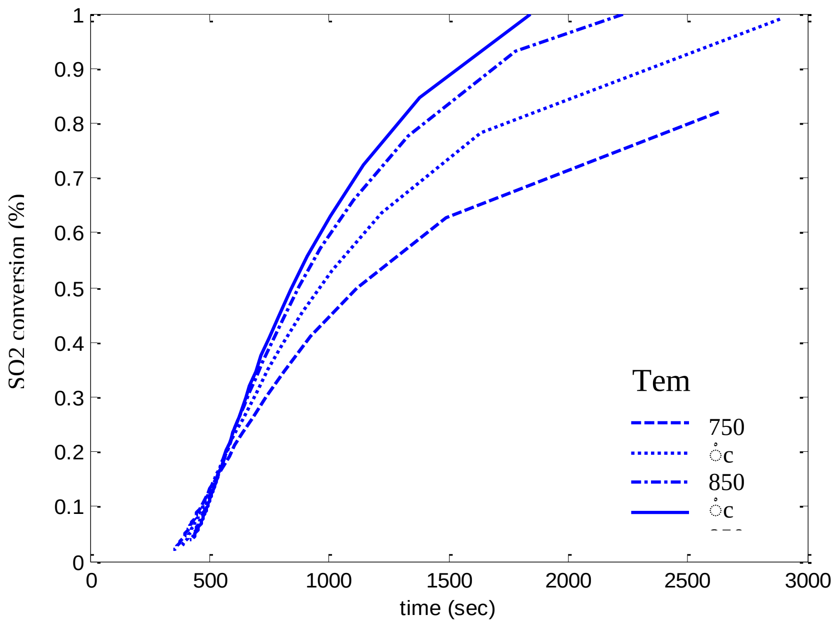


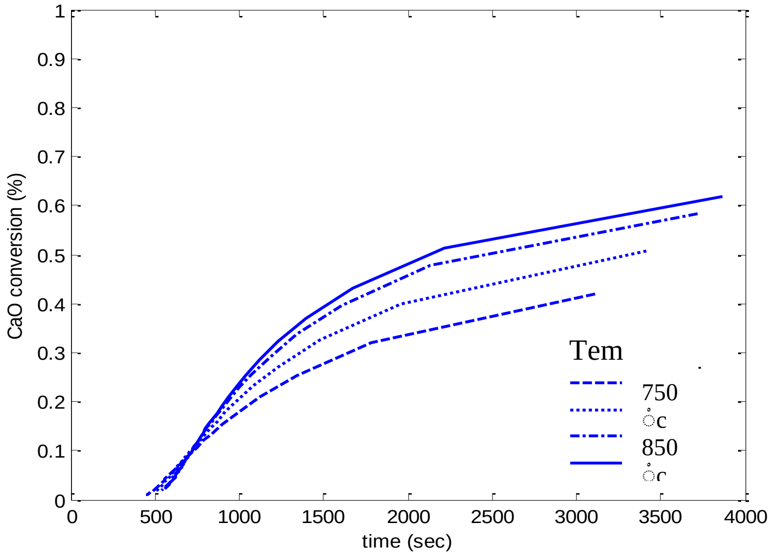


**Fig.2.- Fo=280 *g/s*, dp=0.1*cm*, uo/ umf =3**

## - EFFECT OF MEAN PARTICLES SIZE

The effect of mean particle size on the conversion efficiency is shown in Figs (3)and(4) for the gas and solids. These data are obtained for a fixed feed of solids $F_o$ =280 gm/sec and fluidizing velocity uo=3umf cm/sec. For the range of particle size used in this study(0.1-0.025*cm*) and as it is seen from the plots,a decrease in particle size is to increase the conversion efficiency of both gas and solids for all temperatures used.For instance ,at 750 $^{o}$C the conversion of the gas increased from 62-99% over a particle size decrease from 0.1*cm* down to 0.025*cm*. On the other hand,this increase in efficiencies is accompanied by rapid decrease in the reaction time over the residence time of the particles in the bed. But this residence time showed little change with decreasing particle size and increasing temperature. The heighest conversion efficiencies were obtained with the small size particles(i.e =0.025 *cm*).This is expected,because small size particles offer larger surface area for reaction and solute diffusion than particles of larger size.However,very small size particles are not suitable for fluidized bed reactors due to carry over problems and therfore are not considered in this study .

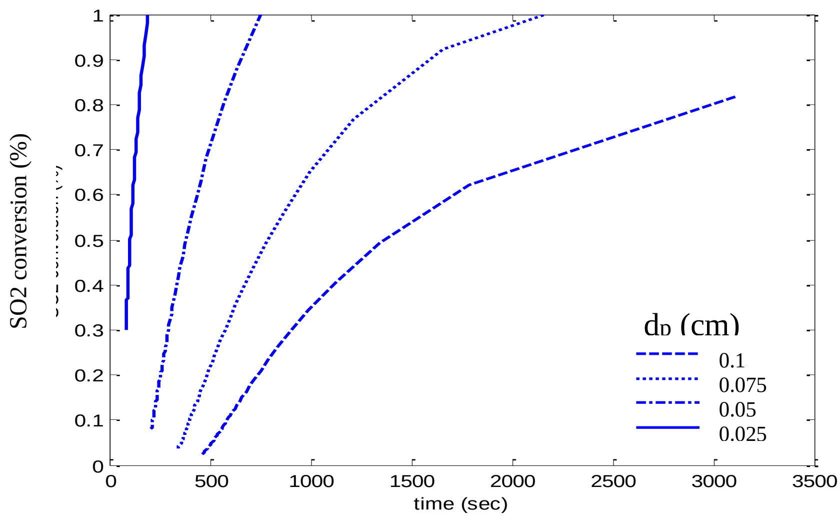


Fig.3.- Fo=280 *g/s*, T= 750 $^{o}$c, uo/ umf =3

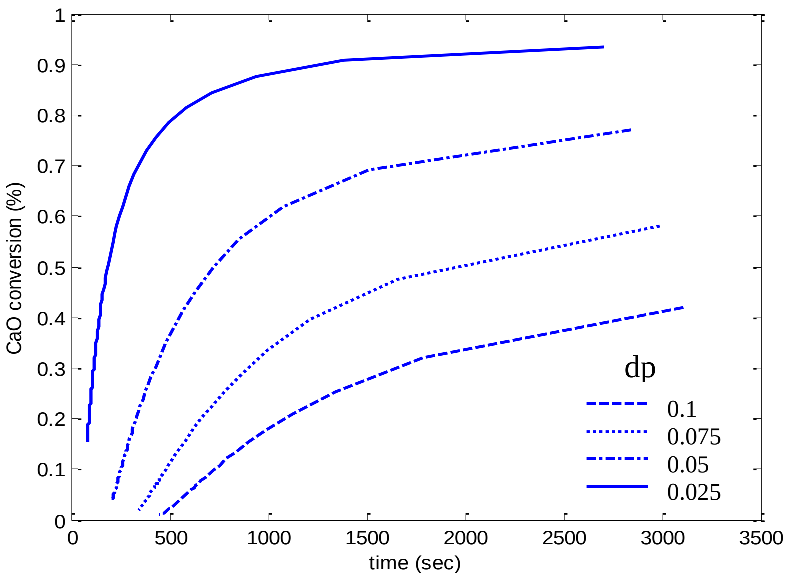


Fig.4.- Fo=280 *g/s*, T= 750 ͦc, uo/ umf =3

## EFFECT OF GAS FLUIDIZING VELOCITY

As stated in Kunni and Levenspiel(1968) recommend a fluidizing velocity in fluidized bed reactors to be greater than $2u_{mf}$ (i,e .$u_o$ >=$2u_{mf}$) for proper reaction and stable operation. However, higher values of uo are not recommended in order to avoid solids carry over.Solids carry over can be prevented if uo is chosen to be well below the terminal velocity of the solid particles in the bed. Accordingly, the range of uo values coverd in this study is taken to be (3-6)$u_{mf}$ cm/sec. Figs.(5) and (6) depict the effect of changing uo on the conversion efficiency of the gas and solid with the operation temperature , solid feed rate and size of particles are kept constant at 950 $^{o}$C , 280 *gm/s*ec and 0.025*cm* respectively. An increase in uo leads to a decrease in %conversion,for solid only (gas conversion remains unchanged). However, both gas and solids almost attain the same conversion(95-96% for the solid and 99% for the gas) within the same range of reaction time of 360-475 *sec*.

This range of reaction time is well below the residence time of the solid particles in the reactor. For proper operation of the reactor, it is essential that the reaction should go to completion before any of the solid particles leave the reactor. In other words, it is essential that the reaction time should , always, be less than the residence time of the solid particles in the bed in order to achieve complete reaction.

From these results, it appears that a fluidizing velocity of 3umf is our choice as an optimum value.The use of fluidizing velocity higher than 3umf does not affect the conversion efficiency of the gas but more reaction time is needed. This would exceed the residence time of the solids in the bed. On the other hand an increase of uo above 3umf entails a decrease in solid conversion. Thus higher values of uo are not desirable. Consequently, the fluidizing velocity is fixed at 3umf and used throughout the calculations of the simulation program.

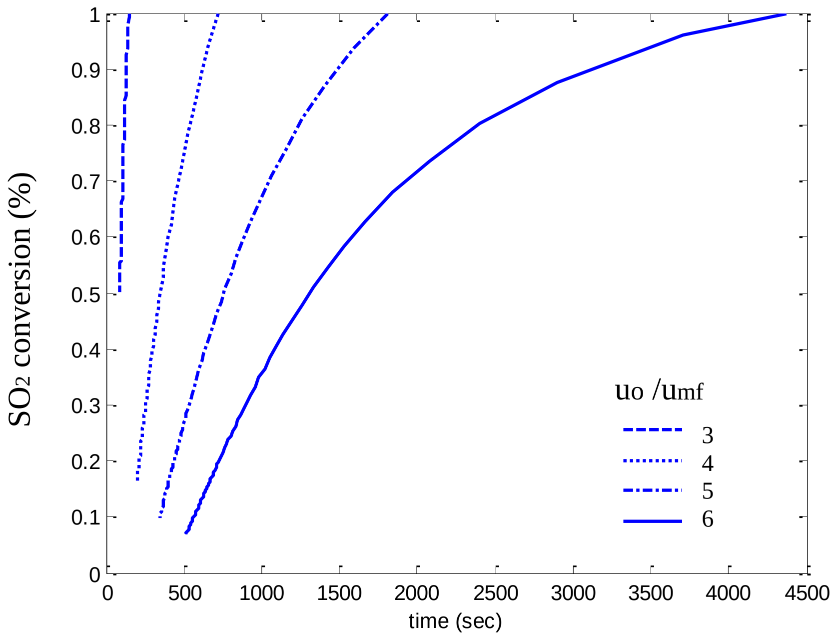


Fig.5.- dp=0.025*cm*, T= 950 ̊c, Fo=280 *g/s*

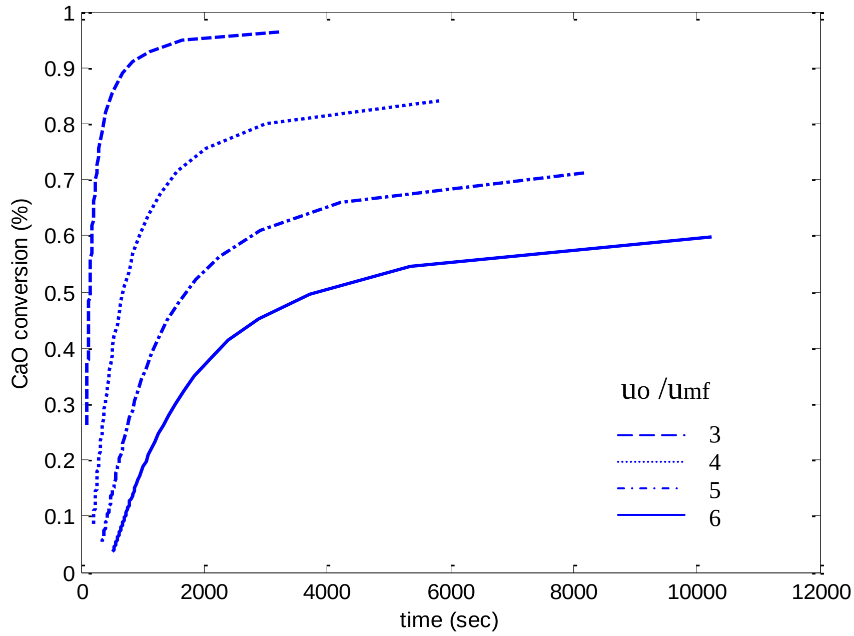


Fig.6.- dp=0.025 *cm*, T= 950 ̊c, Fo=280 *g/s*

**EFFECT OF INLET $SO_2$ CONCENTRATION**

The concentration of $SO_2$ in the feed gas entering the reactor is fixed within the range 3-5% by volume.This concentration originates in the heavy fuel oil used in the combustion. Davidson and Harrison(1968) state that commercial fuel oils used for combustion usually contain sulfur that is finally converted to $SO_2$ within the range 3-5%v/v in the flue gas.

Figs (7-12) show the effect of varying $SO_2$ concentration on the conversion efficiency of the gas and solid respectively. As it is shown, with the other parameters fixed, the reaction time increases as $SO_2$ concenteration is decreased. It should be noted that the inlet concenteration of $SO_2$ is usually fixed as the concenteration of the feed gas to be desulfurized. However, some variations in the quality of fuel used in the combuster could change this composition, but still maximum conversions are obtained. For the simulation programe, the inlet $SO_2$ concenteration is set at 5%v/v in a feed gas of 50000 $cm^3/sec$. It can be noted from the results the conversion of the gas and solid remaine constant regardless of $SO_2$ conversion. However,if the concentration of gas is increased ,the material balance requires a decrases of the gas flow rate and hence a decrase of reaction time and residence time.

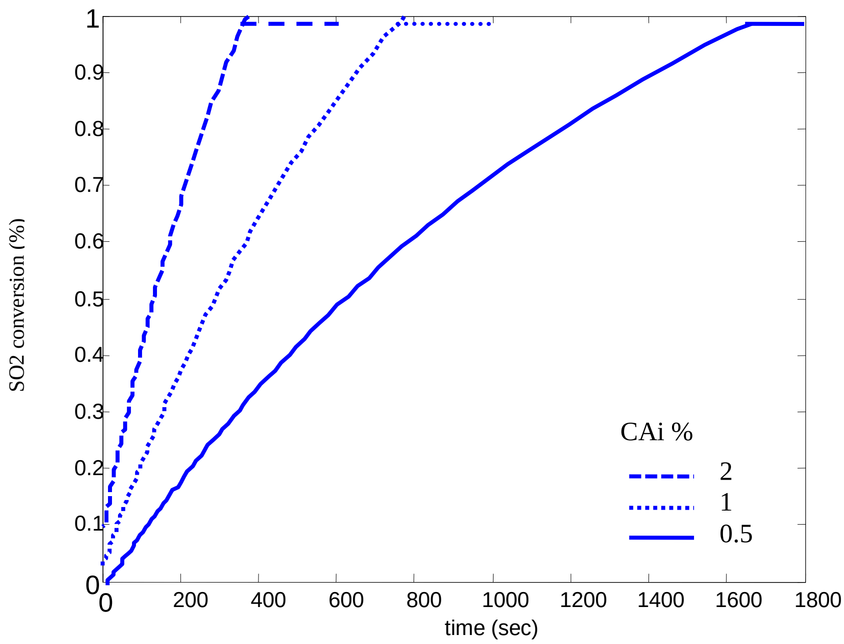


Fig.7.- dp=0.025 *cm*, T= 950 ̊c, uo/ umf =3, Fo=280 *g/s*

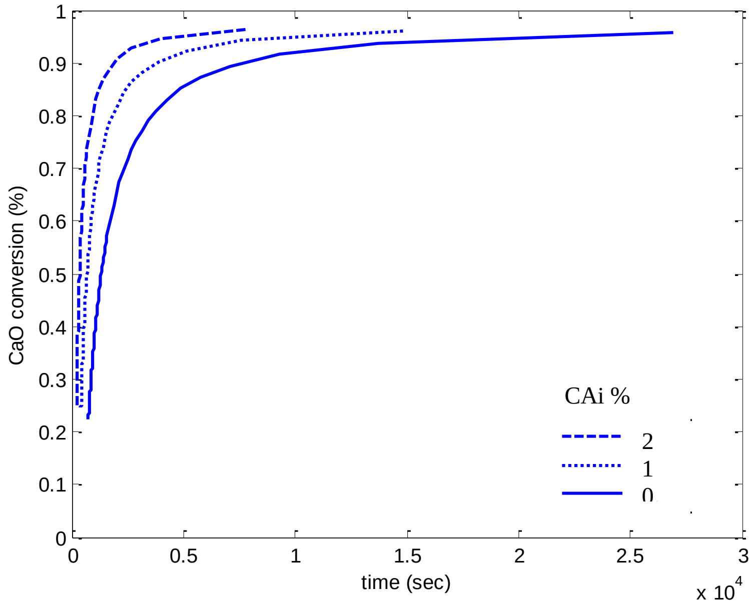


Fig.8.- dp=0.025 *cm*, T= 950 ̊c, uo/ umf =3, Fo=280 *g/s*

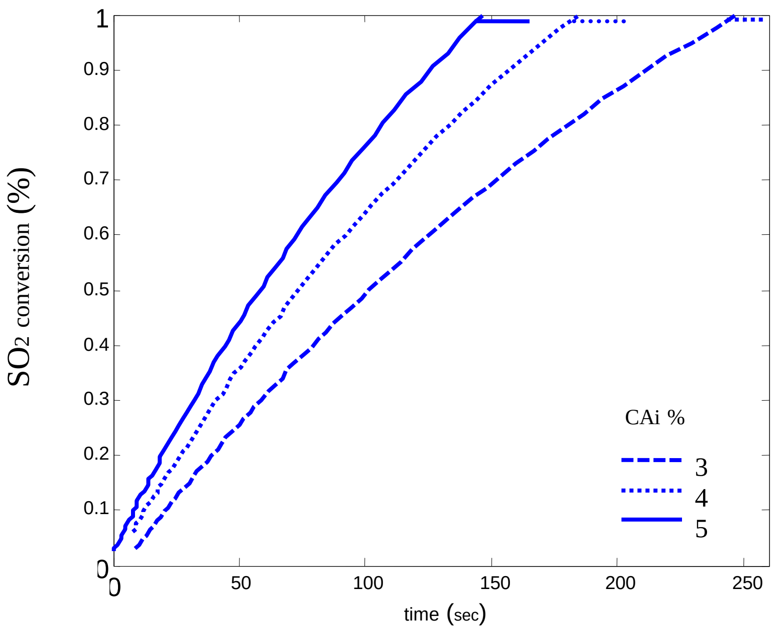


Fig.9.- dp=0.025 *cm*, T= 950 ̊c, uo/ umf =3, Fo=280 *g/s*

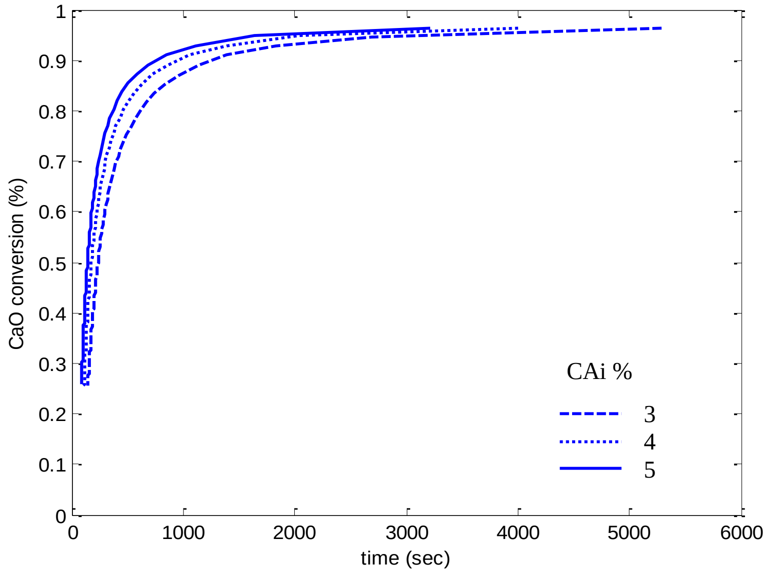


Fig.10.- dp=0.025 *cm* T= 950c, uo/ umf =3, Fo=280 *g/s*

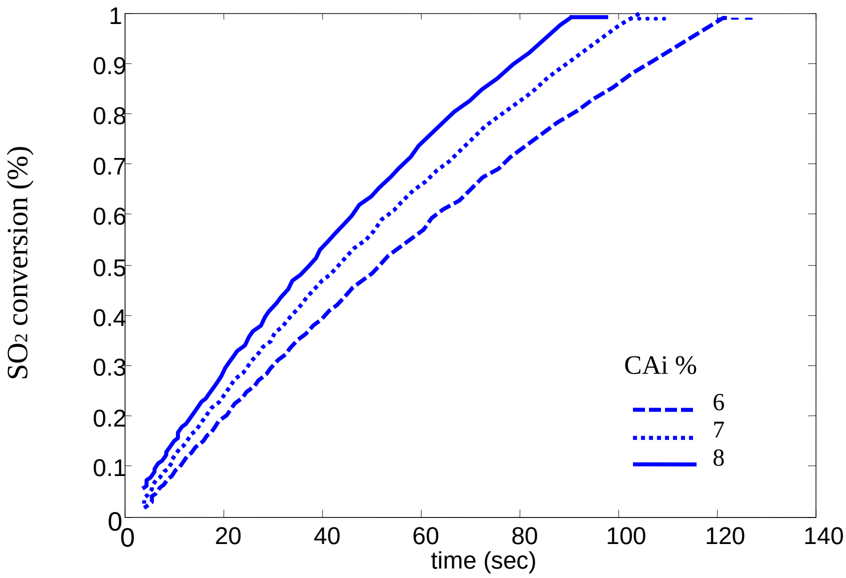


Fig.11.- dp=0.025 *cm*, T= 950 ̊c, uo/ umf =3, Fo=280 *g/s*

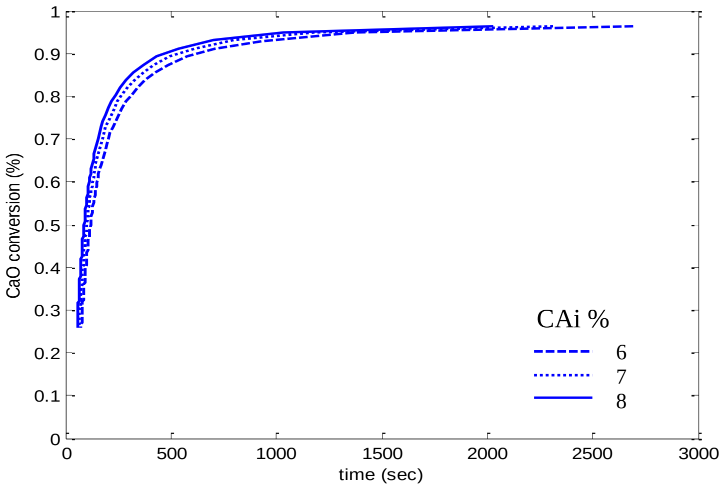


Fig.12.- T=950$^{O}$C, dp=0.025 *cm*, uo/ umf =3, Fo=280 *g/s*

## EFFECT OF SOLID FEED RATE

The effect of solid feed rate has been investigated for a reaction temperature of 950 $^{o}$C and mean particle size=0.025cm with the other parameters are fixed at their desired values.

Increasing the rate of solids entering the reactor has no effect on the conversion efficiency of both gas and solid and the reaction time. As can be seen from Figs(13)and(14), the conversion of the gas and solid rise rapidly to their maximum values within a reaction time of 360-475 *s*ec and this reaction time appears to be well below the residance time of solids in the reactor. However, an increase in solid flow rate involves marked increase in the volumetric flow rate of the input gas to the reactor. Since the range of the input flow of gas is already fixed at 50000 $cm^3/sec$ an increase in solid flow rate above 280*gm/sec* will require higher gas flow rate. Therefore, the recommended solid feed rate is 280*gm /sec*.

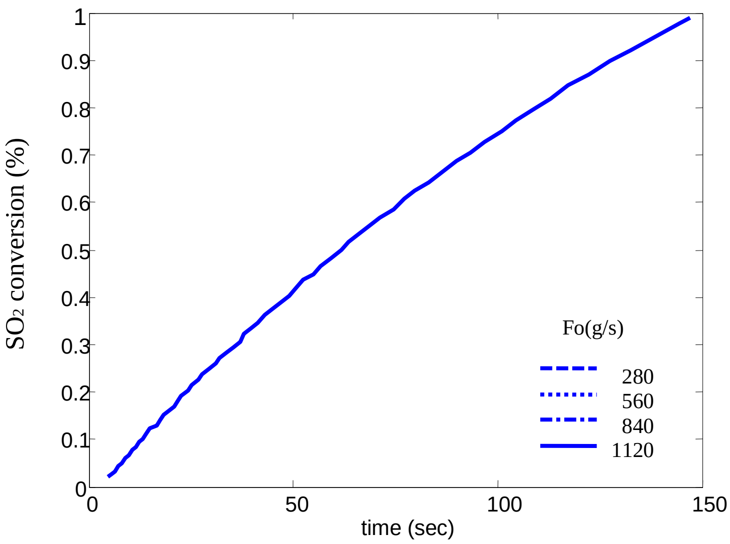


Fig.13.- dp=0.025 *cm*, T= 950 ȯc, uo/ umf =3

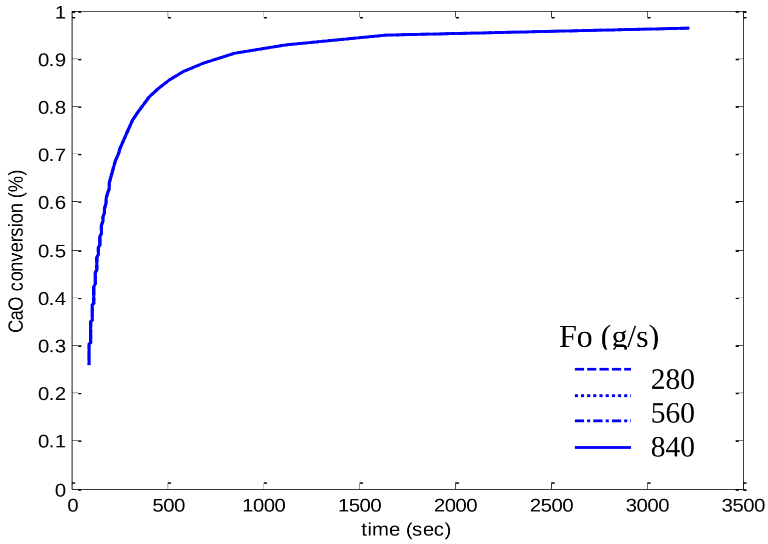


Fig.14.- dp=0.025 *cm*, T= 950 °c, uo/ umf =3

## Effect of Bed Height

Fig(15) depicts the effect of increasing bed height on the reaction time to achieve maximum conversion for the gas and solid at a given bed diameter of 60*cm*. As it is shown the reaction time increases with bed height as well as the residence time. This effect is indirectly linked with equation (26),(19),(23) for the gas concenteration inside the reactor, reaction time and residence time respectively.The results show that the optimum reaction time of 369-475 *sec* corresponds to a fixed bed height of 75-150*cm*. Using higher beds will lead to higher reaction times.

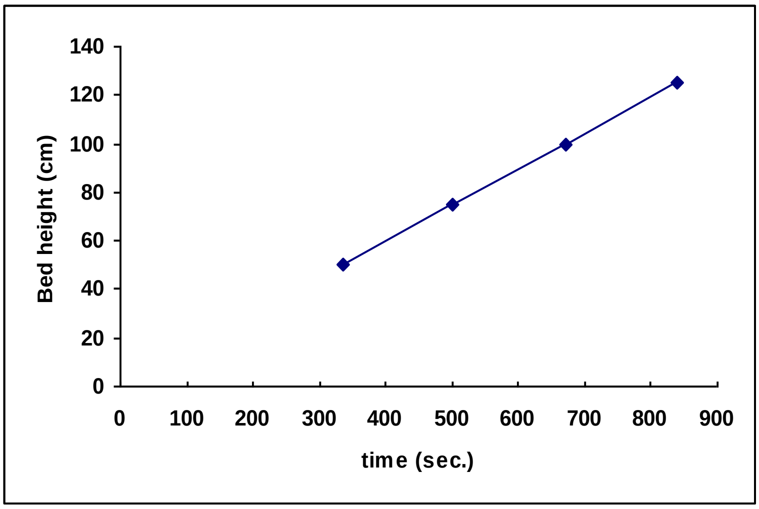


Fig. 15. Fo= 280 *g/s*., $D_B$= 50-75 *cm*, T= 950 °C, $u_o/u_{mf}$=3,$d_p$=0.025*cm*

## EFFECT OF BED DIAMETER

The effect of bed diameter on the conversion efficiency of the gas and solids has been investigated for the range of bed diameters of 50-75*cm* at constant temperature of 950$^o$C,particle size of 0.025*cm*, fluidizing velocity of 3umf cm/sec and solid feed rate of 280*gm/sec* .The inlet concentration of $SO_2$ is taken to be the heighest allowable value of 5% by volume.The results are plot in Figs(16)-(19).The plots show that solid conversion is ranging between 92-97% for bed diameters between 50-75*cm*.This conversion increases until it reaches 99% for beds between 150-300*cm* in diameter.On the other hand the gas conversion exhibits a rapid decrease with increasing bed diameter(i,e. 8% for beds close to 300*cm* in diameter).It is also noted that inorder to achieve a fluidizing velocity of 3umf cm/sec. The feed flow rate of the gas should increase,and as can be seen this flow rate becomes exceedingly high at bed diameters close to 300*cm*. Such high flow rates do not match the design feed rate of 50000$cm^3$/sec .The reaction time remains unchanged at 360-475 *s*ec,but the residence time increases with bed diameter. From these results it is clear that the increase in bed diameter adversely affects the efficiency of gas conversion, but it has little effect on solid conversion.It appears that bed diameters between 50-75*cm* would be the best choice for operation.

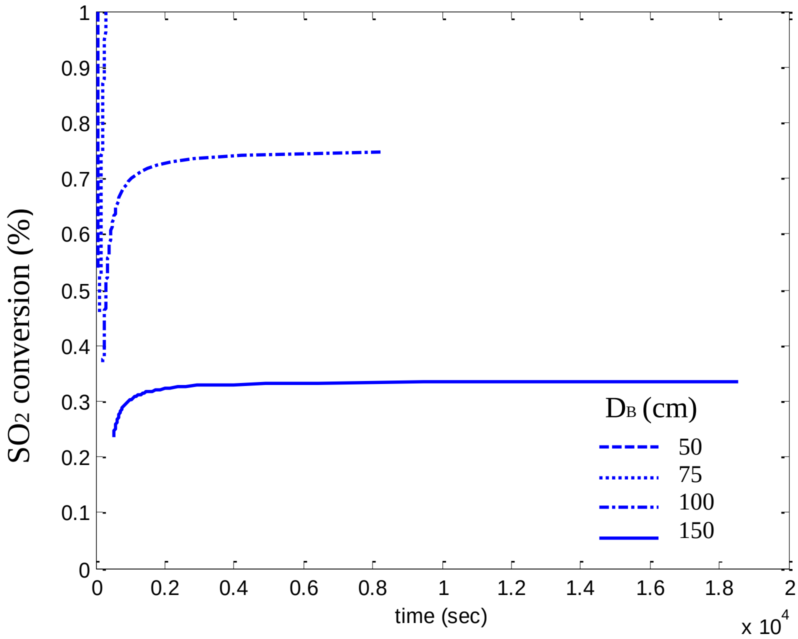


Fig.16. Fo=280 *g/s*, T= 950 °c, uo/ umf =3, dp=0.025

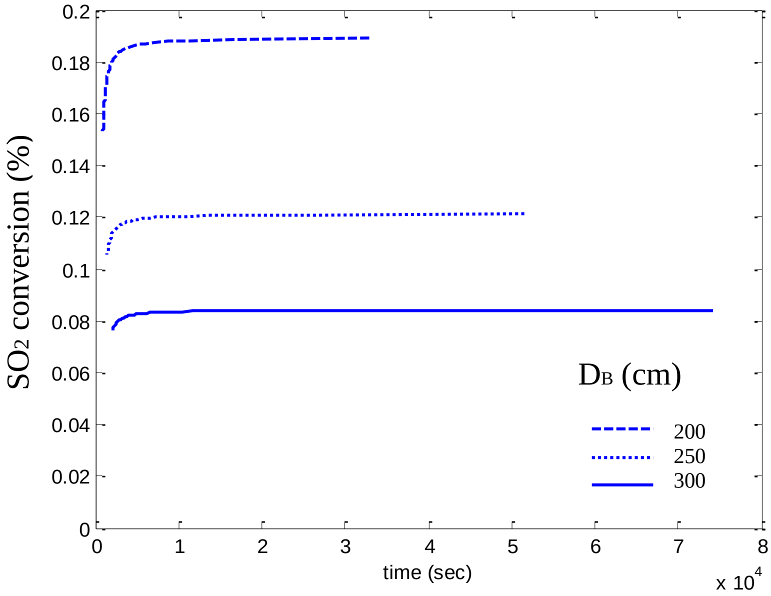


Fig .17. $d_p$=0.025 *cm*, T= 950 ̊c, $u_o/u_{mf}$ =3, $F_o$=280 *g/s*

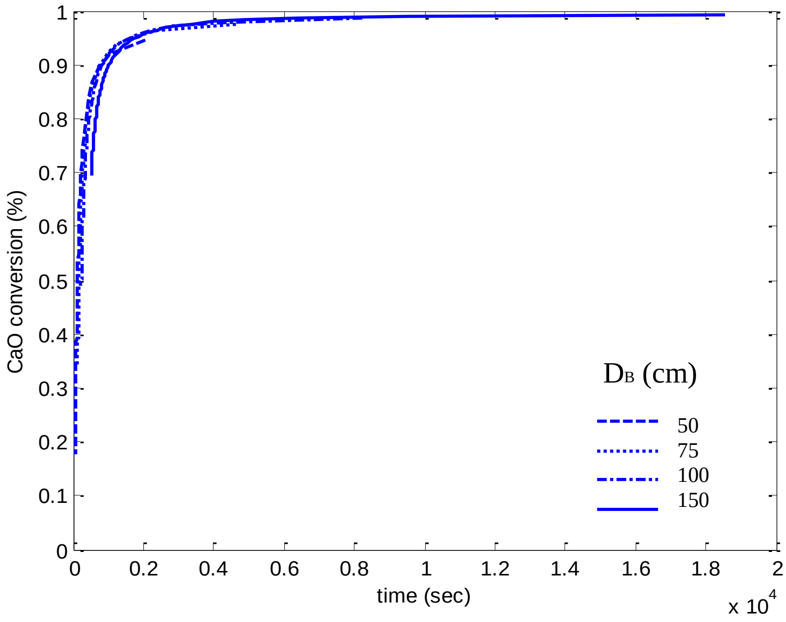


Fig.18. $F_o$=280 *g/s*, T= 950 ̊c, $u_o/u_{mf}$ =3, $d_p$=0.025 *cm*

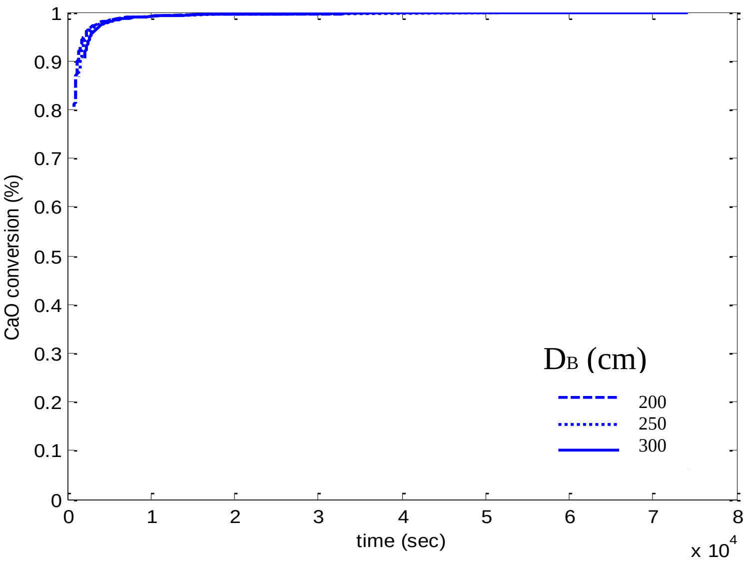


Fig.19.dp=0.025 *cm*, T=950 c$^o$, uo/ umf =3.,Fo=280 *g/s*

## CONCLUSIONS

Recently the bubbling-bed model was applied to the prediction of gas conversion in solid catalysed gas-phase reaction. In the present work this model is used to determine the extent of chemical conversion of both reacting gas and solids in a continuoas flow(for both gas and solid) fluidized bed. This procedure is applied for removal of $SO_2$ from flue gas using $CaO$ as solid reactant in a fluidized bed reactor based on a feed rate of 50000$cm^3/sec$ of flue gas.The results of the simulation programe for maximum conversion of gas and solid are summarized as follows:

-The feed rate of $CaO$ is to be 280gm/sec(about 24.192*Kg/day*) producing 3.617 gm/sec (about 27 *Kg/day*) of $CaSO_4$(99% conversion) as by product,a useful building material.

-The reactor will operate a diabatically at temperature within 950-1000 $^o$C.

-The mean particle size of $CaO$ is 0.025*cm*.

- The fluidizing velocity of the gas(flue gas) should be 3 times the minimum fluidizing velocity of the solid particles.
- The flow rate of the solid feed depends on the flow rate of the feed gas.
- To a chieve the same conversion of both gas and solid an increase in inlet *SO2* concentration requires a decrease in gas flow rate.
- The best ratio of bed height to bed diameter for maximum conversion should not exceed 2.

## NOMENCLATURE

$A_t$ = cross-sectional area of bed $(cm^2)$

$A$ = pre-exponential factor for solid diffusion of $SO_2$ through $CaSO_4$ $(cm^2/s)$.

$b$ = stoichiometeric coefficient in gas/solid reaction equation.

$C_{Ai}$ = concentration of gas in the inlet gase stream $(gmol/cm^3)$

$C_{Ao}$ = concentration of gas (or bubble gas)leaving the bed $(gmol/cm^3)$

$\left.\begin{array}{l} C_{Ab} \\ C_{Ac} \\ C_{Ae} \end{array}\right\}$ = concentration of gas A in bubble,cloud-wake region,and emulsion respectivlely $(gmol/cm^3)$

$\overline{C}_A =$ average concentration of reactant A encountered by solid particles in the bed $(gmol/cm^3)$

$\left.\begin{array}{l} D \\ D_e \\ D_s \end{array}\right\} =$ diffusion coefficient, effective diffusion coefficient in emulsion, and diffusion coefficient through layer of solid product or ash $(cm^2/\sec)$

$D_O$ = diffusivity at standard conditions $(T = 273K, P = 1atm)(cm^2/\sec)$.

$D_B$ = bed diameter $(cm)$.

$d_p =$ particle diameter $(cm)$.

$d_b =$ bubble diameter $(cm)$.

$E_a$ = activation energy for solid diffusion of $CaO$ through $CaSO_4$ $(J/mol)$.

$F_o =$ feed flow rate of solids $(gm/\sec)$.

$F_1 =$ out flow rate of solid $(gm/\sec)$.

$g =$ acceleration of gravity $(gm/\sec)$.

$\left.\begin{array}{l} K_{bc} \\ K_{ce} \end{array}\right\} =$ interchange coefficients between bubble and cloud wake region, and between cloud – wake region and emulsion, respectively $(1/\sec)$.

$Kr =$ reaction rate constant defined in equation (17) $(1/\sec)$.

$K_c =$ rate constant for surface defined in equation (19.a) $(cm/\sec)$.

$k_f =$ reaction rate group defined in equation (17) dimensionless.

$K_m$ = overall rate constant $(cm/\sec)$.

L= height of the reactor $(cm)$.

$\left.\begin{array}{l} L_f \\ L_{mf} \end{array}\right\} =$ height of fluidized bed and static bed respectively $(cm)$.

$M_B =$ molecular weight of solid material $(gm/mol)$.

$\left.\begin{array}{l} m_b \\ m_c \\ m_e \end{array}\right\} =$ weight fraction of solids defined by equation (7,9,11).

$N_A$ = gramme moles of A.

$rc$ = radius of solid unreacted core $(cm)$.

R= gas constant $(atm.cm^3/mol.K)$.

mean residence time of particles in the bed (sec) $\bar{t} =$

$t$ = residence time for particle in the bed ($sec$).

$\left.\begin{matrix} u_b \\ u_{mf} \\ u_o \end{matrix}\right\}$ = velocity of rising bubble, minimum fluidizing velocity, and superficial gas velocity, respectively $(cm/\sec)$.

$u_t$ = terminal or free-falling velocity of the particles $(cm/\sec)$.

$\left.\begin{matrix} V_b \\ V_w \end{matrix}\right\}$ = volume of bubble and of wake, respectively $(cm^3)$..

$V_s$ = volume of a solid particle $(cm^3)$.

$(cm^3)$ $V$T= total volume of the particles

$W =$ weight of bed $(gm)$.

$X_A =$ fractional conversion of reactant gas ($A$).

$\overline{X}_B =$ mean fractional conversion of solid ($B$) material in the exit stream.

$\left.\begin{matrix} y_b \\ y_c \\ y_e \end{matrix}\right\}$ = volume fraction of solids by equations (8,10) , dimensionless.

Greek Letters

$\left.\begin{matrix} \varepsilon_m \\ \varepsilon_{mf} \end{matrix}\right\}$ = void fraction in a fixed bed and in a bed at minimum fluidization, respectively , dimensionless.

$\tau =$ time for complete conversion of a single particle (sec).

$\delta$ = bed fraction of bubble phase .

$\rho_s$ = density of solid $(gm/cm^3)$.

$\rho_g$ = density of gas $(gm/cm^3)$

$\mu_g$ = viscosity of gas $(gm/cm.\sec)$

$\phi$ = sphericity of a particle , dimensionless .

$\alpha =$ ratio of wake volume to bubble volume .

$\rho_B =$ molar density of solid material $(g\,mol/cm^3)$

## REFERANCES


- Allal, K.M., et. al., Collection of Czecho slovak Chemical Communication, Abstracts:57 (11), 2315-2320 (1992).
- Alloway, B.J. and Ayres, D.C., "Chemical Principles of Environmental Pollution",2 nd Ed., Thomas Telford,London, 1997.
- *D*avidson, J.F.and Harrison,D., "Fluidized Particles", Cambridge: Cambridge University Press,1963.
- Incropera, F.P. and Dewit, D.P., "Fundamentals of Heat and Mass Transfer" 4th ed, Jhon Wiley and Sons(1996).
- Lamantia, C.R.and Lunt, R.R, Chem.Eng.Progr.,Vol.70.June,P66,1974.
- Lehle, W.W. "The Manufacture of Sulfuric Acid", Duecker, W.W. and West, J.R., Eds., Reinhlold Publishing Corp., New York,1966.
- Perry,"Chemical Engineering,Hand Book".7ed.1997.
- Rohrman, F.A. and Ludwic,J.H., Chem.Eng.Prog., vol.61.sept.,p.60,1965.
- Sander, U.H.F., Fischer, H., Rothe. U. and Kola, R.,"Sulfur,Sulfur Dioxide and - - Sulfuric Asid",4 th Ed., The British Sulfur Corporation Ltd.,London,1984.

# PREDICTION OF NATURAL CONVECTION HEAT TRANSFER IN COMPLEX PARTITIONS CAVITY

Dr. SATTAR J. HABBEB
Lecturer
Mechanical Engineering Dept.
Technology University

ISRAA Y. DAOUD
Asst. Lecturer
Mechanical Engineering Dept.
Technology University

**ABSTRACT**

A numerical investigation has been carried out to examine the effects of insulated baffle mounted in complex cavity representing as an industrial building on flow pattern and heat transfer characteristics. The cavity is formed by adiabatic horizontal bottom, inclined upper walls and vertical isothermal walls. This problem is solved by using flow-energy equations in terms of stream-vorticity formulation in curvilinear coordinates. Two cases are considered; in the first (case 1) the insulated baffle position attached to the horizontal bottom wall of the cavity while in the second case (case 2) the insulated baffle position attached the upper inclined wall. A parametric study is carried out using following parameters: Rayleigh number from $10^3$ to $10^6$, Prandtl number for 0.7 and 10, baffle height (HB=0, 0.3H$^*$, 0.4H$^*$, and 0.5H$^*$), baffle location for (LB=0.25L and 0.75L) with or without baffle in the cavity (total of 100 tests). For case 1 results show that, the flow strength generally increasing with increasing Ra values, increasing baffle height, and decreasing values of Pr, while in case 2 the same behavior of above could be show except the flow strength decreasing with increasing baffle height, also, increase Ra leads to increase the rate of heat transfer. The configuration of the cavity in case 2 leads to increase in heat transfer rate comparing with that in case 1.

**KEY WORDS:** natural convection, cavity with baffle

**الخلاصة**

تم التوسع بدراسة عددية لاختبار تأثير الحاجز المعزول الموضوع في تجويف معقد يمثل بناية صناعية على حركة الجريان وسمات انتقال الحرارة بالحمل الحر. التجويف متمثل بأسطح معزولة السطح الأفقي السفلي , السطح المائل العلوي وأسطح ثبوت درجة الحرارة العمودية. المسألة حلت باستخدام معادلات الجريان والطاقة بصيغة دالة الانسياب-الدوامية بالإحداثيات المطابقة للجسم. تم اخذ حالتين في هذه الدراسة الحالة الأولى الحاجز المعزول منطبق على السطح السفلي للتجويف بينما في الحالة الثانية يكون منطبق على السطح المائل العلوي للتجويف, المعاملات المدروسة هي:رقم رايلي من $10^3$الى $10^6$,رقم برانتل 0.7 و 10,ارتفاع الحاجز (HB= 0, 0.3H$^*$, 0.4H$^*$, 0.5H$^*$), موقع الحاجز (LB=0.25L, 0.75L), لحالات مختلفة بدون وبوجود الحاجز داخل

التجويف (حوالي 100 اختبار). النتائج للحالة الأولى أوضحت أن قوة الجريان بصورة عامة تزداد مع زيادة رقم رايلي, زيادة ارتفاع الحاجز المعزول, ونقصان قيم رقم برانتل بينما في الحالة الثانية يبقى نفس التصرف أعلاه مع نقصان قوة الجريان بازدياد ارتفاع الحاجز المعزول. كذلك زيادة قيم رقم رايلي تؤدي إلى زيادة معدل انتقال الحرارة. تركيب التجويف في الحالة الثانية يؤدي إلى زيادة معدل انتقال الحرارة مقارنة بالحالة الأولى.

## INTRODUCTION

Heat transfer and fluid flow inside complex cavity with or without baffles has not been investigated widely due to geometric complexity. This case study represented as an industrial building, numerous references deal with enclosures with flat straight walls due to its huge application in engineering like as, solar-collectors and cooling system of electronic devices. Especially for the cooling low powered laptop computers, monitors and TV. These are always complex interaction between the finite fluid content inside the enclosure with enclosure walls. This complexity increase when the wall becomes inclined, wavy or content baffles distributed in the enclosure. In the past, a great number of studies have focused on a vertical of cavity configuration formed with straight walls, mostly cavities of square, rectangular, trapezoidal and parallelogram cross sections. Representative reference that have divulged these efforts are condensed in Iyican et al (1980), Van Doormaal et al (1981), Law et al (1991), and Peric (1993). In these works buoyancy-induced flows are considered in the physical system and descriptive mathematical methodologies in the analysis or the experimental procedures in the laboratory are outlined.

The method of transformed coordinates was originally proposed in Jang et al (2003) as a tool to solve heat transfer problems in the presence of irregular surface of all kinds. This method is not limited to heat transfer problems, but is also applicable to other problems in engineering and science. Karyakin (1989) investigated transient natural convection in a trapezoidal cavity with parallel top and bottom walls and inclined side walls. Lee (1991) presented numerical results up to a Rayleigh number of $10^5$ for natural convection in trapezoidal enclosure of horizontal bottom and top walls that are insulated and isothermal inclined side walls. Moukalled et al (2003) studied numerically the natural convection in a partitioned trapezoidal cavity heated from the side. In particular the effect of Rayleigh number, Prandtl number, baffle height, and buffle location on heat transfer is investigated for two boundary conditions representing buoyancy-assisting and buoyancy-opposing modes along the upper inclined surface of the cavity. Shi et al (2003) performed a numerical study in a square cavity due to thin fin on the hot wall. They concluded that heat transfer capacity on the anchoring wall was always degraded; however, heat transfer capacity on the cold wall without the fin can be promoted for high Rayleigh numbers and with fins placed in the vicinity of the insulated walls.

Tasnim et al (2005) analyzed the laminar natural convection heat transfer in a square cavity with an adiabatic arc shaped baffle. As boundary conditions of the cavity, two vertical opposite walls are kept at constant but different temperatures and the remaining two walls are kept thermally insulated. Results are presented for a range of Rayleigh number, arc lengths of the baffle, and shape parameters of the baffle. Ambarita et al (2006), studied numerically a differentially heated square cavity, which is formed by horizontal adiabatic walls and vertical isothermal walls. Two perfectly insulated baffles were attached to its horizontal walls at symmetric position. The results show that Nusselt number is an increasing function of Rayleigh number, a decreasing one of baffle length and strongly depends on baffle position. Dagtekin et al (2006), studied natural convection heat transfer and fluid flow of two heated partitions within an enclosure have been analyzed numerically. The right side wall and the bottom wall of the enclosure were insulated perfectly while the left side wall and top wall were maintained at the same uniform temperature. The partitioned were placed on the bottom of the enclosure and their temperatures were kept higher than the non-isolated walls. The effects of position and heights of the partitions on heat transfer and flow field for Rayleigh number range from $10^4$ to $10^6$ have been investigated.

Bilgen (2002) investigated numerically the laminar and turbulent natural convection in enclosures with partial partitions. Vertical boundaries are isothermal and horizontal boundaries were adiabatic. Various geometrical parameters were: aspect ratio, partition position, height of the partition and Rayleigh number, the results is reduced in terms of the normalized Nusselt number as a function of the Rayleigh number and other non dimensional geometrical parameters. An experimental study of low level turbulence natural convection in an air filled vertical partitioned square cavity was conducted by Ampofo (2004). The dimension of the cavity, which was 0.75*0.75*1.5, resulted in two dimensional flow. The hot and cold walls of the cavity were isothermal at 50 and 10 $^{\circ}C$ respectively giving a Rayleigh number of $1.58 \times 10^9$. The local velocity and temperature were systematically measured at different locations in the cavity and both mean and fluctuation quantities are presented.

The objective of this study is to examine numerically the natural heat transfer in complex geometry such as industrial building with or without baffles distributed in the cavity. Moreover to study the effect of Rayleigh number, Prandtl number and configuration of these baffles such as height and position for two cases, baffle attached the horizontal bottom wall of the cavity or attached the upper inclined wall on the characteristics of natural convection heat transfer in the cavity.

## PHYSICAL MODEL

The conjugate problem under present consideration is depicted in **Fig. 1,** which show a complex cavity represented in industrial buildings with insulated bottom and inclined top walls. The left wall fixed at hot temperature $T_h$ while the right wall maintained at the cold temperature $T_c$, the inclination of the top surface of the cavity is fixed at 15 degree. The geometry of the cavity in this study fixed at the width of the cavity 4 times the height of the left vertical wall. Results show two cases according to the position of the baffle, which is attached to horizontal bottom wall or attached to inclined top wall of the cavity as shown in **Fig. 1.** Three baffle height (HB = $0.3H^*$, $0.4H^*$, $0.5H^*$) and two position of the baffle (LB= 0.25L, 0.75L) are studied. In all computational the baffle thickness (WB=L/30) to simulate a thin baffle. The viscose incompressible flow inside a closed cavity and a temperature distribution is described by the Navier-Stokes and energy equations for two dimension and steady. The Boussinesq approximation is used with the assumption of constant properties and negligible viscous dissipation. The governing equation in stream function- vortities formulation in dimensionless form is defined as follows:

$$\frac{\partial^2\psi}{\partial^2 x}+\frac{\partial^2\psi}{\partial^2 y}=-\omega \tag{1}$$

$$\frac{\partial\omega}{\partial t}+u\frac{\partial\omega}{\partial x}+v\frac{\partial\omega}{\partial y}=\Pr\left(\frac{\partial^2\omega}{\partial^2 x}+\frac{\partial^2\omega}{\partial^2 y}\right)+\Pr\cdot Ra\,\theta \tag{2}$$

$$\frac{\partial\theta}{\partial t}+u\frac{\partial\theta}{\partial x}+v\frac{\partial\theta}{\partial y}=\left(\frac{\partial^2\theta}{\partial^2 x}+\frac{\partial^2\theta}{\partial^2 y}\right) \tag{3}$$

Hence, introducing the following non-dimensional variables:

$(x,y)=(x^\bullet,y^\bullet)/l$ , $(u,v)=(u^\bullet,v^\bullet)\cdot l/a$ , $\theta=(T-T_c)/(T_h-T_c)$

$\Pr=\nu/a$ , $Ra=g\,\bar{\bar{\beta}}\,l^3(T_h-T_c)/(a\nu)$

The study is completed with the following boundary condition:

$\theta=0$ , $u=v=0.$ $\Rightarrow$ *on the cold wall*

$\theta=1$ , $u=v=0.$ $\Rightarrow$ *on the hot wall*

$\theta_x=0$ , $\theta_y=0$ , $u=v=0.$ $\Rightarrow$ *on the rest*

## NUMERICAL PROCEDURES

The grid generation calculation is based on the curvilinear co-ordinate system applied to fluid flow as described by Thompson (1999). The transformation is as follows: $\xi=\xi(x,y)$ , $\eta=\eta(x,y)$. The problem is now defined in terms of new variables:

$$\left[\lambda\cdot\psi_\xi+\sigma\cdot\psi_\eta+\alpha\cdot\psi_{\xi\xi}-2\beta\cdot\psi_{\xi\eta}+\gamma\cdot\psi_{\eta\eta}\right]/J^2=-\omega \tag{4}$$

$$\begin{aligned}\omega_t+\left[\psi_\eta\cdot\omega_\xi-\psi_\xi\cdot\omega_\eta\right]/J=\Pr\left[\lambda\cdot\psi_\xi+\sigma\cdot\psi_\eta+\alpha\cdot\psi_{\xi\xi}-2\beta\cdot\psi_{\xi\eta}+\gamma\cdot\psi_{\eta\eta}\right]/J^2\\+Ra\cdot\Pr\cdot\left[y_\eta\cdot\theta_\xi-y_\xi\cdot\theta_\eta\right]/J\end{aligned} \tag{5}$$

$$\theta_t+\left[\psi_\eta\cdot\theta_\xi-\psi_\xi\cdot\theta_\eta\right]/J=\left[\lambda\cdot\theta_\xi+\sigma\cdot\theta_\eta+\alpha\cdot\theta_{\xi\xi}-2\beta\cdot\theta_{\xi\eta}+\gamma\cdot\theta_{\eta\eta}\right]/J^2 \tag{6}$$

Where

$$\begin{aligned}&\alpha=x_\eta^2+y_\eta^2 \quad , \quad \gamma=x_\xi^2+y_\xi^2 \quad , \quad \beta=x_\xi x_\eta+y_\xi y_\eta\\&\lambda=\left[x_\eta(\alpha\cdot x_{\xi\xi}-2\beta\cdot x_{\xi\eta}+\gamma\cdot x_{\eta\eta})-y_\eta(\alpha\cdot y_{\xi\xi}-2\beta\cdot y_{\xi\eta}+\gamma\cdot y_{\eta\eta})\right]/J\\&\sigma=\left[y_\xi(\alpha\cdot y_{\xi\xi}-2\beta\cdot y_{\xi\eta}+\gamma\cdot y_{\eta\eta})-x_\xi(\alpha\cdot x_{\xi\xi}-2\beta\cdot x_{\xi\eta}+\gamma\cdot x_{\eta\eta})\right]/J\end{aligned} \tag{7}$$

The boundary condition represented in the following table:

**Table 1 Boundary condition in the typical case study**

| | $\psi$ | $\theta$ | $\omega$ |
|---|---|---|---|
| Left wall | 0 | 1 | $-\alpha\cdot\psi_{\xi\xi}/J^2$ |
| Right wall | 0 | 0 | $-\alpha\cdot\psi_{\xi\xi}/J^2$ |
| Inclined wall | 0 | $\theta_\eta=0$ | $-\gamma\cdot\psi_{\eta\eta}/J^2$ |
| Bottom wall | 0 | $\theta_\eta=0$ | $-\gamma\cdot\psi_{\eta\eta}/J^2$ |
| Baffles | 0 | $\theta_\eta=0$ , $\theta_\xi=0$ | $-\alpha\cdot\psi_{\xi\xi}/J^2$ , $-\gamma\cdot\psi_{\eta\eta}/J^2$ |

The heat transfer rate by convection in a hot left wall of the cavity is obtained from the Nusselt number calculation. The local Nusselt number and average Nusselt number are expressed as:

$$Nu_l = \alpha \cdot \theta_\xi \big/ J\sqrt{\alpha} \quad , \quad Nu_{ava} = \int_0^1 Nu_l \cdot dy \qquad (8)$$

## VALIDATION OF THE CODE

In order to make sure that the developed codes are free of error coding, a validation test was conducted, calculations for an air filled square cavity without baffle for Ra=$10^4$, $10^5$, $10^6$ were carried out and the results are shown in table 1. the results of the previous publication for the same problem are also presented in table. Data from the table shows that the results of the code, even through there are some differences, do agree very well with the previous works results. Those differences are not essential, the maximum difference is 1.01% and probably caused by the different grid sizes and round-offs in the computational process.

**Table 2.** Comparison of the present result and the previous works result.

| Reference | Average Nusselt number $Nu_{ave}$ | | |
|---|---|---|---|
| | Ra =$10^4$ | Ra =$10^5$ | Ra =$10^6$ |
| Collins (2005) | 2.244 | 4.5236 | 8.8554 |
| Shi (2003) | 2.247 | 4.532 | 8.893 |
| Bilgen (2005) | 2.245 | 4.521 | 8.800 |
| Present study | 2.248 | 4.514 | 8.804 |

## RESULTS AND DISCUSSION

In order to understand the flow pattern, temperature distribution and heat transfer characteristics of the typical case study a total of 100 cases were considered. To study the effects of the baffle position (LB = 0.25L, 0.75L), baffle height (HB = 0.3H*, 0.4H*, 0.5H*), Rayleigh number (Ra = $10^3$, $10^4$, $10^5$, $10^6$), and Prandtl number (Pr = 0.7, 10) for two cases according to the baffle, attached to the horizontal bottom wall or attached to the inclined upper wall of the cavity. Flow and temperature fields and Nusselt number are examined. Typical grid generation for the cavity represented as shown in **Fig 2**.

### Flow and Temperature Fields

The flow consists of a recirculating eddy rotating clockwise, indicating that the fluid filling the cavity is moving up along both the left heated vertical wall and the top insulation inclined wall (the slope is positive) until reach to the middle of the cavity, then the flow down along the top insulation inclined wall (the slope is negative), cold right vertical wall, and horizontally to the left along the insulated bottom wall of the cavity. All results of streamline and isothermal contours are takes for Pr=0.7.

**Fig. 3** shows streamline and isothermal maps in the cavity without baffles as depicted, the flow structure consists of a single eddy rotating clockwise. At low Rayleigh number values, the eye of the recirculating vortex is located at the middle of the cavity close to the hot vertical wall of the cavity, where the largest velocities was located as shown in **Fig. 3A,** and **3C**. As Ra increase **Fig. 3E,** and **3G**, the eye of the vortex moves away from the hot wall towards the middle of the cavity and upward towards the top inclined upper wall of the cavity. In addition, at the highest Ra value Ra=$10^6$, the flow separates near the lower right corner of the cavity. For low Ra (Ra=$10^3$) **Fig. 3B**, isotherms values decrease uniformly from hot to cold wall showing dominant weak convection heat transfer. As Ra increase, the distribution of isothermal implies higher stratification levels within the cavity compare **Fig. 3B,** and **3H**, and consequently higher convection contribution.

For case 1 where the baffles attached horizontal bottom wall of the cavity, the flow pattern and isothermal contours are discussed below. **Fig. 4** and **Fig. 5** show that for LB=0.25L, HB=0.4H$^*$ and LB=0.75L, HB=0.4H$^*$ respectively. Streamlines in **Fig. 4** indicated that at the lowest Ra presented (Ra=$10^3$), the recirculating flow exhibits single vortex (**Fig. 4A,** and **4C**) located near the middle of the cavity. This vortex rotates in the clockwise direction. As Ra increase, the two vortices will be appearing in the cavity around the baffle. The left vortex close to the left hot wall (**Fig. 4E,** and **4G**) is more uniform comparing with right vortex. Increase Ra leads to distrom the right vortex which move towards the left and upper inclined wall in the cavity. Moreover, with increasing values of Ra, the flow between the baffle and the cold right wall becomes weaker as compared to the region between the baffle and the hot left wall. The colder fluid tends to stagnate in the lower right-hand section of the cavity between the baffle and right vertical wall (cold wall). Resulting in a thermally stratified region and inhibiting the penetration of the warmer fluid from the cavity left-hand section. Isotherms presented in **Fig. 4** (left side), reflect the above described flow patterns. At low Ra, variation in temperature is almost uniform over the domain. As Ra increase, convection is promoted, and isothermal contours become more distorted.

The effects of positioning of the baffle close to the cold right wall on the streamline and isotherms are depicted in **Fig. 5** for LB=0.75L, HB=0.4H$^*$. At low Ra value **Fig. 5A,** and **5C**, the flow structure is qualitatively similar to that presented in **Fig**. **4A,** and **4C**, with small vortex behind the baffles close to the right cold wall. As Ra values increase **Fig**. **5G,** and **5E**, a more pronounced thermally stratified zone developed in the baffle cold wall region as a compared to the configuration in which the baffle is close to the hot wall (**Fig**. **4G,** and **4E**). This thermally stratified region prevents the bulk of the fluid descending a long the cold wall from penetrating the region. Moreover, to that the two vortices appear in the cavity, first is uniform as a circle close to the cold right wall and the second is similar to the ellipse shape move up to the left wall. The above described behavior is further exemplified by the isothermal plots presented in **Fig**. **5** (left side). At low Ra stratification effects are small and distribution of isotherms is more or less uniform. While as Ra increase, isotherms becomes more distorted and stratification effects are promoted. The effects of baffles height on the hydrodynamics and thermal fields are presented in **Fig**. **6** for baffle position LB=0.25L and Ra=$10^6$. Streamlines and isotherms are displayed for four different baffles height of (HB=0, 0.3H$^*$, 0.4H$^*$, 0.5H$^*$). As HB increase, a weaker flow is observed in both the right and left portions of the doman, two non-similar clockwise rotating eddies are noticed in **Fig. 6C, 6E**, and **6G** with their strength lower than the single vortex flow in the cavity without baffle. For highest HB the left vortex is more uniform and dissipated between the baffle and the hot left wall, while the right vortex is move to up and distributed to the weak flow near to the cold right wall. Isotherms presented in **Fig. 6** (left side) are in accordance with above finding and clearly show the decreases in the convection heat transfer through the spread of the isotherms.

For case 2 where the baffles attached upper inclined wall of the cavity, the flow pattern and isothermal contours are discussed below. **Fig**. **7** and **Fig**. **8** show that for LB=0.25L, HB=0.4H$^*$ and LB=0.75L, HB=0.4H$^*$ respectively. Streamlines in **Fig**. **7** indicated that at the lowest Ra (Ra=$10^3$), the recirculating flow exhibits two clockwise rotating vortices with some communication between them (**Fig**. **7A**). As Ra increase, the deformation of the vortices increase, moreover, the increasing Ra values, the eye of the vortex in the right hand portion of the domain moves upward and to the left as a result of increasing stratification level in the lower right portion of the cavity. Isotherms presented in **Fig**. **7** (left side) reflect the above described flow pattern. At low Ra, variations in temperature are almost uniform over the domain, If Ra increase, convection is promoted and stratification effects are increased. The effects of positioning the baffle closer to the cold vertical wall on the streamlines and temperature fields are depicted in **Fig**. **8** for LB=0.75L, HB=0.4H$^*$. At low Ra values the flow structure is qualitatively similar to the previous **Fig**. **7** but in this case the weak flow region could be show between the baffle and the cold right wall. As Ra values increase **Fig**. **8E,** and **8G**, stratification levels increase and isotherms become more distorted in the baffle cold wall region as compared to the configuration in which the baffle is closer to the hot left wall (**Fig**. **7E,** and **7G**). This indicates stronger convection caused by higher buoyancy effects as a result of the longer distance the flow travels before encountering the baffle. Isothermal contours in this case are similar to that in **Fig**. **7** with some difference in shape and behavior of flow in the cavity due to increase the position of the baffle from the hot wall. The effects of baffles height on the hydrodynamics and thermal fields are presented in **Fig**. **9** for baffle position LB=0.25L and Ra=$10^6$. Streamlines and isotherms are similar to that in case 1 (**Fig. 6**) but it show weaker flow in both sides of the baffle, more decrease in convection heat transfer, and more deformation in streamline and isotherms.

## Heat transfer parameter

Local Nusselt number distribution along hot wall is presented in **Fig. 10** for case 1 the $Nu_l$ levels increase with increasing Ra indications higher convection contribution. If the position of baffle is increase the $Nu_l$ increase because the temperature difference along the hot wall is increase for constant Ra expect for Ra=$10^6$ because the buoyancy effect become more declare and huge. This behavior also shows in case two **Fig. 11** with small difference in shape of the curve and its values. For low Ra, the $Nu_l$ is low too because the limited of convection heat transfer in this case. **Fig. 12** shows the $Nu_l$ distribution along the hot wall for different height baffle and for two cases. Increase HB values leads to decrease the $Nu_l$ because the temperature difference is decrease too. In case 2 (**Fig. 12** right side) increase height baffle leads to increase the values of $Nu_l$ comparing with its values in case 1 (**Fig. 12** left side) due to the location of the baffle in the cavity. **Fig 13** represents the average Nusselt number distribution according to the Rayleigh number for two cases. Figures show that for log scale axis where the relation is linear and if the height of the baffle increase the slope of the curve is increase too, this description is applied for two cases.

**Maximum stream function (flow strength)**

The maximum absolute values of the stream function displayed in table **3** for case 1 (baffle attached the horizontal bottom wall) and to different value of Pr=0.7 and 10. Indicated that the flow strength (maximum velocity in the domain) generally increase with increasing baffle height and decreasing values of Pr, moreover, the strength of flow increase with Ra due to an increase in temperature difference. **Table 4** show that for case 2 (baffle attached the upper inclined wall), indicated that the flow strength generally decreases with increasing baffle height and increasing values of Pr due to the increase in the fluid viscosity. Moreover the strength of the flow increases with Ra values increase due to an increase in temperature difference and consequently in buoyancy forces.

**Table 3. Maximum absolute values of stream function for baffles attached the horizontal bottom wall.**

| Ra | Without baffles | Baffles Height HB | | | | | |
|---|---|---|---|---|---|---|---|
| | | 0.3 H* | 0.4 H* | 0.5 H* | 0.3 H* | 0.4 H* | 0.5 H* |
| | | LB =0.25 L | | | LB =0.75 L | | |
| **Pr = 0.7** | | | | | | | |
| $10^3$ | 0.2520 | 0.2277 | 0.26714 | 0.3310 | 0.2535 | 0.2675 | 0.3289 |
| $10^4$ | 1.8887 | 1.79598 | 1.9339 | 2.1504 | 1.9554 | 1.9808 | 2.0804 |
| $10^5$ | 11.1519 | 7.2596 | 7.3242 | 7.4226 | 6.7567 | 6.7617 | 6.773 |
| $10^6$ | 15.7261 | 16.3829 | 17.6351 | 19.0268 | 16.883 | 16.944 | 17.123 |
| **Pr = 10** | | | | | | | |
| $10^3$ | 0.0176 | 0.0156 | 0.0180 | 0.0219 | 0.0178 | 0.0188 | 0.02366 |
| $10^4$ | 0.1394 | 0.12527 | 0.1327 | 0.1437 | 0.1392 | 0.1419 | 0.1519 |
| $10^5$ | 1.1110 | 1.2202 | 1.2854 | 1.3788 | 1.3602 | 1.3793 | 1.4368 |
| $10^6$ | 7.6564 | 7.0533 | 7.2353 | 7.7474 | 7.1792 | 7.1182 | 7.4256 |

**Table 4. Maximum absolute values of stream function for baffles attached the inclined upper wall.**

| Ra | Without baffles | Baffles Height HB | | | | | |
|---|---|---|---|---|---|---|---|
| | | $0.3\ H^*$ | $0.4\ H^*$ | $0.5\ H^*$ | $0.3\ H^*$ | $0.4\ H^*$ | $0.5\ H^*$ |
| | | LB =0.25 L | | | LB =0.75 L | | |
| **Pr = 0.7** | | | | | | | |
| $10^3$ | 0.2520 | 0.1949 | 0.1935 | 0.1852 | 0.2466 | 0.2451 | 0.2435 |
| $10^4$ | 1.8887 | 1.5714 | 1.5131 | 1.4467 | 1.9469 | 1.9409 | 1.9342 |
| $10^5$ | 11.1519 | 6.9733 | 5.9200 | 4.8871 | 6.8875 | 6.8742 | 6.8690 |
| $10^6$ | 15.7261 | 16.1176 | 14.3799 | 13.0812 | 14.9814 | 13..9628 | 13.1340 |
| **Pr = 10** | | | | | | | |
| $10^3$ | 0.0176 | 0.0139 | 0.0136 | 0.0135 | 0.0171 | 0.0170 | 0.0168 |
| $10^4$ | 0.1394 | 0.1159 | 0.1143 | 0.1107 | 0.1365 | 0.1356 | 0.1347 |
| $10^5$ | 1.1110 | 1.1179 | 1.0917 | 1.0513 | 1.3398 | 1.3329 | 1.3252 |
| $10^6$ | 7.6564 | 6.4921 | 5.6038 | 5.0103 | 7.2502 | 7.3050 | 7.3016 |

## CONCLUSION

For case 1 results show that, the flow strength generally increasing with increasing Ra values, and decreasing values of Pr, while in case 2 the same behavior of above could be show except the flow strength decreasing with increasing baffle height. Also, increase Ra leads to increase the rate of heat transfer, the configuration of the cavity in case 2 leads to increase in heat transfer rate comparing with that in case 1 as shown in figures and tables.

## REFERENCES


- Amberite H., Kishinami K., Daimaruya M., Saitoh T., Takahashih H., and Suzuki J., “Laminar natural convection heat transfer in an air filled square cavity with two insulated baffles attached to its horizontal walls”, Jouornal of Thermal science and engineering, vol. 14,no. 3, 2006.
- Ampofo F., "Turbulent natural convection in an air filled partitioned square cavity", Int. J. of Heat and Fluid Flow, 25(2004)103-114.
- Bilgen E., “Natural convection in enclosures with partial partitions”, Journal of Renewable Energy, 26(2002)257-270.
- Bilgen E., “Natural convection in cavities with a thin fin on the hot wall”, Int. J. Heat and Mass Transfer, 48(2005)3493-3505.
- Dagtekin I., and Oztop H., “Natural convection heat transfer by heated partitions within enclosure”, Int. J. of heat and mass transfer, vol. 28, no. 6, 2006, pp.823-834.
- Iyican L., Bayazitoglu Y., and Witte L.C. , “ An analytical study of natural convection heat transfer within a trapezoidal enclosure”, ASME . J. Heat transfer, 102(1980), 640-647.
- Iyican L., Bayazitoglu Y., and Witte L.C. , “ An experimental study of natural convection in trapezoidal enclosure”, ASME . J. Heat transfer, 102(1980), 648-653.
- Karyakin Y.E., “Transient natural convection in prismatic enclosures of arbitrary cross section”, Int. J. of heat and mass transfer, Vol. 32, no. 6(1989)1095-1103.
- Jang J.H., Yan W.M., and Liu H.C., “Numerical convection heat and mass transfer a long a vertical wavy surface”, Int. J. of heat and mass transfer, 46(2003)1075-1083.
- Law S.W., Gani R., and Symons J.G., “Experimental and numerical studies of natural convection in trapezoidal cavities”, ASME . J. Heat transfer, 111(1991), 372-377.
- Lee T.S., “Numerical experiments with fluid convection in tilted nonrectangular enclosure”, Journal of Numerical heat transfer, A, vol. 10, (1991)487-499.
- Moukalled F., and Darwish M., “Natural convection in a partitioned trapezoidal cavity heated from the side”, Journal of Numerical heat transfer, Part A-43(2003)543-563.
- Peric M.,” Natural convection in trapezoidal cavities”, Journal of Numerical heat transfer, Part B-24(1993)213-219.

- Shi, and Khodadi, “Laminar natural convection heat transfer in a differentially heated squre cavity due to a thin fin on the hot wall”, J. heat transfer 125(2003)624.
- Tasnim S.H., and Collins M., “Suppressing a natural convection in a differentially heated square cavity with an arc shaped baffle”, Int. J. of heat and mass transfer, 32(2005)94-106.
- Thompson J. F., Bharat K. S., and Weatherill N. P., " Handbook of grid generation", 1999 by CRC Press LLC.
- Van Doormaal J.P., Raithby G.D., and Strong A.B., “Predication of natural convection in non-rectangular enclosure using orthogonal curvilinear coordinates”, Journal of Numerical heat transfer, 4(1981)21-38.


**NOMENCLATURE:**

| SYMBOLS | TITLES | UNITS |
|---|---|---|
| a | Thermal diffusivity | m/sec$^2$ |
| g | Gravitational acceleration | m/sec$^2$ |
| H | Cavity height (left vertical wall) | m |
| HB | Baffle height | m |
| $H^*$ | Height of the cavity at the location of the baffle | m |
| J | Jacobian | ----- |
| L | Cavity width | m |
| LB | baffle position | m |
| Nu | Nusslet number | ----- |
| Pr | Prandtl number ($\nu$/a) | ----- |
| Ra | Rayleigh number ( g. $\beta'$ .($T_h$ - $T_c$).$L^3$/$\nu$.a) | ----- |
| T | Temperature | $^{\circ}C$ |
| t | Time | sec |
| u,v | Dimensionless velocity | ----- |
| WB | Baffle thickness | ----- |
| x, y | Dimensionless coordinates | ----- |
| **GREEK SYMBOLS** | | |
| $\theta$ | Dimensinless temperature | ----- |
| $\beta'$ | Thermal expansion coefficient | 1/K |
| $\alpha,\beta,\gamma,\lambda,\sigma$ | Transformation functions | ----- |
| $\xi$ , $\eta$ | Dimensionless curvilinear coordinates | ----- |
| $\psi$ | Stream function | ----- |
| $\omega$ | Vorticity | ----- |
| $\nu$ | Kinematics viscosity | m$^2$/sec |

**SUBSCRIPTS**

| | |
|---|---|
| ave | Average |
| c | Cold wall |
| h | Hot wall |
| l | Local |
| max | Maximum value |
| x , y, $\xi$ , $\eta$ | Derivative relative to x, y, $\xi$, and $\eta$ respectively. |

**SUPERSCRIPT**

| | |
|---|---|
| • | Dimensional form |

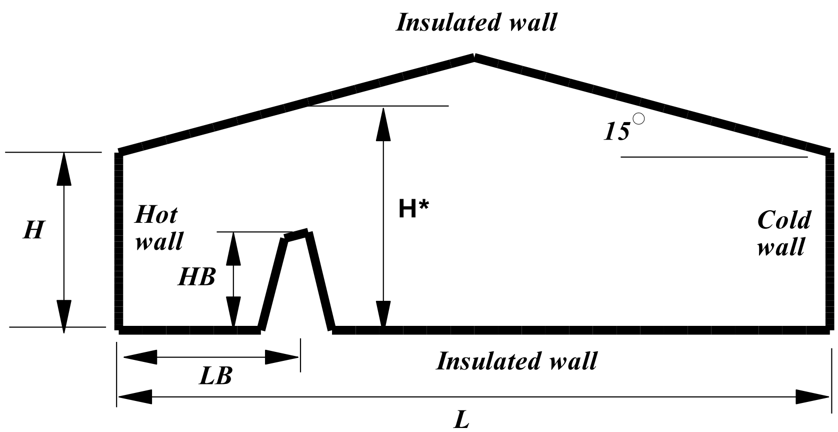


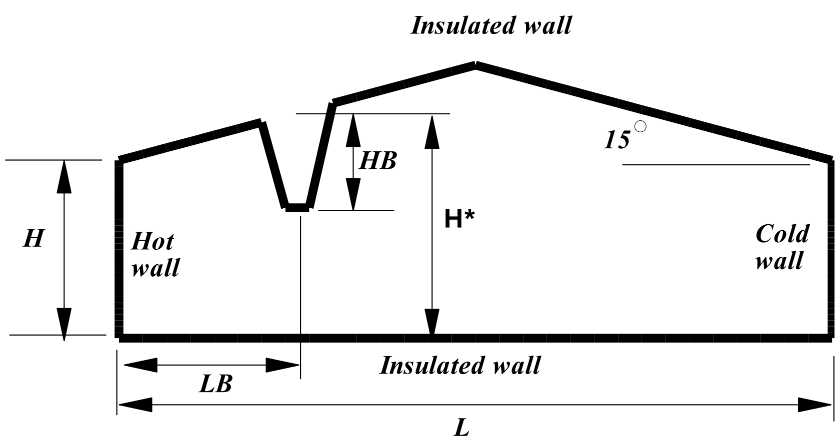


**Fig. 1 Typical cavity with boundary conditions for two cases**
**A. Case 1 (baffle attached to the horizontal bottom wall)**
**B. Case 2 (baffle attached to the upper inclined wall)**

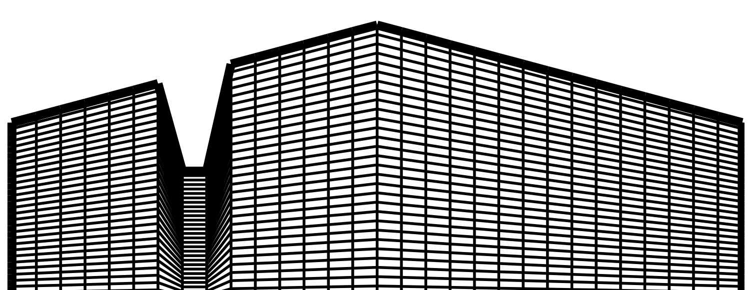

**A** **Ra =$10^3$** **B**

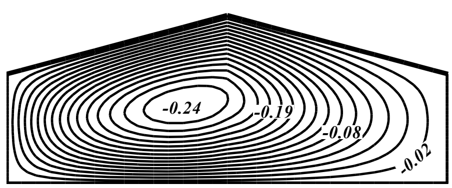


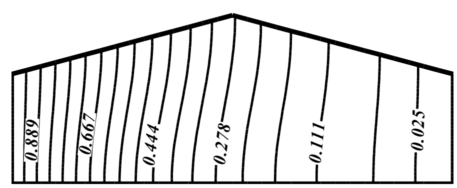


**C** **Ra =$10^4$** **D**

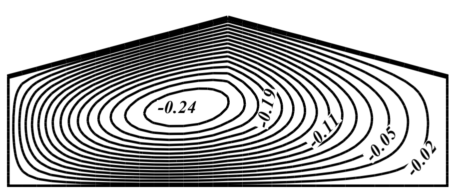


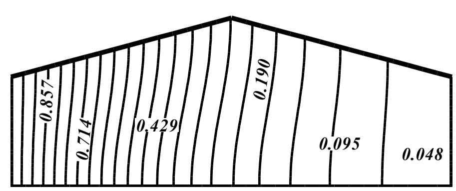


**E** **Ra =$10^5$** **F**

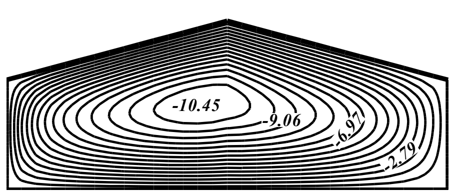


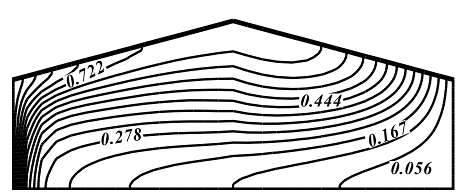


**G** **Ra =$10^6$** **H**

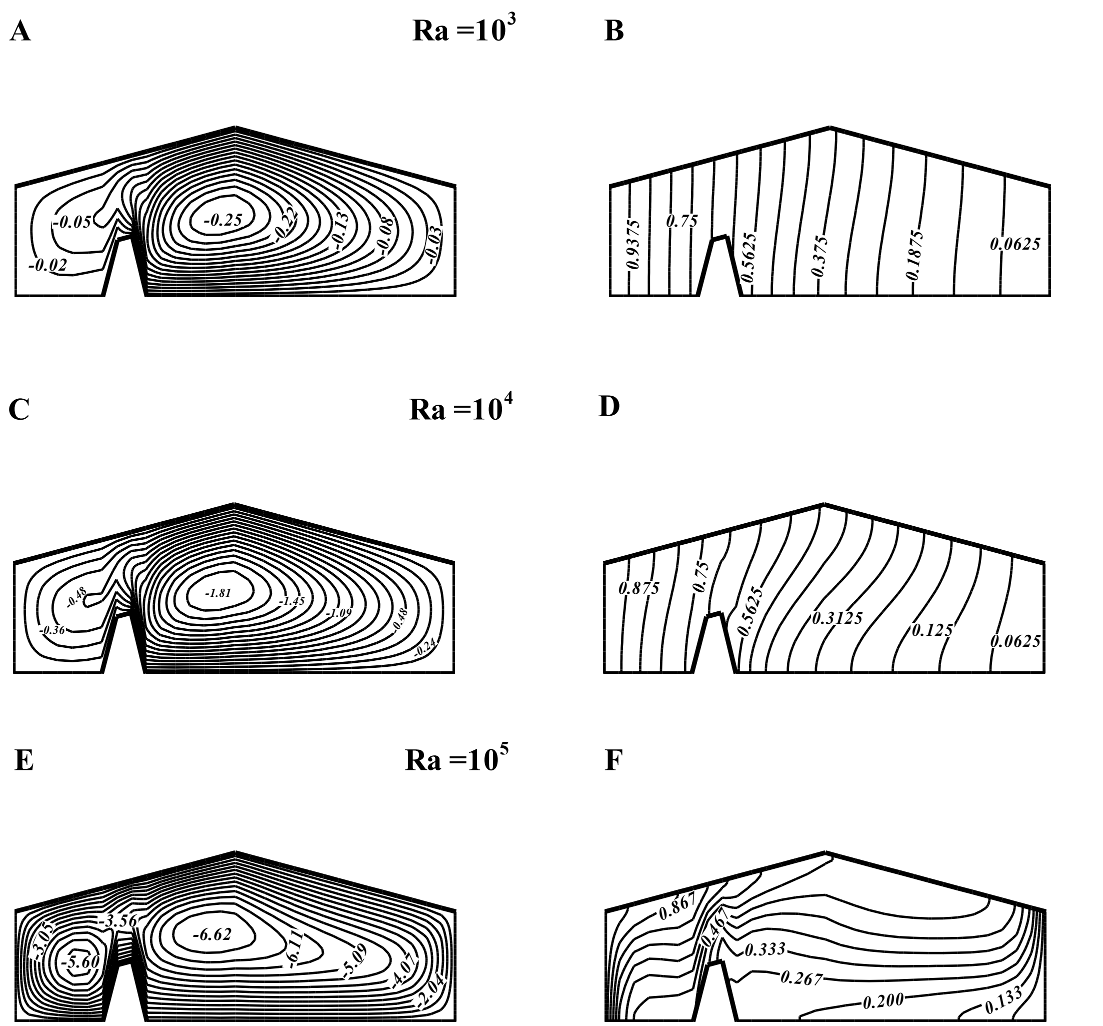

A
Ra =10^3
B
-0.05
-0.25
-0.22
-0.13
-0.08
-0.03
-0.02
0.9375
0.75
0.5625
0.375
0.1875
0.0625
C
Ra =10^4
D
-0.48
-1.81
-1.45
-1.09
-0.48
-0.36
-0.24
0.875
0.75
0.5625
0.3125
0.125
0.0625
E
Ra =10^5
F
-3.03
-3.56
-6.62
-5.60
-6.11
-5.09
-4.07
-2.04
0.867
0.467
0.333
0.267
0.200
0.133

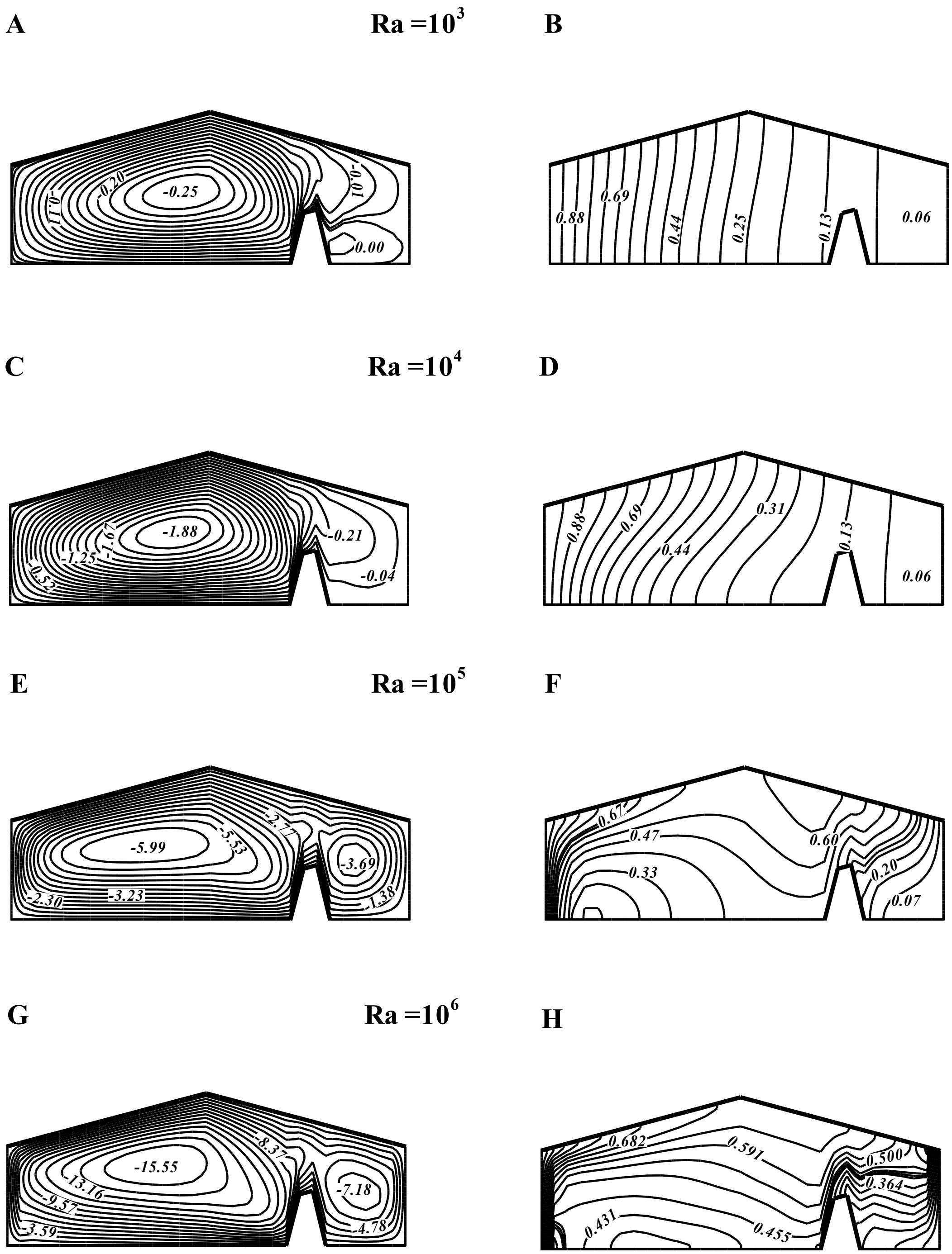


**Fig. 5 Rayleigh number effect on streamlines (left side) and isothermal contours (right side) in the typical cavity for case 1, baffle attached the horizontal bottom wall at LB=0.75L, HB=0.4H***

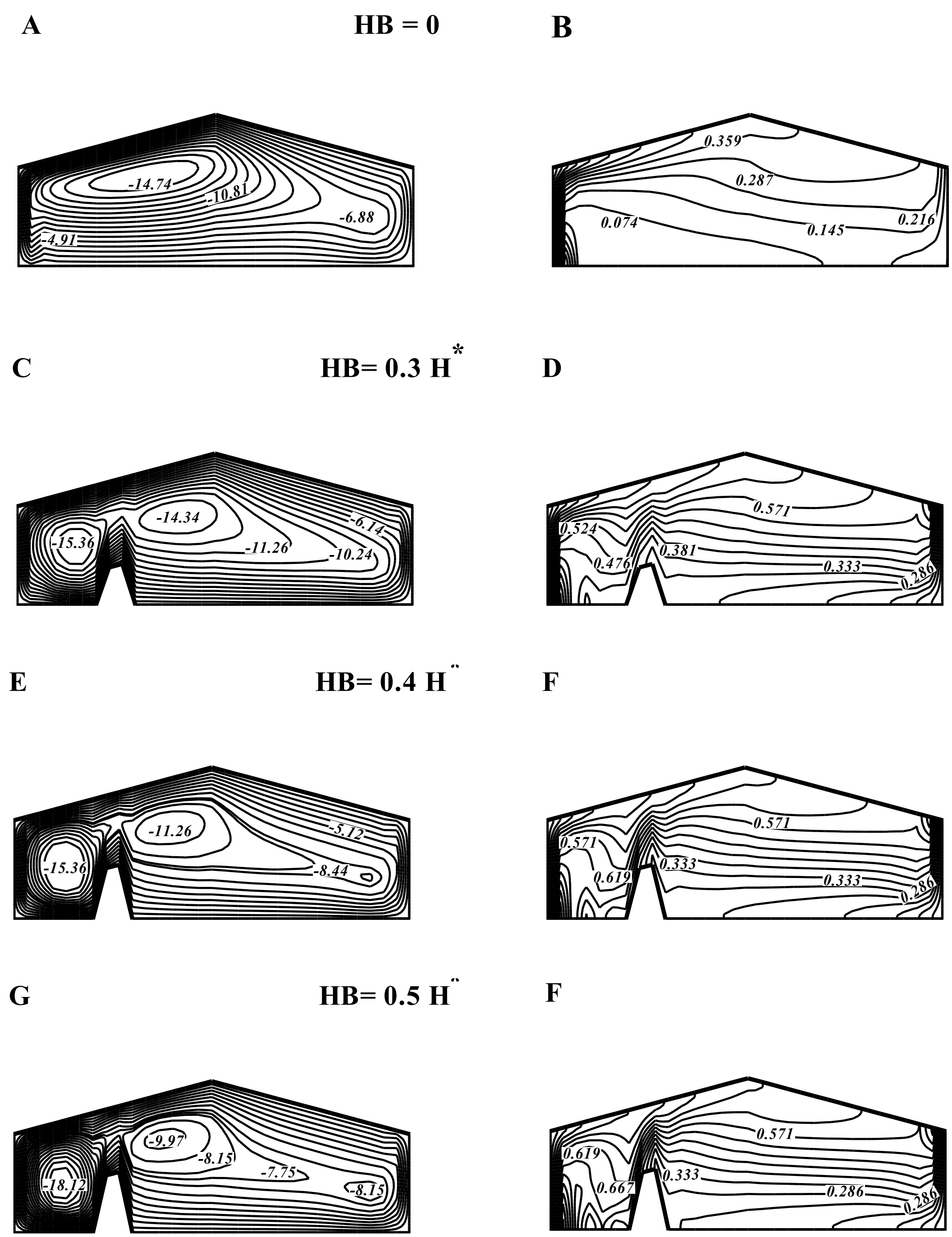


**Fig. 6 Baffle height effect on streamlines (left side) and isothermal contours (right side) in the typical cavity for case 1, baffle attached the horizontal bottom wall at LB=0.25L, Ra=$10^6$**

**Fig. 7 Rayleigh number effect on streamlines (left side) and isothermal contours (right side) in the typical cavity for case 2, baffle attached the upper inclined wall at LB=0.25L, HB=0.4H***

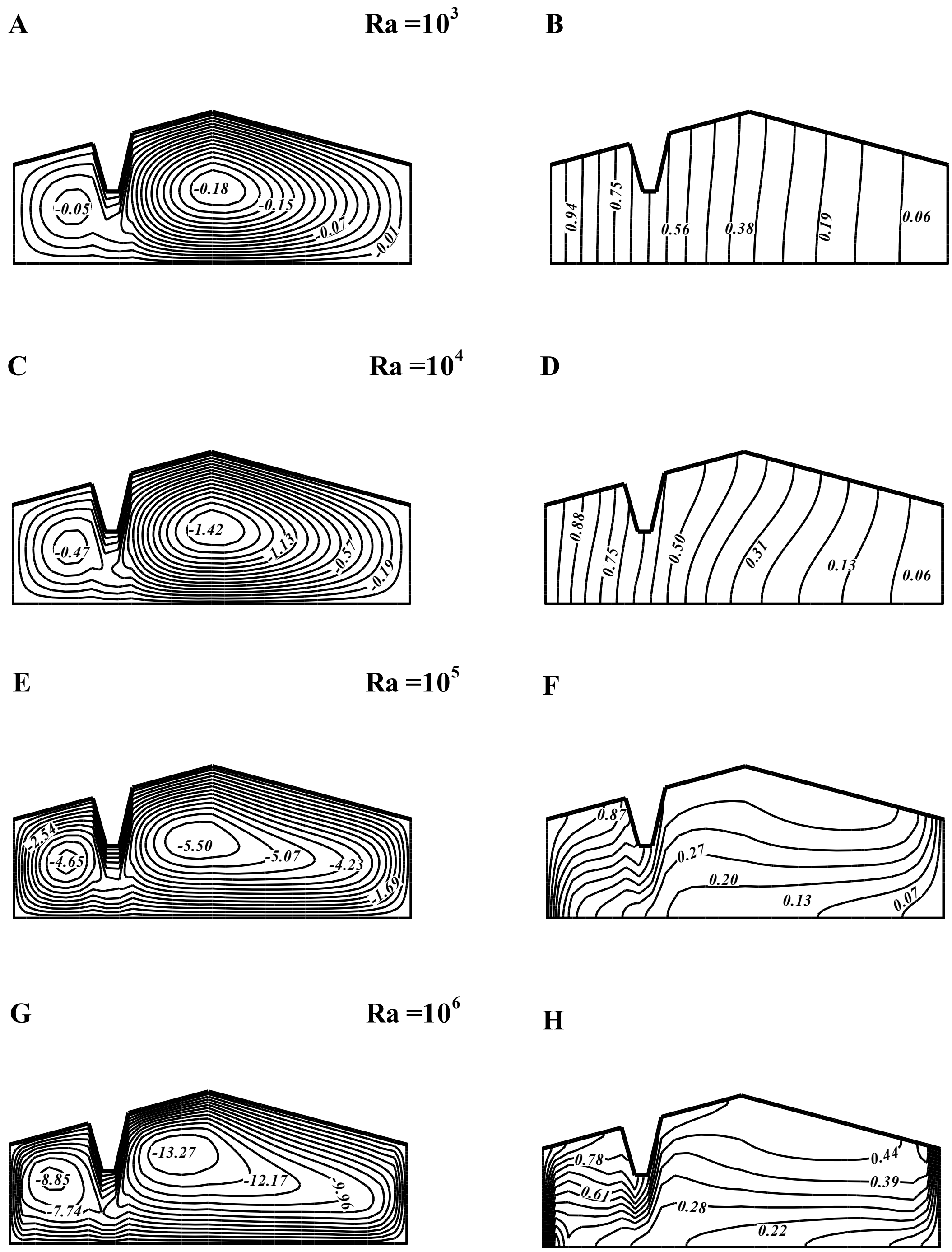
A
Ra =10^3
B
-0.18
-0.05
-0.15
-0.07
-0.01
0.94
0.75
0.56
0.38
0.19
0.06
C
Ra =10^4
D
-1.42
-0.47
-1.13
-0.57
-0.19
0.88
0.75
0.50
0.31
0.13
0.06
E
Ra =10^5
F
-2.54
-4.65
-5.50
-5.07
-4.23
-1.69
0.87
0.27
0.20
0.13
0.07
G
Ra =10^6
H
-13.27
-8.85
-7.74
-12.17
-9.96
0.78
0.61
0.44
0.39
0.28
0.22

**Fig. 8 Rayleigh nu**
**contours (right sid**
**uppe**

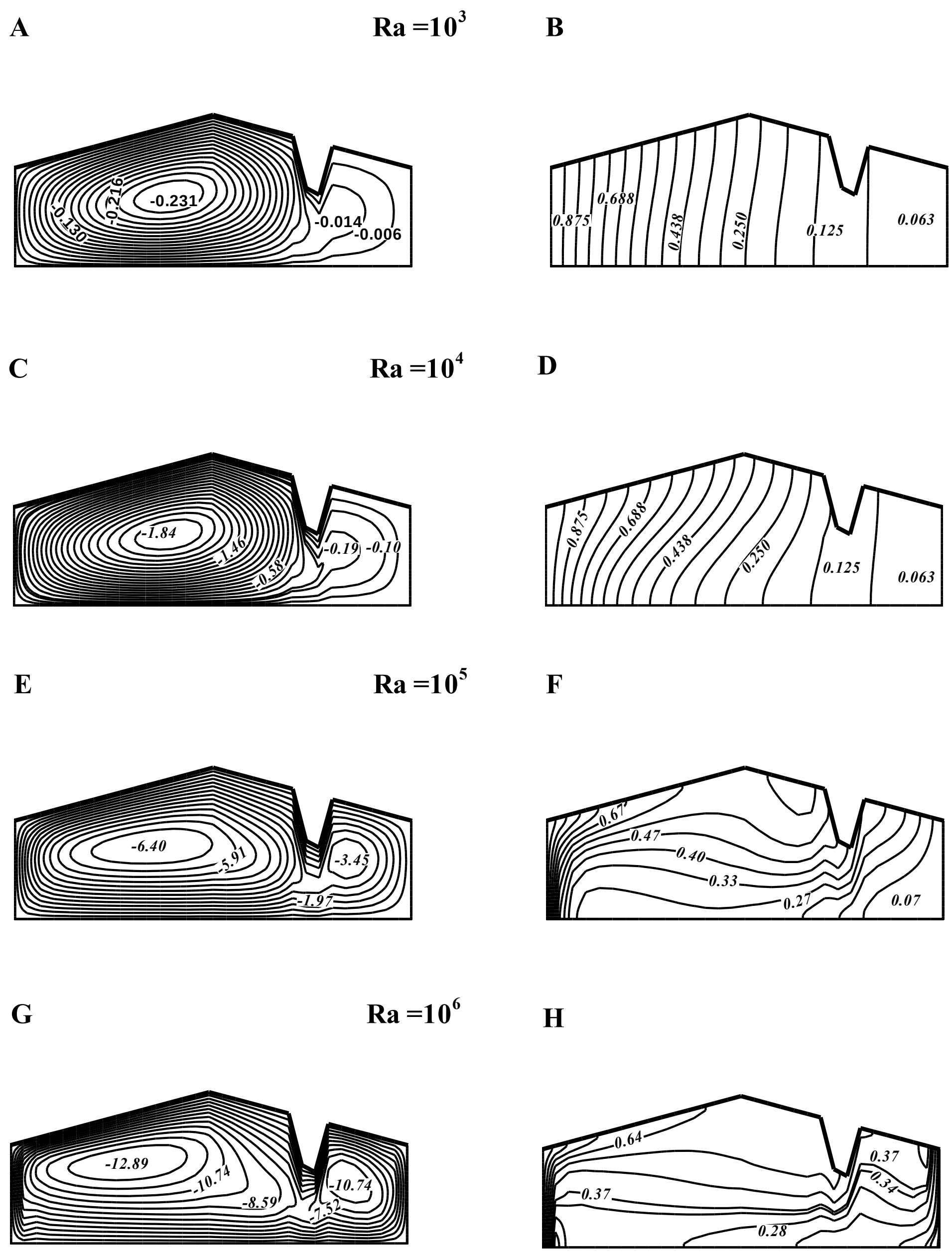

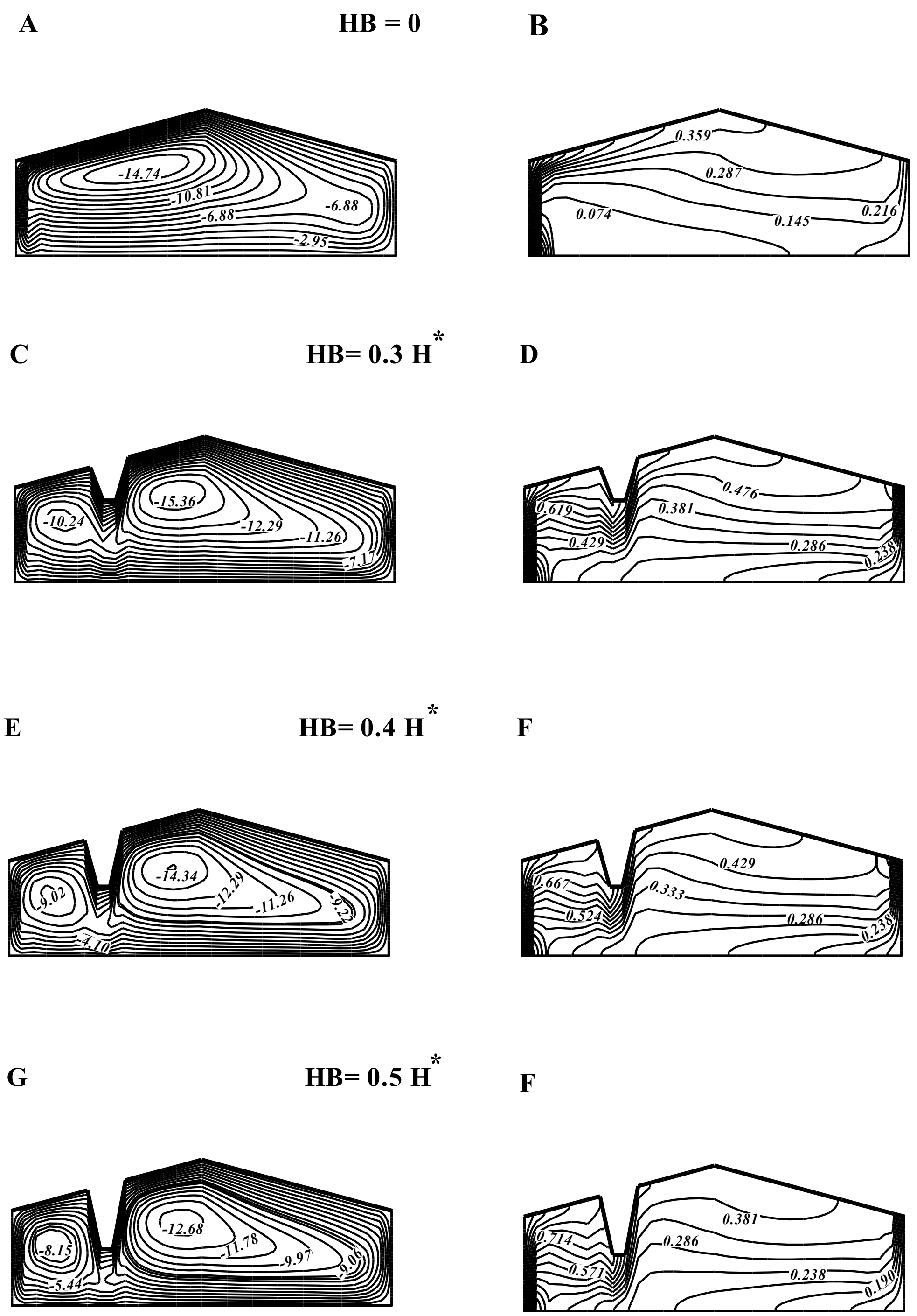


**Fig. 9 Baffle height effect on streamlines (left side) and isothermal contours (right side) in the typical cavity for case 2, baffle attached the upper inclined wall at LB=0.25L, Ra=$10^6$**

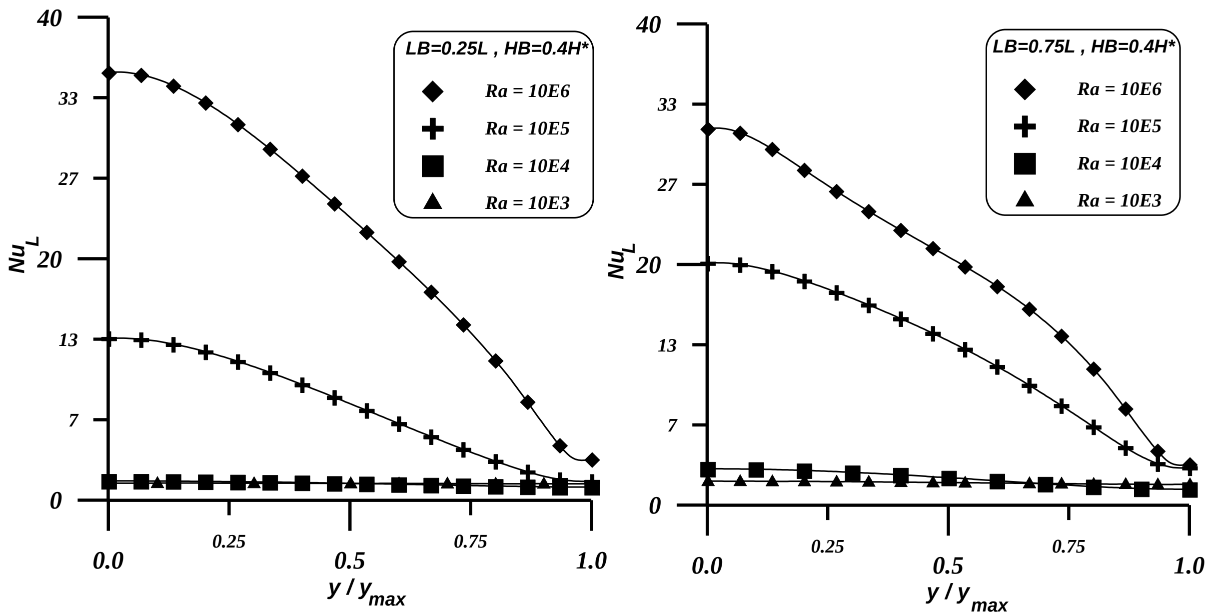


**Fig. 10 Local Nusselt number distribution on the left hot wall for case 1, baffle attached the horizontal bottom wall of the cavity**

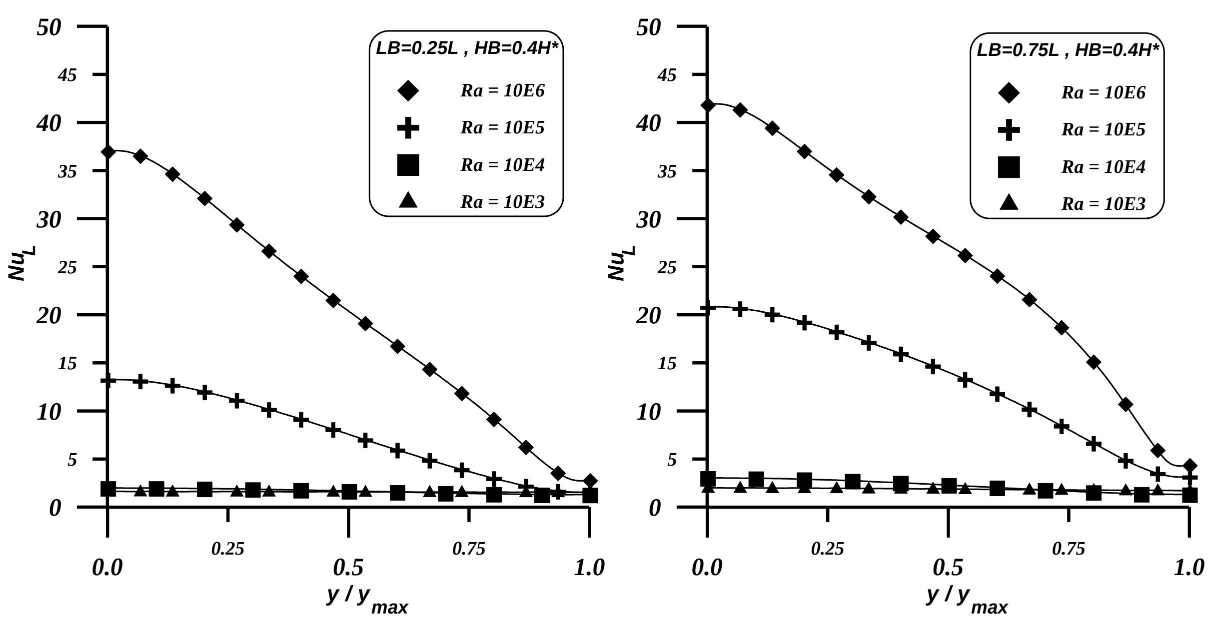


**Fig. 11 Local Nusselt number distribution on the left hot wall for case 2, baffle attached the upper inclined wall of the cavity**

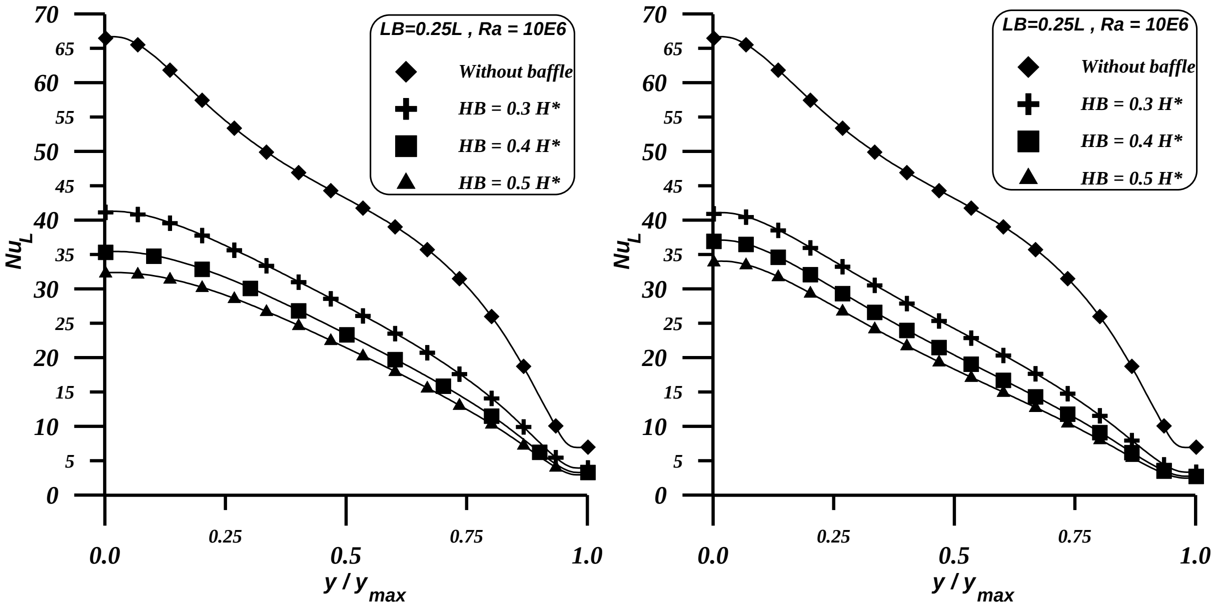


**Fig. 12 Local Nusselt number distribution on the left hot wall for Ra = $10^6$.**
**A. Case 1, baffle attached the horizontal bottom wall.**
**B. Case 2, baffle attached the upper inclined wall.**

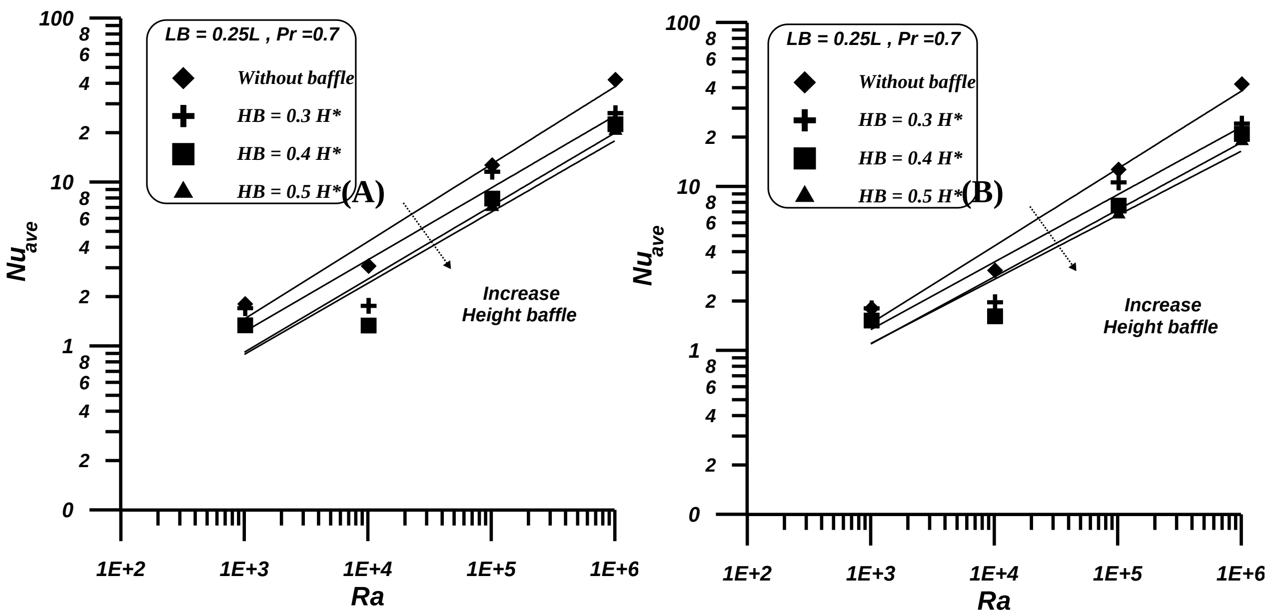


**Fig. 13 Average Nusselt number distribution with Rayleigh number on the left hot wall**
**A. Case 1, baffle attached the horizontal bottom wall.**
**B. Case 2, baffle attached the upper inclined wall.**

# DYNAMIC BEHAVIOR OF NON - RETURN VALVES OPERATING AT SMALL OPENING

Dr. Ali A.M. Al-Asadi
Ministry of Higher Education and Scientific Research

Dr. Hameed D. Lafta
Mechanical Engineering Dep.
College of Engineering
Kufa University

Msc. Ali W. Abbas
Mechanical Engineering Dep.
College of Engineering
Kufa University

## ABSTRACT

In the present work a general dynamic behavior of non return valves subjected to jet flow is presented. The differential equations of valve motion and discharge were developed in a non-dimensional from, in terms of suitable dimensionless variables and parameters of the valve system.

The derived equations are coupled nonlinear differential equations. Thus, a computer program was developed using a package called (MatLab) to solve these equations. The study shows that there are three types of the valve responses depending on the overall hydrostatic pressure difference and it is found that the valve vibrating at a constant limit cycle, which is leading to the failure of the system. It is also shown that the limit cycle frequency decreases with increasing the stiffness parameter and inertia factor. Finally the study shows that the losses factor has negligible effect on valve vibration and discharge.

**KEY WORDS**: - Dynamic, Return valves, Nonlinear equations

**الخلاصة**

في هذا البحث, تمت دراسة التصرف الديناميكي للصمامات اللارجاعية تحت جريان نفاث.اشتقت المعادلات الخاصة بحركة الصمام و جريان المائع بدلالة المتغيرات اللابعدية.

ان معادلات الحركة والجريان هي معادلات تفاضلية غير خطية ومرتبطة التصرف , ولذلك تم بناء برامج حاسوبية باستخدام ما يسمى بـ( MAT LAB) لحل هذه المعادلات عدديا". بينت الدراسة ان هنالك ثلاث حالات لاستجابة الصمام تعتمد على فرق الضغط الهايدروستاتيكي ,ووجد ان الصمام يهتز عند تردد حدي ثابت و الذي يؤدي بدوره الى فشل الصمام , وكذلك بينت الدراسة ان قيمة التردد الحدي الثابت تنقص بزيادة معامل الجساءة و معامل القصور الذاتي وان معامل الخسارة ليس له تأثير ذو قيمة على اهتزاز الصمام وكمية الجريان.

## NOMENCLATURE

| Symbol | Meaning | Units |
|---|---|---|
| a | Acceleration | $m/s^2$ |
| A | Area of the pipe | $m^2$ |
| A2 | Area of the pipe upstream of valves | $m^2$ |
| A3 | Area of vena contract in the valve gap | $m^2$ |
| A4 | Area of the pipe downstream of valves | $m^2$ |
| $A_o$ | Area of the orifice | $m^2$ |
| C | Damping | N.s/m |
| $C_c$ | Valve contraction coefficient | - |
| $C_d$ | Valve velocity coefficient | - |
| $C_v$ | Valve discharge coefficient | - |
| g | Gravity acceleration | $m/s^2$ |
| $h_L$ | Head losses over the length (L) | m |
| $I_{ij}$ | Inertia of the fluid between any section i-j | m |
| k | Stiffness | N/m |
| K | Dimensionless Stiffness | - |
| $L_{eq}$ | Equivalent pipe length | m |
| $L_{ij}$ | Pipe length over section i-j | m |
| $L_o$ | Length of jet through valve | m |
| P | Pressure | $N/m^2$ |
| q | Discharge | $m^3/s$ |
| Q | Dimensionless discharge | - |
| r | Radius of the pipe | $m^2$ |
| t | Time | s |
| v | Velocity | m/s |
| w | Area of the valve | $m^2$ |
| x | Valve displacement measured from seat | m |
| X | Dimensionless Valve displacement | - |
| $x_o$ | Valve initial ( no load ) opening | m |
| $X_o$ | Dimensionless Valve initial opening | - |

## Greek Symbols

| Symbol | Meaning | Unit |
|---|---|---|
| $\Psi$ | Overall losses coefficient | - |
| A | Dimensionless inertia factor | - |
| $\alpha_o$ | Dimensionless inertia factor of the jet | - |
| $\mu$ | Dimensionless mass ratio | - |
| $\tau$ | Dimensionless time | - |
| $\tau_o$ | Shear on the pipe wall | N/m |
| $\zeta$ | Damping factor | - |
| $\theta$ | Dimensionless downstream pipe area | - |
| $\eta$ | Dimensionless down steam pipe | - |
| $\gamma$ | Specific weight | - |
| $\rho$ | Fluid density | $Kg/m^3$ |
| $\omega$ | Reference frequency | - |
| $\Lambda$ | Integration factor | - |

## INTRODUCTION

Check or non return valves are widely used in many power or process plants. They are unique because in their main mode they operate without receiving any out side help usually do not give indication of their setting. Furthermore, they must be reliable and must be able to operate for an extended period, thus they must be carefully designed J. W. Hutchison 1976 .Various types of these valves and their application have been described by Siikonen 1983, in the technical research center of Finland, suggested a computational method for the valve dynamics. The method consists of a hydraulic part and a five equations model describing valve dynamics. These equations are coupled ordinary differential equations. Some important parameters for the boundary condition were determined experimentally, such as losses, discharge coefficient etc. The hydraulic equations were solved using the method of characteristics. The method gives good indication of behavior of non – return valves under unsteady flow condition.

Renold and Soung 1976 examined the hydraulic performance characteristics of large diameter titling desk check valves. In particular, design parameters of pressure drop during normal operation, maximum permissible flow during valve closure, and maximum hammer surge are considered. Equations and coefficients were provided, for evaluation of pressure losses, as a function of desk angle and line Reynolds number .A method of calculating fluid torques on a moving disk In general, all the design techniques developed are general and can be applied to the most check valves design.

Kubie 1982 studied the performance and design of plug type check valves. Full non-linear equations of system, which are consisting of pipeline, pumps and check valve, were developed Using Newton second law, effect of different parameters such as discharge coefficient and inertia was developed. In particular, the work demonstrated that the check valves could not be properly designed without having enough information about the system in which they are to operate where the valves vary sensible to the system components specially inertia effect

Weaver and Dubi 1978 studied experimentally the flow-induced vibration of a check valve with a spring damper to prevent slamming. Both prototype and two- dimensional experiments were conducted to develop an under standing of the mechanism of self-excitation as will as the phenomenon was studied is considered to be the same as that causing vibration in numerous other flow control devices.

More research is being done and attempts are being made to develop an understanding of mechanisms of excitation. However, in many cases it is still necessary to use cut and try methods.

## MATHEMATICAL MODELING

The basic system considered in the analysis is consisting of check valve, constant presser reservoir and connecting pipeline system. The excitation mechanism nature can be understood through the physical modeling and flow visualization. Through the physical model and flow visualization studies, an understanding of the excitation mechanism was developed. Furthermore, it was established that the effect of the unsteady separated flow around the valve is not an important part of the mechanism. Thus it was felt that the behavior of the valve might to be modeled satisfactory using simple one dimensional fluid mechanism Weaver and Ziada 1980. Therefore, the valve can be represented as an orifice with time varying area, in general pipeline system as show in Fig .(2). Water hammer occurred on each closure but was found to die out before valve recluse and, hence, it is not important phenomenon of the valve

Weaver et.al. 1975. Vortex shedding occurred in the wake of valve clapper during each cycle but this also played on role in the excitation mechanism Weaver et.al. 1975 . The pressure difference between up stream and down stream orifice is the same pressure acting on the up and down valve. Dynamic behavior in general pipeline system is influenced by the characteristics of rest of the system, especially the fluid inertia effects.

Referring to Fig.(1), which shows the forces acting on an element in the pipeline system, using Newton's second law and remembering that the flow is incompressible fluid flow, gives .

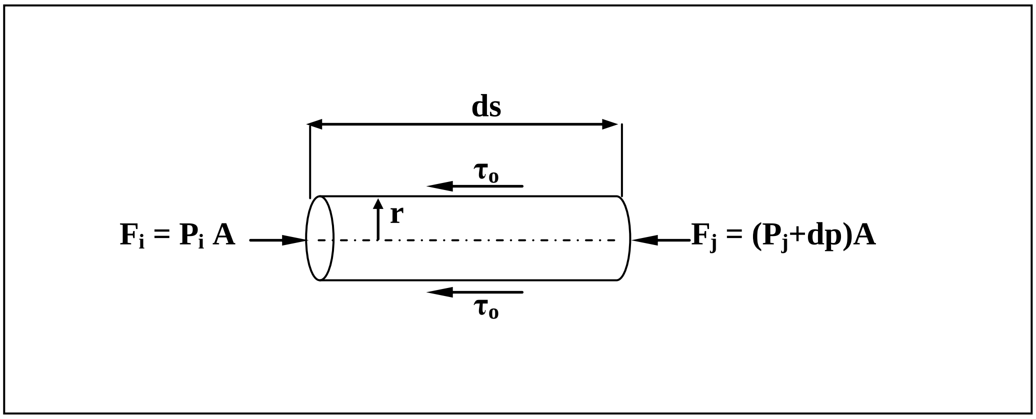


**Fig.(1). Forces acting on an element in the pipeline system.**

$$\sum F = m.a$$

$$PiA - (p_j + dp)A - \tau_o (2\pi r)ds = \rho A ds\left(\frac{dv}{ds} + \frac{dv}{dt}\right) \quad (1)$$

Re – arranging eq. (1), and dividing by $\gamma = \rho g$ , $A = \pi r^2$ ,then

$$-\frac{dp}{\gamma} - \frac{2\tau_o ds}{\gamma r} = v\frac{dv}{g} + \frac{ds}{g}\frac{dv}{dt} \quad (2)$$

Substituting for vdv =1/2 $dv^2$, then eq. (2) becomes

$$-\frac{dp}{\gamma} - \frac{dv^2}{2g} = \frac{2\tau_o ds}{\gamma r} + \frac{ds}{g}\frac{dv}{dt} \quad (3)$$

Eq. (3) applies to unsteady flow of both compressible and incompressible real fluid.

For incompressible flow that are considering here $\gamma$ is constant, so it can be integrate directly between point i and j and substituting for the distance between them L, then eq.(3.3) becomes:

$$\frac{p_i - p_j}{\gamma} + \frac{v_i^2 - v_j^2}{2g} = \frac{2\tau_o L_{ij}}{\gamma R} + \frac{L_{ij}}{g}\frac{dv_J}{dt} \quad (4)$$

$$\frac{2\tau_o L_{ij}}{\gamma R}$$

Where term represents the head losses ($h_L$) over the length (L), thus the Eq. (4) becomes:

$$\frac{p_i}{\gamma}+\frac{v_i^2}{2g}=\frac{p_j}{\gamma}+\frac{v_j^2}{2g}+h_L+\frac{L_{ij}}{g}\frac{dv_J}{dt} \tag{5}$$

Eq. (5) is the same as the steady flow equation, with addition of the last term, $\left[\frac{L_{ij}}{g}\frac{dv}{dt}\right]$ which is called the accelerative head.

The head losses term can be expressed in terms of velocity, v, which is defined as:

$$h_L=\phi_{ij}\frac{v_j^2}{2g} \tag{6}$$

Where:

$\phi_{ij}$ = loss factor

Substituting for eq.(6) in eq.(5), then

$$\frac{p_i}{\gamma}+\frac{v_i^2}{2g}=\frac{p_j}{\gamma}+(1+\varphi_{ij})\frac{v_j^2}{2g}+\frac{L_{ij}}{gA_J}\frac{dq}{dt} \tag{7}$$

where in general q = vA

Equation above is the unsteady Bernoulli equation, where P, γ, v, $\phi$ , and q, are the pressure, specific weight, mean velocity, turbulent losses factor and discharge respectively.

Applying eq.(7) between sections 1 & 2 as shown in Fig.(2) to get the equation of motion of the water column in the upper stream pipeline system, thus:

$$\frac{p_1}{\gamma}+\frac{v_1^2}{2g}=\frac{p_2}{\gamma}+(1+\varphi_{1-2})\frac{v_2^2}{2g}+\frac{L_{1-2}}{g}\frac{dv_2}{dt} \tag{8}$$

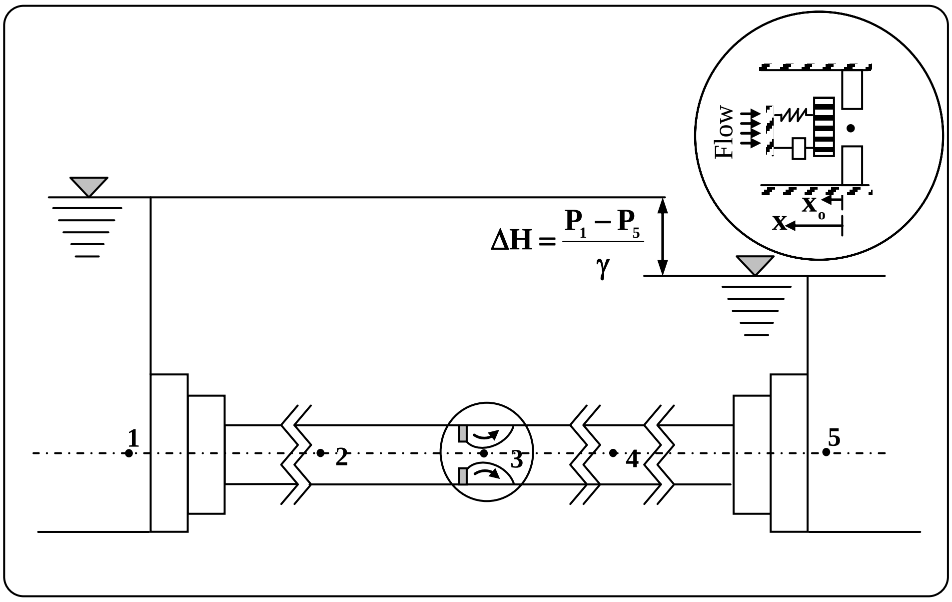


**Fig.( 2). General pipeline system with valve modeled as an orifice**

Applying Eq.(7) between section 2 & 3 to get equation of motion through the orifice, then

$$\frac{p_2}{\gamma} + \frac{v_2^2}{2g} = \frac{p_3}{\gamma} + (1+\phi_{2-3})\frac{v_3^2}{2g} + \frac{L_{2-3}}{gA_3}\frac{dq}{dt} \tag{9}$$

Where:

$L_{2-3}$= is the jet length.

Referring to Fig.( 2), which shows the orifice in the pipeline system, it can be noted that the streamlines continue to converge for short distance downstream of the plane of the orifice. Hence the minimum-flow area is actually smaller than the area of the orifice. To relate area of minimum flow, which is often, called the contracted area of the jet, or vena contract, to the area of the orifice Ao, using the contraction coefficient, which is define as:

$$A_3 = C_c A_o \tag{10}$$

Where:

Cc: contraction coefficient.

The velocity beyond the orifice section,$v_3$, can be eliminated by means of the continuity equation. Solving eq. (9) for $v_3$, then

$$V_3^2 = \frac{2g}{1-\left(\frac{A_3}{A_2}\right)^2}\left[\frac{P_2}{\gamma} - \frac{P_3}{\gamma} - \frac{L_{2-3}}{gA_3}\frac{dq}{dt}\right] \tag{11}$$

The discharge, is given by $V_3A_3$, or, in terms of eq.(10) & eq.(11) is given by:

$$q = C_v A_o \sqrt{\frac{2g}{1-\left(\frac{C_c A_o}{A_2}\right)^2}\left(\frac{P_2 - P_3}{\gamma} - \frac{L_{2-3}}{gA_3}\frac{dq}{dt}\right)} \quad (12)$$

Equation (12) describes the discharge for the flow of an incompressible fluid through an orifice; however, it is valid for relatively high Reynolds number John et.al. 1990. For low and moderate values of Reynolds numbers, viscous effects are signification and, an additional coefficient of viscosity must be applied to the discharge equation to relate the ideal flow to the actual flow. Thus for viscous fluid flowing through an orifice, the following discharge equation can be established:

$$q = C_d A_o \sqrt{\frac{2g}{1-\left(\frac{C_c A_o}{A_2}\right)^2}\left(\frac{P_2 - P_3}{\gamma} - \frac{L_{2-3}}{gA_3}\frac{dq}{dt}\right)} \quad (13)$$

Where $C_d$ is the discharge coefficient and it is given by

$C_d = C_v C_c$

It is should be noted that the contraction and discharge coefficient in eq. (13) will generally depend on valve's geometry, position and velocity in a way that cannot be predicated theoretically Daily and McCloy .

Referring to Fig.(2) and applying eq.(8) between sections 3 and 4 to get the equation of motion for the expanding jet, then:-

$$\frac{p_3}{\gamma} + \frac{v_3^2}{2g} = \frac{p_4}{\gamma} + (1+\phi_{3-4})\frac{v_4^2}{2g} + \frac{L_{3-4}}{gA_4}\frac{dq}{dt} \quad (14)$$

Applying eq.( 8) between sections 3 & 4 , thus:

$$\frac{p_4}{\gamma} + \frac{v_4^2}{2g} = \frac{p_5}{\gamma} + (1+\phi_{4-5})\frac{v_5^2}{2g} + \frac{L_{4-5}}{gA_5}\frac{dq}{dt} \quad (15)$$

Equations (14) & (15) represent the equations of motion of water column in the down stream pipeline system.

As the valves dynamic behavior is strongly influence by characteristics of the rest of the system, especially the fluid inertia effects $L_{ij}$, it is useful to include theses in the expression for the discharge through the valve. This may be done by substituting for $(P_2\text{-}P_3)/\gamma$ in eq.(13) after assuming that the velocity,$V_1 = V_5 = 0$, thus:

$$q = C_d A_o \sqrt{\frac{2g}{1-\left(\frac{C_c A_o}{A_2}\right)^2}} \sqrt{\frac{P_1 - P_5}{\gamma} - \sum h_L - \sum \frac{L_{ij}}{gA_{ij}}\frac{dq}{dt} - \frac{L_{2-3}}{gA_3}\frac{dq}{dt} - \frac{V_2^2}{2g} + \frac{V_3^2}{2g}} \tag{16}$$

In this equation and those, which follow, the summation signs for the values of losses and interfaces exclude those values of the valve, section 2-3 and this attributed to the fact that those coefficients at the valve section are depending on the valve displacement while all others are constants.

Eq. (6) may be substituting for the turbulent losses in terms of losses coefficient, $\phi_{ij}$, and the velocity head in the pipe just downstream of the valve, ($V_4^2/2g$), thus:

$$q = C_d A_o \sqrt{\frac{2g}{1-\left(\frac{C_c A_o}{A_2}\right)^2}} \sqrt{\frac{P_1 - P_5}{\gamma} - \frac{A_4^2}{A_{ij}^2}\sum \phi_{ij}\frac{V_4^2}{2g} - \sum \frac{L_{ij}}{gA_{ij}}\frac{dq}{dt} - \frac{L_{2-3}}{gA_3}\frac{dq}{dt} - \frac{A_4^2}{A_2^2}\frac{V_4^2}{2g} + \frac{A_4^2}{A_3^2}\frac{V_3^2}{2g}} \tag{17}$$

The eq.(17) can be simplified by putting losses coefficients , $\phi_{ij}$ , in terms of overall losses coefficient, $\psi$, which is define as:

$$\psi = A_4^2 \sum \frac{\phi_{ij}}{A_j^2} \tag{18}$$

Substituting for eq. (18) in eq.(17), then

$$q = C_d A_o \sqrt{\frac{2g}{1-\left(\frac{C_c A_o}{A_2}\right)^2}} \sqrt{\frac{P_1 - P_5}{\gamma} - \psi\frac{V_4^2}{2g} - \sum \frac{L_{ij}}{gA_{ij}}\frac{dq}{dt} - \frac{L_{2-3}}{gA_3}\frac{dq}{dt} - \frac{A_4^2}{A_2^2}\frac{V_4^2}{2g} + \frac{A_4^2}{A_3^2}\frac{V_4^2}{2g}} \tag{19}$$

Assume ($L_{eq}$) is the length of pipe, of constant cross section-area A4 that have the same inertia effect as the actual pipe. If the pipe consists of section of different cross-sectional area, then the equivalent length ($L_{eq}$) may be defined as:

$$L_{eq} = A_4 \sum L_{ij} / A_{ij} \tag{20}$$

Therefore it can be simplified the inertia term in Eq.(19) by substituting eq.(20) and substituting for $q = A_4 v_4$, thus: to get:

$$q = C_d A_o \sqrt{\frac{1}{1-\left(\frac{C_c A_o}{A_2}\right)^2}\left[\begin{array}{l} 2g\Delta \mathrm{H} - \frac{1}{A_4^2}\left(\psi + \frac{A_4^2}{A_2^2} - \frac{A_4^2}{C_c A_o}\right)q^2 \\ -\frac{2}{A_4}\left(L_{eq}\frac{A_4 L_o}{C_c A_o}\right)\frac{dq}{dt} \end{array}\right]} \tag{21}$$

Where:

$\Delta H = (P_1 - P_5)/\gamma$, the total pressure drop cross the system and Lo is the length of the jet ($L_{2\text{-}3}$) of area $C_c A_o$ through the valve orifice. However, it is difficult to estimate the length of this jet and in many applications, the inertia of the jet may be neglected in comparison with rest of the system.

Assuming that the valve can be represented by single degree of freedom system [13] and it is equation of motion is given by:

$$m\frac{d^2x}{dt^2} + C\frac{dx}{dt} + k(x - x_o) + F = 0 \tag{22}$$

Where:

m is total effective mass, and C is the system damping including that due to fluid, k is the elastic restoring force of the valve, $x_o$ is the zero load opening displacement of the valve, and F is the dynamic fluid loading on the valve, and it can be determined by integrating the dynamic pressure, $\Delta p$, over the surface of the valve:-

$$F = \int_s \Delta p \, ds \tag{23}$$

where
s : surface area of the valve.
$\Delta p$ : dynamic pressure.

If the pumping action of the valve is neglected and the dynamic pressure is assumed to act uniformly over the upstream and downstream faces of the valve, so that the dynamic load is given by:-

$$F = \lambda s(p2-p3) \tag{24}$$

Where $\lambda$ is an integration factor depends on the valve geometry and arrangement.
Substituting eqs.(10, 14, and 15) for ($P_2$-$P_3$) in eq.(13) and simplifying the resulting equation in a manner similar to that followed for simplifying eq.(21), and assuming that $V_1 = V_5 = 0$, thus

$$F = \lambda s\left[(p_1 - p_5) - \frac{\rho}{2A_4^2}\left(\psi + \frac{A_4^2}{A_2^2} - \frac{A_4^2}{A_3^2}\right)q^2 - \frac{\rho}{A_4}L_{eq}\frac{dq}{dt}\right] \tag{25}$$

Where $\rho$ is the fluid density

For the purpose of analysis it is convenient to represent eq.(21) and eq.(22) in terms of dimensionless form. In addition for most flow control devices operating at small opening, the flow area is linearly related to the valve displacement, thus the dynamic discharge equation and the valve displacement (for more details see Appendix A) are given by:-

$$Q = \frac{C_d X}{\left[\eta^2 - \left(\frac{C_c X}{\theta}\right)^2\right]^{\frac{1}{2}}} \left[\begin{array}{l} \Delta P - \left(\psi + \frac{1}{\theta^2} - \frac{\eta^2}{C_c^2 X^2}\right) Q^2 \\ -\left(\alpha + \frac{\eta \alpha_o}{(C_c X)}\right) \frac{dQ}{d\tau} \end{array}\right]^{\frac{1}{2}} \qquad (26)$$

$$\frac{d^2 X}{d\tau^2} + 2\zeta \frac{dX}{d\tau} + K(X - X_o) + \frac{1}{2}\mu \left[\begin{array}{l} \Delta P - \left(\psi + \frac{1}{\theta^2} - \frac{\eta^2}{C_c^2 X^2}\right) Q^2 \\ -\left(\alpha + \frac{\eta \alpha_o}{C_c X}\right) \frac{dQ}{d\tau} \end{array}\right] = 0 \qquad (27)$$

It should be noted that the discharge (Q) and the inertia factor ($\alpha_o$) represent the dynamic effects and approach zero faster than the displacement X and are equal to zero when the valve is closed.

## - RESULTS & DISCUSSION

The governing differential equations obtained in the present study are coupled non-linear differential equations in terms of valve discharge and displacement and until this time there is no way to be solved analytically. Thus, a numerical solution was adopted to obtain the solution for displacement and discharge. For this purpose computer simulation programs are developed using a package which is called MAT LAB. The flow chart of the program is shown in appendix (B). The general results are presented below for the most instructive and interesting cases. Also, for the purpose of comparison, the present results are compared quantitatively with the experimental data for specific case of a swing check valve.

In parametric study, the valve and discharge contraction coefficients are assumed constant, because there is no way to predict their variation with accelerating and decelerating flows or as a function of the valve motion.

The computations were executed show that there are three types of response depending on the overall hydrostatic pressure difference across the valve:

1- The valve undergo small damped oscillations and come to rest at an opening for which the static pressure drop across the valve is balanced by the valve elastic restraint. This occurs for ($\Delta P \leq 2.6$).
2- The valve closes for several times and come to rest in a closed position. This occurs for ($\Delta P \geq 40$).
3- The valve oscillates at a limit cycle of constant amplitude. This occurs for ($2.6 \leq \Delta P \leq 40$).

The latter case will be carefully discussed because it represents greatest insight into the system's behavior. Also, such results offer the possibility of comparison with experimental observations of vibrating structures.

The numerical values of the system parameters adopted in the present study are of typical values and are shown in table (1).

**Table (4.1). Dimensionless parameters of the system.**

| Parameter | symbo | value |
|---|---|---|
| Stiffness | K | 0.9 |
| Initial opening | X0 | 0.5 |
| Pressure difference | ΔP | 26.7 |
| Damping factor | ξ | 0.45 |
| Inertia factor | α | 1372 |
| Losses factor | ψ | 40 |
| Mass ratio | μ | 0.032 |
| Area ratio | η | 4.64 |
| Discharge coefficient | Cd | 0.85 |
| Contraction coefficient | Cc | 0.8 |

## - EFFECT OF STIFFNESS PARAMETER (K)

Figs (3), (4), and (5) show the variation of the valve displacement against the dimensionless time for different values of stiffness parameter and hydrostatic pressure difference.

It can be see that for low hydrostatic pressure difference ($\Delta P=1.8$) the increase in stiffness leads to increase in the maximum overshoot. In control system the over shoot must be not exceeding 20 percent for design specification Weaver and Dubi [5], this makes the stiffness more than 0.9 unacceptable for the valve application. For high hydrostatic pressure difference ($\Delta p=42.6$) the valve opens for a several time and closed and remains closed. In this case, the increase in stiffness only increases the amplitude. For intermediate hydrostatic pressure difference ($\Delta p=26.7$), the behavior is similar to that observed in both the prototype valve model experiments reported by Weaver and Dubi [5].

Further insight is obtained by examining the discharge variation as a function of the valve displacement as shown in Fig (6). The plot is similar to the experimental curve reported by [6] and show that the maximum discharge occurs after the valve has reached its maximum opening.

## - EFFECT OF INERTIA FACTOR (A)

Figs.(7), (8) and (9) show the variation of the displacement against dimensionless time for different values of inertia factor and hydrostatic pressure difference . Whereas Fig. (7) shows that the increase in inertia factor has no effect on the amplitude of oscillation for low hydrostatic pressure difference ($\Delta p=1.8$), the effect only appears at small inertia on the final rest of the valve. While, Figs. (8) and (9) show there are no effect of inertia factor on the amplitude at moderate and high hydrostatic pressure differences.

It also has been shown in Fig.(10) that for intermediate hydrostatic pressure difference the flow reaches its maximum discharge very shortly after the valve reaches its maximum displacement for small fluid inertia. Significantly, the discharge also reduces much more gradually during closure so that the rate of change of discharge and dynamic pressure is considerably reduced. This resulting in that the valve oscillates at a higher frequency (near its natural frequency) and the motion is much more nearly simple harmonic motion.

## EXPERIMENTAL VERIFICATION OF MODEL

Figs (11-a) and (11-b) show comparison of the theoretical predications with experimental results of limit cycle amplitude and frequency respectively. The spring stiffness and the frequency has been normalized with respect to the natural frequency of the valve in quiescent fluid in order to emphasize that these self-excited vibrations do not generally occur at the structural natural frequency.

While the results of the foregoing section shown that the displacement and discharge characteristics agree qualitatively with experimental observation, these curves demonstrate that the quantitative agreement is reasonable as well. Apparently, the theory underestimates the limit cycle amplitude by about 20 percent while overestimating the frequency by similar amount. It is thought that the difference is primarily due to the assumption of constant discharge coefficient.

## - CONCLUSIONS

The main conclusions can be summarized as follows:

- A theoretical model has been derived for self-excited vibrations of valves subject to the jet flow mechanism of instability is sufficiently general that it is considered applicable to a large variety of flow control devices operating at small openings.
- When the valve is considered to be elastically restrained by support stiffness K at small initial opening (zero hydrodynamic load), its response to some disturbance can be classified into a three categories:
    - It may undergo small damped oscillation and come to rest at an opening for which the static pressure drop across the valve is balanced by the valves elastic restraint. Such behavior is dynamically stable and is the desired response for flow control structures.
    - It may open, perhaps bounce several times, and come to rest in a closed position.
    - Valve may repeatedly open and close again and thus oscillate at some constant limit cycle amplitude. This represents a dynamically unstable system.
- 3 -Motion of the flow control device is far from simple harmonic and the discharge does not reach its maximum value until the valve has completely opened.
- 4 -Numerical results show that for systems in which the discharge variations are large and the fluid inertia is significant the system behaviors highly nonlinear.
- 5 -For the systems which have little fluid inertia the self-excited motion is more nearly simple harmonic and a much simpler analysis may be applicable.

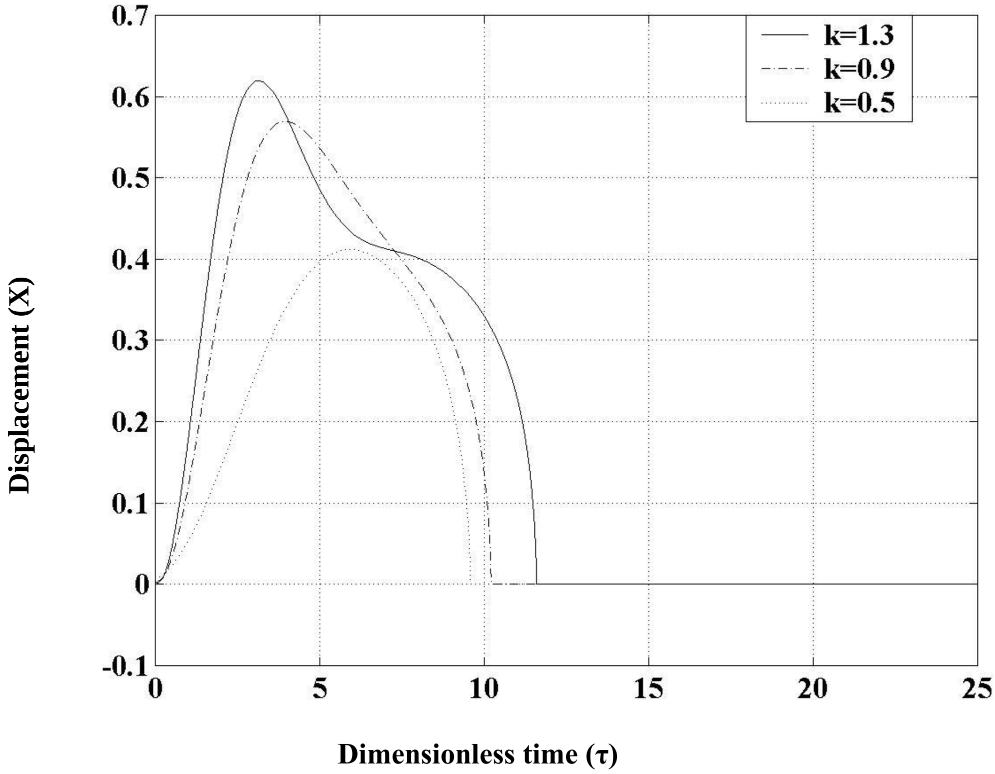


Fig.(4) Effect of stiffness variation on valve displacement,(Δp=42.6).

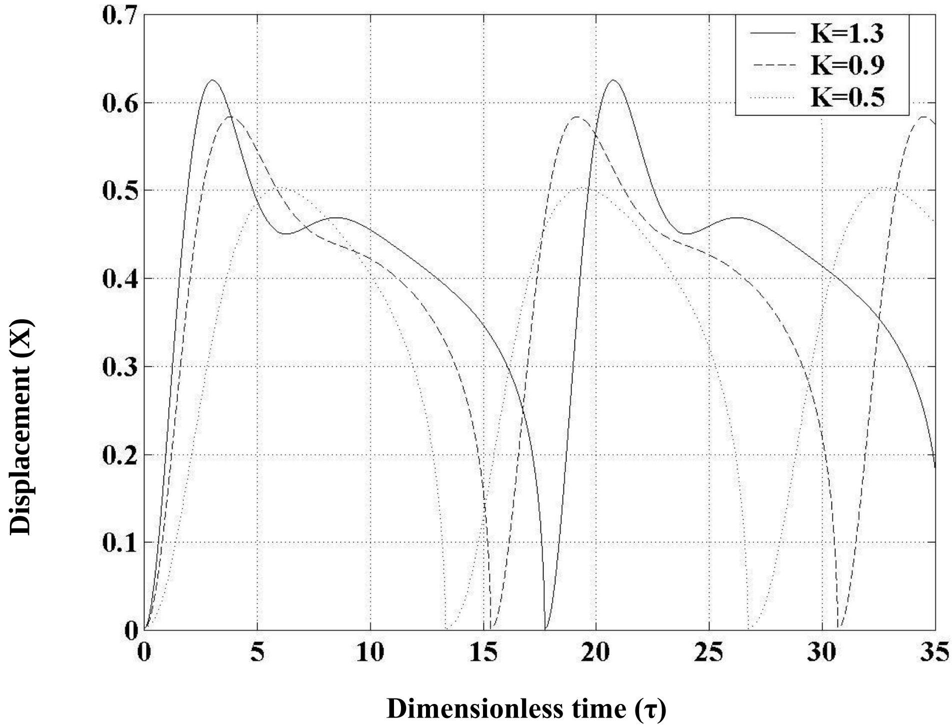


Fig.(5) Effect of stiffness variation on valve displacement at (Δp=26.7).

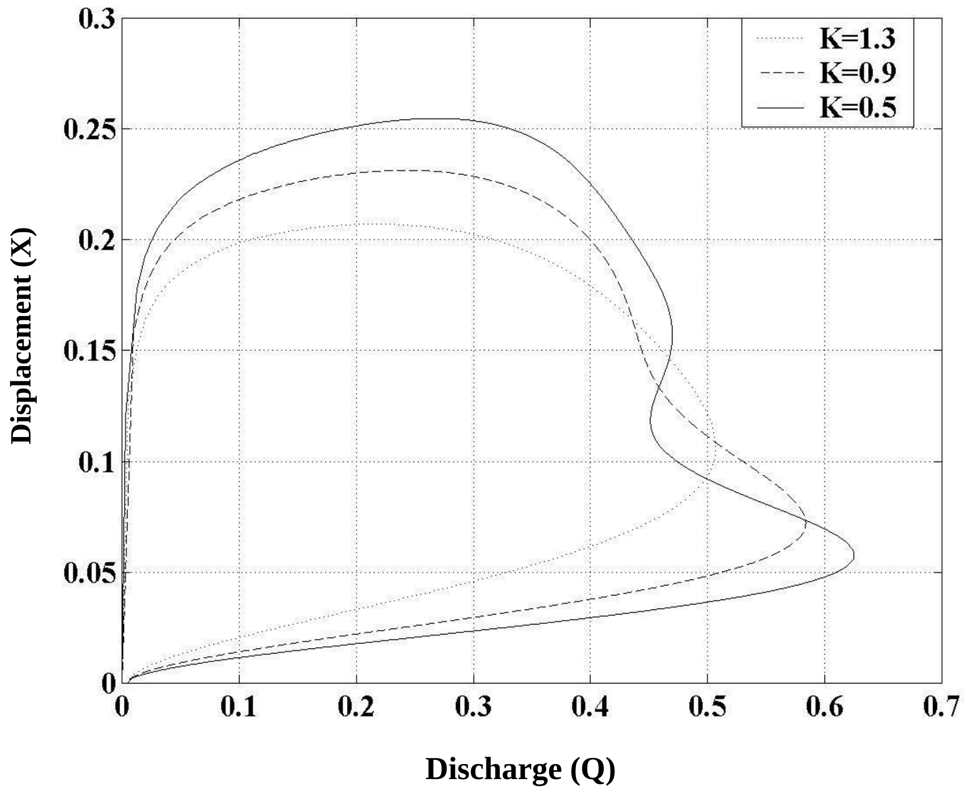


**Fig.(6) Effect of stiffness on valve dynamic discharge at (Δp=26.7).**

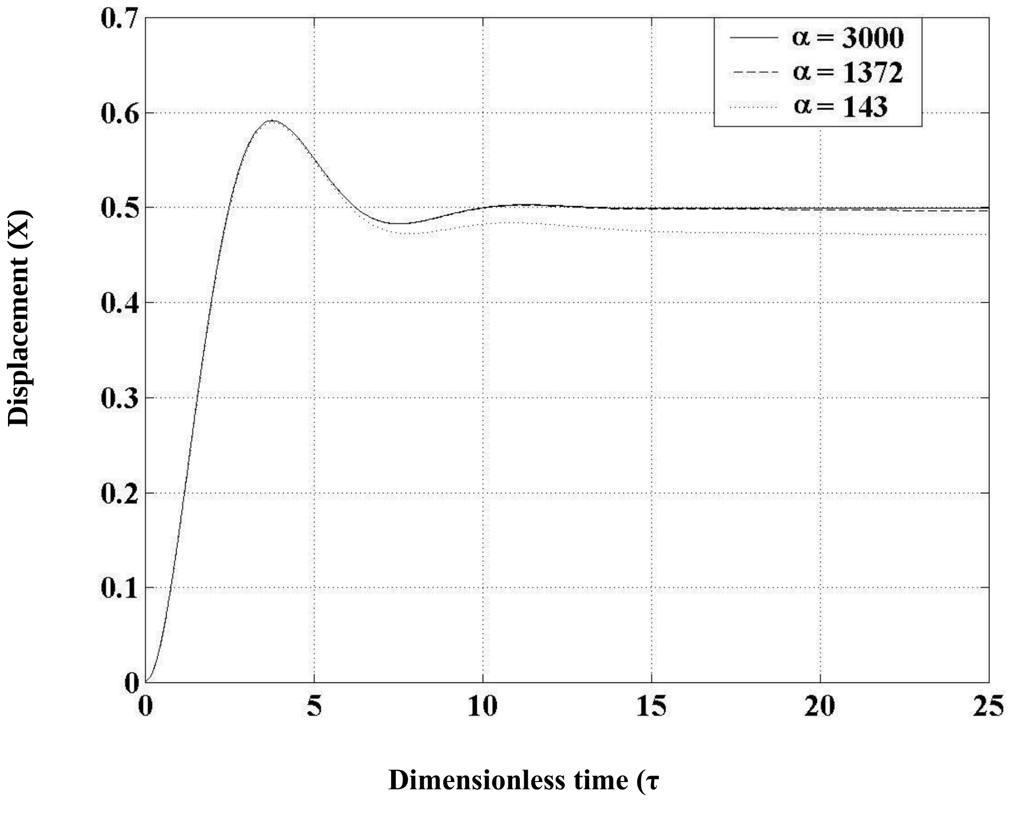


**Fig.(7) Effect of inertia factor variation on valve displacement at (Δp=1.8).**

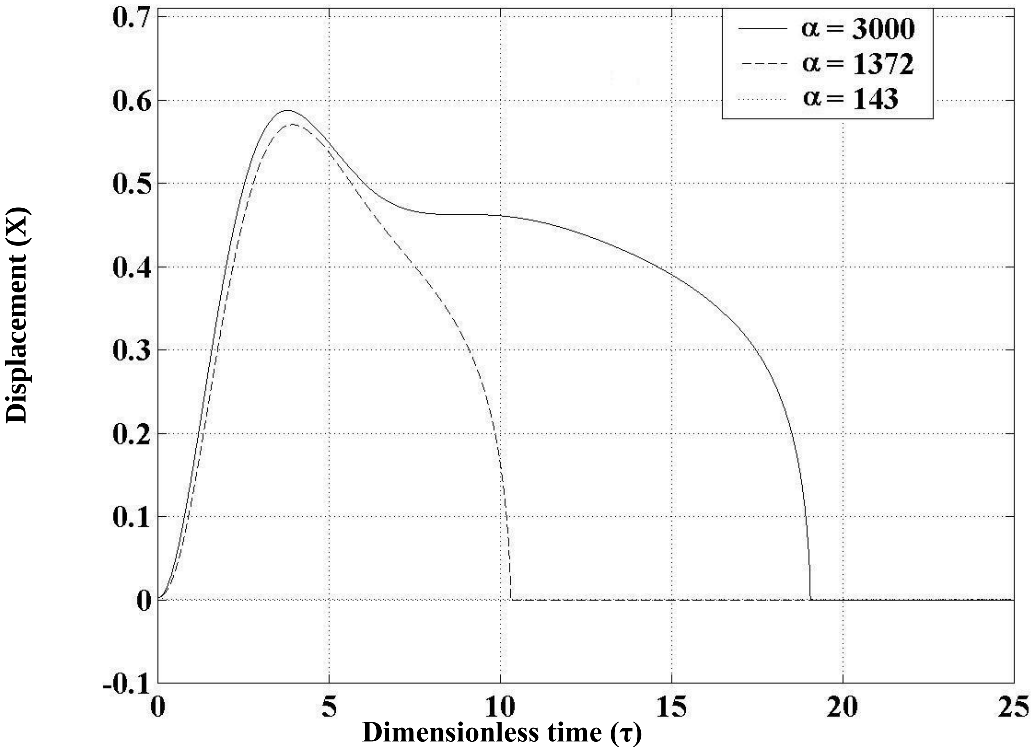


**Fig.(8) Effect of inertia factor variation on valve displacement at (Δp=42.6).**

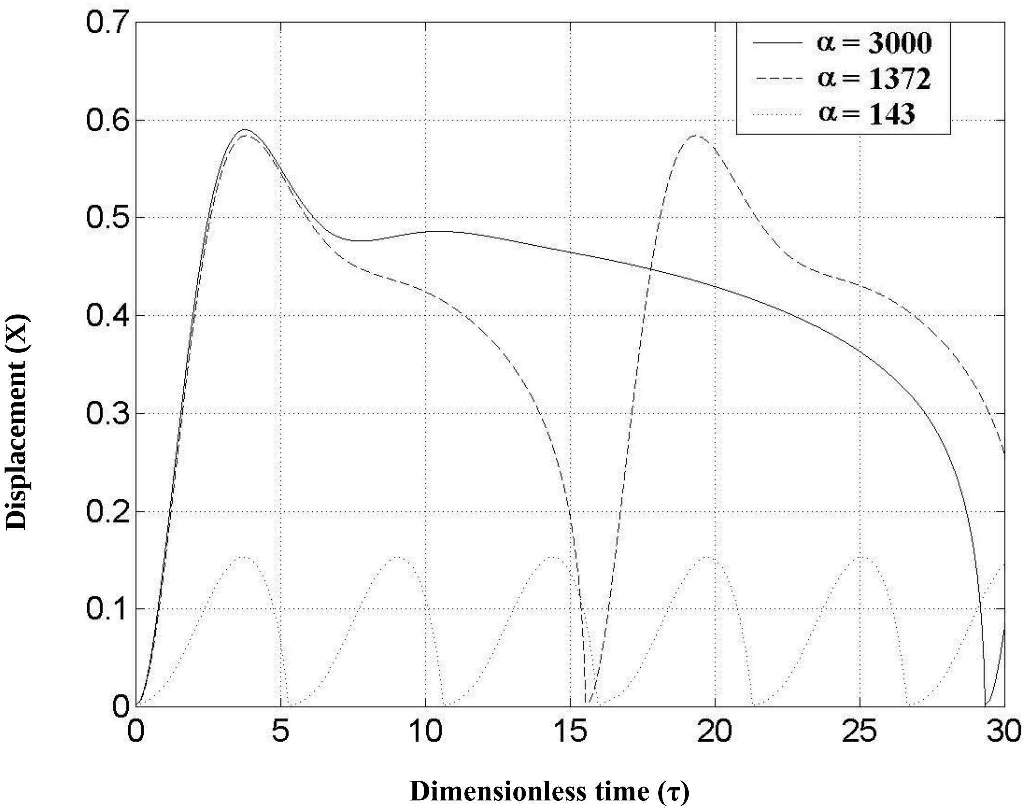


**Fig.(9) Effect of inertia factor variation on valve displacement at (Δp=26.7).**

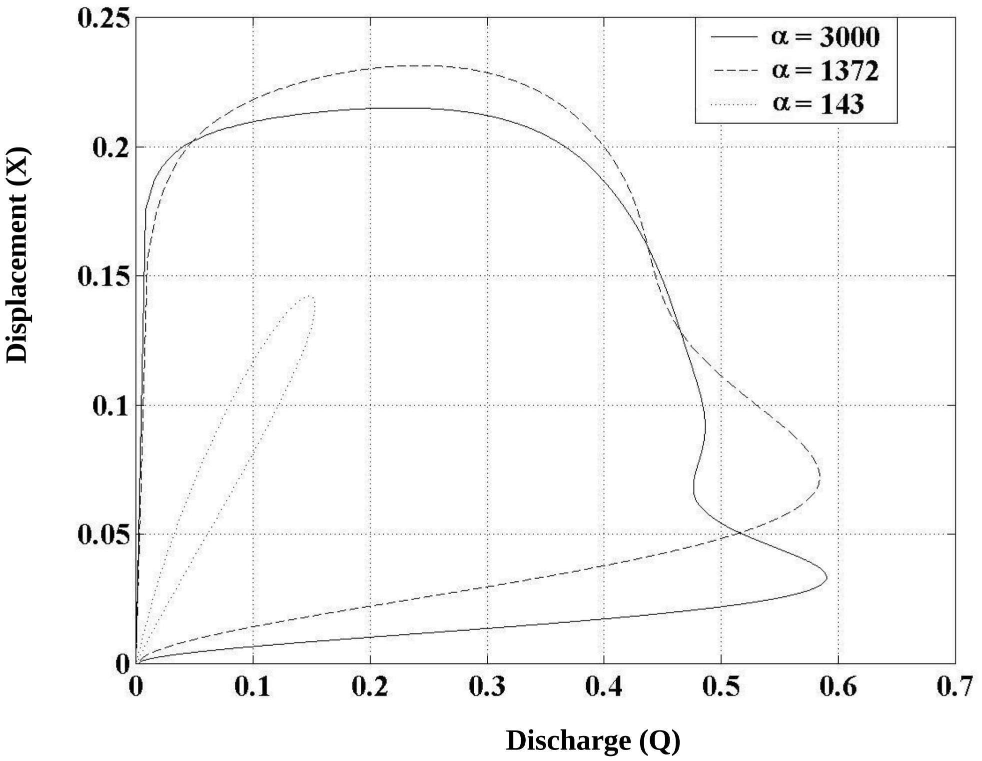


**Fig.(10) Effect of inertia factor on valve dynamic discharge at ($\Delta$p=26.7).**

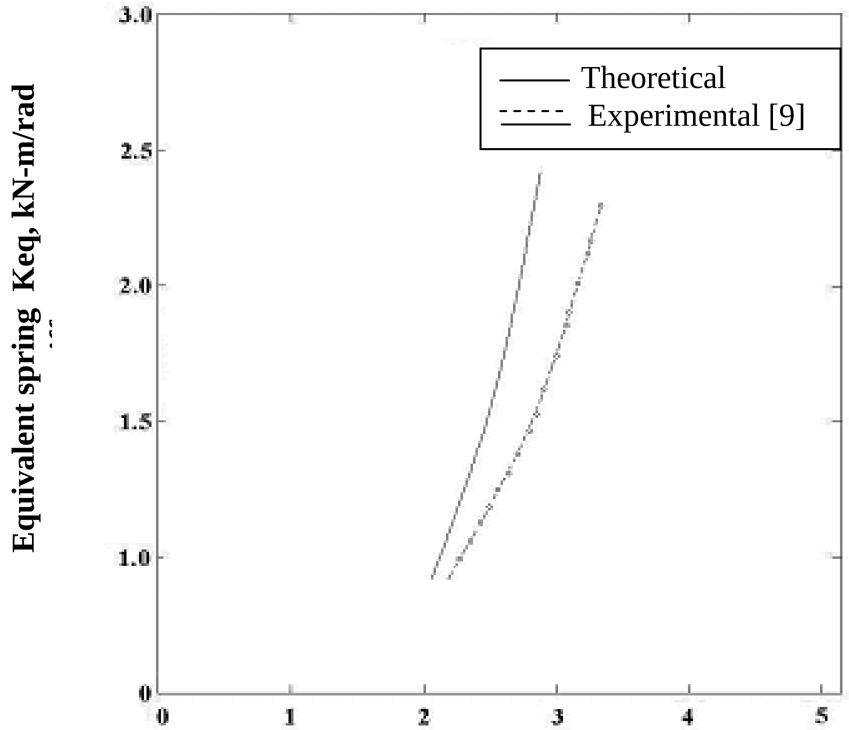


(a) Frequency ratio ($\omega/\omega_n$)

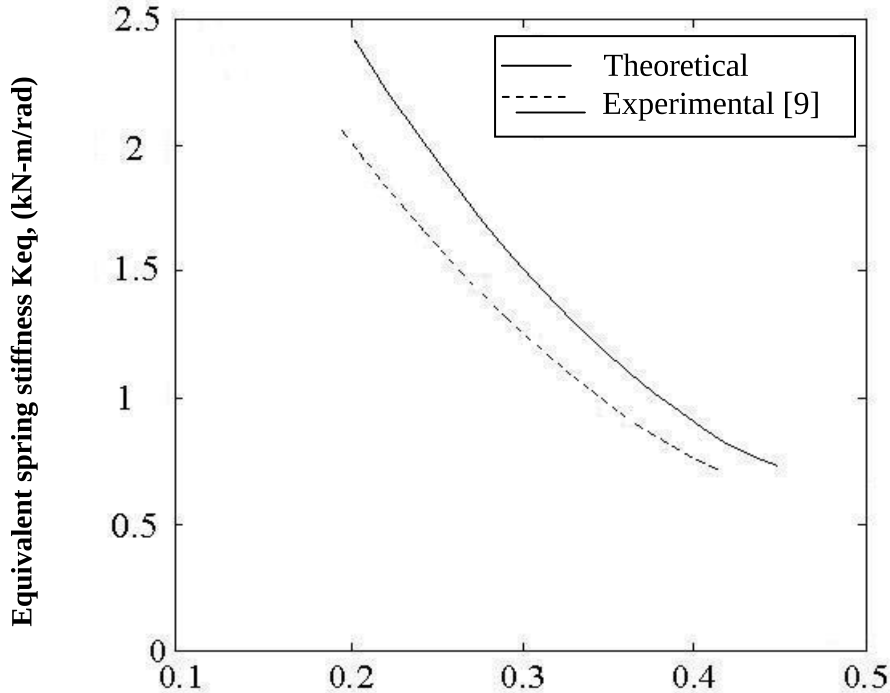


(b) Amplitude of oscillation ( Deg )

**Fig.(11). Comparison between theoretical and experimental results for a swing check valve.**

## REFERENCES


- J. W. Hutchison “ISA Handbook of Control Valves” Second Edition U.S.A, 1976.
- T. Siikonen “Computational Method for the Analysis of the Valve Transients” Journal of the Pressure Vessel Technology. August 1983. Vol. 105, pp. 227-233.
- Renold S. Kone and Soung M. Cho “Hydraulic Performance of Titling-Desk Check Valves” Journal of the Hydraulics Division, Proceedings of the American society of Civil Engineering, Vol. 102, No.hy1, January, 1976. pp 57-71.
- J. Kubie “Performance and Design of Plug-Type Check Valves” Engineering Sciences Division 1982 Vo. 196 pp. 47-56.
- D.S. Weaver and F. A. Dubi, “Flow Induced Vibrations of a Hydraulic Valve and Their Elimination”, ASME J .of Fluids Engineering, Vol 100 1978, pp 239-145.
- D.S. Weaver and S. Ziada “A Theoretical Model for Self-Excited Vibrations in Hydraulic Gates, Valves and Seals” Transactions of the ASME. May 1980. Vol.102, pp 146-151.
- Weaver, D.S., Ziada, “Flow Visualization Studies of Check Valve Vibrations” Proc. 4th Biennial Symposium on Turbulence in Liquids, Science Press, Princeton, N.J., 1975, PP.201-208.
- Joun A. Robenson and Clayton T. Crowe “Engineering Fluid Mechanics” Fourth edition U.S.A, 1990.
- J. W. Daily “Resistance Coefficient for Accelerated and Decelerated Flows through Small Tubes and Orifice”. Transaction of the ASME, Vol. 78, pp 1071-1077.
- D.McCloy “Effects of Fluid Inertia and Compressibility on the Performance of Valves and Flow Meters Operating under Unsteady Conditions”. Mechanical engineering science, Vol. 8, No.7, pp 52-61.

**APPENDIX (A)**

In addition, for most flow control device operating at small opening, the flow area is linearly related to the valve displacement, thus:

$$Ao = Wx \tag{A.1}$$

Where:

W: area of the valve and x is valve displacement.

Consequently, the following dimensionless parameters are defined by:

$$
\begin{aligned}
&\text{Damping} && \zeta = \frac{c}{2m\omega} \\
&\text{Frequency} && \omega^2 = \frac{k_r}{m} \\
&\text{Displacement} && X = \frac{x}{d} \\
&\text{Zero load opening} && X_o = \frac{x_o}{d} \\
&\text{Stiffness} && K = \frac{k}{k_r} \\
&\text{Time} && \tau = \omega t \\
&\text{Down stream pipe area} && \eta = \frac{A_4}{Wd} \qquad\qquad (A.2) \\
&\text{Upstream pipe area} && \theta = \frac{A_2}{A_4} \\
&\text{Over all pressure difference} && \Delta P = \frac{2\Delta p}{\rho(\omega\lambda d)^2} \\
&\text{Discharge} && Q = \frac{q}{A_4(\omega d\lambda)} \\
&\text{Inertia factor of pipe} && \alpha = \frac{2L_{eq}}{\lambda d} \\
&\text{Inertia factor of the jet} && \alpha_o = \frac{2L_o}{\lambda d} \\
&\text{Mass ratio} && \mu = \frac{\lambda^3 s \rho d}{m}
\end{aligned}
$$

The dynamic discharge equation (23) is given in terms of dimensionless parameters and displacement, by substituting Eqs. (A.1) and (A.2) thus:

$$q=\frac{C_d WXd}{\sqrt{1-\left(\frac{C_c WXd}{A_2}\right)^2}}\sqrt{\begin{matrix}\frac{2(P_1-P_5)}{\rho}-\frac{1}{A_4^2}\left(\psi+\frac{1}{\theta^2}-\frac{A_4^2}{(C_c WXd)^2}\right)q^2\\-\frac{2\omega}{A_4}\left(L_{eq}+\frac{A_4 L_o}{(C_c WXd)}\right)\frac{dq}{d\tau}\end{matrix}} \qquad \text{(A.3)}$$

Multiplying and dividing Eq.(A.3) by (λωd), then:

$$q=\frac{C_d WXd}{\sqrt{1-\left(\frac{C_c WXd}{A_2}\right)^2}}\sqrt{\frac{(\lambda\omega d)^2}{(\lambda\omega d)^2}\left(\begin{matrix}\frac{2(P_1-P_5)}{\rho}-\frac{1}{A_4^2}\left(\psi+\frac{1}{\theta^2}-\frac{A_4^2}{(C_c WXd)^2}\right)q^2\\-\frac{2\omega}{A_4}\left(L_{eq}+\frac{A_4 L_o}{(C_c WXd)}\right)\frac{dq}{d\tau}\end{matrix}\right)} \qquad \text{(A.4)}$$

Or

$$q=\frac{C_d WXd}{\sqrt{1-\left(\frac{C_c WXd}{A_2}\right)^2}}\sqrt{(\lambda\omega d)^2\left(\begin{matrix}\frac{2(P_1-P_5)}{\rho(\lambda\omega d)^2}\frac{1}{A_4^2}\left(\psi+\frac{1}{\theta^2}-\frac{A_4^2}{(C_c WXd)^2}\right)\frac{q^2}{(\lambda\omega d)^2}\\-\frac{2}{A_4\lambda^2\omega d^2}\left(L_{eq}+\frac{A_4 L_o}{(C_c WXd)}\right)\frac{dq}{d\tau}\end{matrix}\right)} \qquad \text{(A.5)}$$

Substituting Eq.(A.2), in Eq.(A.5), and dividing by (A4ωπ),then:

$$Q=\frac{C_d X}{\left[\eta^2-\left(\frac{C_c X}{\theta}\right)^2\right]^{\frac{1}{2}}}\left[\begin{matrix}\Delta P-\left(\psi+\frac{1}{\theta^2}-\frac{\eta^2}{C_c^2 X^2}\right)Q^2\\-\left(\alpha+\frac{\eta\alpha_o}{(C_c X)}\right)\frac{dQ}{d\tau}\end{matrix}\right]^{\frac{1}{2}} \qquad \text{(A.6)}$$

In order to obtain the valve equation of motion (displacement) in terms of dimensionless parameter using Eqs. (A.2) and (A.6) then Eq. (22) becomes:-

$$\frac{d^2X}{d\tau^2}+2\zeta\frac{dX}{d\tau}+K(X-X_o)+\frac{1}{2}\mu\left[\begin{matrix}\Delta P-\left(\psi+\frac{1}{\theta^2}-\frac{\eta^2}{C_c^2 X^2}\right)Q^2\\-\left(\alpha+\frac{\eta\alpha_o}{C_c X}\right)\frac{dQ}{d\tau}\end{matrix}\right]=0 \qquad \text{(A.7)}$$

Or

$$\frac{d^2X}{d\tau^2}+2\zeta\frac{dX}{d\tau}+K(X-X_o)+\frac{1}{2}\mu\Delta P^*=0 \qquad \text{(A.8)}$$

Where ΔP* is given by

$$\Delta P^* = \left[ \Delta P - \left( \psi + \frac{1}{\theta^2} - \frac{\eta^2}{C_c^2 X^2} \right) Q^2 - \alpha \frac{dQ}{d\tau} \right] \qquad \text{(A.9)}$$

## APPENDIX ( B)

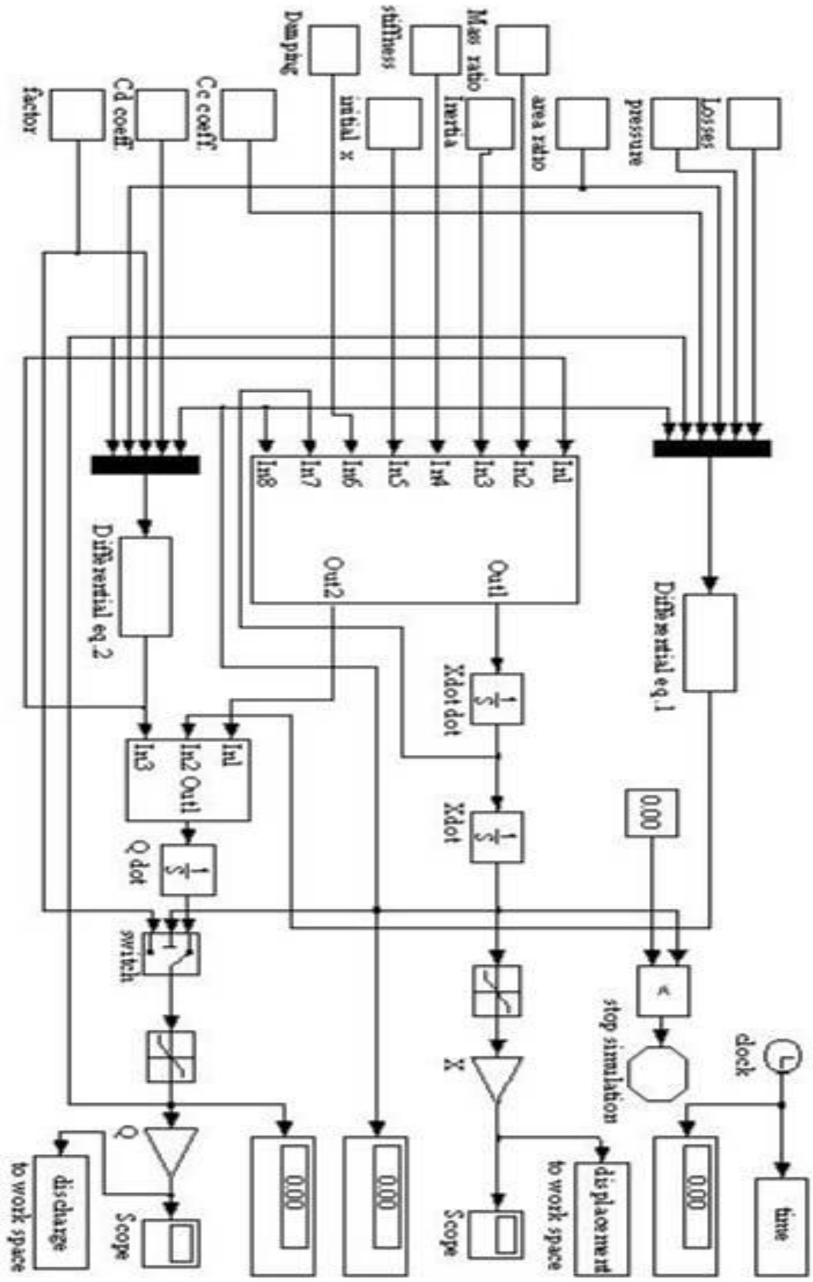


**Fig.(B.1). Flow chart of computer simulation program.**

# SEPARATION OF OIL FROM O/W EMULSION BY ELECTROFLOTATION TECHNIQUE

Ahmed A.Mohammed,Ali Jassim Mohammed Al-Gurany
Environmental Engineering Department, College of Engineering, University of Baghdad,

**ABSRACT**

Dilute emulsified oil in water (50-500 ppm) was removed by electrocoagulatin and electroflotation process. Effects of various parameters such as current density, initial pH, sodium chloride concentration, different electrodes material, gap, temperature, electrodes surface area, and treatment time on the removal efficiency were studied in batch and continuous mode.It was found that the higher removal efficiency (99%) achieved at pH of 7.5 for Al/Al electrodes while for iron electrodes at pH 8 in the batch mode.

The removal efficiency increased and the treatment time decreased with increasing the current density and decreasing the gap distance between electrodes.

The removal efficiency was (99%) at 10 min for Al/Al electrodes, (98.6%) at 12 min for Al/St.St. electrodes, and (97.4%) at 12 min for Fe/St.St. electrodes.

The present results showed that the best temperature was 60ºC .The best concentration of sodium chloride was found to be (400 ppm) when the oil concentration was (500 ppm). Also it was found that a vertical Al/Al electrode was the best type with an electrical energy consuming (3.36 $kWh/m^3$).

In the continuous experiments, the removal efficiency enhanced with increasing flow rate. A multiple linear regression model was used in order to relate experimental data to a statistical model with a correlation coefficient of (0.909) and variance (0.827).

**KEYWORDS: emulsion, electroflotation, separation**

**الخلاصة**

. الزيت المستحلب في الماء (50-500 ppm) فصل بطريقة التطويف الكهربائي . تم دراسة تأثير عدة متغيرات مثل كثافة التيار,الدالة الحامضية ,تركيز كلوريد الصوديوم,نوعية الاقطاب ,درجة الحرارة,المساحة السطحية ,المسافة بين الاقطاب ,وزمن المعالجة على كفاءة ازلة الزيت وبأسلوب الوجبة. ومن التجارب وجد ان اعلى كفاءة (99%) وبدالة حامضية (pH=7.5) لاقطاب Al/Al اما بالنسبة لاقطاب Fe/St.St عندما تكون الدالة الحامضية هي (pH=8).

وقد تبين ان كفاءة الازالة تزداد وزمن المعاجة يقل بزيادة كثافة التيار الكهربائي في حين عند زيادة المسافة بين الاقطاب يؤدي الى نقصان كفاءة الازلة مع زيادة زمن المعالجة. ومن خلال النتائج المختبرية الكفاءة المستحصلة (99%) بزمن (10 min) لاقطاب Al/Al وكفاءة (98.6%) وزمن (12 min) بالنسبة لاقطاب Al/St.St. واما اقطاب Fe/St.St. تكون الكفاءة (97.4%) وزمن (12 min).

أفضل درجة حرارة هي (60 ºC) وأفضل تركيز لملح كلوريد الصوديوم هو(400 ppm) .ونستنتج من التجارب المختبرية ان اقطاب Al/Al العمودية هي الافضل باسنهلاك للطاقة الكهربائية بمقدار ($3.36\ kWh/m^3$).
وجد ان كفاءة الازالة تتحسن مع زيادة الجريان.من خلال احتساب الانحدار اللاخطي المتعدد للنتائج المختبرية تم ايجاد معادلة تربط كافة المتغيرات المدروسة وبمعامل تصحيح (90.9%) وتباين (82.7%).

## INTRODUCTION

Oily wastewater has remained problematic in various industries four decades. The major industrial sources of oily wastewater include petroleum refining, metals manufacturing, and food processing. This wastewater contains lubricating oil, grinding oils, cutting oils, and coolant oil–water emulsions with a possible soluble and emulsified oil content that varies from 100 to 5000 mg/l (Yang, 2006).

Types of oil-water mixture may be classified as oil and grease present as free oil, dispersed oil, emulsified oil or dissolved oil. Free oil is usually characterized by an oil-water mixture with droplets greater than or equal to 150 microns in size while a dispersed oil mixture has a droplet size range between 20 and 150 microns, and an emulsified oil mixture have droplet sizes smaller than 20 microns. Wastewater with an oil-water mixture where the oil is said to be soluble is a liquid where oil is not present in the form of droplets (the oil particle size would be typically less than 5 microns) (Rhee et al., 1985).

## SOURCES OF OIL AND GREASE IN OILY WASTEWATER

Petroleum refining and oil re-refining, used oil and re-refining operation, from fractions oil and primary distillation through final treatment, contains various oils and organosulfur compounds in their wastewaters. Crude oil producing facilities emulsified of wastewater from oil field operations may contain drilling muds, brine, free and emulsified oil, tank-bottom sludge and natural gas. Many oil-bearing beds have brine-bearing formations. Oil and gas must then be separated from the wastewater; this wastewater is typically a brine waste containing some oil contamination and must be disposed (Rhee et al., 1985).

## CONVENTIONAL METHODS OF TREATING OILY WASTEWATER

The treatment of oily wastewater has been addressed by different techniques; the most commonly used are the physical methods include heating, centrifugation, precoat filtration, ultrafiltration, and membrane process. ultrafiltration and membrane processes have been actively pursued (Um et al., 2001; Gryta et al., 2001).

The chemical destabilization (conventional coagulation) is used directed toward the destabilization of the dispersed oil droplets or the destruction of emulsifying agents present in a first stage followed by the removal of the separated oil. This treatment accomplished by addition of hydrolyzing metal salts ($Fe^{3+}$ or $Al^{3+}$) as coagulant reagents, which are still the most widely used reagents for demulsification. The process usually consists of rapid mixing of the coagulant with the wastewater followed by flocculation and flotation or settling.

Currently the treatment of oily wastewater applies a primary treatment to separate the floatable oils from the water and emulsified oils. A secondary treatment phase is then required to break the oil–water emulsion and separate the remaining oil from the water. Primary treatment takes advantage of the differences in the specific gravities of the oils and grease and the water. Then subsequently skimmed oils and grease floated from the wastewater surface.

Dissolved-air flotation is another process for the supplemental treatment of oil-water separator effluents for reducing oil and suspended solids to low levels. Its success depends on the use of very fine air bubbles to increase the rate of suspended particles so they can be floated to the surface for removal. It is, in effect, the opposite of sedimentation. Dissolved-air flotation can be used alone or in combination with flocculation (flocculation-flotation) (Canizares et al., 2007).

## ELECTROCHEMICAL TECHNOLOGIES FOR WASTEWATER TREATMENT

Electrochemical technologies have recuperated their importance in the world during the past two decades. There are different companies supplying facilities for metal recoveries, treating drinking water or process water, treating various wastewaters resulting from tannery, electroplating, dairy, textile processing, oil and oil-in-water emulsion, etc. At the present time, electrochemical technologies have reached such a state that they are not only comparable with other technologies in terms of cost, but also more efficient and compact.

The development of design and application of electrochemical technologies in water and wastewater treatment have been focused particularly to some technologies such as electroflotation, electrocoagulation, and electrooxidation.

This new rise of electrochemical has also been due to the relative reduction in the operation and investment costs. The electrochemical has the potential to be competitive with respect to both economical and environmental criteria for treatment of wastewater and other related water management issues (Saur et al., 1996; Hosny, 1992; Mollah et al., 2001; Chen et al., 2002).

## EXPERIMENTAL WORK AND PROCEDURE

This paper contains description of apparatus, materials and analysis measurement methods of oil emulsion which were used in the test of experimental work.

The experimental work was performed in two parts (batchwise and continuous) for the treatment of emulsified oil. The effect of oil concentration, electrode type, gape, pH, NaCl concentration, applied potential, surface area and treatment time were studied.

## EQUIPMENTS AND APPARATUS

The following measuring devices were used in experiments

- Digital pH meter, model orion 3star, thermo electron, USA.
- Combo meter, model combo (Conductivity/TDS/Temp.), HM Digital, Korea, with a range (0-9990 µS/cm), Temp. =0-80 ºC.
- Power supply, Iraqi model VS/CS 25A, 35 V, Iraq.
- Blender mixer, AL-Arabi blender MX-5200, Egypt.
- Ultraviolet spectrophotometer (model GENESYS$^{TM}$ 10 spectrophotometers; thermo), USA.
- Dosing pump ,H.R. flow inducer ,Watson –Marlow limited ,England
- Electrical balance, Sartorius, digital indicator with capacity (210gm).
- Beaker, pipettes of various size.
- Electrical heater, power= 100 w, china.

## O/W EMULSIONS PREPARATION

The oily phase of the emulsion is prepared from using a common lubricant oil (Babel-40 provided by AL-Doura refinery, Iraq), and an emulsifying agent (R.T.K. provided by BRB CO., UK), 0.5 gm oil and 0.12 gm emulsifying agent mixed together in separate beakers, to prepared 500 ppm of emulsified oil then stirred until a homogenous liquid was obtained. The salt content of the emulsion was adjusted by adding a suitable amount of sodium chloride solution which prepared separately by dissolving 0.2 gm of NaCl in 1 liter of distilled water. Conductivity of Sodium chloride (NaCl) solution was measured by combo meter to achieve a conductivity of (up to 452 µS/cm). Then the contents of the two beakers were mixed and stirred by using blender mixer to obtain the oil emulsion desired.

## BATCH EXPERIMENTS

The experiments were carried out in batch laboratory electroflotation cell (Fig.1-a) a glass cell of internal size 12 cm × 12 cm × 30 cm (width × length ×height) with an effective volume of 4L. It is provided with two electrodes: aluminum or iron as anode and stainless steel as cathode. In the electroflotation cell configuration, the monopolar aluminum or iron plate electrodes were used. The spacing between electrodes varies from 1-4 cm. whereas, the oil emulsion batch 3L for each experiment we used. Electrodes were placed in the oil emulsion and connected to terminals of a DC Power Supply. The voltage and current flowing through the cell were measured with a multimeter. The emulsion was maintained at the desired temperature by portable immersed heater. Samples were taken from the cell using a pipette tube to avoid passivation of the electrodes, the electrochemical cell and electrodes were entirely cleaned after each experiment with detergent and ethanol. All experiments were carried out at room temperature near 30ºC. pH of the emulsion was adjusted at the desired value by adding 1M (NaOH or $H_2SO_4$) . pH meter was used to measure the pH value. While conductivity of emulsion was measure using Combo meter. The same procedure applied in batch mode was applied in continuous experiments.

## CONTINUOUS EXPERIMENTS

In continuous experiments, the electroflotation cells with a total volume of 3.5 liters are shown in (Fig.1-b). It is divided into two compartments. The first size of compartment is (9cm×12 cm × 30 cm) which provided with two electrodes. This compartment receives the influent from a hold conical flask by a dosing pump. The size second compartment is (9 cm× 12 cm × 9 cm) which received the effluent and undergoes to settling of the suspended solids .The bubbles formed at electrodes and effluent are in co-current movement. Electrodes were connected to terminals of a DC Power Supply. Multimeter was used to measure the current passing through the circuit and the applied potential, respectively. The pH values in the cell were measured using a pH meter and adjusting pH of emulsion by 1M (NaOH or H2SO4).while, the conductivity of emulsion was measured using Combo meter.

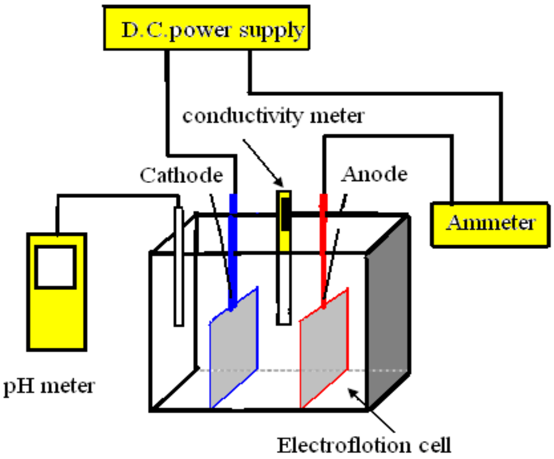


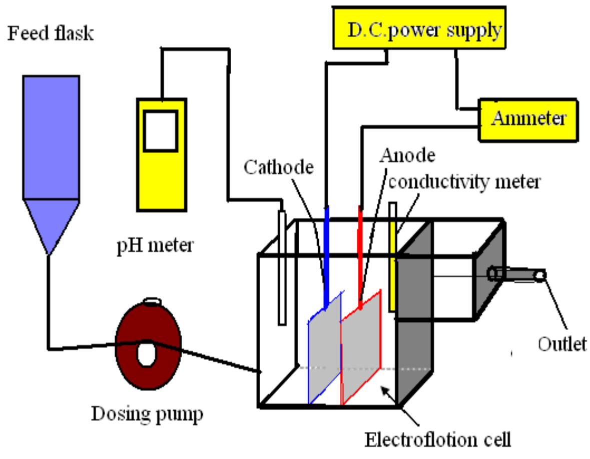


**(a)** **(b)**

**Fig.(1): Schematic diagram of batch and continuous experimental.**

**(a) batch mode, (b) continuous mode**

## RESULTS AND DISCUSSION

This research is mainly focused on the electrocoagulatin treatment of emulsified oil. The effects of: initial pH, initial oil concentration, temperature, NaCl concentration, electrodes type, surface area, applied potential and treatment time value were studied to evaluate the EC progress. The oil removal efficiency was estimated from experimental tests for all electrodes types. Two parts were used during electroflotation treatment:
(i) Batch experiments.
(ii) Continuous experiments.

## BATCH EXPERIMENTS

**- Effect of applied potential**

The variation of removal efficiency and energy consumption with time for different applied potentials are shown in figs.(2 and 3) from these figures it can be seen that both the energy consumption and the removal efficiency increase with increasing applied potential (5V- 35V). This can be explained by the fact that with an increased in the current density, the aluminum production on both anode and cathode increased resulted in an increased in the floc production in the solution .in addition bubbles density increases and their size decreases resulting in both greater upward momentum flux and increased mixing. Therefore, the highest removal efficiency 98.2% with lowest electrolysis time (28 min) at applied potential 35V by using horizontal (A/Al) electrodes was achieved.

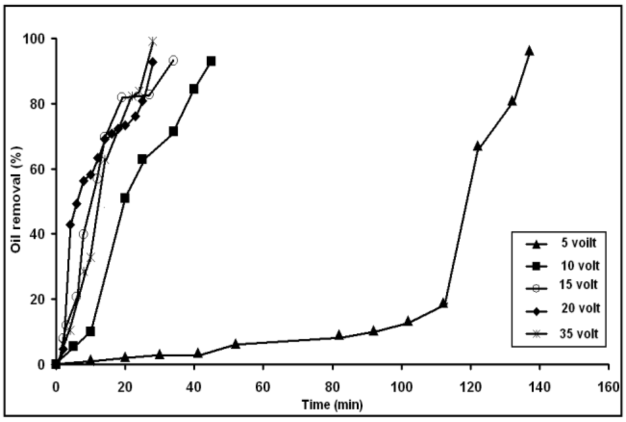


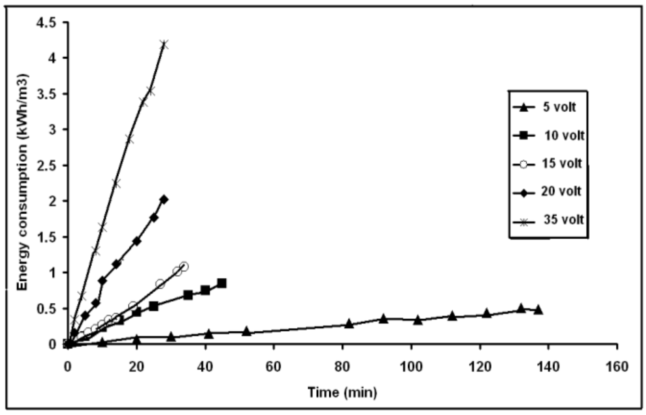


Fig.(2)Variation of oil removal efficiency with different applied potential (Horizontal Al/Al electrodes, [oil] =500 ppm, [NaCl] =200 ppm, gap=1 cm,30ºC, AAA=182.47cm$^2$ ).

Fig.(3)Variation of energy consumption with different applied potential (Horizontal Al/A electrodes, [oil] =500 ppm, [NaCl] =200 ppm, gap=1 cm,30ºC, AAA=182.47cm$^2$ ).

**- Effect of initial pH**

pH is an important parameter in chemical and electrochemical coagulation. The effect of pH on the removal efficiency is plotted in fig.(4). Adjusting the pH in the range (3.5-8.5) using 1M (NaOH or $H_2SO_4$) and applying 35V, this figure shows the removal efficiency as a function of treatment time at different initial oil emulsion pH values. The higher oil removal efficiency (98.2-98.3%) attained in the pH range of (3.5–8.5). The pH effect in the removal efficiency is very significant in pH 7.5 (98.2%) with electrolysis time 28 min and energy consumption of 4.19 kW/m$^3$. While for the other values of pH the time required to achieve the same removal efficiency increased in the range (46-62 min) in the acidic medium and about (40 min) at pH 8.5. With increasing the treatment time (28-62 min) the electrical energy consumption increased from (0.93 -8.19 $kWh/m^3$), this is shown in fig.(5) by plotting energy consumption against time at different initial pH. It is that increasing pH from acidic to neutral values lead to stands for the whole oil droplets/precipitate particles system. This behavior can be explained in terms of the charge reversal of the aluminum hydroxide precipitates from positive to negative, for pH values over 8. These negative charges produce repulsion forces between the oil droplets (negatively charged) and the particles of precipitate, and consequently avoid the attachment of more than one droplet to a particle of precipitate, and the subsequent coalescence of the droplets, causing therefore increase time of oil removal efficiency.

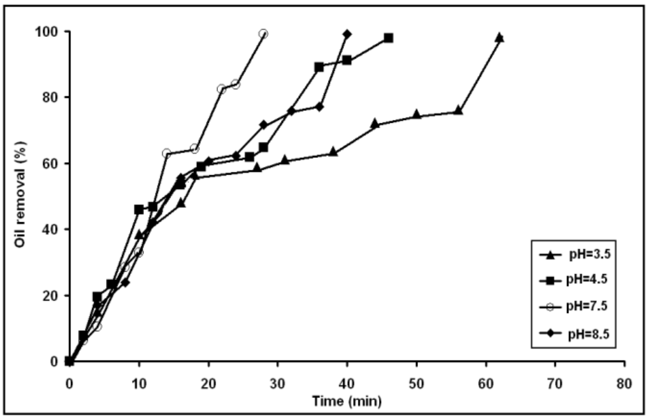


Fig.(4) Variation of oil removal efficiency with different pH (Horizontal Al/Al electrodes, 35 V, [oil] =500 ppm, [NaCl] =200 ppm, gap=1 cm ,30ºC, AAA=182.47 $cm^2$).

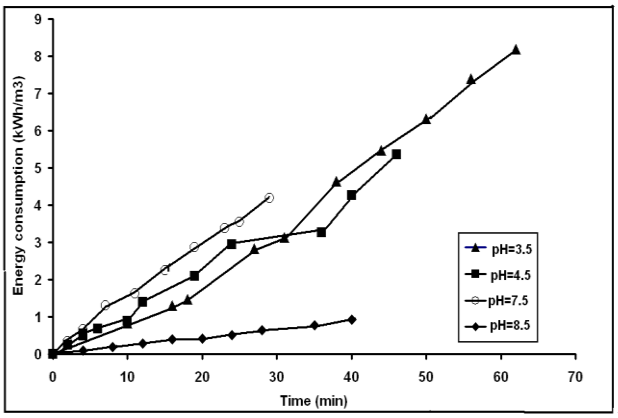


Fig.(5) Variation of energy consumption with different pH (Horizontal Al/Al electrodes, 35 V, [oil] =500 ppm, [NaCl] =200 ppm, gap=1 cm ,30ºC, AAA=182.47 $cm^2$).

**-Effect of initial oil concentration**

The removal efficiency of emulsified oil at various initial oil concentration (50-500ppm) with different electrodes direction are shown in figs.(6 and 7).In the case of horizontal (Al/Al)electrodes, figure(4.5) the time required to achieved the higher removal efficiency (98.2%) increased from (16-28 min ) with increasing initial oil concentration from (50 -500 ppm).while vertical (Al/Al) electrodes had a better removal efficiency (98.6%) achieved at time 10 min for initial concentration (300 ppm). From the two figures below it can be seen that the electrodes direction effect on time and removal efficiency.

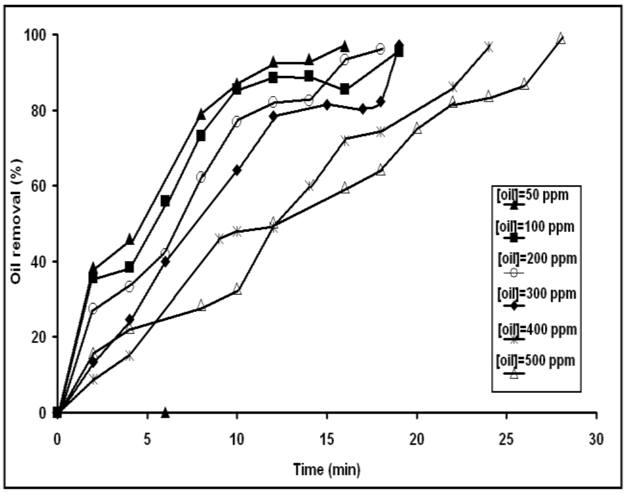


Fig.(6)Variation of oil removal efficiency with different oil concentration (horizontal Al/Al electrodes, 35V, gap=1cm, pH=7.5, 30 ºC, AAA=182.47 $cm^2$).

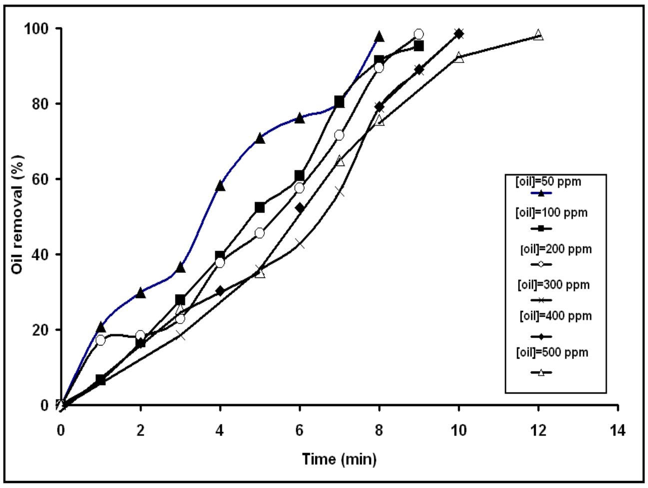


Fig.(7)Variation of oil removal efficiency with different oil concentration (horizontal Al/Al electrodes, 35V, gap=1cm, pH=7.5, 30 ºC, AAA=182.47 $cm^2$).

## -Effect of initial temperature

The effect of the electroflotation cell temperature on the oil removal efficiency is shown in fig.(8).The removal efficiency showed a tendency to increase with an increase in temperature. The higher removal efficiency (98.8%) achieved when the solution temperature 60ºC with treatment time 9 min. An increase in the temperature resulted a decrease in the oil emulsion stability due to an increase in the adsorption rate, because the Van der Waals forces and Brownian motion increase and decrease the viscosity of the continuous phase film. This would contribute to increase coalescence rate, through an increased probability of film rupture (Becher, 1966).

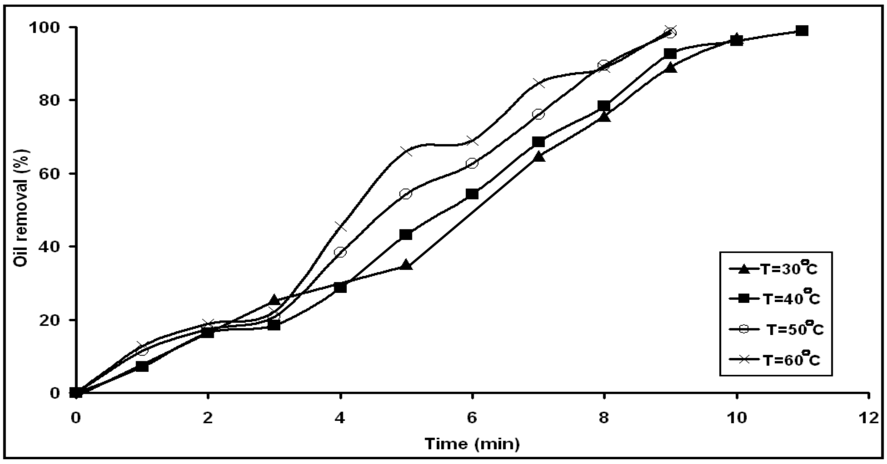


**Fig.(8) Variation of oil removal efficiency with different temperature (Horizontal Al/Al electrodes, 35V,[oil] =500 ppm, [NaCl] =200ppm, gap=1 cm, pH=7.5, AAA=182.47 $cm^2$).**

## -Effect of sodium chloride concentration

Sodium chloride concentration was varied to evaluate the impact of solution conductivity on electrocoagulation. Figure(9) shows the relationship between sodium chloride concentration and removal efficiency with time. From this figure it can be seen that increasing sodium chloride concentration (50-400 ppm) leads to an increase in the removal efficiency with decreasing in treatment time required to achieve the highest removal percent. When using 50 ppm NaCl, the maximum removal efficiency achieved (98%) at time 13 min. while increasing the NaCl concentration to 400ppm resulted in 98.9% removal efficiency at 7 min. This means that the time decreased as the solution conductivity increases.

The increase in the oil removal efficiency attributed to a change in the ionic strength due to changing conductivity of the emulsion medium. Ionic strength affects on the oil emulsion destabilizing which occurring between charged species and oil droplets during EC.

The relationship between solution conductivity and energy consumptions is plotted in fig.(10). From this figure it can be concluded that the energy consumption increases from 1.99 to 4.12 $kWh/m^3$ with increasing conductivity.

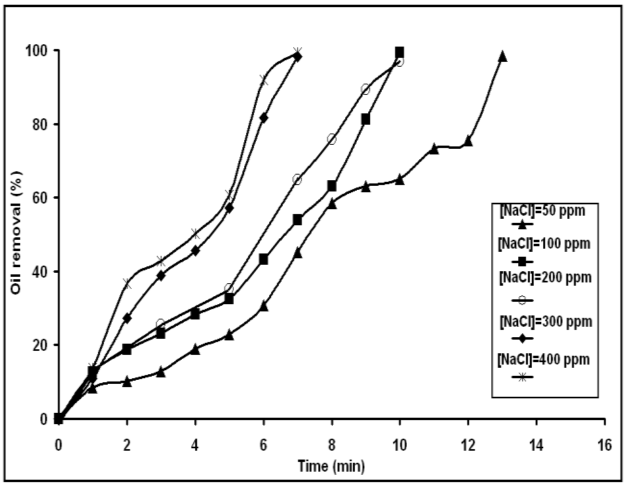


Fig.(9) Variation of oil removal efficiency with different NaCl concentration(vertical Al/Al electrodes, 35V,[oil] =500 ppm,gap=1cm, pH=7.5,60 ºC,AAA=182.47 $cm^2$).

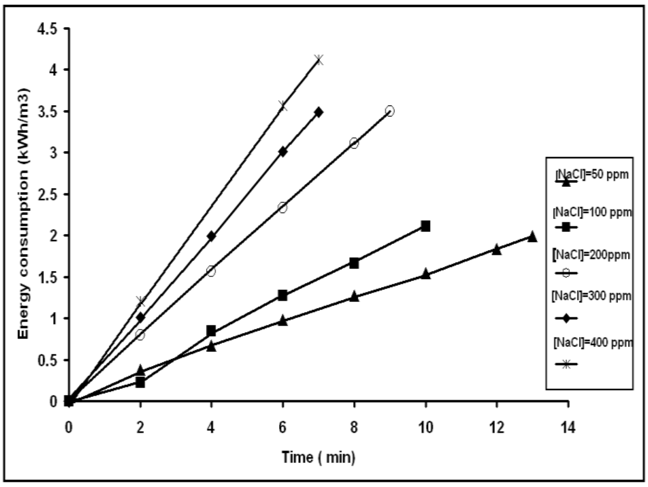


Fig.(10) Variation of energy consumption with different NaCl concentration(vertical Al/Al electrodes, 35V,[oil] =500 ppm,gap=1cm, pH=7.5,60 ºC,AAA=182.47 $cm^2$).

## -Effect of electrodes surface area with different gap

Three electrodes types with two different sizes are used to investigate the effect of electrode size and gap between electrodes on the removal efficiency. The results are shown in fig.(11 and 12) for (Al/Al) electrodes. It can be observed that increasing the active area from (182.217 -273.12 $cm^2$) enhanced the removal efficiency and reducing the treatment time required.

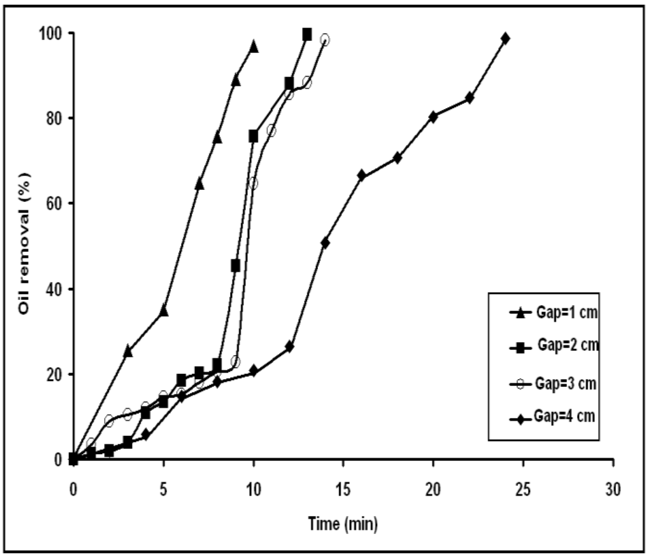


Fig.(11)Variation of oil removal efficiency with gap (Vertical Al/Al electrodes, 35V ,[oil] =500 ppm,[NaCl]=200 ppm,pH=7.5, 30ºC,AAA= 182.47 $cm^2$).

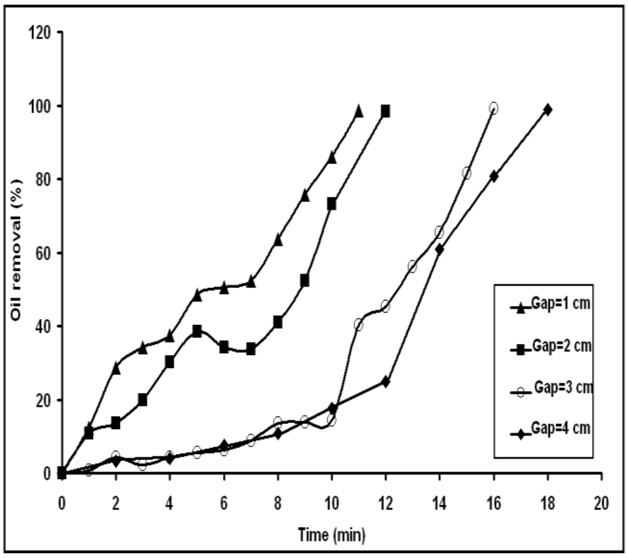


Fig.(12)Variation of oil removal efficiency with gap (Vertical Al/Al electrodes, 35V, [oil] =500 ppm,[NaCl]=200 ppm,pH=7.5, 30ºC,AAA=273.12 $cm^2$).

**-Effect of electrodes material and current density**

The influence of different electrodes type and current density on oil removal efficiency are shown in fig(13). The optimum electrode type is the vertical (Al/Al) electrode which achieved 99% removal efficiency in 10 minutes and current density (6.33 $mA/cm^2$).

This is ascribed to the fact that at Al/Al electrodes under higher applied potential the amount of aluminum oxidized increased, resulting in a greater amount aluminum hydroxide. In addition, it was demonstrated that bubble density increases, and their size decreases with increasing current density for same electrodes type, resulting in a greater upwards flux and a faster removal of oil. As the current density decreased, the time needed to achieve similar efficiencies increased and the results of this research confirm this fact.

The amount of metal released with different electrodes gap is shown in fig.(14),from this figure it can be seen that the amount of metal released depend on the gap and time. Cell with Al/Al electrodes release an amount much than that in the Al/St.St..

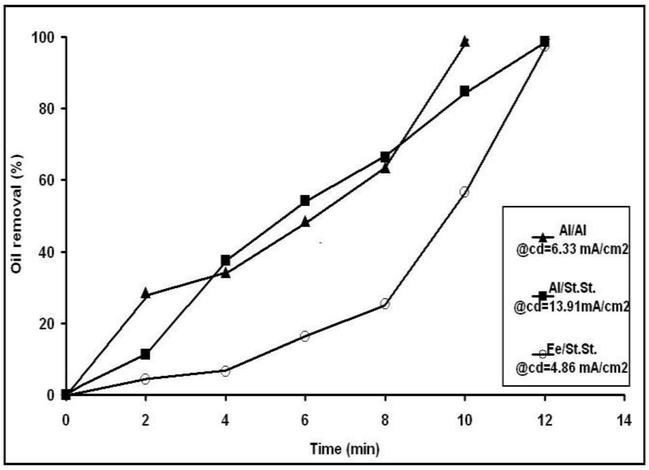


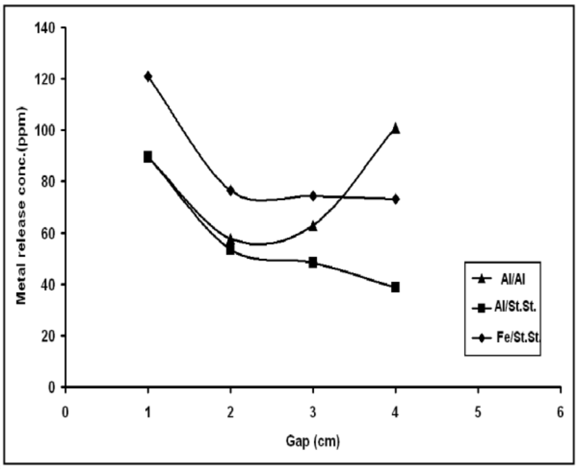


Fig.(13) Variation of oil removal efficiency with electrodes type(Vertical (Al/Al) 35V, 30 ºC, [oil] =500 ppm,gap=1cm,[NaCl]=200ppm,).

Fig.(14) Variation of oil removal efficiency with gap (Vertical (Al/Al) 35V, 30 ºC, [oil] =500 ppm,gap=1cm,[NaCl]=200ppm,).

## CONTINUOUS EXPERIMENTS

### Effect of liquid flow rate

The effect of liquid flow rate on the electrocoagulatin efficiency of emulsified oil has been investigated. The relationship between oil removal at different flow rates for (Al/Al), (Al/St.St.), and (Fe/St.St.) electrodes are plotted in fig.(15~17).from those figures it can be seen that the removal efficiency increased with increasing solution flow rate. This result could be explained by the fact that more steady convection allowed by higher flow rates are to improve the rates of transport and transfer phenomena of the various species in the electrochemical cell. In addition, higher flow velocity induce a greater number of collisions between the particle of $Al(OH)_{3(s)}$ and the destabilized oil droplets, thus improving the flocculation.

However, it is observed that the flow rate effect on the oil removal was more significant for the highest values when using (Al/Al) electrodes in (fig.15). This exhibit the effect of: (i) the anode and cathode dissolution, forming $Al^{3+}$ and allowing coagulation, (ii) the transfer phenomena by convective diffusion, and (iii) the flocculation phenomena. However, the influence of the flow rate on the oil removal was more significant at high current densities. From these figures it was found that the highest removal efficiency (99%) after 11 min electrolysis time and 10.58 mA/cm$^2$ current density is achieved by higher flow rate (0.15 l/min),while for (Al/St.St.) electrodes fig.(16) the highest removal efficiency 98.6% after 16 min electrolysis time and 5.6 mA/cm$^2$ current density is achieved at higher flow rates( 0.15 l/min),and for (Fe/St.St.) electrodes fig.(17) the highest removal efficiency 96.2 % after 26 min electrolysis time and 7.51 mA/cm$^2$ current density.

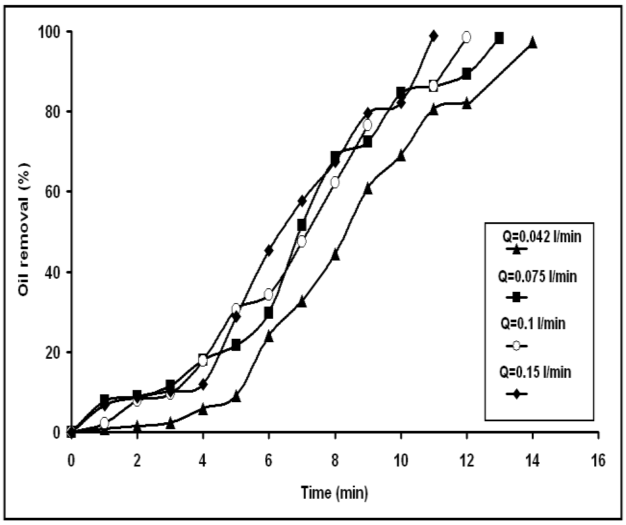


Fig.(15) Variation of oil removal efficiency different flow rate (Vertical Al/Al electrodes, 35V,[oil] =500 ppm,[NaCl]=200ppm, pH=7.5, 30 ºC, AAA=273.12 $cm^2$).

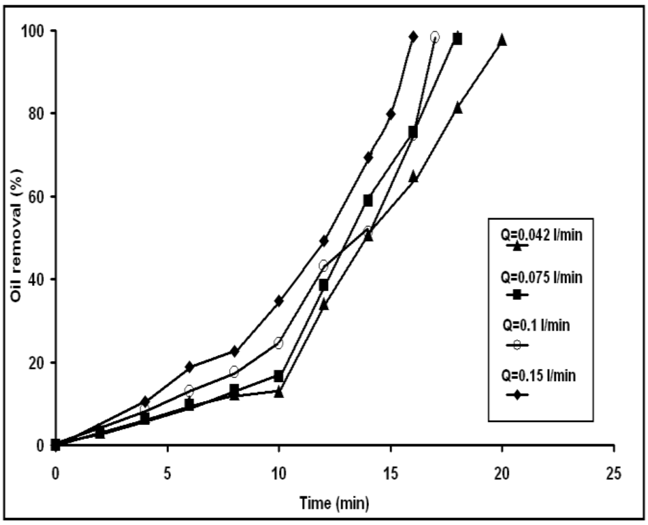


Fig.(15) Variation of oil removal efficiency with different flow rate(Vertical (Al/St.St. electrodes 35V,[oil] =500 ppm,[NaCl]=200ppm, pH=7.5, 30 ºC, AAA=273.12 $cm^2$).

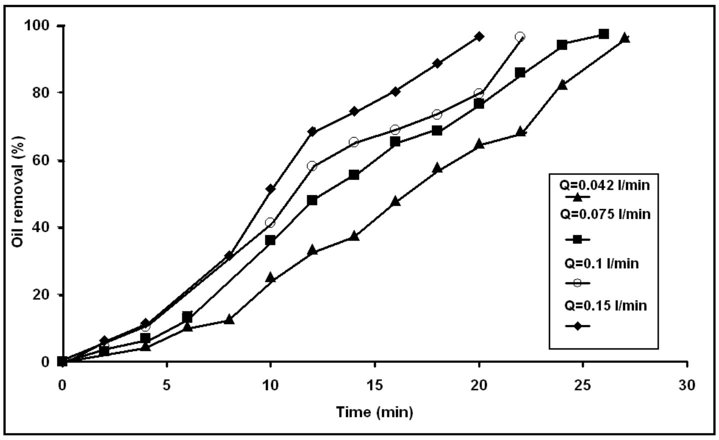


Fig.(17) Variation of oil removal efficiency with different flow rate (Vertical (Fe/St.St.) electrodes, 35V,[oil] =500 ppm,[NaCl]=200ppm, pH=8,30 ºC, AAA =271.44 $cm^2$).

## CONCLUSIONS

The demulsification of oil in water was achieved by electrocoagulatin and the results can be summarized as follows;-

- An aluminum electrode was preferable for electrical demulsification due to higher oil removal efficiency (99%) than iron electrodes which reached a maximum removal efficiency of (97.4%).
- The effects of the current density on oil removal efficiencies, for aluminum and iron electrode materials. The current densities are in favor of both removal efficiencies for both electrode materials between (4.86-6.33 $mA/cm^2$).the higher efficiencies are obtained (99%) with aluminum and (97.4%) with iron electrodes.

- It is possible to achieved (99%) removal efficiency using a current density of ($1.78\ mA/cm^2$) with an energy consumption of ($6.37\ kWh/m^3$) with (Al/Al) electrodes.
- The optimum temperature was 60ºC for vertical Al/Al electrodes, the removal efficiency reached (98.8%) at 9 min.
- The smaller electrodes gap (1cm) resulted in higher removal efficiency at lowest time due to a higher consumed of the electrode.
- With regard to pH, the treatment time increased with decreasing the pH or increasing it above 7.5. The optimum pH was 7.5 for aluminum electrodes.
- With increasing volumetric flow rate (0.042 - 0.15 l/min) the removal efficiency increased in the range (96.3 - 99%).
- The presence of sodium chloride enhances the oil removal efficiency and
- decrease treatment time.
- The best equation which represents the experimental values is obtained
- with a correlation coefficient of 90.9% and variance 82.7%.

$$\mathbf{R\%=98.05211*X_1^{-0.00561}*X_2^{-0.00182}X_3^{-0.00182}*X_4^{0.00364}*X_5^{-0.00491}*X_6^{0.00247}}$$

**NOMENCLATURE**

R%=percentage of oil removal efficiency.

$X_1$=pH.

$X_2$=gap(cm).

$X_3$=current density (mA/cm2).

$X_4$= temperature (ºC).

$X_5$= treatment time (min).

$X_6$=oil concentration (ppm).

**ABBREVIATION**

AAA=Active anode area
Al=Aluminum electrodes
Fe=Iron electrodes
St.St.=Stainless steel

**REFERENCE**

- Becher, P. (1966) Emulsions: Theory and Practice. 2nd edition, Reinhold Publishing Corporation.
- Canizares, P., Louhichi, B., Gadri, A., Nasr, B., Paz M.R., Rodrigo A., and Saez,C. (2007) Electrochemical treatment of the pollutants generated in an ink-manufacturing process.
- Chen, X., Chen G., polockyue (2002) Novel Electrode System for Electroflotation of Wastewater, Environ. Sci. Technol., 36, 778-783
- Gryta, M., Karakulski,K., and Morawki, A.W. (2001) Purification of oily wastewater by hybrid UF/MD. Water Research 35,(15) , 3665–3669.

- Hosny, A.Y. (1996) Separating oil from oil-water emulsions by electroflotation technique. Separation Technology (6),9–17. (www.inderscience.metapress.com)
- Mollah, M.Y. A., Schennach. R., Parge. J. R. and Cocke. D.L. (2001) Electrocoagulation (EC) science and application. Journal of Hazardous Materials B84, 29-41.
- Rhee ,C. H., Martyn, P.C., Kremer,J.G.(1985) Removal of oil and grease in oil processing wastewater ,the Sanitation Districts of Los Angeles County
- Saur,I.F., Rubach, S. ,Forde, J.S., Kjaerheim, G.and Syversen, U. (1996) Electroflocculation: removal of oil, heavy metals and organic compounds from oil-in-water emulsions. Filtration and Separation 303.295–303.
- Um, M.J., Yoon, S.H., Lee, C.H., Chung, K.Y. and Kim, J.J. (2001) Flux enhancement with gas injection in cross flow ultrafiltration of oily wastewater. Water Research 35 (17), 4095–4101.

# VERTICAL VIBRATIONS OF BASE ISOLATED MACHINE FOUNDATIONS

Professor Dr.Thmir K. Mahmood
Baghdad University
Civil Eng.Dept.

Salim Y. Awad
PhD. Candidate Baghdad University
Civil Eng.Dept.

## ABSTRACT

Vibration of base isolated machine foundations has been studied using the Scaled Boundary Finite Element Method (SBFEM) and the cone model method. The dynamic stiffness of soil supporting rigid massless foundation was determined. This stiffness is of complex value. The real part represents the reflected energy of the restoring and inertial forces while the imaginary part represents the energy dissipated within the endless extent of the soil as a geometric damping. The effect of geometric and material properties of soil upon the real and imaginary parts of the dynamic stiffness was determined and represented in terms of dimensionless charts for the frequency range of interest. Results have shown that increasing the embedment ratio has a significant effect on the dynamic stiffness, it increases the dynamic stiffness considerably. The effect of stiffness ratio(stiffness of isolator/ stiffness of soil) was demonstrated for isolated machine foundations. The use of soft isolators reduces the dynamic response of foundation and the soil reaction.

## الخلاصة

يتناول البحث ألاهتزازات الشاقولية لأسس المكائن المعزولة, مستخدمة طريقة العناصر المحيطية المحددة المقايسة و طريقة النموذج المخروطي لاحتساب مصفوفة الصلابة الديناميكية للتربة تحت الأساس. عناصر مصفوفة الصلابة الديناميكية ذات قيم معقدة يمثل الجزء الحقيقي منها طاقة الانفعال المنعكسة والتي تحاول إرجاع الأساس إلى وضع السكون بينما يمثل الجزء الخيالي الطاقة المتبددة في المدى اللانهائي للتربة.
تم حساب تأثير الشكل الهندسي وعمق الدفن على مصفوفة الصلابة مع تغير التردد, حيث تم احتساب كل من ثابت المرونة ومعامل التخميد للتربة تحت الأساس و رسم تغاير هذه المعاملات مع التردد باستخدام مخططات لا بعدية لمديات التردد العملية. تبين من خلال الدراسة أن الصلابة الديناميكية تزداد بزيادة عمق الأساس. لدراسة تأثير العوازل على الاستجابة الديناميكية للأساس تم استخدام عوازل نابضة وبصلابة معينة (جزء صغير من صلابة التربة) وتبين ان كفاءة العزل تزداد كلما قلت نسبة الصلابة.

**KEY WORDS:** machine foundations, dynamic stiffness, wave propagation, scaled boundary finite element method, cone model, vibration isolation.

## INTRODUCTION

The idealization of soil media by means of a conventional finite element method has a limitation, since it truncates the soil domain at pre specified artificial boundaries and this leads to spurious reflections at the assumed boundaries (Dominguez, 1993). The whole concern is to assemble the **dynamic stiffness matrix** of soil, this matrix is of a complex form , and can be decomposed into real and imaginary parts. The imaginary part corresponds to the absorbed energy dissipated in the endless extent of the infinite domain, while the real part corresponds to the reflected energy at boundaries. The dissipation of energy through soil is called **radiation damping**. Radiation condition states that the soil as an infinite media is an energy sink. (Wolf,1985).

The foundations for machines are usually in the form of reinforced concrete blocks. Brick finite elements may be used to idealize the block foundations. The soil may be idealized by a linear elastic or linear viscoelastic material.

## REVIEW OF LITERATURE

Lamb(1904) studied the response of the elastic half space subjected to oscillating vertical forces. Thus, he solved the two-dimensional wave propagation problem. In 1936, Reissner developed the first analytical solution for the vertically loaded cylindrical disk on an elastic half-space. His solution is considered to be the first engineering model. He reached a solution by integrating Lamb's solution over a circular area for the center displacement; he assumed a state of uniform stress under the footing. Barkan (1962) conducted some plate bearing tests to get an equivalent soil spring constant k. From these tests, he prepared tables and empirical formulas to easily estimate the design values of the subgrade reaction for several types of soil for each possible mode of vibration. In 1965, Lysmer in his doctoral thesis, studied the vertical vibration of circular footings by discretizing the circular area into concentric rings (Asik, 2001). Wong and Luco (1976) presented an approximate numerical procedure for calculation of harmonic force-displacement relationship of rigid foundations of arbitrary shape and placed on an elastic half-space.The first Boundary Element Method(BEM) application for soil problems was presented by Dominguez in (1978) who applied the BEM to compute the dynamic stiffness of rectangular foundations resting on, or embedded in, a viscoelastic half-space in frequency domain(Dominguez, 1993). The dynamic stiffness of rigid rectangular foundations on the halfspace was determined by (Triantafyllidis, 1986) for different aspect ratios of *(L/B =1, 2, 5 and 10)* and for Poisson's ratio *(ν =0.25, 0.33 and 0.40)*. All modes of vibration were considered and the stiffness and damping coefficients were represent in dimensionless charts for dimensionless frequency up to *3.5*. (Gazetas et al, 1985, 1986a, 1986b, 1987, 1989a, 1989b, 1991a, 1991b) treated the subject in a simple physical manner based on an improved understanding of the physics of the problem. This has been enhanced by the results of the extensive rigorous parametric studies including several analytical results compiled from the literature. Mita and Luco (1989) had tabulated dimensionless impedance functions and effective input motions of square foundation embedded in a uniform half space. Alhussaini (1992) studied the vibration isolation of machine foundation using open and in-filled trenches as a wave barriers using boundary element method (BEM). Meek and Wolf (1992) used the cone model to idealize homogenous soil under base mat, they also used cone model to idealize soil layer on rigid rock. Asik (1993) developed a simplified semi-analytical method, to compute the response of rigid strip and circular machine foundations subjected to harmonic excitation. Wolf and Song (1996) had developed the scaled boundary finite element method for modeling the unbounded media in analysis of DSSI. (Wolf, 1997) developed a spring-dashpot-mass model with frequency-independent coefficients and a few internal degrees of freedom. Spyrakos and Xu (2004) studied the dynamic response of flexible massive strip foundations embedded in a layered soil using coupled FEM/BEM. Chen and Yang (2006) presented a simplified model for simulating unbounded soil in the vertical vibration problems of surface foundations. The model comprises a mass, a spring, and a dashpot without any internal degree of freedom. Kumar and Reddy (2006) investigated experimentally the response of a machine foundation subjected to vertical vibration by sandwiching a spring cushioning system between the machine base and its footing block. Kumar and Boora (2008) also examined experimentally the effect of two different combinations of a spring mounting base and a rubber pad sandwiched between the machine base and its concrete footing block. Using modal analysis (Chen and GangHou, 2008) presented a methodology to evaluate dynamic displacements of a circular flexible foundation on soil media subjected to vertical vibration.

## MATHEMATICAL MODELS FOR MACHINE FOUNDATIONS

The idealization of soil-foundation system is the most important task of the designer, either simple or complex models may be used. It depends on the degree of accuracy required and on the importance of the project. Simple mathematical models are frequently used by office designer as it needs basic knowledge to build and to run the model, these models consist of discrete springs with lumped masses.

A boundary condition capable of eliminating the reflection of waves to the computational domain has to be applied on the artificial boundary. The boundary condition at infinity should be able to irreversibly transfer energy from the bounded domain to the unbounded domain and to eliminate the reflection of waves impinges the boundary. Such a boundary condition is called the radiation condition. Obtaining the radiation condition for large scale engineering problems is the most challenging part of the dynamic soil-structure interaction analysis.

The scaled boundary finite-element method is a powerful semi-analytical computational procedure to calculate the dynamic stiffness of the unbounded soil at the structure–soil interface. This permits the analysis of dynamic soil–structure interaction using the substructure method(Wolf and Song, 1996).

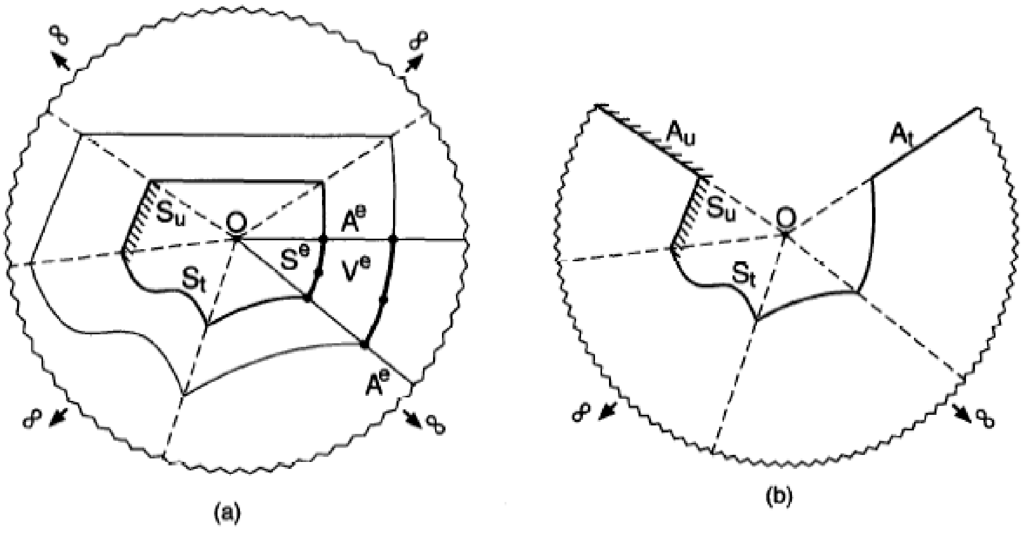


**Fig. 1** Modeling of unbounded medium with surface finite elements (section) with: (a) scaling centre outside of medium; (b) extension of boundary passing through scaling centre.

The total boundary must be visible from a point within the medium which is called the scaling center *O*. On the doubly-curved boundary *S* of the medium, the displacements and surface tractions are prescribed on ***Su*** and **S*t*** respectively. The radial direction points from the scaling centre to a point on the boundary, where two circumferential directions tangential to the boundary are identified. The boundary is discretized with doubly-curved surface finite elements with any arrangement of nodes. The dynamic behavior is described by the dynamic-stiffness matrix in the frequency domain [S(w)] relating the displacement amplitudes in the degrees of freedom on the boundary *S* to the corresponding force amplitudes.
By scaling the boundary in the radial direction with respect to the scaling centre *O* with a scaling factor larger than 1, the whole domain is covered. The scaling corresponds to a transformation of the coordinates for each finite element, resulting in the two curvilinear local coordinates in the circumferential directions on the surface and the dimensionless radial coordinate representing the scaling factor. This transformation is unique due to the choice of the scaling centre. This transformation of the geometry involving the discretization of the boundary with finite elements and scaling in the radial direction leads to a system of linear second-order differential equations for the displacements with the dimensionless radial coordinate as the independent variable.
After substituting the definition of the dynamic-stiffness matrix in the differential equations, it is shown that the dynamic-stiffness matrix is a function of the dimensionless frequency which is proportional to the product of the frequency and the dimensionless radial coordinate. This permits the equation for the dynamic-stiffness matrix on the boundary to be expressed as a system of nonlinear first-order ordinary differential equations in the frequency as the independent variable with constant coefficient matrices.

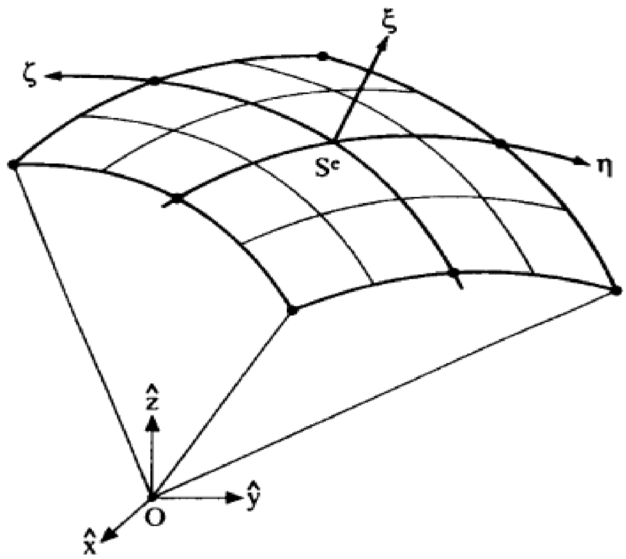


**Fig. 2** Scaled boundary transformation of geometry of surface finite element .

Denoting points on the boundary with x, y, z, the geometry is described in the local coordinate system $\eta, \zeta$

$$x(\eta,\zeta)=[N(\eta,\zeta)]\{x\}$$
$$y(\eta,\zeta)=[N(\eta,\zeta)]\{y\} \qquad (1)$$
$$y(\eta,\zeta)=[N(\eta,\zeta)]\{y\}$$

with the mapping functions ***[N(η,ζ)]*** and the coordinates of the nodes *{x}, {y}, {z}*. The three-dimensional medium is defined by scaling the boundary points with the dimensionless radial coordinate ***x*** measured from the scaling centre with $\xi = 1$ on the boundary and is 0 at the scaling centre The new coordinate system is defined by $\xi$ and the two circumferential coordinates $\eta,\zeta$, for an unbounded medium $1 < \xi < \infty$

**1. Governing Equations in Scaled boundary Coordinates**

The differential equations of motion in the frequency domain expressed in displacement amplitudes:

$$\{u\} = \{u(x,y,z)\} = [u_x\ u_y\ u_z]^T \qquad (2)$$

are formulated as

$$L^T\sigma(\omega) + b(W)+w^2\rho u(\omega) = 0 \qquad (3)$$

with the mass density $\rho$ and the amplitudes of the body loads $b$.

The stress amplitudes $\{\sigma\}$ follows from Hooke's law with the elasticity matrix *[D]* as

$$\{\sigma\} = [\sigma_x\ \sigma_y\ \sigma_z\ \tau_{yz}\ \tau_{xz}\ \tau_{xy}]^T = [D]\{\varepsilon\} \qquad (4)$$

The strain amplitudes $\{\varepsilon\}$ are defined from the strain-displacement relationship

$$\{\varepsilon\} = [\varepsilon_x\ \varepsilon_y\ \varepsilon_z\ \gamma_{yz}\ \gamma_{xz}\ \gamma_{xy}]^T = [L]\{u\} \qquad (5)$$

Where ***[L]*** is the differential operator

$$L=\begin{bmatrix} \frac{\partial}{\partial\hat{x}} & 0 & 0 \\ 0 & \frac{\partial}{\partial\hat{y}} & 0 \\ 0 & 0 & \frac{\partial}{\partial\hat{z}} \\ 0 & \frac{\partial}{\partial\hat{z}} & \frac{\partial}{\partial\hat{y}} \\ \frac{\partial}{\partial\hat{z}} & 0 & \frac{\partial}{\partial\hat{x}} \\ \frac{\partial}{\partial\hat{y}} & \frac{\partial}{\partial\hat{x}} & 0 \end{bmatrix} \qquad (6)$$

The derivatives with respect to X,Y,Z are transformed to those with respect to $\xi,\eta,\zeta$

$$\begin{Bmatrix} \dfrac{\partial}{\partial \hat{X}} \\ \dfrac{\partial}{\partial \hat{y}} \\ \dfrac{\partial}{\partial \hat{z}} \end{Bmatrix} = \left[\hat{J}\right]^{-1} \begin{Bmatrix} \dfrac{\partial}{\partial \xi} \\ \dfrac{\partial}{\partial \eta} \\ \dfrac{\partial}{\partial \zeta} \end{Bmatrix} = \left[J\right]^{-1} \begin{Bmatrix} \dfrac{\partial}{\partial \xi} \\ \dfrac{1}{\xi}\dfrac{\partial}{\partial \eta} \\ \dfrac{1}{\xi}\dfrac{\partial}{\partial \zeta} \end{Bmatrix} \tag{7}$$

Applying the weighted residuals method leads to the scaled boundary finite element equations of displacements $\{u(\xi)\}$

$$\begin{aligned} &\left[E^0\right]\xi^2\{u(\xi)\}_{,\xi\xi} + \left(2\left[E^0\right] - \left[E^1\right] + \left[E^1\right]^T\right)\xi\{u(\xi)\}_{,\xi} + \left(\left[E^1\right]^T - \left[E^2\right]\right)\{u(\xi)\} \\ &\omega^2\left[M^0\right]\xi^2\{u(\xi)\} + \{F(\xi)\} = 0 \end{aligned} \tag{8}$$

Where the coefficient matrices

$$\left[E^0\right] = \int_{S^\xi} \left[B^1\right]^T [D]\left[B^1\right]|J|\, d\eta d\zeta \tag{9 a}$$

$$\left[E^1\right] = \int_{S^\xi} \left[B^2\right]^T [D]\left[B^1\right]|J|\, d\eta d\zeta \tag{9 b}$$

$$\left[E^2\right] = \int_{S^\xi} \left[B^2\right]^T [D]\left[B^2\right]|J|\, d\eta d\zeta \tag{9 c}$$

$$\left[M^0\right] = \int_{S^\xi} [B(\eta,\zeta)]^T \rho [B(\eta,\zeta)]|J|\, d\eta d\zeta \tag{10}$$

and

$$\{F(\xi)\} = \xi\left\{F^t\right\} + \xi^2\left\{F^b\right\} \tag{11}$$

Applying the conditions of equilibrium and compatibility at soil-structure interface, getting the scaled boundary equations in dynamic stiffness matrix:

$$\begin{aligned} &\left(\left[S^\infty(\omega)\right] + \left[E^1\right]\right)\left[E^0\right]^{-1}\left(\left[S^\infty(\omega)\right] + \left[E^1\right]^T\right) - \left[S^\infty(\omega)\right] \\ &- \omega\left[S^\infty(\omega)\right]_{,\omega} - \left[E^2\right] + \omega^2\left[M^0\right] = 0 \end{aligned} \tag{12}$$

The dynamic stiffness matrix $[S\infty(\omega)]$ at high frequency is expanded in a polynomial of $(i\omega)$decreasing order starting at one:-

$$\left[S^\infty(\omega)\right] \approx i\omega[C_\infty] + [K_\infty] + \sum_{j=1}^{m} \frac{1}{(i\omega)^j}\left[A_j\right] \tag{13}$$

The first two terms on the right hand side represent the constant dashpot matrix $[C_\infty]$ and the constant spring $[K_\infty]$ (subscript $\infty$ for $\omega \rightarrow \infty$). Substituting Equation (13) into Equation (12), and setting the coefficients of terms in descending order of the power of $(i\omega)$ equal to zero

determines analytically the unknown matrices in Equation (13) sequentially.
The scaled boundary finite element equation is solved numerically. To start the algorithm for these nonlinear first order differential equations. The dynamic stiffness matrix $[S^{\infty}(\omega_h)]$ at high but finite $\omega_h$ is calculated from the asymptotic expansion polynomials equation as the boundary condition. A standard numerical integration procedure then yields $[S^{\infty}(\omega)]$ for decreasing $\omega$. The error introduced through the boundary condition diminishes for decreasing $\omega$. The numerical implementation of the aforementioned algorithm is done using the computer program of Wolf (Wolf and Song, 1996) with little modifications.

## 2. Cone Model

The soil is idealized as a truncated semi cone of initial radius $r_o$ and apex distance $z_o$, with an opening angle depends on the static stiffness of half space under rigid disk of radius $r_o$, which can be exactly determined from theory of elasticity.

$$A(z) = A_o\left(\frac{z}{z_o}\right)^2 \qquad (14)$$

$$A_o = \pi r_o^2 \qquad (15)$$

From static equilibrium

$$p_o = \frac{E_c \pi r_o^2}{z_o} u_o \qquad (16)$$

$$K_o = \frac{E_c \pi r_o^2}{z_o} \qquad (17)$$

but $K_{exact} = \dfrac{4Gr_o}{1-v}$ (18)

comparing Eq.(17) with Eq.(18) leads to,

$$\frac{z_o}{r_o} = \frac{\pi}{2}\frac{(1-v)^2}{1-2v} \qquad (19)$$

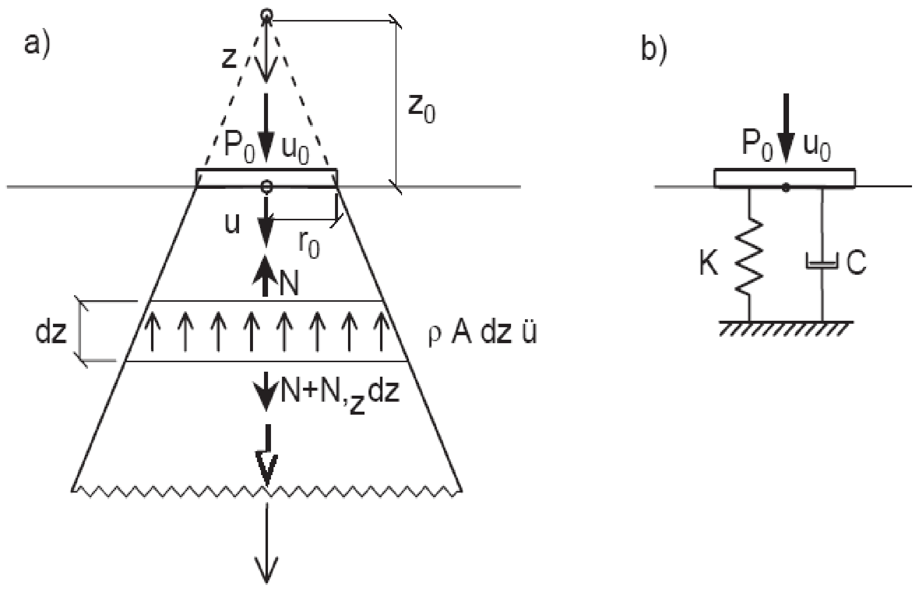


**Fig. 3 Disk on surface of homogeneous half-space.**
**a) Truncated semi-infinite cone. b) Lumped-parameter model**

Solving the one dimensional wave equation for out-coming waves only

$$u(z,t) = \frac{z_o}{z} f(t - \frac{z - z_o}{c_p}) \qquad (20)$$

$$p_o = \rho c_p^2 A_o \left[ \frac{1}{z_o} u_o(t) + \frac{1}{c_p} \dot{u}_o(t) \right] \qquad (21)$$

$$p_o = K u_o(t) + C\, \dot{u}_o(t) \qquad (22)$$

$$K = \rho c_p^2 A_o \frac{1}{z_o} \qquad (23)$$

$$C = \rho c_p^2 A_o \qquad (24)$$

$$S(\omega) = (K + i\omega C)(u(\omega)) \qquad (25)$$

As $\omega \rightarrow \infty$ the $i\omega C \gg K$ i.e. $K$ can be neglected as compared to $\omega C$ . knowing that the $C$ is the same as that of prismatic rod with constant area , it means that wave propagation is perpendicular to the disk. This is the exact wave pattern of disk on a half space in the high frequency limits. Thus, the cone model also yields exact results for $\omega \rightarrow \infty$. As the opening angle of the cone is calculated by matching the static stiffness coefficients, a doubly-asymptotic approximation results for the cone, correct both for zero frequency (the static case) and for the high frequency limit dominated by the radiation dashpot *C*. Cone model analysis is done making use of the computer program(Conan) provided by Wolf and Deek's (2004).

**- Dynamic Stiffness of Soil under Foundation**

The vertical dynamic stiffness of soil under machine foundations is addressed here. Initially the dynamic stiffness of flexible foundation by the SBFEM or by the cone model is determined, and then it will pre and post multiplied by the vectors of rigid body motion to retain the dynamic stiffness for the given mode. A complex value stiffness matrix is calculated for each frequency step, starting from a high but finite frequency down to zero frequency i.e. static stiffness. The frequency range of the dynamic stiffness should cover practical range of frequencies for machine foundations. Worked examples, verification problems and parametric studies have been achieved, to show the effects of the geometrical and material parameters on the dynamic stiffness of soil under foundation.

The effects of Poisson's ratio on vertical dynamic stiffness and on damping coefficient of embedded foundation are sown in (Fig. 4).

A verification example of a square foundation with ($v$=0.4) and with different embedment ratios were compiled by SBFEM, the results were compared with the cone model and with boundary element method of (Mita and Luco, 1989). Acceptable agreements are shown (Fig. 4), with some deviations perhaps due to different discretization schemes.

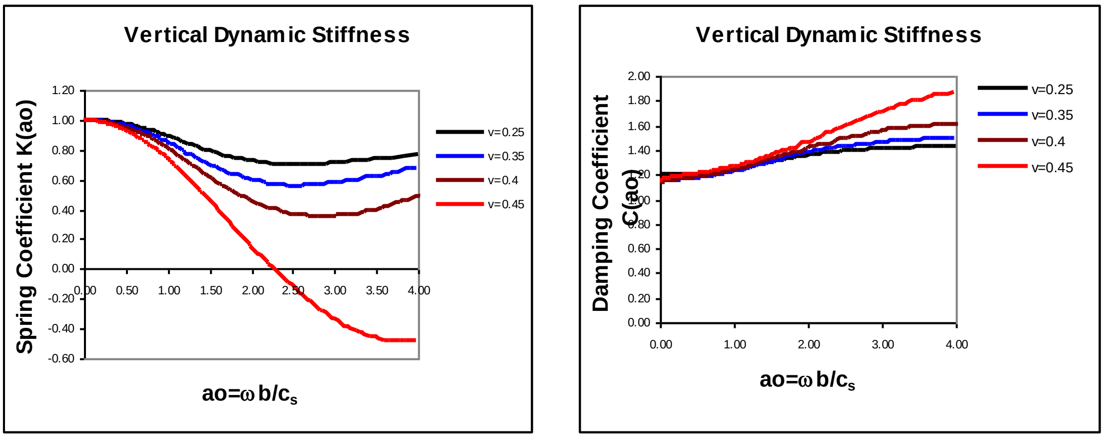


Fig. 4 Effect of Poisson's' Ratio (v) on Vertical Dynamic Stiffness of Rigid Rectangular Foundation .

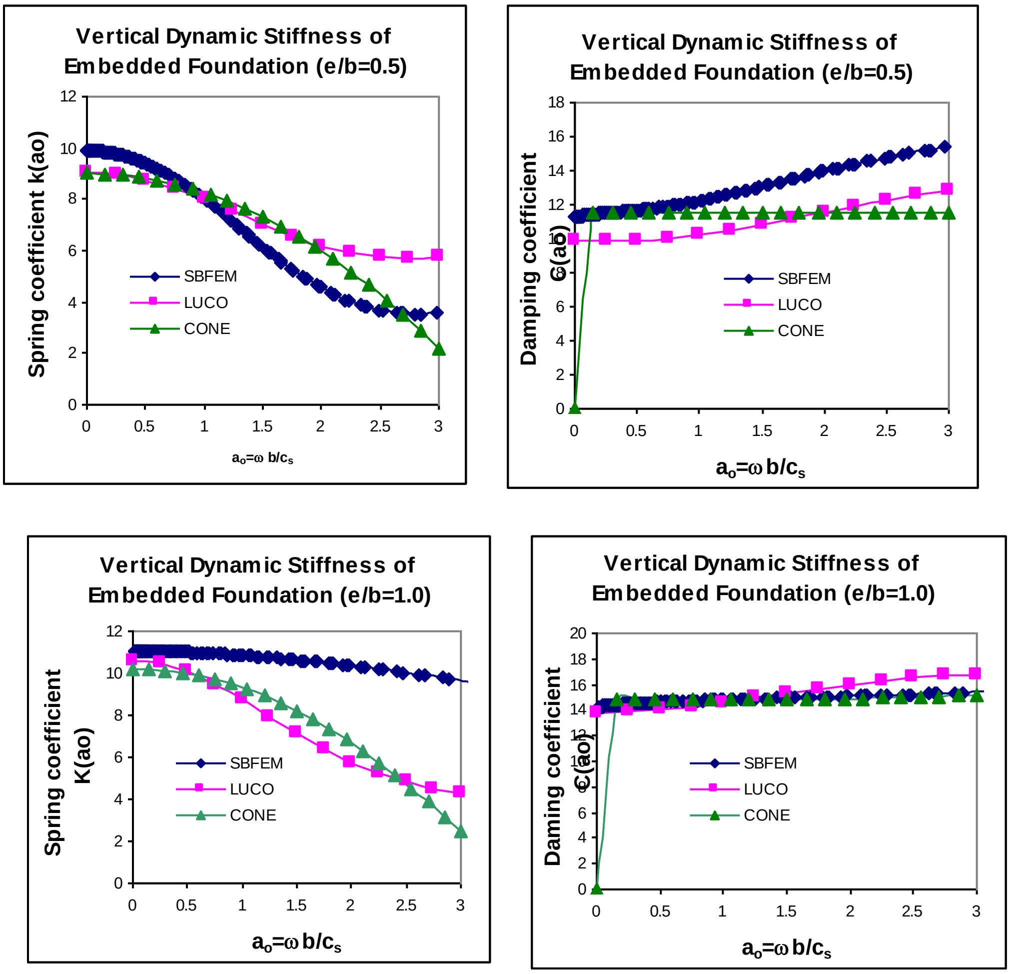


**Fig. 5** Vertical Dynamic Stiffness of a Rigid Prism Foundation Resting on/in Half Space (v=0.40), with Different Embedment Ratios.

## - DATA PREPARATION, SPATIAL AND TEMPORAL DISCRETIZATION

The soil foundation interface is discretized in a finite element manner i.e. an eight nodded element for general three dimensional foundations, a tabulated joint coordinates, element incidence and boundary conditions are specified. Material properties for each element are fed. These include the mass density and the elastic constants. Elastic constants may be fed using different options, either two modulus option of elastic shear modulus and the Poison's ratio for isotropic soil or lower triangle of the material constitutive matrix for general anisotropic material.

The spatial discretization of soil foundation interface depends on the wave length [λ]. Extreme minimum value of λ is retained by dividing the shear wave velocity by the highest frequency. The recommended element length or node to node distance is [λ/4 to λ/6] (Wolf, 2003). The solution of the nonlinear differential equation of SBFE in dynamic stiffness is in the form of power series. The solution starts with expansion of dynamic stiffness into power series at high but finite frequency. This high valued frequency should be fed by analyst to start the numerical solution. The dynamic stiffness matrix is calculated for each frequency step from the high frequency down to low or zero frequency value corresponding to the static stiffness matrix. The initial decrement of frequency is fed, and a minimum frequency step should be specified to terminate the solution algorithm.

For cone model, the spatial discretization i.e. the distances between disks should not be more than [$\lambda/5$] (Wolf and Deek's, 2004), where $\lambda$ is the shear wave length. There is no restriction on the selection of the upper or lower frequency, and any frequency may be used.

## APPLICATIONS

For a given frequency, the dynamic stiffness of soil supporting a rigid foundation is determined using the scaled boundary finite element method, or cone model. The equivalent springs and dampers coefficients for each nodal degree of freedom are calculated. Each node assumes its share of stiffness and damping due its tributary area. The springs and dampers form the boundary conditions for the finite element model of the foundation mass.

A parametric study shows the effect of mass ratio ($b_z$) (mass of foundation plus machine/ $\rho b^3$) upon the dynamic response, resonant frequency and damping ratios, for an embedded rectangular foundation of (e/b=0.5) with aspect ratio of length to width of (L/b=3) in (Figs. 6 and 7).

Interpretation of these graphs indicates that as the mass ratio increases the resonant frequency decreases and the damping ratio decreases and the dynamic response increases at distinct peaks. For low mass ratio no peaks seam distinct and the dynamic response always decreases.

The next parametric study shows the effect of stiffness ratio ($K_{(isolator)}/K_{(soil)}$) of a square embedded foundation on the forces transmitted to soil. This is the dynamic soil reaction as a fraction of the driving dynamic force, or in a conventional form it is the isolation efficiency as seen in (Fig. 8). The effect of stiffness ratio on the fundamental frequency is shown in (Fig. 9). It is clear that isolation effectiveness increases with the decrease in the stiffness ratio i.e. when using more flexible isolator sandwiched between the base and machine. Noting that an increase in the displacement of the machine itself, however, can be controlled by enhancing the isolation system with an energy dissipation devices i.e. dampers. The use of more flexible isolators decreases the fundamental frequency considerably , down to the rigid body mode of lowest frequency when one can get the best isolation effectiveness at the so called isolation frequency.

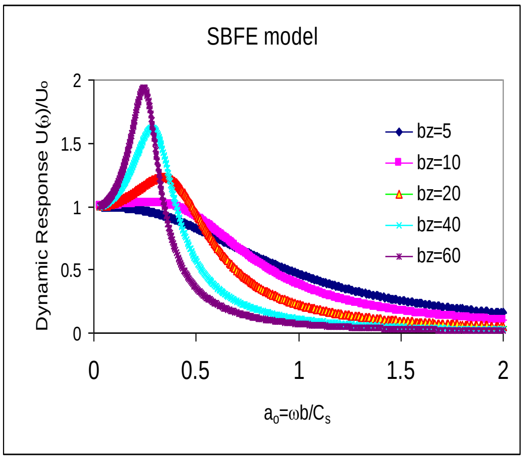


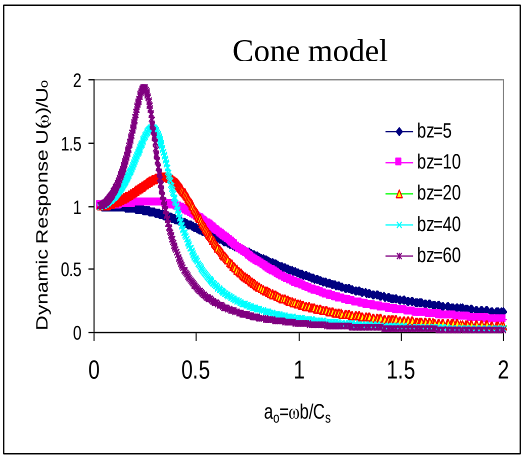


**Fig. 6** Effect of Mass Ratio on Dynamic Response of Embedded Rectangular Foundations (E/B=0.5), (L/B=3.0).

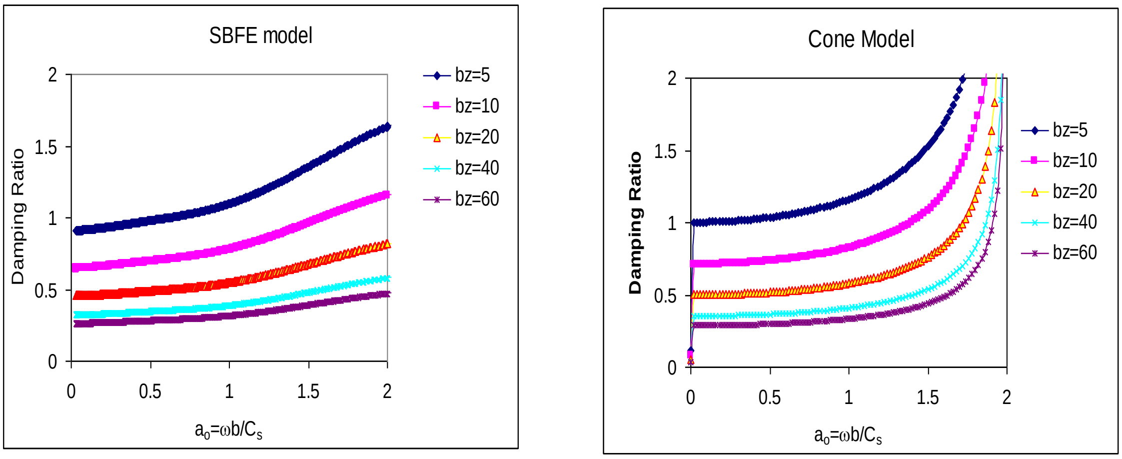


**Fig. 7** Effect of Mass Ratio on Damping Ratio of Embedded Rectangular Foundations (E/B=0.5), (L/B=3.0).

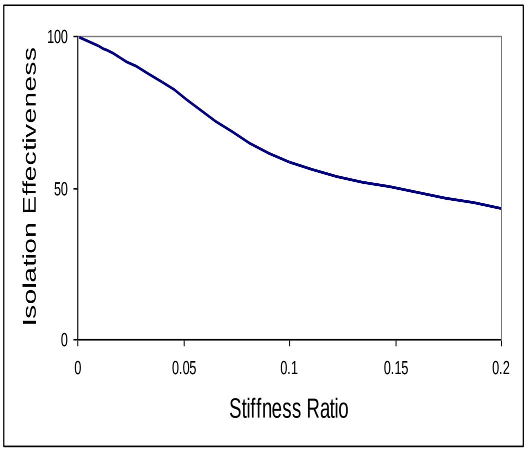


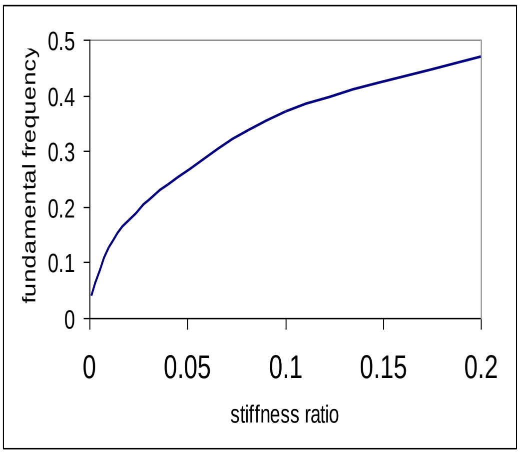


**Fig. 8** Effect of Stiffness Ratio on Isolation Efficiency.

**Fig. 9** Effect of Stiffness Ratio on Resonant Frequency.

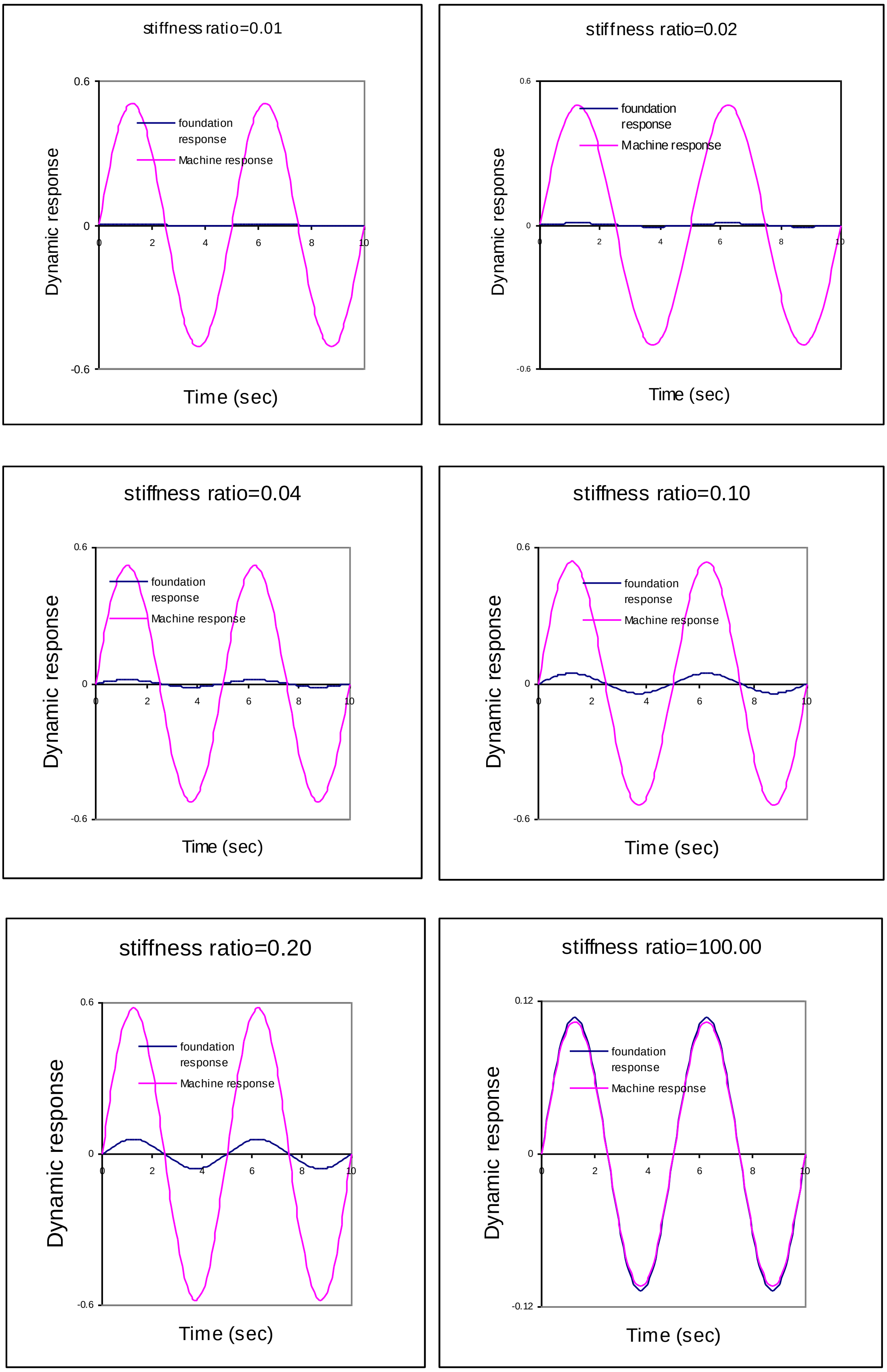


**Fig. 10** Effect of Stiffness Ratio on Vertical Dynamic Response of Machine and Foundation.

The presence of isolation between the machine and its base forms a discrete system of two degrees of freedom. The effect of the stiffness ratio on the vertical dynamic displacements of the machine and its supporting foundation is shown in (Fig.10). The uncoupled motion maintained at high isolation effectiveness leads some designers to design the isolated foundation under static loads only. This is a major advantage of using effective base isolation it will not only reduce the dynamic problem into static one but it will make it possible to place the machine even on a tenth floor of a multi story building or in/on soil with uncertain dynamic properties. In addition there is no need for a thorough sophisticated soil dynamics investigations.

## - CASE STUDY

A turbine machine of (762,000 kg )mass rests on a reinforced concrete foundation block of dimensions (24.0mx 8.0m x4.0m) and of (1,920,000 kg) mass (Fig.11) The operational frequencies are 50 Hz, 314 rad/sec. The corresponding vertical stiffness and damping of soil obtained from the scaled boundary finite element method are ($76 \times 10^8$ N/m) and ($15 \times 10^{10}$ N/m) respectively. The mass of foundation block and machine is ($2.592 \times 10^6$ kg) and the damping ratio is more than 100% , however , 25% of critical damping will be used , according to (DIN 4024, after ACI 351.3R-04) the corresponding damping coefficient is ($0.70 \times 10^8$ N.sec/m). The amplitude of harmonic dynamic force of ($1.344\ 10^6$ N) was assumed, which is 20% of the weight of the machine($F(t)=1.344x10^6 sin(314t)$).
For isolated rigid mass model a spring isolator with stiffness of one tenth of that of soil was used, results in two degrees of freedom system. The results of vibration analysis of both isolated and non-isolated foundations are listed in (Table 1)
Several finite element models were used for analyzing this case with different element sizes.

- One element model of 24 x 8 x 4 m element size,
- 12-element model with 4 x 4 x 4 m element size,
- 96-element model with 2 x 2 x 2 m element size,
- 768-element model with 1 x 1 x 1 m element size.
- Two cases of isolated finite element model with stiffness ratio of ten percent, these are one-element and 12-element models were investigated. (Table 2) lists the results of the finite element models of vertical vibration of block foundations with and without isolation.

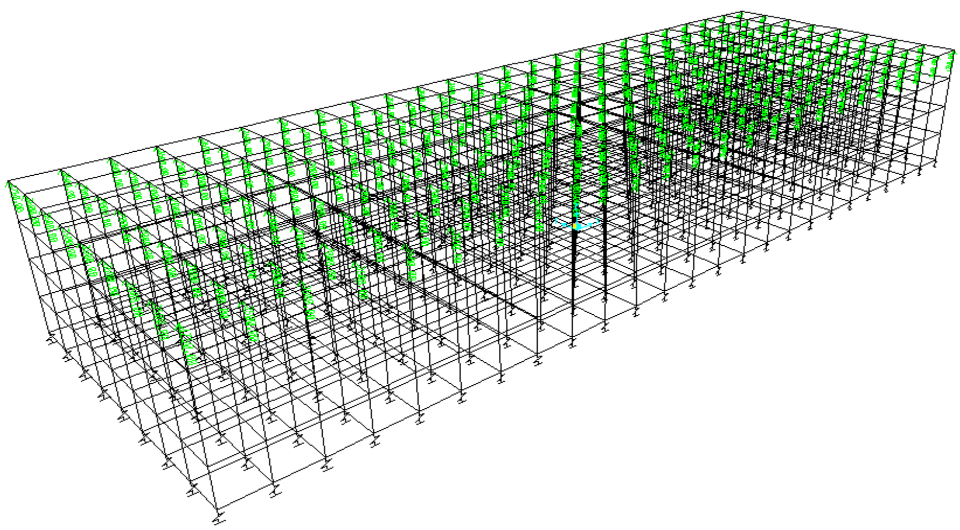

**Fig. 11** Finite Element Idealization of Machine Foundations

**Table 1 Vertical Dynamic Responses Of Rigid Mass Foundation.**

| case | Natural frequency (rad/sec) | Displacements micron ($10^{-6}$meter) | | Transmissibility Ratio % |
|---|---|---|---|---|
| | | foundation | machine | |
| Non-isolated | 54 | 5.3 | | 3 |
| isolated | 32 | 1.8 | 20 | 1.0 |

**Table 2 Vertical Dynamic Responses Of Block Foundation Using Finite Element Method.**

| case | Natural frequency (rad/sec) | Displacements micron ($10^{-6}$meter) | | Transmissibility Ratio % |
|---|---|---|---|---|
| | | foundation | machine | |
| One element | 53.7 | 5.25 | | 3.2 |
| 12-element | 53.69 | 5.24 | | 3 |
| 96-element | 53.6 | 5.2 | | 2.96 |
| 768-element | 52.8 | 5.07 | | 2.85 |
| Isolated one-element model | 32 | 2.6 | 20 | 1.5 |
| Isolated 12-element model | 31 | 2.32 | 20 | 1.3 |

Examination of (Table 1) and (Table 2) leads to the following non surprising conclusions: Resonant frequency decreases considerably with the use of isolators, the vertical

displacement and the dynamic soil reaction of foundation decrease, while the displacement of machine increases with the use of isolators; Resonant frequency decreases slightly with the use of finite element model and as the number of element increases, this result is not surprising because increasing of element numbers means the use of more flexible (less stiffness) system keeping the mass(s) not changed. The use of isolators in the finite element model results in the same response for foundation and machines with slight reduction in foundation response (displacements and dynamic soil reactions )with the increasing of element number.
Both dynamic responses of machine and foundation in non-isolated and in isolated systems are within acceptable limits(section 3.3). As the non-isolated natural frequency(54 rad/sec) is sufficiently far away from the driving frequency(314 rad/sec). The use of isolators has no practical values if it is not detrimental. However it may be beneficial when the machine assumes unusual frequencies when turn on/off conditions or emergency shutdown.

## CONCLUSIONS

Comparing the SBFEM and the cone model results with the published boundary element, the applicability of these models are demonstrated. The important observations of the effect of the geometrical and material properties of soil under foundation upon the dynamic stiffness and dynamic response are presented separately in the following paragraphs. The vertical vibration of rectangular foundations have been studied by the SBFEM and by the cone model, some conclusions may be drawn as follows:-

- The results for the vertical dynamic stiffness of rectangular foundations indicate that the real part for the spring coefficient decreases by (0% to 80%) and may posses negative values and the damping coefficient increases up to (50%) as Poisson's ratio increases from (0.25) to (0.45). The frequency effect on spring and damping coefficients of embedded foundations with different embedment ratios (e/b= 0.5,1.0,1.5,2.0)has been found. Both spring and damping coefficients increase with the increasing of embedment ratio.

- The mass ratio($M_f/\rho b^3$) of foundation has a significant role in the dynamic response. As the mass ratio increases from(5) to (20) the resonant frequency decreases by (70%), damping ratio decreases by (50%) and the dynamic response increases by (100%) with a distinct peaks. For low mass ratio (less than 5) no peaks seem distinct and the dynamic response always decreases.
- The effect of stiffness ratio ($K_{(isolator)}/K_{(soil)}$) on the isolation efficiency or on tuning of fundamental frequency. It seems that isolation effectiveness increases from(50%) to (80%) with decreasing in stiffness ratio from(0.20) to (0.05). The use of more flexible isolators decreases the fundamental frequency by(50%) when the stiffness ratio decreases from(0.20) to (0.05).
- The presence of isolation between machine and its base forms a system of two degrees of freedom at each mass of both the machine and the foundation. These two degrees of freedom systems seem to be gradually uncoupled as much as the isolation stiffness being more flexible (stiffness ratio less than 0.05). The major advantage of base isolation, not only reduces the dynamic problem into static one but also it reduces the need for a thorough sophisticated soil dynamic investigations.
- For vertical mode, the use of finite element model affects the response slightly (less than 10%) due to the flexibility of finite element model as compared with rigid mass model. Resonant frequency decreases slightly(less than 1%) with the use of finite element model and as the number of elements increases. This result is not surprising

because increasing of element numbers means the use of more flexible (less stiffness) system keeping the mass(s) not changed.

## REFERENCES


- Achenbach, J. D.(1973). *Wave propagation in elastic solids*. North-Holland Publishing Company-Amsterdam.
- Al-jaberi Zuhair, (2006), *Dynamic analysis of Block type Machine Foundations*. MSc. Thesis, Baghdad university.
- American Concrete Institute. (2004), *Foundation for Dynamic Equipment*, Reported by ACI Committee 351.
- Arya, S.C., O'Neill, M.W. and Pincus, G. (1984), *Design of structures and foundations for vibrating machines,* Gulf Publishing Company, Houston.
- Asik M. Z. (1993), *Vertical vibration analysis of rigid footing on a soil layer with a rigid base*. PhD Thesis, Texas Tech University.
- Asik M Z and Vallabhan C. V. J. (2001). A Simplified Model for the Analysis of Machine Foundations on a Non-saturated, Elastic and Linear Soil Layer. *Computers and Structures*, Vol. 79, pp 2717-2726.
- Barkan, D. D. (1962). *Dynamics of bases and foundations.* McGraw-Hill Book Co., New York, N.Y.
- Bazyar M. H. (2007), *Dynamic Soil-Structure Interaction Analysis Using The Scaled Boundary Finite-Element Method*. PhD thesis, The University of New South Wales Sydney, Australia.
- Beskos D.E.,(1987) *Boundary element methods in structural analysis*, *ASCE*, 0-87262-694-6,1989,352pp.
- Bu S. and Lin C., (1999). Coupled Horizontal-Rocking Impedance Functions For Embedded Square Foundations At High Frequency Factors. Journal of Earthquake Engineering, Vol. 3, No. 4 : 561-587, Imperial College Press.
- Chen Shi-Shuenn and Shi Jun-Yang (2006).Simplified Model for Vertical Vibrations of Surface Foundations, *Journal of Geotechnical and Geo-environmental Engineering, ASCE*, Vol. 132, No. 5, May 1.
- Chen Shi-Shuenn, Jr-GangHou, (2008). Modal analysis of circular flexible foundations under vertical vibration. *Soil Dynamics and Earthquake Engineering* :article in press, doi:10.1016/j.soildyn.2008.10.004.
- Dobry, R., and Gazetas, G. (1986). "Dynamic response of arbitrarily shaped machine foundations." *Journal of Geotechnical engineering, ASCE*, 112(2), 109-135.
- Dominguez J.,(1993) Boundary Elements in Dynamics, Computational Mechanics Publications, Southampton.
- Gazetas G and Rosset J M(1979). Vertical Vibration of Machine Foundations. *Journal of Geotechnical engineering, ASCE*, 105(12), pp 1435-1454.
- Gazetas, G. (1991). Formulas and charts for impedances of surface and embedded foundation." *Journal of Geotechnical engineering, ASCE*, 117(9), 1363-1381
- Kausel E. (2006), *Fundamental Solutions in Elastodynamics*. Cambridge University Press, New York
- Kausel E. (1974), *Forced vibration of circular foundations on layered media*. PhD thesis, Massachusetts Institute of Technology.

- Kumar J. and Boora V. (2008), Dynamic response of machine foundation in combination with spring mounting base and rubber pads. *Geotech. Geol. Eng. Springer* DOI 10.1007/s 10706-008-9239-7
- Kumar J. and Reddy C.(2006), Dynamic response of footing and machine with spring mounting base, *Geotech. Geol. Eng. Springer* (24), pp 15-27.
- Lehmann L. (2007). *Wave Propagation in infinite domains with applications to structure interaction*. Springer-Verlag Berlin Heidelberg
- Meek, J. W., and Wolf, J. P._(1992). Cone models for Homogenous soil, *Journal of Geotechnical Engineering, ASCE*, 118(5), 667–685.
- Meek, J. W., and Wolf, J. P. _(1994)_. Cone models for Embedded Foundations, *Journal of Geotechnical Engineering, ASCE,* 120(1), 60–80.
- Mita, A., and Luco, J. E. (1989). "Impedance functions and input motions for embedded square foundations. *Journal of Geotechnical engineering, ASCE*, 115(4), 491-503.
- Richart, F. E., Hall, J. R., and Wood, R. D. (1970). *Vibrations of soils and foundations.* Prentice-Hall, Englewood Cliffs, N.J.
- Spyrakos C.C. and Xu C. (2004), Dynamic analysis of flexible massive strip foundations embedded in layered soil by hybrid BEM-FEM. *Soil Dynamic and Earthquake Engineering*, 82: 2541-2550.
- Traintafyllidis TH. (1986) Dynamic stiffness of rigid rectangular foundations of the halfspace, *Earthquake Engrg. Struct. Dyn.*, Vol. 14, pp. 391-412.
- Wolf, J. P. (1985), *Dynamic soil-structure interaction.* Prentice-Hall, Inc., Englewood Cliffs, N.J.
- Wolf, J. P. and Somaini D. R. (1986) Approximate dynamic model of embedded foundation in time domain. *Earthquake Eng. Struct. Dyn.*, 14, 683–703
- Wolf, J. P. (1988). *Dynamic soil-structure interaction in the time-domain.* Prentice-Hall, Englewood Cliffs, N.J.
- Wolf, J. P. (1994) *Foundation vibration analysis using simple physical models*, Prentice-Hall, Englewood Cliffs, N.J.
- Wolf J.P. and Song Ch. (1996*),Finite Element Modeling of Unbounded Media*, John Wiley & Sons, Chichester.
- Wolf J.P. and Song C. (1996), Consistent infinitesimal finite-element cell method in frequency domain, *Earthquake Engrg. Struct. Dyn*. 25 :307–1327.
- Wolf JP. (1997),Spring-Dashpot-Mass models for foundation vibrations. *Earthquake Eng Struct Dyn*;26:931–49
- Wolf J.P., Song Ch. (2000), The scaled boundary finite-element method—a primer: derivations, *Comput. Struct*. 78 : 191-210.
- Wolf, J. P., and Song, C. (2002) Some cornerstones of dynamic soil structure interaction. *Eng. Struct.*, 24, 13–28.
- Wolf John P. (2002). Response of unbounded soil in scaled boundary finite-element method, *Earthquake Engng Struct. Dyn*. 31:15–32
- Wolf, J.P. (2003), The Scaled Boundary Finite Element Method, John Wiley & Sons, Chichester, U.K.
- Wolf, J. P. and Deeks, A. J. (2004). *Foundation vibration analysis: A strength of materials approach,* Elsevier, New York.
- Wong, H. L. and Luco, J. E. (1976). "Dynamic response of rigid foundations of arbitrary shape." *Earthquake Eng. Struct. Dyn.*, 4(6), 579-587.

## NOMENCLATURE

The major symbols used in this paper are listed below; others are indicated with their equations where they first appear.

| | |
|---|---|
| $A$ | Plan area of foundation |
| $a_o$ | Dimensionless frequency $a_o = \dfrac{\omega b}{C_s}$ |
| $A_u$ | Side face with pre-specified displacements |
| $A_t$ | Side face with pre-specified forces |
| $b$ | Half width of foundation (characteristic length) |
| $[b^1],[b^2],[b^3]$ | Scaled boundary finite element differential operators |
| $b_z$ | Mass ratio |
| $C$ | Wave velocity |
| $C$ | Damping coefficient |
| $[C]$ | Damping matrix |
| $[C_\infty]$ | Damping matrix of unbounded media |
| $E$ | Modulus of elasticity |
| $[E^o],[E^1],[E^2]$ | Elastic Matrices of Scaled boundary finite element |
| $[E^{o*}],[E^{1*}],[E^{2*}]$ | Complex Elastic Matrices of Scaled boundary finite element involving material damping |
| $e$ | Volumetric strain |
| $e/b$ | Embedment ratio |
| $f(t)$ | Incident wave |
| $G$ | Shear modulus of elasticity |
| $[G(\omega)]$ | Dynamic flexibility matrix |
| $g(t)$ | reflected wave |
| $h(t)$ | refracted wave |
| $I$ | Moment of inertia of plan of foundation |
| $i$ | Imaginary part $= \sqrt{-1}$ |
| $J$ | Jacobean matrix |
| $k$ | Stiffness coefficient |
| $[K]$ | Stiffness Matrix |
| $[K_\infty]$ | Stiffness Matrix of unbounded media |

| | |
|---|---|
| $L$ | Half length of foundation |
| $[L]$ | Differential operator |
| $m$ | Lumped Mass |
| $[M]$ | Mass matrix |
| $[M^o]$ | Mass matrix of Scaled boundary finite element |
| $N(z,t)$ | Normal force |
| $O$ | Similarity centre |
| $r$ | Radial coordinates |
| $r_o$ | Characteristic length of foundation |
| $S(\omega)$ | Dynamic stiffness |
| $[S(\omega)]$ | Dynamic stiffness matrix |
| $\bar{t}_i$ | Traction forces |
| $u_i$ | Component of displacement |
| $\dot{u}_i$ | Component of velocity |
| $\ddot{u}_i$ | Component of acceleration |
| $v$ | Poisson's ratio |
| $x, y, z$ | Cartesian's coordinates |
| $\alpha$ | Reflection coefficient of waves |
| $\beta_m$ | Material hysteretic damping |
| $\beta$ | Frequency ratio |
| $\varepsilon_i$ | Normal strain component |
| $\varepsilon_{ij}$ | Shear strain component |
| $\lambda$ | Wave length |
| $\lambda, \mu$ | Lame' constants |
| $\rho$ | Mass density |
| $\sigma_i$ | Normal stress component |
| $\tau_{ij}$ | Shear stress component |
| $\omega$ | Frequency |
| $\omega_{ij}$ | Rotational strain |
| $\zeta$ | Damping ratio |
| $\xi, \zeta, \eta$ | Natural coordinates |

# EXPERIMENTAL STUDY ON THE PRESENCE OF OPEN CAVITY EFFECTS ON INTERNAL FLOW AND CONVECTION HEAT TRANSFER CHARACTERISTICS

Dr. IKHLASE M. FAYED Dr. MOAYED R. HASAN Dr. ANEAS A. AL-FAKHRI


## ABSTRACT

An experimental study is conducted to investigate the effect of open cavity on the pattern of fully developed internal flow and convection heat transfer. In this experimental work the velocity profile, temperature distribution, heat transfer coefficient and Nusselt number were determined at various Reynolds numbers ($1.9*10^4 \le Re \le 2.7*10^4$) for smooth surface as well as for flow over open cavity (with and without excitation). The results showed that the presence of the cavity led to change the downstream velocity profile and the dissimilarity of downstream skin friction coefficient between the upper and lower surfaces around (64 %) at distance to the length cavity (x/L= + 20.5). As a result the heat transfer coefficient and Nu increased downstream of the cavity especially at (x/L= + 20.5) around (30 %). The effect of cavity excitation with different sound levels (100,107.5 and 115) dB and frequencies (25,50 and 100) Hz was small compared with the cavity itself.



## الخلاصة

يتناول البحث دراسة عملية لتاثير الفجوة المفتوحة على طبيعة الجريان و انتقال الحرارةبالحمل‌ا جري ان كامل الـ تطور .تم
ايجاد منحنى السرعة, توزيع درجات الحرارة, معامل انتقال الحرارة اضافة الى حساب رقم نسلت لمواقع مختلفة على سطح
املس و سطح يتضمن فجوة مفتوحة (بعدم وجود اثارة و بوجود اثارة) عند اعداد رينولدز مختلفة $(1.9*10^4 \le Re \le$
$2.7*10^4)$. اشارت النتائج الى ان وجود الفجوة يؤدي الى تغير منحنى توزيع السرعة خلف الفجوة اضافة الى عدم التماثل لقيم
معامل الاحتكاك الموضعي للسطح العلوي و السفلي بحدود (64 %) عند ساف ة الى طول ف جوةم(x/L= +20.5 ) .
نتيجة لذلك فان كل من معامل انتقال الحرارة الموضعي و عدد ن سلت ازداد بصورة ملحوظة و خصوصاً عند (
x/L= +20.5 ) دودحب (30 %) . كما اشارت الدراسة الى ان تأثير الاثارة للفجوة ضغط (100,107.5&115dB)
ب م س توي ات (25,50&100 Hz) ت و ت رددا على النتائج الم س تح صلة يكون صغير مقارنةً بتأثير الفجوة نفسها.

## INTROUDACTION

The problem deals with the internal flows encountered in many industrial processes, where a fluid has to transport in a piping system. All the valves or other elements may great flush mounted cavity. Flow interaction with a structure produces vortices with shed at a prescribed frequency. If the shedding frequency coincides with the resonance frequency of an adjoining elastic structure or acoustic fluid volume within the cavity, the resulting oscillation can reinforce the vortices creating a feed back mechanism responsible for producing high energy at resonance. This phenomenon is called lock-in and at low Mach number can result in a strong narrow band sound source. Lock-in is often undesirable and can promote rapid fatigue failure [3]. The flow over open cavity can be explained according to [4] which showed that at the up-stream edge of the cavity a boundary layer separates. The resulting shear layer develops based upon its initial conditions and the instability characteristics of the mean shear-layer profile. The shear layer spans the length of the cavity and ultimately reattaches near the trialing edge of the cavity in an open cavity flow. The reattachment region acts as the primary acoustic source. The incident acoustic waves force the shear layer, setting the initial amplitude and phase of the instability waves through a receptivity process. The effect of sound on a free convection heat transfer from a vertical flat plate had been studied in [2] and showed that, intense acoustic fields result in significant increase in the rate of free convection heat transfer and heat transfer coefficient with increasing intensity of a caustic field. The cavity problem has long been an attractive problem for researchers due to the rich nature of the flow physics and it relevance to practical applications [8]. Even though many researches studied the flow and heat transfer a long smooth surface in the rectangular duct [5] and the flow over open cavity and it attempted to control the flow over it using open-loop and closed-loop control [1, 4, 6, 9]. These studies did not deal with the effect of these methods and cavity effect on the flow pattern and at the same time on the heat transfer characteristics.

The goal of this work is to investigate experimentally the effect of open cavity (with and without excitation) on the internal flow and heat transfer characteristics.

## EXPERIMENTAL FACILITY

The experiments were performed in an open rectangular duct, using air as the working fluid. The duct has cross section (1.006*.03 m) and is over 10.35 m long. At the outlet section of the duct two centrifugal fans were fixed. The upper and lower walls of the duct made of plywood of (15 mm) thickness. The lower wall was instrumented with embedded thermocouples to measure the local temperature of the surface. The thermocouples junction was embedded with epoxy resin in the holes drilled upward from the lower wall. The lower surface was electrically heated by using strips foil of nichrome to serve as a source of heat. The heating element consists of strips of (2 cm) width. Foil strips were placed adjacent to each other with spacing of around (1 mm) between them and heated by alternating current to serve as constant heat flux. The lower wall was insulated to ensure that the input heat was mainly dissipated to the air. The side walls of the duct made of Perspex pieces. The first section of the duct with length (3.625 m) was used as working section and practically all the measurements were recorded. A cavity with length (6 mm), depth (50 mm) and width (750 mm) was formed on the lower surface of the duct at a distance (1.2 m) from the working section. Loudspeaker was fixed at the lower end of the cavity.

A 20 mm hole was provided at one wall of the cavity box for the insertion of the microphone. Fig (1) shows the working section and measurement locations. The excitation of the cavity with different frequencies and amplitudes was generated from signal generator and transmitted to the cavity through loudspeaker. The output from microphone was fed to a sound level meter which its reading is in dB. For static and total pressure measurements, holes were drilled due to (British-Standard) at the upper wall of the duct. For static pressure measurements the tapings were connected to micro manometer with (1%) accuracy and a range (1-10 mm $H_2O$). Measurements of local velocity within the boundary layer were made using a Pitot probe (with outer diameter 1.5 mm) and its working end chamfered to obtain measurement at 0.25 mm from the attachment wall. The tube was screwed to a special probe carrier in which Dial gauge was connected. The dial gauge gave 30 mm reading range with accuracy of 0.01 mm.

## DATA ANALYSIS

Surface temperatures were measured with thermocouples embedded along the foils. The net convective heat from the face of foils was obtained by subtracting losses from insulated surfaces and radiation losses from metered electric energy input to the foil [ 5], as follow,

$$Q_{con} = Q_{gen} - Q_{loss} \tag{1}$$

$$Q_{gen} = I^2 \times R \tag{2}$$

$$R = 14.475 + 0.061 \times (T - T_o) \tag{3}$$

$$Q_{loss} = -0.41 + 0.0784 \times \Delta T - 4.863 \times 10^{-4} \times \Delta T^2 \tag{4}$$

Where,

$\Delta T = T - T_o$

$$h = \frac{Q_{con}}{A \times (T - T_{bn})} \tag{5}$$

$$Nu = \frac{h \times D}{k} \tag{6}$$

## RESULTS AND DISSCSION

The experiments had been tried with three cases,

1- smooth surface (cavity covered with tape)
2- cavity without excitation
3- cavity with excitation at different frequencies and levels.

### Velocity Profile

Velocity was measured using a total head tube and wall static pressure tapings. The velocity measurements were carried out upstream of the cavity at distance to the cavity length (x/L= -16.25) and downstream of the cavity (x/L= +20.5, x/L= +78.9, x/L= +137.9) as shown in figure (2). The velocity profiles were found to be identical in the flow direction. The existence of cavity led to change the velocity profile especially at (x/L= +20.5) as shown in figure (3) due to a periodic vortex organization which periodical impacts the downstream edge of the cavity and caused the change of velocity profile [4]. The dissimilarity of velocity profile down stream the cavity diminished at (x/L= +137.9). The effect of cavity excitation with 25 Hz and 100 dB on velocity profile have been insensitive compared without excitation, except of a certain variation in the inner region at (x/L= +20.5) as shown in figure (4). Figure (5) shows the effect of changing the pressure level of excitation from 100-115 dB at the same frequency at x/L= +20.5. From the figure it is clear that the highest value of pressure level has the greater effect.

### Skin Friction Coefficient

The values of $C_f$ were measured for the above three cases using Preston tube (Di/Do=0.6) [7]. The measurement for upper and lower surfaces gave nearly the same values for smooth surface, maximum difference (9%) as shown in figure (6). The existence of cavity caused a large difference between these values particularly at x/L= 20.5 (64%) as shown in figure (7). The difference between these values related to the variation of velocity profile for two surfaces. The comparison between $C_f$ for smooth surface and that for cavity is shown in figure (8). The excitation of cavity did not cause clear effect on the values of skin friction coefficient in comparison with that for cavity without excitation except at x/L= +20.5 as shown in figure (9, 10).

### Heat Transfer Coefficient And Nusselt Number

Figure (11) shows the heat transfer coefficient (h) along the test section for smooth surface at different values of Reynolds number. From the figure it is clear that (h) is nearly constant along smooth surface. The existence of cavity led to a sharp increase in heat transfer coefficient at x/L= +20.5, which disappeared along the remainder distance as shown in figure (12). The excitation of cavity with different values of frequency and amplitude maintained the same trend of heat transfer coefficient as that for cavity without excitation although the excitation caused a certain increase in (h) at x/L= +20.5 as shown in figures (13, 14). From eq. (6) Nu number was calculated for smooth, cavity and cavity with excitation, and from figures (15-18) the same results and trend of variation for Nu were obtained as that for h.

The weak effect of excitation of the cavity on the above results may be related to the amplitudes and frequencies lying around the values of that for cavity without excitation as shown in figure (19). All the above results of smooth surface in the fully developed region were compared with [5] and gave good agreement as shown in Table. 1.

## CONCLUSIONS

- The greater effect of cavity confined to x/L= +20.5 downstream of the cavity.
- Vortex organization within the cavity led to alter the velocity profile and caused the dissimilarity of skin friction coefficient for upper and lower surfaces around (64%) at x/L = +20.5 as well as increased heat transfer coefficient (h) and Nusselt number around (30 %) at x/L= +20.5.
- The excitation of cavity with different amplitudes and frequencies had small effect on the results compared with self cavity and almost confined to x/L= +20.5.
- The variation of Re number ($1.9*10^4 \leq Re \leq 2.7*10^4$) had not significant effect of the obtained results.

## REFERENCES


- Hamed A., Das K., and Basu D. (2004), Numerical simulations of fluidic control for transonic cavity flows. 42nd AIAA Aerospace Sciences Meeting & Exhibit. pp. 1-8.

- June R.R., and Baker M. J. (1963), The effect of sound on free convection heat transfer from a vertical plate. Journal of heat transfer. pp.279.

- Klai-Fook Cody, Hambric S. and Pollack M. (2005). Challenges of investigating fluid-elastic lock- in of a shallow cavity and a cantilevered beam at low Mach numbers. LM-05K127. pp. 1-9.

- Louis Cattafesta, David Williams, Clancy Rowley and Farruk Alvi. (2003). Review of active control of flow- induced cavity resonance. 33rd AIAA Fluid dynamics conference. pp.1-20.

- Lwaa N. (1992). Experimental study to flow and heat transfer in the rectangular duct centered with diffuser section at different angles. M.Sc. Thesis, University of Technology, Mech. Dept.

- Pascal Hemon, Xavier Amandolese, Francoise Santi and Jan Wojciechowski (2002). Study the acoustic oscillation of flow over cavities. Part 2. Sound Reduction. ASME International Engineering Congress & Exposition. pp. 1-7.

- Patel V.C. (1965). Calibration of Preston tube and limitation on its use pressure gradients. J. Fluid Mec., vol. 23. pp. 185-208.

- Samimy M., Debiasi M. and Caraballo E. (2003). Development of closed-loop control for cavity flows. 33rd AIAA Fluid Dynamics Conference and Exhibit. pp. 1-17.

- Xavier Amandolese, Pascal Hemon and Clotide Regardin. (2002). Study the acoustic oscillation of flow over cavities. Part 1.Internal Fl;ows. ASME International Engineering Congress & Exposition. pp. 1-9.


## NOTATION

A foil surface area ($m^2$)
Cf skin friction coefficient
D cavity depth, effective diameter (mm,m)
dB decibel
F frequency (Hz)
h heat transfer coefficient ($W/m^2.\,^oC$)
I electric current flow rate (amp)
k thermal conductivity ($W/m.^oC$)
L cavity length (mm)
Nu Nusselt number
Q heat transfer rate (W)
R electric resistance ($\Omega$)
Re Reynolds number ($U_c.D/\nu$)
T foil temperature ($^oC$)
U stream wise velocity component (m/s)
w cavity width (mm)
x stream wise coordinate
y vertical coordinate

## SUBSCRIPTS

b baulk
c center
con convective
gen generated
loss losses
n number of foil
o ambient
bn baulk at specified foil

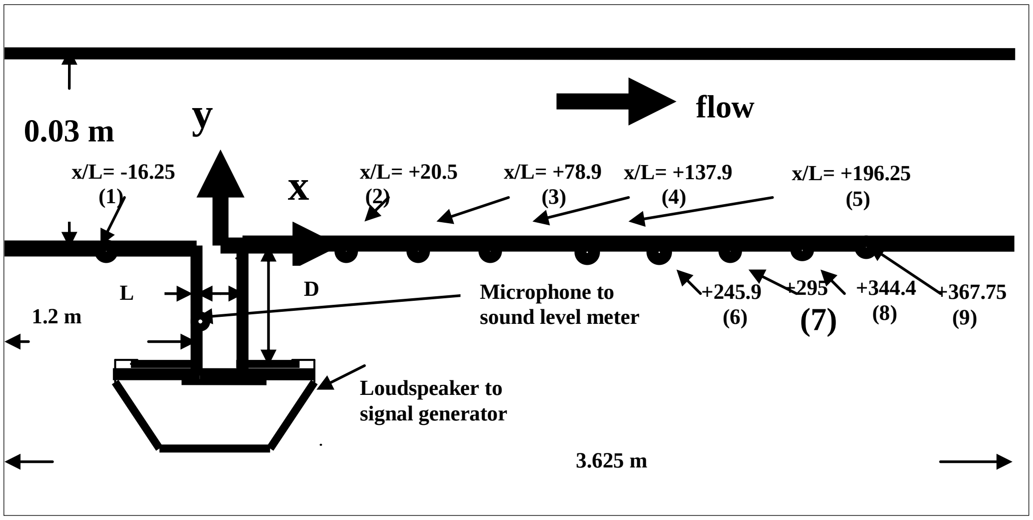


**Fig.1. working section and measurement locations**

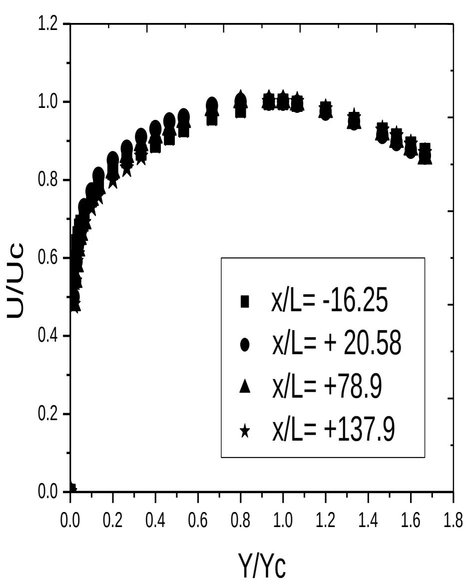


**Fig.2. velocity profile for smooth surface at Re= $2.3*10^4$.**

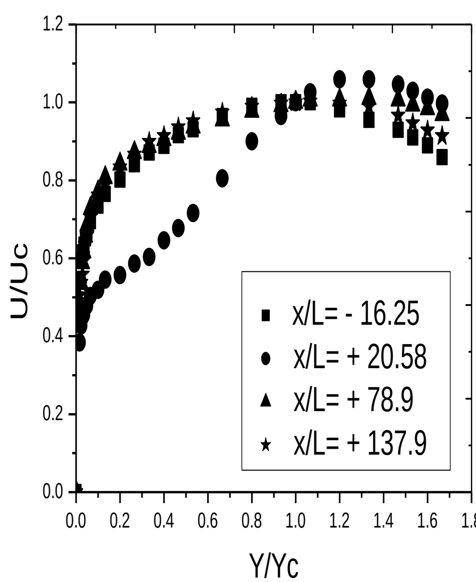


**Fig.3. velocity profile for cavity without excitation at Re= $2.3*10^4$.**

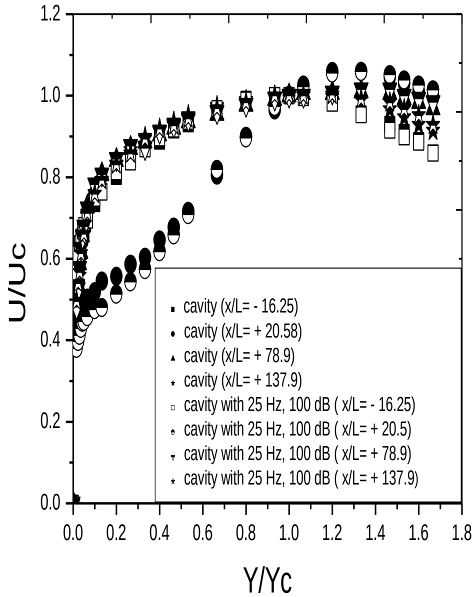


**Fig.4. velocity profile for cavity with excitation and without excitation at Re= $2.3*10^4$**

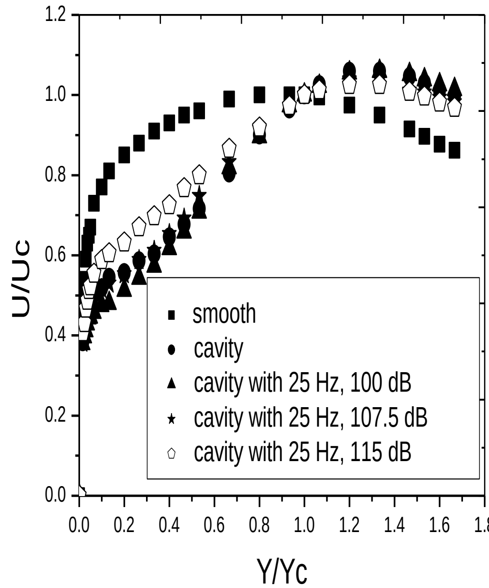


**Fig.5. velocity profile for smooth, cavity with excitation and without excitation at x/L= 20.5 and Re= $2.3*10^4$.**

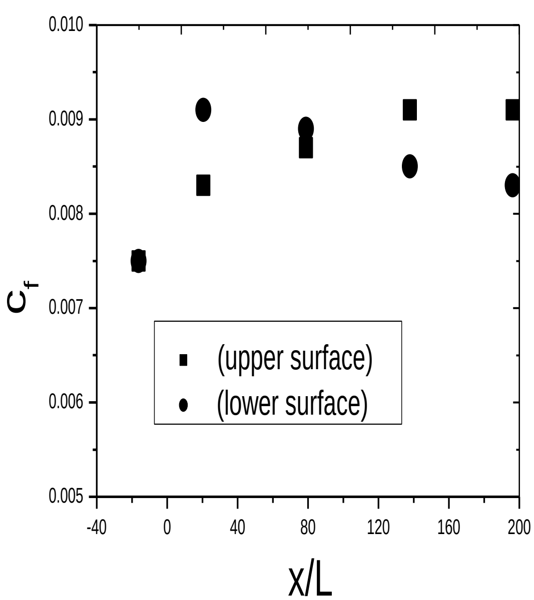


**Fig.6. local skin friction coefficient for smooth surface at Re= $2.3*10^4$.**

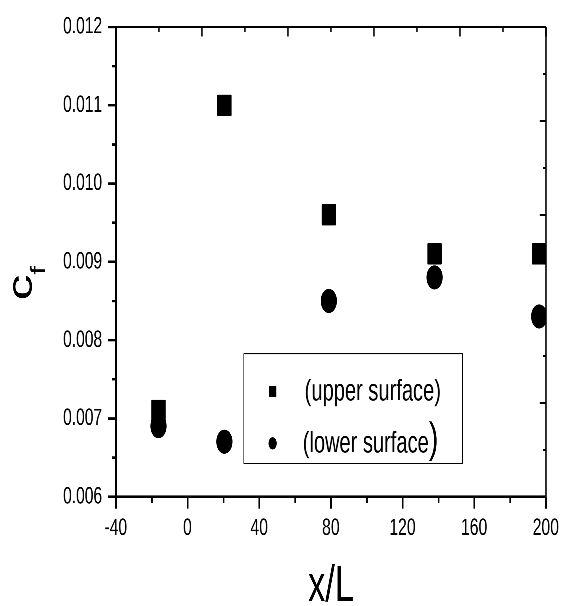


**Fig.7. local skin coefficient for cavity without excitation at Re= $2.3*10^4$.**

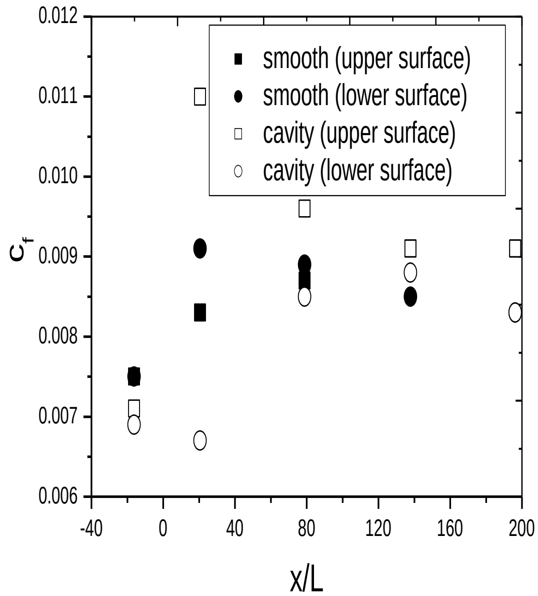


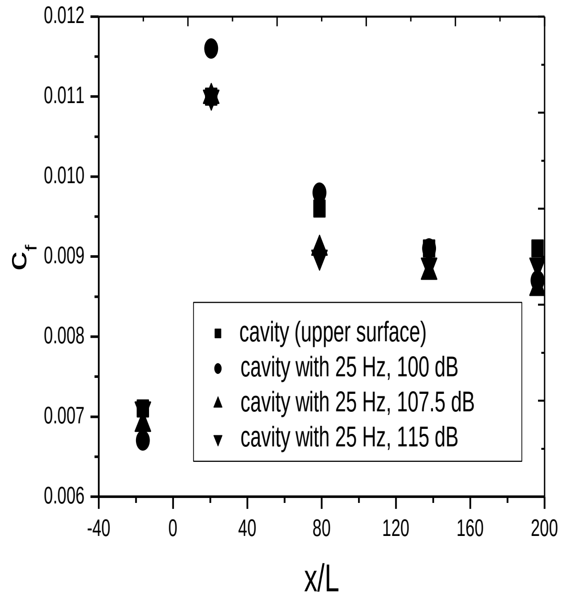


**Fig.8. local skin friction coefficient for smooth and cavity without excitation at Re= 2.3*10$^4$.**

**Fig.9. local skin coefficient for cavity with excitation and without excitation with different levels at Re= 2.3*10$^4$.**

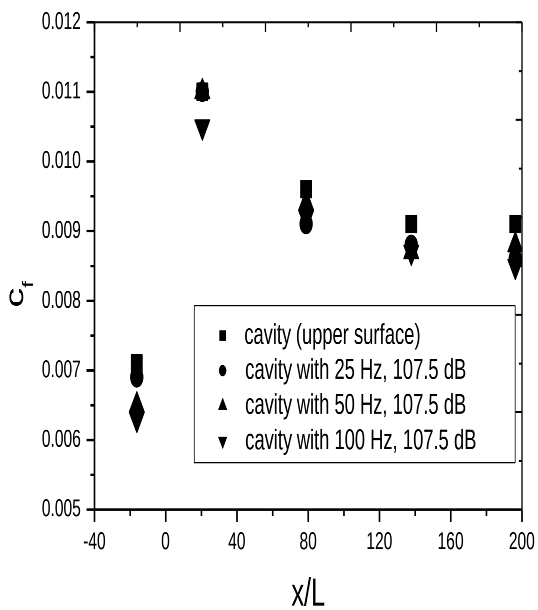


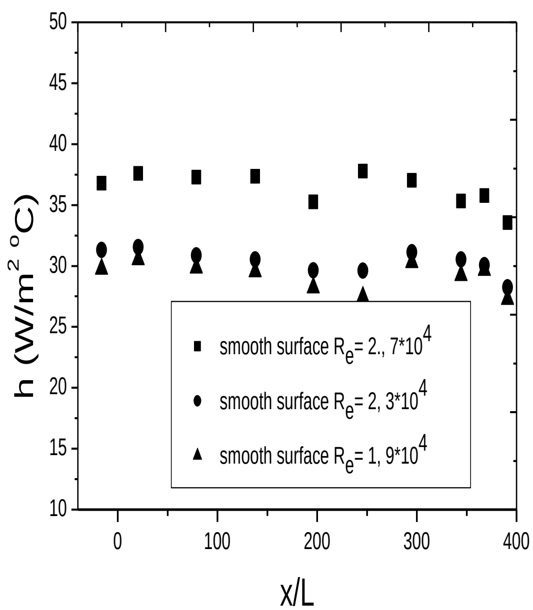


**Fig.10. local skin friction coefficient for cavity with excitation and without excitation with different frequencies at Re= 2.3*10$^4$.**

**Fig.11. variation of local heat transfer coefficient along smooth surface at different Re numbers**

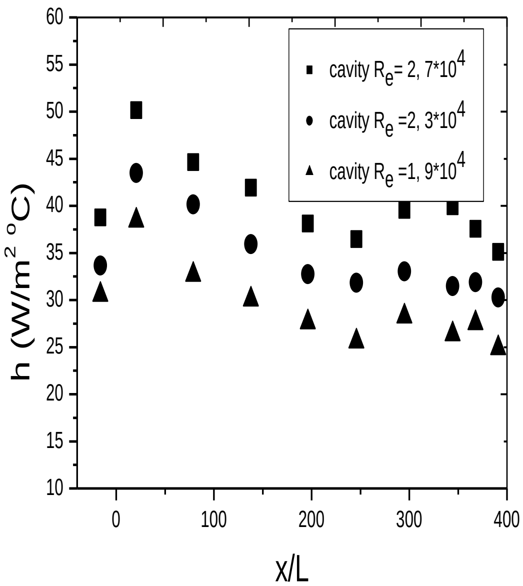


**Fig.12. variation of local heat transfer coefficient along cavity without excitation.**

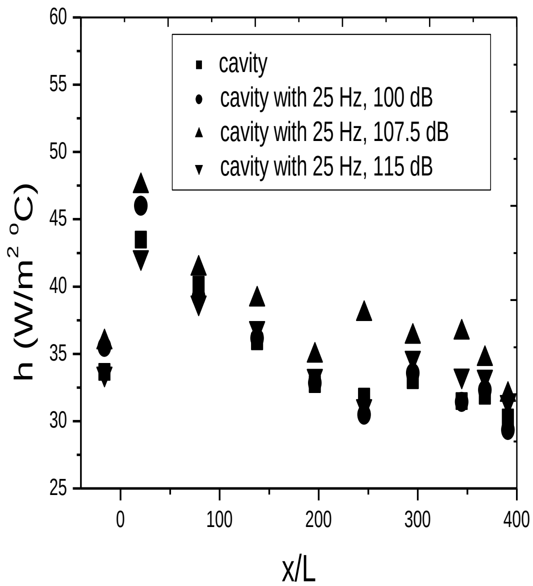


**Fig.13. influence of excitation the cavity with different levels on the local heat transfer coefficient at Re= $2.3*10^4$.**

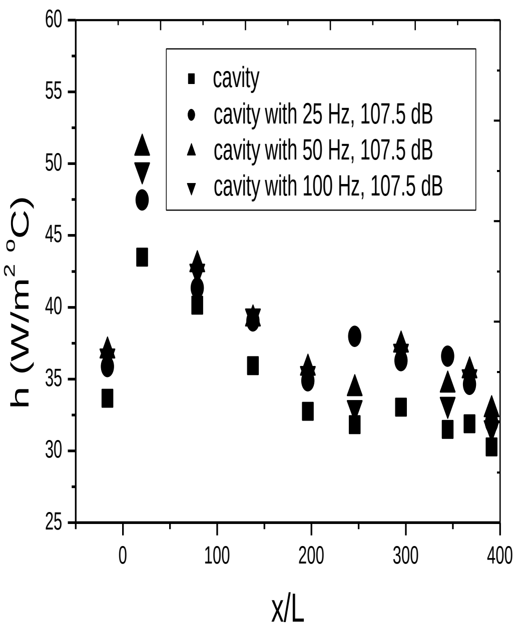


**Fig.14.influnce of excitation the cavity with different frequencies on the local heat transfer coefficient at Re= $2.3*10^4$.**

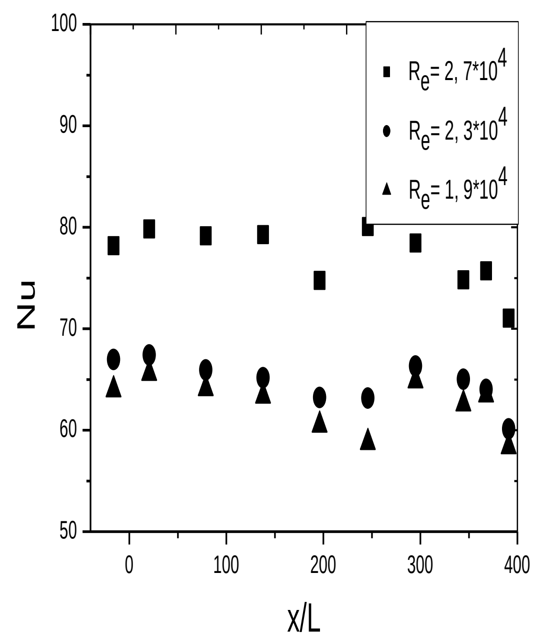


**Fig.15. variation of local Nu along smooth surface at different Re numbers.**

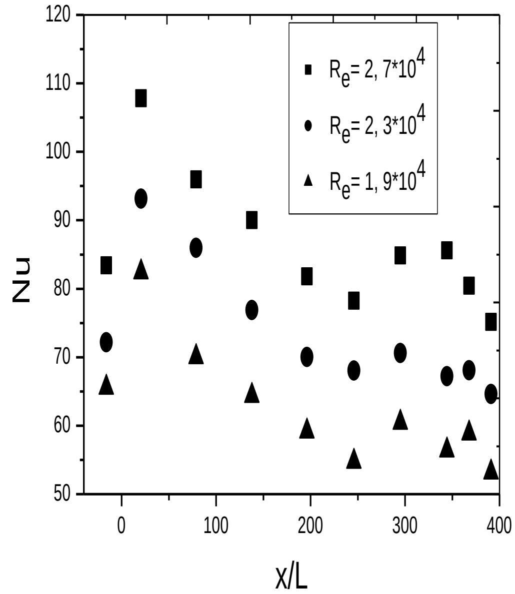


**Fig.16. variation of Nu along cavity without excitation at different Re numbers.**

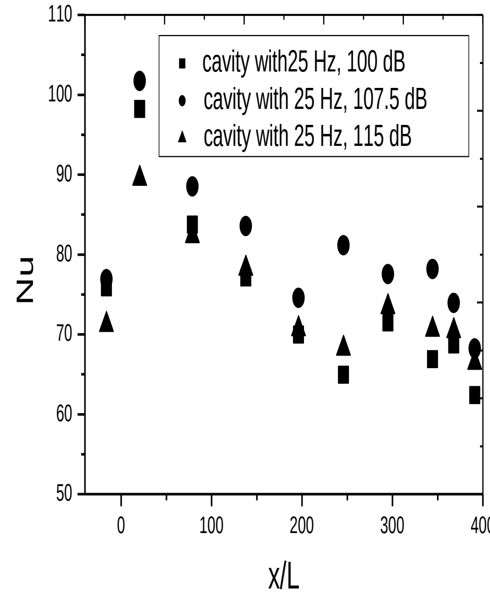


**Fig.17. influence of excitation cavity with different levels on local Nu at Re= 2.3*10$^4$.**

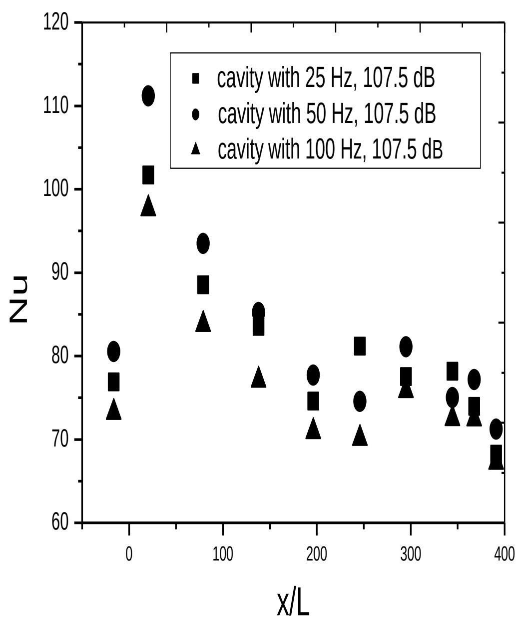


**Fig.18. influence of excitation cavity with different frequencies on local Nu at Re= 2.3*10$^4$.**

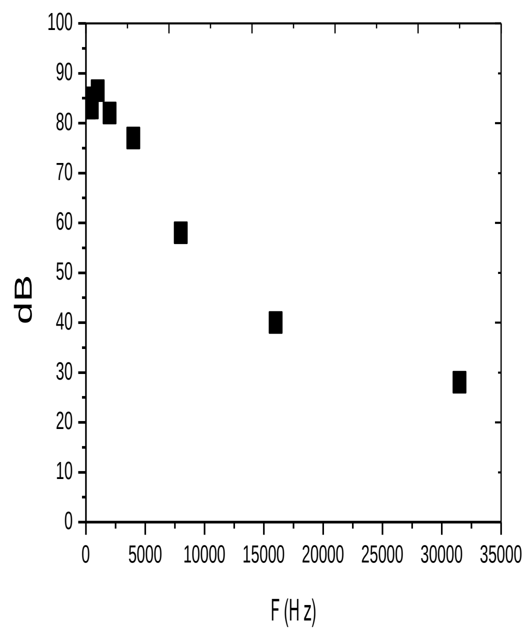


**Fig.19. sound pressure level for cavity without excitation at Re= 2.3*10$^4$.**

**Table.1. Comparison between present work and reference [5]**

| | Re | $C_f$ | Nu |
|---|---|---|---|
| present work | $2.3*10^4$ | 0.0085 | 65.0 |
| | $1.9*10^4$ | 0.0091 | 62.0 |
| refrence [5] | $4.0*10^4$ | 0.0064 | 76.0 |
| | $3.0*10^4$ | 0.0070 | 61.0 |

# DAMAGE DETECTION IN ROTATING BLADE BY VIBRATIONAL ANALYSIS USING FINITE ELEMENT METHOD

Dr.Nabil H. H. Univ. of Baghdad College of Eng.

Shwan A. Z. Univ. of Baghdad College of Eng.

**ABSTRACT**

The development of monitoring systems for rotating blade has been driven by a desire to reduce the maintenance costs and human interaction to improve the safety, reliability and operational life, so it is urgent to monitor the integrity of a structural systems. In this study four different coordinate system has been used to describe the blade motion, then an element stiffness and mass matrices has been formulated by using Hamilton's principle and finite element method, where each element has been described by seven degrees of freedom, so the method has been demonstrated analytically on a finite element model to estimate the modal parameters under rotating and non-rotating conditions in vacuum (to eliminate aerodynamic effect and damping coefficient) and to capture centrifugal effect, so the damage has been simulated by stiffness reduction of assumed elements and by crack form . These results was reasonable, so many parameters has been investigated such as, damage severity, damage location and the effect of rotation speed on these methods have been studied, as well as an assessment has been provided for these methods via statistic to suggest the effective method and this is the main objective, so The Residual Error Method was the best,compared with other methods. All formulations and computations has been coded in MATLAB version 7.

**الخلاصة:**

حصل التطوير في مراقبة الريش الدوارة لتقليل كلفة الصيانة وتقليل استخدام الايدي العاملة لتحسين ظروف السلامة والمحافظة على العمر الافتراضي للريشة , لذا كان من الضروري مراقبة كمالية الريشة.

استخدمت في هذه الدراسة اربعة Coordinate Systems لوصف حركية الريشة ومن ثم صياغة مصفوفتي الجساءة والكتلة باستخدام مبدأ Hamilton Principle هاملتون وطريقة العناصر المحددة FEMمحاور , حيث ان كل عنصر يحوي سبع درجات من الحرية, وبهذا استخدم الحل العددي لحساب الترددات الطبيعية واشكالها الاهتزازية اثناء سكون الريشة واثناء دورانها في الفراغ (لتقليل تأثيرقوة الهواء) و ألتماس تأثير القوة الطاردة المركزية, ومن ثم تمثيل الضرر في الريشة على شكل نقصان في الجساءة وعلى شكل شقوق Cracks .

بالاعتماد على الترددات الطبيعية واشكالها الأهتزازية تم استخدام عدة طرق لكشف الأضرار وذلك باستخدام سيناريوهات خاصة بهذه الاضرار ومواقعها على الريشة.

تم التوصل الى نتائج معقولة , وقد تم دراسة بعض المتغيرات مثل شدة الضرر , موقعه وتأثير سرعة دوران الريشة على طرق الكشف المستخدمة , ومن ثم تقييم هذه الطرق لاقتراح الطريقة الفعالة وهذا هو الغرض الرئيسي من هذه الدراسة, تم استخدام برنامج الحاسبةMATLAB7 كما تم الوصول الى استنتاجات مقبولة ايضا.

**KEYWORDS: Damage, Rotating blade, Finite element method.**

## INTRODUCTION:

In the past few years the problem of health monitoring and fault detection of structures has received considerable consideration. It was noted that fault causes changes in the dynamic response of the structure, so the change can be considered as an indication of damage in a structure, consequently the scheme of fault detection are based on the comparison of the dynamic response of healthy structure with the dynamic response of defected structure.Vibration analysis has been found as an important tool in the investigations of the dynamical behavior of many industrial applications like many types of rotating blade such as axial fan, impeller, turbine, helicopter and wind turbine blades … etc.

Blade failure normally occurs when the blade is vibrating at or near resonant condition and there are many factors that can induce a damage in a mechanical structure such as , a general environmental attacks, erosion, corrosion, creep, fatigue, where the fact that many factors can contribute to form a crack (**Al-said** et al 2006), so it is the most common type of defects that occurs in structures(**Mohammad** and **Omar** 2003).

A crack in a structure introduces a local flexibility which is a function of the crack depth, and this flexibility changes the stiffness and the dynamic behavior of the structure (**Ricci** and **Viola** 2002) , so numerous attempts to quantify local defects are reported to the literature, generally the damage reduce the natural frequencies of a structure because it becomes more flexible, where this fact had been extensively used to detect the presence of damage in a structural component, so the damage is simulated by reducing the stiffness of assumed elements and by crack form also.

An important factor which based on damage detection research is the implementation of reasonable damage models. The models must accurately reflect the physics of the damage, and be compatible with the damage evaluation techniques which discussed in chapter five. Although there are many ways in which the rotor system can be damaged, this work will be limited to two categories of faults:

1- Distributed stiffness faults. 2-Cracks.

The global stiffness matrix has been developed for the eigenvalue problem ( **Herrera** 2005).

## BLADE KINEMATICS AND COORDINATE SYSTEMS:

Four different coordinate system are used to describe the blade motion. These coordinate systems, as listed, are the inertial, hub-fixed, undeformed-blade and deformed-blade coordinate systems. The inertial coordinate system $(X_1, Y_1, Z_1)$ with unit vectors $\hat{\imath}_1, \hat{\jmath}_1, \hat{k}_1$ is a ground-fixed reference frame and there is no fuselage motion and the hub fixed coordinate system $(X_H, Y_H, Z_H)$ with unit vectors $\hat{\imath}_H, \hat{\jmath}_H, \hat{k}_H$ is assumed parallel to the inertial coordinate system, as shown in Fig. (1) .

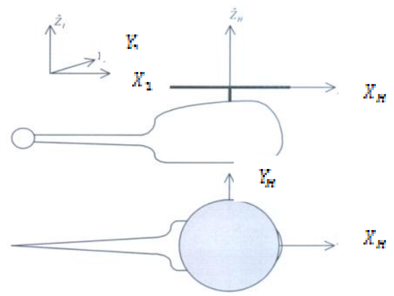

**Fig. (1) Inertial and hub fixed coordinate system**

The undeformed-blade coordinate system(x,y,z)with unit vectors $\hat{\imath}, \hat{\jmath}, \hat{k}$ is attached to the undeformed blade. The *z* axis of the undeformed-blade coordnate is parallel to the $Z_H$ axis of the hub fixed coordinate system and the blade is rotating about this axis at a constant angular velocity Ω, as in Fig.(2) as well as the x-axis lies along the blade elastic axis and the *y*-axis is in the plane of rotation. In some rotor systems the equilibrium flap position is not parallel to the hub plane and this "precone" is incorporated to relieve stress in the blade root, so precone angle is neglected in this derivation because it is very small (**Hodges** and **Dowell** 1974). The transformation between the hub-fixed non-rotating and undeformed-blade coordinate systems is defined as:

$$\begin{Bmatrix} \hat{\imath} \\ \hat{\jmath} \\ \hat{k} \end{Bmatrix} = \begin{bmatrix} \cos\psi & \sin\psi & 0 \\ -\sin\psi & \cos\psi & 0 \\ 0 & 0 & 1 \end{bmatrix} \begin{Bmatrix} \hat{I}_H \\ \hat{J}_H \\ \hat{k}_H \end{Bmatrix} = T_{UH} \begin{Bmatrix} \hat{I}_H \\ \hat{J}_H \\ \hat{k}_H \end{Bmatrix} \tag{1}$$

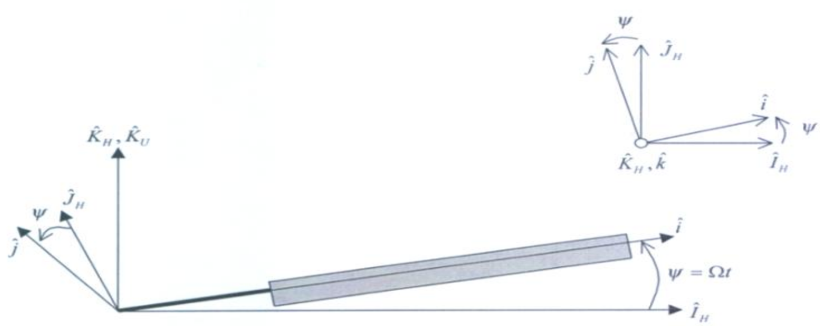

**Fig. (2) Transformation between hub and undeformed blade coordinate systems**

The final coordinate system to discuss is the deformed-blade coordinate system (ξ , η , ζ) with unit vectors $\hat{\imath}_\xi, \hat{\jmath}_\eta, \hat{k}_\zeta$ . The transformations to get this last coordinate system is shown in Fig.(3).The elastic axis undergoes flap deflection, which contributes both a translation (*w*) and then undergoes a negative rotation( $w'$ ), about the undeformed-blade axis-*y* , as shown in Fig. (3 a) . At this point the blade elastic axis is coincident with the $\xi$ axis of the deformed-blade coordinate system, then the blade cross section undergoes twist $(\theta_1)$ about the elastic axis $\xi$, as shown in Fig.(3 b), where the total blade pitch $\theta_1$ is expressed as:

$$\theta_1 = \theta_0 + \phi \tag{2}$$

Where $\Theta_0$ is the pitch angle due to control and it is very small, and $\phi$ is the elastic twist.

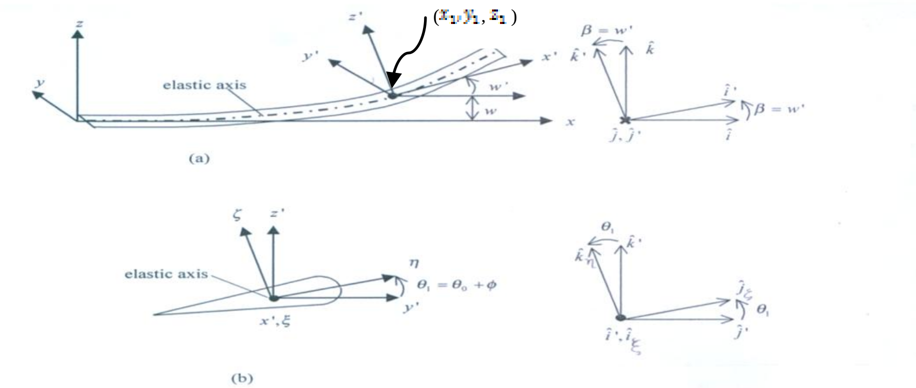

**Fig. (3) Transformations from undeformed-blade to deformed-blade coordinate systems and blade cross section coordinate system**

The transformation from the deformed-blade to undeformed-blade coordinate systems as in Fig. (3) is given as following(**Stevens** 2001):

$$\begin{Bmatrix} \hat{i} \\ \hat{j} \\ \hat{k} \end{Bmatrix} = \begin{bmatrix} \cos\beta & -\sin\beta\sin\Theta & -\sin\beta\cos\Theta \\ 0 & \cos\Theta & -\sin\Theta \\ \sin\beta & \cos\beta\sin\Theta & \cos\beta\cos\Theta \end{bmatrix} \begin{Bmatrix} \hat{i}_\xi \\ \hat{j}_\eta \\ \hat{k}_\zeta \end{Bmatrix} = T_{UD} \begin{Bmatrix} \hat{i}_\xi \\ \hat{j}_\eta \\ \hat{k}_\zeta \end{Bmatrix} \tag{3}$$

Where $\beta$ and $\Theta$ are Euler angle and can be approximated by Eq. (4).

$$\cos\beta = \sqrt{1 - w'^2} \quad , \quad \sin\beta = w' \quad , \quad \Theta = \Theta_1 \tag{4}$$

Substituting these approximations into Eq.( 3) yields a more useful form of the transformation from deformed to undeformed coordinate systems, and by using local linear approximation .

$$T_{UD} = \begin{bmatrix} \left(1 - \frac{w'^2}{2}\right) & -w'\sin\Theta_1 & -w'\cos\Theta_1 \\ 0 & \cos\Theta_1 & -\sin\Theta_1 \\ w' & \left(1 - \frac{w'^2}{2}\right)\sin\Theta_1 & \left(1 - \frac{w'^2}{2}\right)\cos\Theta_1 \end{bmatrix} \tag{5}$$

The origin of the deformed - blade coordinate system is the blade elastic axis, and a chordwise locations must be defined relative to this point, as shown in Fig.(4), where the center of gravity is at a distance ($eg$) from the elastic axis; and ($eg$) is assumed positive forward.

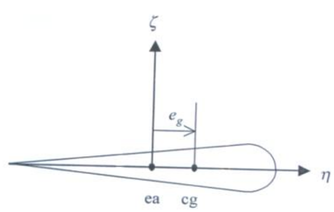


**Fig. (4) The location of elastic axis and center of gravity on the chord**

**HAMILTON'S PRINCIPLE:**

Hamilton's principle is used to derive the finite element equations to describe the rotor systems. Hamilton's principle for conservative systems states that the true motion of a system between two arbitrary moments in time integral of the difference between potential and kinetic energies . If the system is subject to non-conservative forces, such as the aerodynamic forces imposed , so the virtual work terms must be included , and Hamilton's Principle may be expressed as ( **Hodeges** and **Dowell** 1974):

$$\delta\Pi = \int_{t_1}^{t_2} (\delta T - \delta U + \delta W)dt = 0 \tag{6}$$

Where the variation of blade strain energy $\delta U$in terms of engineering stress-strain relation, is given by:

$$\delta U = \int_0^R \iint_A (\sigma_{xx}\delta\varepsilon_{xx} + \sigma_{x\eta}\delta\varepsilon_{x\eta} + \sigma_{x\zeta}\delta\varepsilon_{x\zeta})\, d\eta d\zeta dx \tag{7}$$

$$(\sigma_{xx} = E\varepsilon_{xx} \quad , \quad \sigma_{x\eta} = G\varepsilon_{x\eta} \quad , \quad \sigma_{x\zeta} = G\varepsilon_{x\zeta}) \tag{8}$$

The engineering strains can be expressed in terms of translation displacement ( $w$ ) , rotation ( $w'$), curvature ($w''$), twist ($\phi$), twist rate($\phi'$), also we should refer that the non-dimensional scheme is used for the ensuing derivations, where this scheme is necessary in order to increase the generality of the analysis in the numerical implementation , therefore for the flap-torsion case the non-dimensional variation in strain energy becomes (**Stevens** 2001):

$$\frac{\delta U}{m\Omega^2 R^3} = \int_0^1 (EI_{yy}(\cos\theta_0)^2 w''\delta w'' + \frac{m\Omega^2}{2}(R^2 - x^2)w'\delta w' + GJ\phi'\delta\phi' )\, ds \tag{9}$$

Where the tension is given as (**Solaiman** 1999). As well as the kinetic energy of the blade depends on the blade velocity. Since fuselage motion is not accounted for this derivation , the blade velocity is due only to the blade motion relative to the hub , as well as the derivation describes only flap and twist motion of the blade , so the position of an arbitrary point after the beam has deformed is given by ($x_1, y_1, z_1$ ), see Fig. (3)

$$\left.\begin{aligned} x_1 &= x + u - w'(\eta\sin\theta_1 + \zeta\cos\theta_1) \\ y_1 &= \eta\cos\theta_1 - \zeta\sin\theta_1 \\ z_1 &= w + \eta\sin\theta_1 + \zeta\cos\theta_1 \end{aligned}\right\} \tag{10}$$

Then differentiating the position vector with respect to the hub-fixed non-rotating coordinate system yield (**Stevens** 2001):

$$\overrightarrow{V_b} = \overrightarrow{V_{bx}}\hat{\imath} + \overrightarrow{V_{by}}\hat{\jmath} + \overrightarrow{V_{bz}}\hat{k} \tag{11}$$

$$\delta T = \int_0^R \iint_A \rho\overrightarrow{V_b}.\delta\overrightarrow{V_b}\, d\eta d\zeta dx \qquad \text{(variation in kinetic energy)} \tag{12}$$

From Eq.(12)-( 14) and via integrating by parts as in reference, the non−dimensional variation of kinetic energy becomes:

$$\frac{\delta T}{m\Omega^2 R^3} = \int_0^1 (T_w\delta w + T_{w'}\delta w' + T_\phi\delta\phi)\, ds \tag{13}$$

$$\left.\begin{aligned}
&T_w = -m\ddot{w} - \ddot{\phi} m e_g \cos\Theta_0 \\
&T_{w'} = -x m e_g \Omega^2 \sin\Theta_0 - \phi x m e_g \Omega^2 \cos\Theta_0 \\
&T_\phi = -\ddot{w} m e_g \cos\Theta_0 - \ddot{\phi} m \mathrm{k}_m^2 - w' x m e_g \Omega^2 \cos\Theta_0 \\
&\;-m\Omega^2 (\mathrm{k}_{m2}^2 - \mathrm{k}_{m1}^2)\cos\Theta_0 \sin\Theta_0 - \phi m\Omega^2 (\mathrm{k}_{m2}^2 - \mathrm{k}_{m1}^2)\cos 2\Theta_0 \\
&\mathrm{m}\mathrm{k}_{m1}^2 = \iint_A \rho\, \zeta^2 \, d\eta d\zeta \,;\, m\mathrm{k}_{m2}^2 = \iint_A \rho\, \eta^2 \, d\eta d\zeta \,;\, \mathrm{k}_m = \sqrt{\mathrm{k}_{m1}^2 + \mathrm{k}_{m2}^2}
\end{aligned}\right\} \tag{14}$$

So the virtual work $\delta W$ of non-concentrative forces may be expressed as:

$$\delta W = \int_0^R (\mathrm{L}_w^A \delta w + \mathrm{M}_\phi^A \delta\phi)\, dx \tag{15}$$

The terms due to the blade airfoil are ($\mathrm{L}_w^A$), where the distributed air load in the($z$)direction, and ($\mathrm{M}_\phi^A$) the aerodynamic pitching moment about undeformed elastic axis, but In this study the aerodynamic effects are not included .

## BLADE FINITE ELEMENT:

The spatial finite element equations of motion are derived in this section , and the generalized Hamilton's principle must be written in the non-dimensional form, so the discredited form in Eq.( 16):

$$\delta\Pi = \int_{\bar{\psi}_1}^{\bar{\psi}_2} \sum_{i=1}^{N} (\delta T_i - \delta U_i + \delta W_i)\, d\bar{\psi} = 0 \tag{16}$$

The blade finite element discretization is shown in Fig. (5), where the blade is discredited into $N$ beam elements, each consisting of seven degrees of freedom , so these degrees of freedom are distributed among three nodes, two external and one internal, as well as the displacement of the left hand node is described by lateral displacement, slope and twist denoted as ($w_A$ , $w_A'$ and $\phi_A$ ), likewise the displacement of the right hand node is described by ($w_B$ , $w_B'$ and $\phi_B$ ), and the displacement of the internal node is described only by a twist ($\phi_M$). Elemental boundary conditions requires continuity of displacement and slope of flap deflection and continuity of displacement of elastic twist.

Within each element, deformations between the nodes are described using shape functions, where these shape functions, are derived from a cubic Hermetian polynomial for flap deformation and a quadratic polynomial for torsion deformation (Rao S. S. 1989), and by using these shape functions the continuous deflections over a beam elements can be expressed in terms of the nodal displacements $\boldsymbol{q}_i$ , as in Eq. (17).

$$\mathbf{u}(s) = \begin{Bmatrix} w(s) \\ \phi(s) \end{Bmatrix} = \begin{bmatrix} H_w & 0 \\ 0 & H_\phi \end{bmatrix} \boldsymbol{q}_i \tag{17}$$

$$\mathbf{q}_i^T = [w_A , w_A' , w_B , w_B' , \phi_A , \phi_M , \phi_B ] \quad \text{(elemental nodal displacement vector)} \tag{18}$$

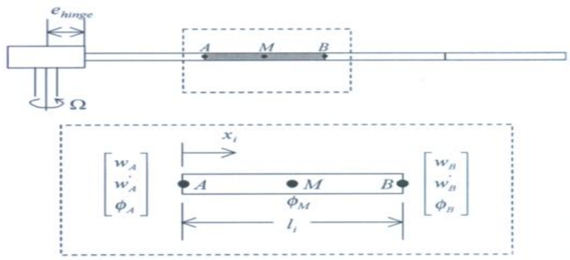


**Fig. (5) Finite element discretization and elemental degrees of freedom**

The polynomials for the bending and torsion shape functions are given in Eq.(19), respectively, where $s=\frac{x_i}{L_i}$ and $L_i$ is the length of the $i^{th}$ beam element.

$$H_w^T=\begin{Bmatrix}H_{w1}\\H_{w2}\\H_{w3}\\H_{w4}\end{Bmatrix}=\begin{Bmatrix}2s^3-3s^2+1\\l_i(s^3-2s^2+s)\\-2s^3+3s^2\\l_i(s^3-s^2)\end{Bmatrix}\quad,\quad H_\phi^T=\begin{Bmatrix}H_{\phi1}\\H_{\phi2}\\H_{\phi3}\end{Bmatrix}=\begin{Bmatrix}2s^2-3s+1\\-4s^2+4s\\2s^2-s\end{Bmatrix}\tag{19}$$

The variations in displacements $(\delta w)$ and $(\delta\phi)$ can be written in terms of variations in nodal displacements as in Eq. (20).

$$\delta\mathbf{u}(s)=\begin{Bmatrix}\delta w(s)\\\delta\phi(s)\end{Bmatrix}=\begin{bmatrix}H_w&0\\0&H_\phi\end{bmatrix}\delta\boldsymbol{q}_i\tag{20}$$

Looking more closely at the expression for variations in strain and kinetic energies, as in Eq. (9) and (13). It is clear that the total energy also depends on ($\delta w'$,$\delta w''$ and $\delta\phi'$), so these variations are found by spatially differentiating for Eq.(20). Since the variations in nodal degrees of freedom $(\delta\boldsymbol{q}_i)$are discrete; the shape functions capture the spatial variation as in Eq. (21) , where :

$$\{\delta w'(s)\}=[H'_w]\begin{Bmatrix}\delta w_A\\\delta w'_A\\\delta w_B\\\delta w'_B\end{Bmatrix}\ ,\ \{\delta w''(s)\}=[H''_w]\begin{Bmatrix}\delta w_A\\\delta w'_A\\\delta w_B\\\delta w'_B\end{Bmatrix}\ ,\ \{\delta\phi'(s)\}=[H'_\phi]\begin{Bmatrix}\delta\phi_A\\\delta\phi_M\\\delta\phi_B\end{Bmatrix}\tag{21}$$

## ELEMENTAL MATRICES:

The expressions is integrated by parts, so the mass and stiffness matrices are identified by separating acceleration, and displacement terms, then the virtual energy expression in terms of the elemental matrices becomes:

$$\delta\Pi=\int_{\bar\psi_1}^{\bar\psi_2}[\textstyle\sum_{i=1}^{N}\delta\boldsymbol{q}_i^T(\boldsymbol{M}_i^b\,\ddot{\boldsymbol{q}}_i+\boldsymbol{K}_i^b\,\boldsymbol{q}_i)]\,d\bar\psi\quad=0\tag{22}$$

There are no structural contributions for damping in the preceding formulation to facilitate the simulation in *vacuum* cases, so there are no aerodynamic effects.The elemental mass and stiffness matrices can be partitioned to indicate contributions from flap bending and elastic torsion.

$$[\boldsymbol{M}_i^b] = \begin{bmatrix} M_{ww}^b & M_{w\phi}^b \\ M_{\phi w}^b & M_{\phi\phi}^b \end{bmatrix} \quad , \quad [\boldsymbol{K}_i^{str}] = \begin{bmatrix} K_{ww}^{str} & K_{w\phi}^{str} \\ K_{\phi w}^{str} & K_{\phi\phi}^{str} \end{bmatrix} \quad , \quad [\boldsymbol{K}_i^{CF}] = \begin{bmatrix} K_{ww}^{CF} & K_{w\phi}^{CF} \\ K_{\phi w}^{CF} & K_{\phi\phi}^{CF} \end{bmatrix} \tag{23}$$

$$[\boldsymbol{K}_i^b] = [\boldsymbol{K}_i^{str}] + [\boldsymbol{K}_i^{CF}] = \begin{bmatrix} K_{ww}^b & K_{w\phi}^b \\ K_{\phi w}^b & K_{\phi\phi}^b \end{bmatrix} \tag{24}$$

$$\left.\begin{array}{l} [M_{ww}^b] = \int_0^1 mH_w^T H_w ds \quad , \quad [M_{\phi\phi}^b] = \int_0^1 mK_m^2 H_\phi^T H_\phi ds \qquad \text{(mass terms)} \\ [M_{w\phi}^b] = \int_0^1 me_g \cos\Theta_0 H_w^T H_\phi \, ds \quad , \quad [M_{\phi w}^b] = \int_0^1 me_g \cos\Theta_0 H_\phi^T H_w \, ds \end{array}\right\} \tag{25}$$

The blade stiffness terms will have components due to both structural and centrifugal terms, where the stiffness terms due to structural properties are:

$$[K_{ww}^{str}] = \int_0^1 EI_{yy} (\cos\Theta_0)^2 H_w''^T H_w'' ds \quad , \quad [K_{\phi\phi}^{str}] = \int_0^1 GJH_\phi'^T H_\phi' ds \quad , \quad [K_{w\phi}^{str}] = [K_{\phi w}^{str}] = 0 \tag{26}$$

Since the rotor blade rotates, the centrifugal forces contribute a significant stiffening effect,where the stiffness terms due to centrifugal loading are given in Eq.(27) .

$$\left.\begin{array}{l} [K_{ww}^{CF}] = \int_0^1 \frac{m\Omega^2}{2}(R^2 - x^2) H_w'^T H_w' ds \quad , \quad [K_{\phi\phi}^{CF}] = \int_0^1 m\,\Omega^2 (K_{m2}^2 - K_{m1}^2) \cos 2\,\Theta_0 H_\phi^T H_\phi \, ds \\ [K_{w\phi}^{CF}] = \int_0^1 xme_g \,\Omega^2 \cos\Theta_0 \, H_w'^T H_\phi ds \quad , \quad [K_{\phi w}^{CF}] = \int_0^1 xme_g \,\Omega^2 \cos\Theta_0 \, H_\phi^T H_w' ds \end{array}\right\} \tag{27}$$

In Eq.(27), the term $\frac{m\Omega^2}{2}(R^2 - x^2)$ is the axial loading due to centrifugal forces at the location $x$ , so in Eq.( 27) $x$ is the distance from the shaft axis to the point on the blade, where a centrifugal force will be at maximum value when $x = 0$ , and a centrifugal force will be zero at $x = R$ .

## ASSEMBLY OF GLOBAL MATRICES:

The elemental degrees of freedom has been ordered according to flap or torsional motion, thus the order was:( $w_A$ , $w_A'$ , $w_B$ , $w_B'$ , $\phi_A$ , $\phi_M$ and $\phi_B$ ).

Via multiplying the elemental mass and stiffness matrices by transformation matrix $t_r$ as in Eq. (28) to get a new reordered stiffness and mass matrices for assembly .

$$[t_r] = \begin{bmatrix} 1 & 0 & 0 & 0 & 0 & 0 & 0 \\ 0 & 1 & 0 & 0 & 0 & 0 & 0 \\ 0 & 0 & 0 & 0 & 1 & 0 & 0 \\ 0 & 0 & 0 & 0 & 0 & 1 & 0 \\ 0 & 0 & 1 & 0 & 0 & 0 & 0 \\ 0 & 0 & 0 & 1 & 0 & 0 & 0 \\ 0 & 0 & 0 & 0 & 0 & 0 & 1 \end{bmatrix} \quad , \quad [\mathrm{K}_{ei}] = [t_r] * [K_i^b] * [t_r] \quad , \quad [\mathrm{M}_{ei}] = [t_r] * [M_i^b] * [t_r] \tag{28}$$

Where $[\mathrm{K}_{ei}]$ is reordered stiffness matrix for $i^{th}$ element and $[\mathrm{M}_{ei}]$ is reordered mass matrix for $i^{th}$ element, so the global matrices is more straightforward if the degrees of freedom are reordered spatially, and the reorder result becomes:( $w_A$ , $w_A'$ , $\phi_A$ , $\phi_M$ , $w_B$ , $w_B'$ , $\phi_B$ ), so the virtual energy becomes:

$$\delta\Pi = \int_{\bar\psi_1}^{\bar\psi_2} \delta \boldsymbol{q}^T (\boldsymbol{M}\ddot{\boldsymbol{q}} + \boldsymbol{K}\boldsymbol{q}) d\bar\psi \quad = 0 \tag{29}$$

Since the virtual displacements $\delta \boldsymbol{q}$ are arbitrary (between any two moments), so the integrand in Eq. (29) must be vanished, then the equation of motion becomes:

$$\boldsymbol{M}\ddot{\boldsymbol{q}} + \boldsymbol{K}\boldsymbol{q} = \boldsymbol{0} \qquad (30)$$

So the modal parameters of a blade is considered(with centrifugal effect and without centrifugal effect) for the undamaged and damaged cases. For the undamped system of several degrees of freedom , the equations of motion expressed in matrix form become:

$$[\mathbf{M}_g]\{\ddot{u}\} + [\mathbf{K}_g]\{\,u\,\}=\{0\} \qquad (31)$$

By using the characteristic equation of the system, so the roots $\lambda_i$ of the characteristic equation are called eigenvalues (Thomson W. T. 1975), so it is possible to find the eigenvectors from the adjoint matrix , and the complete free vibration solution is expressed also. The mode shape vectors has very important properties and known as the orthogonality properties which are described by ( Meirovitch L. 1975), so the most common normalization scheme has been used in modal analysis to normalize the modes with respect to the mass matrix $[\mathbf{M}_g]$.The global displacement vector and matrices has been defined as:

$$\boldsymbol{q}_g = \textstyle\sum_{i=1}^{N} \boldsymbol{q}_i \;, \quad \mathbf{M}_g = \sum_{i=1}^{N} \mathrm{M}_{ei} \;, \quad \mathbf{K}_g = \sum_{i=1}^{N} \mathrm{K}_{ei} \qquad (32)$$

The summations represent the assembly procedure as shown in Fig.(6), where the matrix rows and columns has been reordered to facilitate assembly , then the structural mass and stiffness matrices has been banded. The assembly procedure can be easily modified to accommodate different types of rotor systems, and the assembly method which described in Fig.(5) assumes cantilevered boundary conditions between each element, so the boundary conditions between two elements states that the displacement, slope and twist are continuous at the nodes as :

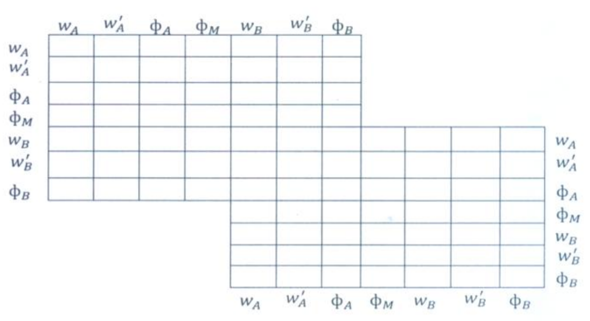


$$\left.\begin{aligned} w_A(i) &= w_B(i-1) \\ w'_A(i) &= w'_B(i-1) \\ \phi_A(i) &= \phi_B(i-1) \end{aligned}\right\} \qquad (33)$$

**Fig. (6) The assembly procedure**

## APPLICATION OF KINEMATICS BOUNDARY CONDITIONS:

Kinematic boundary conditions are applied to the global matrices, and the rotor model assumes that the blade is cantilevered at the root, so the degrees of freedom ($w$, $w'$ and $\phi$) are constrained, and the corresponding rows and columns are removed from the FEM.

## DAMAGE MODELS:

The distributed stiffness fault is modeled as a 10% and 20% reduction in blade bending and torsional stiffness, but for the crack form the damaged element of the beam is modeled with two nodes and two degrees of freedom(transverse displacement and slope) at each node, where the goal is to find a beam finite element that represents the effects of a crack in a beam as shown in Fig(8).In this study the finite element model for the cracked beam with an one-edge and non-propagating was proposed by Qian et al and also used by(**Cacciola** et al 2003), so a crack affects the bending stiffness of the blade only.

## STIFFNESS MATRIX OF THE CRACKED ELEMENT:

An element stiffness matrix of a beam with a crack has been formulated and then a finite element model of a cracked beam has been developed. The strain energy of an element without a crack is:

$$W^{(0)} = \frac{1}{2EI}\int_0^l (M+Pz)^2 dz = \frac{1}{2EI}\left(M^2 l + \frac{P^2 l^3}{3} + MPl^2\right) \quad (34)$$

The flexibility coefficients are expressed by a stress intensity factor in the linear elastic range using Castigliano theorem, so the additional energy in the case of rectangular beam of height $h$ and width $b$ due to the crack can be written as:

$$W^{(1)} = b\int_0^a \left(\frac{K_I^2+K_{II}^2}{E_p} + \frac{(1+\upsilon)K_{III}^2}{E}\right) da \quad (35)$$

Where $E_p = E$ for plane stress, $E_p = E/(1-\upsilon^2)$ for plane strain and(a) is the crack depth, as well as by taking into account only bending, so Eq. (35) leads to:

$$W^{(1)} = b\int_0^a \frac{(K_{IM}+K_{IP})^2+K_{IIP}^2}{E_p}\, da \quad (36)$$

$$K_{IM} = \frac{6M}{bh^2}\sqrt{\pi a}\, F_I(S), \quad K_{IP} = \frac{3Pl}{bh^2}\sqrt{\pi a}\, F_I(S), \quad K_{IIP} = \frac{P}{bh}\sqrt{\pi a}\, F_{II}(S) \quad (37)$$

Where $K_{IM}$, $K_{IP}$, and $K_{IIP}$ are the stress intensity factors for opening type and sliding type of cracks, due to $M$ and $P$ respectively, and $F_I(s)$ and $F_{II}(s)$ are the correction factor , see Fig.(7).

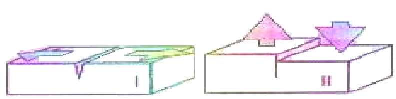


**Mode I : opening mode Mode II :sliding mode**

**Fig. (7) The modes of loading**

$$F_I(s) = \sqrt{\left(\frac{2}{\pi s}\right)\tan\left(\frac{\pi S}{2}\right)}\,\frac{0.923+0.199\left[1-\sin\left(\frac{\pi S}{2}\right)\right]^4}{\cos\left(\frac{\pi S}{2}\right)}, \quad F_{II}(s) = (3S-2S^2)\frac{1.122-0.561S+0.085S^2+0.18S^3}{\sqrt{1-S}} \quad (38)$$

Where (S) is the ratio between crack depth and height of element (a/h), so the elements of the flexibility matrix $c_e^{(0)}$ of the undamaged element can be derived as :

$$c_e^{(0)} = \frac{\partial^2 w^{(0)}}{\partial P_i \partial P_j} \; ; \quad i,j = 1,2 \qquad P_1 = P \;,\; P_2 = M \tag{39}$$

And the element of the additional flexibility matrix $c_e^{(1)}$ are :

$$c_e^{(1)} = \frac{\partial^2 w^{(1)}}{\partial P_i \partial P_j} \; ; \quad i,j = 1,2 \qquad P_1 = P \;,\; P_2 = M \tag{40}$$

Finally the total flexibility matrix for the element with a crack is :

$$c_e = c_e^{(0)} + c_e^{(1)} \tag{41}$$

From equilibrium conditions the following matrix has been found:

$$[\boldsymbol{T}] = \begin{bmatrix} -1 & -L & 1 & 0 \\ 0 & -1 & 0 & 1 \end{bmatrix}^T \tag{42}$$

From the principle of virtual work the stiffness matrix of cracked element can be written as :

$$[K_c] = \boldsymbol{T}\, c_e^{-1}\, \boldsymbol{T}^{\boldsymbol{T}} \quad , \quad [K_u] = [K_{ww}^{str}] = \boldsymbol{T}\; c_e^{(0)-1}\; \boldsymbol{T}^{\boldsymbol{T}} \tag{43}$$

Then the stiffness matrix of cracked element can be written as:

$$[K_c] = [K_{ww}^{str}] \tag{44}$$

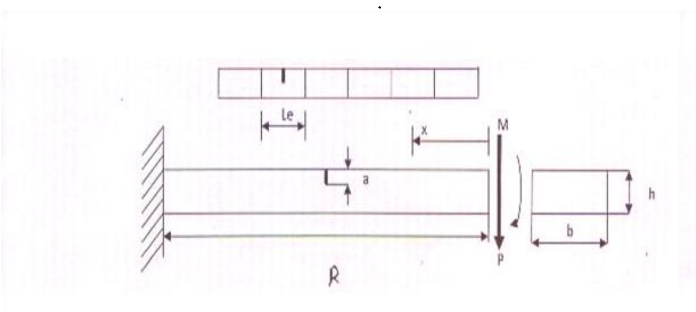


**Fig. (8) Cracked cantilever**

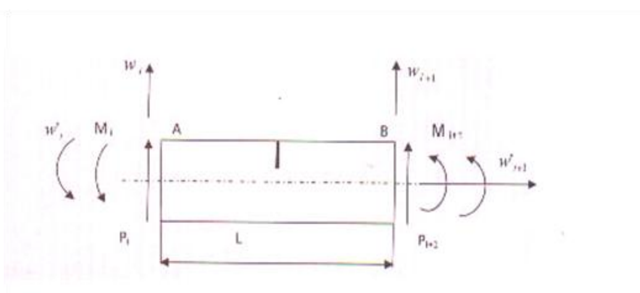


**Fig. (9) Equilibrium conditions of a cracked element**

Then:

$$[K_i^{str*}] = \begin{bmatrix} K_c & K_{w\phi}^{str} \\ K_{\phi w}^{str} & K_{\phi\phi}^{str} \end{bmatrix} \quad , \quad [K_i^{CF}] = \begin{bmatrix} K_{ww}^{CF} & K_{w\phi}^{CF} \\ K_{\phi w}^{CF} & K_{\phi\phi}^{CF} \end{bmatrix} \tag{45}$$

$$[K_i^{b*}] = [K_i^{str*}] + [K_i^{CF}] = \begin{bmatrix} K_{ww}^{b} & K_{w\phi}^{b} \\ K_{\phi w}^{b} & K_{\phi\phi}^{b} \end{bmatrix} \quad , \quad [K_{ei}^{*}] = [t_r] * [K_i^{b*}] * [t_r] \tag{46}$$

Where $[K_{ei}^{*}]$ is the reordered stiffness matrix for $i^{th}$ cracked element, and as mentioned that the damage does not alter the mass of the structure, so :

$$[M^*_{ei}] = [M_{ei}] \qquad (47)$$

## DAMAGE EFFECT ON MODAL PARAMETERS :

The free vibration analysis of a blade with and without damage has been performed, so the cantilever beam is an idealized model for a blade which described. The stiffness and mass matrices will be used for a simple model of blade for analytical study . The following dimensions and material properties of the aluminum blade are listed in table ( 1 ) .

**Table (1) Material properties of the blade**

| | |
|---|---|
| Blade length (R) | 0.594 m |
| Blade width (b) | 0.037 m |
| Blade height (h) | 0.0015 m |
| Modulus of elasticity (E) | 62.1 GPa |
| Modulus of rigidity (G) | 23.3 GPa |
| Mass density (ρ) | 2700 $Kg/m^3$ |
| Poisson's ratio (υ) | 0.34 |

## DAMAGE SCENARIOS:

20 damage scenarios has been investigated and summarized in table (2), where in $1^{st}$ 10 scenarios the damage has been simulated by stiffness reduction of assumed elements, and in $2^{nd}$ 10 scenarios the damage has been simulated in the form of crack, so the finite element model of the blade has been used for the stiffness matrix of the cracked element which described in chapter three. For the finite element analysis the blade has been divided into 20 elements to locate the damage accurately.

Table (2) Damage scenarios

| Damage scenarios | Damaged element | Stiffness reduction % | a/h |
|---|---|---|---|
| D1 | $1^{st}$ (0-0.0297)m | 10 | - |
| D2 | $1^{st}$ (0-0.0297)m | 20 | - |
| D3 | $5^{th}$ (0.1188-0.1485)m | 10 | - |
| D4 | $5^{th}$ (0.1188-0.1485)m | 20 | - |
| D5 | $10^{th}$ (0.2673-0.297)m | 10 | - |
| D6 | $10^{th}$ (0.2673-0.297)m | 20 | - |
| D7 | $15^{th}$ (0.4158-0.4455)m | 10 | - |
| D8 | $15^{th}$ (0.4158-0.4455)m | 20 | - |
| D9 | $5^{th}$ & $10^{th}$ | 10 | - |
| D10 | $5^{th}$ & $10^{th}$ | 20 | - |
| C1 | $1^{st}$ (0-0.0297)m | - | 0.1 |
| C2 | $1^{st}$ (0-0.0297)m | - | 0.2 |
| C3 | $5^{th}$ (0.1188-0.1485)m | - | 0.1 |
| C4 | $5^{th}$ (0.1188-0.1485)m | - | 0.2 |
| C5 | $10^{th}$ (0.2673-0.297)m | - | 0.1 |
| C6 | $10^{th}$ (0.2673-0.297)m | - | 0.2 |
| C7 | $15^{th}$ (0.4158-0.4455)m | - | 0.1 |
| C8 | $15^{th}$ (0.4158-0.4455)m | - | 0.2 |
| C9 | $5^{th}$ & $10^{th}$ | - | 0.1 |
| C10 | $5^{th}$ & $10^{th}$ | - | 0.2 |

## ROTATION SPEED EFFECTS ON MODAL PARAMETERS :

The purpose of this section is to study the centrifugal effect on detection methods, so four rotation speed scenarios has been assumed for two speed of rotation as listed in table (3), where the first two scenarios associated with the stiffness reduction conditions and the second two scenarios associated with the crack conditions .

**Table (3) Rotation speed scenarios**

| Rotation speed scenarios | Damaged element | a/h | Stiffness reduction % | Ω rad/sec |
|---|---|---|---|---|
| SD1 | $5^{th}$ (0.1188-0.1485)m | - | 20 | 0 |
| SD2 | $5^{th}$ (0.1188-0.1485)m | - | 20 | 30 |
| SC1 | $5^{th}$ (0.1188-0.1485)m | 0.2 | - | 0 |
| SC2 | $5^{th}$ (0.1188-0.1485)m | 0.2 | - | 30 |

## METHODS OF DAMAGE DETECTION:

These techniques commonly employed are based on vibration measurement, so in these methods the damage has been detected from alternations in dynamic parameters for healthy and damaged states , so these methods are :

1. Methods based on changes in frequencies and mode shapes like:
   a. Changes in Natural Frequencies .
   b. Eigenparameter Method .
   c. Residual Error Method in The Movement Equation .
2. Methods Based on The Mode Shape Curvature ( Mode Shape Curvature Method).

## A. CHANGE IN NATURAL FREQUENCIES :

Modal frequency shift was presented as a common damage indicator , this section explores the applications and limitations of using modal frequency shifts as damage indicators in rotating blade, where the eigenvalue problem of the undamaged and damaged structure has been estimated by using characteristic equation (**Thomson** 1975) .

## B. EIGENPARAMETER METHOD :

The eigenparameter method was proposed by(**Yuen** 1984), to detect and locate the damage in a cantilever beam, so the eigenequation for undamaged and damaged cantilever can be written as:

$$([\mathbf{K}_g] - \lambda_i[\mathbf{M}_g])\{u_N^{(i)}\} = 0 \;;\; ([\mathbf{K}_g^*] - \lambda_i^*[\mathbf{M}_g^*])\{u_N^{(i)*}\} = 0 \qquad (48)$$

The eigenvalue is chosen in normalized form of damage, and the following eigenparameters has been estimated in the analysis :

$$\{\boldsymbol{U}_{i}\} = \frac{\{u_N^{(i)*}\}}{\lambda_i^*} - \frac{\{u_N^{(i)}\}}{\lambda_i} \tag{49}$$

## C. RESIDUAL ERROR METHOD IN THE MOVEMENT EQUATION:

The Residual error method in the movement equation was proposed by Genovese, and also used by (**Brasiliano** 2003). This method is used to identify a damage present in a structure and locate it by observing the error present in the movement equation:

$$\boldsymbol{Er}=[\mathbf{K}_g][u^*]-([\mathbf{M}_g][u^*])[\Lambda^*] \tag{50}$$

$$\boldsymbol{Er}= [\ e_1\, e_2\, e_3\, e_4 \ldots\ldots\ldots\ldots e_n] \tag{51}$$

$$[u^*]=[\{u^{(1)*}\}\ \{u^{(2)*}\}\ \{u^{(3)*}\} \ldots\ldots\ldots \{u^{(n)*}\}] \tag{52}$$

$$[\Lambda^*] = \begin{bmatrix} \omega_{n1}^{2*} & 0 & \dots & 0 \\ 0 & \omega_{n2}^{2*} & \cdots & 0 \\ \vdots & \vdots & \ddots & \vdots \\ 0 & 0 & \cdots & \omega_{ni}^{2*} \end{bmatrix} \tag{53}$$

Each column of matrix ***Er*** is a vector corresponding to one mode shape and each value of this vector represents the error that occurs in some positions of the blade.

## MODE SHAPE CURVATURE :

This method was proposed by ( **Pandey** et al.1991) , and also used by (**Herrera** 2005) , so this method demonstrate that the absolute changes in mode shape curvature can be used as a good indicator for damage presence of FEM beam structures. The curvature values has been computed from the displacement mode shape by using the central difference approximation for mode *i* and DOF q:

$$\{u_N^{(i)''}\}= \frac{\{u_N^{(i)}\}_{q-1}-2\{u_N^{(i)}\}_q+\{u_N^{(i)}\}_{q+1}}{L_e^2}\ ;\ \{u_N^{(i)''*}\}= \frac{\{u_N^{(i)*}\}_{q-1}-2\{u_N^{(i)*}\}_q+\{u_N^{(i)*}\}_{q+1}}{L_e^2} \tag{54}$$

$$\left\{\Delta\, u_N^{(i)''}\right\}=\left|\left\{u_N^{(i)''*}\right\}-\left\{u_N^{(i)''}\right\}\right| \tag{55}$$

## RESULTS AND DISCUSSION:

The present study is based on bending mode only, where the cracked element associated with the bending mode and only the translation degrees of freedom along the perpendicular axis to the elements (vertical **DOF** in the blade)has been considered,where the rotation degrees in an experimental work are not obtained because of the difficulty in their measurement. As well as the torsion mode affected by rotation speed less than bending mode, for these reasons this study is concentrated on the bending.

## DAMAGE EFFECT ON MODAL PARAMETERS :

The first five natural frequencies for the blade at Ω = 0 (rad/sec) and at Ω = 30 (rad/sec) has been tabulated in tables (4) and (5) for assumed scenarios.

**Table (4) Natural frequencies for the blade at Ω = 0 (rad/sec)**

| scenarios | 1st mode | 2nd mode | 3rd mode | 4th mode | 5th mode |
|---|---|---|---|---|---|
| Present undamaged | 20.6939 | 129.6868 | 363.1318 | 711.6263 | 1176.5 |
| D1 | 20.4826 | 128.5971 | 360.5878 | 707.5026 | 1170.8 |
| D2 | 20.2271 | 127.3253 | 357.7042 | 702.9457 | 1164.7 |
| D3 | 20.5847 | 129.68 | 362.13 | 708.3462 | 1173.8 |
| D4 | 20.4506 | 129.6717 | 360.9180 | 704.4352 | 1170.7 |
| D5 | 20.6626 | 128.9964 | 363.0529 | 708.1019 | 1175.5 |
| D6 | 20.6236 | 128.1537 | 362.956 | 703.8758 | 1174.3 |
| D7 | 20.6908 | 129.3639 | 360.8984 | 709.054 | 1176.2 |
| D8 | 20.6868 | 128.9621 | 358.1819 | 706.01 | 1175.8 |
| D9 | 20.6272 | 129.3548 | 362.6206 | 708.3669 | 1174.7 |
| D10 | 20.5539 | 128.9901 | 362.0612 | 704.8110 | 1172.9 |
| C1 | 20.6851 | 129.6410 | 363.0250 | 711.4557 | 1176.3 |
| C2 | 20.6592 | 129.5061 | 362.7112 | 710.9558 | 1175.6 |
| C3 | 20.6894 | 129.6867 | 363.0910 | 711.4889 | 1176.4 |
| C4 | 20.6761 | 129.6865 | 362.9703 | 711.0838 | 1176.1 |
| C5 | 20.6926 | 129.6581 | 363.1296 | 711.4793 | 1176.5 |
| C6 | 20.6888 | 129.5736 | 363.1229 | 711.0457 | 1176.4 |
| C7 | 20.6938 | 129.6735 | 363.0391 | 711.5199 | 1176.5 |
| C8 | 20.6934 | 129.6344 | 362.7652 | 711.2064 | 1176.5 |
| C9 | 20.6881 | 129.6581 | 363.0887 | 711.3419 | 1176.4 |
| C10 | 20.671 | 129.5733 | 362.9615 | 710.5092 | 1175.9 |
| Frequency decreasing% | 0-2.3 | 0-1.85 | 0-1.51 | 0-1.23 | 0-1.01 |

**Table (5) Natural frequencies for the blade at Ω = 30 (rad/sec)**

| Scenarios | 1st mode | 2nd mode | 3rd mode | 4th mode | 5th mode |
|---|---|---|---|---|---|
| Undamaged | 38.4810 | 150.5482 | 384.6151 | 734.0786 | 1199.6 |
| D1 | 38.2927 | 149.5488 | 382.1778 | 730.0604 | 1194 |
| D2 | 38.0690 | 148.3912 | 379.4244 | 725.6270 | 1188 |
| D3 | 38.4343 | 150.5407 | 383.7020 | 730.9727 | 1196.9 |
| D4 | 38.3774 | 150.5314 | 382.5917 | 727.2765 | 1193.9 |
| D5 | 38.4732 | 149.9810 | 384.5330 | 730.7424 | 1198.5 |
| D6 | 38.4635 | 149.2921 | 384.4325 | 726.7488 | 1197.3 |
| D7 | 38.4804 | 150.2511 | 382.4578 | 731.6352 | 1199.3 |
| D8 | 38.4795 | 149.8832 | 379.8411 | 728.7463 | 1198.9 |
| D9 | 38.4550 | 150.2743 | 384.1418 | 730.9915 | 1197.8 |
| D10 | 38.4266 | 149.9741 | 383.6247 | 727.6265 | 1195.9 |
| C1 | 38.4732 | 150.5061 | 384.5129 | 733.9127 | 1199.3 |
| C2 | 38.4499 | 150.3824 | 384.2125 | 733.4265 | 1198.7 |
| C3 | 38.4791 | 150.5480 | 384.5776 | 733.9484 | 1199.4 |
| C4 | 38.4734 | 150.5476 | 384.4669 | 733.5645 | 1199.1 |
| C5 | 38.4807 | 150.5246 | 384.6126 | 733.9394 | 1199.5 |
| C6 | 38.4798 | 150.4550 | 384.6053 | 733.5288 | 1199.4 |
| C7 | 38.4810 | 150.5360 | 384.5255 | 733.9777 | 1199.6 |
| C8 | 38.4809 | 150.4999 | 384.2606 | 733.6803 | 1199.5 |

| | | | | | |
|---|---|---|---|---|---|
| C9 | 38.4788 | 150.5245 | 384.5751 | 733.8092 | 1199.4 |
| C10 | 38.4721 | 150.4545 | 384.4571 | 733.0145 | 1199 |
| Frequency decreasing% | 0-1.07 | 0-1.43 | 0-1.34 | 0.013-1.15 | 0-0.97 |

The shifting in natural frequencies at (Ω=30 rad/sec)is smaller than the shift at (Ω=0 rad/sec)where the centrifugal effect stiffening the blade so the effect of damage becomes smaller, so the indication for damage presence is clearest at (Ω=0 rad/sec). It is clear also that the maximum shifting occurred at the scenario D2(clearest scenario as it has been mentioned) for the first five natural frequencies where D2 has the severest damage value and the nearest damaged element to the fixed end.

**DAMGE SEVERITY EFFECT:**

The first three natural frequencies have been observed for variant damage severity (from 5% to 60% stiffness reduction and crack depth) at 1st element. It was observed that 1st natural frequencies decrease when the damage severity(stiffness reduction,crack depth)increase, and it was observed also that the, so it is clear also from Fig.(10)that the natural frequencies affected by stiffness reduction more than crack.

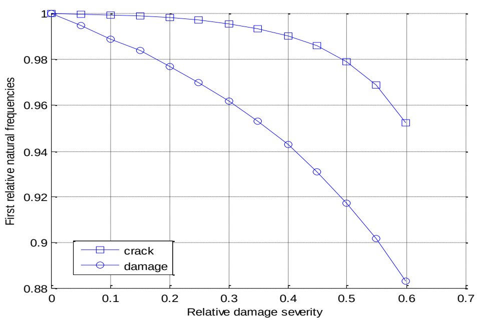


**Fig.(10) Relative natural frequencies and relative damage severity and crack depth (1st mode)**

**ROTATION SPEED EFFECT ON NATURAL FREQUENCIES FOR UNDAMAGED BLADE:**

In order to investigate the effect of the rotation speed nine values have been used (10- 90)rad/sec, and it was clear from Fig.(11) that the natural frequencies increase by rotational speed increasing where the centrifugal force stiffening the blade (due to presence of $K^{CF}$ terms).

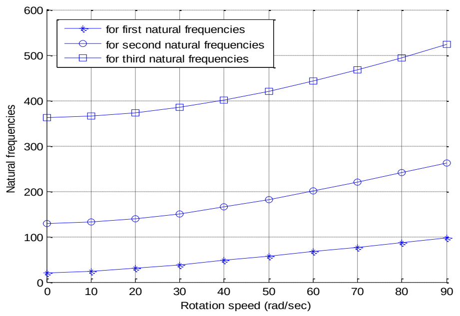


**Fig. (11) The relation between natural frequencies and rotation speed**

**CHANGES IN NATURAL FREQUENCIES:**

The measurement of natural frequencies is the first method to detect the damage, so the results have been tabulated in tables(4)and (5). It is clear from these results that the shifting in natural frequencies is insufficient detection indicator especially at Ω=30 (rad/sec), so changes in natural frequencies being more small when the damaged zone shifted toward free end.

## EIGENPARAMETER METHOD:

For the first mode the slope starts at the damaged location and this slope becomes steeper when the damaged location shifted closer to the fixed end, where the maximum bending has been occurred at this point and when the damage being more sever as shown in Fig.(12)and(13). This method is efficient for damage identification for the cases of single damages. In the cases of multiple damage the method is ineffective, where this method is able to locate the damage at one location only, as shown in Fig.(14) and (15).

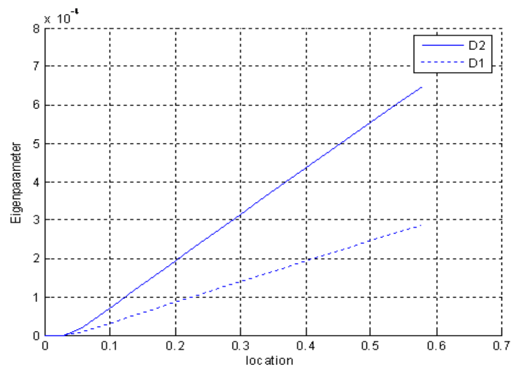


**Fig(12) Eigenparameter for D1,D2 (1st mode)**

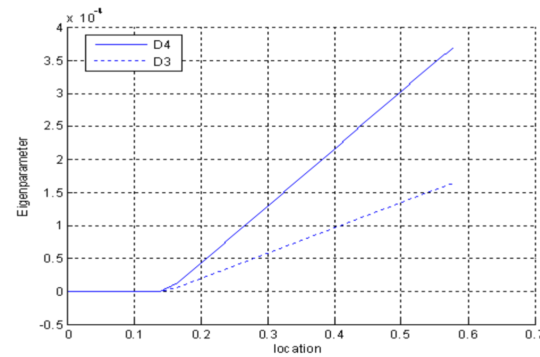


**Fig.(13) Eigenparameter for D3,D4 (1st mode)**

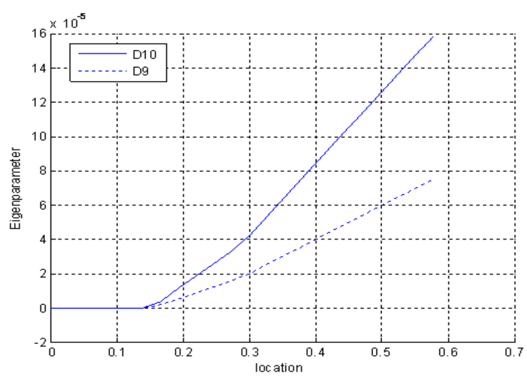


**Fig.(14) Eigenparameter for D9,D10 (1st mode)**

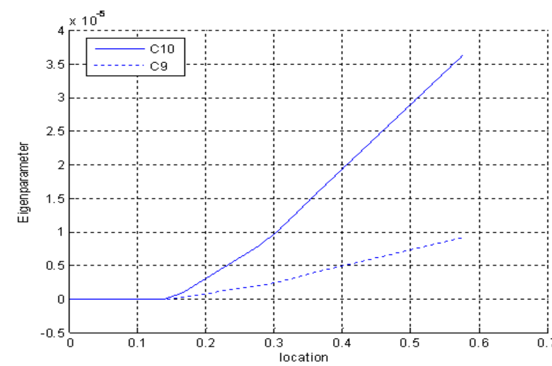


**Fig.(15) Eigenparameter for C9,C10 (1st mode)**

## RESIDUAL ERROR METHOD IN THE MOVEMENT EQUATION:

Error has been presented in the movement equation for damage scenarios and for first three modes as shown in Fig.(16) to Fig.(19), where a positive peak has been displayed at the damaged regions clearly and precisely for all investigated modes and scenarios (single and multiple damage). It is clear that the indication for damage presence will be perceptible when the damage being more sever and closer to the fixed end where the maximum bending has been occurred at this point.

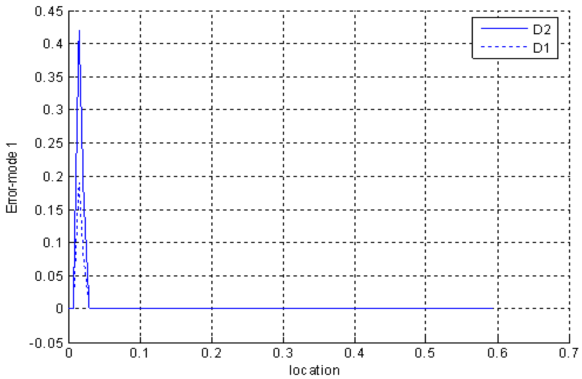


Fig.(16) Residual error for D1.D2 (1st mode)

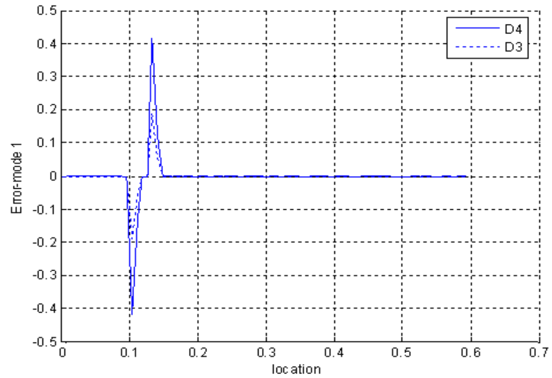


Fig.(17) Residual error for D3.D4 (1st mode)

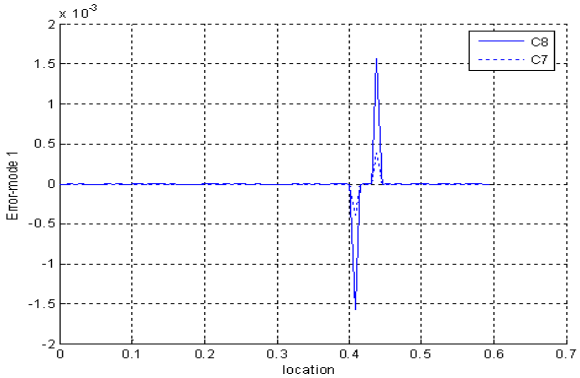


Fig.(18) Residual error for C7,C8 (1st mode)

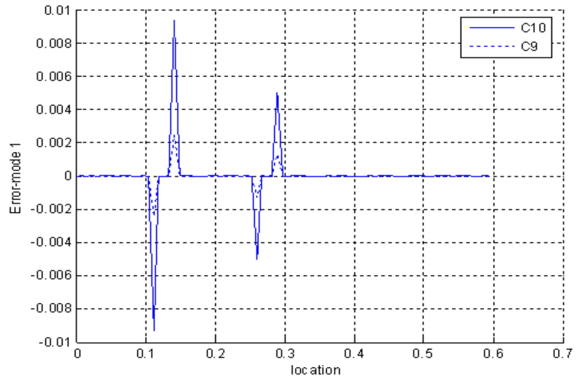


Fig.(19) Residual error for C9,C10 (1st mode)

## MODE SHAPE CURVATURE:

The absolute differences between mode shape curvature of healthy and defected blade for the damage scenarios are plotted. For the cases of single damage the maximum difference for each mode shape curvature has been occurred at damaged zone as shown in Fig.(21)and(22) except scenarios (D1,D2,C1 and C2)where the differences of mode shape curvature are localized near the damaged zone (not at the damaged zone) and it is a difficult task to detect the damage which locates close to the fixed end as in Fig(20),For the cases of multiple damage it has been able to locate the damage at two zone,see Fig.(23)

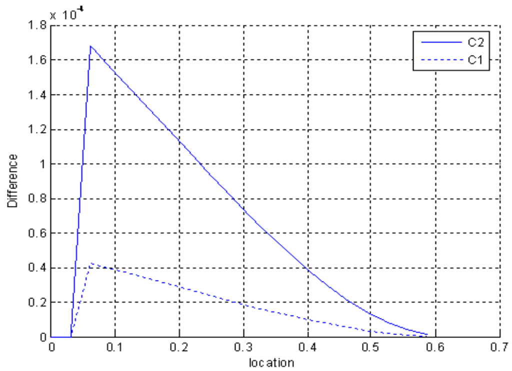


Fig.(20) Absolute diff. for C1,C2 ($1^{st}$ mode)

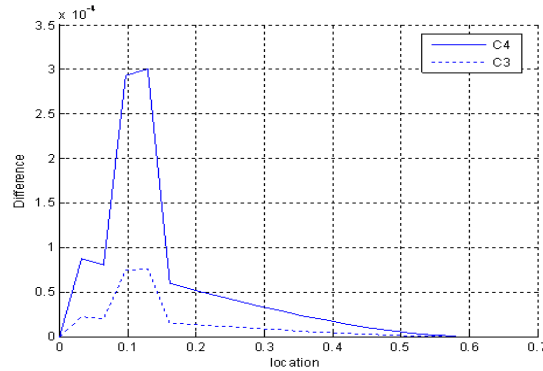


Fig.(21) Absolute diff. for C3,C4 ($1^{st}$ mode)

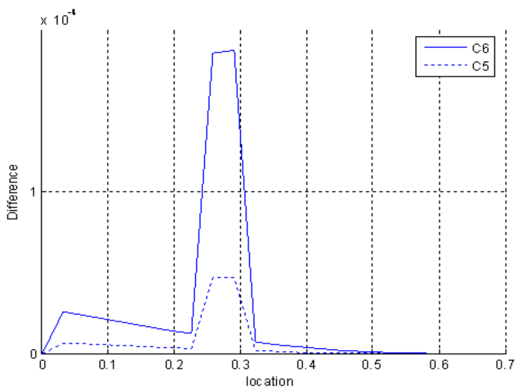


Fig.(22) Absolute diff. for C5,C6 ($1^{st}$ mode)

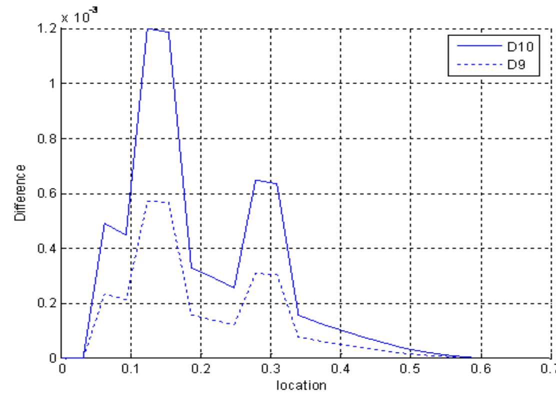


Fig.(23)Absolute diff. for D9,D10 ($1^{st}$ mode)

## ROTATION SPEED EFFECT ON DETECTION METHODS:

The effect of rotation speed on detection methods has been investigated for rotation speed scenarios which listed in table (3) for the first mode only because it is the clearest mode to present the facts as shown in Fig. (24-26) .

The effect of rotation speed has been investigated on the first method (as in tables(4) and (5)) and on the other used methods at two values of $\Omega$ =(0 and 30) rad/sec, as shown in Fig.(24-26). It is clear that the identification for damage presence under non-rotating conditions noticeable, compared with the identification under rotating conditions, where the centrifugal effect stiffening the blade.

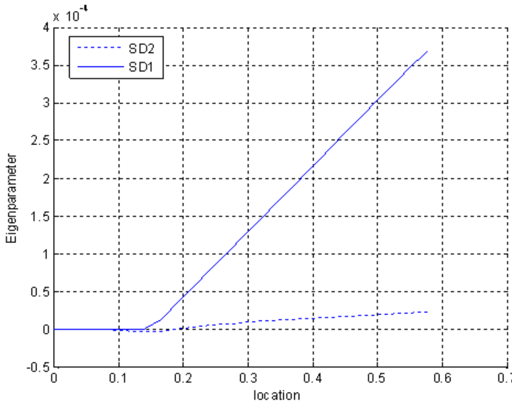


**Fig.(24)Eigenparameter for SD1,SD2**

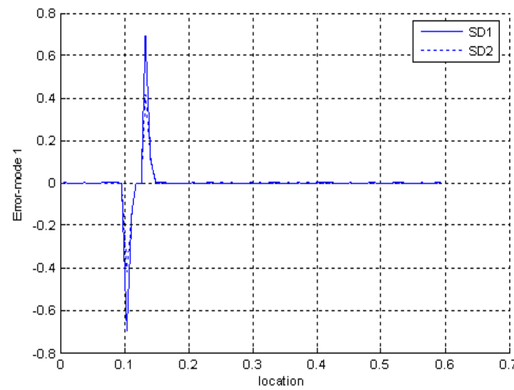


**Fig.(25) Residual error for SD1,SD2**

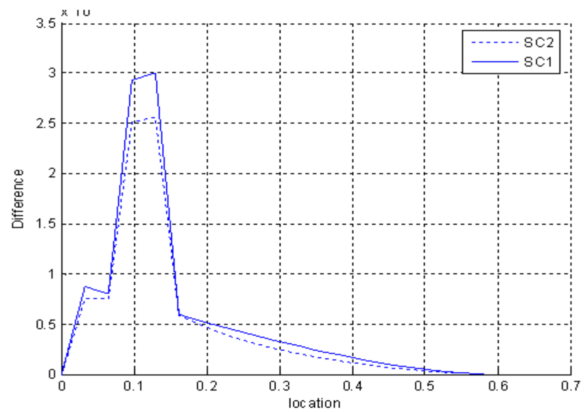


**Fig.(26) Mode shape curvature for SC1,SC2**

## CONCLUSIONS

The main conclusions of the present work according to the results may be summarized as:

- The shifting at natural frequencies only are insufficient to detect the damage , so these frequencies affected by crack depth and stiffness reduction imperceptibly, specially when the damage located far from fixed end, as well as the decreasing in natural frequencies only can not locate the damage .
- The maximum decreasing occurred for the natural frequencies at the severest damage value and the nearest damaged element to the fixed end , and these frequencies decrease with damage accumulation.
- For the same values of damage percent and crack ratio ; the indication for the damage percent case is clearer than the indication for the crack ratio case.
- The natural frequencies increase when the rotational speed increasing , where the centrifugal force stiffening the blade, so the indication for damage presence under non- rotating conditions is clearer than the indication under rotating conditions .
- Residual Error Method in The Movement Equation is very efficient for damage identification, where this method has the ability to identify the damage succefully for the cases of single and multiple damage , so it is effective method to detect and locate the damage.

## REFERENCES


- Al-said Samer Masoud, Naji Malak and Al-Shukry Adnan A., (2006). "Flexural vibration of rotating cracked Timoshenko beam". Journal of vibration and control .
- Mohammad H.F. Dado and Omar A. Shpli, (2003). "Crack parameter estimation in structures using finite element modeling". International Journal of solids and structures .
- Ricci P. and Viola E., (2002). "Formulation of the dynamic behavior of cracked plane frame structures". University of Bologna, Viale Risorgimento 2-40136, Bologna, Italy.
- Herrera J. C., (2005). "Evaluation of structural damage identification methods based on dynamic characteristics". A thesis submitted in partial fulfillment of the requirements for the degree of Doctor of Philosophy in civil engineering / University of Puerto Rico.
- Stevens Patricia Lynn, (2001)."Active interrogation of helicopter main rotor faults using trailing edge flap actuation". A thesis submitted in partial fulfillment of the requirements for the degree of Doctor of Philosophy in Mechanical Engineering/The Pennsylvania state university.
- Hodges D. H. and Dowell E. H., (1974). "Nonlinear equations of motion for the elastic bending and torsion of twisted nonuniform rotor blades". Ames Research Center and U. S. Army Air Mobility RED laboratory Moffett Field , Calif. 94035.
- Rao S. S., (1989). "The finite element method in engineering", (Book). Second edition, Purdue university, West Lafayetta, Indiana, USA.
- Thomson W.T, (1975)."Theory of vibration with applications".(Book ). University of California, USA, printed in India.
- Meirovitch L., (1975)."Elements of vibration analysis". (Book) International student edition.
- Yuen M. M. F., (1984). "A numerical study of the eigenparameters of a damaged cantilever". Journal of Sound and Vibration 103(3), 301-310.
- Brasiliano A., Doz G. N. and Brito J. L.,(2003). "Damage identification in continuous beams and frame structures using the Residual Error Method in the movement equation". Nuclear Engineering and Design 227, 1-17. Cacciola P., Impollonia N. and Muscolino G., (2003). "Crack detection and location in a damaged beam vibrating under white noise". Comuters and Structures 81, 1773-1782.
- Solaiman Solly, (1999). "Dynamic modeling and stability analysis of a smart Hingeless helicopter blade". A thesis submitted in partial fulfillment of the requirements for the degree of Master of Mechanical Engineering/Carleton university.

# ANALYSIS OF CONCRETE FLEXURAL MEMBERS REINFORCED WITH FIBRE POLYMER

Asst. Prof. Dr. Nazar K. Oukaili, Ahlam Ali Al-Asadi
Civil Engineering Department, College of Engineering, University of Baghdad

**ABSTRACT:**

Analytical model is used in this paper to predict the load carrying capacity of structural concrete members under flexural and normal force which can be concentric or eccentric. The analysis is based on requirement of equilibrium and compatibility of strain in concrete and steel or FRP. The adopted model is based on the real stress - strain diagrams for materials. In accordance with this model, the member cross section is covered by a mesh with the smallest cells. After that, stress or strain is determined in each cell and the integral is substituted by the process of summation to define the elements of stiffness matrix. The force vectors equations have nonlinear behaviour. However, in this model, these nonlinear equations are changed to linear equations using the iteration methods with fixity of secant modulus of elasticity in each iteration cycle. In this paper, FORTRAN computer program language is used to compute the force and strains vectors. The comparison between the analytical results obtained from the used model and experimental data for other researchers is performed. The analytical model is giving a reasonable agreement between the theoretical and experimental results.

## تحليل الأعضاء الخرسانية المنحنية المسلحة بالألياف البوليميرية

**الخلاصة:**

في هذه الورقة البحثية تم أقتراح أنموذج تحليلي لتحديد السعة الحملية لعناصر الخرسانية الأنشائية المعرضة للأنحناء والقوة المحورية مركزية اوغيرمركزية. ان طبيعة التحليل تعتمد على شروط الأتزان والتوافق في الأنفعالات في الخرسانة والحديد. يستند الأنموذج المستخدم على المخططات البيانية الحقيقية الكاملة لتشوه الخرسانة والحديد. ان أسلوب الحل وفقآ للأنموذج المقترح يعتمد بشكل أساسي على تغطية المقطع العرضي بشبكة ذات خلايا صغيرة جداً. بعد ذلك يؤخذ متوسط الأجهادات اوالأنفعالات في حدود كل خلية وبالتالي يتم الأنتقال من التكامل التفاضلي الى المجموع التكاملي لتحديد عناصر مصفوفة صلادة المقطع. من جهة أخرى، فان المعادلات الرئيسية لمتجهات القوى لها صفة لا خطية، الا أنه يتم في النموذج المدروس تحويل المعادلات اللاخطية الى معادلات خطية باستخدام الطرق التكرارية مع تثبيت معامل المرونة القاطعي خلال كل دورة تكرار. في هذه الورقة البحثية استخدم برنامج بلغة فورتران لتحديد متجهة القوى والانفعالات الخطية. تمت مقارنة النتائج المستحصلة من هذا الأنموذج مع النتائج المختبرية لعدد من الباحثين. ولوحظ ان الأنموذج التحليلي يعطي توافق معقول بين النتائج النظرية والمختبرية.

**KEYWORDS: Flexural Member, Fibre Reinforced Polymer, Ultimate Moment Capacity, Moment-Curvature diagram**

## INTRODUCTION

Conventional concrete structures are reinforced with nonprestressed and/or prestressed steel. The steel is initially protected against corrosion by the alkalinity of the concrete, usually resulting in durable and serviceable construction. For many structures subjected to aggressive environments, such as marine structures, bridges and parking garages exposed to deicing salts, combinations of moisture, temperature and chlorides reduce the alkalinity of the concrete and result in the corrosion of reinforcing and prestressing steel. The corrosion process ultimately causes concrete deterioration and loss of serviceability. To address corrosion problems, professionals have turned to alternative metallic reinforcement, such as epoxy-coated steel bars. While effective in some situations, such remedies may still be unable to completely eliminate the problems of steel corrosion (cited in ACI 440H, 2000).

Recently, composite materials made of fibres embedded in a polymeric resin, also known as fibre-reinforced polymers (FRP), have become an alternative to steel reinforcement for concrete structures. Because FRP materials are nonmagnetic and non-corrosive, the problems of electromagnetic interference and steel corrosion can be avoided with FRP reinforcement. Additionally, FRP materials exhibit several properties, such as high tensile strength, that make them suitable for use as structural reinforcement (Dolan et al., 1999).

## STRESS-STRAIN MODEL FOR MATERIALS

In 1986, Korpenko (Korpenko et al., 1986) suggested a relationship to predict the stress-strain diagram for concrete and steel under unaxial loads. This relationship unified the stress-strain diagram represented for concrete in tension or compression and all types of steel (mild or high strength steel).

Let:

$$\tilde{\sigma}_m = \left|\frac{\sigma_m}{\hat{\sigma}_m}\right| \quad ; \quad \tilde{\varepsilon}_m = \left|\frac{\varepsilon_m}{\hat{\varepsilon}_m}\right| \tag{1}$$

where:

$\tilde{\sigma}_m$, $\tilde{\varepsilon}_m$: relative level of stress and strain, respectively; $\hat{\sigma}_m$, $\hat{\varepsilon}_m$: stress and strain at the peak of stress-strain diagrams for materials (concrete and steel); $\sigma_m$ , $\varepsilon_m$: stress and strain for materials (concrete or steel); $m$: represents the parameters for concrete and steel, ($m = c, t$: represents the compression or tension in concrete, respectively. $m = s, ps, f$ : represents the nonprestressing, prestressing steel or fibre reinforced polymer, respectively).

The nonlinear behaviour of the stress-strain diagram for materials (concrete or steel) can be represented by the following expression (Korpenko et al., 1986):

$$\sigma_m = \varepsilon_m E_m v_m \tag{2}$$

where:

$E_m$: initial modulus of elasticity for material (concrete or steel); $v_m$: coefficient of elastic strain (represents the elastic strain to the total strain) (Korpenko et al., 1986).

$$\begin{aligned} v_m &= 1, && |\sigma_m| \le |\sigma_{m,el}| \\ v_m &= \hat{v}_m \pm (v_o - \hat{v}_m)\sqrt{1 - e_{1m}\eta_m - e_{2m}\eta_m^2}, && |\sigma_m| > |\sigma_{m,el}| \end{aligned} \tag{3}$$

Where (Korpenko et al., 1986):

$$\eta_m = \frac{\sigma_m - \sigma_{m,el}}{\hat{\sigma}_m - \sigma_{m,el}} = \frac{\tilde{\sigma}_m - \sigma_{m,el}}{1 - \tilde{\sigma}_{m,el}} \le 1 \tag{4}$$

where:
$\sigma_{m,el}$ : proportional limit of material; $\tilde{\sigma}_{m,el}$ : relative level of proportional limit of material; $\hat{v}_m$ : coefficient of elastic strain when the stress $\sigma_m$ reaches the ultimate stress $\hat{\sigma}_m$ ; $v_o$ : coefficient depended on relative level stress for material; $e_{1m}, e_{2m}$ : coefficient depending on type of material (steel or concrete).

$$e_{2m} = 1 - e_{1m} \tag{5}$$

To use Eq.(3), the $e_{1m}$ must be less than 2 (Korpenko et al., 1986).

## Stress-Strain Model for Concrete

The stress-strain diagram of concrete (Fig.1) is represented using Eq.(2) and Eq.(3) by taking the following expressions for coefficient $v_m$ and $e_{1c}$ (Korpenko et al., 1986):

$$\begin{aligned} v_o &= 1 \quad ; \quad \tilde{\varepsilon}_c \le 1 \\ v_o &= 2.05\,\hat{v}_c \quad ; \quad \tilde{\varepsilon}_c > 1 \end{aligned} \tag{6}$$

$$\begin{aligned} e_{1c} &= 1.72 - 1.82\,\hat{v}_c \quad ; \quad \tilde{\varepsilon}_c \le 1 \\ e_{1c} &= 1.95\,\hat{v}_c - 0.138 \quad ; \quad \tilde{\varepsilon}_c > 1 \end{aligned} \tag{7}$$

where:
$\hat{\sigma}_c$: stress at the peak of stress-strain diagram for concrete; $\hat{\varepsilon}_c$: strain at the peak of stress-strain diagram for concrete; $\hat{v}_c$: coefficient of elastic strain when $\sigma_c = \hat{\sigma}_c$; $E_c$: initial modulus of elasticity for concrete; $v_o$: coefficient that depends on the stress level of concrete; $e_{1c}$: coefficient that depends on type of materials.

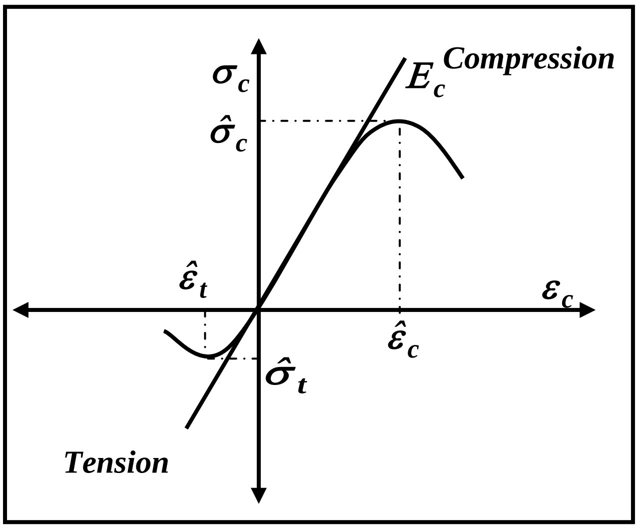


**Figure 1: Stress-strain diagram for concrete (Oukaili, 1998)**

## Stress-Strain Model for Steel

In addition to the general mechanical properties in concrete and steel which are required to simulate the $\sigma - \varepsilon$ diagram; steel has special mechanical characteristics such as yield stress $\sigma_y$ or $\sigma_{0.2}$ and yield strain $\varepsilon_{0.2}$ and coefficient of elastic strain $\nu_{0.2}$.

The elastic stress for high strength steel (Fig.2a) is determined by:

$$\sigma_{s,el} = \beta_{el}\, \sigma_{0.2} \tag{8}$$

Where:
$\sigma_{0.2}$: stress for steel at yield state; $\beta_{el}$: coefficient that depends on steel type.
The coefficient $e_{1s}$ can be found from equation below (Korpenko et al., 1986):

$$e_{1s} = \frac{(v_o - \hat{v}_s)^2 (\eta_{0.2}^2 - 1) + (v_{0.2} + \hat{v}_2)^2}{(\eta_{0.2}^2 - \eta_{0.2})(1 - \hat{v}_s)^2} \le 2 \tag{9}$$

In mild steel the linear branch until proportional limit is determined using Eq.(2) with taking $v_s = 1$.

When the stress-strain diagram for mild steel is represented, the yield plateau is observed (see Fig.2a). In this Figure $\hat{\sigma}_s$, $\hat{\varepsilon}_s$ represent the stress and strain in the end yield plateau, and determined as follows (Korpenko et al., 1986):

$$\hat{\sigma}_s = (1.01 : 1.03)\sigma_y \quad ; \quad \hat{\varepsilon}_s = \frac{\hat{\sigma}_s}{E_s} + \lambda_y \quad ; \quad \sigma_{0.2} = 0.99\sigma_y \tag{10}$$

where:
$\lambda_y$: length of yield plateau depends on steel type (0.008-0.015).

After the yield point, mild steel will undergo a period of strain hardening, in which the stress slowly increases with a rapid increasing of strain up to rupture. The strain hardening region is represented using Eq.2; Eq.3; and Eq.9, with taking: point c to complete the strain hardening diagram (Fig.2b), its coordinate is (Korpenko et al., 1986):

$$\sigma_{s(c)} \approx 1.2\,\sigma_y \quad ; \quad \varepsilon_{s(c)} = 0.05 + \frac{\sigma_{s(c)}}{E_s} \tag{11}$$

With taking:

$$\eta_{s(c)} = \frac{\sigma_{s(c)} - \hat{\sigma}_s}{\dot{\sigma}_s - \hat{\sigma}_s} \quad ; \quad v_{s(c)} = \frac{\sigma_{s(c)}}{E_s \varepsilon_{s(c)}} \tag{12}$$

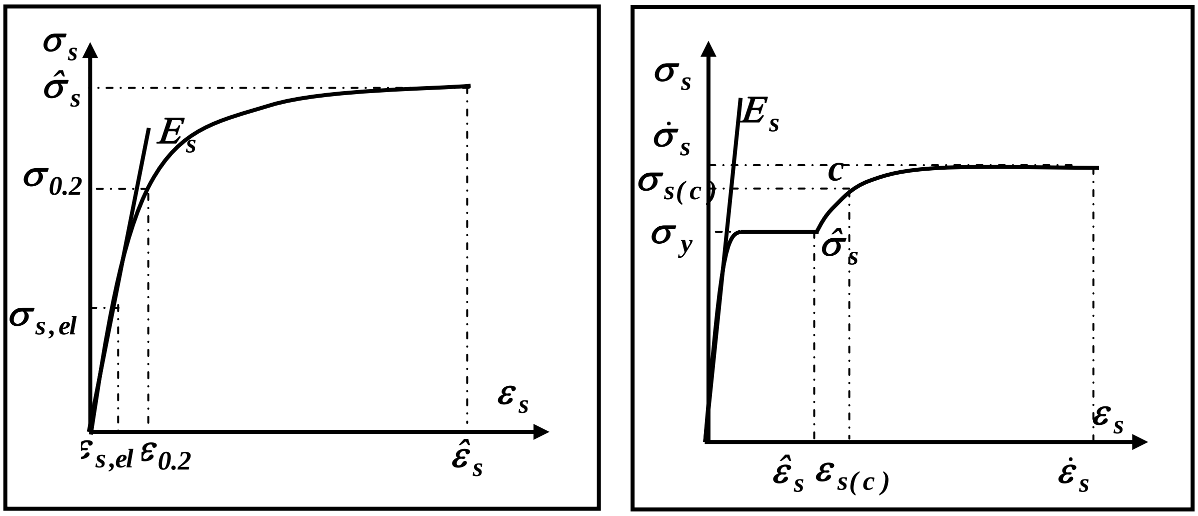


**(a)** **(b)**

**Figure 2:** Stress-strain diagrams for (a) mild steel, (b) high strength steel (Oukaili, 1998)

## Fibre Reinforced Polymer (FRP) Model

For FRP materials, an ideal elastic behaviour is assumed until the failure **(Pešić and Pilakoutas**, 2005) (Fig.3) and the unaxial tensile stress-strain ($\sigma_f - \varepsilon_f$) relation is simply given by:

$$\sigma_f = E_f \varepsilon_f \quad , \qquad 0 \le \varepsilon_f \le \varepsilon_{fu} \tag{13}$$

where:

$E_f$ : elastic modulus for FRP; $\varepsilon_f$ : strain for FRP; $\varepsilon_{fu}$ : strain at rupture.

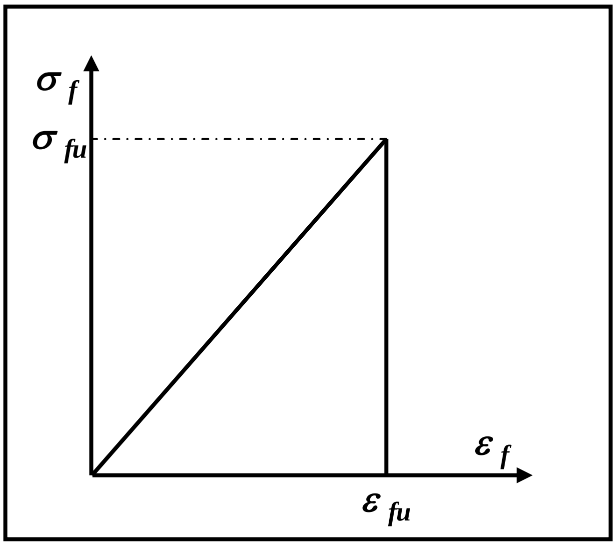


**Figure 3: Stress-strain diagrams for FRP (Pešić and Pilakoutas, 2005)**

## COMPARISON BETWEEN KORPENKO MODELS WITH EXPERIMENTAL RESULTS FOR CONCRETE

The analysis and design of structural concrete depend on the prediction of stress-strain relationship for concrete in compression. According to that, there is a mathematical model in the present study to predict the stress-strain diagram for concrete under unaxial load. It is compared with actual experimental data which are collected from the following works: Wang et al., 1978; Nilson et al., 1986; and Tasnimi, 2004. These data are classified into three groups according to strength: low strength concrete (LSC), normal strength concrete (NSC), and high strength concrete (HSC). Fig.4 illustrates detailing comparison between of Korpenko´s stress-strain relationship and the experimental data for the LSC, NSC, and HSC and the comparison between the analytical and experimental data shows good agreement.

## COMPARISON BETWEEN KORPENKO MODELS WITH EXPERIMENTAL RESULTS FOR STEEL

Korpenko´s analytical steel model for mild and high strength steel is compared with experimental data. In mild steel the experimental data collected from the following studies: Goto et al., 1998; and Cho et al., 2004, while the experimental data for high strength steel collected from: Leax et al and Canfield, 2005. The Fig.5 demonstrates these comparisons and a good agreement between the analytical and experimental results can be observed.

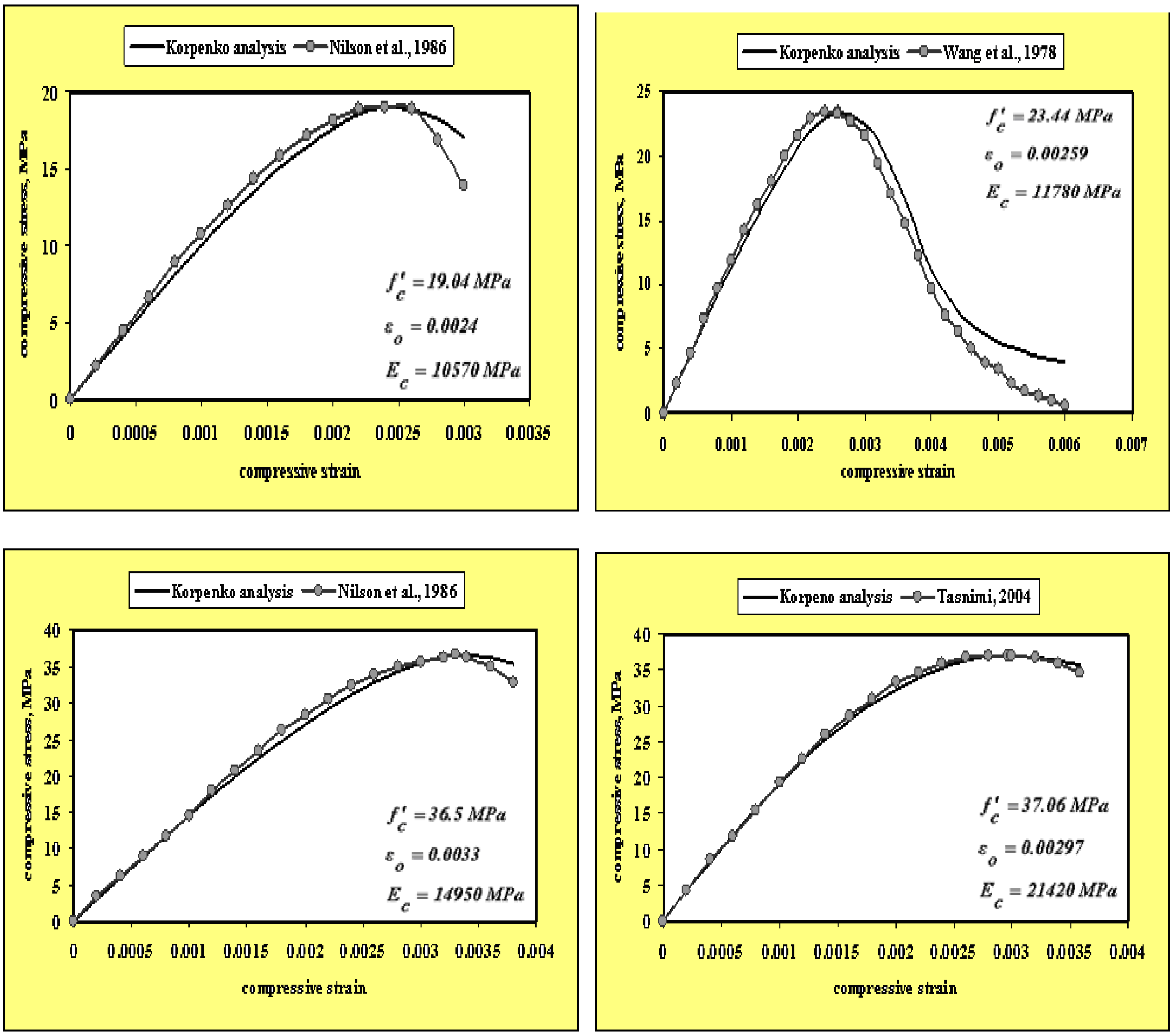

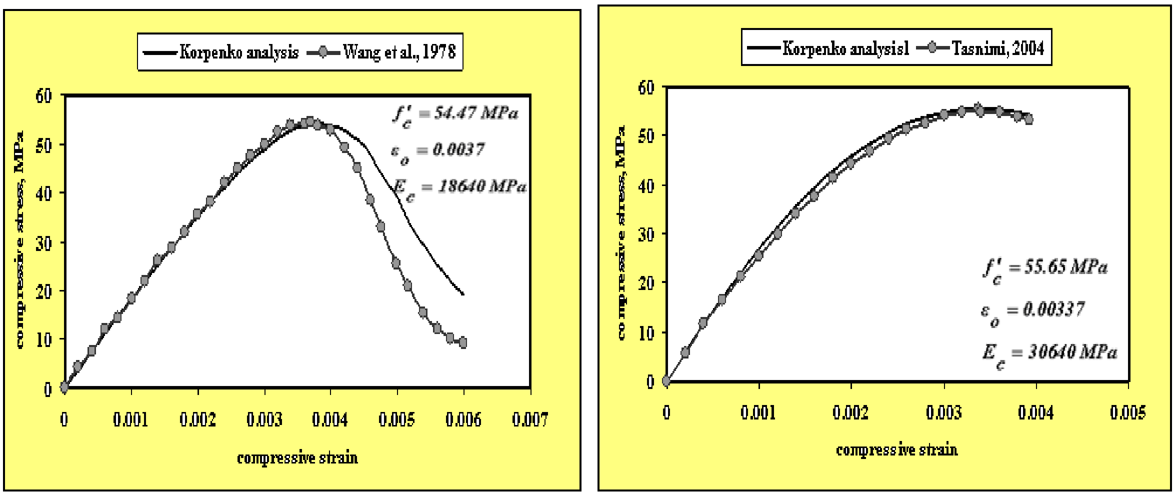


**Figure 4:** Comparison of proposed model with experimental data to LSC, NSC, HSC

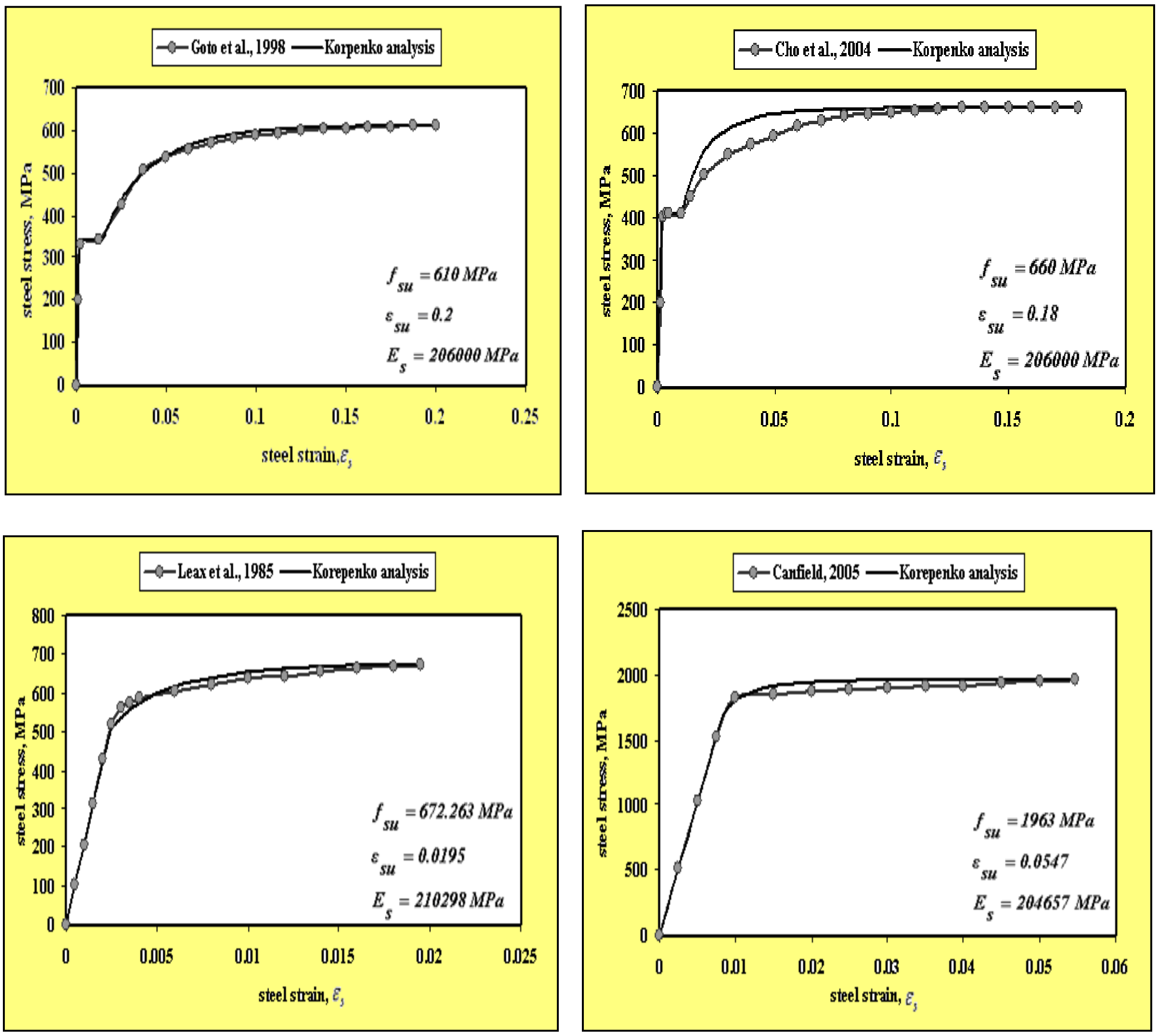


**Figure 5: Comparison of proposed model with test data for mild steel and high strength steel**

## DERIVATION OF ANALYTICAL RELATIONSHIPS TO PREDICT THE LOAD OR MOMENT CAPACITY FOR STRUCTURAL CONCRETE MEMBERS

The analytical model adopts the following assumption (Oukaili, 1998 and Oukaili and Akasha, 2002):

- Cross section is designed to resist the shear and the failure dose not occur because of this effect;
- Linear strain distribution is assumed for across the section depth (Navier law);
- To determine the strain during all load levels until failure, the section between two cracks is assumed;
- The model is based on real stress-strain diagrams for concrete (subjected to tension or compression) and steel;
- Steel and concrete are behaving as nonlinear elastic materials;
- Total stresses are associated with total strains in concrete and steel by secant modulus of elasticity;

In addition to the assumption above it is assumed that (ACI440, 2000)

- The tensile behaviour of the FRP reinforcement is linearly elastic until failure;
- Prefect bond exists between concrete and steel or FRP reinforcement.

The analysis is based on the requirement of equilibrium and compatibility of strain in concrete and steel or FRP. The equilibrium equations take the following form:

$$
\begin{aligned}
N &= \int_{\Omega_c} \sigma_c \, d\Omega_c + \sum_{i=1}^{m} \sigma_{si} A_{si} + \sum_{i=1}^{n} \sigma_{psi} A_{psi} + \sum_{i=1}^{j} \sigma_{fi} A_{fi} \\
M_x &= \int_{\Omega_c} \sigma_c y \, d\Omega_c + \sum_{i=1}^{m} \sigma_{si} A_{si} y_{si} + \sum_{i=1}^{n} \sigma_{psi} A_{psi} y_{psi} + \sum_{i=1}^{j} \sigma_{fi} A_{fi} y_{fi} \qquad \textbf{(14)} \\
M_y &= \int_{\Omega_c} \sigma_c x \, d\Omega_c + \sum_{i=1}^{m} \sigma_{si} A_{si} x_{si} + \sum_{i=1}^{n} \sigma_{psi} A_{psi} x_{psi} + \sum_{i=1}^{j} \sigma_{fi} A_{fi} x_{fi}
\end{aligned}
$$

where:

$N$ : axial force; $M_x$: bending moment in $Y$ direction; $M_y$: bending moment in $X$ direction; $\Omega_c$: concrete area; $\sigma_c$, $\sigma_{si}$, $\sigma_{psi}$, $\sigma_{fi}$: the stresses in concrete, nonprestressing steel, prestressing steel, and fibre reinforced polymer (FRP), respectively; m, n, j: number of nonprestressing steel, prestressing steel, and FRP, respectively; $A_{si}$, $A_{psi}$, $A_{fi}$: area of nonprestressing steel bars, prestressing steel bars, and FRP elements, respectively (Fig.6); $x_{si}$, $y_{si}$, $x_{psi}$, $y_{psi}$, $x_{fi}$, $y_{fi}$: distance from the centre of gravity of nonprestressing steel, prestressing steel, and FPR to the local coordinate axes, respectively (Fig.7).

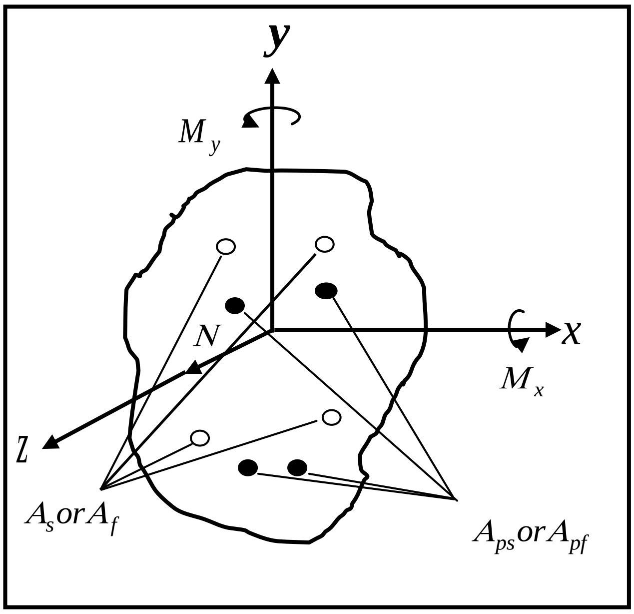


**Figure 6: Cross section for member**

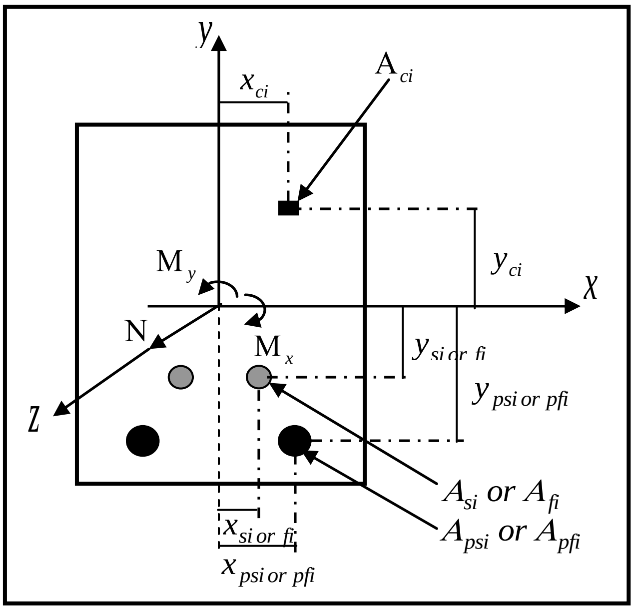


**Figure 7: Positive sign for forces on the cross section**

The physical relationship is used to determine the stress, which is shown as follows:

$$\sigma = \overline{E}\varepsilon = E\nu\varepsilon \tag{15}$$

where:

$\overline{E}$ : secant modulus of elasticity for materials; $\nu$ : coefficient of elastic strain.

According to Bernoullis' theory "the plane cross-section before loading remains plane after loading", the strain in any point is expressed as follows (Oukaili, 1998 and Oukaili and Akasha, 2002):

$$\varepsilon = \varepsilon_{om} + \varepsilon_o + K_x y + K_y x \tag{16}$$

where:

$\varepsilon_{om}$ : initial strain in materials (concrete , nonprestressed steel, prestressed steel, and FRP) resulted from effective prestressing force, $\varepsilon_o$ : strain that result from axial load.

$K_x$: curvature in Y-direction, $K_y$: curvature in X-direction, x, y: distance between centre of gravity for concrete, prestressing steel, and nonprestressing steel and the local coordinate axes.

The substitution of Eq.(15) and Eq.(16) in Eq.(14) results in:

$$\begin{Bmatrix} N \\ M_x \\ M_y \end{Bmatrix} = \begin{bmatrix} C_{11} & C_{12} & C_{13} \\ C_{21} & C_{22} & C_{23} \\ C_{31} & C_{32} & C_{33} \end{bmatrix} * \begin{Bmatrix} \varepsilon_o \\ K_x \\ K_y \end{Bmatrix} \tag{17}$$

where:

$$C_{11} = \int_{A_c} E_c\, v_c\, dA_c + \sum_{i=1}^{m} E_{si}\, v_{si}\, A_{si} + \sum_{i=1}^{n} E_{psi}\, v_{psi}\, A_{psi} + \sum_{i=1}^{j} E_{fi}\, A_{fi} \quad (18)$$

$$C_{12} = C_{21} = \int_{A_c} E_c\, v_c\, y_c\, dA_c + \sum_{i=1}^{m} E_{si}\, v_{si}\, A_{si}\, y_{si} + \sum_{i=1}^{n} E_{psi}\, v_{psi}\, A_{psi}\, y_{psi} + \sum_{i=1}^{j} E_{fi}\, A_{fi}\, y_{fi} \quad (19)$$

$$C_{13} = C_{31} = \int_{A_c} E_c\, v_c\, x_c\, dA_c + \sum_{i=1}^{m} E_{si}\, v_{si}\, A_{si}\, x_{si} + \sum_{i=1}^{n} E_{psi}\, v_{psi}\, A_{psi}\, x_{psi} + \sum_{i=1}^{j} E_{fi}\, A_{fi}\, x_{fi} \quad (20)$$

$$C_{22} = \int_{A_c} E_c\, v_c\, y_c^2\, dA_c + \sum_{i=1}^{m} E_{si}\, v_{si}\, A_{si}\, y_{si}^2 + \sum_{i=1}^{n} E_{psi}\, v_{psi}\, A_{psi}\, y_{psi}^2 + \sum_{i=1}^{j} E_{fi}\, A_{fi}\, y_{fi}^2 \quad (21)$$

$$C_{23} = C_{32} = \int_{A_c} E_c\, v_c\, x_c\, y_c\, dA_c + \sum_{i=1}^{m} E_{si}\, v_{si}\, A_{si}\, x_{si}\, y_{si} + \sum_{i=1}^{n} E_{psi}\, v_{psi}\, A_{psi}\, x_{psi}\, y_{psi} + \sum_{i=1}^{j} E_{fi}\, A_{fi}\, x_{fi}\, y_{fi} \quad (22)$$

$$C_{33} = \int_{A_c} E_c\, v_c\, x_c^2\, dA_c + \sum_{i=1}^{m} E_{si}\, v_{si}\, A_{si}\, x_{si}^2 + \sum_{i=1}^{n} E_{psi}\, v_{psi}\, A_{psi}\, x_{psi}^2 + \sum_{i=1}^{j} E_{fi}\, A_{fi}\, x_{fi}^2 \quad (23)$$

The direct integration to determine the stiffness matrix elements is not defined mathematically, because secant modulus of elasticity depends on the strain value for material. For that, the numerical integration method is used to determine the stiffness matrix element. In accordance with this model, the member cross section is covered by a mesh with the smallest cells. After that, stress (strain) is determined in each cell and the integral substituted by the process of summation to define the elements of stiffness matrix (Oukaili and Akasha, 2002).

The force vectors equations (Eq.17) have nonlinear behaviour. However in this model, these nonlinear equations are changed to linear equations using the iteration methods with fixity of secant modulus of elasticity in the current iteration cycle (Oukaili, 1998). So that, the stiffness matrix elements take the following form:

$$C_{11} = \sum_{i=1}^{k} E_{ci}\, v_{ci}\, A_{ci} + \sum_{i=1}^{m} E_{si}\, v_{si}\, A_{si} + \sum_{i=1}^{n} E_{psi}\, v_{psi}\, A_{psi} + \sum_{i=1}^{j} E_{fi}\, A_{fi} \quad (24)$$

$$C_{12} = C_{21} = \sum_{i=1}^{k} E_{ci}\, v_{ci}\, A_{ci}\, y_{ci} + \sum_{i=1}^{m} E_{si}\, v_{si}\, A_{si}\, y_{si} + \sum_{i=1}^{n} E_{psi}\, v_{psi}\, A_{psi}\, y_{psi} + \sum_{i=1}^{j} E_{fi}\, A_{fi}\, y_{fi} \quad (25)$$

$$C_{13} = C_{31} = \sum_{i=1}^{k} E_{ci}\, v_{ci}\, A_{ci}\, x_{ci} + \sum_{i=1}^{m} E_{si}\, v_{si}\, A_{si}\, x_{si} + \sum_{i=1}^{n} E_{psi}\, v_{psi}\, A_{psi}\, x_{psi} + \sum_{i=1}^{j} E_{fi}\, A_{fi}\, x_{fi} \quad (26)$$

$$C_{22} = \sum_{i=1}^{k} E_{ci}\, v_{ci}\, A_{ci}\, y_{ci}^2 + \sum_{i=1}^{m} E_{si}\, v_{si}\, A_{si}\, y_{si}^2 + \sum_{i=1}^{n} E_{psi}\, v_{psi}\, A_{psi}\, y_{psi}^2 + \sum_{i=1}^{j} E_{fi}\, A_{fi}\, y_{fi}^2 \quad (27)$$

$$C_{23} = C_{32} = \sum_{i=1}^{k} E_{ci}\, v_{ci}\, A_{ci}\, x_{ci}\, y_{ci} + \sum_{i=1}^{m} E_{si}\, v_{si}\, A_{si}\, x_{si}\, y_{si} + \sum_{i=1}^{n} E_{psi}\, v_{psi}\, A_{psi}\, x_{psi}\, y_{psi} + \sum_{i=1}^{j} E_{fi}\, A_{fi}\, x_{fi}\, y_{fi} \quad (28)$$

$$C_{33} = \sum_{i=1}^{k} E_{ci}\, v_{ci}\, A_{ci}\, x_{ci}^2 + \sum_{i=1}^{m} E_{si}\, v_{si}\, A_{si}\, x_{si}^2 + \sum_{i=1}^{n} E_{psi}\, v_{psi}\, A_{psi}\, x_{psi}^2 + \sum_{i=1}^{j} E_{fi}\, A_{fi}\, x_{fi}^2 \quad (29)$$

Where:
$C_{11}$: axial stiffness, which depends on loading level and geometric properties of the cross section; $C_{12}$: axial-flexural stiffness, due to axial force (compression or tension) and bending moment in Y-direction, which depends on the geometric properties of cross section, stress-strain condition and the location and direction of selected coordinates axes; $C_{13}$: axial-flexural stiffness, due to axial force and bending moment in X-direction; $C_{22}$: flextural stiffness in Y-direction; $C_{23}$: stiffness, due to bending in X and Y direction, which depends on geometric properties of the section and locations of selected coordinates; $C_{33}$: flextural stiffness in X-direction; $k$ : number of effective concrete cells; $A_{ci}$: the cross sectional area of the concrete cell i; $x_{ci}$, $y_{ci}$: distance from the centre of gravity of the concrete cell i to the selected coordinates; $m$: number of nonprestressed longitudinal steel bar in the cross section; $A_{si}$: the cross sectional area of nonprestressed longitudinal steel bar i;
$x_{si}$, $y_{si}$: distance from centre of gravity for nonprestressed longitudinal steel bar i to the selected coordinates; $n$: number of prestressed longitudinal steel bar in the cross section; $A_{psi}$: the cross sectional area of prestressed steel bar i; $x_{psi}, y_{psi}$: distance from the centre of gravity for prestressed longitudinal steel bar i to the selected coordinates; $j$: number of longitudinal FRP bar in the cross section; $A_{fi}$: the cross sectional area of the FRP bar i; $x_{fi}, y_{fi}$: distance from the centre of gravity of longitudinal FRP bar i to the selected coordinates.
The equation (17) can be rewritten in the following shape:

$$\{F\} = [C] * \{\lambda\} \quad (30)$$

Where:
$\{F\} = \lfloor N, M_x, M_y \rfloor$: load vector; $[C]$: section stiffness matrix; $\{\lambda\} = \{\varepsilon_o, K_x, K_y\}^T$ : axial strain vector.

The stiffness matrix elements depend on the secant modulus of elasticity and the last depends on stress-strain diagrams. Therefore, Eq.(30) takes the following new shape:

$$\{F\} = [C(\varepsilon)] * \{\lambda\} \quad (31)$$

The strain in cross-section determined by Eq.(16). Eq.(31) can take the new shape:

$$\{F\} = [C(\lambda)] * \{\lambda\} \tag{32}$$

In the nonlinear system, Eq.(5-32) represents a compatibility relationship which is used to determine the moment capacity of the structural concrete members.

The analytical model is attributable to using discrete approaches and nonlinear analysis using modern electronic computers and using numerical methods (Oukaili and Akasha, 2002**)**. Oukaili program (Oukaili, 1999) called SECTION is used in this paper.

## 6. Structural Concrete Members Reinforced with Fibre Reinforced Polymer (FRP) Bars

Simply supported beams for other investigators are examined to study the flexural behaviour of the structural concrete members reinforced with FRP bars. These beams are shown as follows:

### 6.1 Aiello and Ombres (2000)

Aiello and Ombres (2000) cast nine concrete beams reinforced with AFRP rebars for flexural tests to examine the failure load. The tensile reinforcement area is 176.7mm$^2$. The beam spanning 2610 mm was subjected to four-point bending. The cross sectional geometry and test set-up beam are as shown in Fig.8.

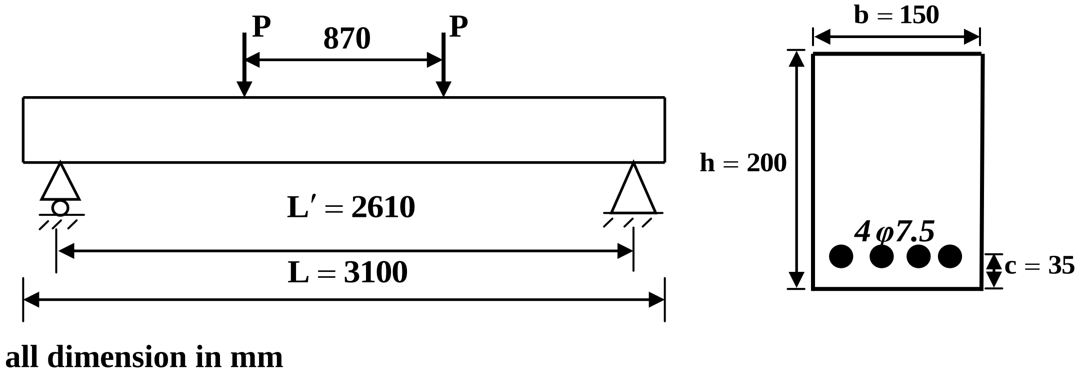


**Figure 8: Cross section and test set-up of beam A**

Average value of the tensile strength and modulus of elasticity of the rebars determined by standard tensile test, are 1506 and 50100 MPa, respectively. The average compressive strength of the concrete is 46.2 MPa. ACI 318 Committee (ACI 318, 2008) expression is used to determine the modulus of rupture and modulus of elasticity and shown as follows:

$$f_r = 0.62\sqrt{f_c'} \tag{33}$$

$$E_c = 4730\sqrt{f_c'} \tag{34}$$

To determine the strain corresponding to the maximum stress $\varepsilon_o$ the empirical equation assumed by Smith and Young (Smith and Young, 1956) is used and shown as follows:

$$\varepsilon_0 = (0.71\ f_c' + 168) \times 10^{-5} \tag{35}$$

Number 3 Volume 16 September 2010 Journal of Engineering

For that, the compressive strain $\varepsilon_o$, modulus of rupture and modulus of elasticity for concrete are 0.002, 4.214 and 32286 MPa, respectively.

The analytical moment-curvature relationship at critical section is evaluated for beam A, which is shown in Fig.9.

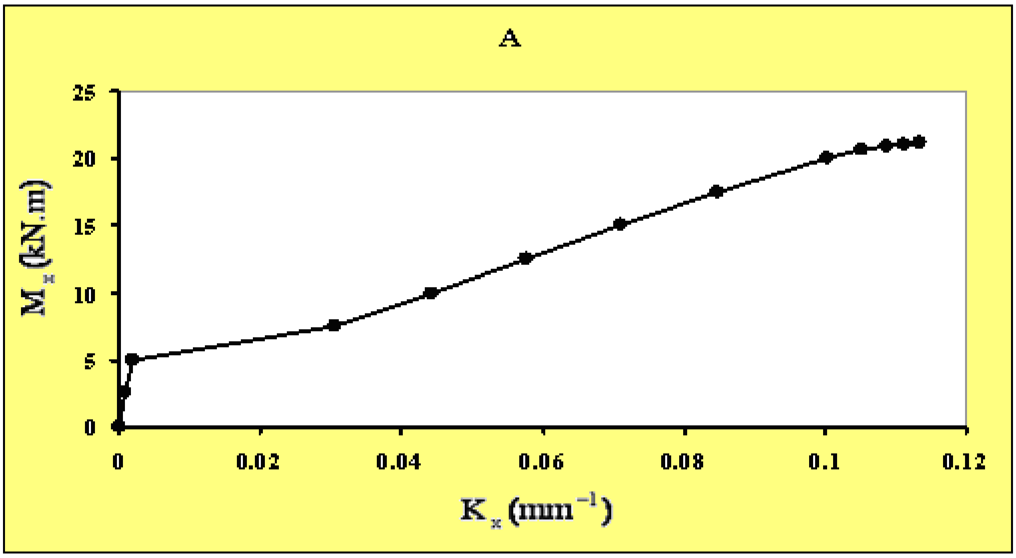


**Figure 9: Theoretical moment-curvature diagram for beams A**

Beam A failed experimentally at a bending moment of 22.84 kN.m. Analytical moment capacity is determined based on the used model in this study and the model recommended by ACI 440H Committee; these moments are 21.17 kN.m and 19.062 kN.m, respectively.

**Dolan and Burke (2001)**

Two rectangular and T-section beams reinforced with prestressed CFRP bar were tested by Dolan and Burke (2001). Beam strawman 3 is studied in this section. This beam is simply supported and was subjected to four-point flexural testing. The cross section dimension and flexural testing of beam is shown in Fig.10.

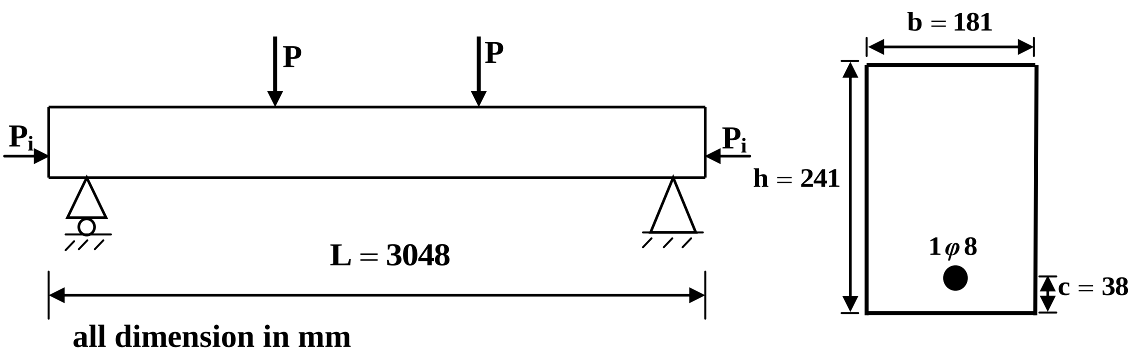


**Figure 10: Cross section dimension and flexural testing for strawman 3**

The measure compressive strength of concrete used in the beam is 31 MPa. The other mechanical properties of concrete are determined using the same empirical equation in section 6. 1.

Therefore, the calculated value of the compressive strain $\varepsilon_o$, modulus of rupture and modulus of elasticity is 0.0019, 3.452, 26336 MPa, respectively. The mean tensile strength of FRP is 1862 MPa, and the mean modulus of elasticity for the CFRP bars is 146 GPa. The tensile reinforcement area is 50.3 mm$^2$ and the initial prestressing force is 53.4 kN.

The analytical moment-curvature diagram for Strawman 3 beam is shown in Fig.11.

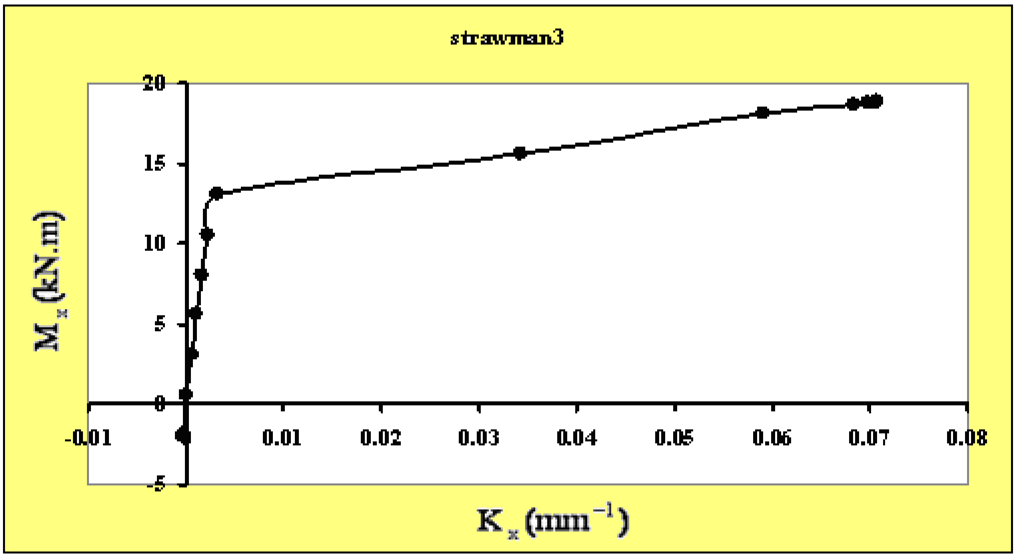


**Figure 11: Theoretical moment-curvature diagram for beam strawman 3**

Strawman 3 beam is failed experimentally at moment 19.1 kN.m, while the moment from the used model and Burke and Dolan is 18.856 and 18.293 kN.m, respectively.

## STRUCTURAL CONCRETE MEMBERS REINFORCED WITH FIBRE REINFORCED POLYMER (FRP) PLATE

External reinforcement with nonprestressed and prestressed FRP plate for simply supported concrete beams under flextural test for many investigators are used in this study. Detailed study for some beams is shown as follows:

### Nguyen et al. (2001)

Simply supported beams strengthened with CFRP plate were studied by Nguyen et al. 2001. A1500 beam has 120 × 150 mm cross section and 1500 mm length, this beam is subjected to four point loads. Detail of the beam and test loading is shown in Fig.12.

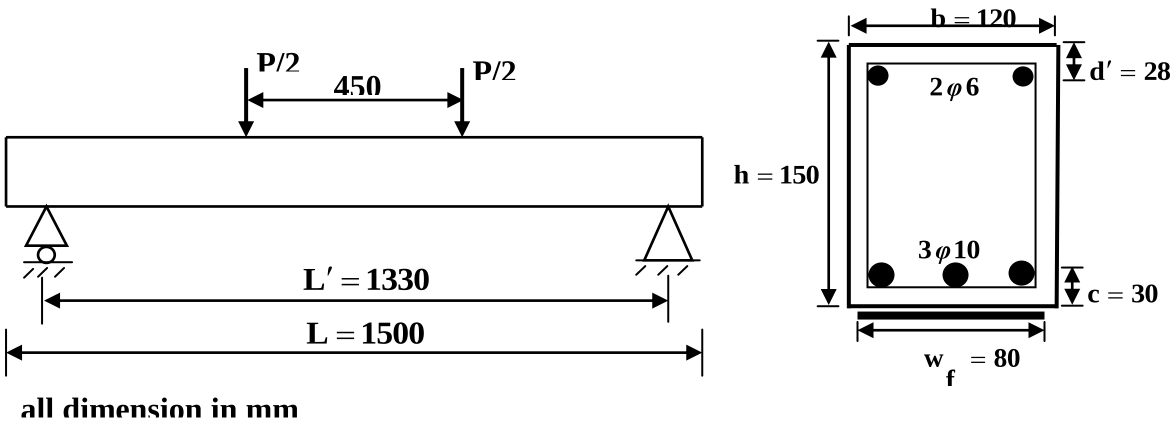

The tension and compression reinforcement areas of the beam are 236 and 56.5 $mm^2$. The CFRP plate of 80 × 1.2 mm cross section is used. The compressive strength of concrete is 44.6 MPa. Table (1) presents the mechanical properties for materials.

**Table (1): Mechanical properties of materials**

| Materials | Reinf. Area $mm^2$ | Yield Strength MPa | Ultimate Strength Mpa | Modulus of Rupture MPa | Modulus of Elasticity GPa | Ultimate Strain | Strain at Maximum Stress |
|---|---|---|---|---|---|---|---|
| CFRP plate | *96* | - | *3140* | - | *181* | - | - |
| Tension reinforcement bar | *236* | *384* | *461** | - | *200** | *0.17** | - |
| Compression reinforcement bar | *56.2* | *400* | *480** | - | *200** | *0.17** | - |
| Concrete | - | - | *44.6* | *4.141*$^{\dagger}$ | *31.588*$^{\dagger}$ | - | *0.002*$^{\dagger}$ |

$^{\dagger}$*assumed* ( $f_r = 0.62\sqrt{f'_c}$ , $\varepsilon_0 = (0.71\, f'_c + 168) \times 10^{-5}$ , $E_c = 4730\sqrt{f'_c}$ ) * *assumed*

The moment-curvature of this beam is shown in Fig.13.

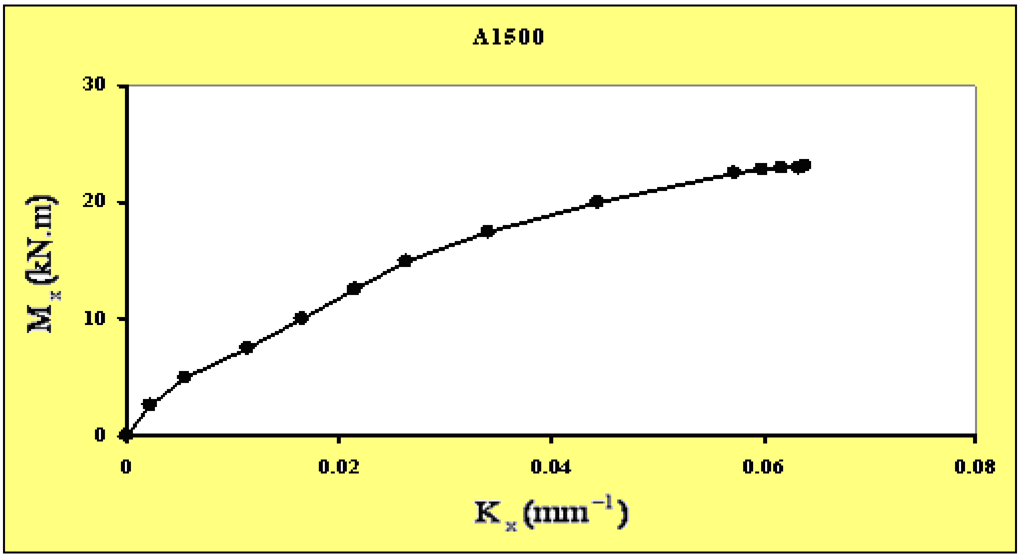


**Figure 13: Theoretical moment-curvature diagram for beam A1500**

The beam A1500 failed at the experimental applied moment of 25.96 kN.m. While, the ultimate moment from the used model and ACI 440H Committee is 23.066 and 18.311 kN.m, respectively.

## <u>Zou et al. (2005)</u>

Zou et al., (2005) has studied the flexural behaviour of five reinforced concrete beams strengthened by prestressed CFRP. Three of these beams are used in this study. All beams have the same dimension of 100 × 150 × 2200 mm (width × depth × length). The clear span 2000 mm of the beams have been loaded by two equal forces. The cross section dimension and test of set-up are shown in Fig.14.

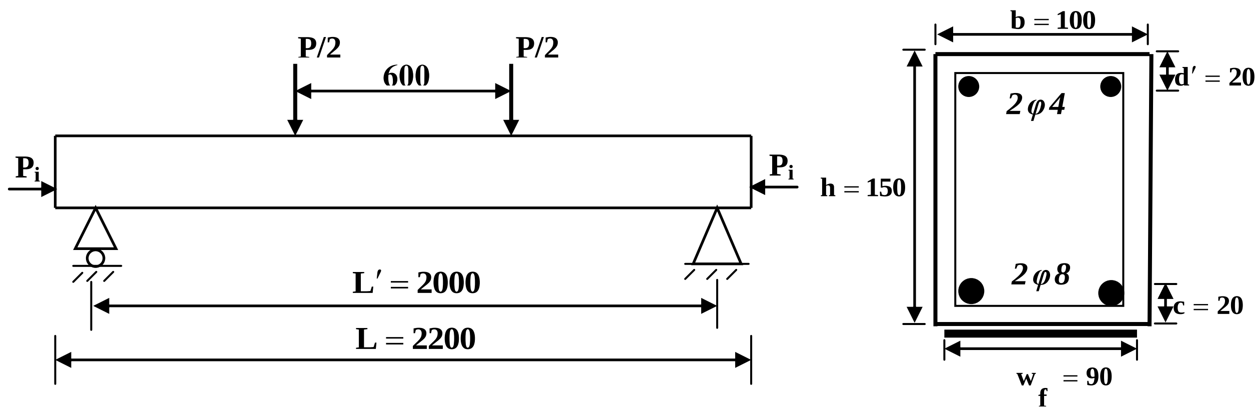


**Figure 14: Cross section dimensions and flexural testing**

The average compressive strength of concrete is 19.92 MPa for three specimens. The area of CFRP sheet used is 90 mm wide with an average thickness of 0.167 mm and the initial prestressing force is 22 kN. Table (2) shows details of mechanical properties for materials.

**Table (2): Mechanical properties for materials**

| Materials | Reinf. Area $mm^2$ | Yield Strength MPa | Ultimate Strength MPa | Modulus of Rupture MPa | Modulus of Elasticity GPa | Ultimate Strain | Strain at Maximum Stress |
|---|---|---|---|---|---|---|---|
| CFRP plate | *15.03* | - | *2941* | - | *207.2* | - | - |
| Tension reinforcement bar | *101* | *309.9* | *372** | - | *224.5* | *0.17** | - |
| Compression reinforcement bar | *25* | *595* | *714** | - | *201.2* | *0.2** | - |
| Concrete | - | - | *19.92* | *2.767†* | *21111†* | - | *0.00182†* |

†*assumed* ( $f_r = 0.62\sqrt{f'_c}$, $\varepsilon_0 = (0.71\, f'_c + 168)\times 10^{-5}$, $E_c = 4730\sqrt{f'_c}$ ), ** assumed*

**Fig. 15 shows the moment curvature diagram for beam B5.**

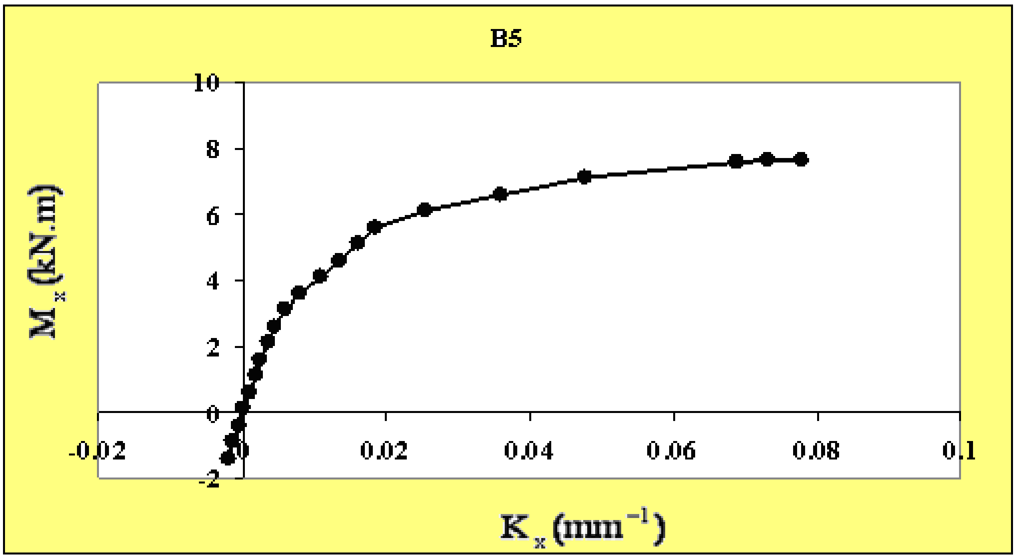


**Figure 15: Moment-curvature diagrams for prestressed beam B5**

Beam B5 has failed at moment 8.75 kN.m, while the ultimate analytical moment is 7.647 kN.m.

## CONCLUSIONS

- The modelling of materials presented in this study is good to represent the actual stress-strain diagrams of LSC, NSC and HSC and mild and high strength steel.
- The presented model gives good agreement with experimental results for the structural concrete member reinforced with nonprestressed FRP bar and plate.
- A reasonable agreement between the analytical and experimental results of the structural concrete member reinforced with external FRP plate is observed.

## REFERENCE


- ACI Committee 318, 2008, ***Building Code Requirements for Structural Concrete***, American Concrete Institute, Detroit (MI).

- ACI Committee 440H, 2000***, Guide for Design and Construction of Concrete Reinforced with FRP Bars***, American Concrete Institute, Detroit, Mich., pp.1-97.

- Aiello, M.; and Ombres, L.; 2000, ***Load-Deflection Analysis of FRP Reinforced Concrete Flexural Members***, Journal of Composites for Construction, Vol.4, No.4, pp.164-171.

- Canfield, S.R.; 2005, ***Full Scale Testing of Prestressed, High Performance Concrete, Composite Bridge Girders***, M.Sc.Thesis, Georgia Institute of Technology, The Academic Faculty.

- Cho, J.; Kim, N.; Cho, N.; and Choi, I.; 2004, ***Cracking Behaviour of Reinforced Concrete Panel Subjected to Biaxial Tension***, ACI Structural Journal, Vol.101, No.1, pp.76-84.

- Goto, Y.; Wang, Q.; and Obata, M.; 1998, ***FEM Analysis for Hysteretic Behaviour of Thin-Walled Columns***, Journal of Structural Engineering, Vol.124, No.11, pp.1290-1301.

- Dolan, C.W.; Rizkalla, S.; and Nanni, A.; 1999, ***Fibre-Reinforced-Polymer Reinforcement for Reinforced Concrete Structure, SP-188***, American Concrete Institute, Farmington Hills, MI, pp.1182.

- Dolan, C.; and Burke, C.R.; 2001, ***Flexural Design of Prestressed Concrete Beams Using FRP Tendons***, PCI Journal, Vol.46, No.2, pp.76-87.

- Korpenko, N.I.; Mukhamediev, T.A.; and Petrov, A.N.; 1986, ***The Initial and Transformed Stress-Strain Diagrams of Steel and Concrete***, Special Publication, Stress–Strain Condition for Reinforced Concrete Construction, Reinforced Concrete Research Centre, Moscow, pp.7-25.

- Leax, T.R.; Dowling, N.E.; Brose, W.R.; and Peck, M.G.; 1985, ***Methodology for Correlating Fatigue Data Obtained under Different Test Conditions***, Journal for Testing and Evaluation, JTEVA, Vol.13, No.6, pp.393-404.

- Nguyen, D.M.; Chan, T.K.; and Cheong, H.K.; 2001, ***Brittle Failure and Bonded Development Length of CFRP-Concrete Beams***, Journal of Composite for Construction, Vol.5, No.1, pp.12-17.

- Nilson, A.H.; Slate, F.O.; and Martinez, S.; 1986, ***Mechanical Properties of High-Strength Light Weight Concrete***, ACI Journal Proceeding, Vol.83, No.4, pp.606-613.

- Oukaili, N.K.; 1998, ***Moment Capacity and Strength of Reinforced Concrete Members Using Stress-Strain Diagrams of Concrete and Steel***, Journal King Saud Univ., V.10, No.2, pp.23-44 (in Arabic).

- Oukaili, N.K.; 1999, ***Model for Predicting the Cracking Moment in Structural Concrete Members***, Al-Yarmok Searches (Sciences Series of Essential and Engineering), V.8, No.2, pp.9-39 (in Arabic).

- Oukaili, N.K.; and Akasha, A.M.; 2002, ***General Program to Study the Behaviour of Concrete Structural under Static Loads***, First Civil Engineering Conference, Sebha University, (Sebha, Liyba), pp.1-19, (in Arabic).

- **Pešić**, N.; and Pilakoutas, K.; 2005, ***Flexural analysis and design of reinforced concrete beams with externally bonded FRP reinforcement***, Materials and Structures, Vol.38, pp.183-192.

- Smith, G.M.; and Young, L.E.; 1956, ***Ultimate Flexural Analysis Based on Stress-Strain Curves of Cylinders***, ACI Journal, Proceedings, V.53, No.6, pp.597-609.

- Tasnimi, A.A.; 2004, ***Mathematical Model for Complete Stress-Strain Curve Prediction of Normal, Light-Weight and High-Strength Concretes***, Magazine of Concrete Research, Vol.56, No.1, February, pp.23-34.

- Wang, P.T.; Shah, S.P.; and Naaman, A.E.; 1978, ***Stress-Strain Curve for Normal and Light Weight Concrete in Compression***, ACI Journal Proceeding, Vol.75, No.11, pp.603-611.

- Zou, P.; Shang, S.; Peng, H.; and Wang, H.; 2005, ***Avoiding De-bonding in FRP Strengthened Reinforced Concrete Beams Using Prestressing Techniques***, Proceeding of The International Symposium on Bond Behaviour of FRP in Structure (BBFS) Chen and Teng (eds).

# DESIGN OF A SLIDING MODE CONTROLLER FOR A TORA SYSTEM

Prof. Dr. Waladin Khairi Sa'id
Control & System Eng. Dept.
University of Technology
Baghdad-Iraq

Mr. Shibly Ahmed Hameed
Control & System Eng. Dept.
University of Technology
Baghdad-Iraq

## ABSTRACT

This paper presents the design of a sliding mode controller for an uncertain model of a TORA system (Translational Oscillations with a Rotational Actuator) as a two DOF underactuated mechanical system. The switching function is selected to make the TORA system an asymptotically stable mass-spring system with a nonlinear damping effect when the sliding mode controller constrains the state to the sliding manifold. This sliding mode controller is derived here according to a new formula consisting of continuous and discontinuous parts. The main obstacle in the controller design is the uncertainty in the switching function, which appears in the controller formula. The sliding controller is found effective in bringing the system state to the neighborhood of the equilibrium point in spite of the uncertainty in the switching function. In addition, the chattering problem is solved via the use of approximate signum function.

## الخلاصة:

يتناول هذا البحث تصميم مسيطر ذو شكل منزلق لمنظومة أل TORA كمنظومة تحت الدفع ذات درجتين للحرية. تم اختيار دالة التبديل لتجعل منظومة أل TORA كمنظومة كتلة-نابض مستقرة مع مخمد لا خطي وذلك عندما يحدد المسيطر الحالة إلى سطح الانزلاق. تم اشتقاق صيغة المسيطر المنزلق في هذا البحث تبعا لصيغة جديدة تتكون من جزء مستمر و جزء غير مستمر. إن العقبة الأكبر في تصميم المسيطر هي الغموض في دالة التبديل والتي تظهر في صيغة المسيطر. وجد المسيطر المنزلق فعالاً في جلب حالة المنظومة إلى منطقة تجاور نقطة الاستقرار على الرغم من الغموض في دالة التبديل. بالإضافة إلى ذالك تم حل مشكلة الارتجاج باستخدام دالة تقريبية لدالة الإشارة.

**KEYWORDS: under actuated mechanical system, sliding mode controller, uncertainty**

## INTRODUCTION

Underactuated system is a mechanical system with number of actuators less than the number of configuration variables that describe the mechanical system behavior according to Euler-Lagrange equation. The TORA system is a two DOF mechanical system where the mass-spring system is actuated via the rotation of an eccentric mass, as shown in Fig. 1. During the past decade many nonlinear controller design techniques were applied to the TORA system. Jankovic et. al. (Jankovic et. al. 1996) applied a passivity-based approach to the TORA system. Olfati-Saber

(Olfati-Saber 2001) transformed the underactuated system to a normal form that depends on the relative degree, and then applied known control strategies like the backstepping. The same approach of Olfati-Saber was applied by Qaiser et. al. (Qaiser et. al. 2007) to the TORA system. Zhong-Ping J. and Kanellakopoulos I. (Zhong-Ping and Kanellakopoulos 2000) proposed an observer/controller backstepping design in which one of the unmeasured state appears quadratically in the state equation. The backstepping approach applied to a nonlinear system assume exact system model. A complicated formula may result due to the application of the backstepping approach as reported in reference (Jankovic et. al. 1996).

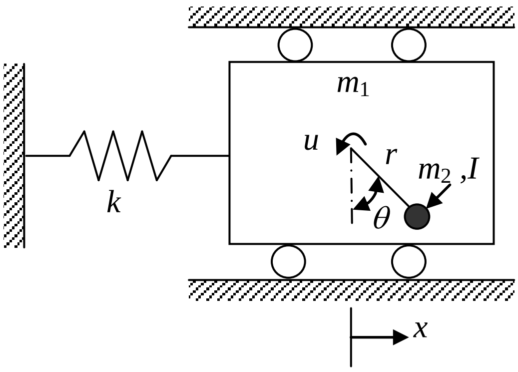


Fig 1: The TORA system.

The systems considered thus far are assumed certain systems. However, uncertainty is a major problem that has not been considered in controller design of underactuated systems thus far. Application of uncertainty is a unique, challenging and interesting research area (Spong 1997). In this work, the sliding mode controller design is accomplished for an uncertain TORA system model after transforming it to a form known as the *regular form* (Luk'yanov and Utkin 1981). A suitable switching function for the sliding controller is selected to constrain the system state to its zero-level (sliding manifold). A successful design implies that the dynamic of the underactuated system at this manifold is asymptotically stable.

Uncertainty in system parameters of an underactuated system leads to many problems like the non-linearizability, difficulty in selecting an attractive surface and the uncertainty in switching function. An attractive switching surface is proposed in reference (Hameed 2007) based on the flatness property of the TORA system. In addition, using uncertain switching function in controller formula ensures only the state is constrained in a region about the equilibrium point (Hameed 2007).

The organization of this paper is as follows: the mathematical model is derived in section two. Section three is devoted to the design of a sliding mode controller which includes the selection of switching manifold based on flatness theory, the effects of using approximate signum function and the presence of uncertainty in switching function. The new sliding mode controller formula is presented in section four and the derivation are given in appendix (A). Section five presents the results and discussion of four numerical simulation tests and finally the conclusion is presented in section six.

## MATHEMATICAL FORMULATION

As shown in Fig. 1, the TORA system consists of translational oscillating platform, which is controlled via a rotational eccentric mass. The inertia matrix, potential energy and the force vector (one-form) assume the following form (Olfati-Saber 2001);

$$M = \begin{bmatrix} m_1 + m_2 & m_2 r\cos(\theta) \\ m_2 r\cos(\theta) & m_2 r^2 + I \end{bmatrix} \text{ , } V(x,\theta) = \frac{1}{2}Kx^2 + (r - r\cos(\theta))m_2 g_0 \text{ , } F = d\theta$$

The dynamical equation of the TORA system are (Hameed 2007):

$$\left.\begin{aligned}\ddot{x} &= \frac{1}{\Delta}\left[\left(m_2 r^2 + I_2\right)m_2 r\sin(\theta)\left(\dot{\theta}\right)^2 - \left(m_2 r^2 + I_2\right)Kx + \left(m_2 r\right)^2 g_0 \sin(\theta)\cos(\theta)\right] \\ &\quad - \frac{\left(m_2 r\cos(\theta)\right)}{\Delta}u \\ \ddot{\theta} &= \frac{1}{\Delta}\left[-\left(m_2 r\right)^2 \sin(\theta)\cos(\theta)\left(\dot{\theta}\right)^2 + \left(m_2 r\right)Kx\cos(\theta) - \left(m_1 + m_2\right)m_2 g_0 r\sin(\theta)\right] \\ &\quad + \frac{\left(m_1 + m_2\right)}{\Delta}u\end{aligned}\right\} \tag{1}$$

where,

$$\Delta = \left(m_1 + m_2\right)\left(m_2 r^2 + I_2\right) - \left(m_2 r\right)^2 \cos^2(\theta) = m_1\left(m_2 r^2 + I_2\right) + m_2 I_2 + \left(m_2 r\right)^2\left(\sin(\theta)\right)^2 > 0$$

Corollary (3.1) in reference (Hameed 2007) proves that the TORA system is a flat system since $m_{11}$ is constant for the actuated shape variable. The flat output is given by;

$$y = x + \left(\frac{m_2 r}{m_1 + m_2}\right)\sin(\theta) \tag{2}$$

Differentiating eq.(2) twice and with the aid of eq.(1) yields the underdetermined differential equation, i.e.;

$$\ddot{y} = -\left(\frac{K}{m_1 + m_2}\right)x \tag{3}$$

Eliminating $x$ from eqs. (2) and (3), the underdetermined equation assumes the following form;

$$\ddot{y} = -\left(\frac{K}{m_1 + m_2}\right)y + \frac{K m_2 r}{\left(m_1 + m_2\right)^2}\sin(\theta) \tag{4}$$

The design of the sliding controller in the next item assumes the following statements;

*i.* The output $y$ and its derivatives are assumed to be known precisely, which is an essential assumption.

*ii.* The rest points for the TORA system in terms of the configuration variables $(x, \theta)$ is the rest point set $\{(0, \theta) : \theta \in (-\pi, +\pi)\}$.

According to statement (ii), the controller must be able to translate the state from any condition (any perturbed condition) to the rest point set described here only.

## SLIDING MODE CONTROLLER DESIGN

The work reported in this section is based on the results of three propositions; namely propositions (4.2), (5.7) and (5.5) and lemma (5.1) of reference (Hameed 2007). The interested reader may refer to reference (Hameed 2007) for the proof of these propositions and the lemma. For convenience, however, only the proof of proposition (5.7) is presented here due to its importance.

### Selection of Switching Manifold

Selection of the switching manifold is the subject of proposition (4.2), (Hameed 2007). It states that; *The selection of the function* $s$ *,where*

$$e = f_0(y, q_0) + k_1\dot{y} + k_2 y$$
$$s = \dot{e} + \lambda e$$
,

*will globally asymptotically stabilizes the 2DOF flat underactuated mechanical system with sliding mode controller provided that:* $(i) k_1, k_2 > 0$, and $(ii) f_0(0, q_0) = 0 \Rightarrow q_o = 0$.

A TORA system with this switching manifold becomes globally asymptotically stable (GAS) according to proposition (5.7), (Hameed 2007). The statement of this proposition is;

**Proposition:** *Consider the TORA system dynamic given by eq. (1), the sliding controller* $u$ *that use the following switching function:*

$$s = \dot{e} + e$$
$$e = \theta + \tan^{-1} c\dot{y} \tag{5}$$

*Render the TORA system GAS system, where* $c$ *is a design parameter in the error function, which has a damping effect.*

**Proof:** To prove the validity of the switching function in eq. (5), first it is needed to show that $\ddot{y}$ is asymptotically stable (AS) with $e = 0$, i.e., if we write $\ddot{y} = f(y, \dot{y}, e)$ at any $e$, then $\ddot{y} = f(y, \dot{y}, 0)$ is AS. Then it is required to show that the upper sub system given by eq. (4) is (ISS) with $e$ regarded as a disturbance. Finally it is required to show that the selection of $s$ will not lead to a singularity in input channel i.e. $L_g s \neq 0$ at any point of $(x, \theta)$. The underdetermined equation $\ddot{y}$ given by eq. (4) may be written in state space form as;

$$\dot{y}_1 = \dot{y} = y_2$$
$$\dot{y}_2 = -\left(\frac{K}{m_1 + m_2}\right) y_1 + \frac{K m_2 r}{(m_1 + m_2)^2} \sin(\theta) \tag{6}$$

When $e = 0$, we have $\theta = -\tan^{-1}(c\dot{y})$ or $\tan(\theta) = -c\dot{y} \Rightarrow \sin(\theta) = \frac{-c\dot{y}}{\sqrt{1 + (c\dot{y})^2}}$, then eq. (6) becomes;

$$\dot{y}_2 = -\frac{K}{(m_1 + m_2)} y_1 - \frac{K m_2 r c}{(m_1 + m_2)^2} \frac{y_2}{\sqrt{1 + (c y_2)^2}} \tag{7}$$

Now let the Lyapunov function be given by;

$$V = \frac{A}{2} y_1^2 + \frac{1}{2} y_2^2, \; A > 0 \tag{8}$$

$$\dot{V} = A y_1 y_2 + y_2 \dot{y}_2 = A y_1 y_2 + y_2 \left[ -\frac{K}{(m_1 + m_2)} y_1 - \frac{K m_2 r c}{(m_1 + m_2)^2} \frac{y_2}{\sqrt{1 + (c y_2)^2}} \right]$$
$$= \left( A - \frac{K}{m_1 + m_2} \right) y_1 y_2 - \left[ \frac{K m_2 r c}{(m_1 + m_2)^2} \frac{1}{\sqrt{1 + (c y_2)^2}} \right] y_2^2 \tag{9}$$

Therefore, $\dot{V}$ is negative semi definite when $A$ is chosen as $A = \frac{K}{m_1 + m_2}$ and $V$ is a proper Lyapunov function provided that the only equilibrium point is at the origin. To show that the TORA system is ISS, re-write eq. (5) with $e \neq 0$, i.e.;

$$\dot{y}_2 = -\frac{K y_1}{(m_1 + m_2)} - \frac{K m_2 r}{(m_1 + m_2)^2} \sin\left(e - \tan^{-1}(c y_2)\right) \tag{10}$$

Clearly $\dot{y}_2$ is globally Lipstize function. It means that $g(e, y_1, y_2)$ is a bounded quantity defined as;

$$g(e, y_1, y_2) = \int_0^1 \frac{\partial \dot{y}_2(y_1, y_2, \kappa e)}{\partial e} d\kappa \ , \ \ |g(e, y_1, y_2)| < L_g \ , \ L_g > 0 \tag{11}$$

The TORA system is ISS because the following integral $\int_0^\infty e d\tau$ is bounded since $\max_{t\in(0,\infty)} |e| < \infty$ for $t \in (0, t_s)$. It is GAS according to theorem (4.4) in reference (Hameed 2007). Finally, $L_g s$ is greater than zero as will be shown later on when the controller is designed.

■

## Approximate Signum Function

To avoid chattering, the approximate form of the signum function will be used. It is given by;

$$\text{sgn}(s) \approx \text{sgn}(s)_{app} = \begin{cases} \sin\left(\dfrac{\pi s}{2\delta_0}\right) & |s| \le \delta_0 \\ \text{sgn}(s) & otherwise \end{cases} \tag{12}$$

The effect of the *approximate signum function* on the attractiveness of the sliding manifold is governed by lemma (5.1), (Hameed 2007). It states that; *The use of the approximate signum function in eq. (12) guarantee the existence of the following attractive boundary layer around the switching manifold* $s = 0$ *:*

$$-\delta_0 < s < \delta_0 \tag{13}$$

Using $\text{sgn}(s)_{app}$ guarantees only the attractiveness of a region bounded by a boundary layer in eq. (13).

## Uncertainty in Switching Function *s*

The effect of using uncertain switching function in the sliding mode controller design will now be considered. The uncertainty in switching function is due to many reasons like the measurement error and/or the uncertainty in the output function calculation and its derivatives. Since the switching function is constructed from these quantities, then this function becomes uncertain. The uncertainty in switching function *s* is treated by proposition (5.5), (Hameed 2007). It states that: *Consider the underdetermined equation for a system given in the following form*

$$\dot{x} = f(x) + g(x)u \tag{14}$$

*then the use of uncertain switching function in the controller design renders the system stable and stay in a bounded region around the origin if and only if the underdetermined equation is ISS.*

## SLIDING CONTROLLER FORMULA

An approach is developed in reference (Hameed 2007) for formulating sliding mode controller law for the dynamic system given by eq.(14) with scalar input ***u*.** The approach utilizes bounded estimation for the uncertainty in the Lie derivative of the switching function $s$ with respect to *f* and *g* respectively. Starting from the time rate of change of the switching function $s$ with respect to the system dynamic of eq. (14) as;

$$\dot{s} = L_f s + (L_g s)u \tag{15}$$

where $L_f s$ and $L_g s$ are the lie derivatives of *s* with respect to *f* and *g*, respectively. Re-writing $L_f s$ terms of its nominal value as follows;

$$L_f s = \left(L_f s\right)_{nom} + \left[L_f s - \left(L_f s\right)_{nom}\right] = \left(L_f s\right)_{nom} + \Delta\left(L_f s\right) \tag{16}$$

where, $L_f s - \left(L_f s\right)_{nom} = \Delta\left(L_f s\right)$, and;

$$\Rightarrow \left|L_f s - \left(L_f s\right)_{nom}\right| = \left|\Delta\left(L_f s\right)\right| < \delta_f \left|\left(L_f s\right)_{nom}\right| \tag{17}$$

Similarly, for $L_g s$ and noting that $L_g s > 0$;

$$L_g s = \left(L_g s\right)_{nom} + \Delta\left(L_g s\right) \tag{18}$$

$$\left|L_g s - \left(L_g s\right)_{nom}\right| = \left|\Delta\left(L_g s\right)\right| < \delta_g \left(L_g s\right)_{nom} \tag{19}$$

where $\left(L_f s\right)_{nom}$ and $\left(L_g s\right)_{nom}$ are the $L_f s$ and $L_g s$ at the system nominal parameter values and $\delta_f$ and $\delta_g$ are the percent estimation of the variation of $L_f s$ and $L_g s$ from their nominal values, respectively. Now the design of the controller law can be implemented using proposition (5.1), (Hameed 2007). The proposition states that: *Consider the uncertain dynamical model described by eq. (14), the sliding mode controller that constrains the state to the switching manifold takes the following form;*

$$u = -\left(\frac{L_f s}{L_g s}\right)_{nom} - v_0 \operatorname{sgn} s \tag{20}$$

*with* $v_0$ *equal to:*

$$v_0 = 1.1\left(\frac{\delta_f + \delta_g}{1-\delta_g}\right)\left|\left(\frac{L_f s}{L_g s}\right)_{nom}\right| \tag{21}$$

The estimation of the upper and lower variation of $L_f s$ and $L_g s$ is not an easy task, it requires that each parameter variation should be considered separately. To overcome the problem of the uncertainty in system model, the Lie derivative of the switching function $L_f s$ is decomposed into uncertain and certain terms. Also, the uncertain term is decomposed to *l* terms as:

$$L_f s = \sum_{i=1}^{l} \left(L_f s\right)_{unc,i} + \left(L_f s\right)_{cer} \tag{22}$$

This approach is suitable for a more complicated type of system, which frequently appear in the underactuated mechanical system. Let each of the uncertain terms satisfy the following bounded formula:

$$\left|\left(L_f s\right)_{unc,i} - \left(\left(L_f s\right)_{unc,i}\right)_{nom}\right| = \left|\Delta_i\left(L_f s\right)\right| < \delta_i \left|\left(\left(L_f s\right)_{unc,i}\right)_{nom}\right|, i = 1,....,l \tag{23}$$

The difference $L_f s - \left(L_f s\right)_{nom}$ can be related to the uncertainty in eq. (23) as follows;

$$L_f s - \left(L_f s\right)_{nom} = \Delta\left(L_f s\right) = \sum_{i=1}^{l} \Delta_i\left(L_f s\right) = \sum_{i=1}^{l}\left[\left(L_f s\right)_{unc,i} - \left(\left(L_f s\right)_{unc,i}\right)_{nom}\right] \tag{24}$$

Now take the absolute value of both sides:

$$\left|L_f s - \left(L_f s\right)_{nom}\right| = \left|\Delta\left(L_f s\right)\right| = \left|\sum_{i=1}^{l} \Delta_i\left(L_f s\right)\right| = \left|\sum_{i=1}^{l}\left[\left(L_f s\right)_{unc,i} - \left(\left(L_f s\right)_{unc,i}\right)_{nom}\right]\right|$$

$$< \sum_{i=1}^{l}\left|\left(L_f s\right)_{unc,i} - \left(\left(L_f s\right)_{unc,i}\right)_{nom}\right| < \sum_{i=1}^{l}\delta_i\left|\left(\left(L_f s\right)_{unc,i}\right)_{nom}\right| = \delta_f \sum_{i=1}^{l}\left(\frac{\delta_i}{\delta_f}\right)\left|\left(\left(L_f s\right)_{unc,i}\right)_{nom}\right| \tag{25}$$

where $\delta_f = \min[\delta_1,........,\delta_l]$. Add the absolute value of the certain term to the right hand side of the inequality above we get;

$$\left|L_f s-\left(L_f s\right)_{nom}\right| < \delta_f\left[\sum_{i=1}^{l}\left(\frac{\delta_i}{\delta_f}\right)\left|\left(L_f s\right)_{nom,i}\right|+\left|\left(L_f s\right)_{cer}\right|\right] = \delta_f\left|\left(\overline{L_f s}\right)_{nom}\right| \tag{26}$$

Hence, the following estimation is obtained;

$$\frac{\left|L_f s-\left(L_f s\right)_{nom}\right|}{\left|\left(\overline{L_f s}\right)_{nom}\right|} = \frac{\left|\Delta\left(L_f s\right)\right|}{\left|\left(\overline{L_f s}\right)_{nom}\right|} < \delta_f \tag{27}$$

Note that $\left|\left(\overline{L_f s}\right)_{nom}\right| > \left|\left(L_f s\right)_{nom}\right|$ and because of this inequality requirement the certain part of $L_f s$ is added.

The following general formula for the sliding mode controller design in the presence of uncertainty in system parameters can now be stated. This is the subject matter of proposition (5.2), (Hameed 2007); it states that**:** *Consider the dynamical system given in eq. (14). Assume that the Lie derivative of the switching function $s = s(x)$ with respect to $f$ given by the form in eq. (22) and each of its i<sup>th</sup> component satisfy inequality (23), then the sliding controller that render the dynamical system AS in the presence of uncertainty in system model is given by:*

$$u = -\left(\frac{L_f s}{L_g s}\right)_{nom} - \nu_0 \operatorname{sgn} s \tag{28}$$

$$\nu_0 = 1.1\left(\frac{\delta_f + \delta_g}{1-\delta_g}\right)\left|\left(\frac{\overline{L_f s}}{L_g s}\right)_{nom}\right| \tag{29}$$

Appendix (A) presents sliding mode controller design details for the TORA system and the control law is given by eq. (A.22).

## SIMULATION RESULTS

The results of a set of numerical experiments using the designed sliding mode controller were carried out and Figs. 2 to 15 summarize the results. Throughout the simulations, the parameters value are taken as: $m_1 = 10.25$, $m_2 = 0.97$, $r = 1.02$, $I = 1$, $K = 5.17$, and the initial conditions are; $(x,\dot{x},\theta,\dot{\theta}) = (1,0,0,0)$. The units of the physical quantities are taken as meter, kilogram and Newton for length quantity, mass and force, respectively.

Responses shown in Figs. 2 to 7 are carried out with $c = 1$(eqs. (5) and (7)), exact signum function and without uncertainty in switching function. Figure 2 shows the position $x$ with time where a damping like behavior is obtained with $c = 1$. This is due to the selection of the error function where the $\sin(\theta)$ term (after reaching $e = 0$) provide the damping effect. This effect stabilizes the mass-spring system. The system is highly undamped and the settling time is of the order of 200 seconds. The plots of $\dot{x}$, $\theta$, and $\dot{\theta}$ with time are shown in Figs. 3, 4, and 5, respectively.

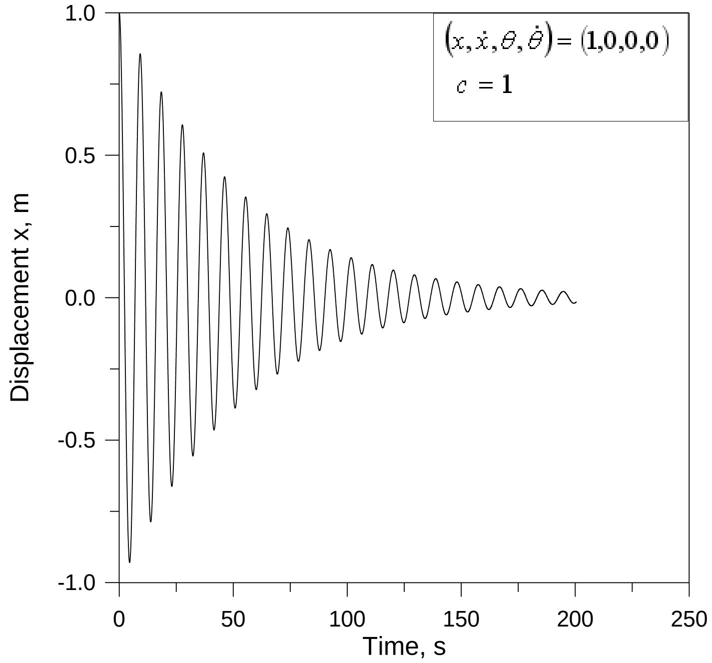


**Fig. 2: Displacement versus time.**

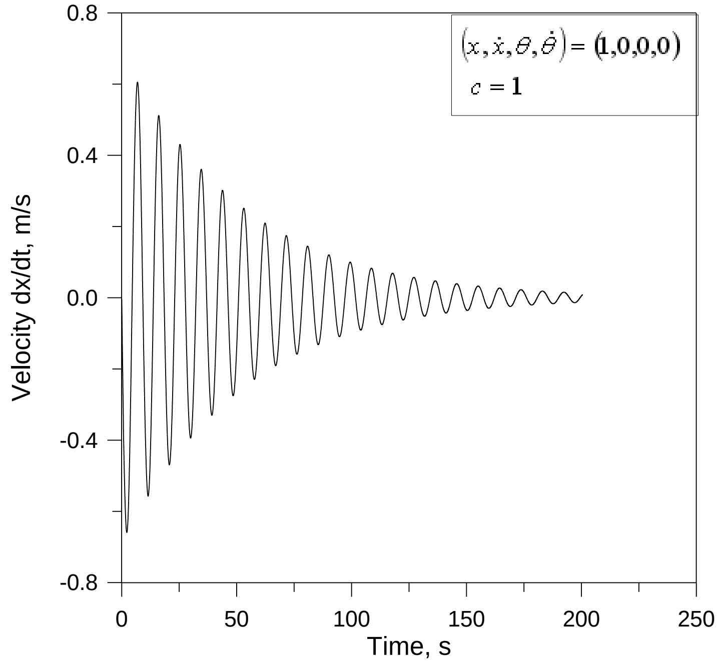


**Fig. 3: Velocity versus time.**

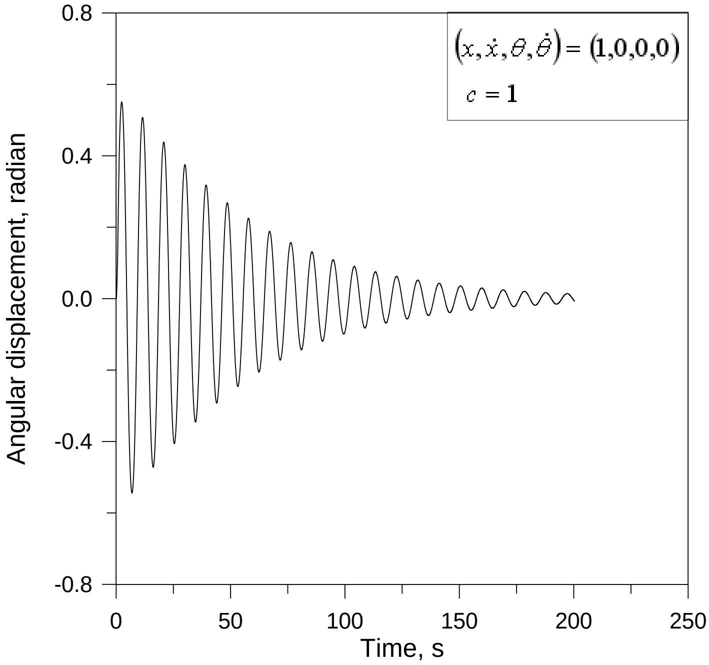


**Fig. 4: Angle of eccentric mass versus time.**

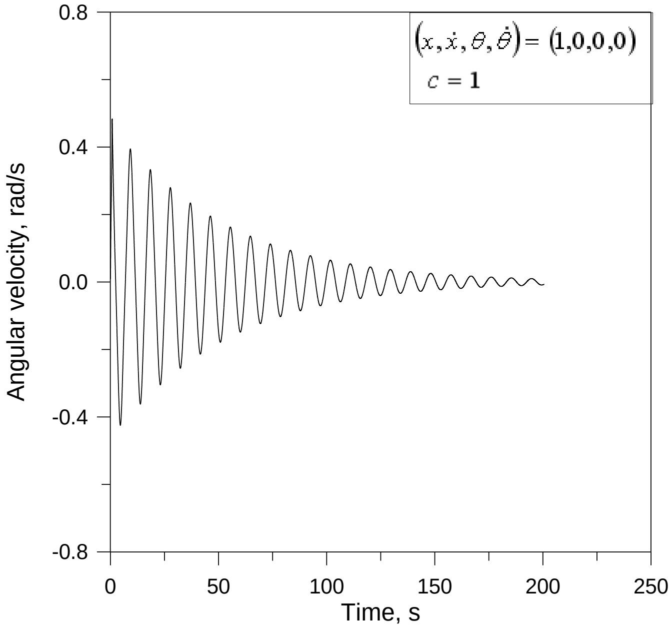


**Fig. 5: Angular velocity versus time.**

Figure 6 shows the switching function response with time. The figure shows that the time required to reach zero-level is less than one seconds. In order to reduce the reaching time to the switching manifold a higher discontinuous gain value is required. However, this causes a high chattering effect. Also, the state is constraint to the switching manifold with very small amplitude of oscillation around it and this is because of the very small switching time interval used in the simulation. Indeed a larger value of the switching time interval causes an oscillation with higher amplitude around the switching manifold and consequently the motion is known as "zig-zag" motion (Drakunov and Utkin 1989).

The sliding control action is shown in Fig. 7. From this figure, it can be noticed that the discontinuous action nature is clear through the black region. In addition, the amplitude of the controller reduces to zero with time and it is guaranteed due to the use of variable amplitude $\left(L_f s / L_g s\right)$ (eq. (27)).

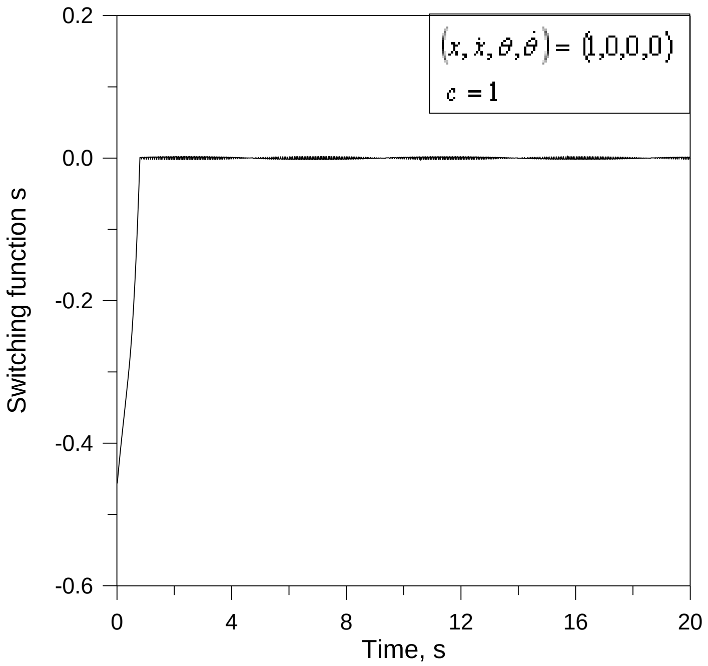


**Fig. 6: Switching function versus time.**

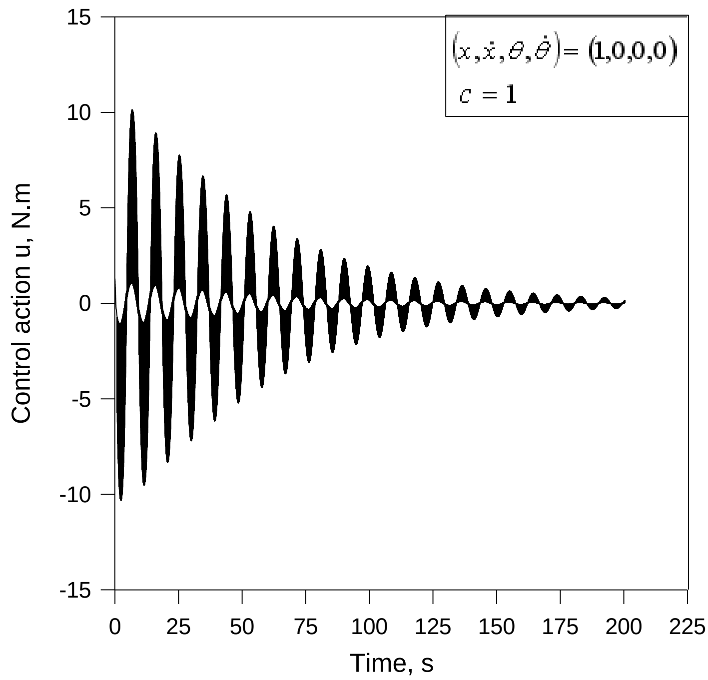


**Fig. 7: Control action (torque) versus time.**

For a certain model of the TORA system, Olfati-Saber (Olfati-Saber 2001) designed a nonlinear controller based on backstepping technique with certain parameter values. By utilizing these nominal values in this work, it is deduced from Fig. 8 that the displacement $x$ is similar to those of Olfati-Saber. However, in reference (Olfati-Saber 2001) the maximum torque required do not exceed $3\,N.m$, while in Fig. 7 the control action reaches $10\,N.m$. The increase in torque is mainly due to the uncertainty taken into account in the controller design.

Increasing the damping effect by selecting $c = 5$ will greatly improve the response, as can be clearly seen in Figs. 8 and 9. Figure 8 shows the plot of displacement $x$ with time where the settling time is reduced to about 60 seconds. While Fig. 9 plots the control $u$ with time. The maximum controller action increases due to higher damping property required. A comparison between Figs. 7 and 9 clearly shows the torque has increased by about 100%.

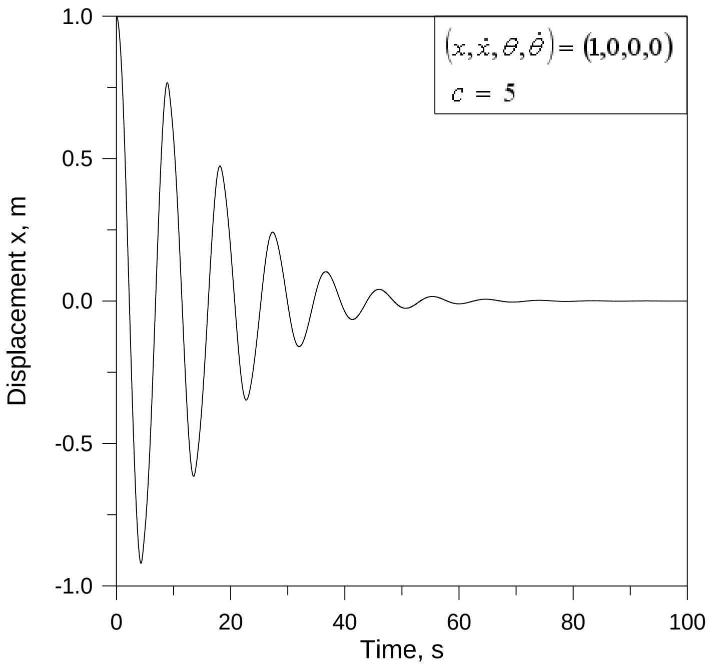


**Fig. 8: Displacement versus time.**

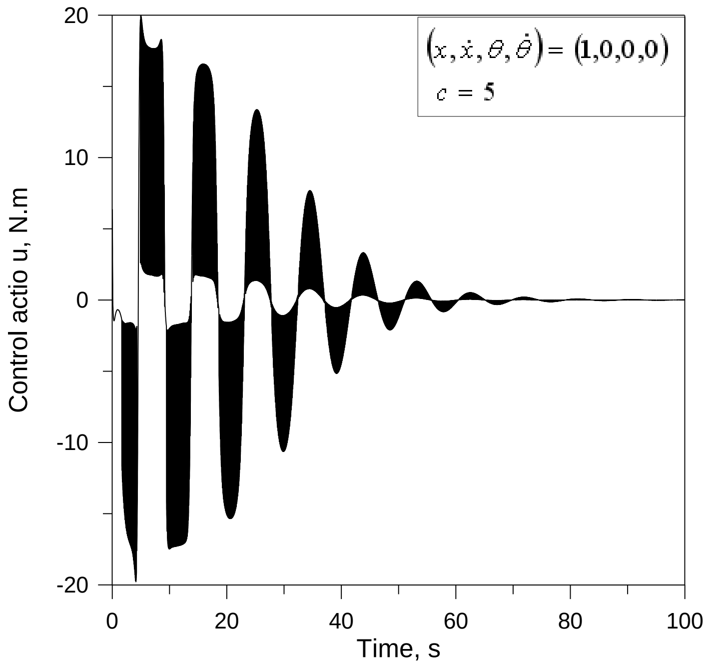


**Fig. 9: Control action versus time.**

A series of numerical tests were carried out where instead of the signum function the approximate one is used with $c = 5$. The plot of displacement $x$ with time (Fig. 10) is unaffected due to the use of approximate signum function in comparison with the exact signum function shown in Fig. 8. Figures 11 and 12 show the switching function plot. A smooth sliding mode controller action versus time is obtained due to the use of the approximate switching function.

It can be observed from Fig. 11, the state stays at the switching manifold without chattering, that is smooth system behavior. A comparison between Figs. 9 and 12 reveals that the maximum torque has been reduced to approximately 10 *N.m*. This is because of the discontinuous part amplitude near the switching manifold is smaller due to the use of the approximate signum function.

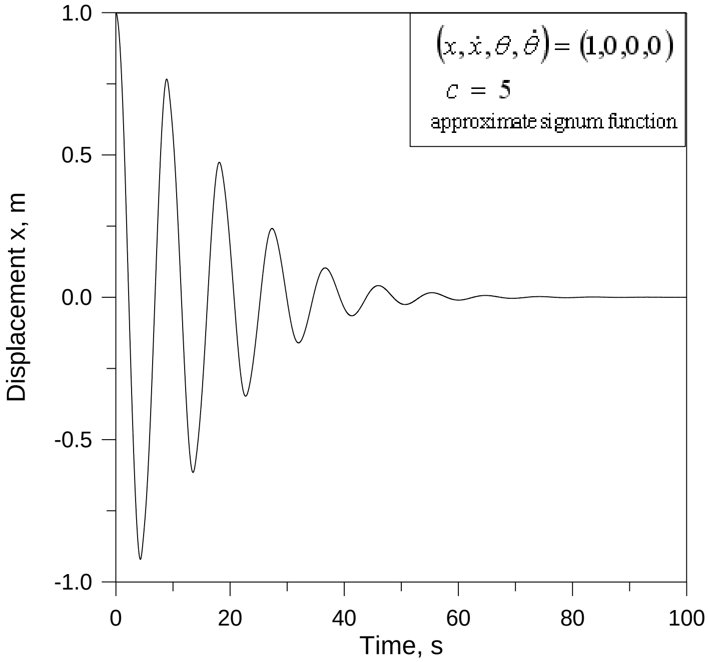


**Fig. 10: Displacement versus time.**

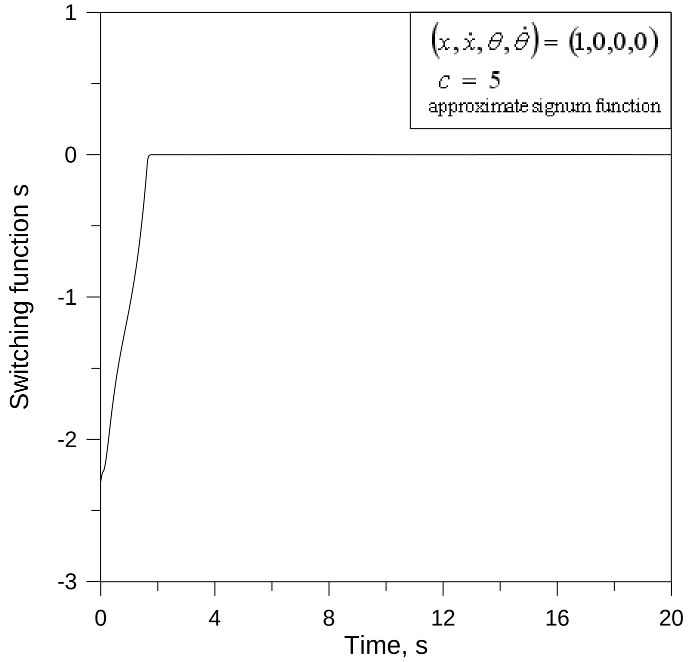


**Fig. 11: Switching function versus time.**

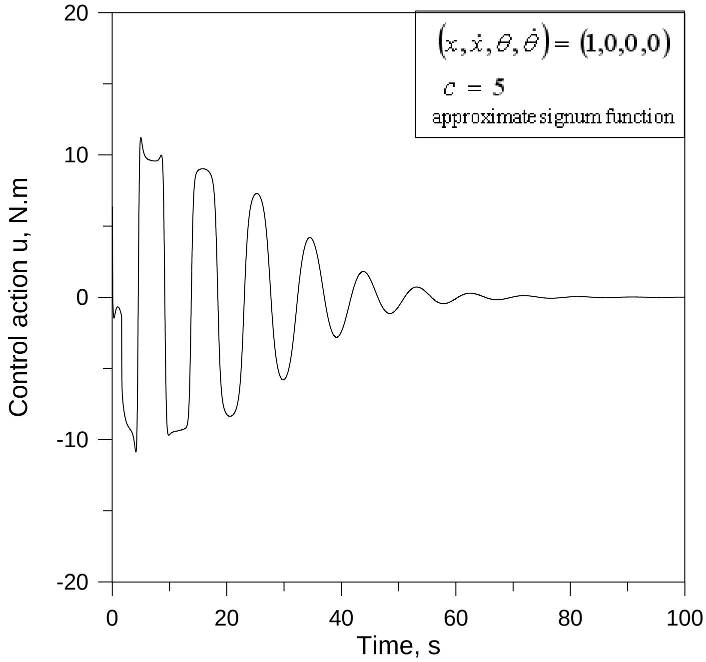


**Fig. 12: Control action versus time.**

The uncertainty of the switching function (proposition (5.5), (Hameed 2007) (section (3.2))) is also tested. Figures 13 to 15 summarize the main results. Figure 13 shows the plot of displacement $x$ with time while Figs. 14 and 15 show the plot of the switching function $s$ and the controller $u$ with time, respectively. The results shown in Figs. 13, 14, and 15 show that the system is AS in spite of the presence of the uncertainty in the switching function (the nominal parameter values is used in the calculation of switching function). On the other hand, the boundary layer does not appear clearly in the plot of the switching function in Fig. 14 due to the small uncertainty assumption in system parameters ($\pm 5\%$).

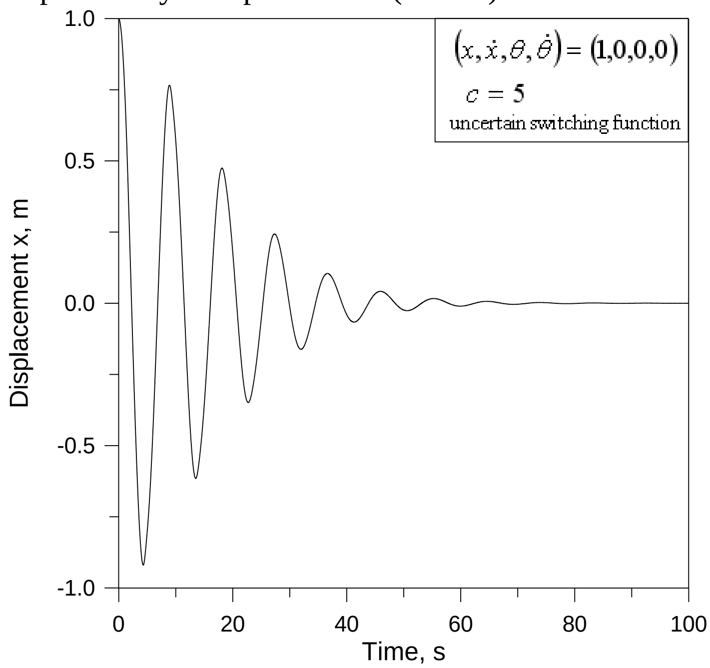


**Fig. 13: Displacement versus time.**

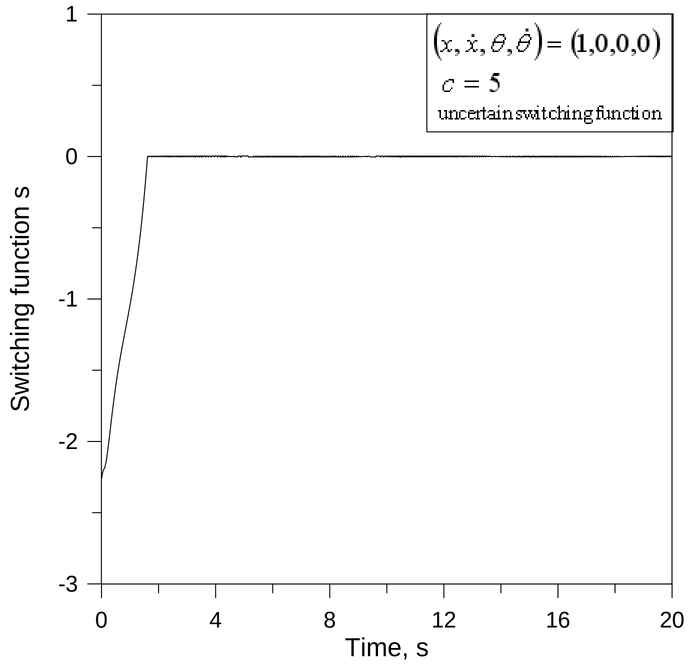


**Fig. 14: Switching function versus time.**

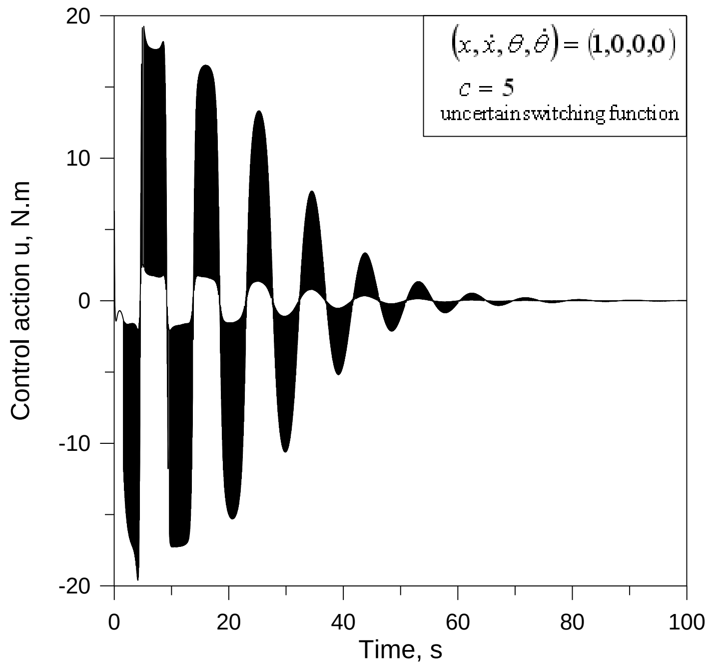


**Fig. 15: Control action versus time.**

## CONCLUSIONS

The present work shows the effectiveness of the sliding mode control theory for the design of a nonlinear controller for the TORA system as a two DOF underactuated mechanical system with model uncertainty. When the sliding controller force the state to the sliding manifold, the TORA system behaves like a spring–mass system with nonlinear damping effect due to the actuation of the eccentric mass. A numerical simulation shows that the proposed controller is robust with respect to the disturbances and uncertainty in system model. In addition the sliding mode controller is found effective in spite of the uncertainty in the switching function. Finally, these simulations prove the applicability of the new sliding controller formula in equations (28) and (29).

## REFERENCES


- Drakunov S. V. and Utkin V. I.. "On discrete-time sliding modes". *IFAC*, pp. 273-278, Capri, Italy, June 1989. (case of two authors)
- Jankovic M., Fontaine D., and Kokotovic P. V.. "TORA example: Cascade and passivity-based control designs". *IEEE Trans. On Control Systems Technology*, vol. 4, No. 3, pp. 292-297, 1996. (case of three authors)
- Luk'yanov A. G. and Utkin V. I.. "Methods of reducing equations for dynamic systems to a regular form". *Automation and Remote Control*, vol. 42, No. 4, (P.I), pp. 413-420, 1981. (case of two authors)
- Olfati-Saber R.. "*Nonlinear control of underactuated mechanical systems with application to robotics and aerospace vehicles*". Ph.D. dissertation, Dept. Elect. Eng. Comput. Sci., Massachusetts Inst. Technol., Cambridge, MA, 2001. (case of one author)
- Qaiser N., Hussein A., Iqbal N., and Qaiser N.. "Dynamic surface control for stabilization of the oscillating eccentric rotor". *J. Systems and Control Engineering*, vol. 221, Part I, 2007. (case of four authors)
- Shibly A. Hameed. "*Design of a Sliding Mode Controller for Underactuated Mechanical System*". Ph.D.. thesis, Baghdad University, Baghdad, Iraq, 2007.
- Spong M. W.. "Underactuated mechanical systems". In B. Siciliano and K. P. Valavanis, editor, *Control Problems in Robotics and Automation*, Springer-Verlag, London, UK, 1997. (case of one author)
- Zhong-Ping Jiang and Ioannis Kanellakopoulos. "Global output-feedback tracking for a benchmark nonlinear system". *IEEE Trans. On Automatic Control*, vol. 45, No. 5, pp. 1023-1027, 2000. (case of two authors)


## NOMENCLATURE

**Symbols**

AS: Asymptotically Stable.
DOF: Degree Of Freedom.
GAS: Globally Asymptotically Stable.
ISS: Input-to-State Stable.
$g_o$: Acceleration due to gravitational attraction ( $g_0 \approx 9.8\, m/s^2$ ).

$I$ : Moment of inertia of the eccentric mass about its own center.
$K$ : Spring constant [ $N/m$ ].
$L_f s, L_g s$ : Lie derivative of switching function with respect to *f* and *g* vector felids respectively.
$(L_f s)_{cer}, (L_f s)_{unc}$: Certain and uncertain parts of $L_f s$
$m_1$: Platform mass [ $Kg$ ].
$m_2$ : Eccentric mass [ $Kg$ ].
$r$ : Rotor radius [ $m$ ].
$\mathrm{sgn}()$ : The signum function.
$\mathrm{sgn}(\ )_{app}$: Approximate signum function.

**GREEK SYMBOLS**

$\Delta$ : Determinant of the inertia matrix ( $\Delta = \det M$ ).
$\delta_f\ ,\delta_g$ : percent estimation of the variation of $L_f s$ and $L_g s$ from their nominal values, respectively.
$\lambda, c$ : controller design parameters

**APPENDIX A**

**Computing Controller Formula For The Tora System**

To compute the control action $u$ for the TORA system the rate of change of the switching function is computed first as:

$$e = \theta + \tan^{-1}(cy_2) = \theta + \tan^{-1}(\eta) \tag{A.1}$$

$$\dot{e} = \dot{\theta} + \frac{\dot{\eta}}{1+(\eta)^2} \tag{A.2}$$

$$\ddot{e} = \ddot{\theta} + \frac{\ddot{\eta}}{1+(\eta)^2} - \frac{2(\eta)(\dot{\eta})^2}{\left[1+(\eta)^2\right]^2} \tag{A.3}$$

where $\eta = cy_2 = c\dot{y}$ then;

$$\dot{s} = \ddot{\theta} + \frac{\ddot{\eta}}{1+(\eta)^2} - \frac{2\eta(\dot{\eta})^2}{\left[1+(\eta)^2\right]^2} + \dot{\theta} + \frac{\dot{\eta}}{1+(\eta)^2} \tag{A.4}$$

In addition $L_f s$ and $L_g s$ are given by;

$$L_f s = -\frac{(m_2 r)^2 \sin(\theta)\cos(\theta)}{\Delta}\left(\dot{\theta}\right)^2 + \frac{(m_2 rK)\cos(\theta)x}{\Delta} + \frac{(m_1+m_2)m_2 g_0 r\sin(\theta)}{\Delta} + \frac{\ddot{\eta}}{1+(\eta)^2} - \frac{2\eta(\dot{\eta})^2}{\left[1+(\eta)^2\right]^2} + \dot{\theta} + \frac{\dot{\eta}}{1+(\eta)^2} \tag{A.5}$$

$$L_g s = \left(\frac{m_1+m_2}{\Delta}\right) \tag{A.6}$$

Following eq. (21), $L_f s$ is decomposed to the following form;

$$L_f s = \sum_{i=1}^{3}\left(L_f s\right)_{unc,i} + \left(L_f s\right)_{cer} \tag{A.7}$$

where,

$$\left(L_f s\right)_{cer} = \frac{\ddot{\eta}}{1+(\eta)^2} - \frac{2\eta(\dot{\eta})^2}{\left[1+(\eta)^2\right]^2} + \dot{\theta} + \frac{\dot{\eta}}{1+(\eta)^2} \tag{A.8}$$

$$\left(L_f s\right)_{unc,1} = -\frac{(m_2 r)^2}{\Delta}\sin(\theta)\cos(\theta)(\dot{\theta})^2 \tag{A.9}$$

$$\left(L_f s\right)_{unc,2} = \frac{(m_2 r K)}{\Delta}\cos(\theta)x \tag{A.10}$$

$$\left(L_f s\right)_{unc,3} = \frac{(m_1+m_2)m_2 g_0 r}{\Delta}\sin(\theta) \tag{A.11}$$

The nominal parameter values[1] are $m_1 = 10$, $m_2 = r = I_2 = 1$, $K = 5$ (Olfati-Saber 2001), $g_0 = 9.81$. Assuming the maximum/minimum variation values are bounded by $\pm 5\%$ of its nominal values, then $\left(\left(L_f s\right)_{unc,i}\right)_{nom}$, $\left(L_f s\right)_{nom}$ and $\left(L_g s\right)_{nom}$ are;

$$\left(\left(L_f s\right)_{unc,1}\right)_{nom} = -\left[\frac{1}{21+(\sin(\theta))^2}\right]\sin(\theta)\cos(\theta)(\dot{\theta})^2 \tag{A.12}$$

$$\left(\left(L_f s\right)_{unc,2}\right)_{nom} = \left[\frac{5}{21+(\sin(\theta))^2}\right]\cos(\theta)x \tag{A.13}$$

$$\left(\left(L_f s\right)_{unc,3}\right)_{nom} = \left[\frac{110}{21+(\sin(\theta))^2}\right]\sin(\theta) \tag{A.14}$$

$$\left(L_f s\right)_{nom} = \frac{-\sin(\theta)\cos(\theta)(\dot{\theta})^2 + 5\cos(\theta)x + 110\sin(\theta)}{21+(\sin(\theta))^2} + \frac{\ddot{\eta}}{1+(\eta)^2} - \frac{2\eta(\dot{\eta})^2}{\left[1+(\eta)^2\right]^2} + \dot{\theta} + \frac{\dot{\eta}}{1+(\eta)^2} \tag{A.15}$$

$$\left(L_g s\right)_{nom} = \frac{11}{21+(\sin(\theta))^2} \tag{A.16}$$

For $\left|\left(\overline{L_f s}\right)_{nom}\right|$, compute first $\delta_i$, $i = 1,2,3$ of the bounded estimation for each component of $\left(L_f s\right)_{unc}$ with $\min\Delta = 18.07 + 0.81(\sin(\theta))^2$ as in the following;

$$\left|\left(L_f s\right)_{unc,1} - \left(\left(L_f s\right)_{unc,1}\right)_{nom}\right| < \left|\frac{(1.05)^4}{18.07+0.81(\sin(\theta))^2} - \frac{1}{21+(\sin(\theta))^2}\right|\sin(\theta)\cos(\theta)(\dot{\theta})^2$$

$$= \left|\frac{\left((1.05)^4 * 21 - 18.07\right) + \left((1.05)^4 - 0.81\right)(\sin(\theta))^2}{18.07+0.81(\sin(\theta))^2}\right|\left(\frac{\sin(\theta)\cos(\theta)(\dot{\theta})^2}{21+(\sin(\theta))^2}\right)$$

[1] Throughout the simulations in this work the units of physical quantities is taken as meter unit for length quantity, kilogram for mass, and Newton for force.

However, $\max\left|\frac{\left((1.05)^4 * 21-18.07\right)+\left((1.05)^4-0.81\right)(\sin(\theta))^2}{18.07+0.81(\sin(\theta))^2}\right| < 0.42 = \delta_1$ at $\sin(\theta)=1$. Then we have:

$$\left|\left(L_f s\right)_{unc,1} - \left(\left(L_f s\right)_{unc,1}\right)_{nom}\right| < 0.42\left|\left(\left(L_f s\right)_{unc,1}\right)_{nom}\right| \tag{A.17}$$

In the same way, we get;

$$\left|\left(L_f s\right)_{unc,2} - \left(\left(L_f s\right)_{unc,2}\right)_{nom}\right| < 0.29\left|\left(\left(L_f s\right)_{unc,2}\right)_{nom}\right| \tag{A.18}$$

$$\left|\left(L_f s\right)_{unc,3} - \left(\left(L_f s\right)_{unc,3}\right)_{nom}\right| < 0.35\left|\left(\left(L_f s\right)_{unc,3}\right)_{nom}\right| \tag{A.19}$$

The term $\left|\overline{L_f s}\right|$ takes the following form;

$$\begin{aligned}\left|\overline{L_f s}\right|_{nom} &= \sum_{i=1}^{3}\frac{\delta_i}{\delta_f}\left|\left(\left(L_f s\right)_{unc,i}\right)_{nom}\right| + \left|\left(L_f s\right)_{cer}\right| = \left(\frac{0.42}{0.29}\right)\left|\left(\overline{L_f s_1}\right)_{nom}\right| \\ &+ \left|\left(\overline{L_f s_2}\right)_{nom}\right| + \left(\frac{0.35}{0.29}\right)\left|\left(\overline{L_f s_3}\right)_{nom}\right| + \left|\frac{c\ddot{y}}{1+(c\dot{y})^2} - \frac{2c^3\dot{y}(\ddot{y})^2}{\left[1+(c\dot{y})^2\right]^2} + \dot{\theta} + \frac{c\ddot{y}}{1+(c\dot{y})^2}\right|\end{aligned} \tag{A.20}$$

where $\delta_f = \min[\delta_1, \delta_2, \delta_3] = \min[0.42, 0.29, 0.35] = 0.29$.

Also for $L_g s$ , $\delta_g$ is computed as;

$$\left|L_g s - \left(L_g s\right)_{nom}\right| < \left|\frac{(10.5+1.05)}{18.07+0.81(\sin(\theta))^2} - \frac{11}{21+(\sin(\theta))^2}\right| < \delta_g\left(L_g s\right)_{nom} = 0.23\left(L_g s\right)_{nom} \tag{A.21}$$

Now the sliding controller as in proposition (5.2), (Hameed 2007) is given by:

$$u = -\left(\frac{L_f s}{L_g s}\right)_{nom} - \nu_0 \operatorname{sgn} s \tag{A.22}$$

$$\nu_0 = 1.1\left[\frac{0.29+0.23}{1-0.23}\right]\left|\left(\frac{\overline{L_f s}}{L_g s}\right)_{nom}\right| = 0.68\left|\left(\frac{\overline{L_f s}}{L_g s}\right)_{nom}\right| \tag{A.23}$$

# INVESTIGATION AND MODIFICATION OF AERODYNAMIC CHARACTERISTICS OF SUPERSONIC AIRCRAFT

Dr. Jafar M. Hassan
Department of Mechanical Engineering
University of Technology
Baghdad, Iraq, P.O. Box :35010

Dr. Laith K. Abbass
Department of Technical Education
University of Technology
Baghdad, Iraq, P.O. Box :35010
E-mail: laithabbass@yahoo.com

Eng. Laith W. Ismail
Center of Training and workshops
University of Technology
Baghdad, Iraq, P.O. Box :35010

**الخلاصة:-**

زيادة الكفاءة الأيروديناميكية مع ضمان المناورة الخارقة للطائرة ذات السرعة فوق الصوتية (F-16A) يتم تقديمها. الخواص الأيروديناميكية, توزيع الضغط على سطح الطائرة وأعلى رفع يتم حسابه للشكل الرئيسي للطائرة لأعداد ماخ وزوايا هجوم مختلفة في حالة الطيران تحت وفوق الصوتي, بأستخدام طريقة الأشرطة (Panel Method) والمعادلات شبه التجريبية (DATCOM).

تم بناء برنامج حاسوبي فرض فيه آلية الدفع الموجه (TVFC) مع أسطح السيطرة (Canards), النتائج بينت أن أسطح السيطرة مع آلية الدفع الموجه قد ولدت عزم ترجح (Nose-down pitching moment) يستطيع إسناد الذيل الأفقي في حالة المناورات العالية. أما من الناحية الأيروديناميكية فأن (5-6%) زيادة في الكفاءة الأيروديناميكية وجدت بعد إضافة أسطح السيطرة عن الشكل الأصلي للطائرة في حالة الطيران تحت وفوق الصوتي.

## ABSTRACT

Increasing the aerodynamic efficiency and enhancing the supermaneuverability for the selected supersonic aircraft (F-16A) is presented. Aerodynamic characteristics, surface pressure distribution and maximum lift are are estimated for the baseline configuration for different Mach number and angles of attack in subsonic and supersonic potential flow, using a low order three-dimensional panel method supported with semi-empirical formulas of Datcom.

Estimation of the total nose-up and nose-down pitching moments about the center of gravity of the completed aircraft in subsonic region depending on the flight conditions and aircraft performance limitations. A modern program was implemented by suggesting a two dimensional thrust vectoring technique (pitch vectoring up and down) controlled by the best design of advanced aerodynamic and control surface (foreplane or canard). Work results shows that the canard (as a control surface) with thrust vectoring produces enough nose-down moment and can support the stabilator at high maneuvers, while for an aerodynamic surface, a rate of (5-6%) increase was achieved in the aerodynamic efficiency (lift-to-drag ratio) of the baseline configuration in both subsonic and supersonic flight.

## NOMENCLATURE

| | | |
|---|---|---|
| $A_i$ | Panel area | m2 |
| AR | Lifting surface aspect ratio | - |
| b | Lifting surface span | m |
| c | Lifting surface chord | m |
| $c_{avg}$ | Mean geometric chord of the wing | m |
| $C_D$ | Drag coefficient | - |
| $C_{D0}$ | Drag coefficient at zero lift (parasite drag coefficient) | - |
| $C_L$ | Lift coefficient | - |
| $C_L^\alpha$ | Lift curve slope | 1/deg |
| $C_l^\alpha$ | Airfoil two dimensional lift curve slope | 1/deg |
| $C_M$ | Pitching moment coefficient | - |
| $C_{M\,cg}$ | Pitching moment coefficient about the center of gravity | - |
| $C_{M\,0}$ | Pitching moment coefficient at zero angle of attack | - |
| $C_N$ | Normal force coefficient | - |
| $C_P$ | Pressure coefficient | - |
| $C_T$ | Tangential force coefficient | - |
| g | Aircraft load factor | - |
| $l_c$ | Distance from the wing's quarter chord to the canard's quarter chord | m |
| $l_h$ | Distance from the quarter chord point of the average chord of the main wing to the quarter average chord point on the horizontal surface in subsonic speed | m |
| $M_i$ | Pitching moment about the origin of panel i | - |
| $M_\infty$ | Free stream Mach number | - |
| $N_i$ | Normal force of panel I | N |
| $q_i$ | Resultant velocity at panel i | m/s |
| S | Lifting surface reference area | m2 |
| $T_i$ | Tangential force of panel i | N |
| $T$ | Engine thrust | N |
| $u_i$ ,$v_i$ ,$w_i$ | Components of the velocity at panel i in x, y and z coordinates | m/s |
| V | Stream velocity | m/s |
| $W$ | Aircraft weight | N |
| $x_i$ , $y_i$ ,$z_i$ | Coordinates of the panel control point | m |
| $z_h$ | Vertical distance of the horizontal surface above the plane of the main wing | m |
| $\alpha$ | Angle of attack | deg. |
| $\theta$ | Inclined angle for the panel with respect to y-direction | |
| $\beta^2$ | Compressibility parameter $=\sqrt{1-M^2}$ or $\sqrt{M^2-1}$ | deg. |
| $\gamma$ | Singularity strength | M3/s.m |
| $\delta$ | Inclined angle for the panel with respect to x-direction | deg. |
| $\delta_C$ | Deflection angle of the canard | deg. |

| | | |
|---|---|---|
| $\delta_S$ | Deflection angle of the horizontal tail (Stabilator) | deg. |
| $\delta_{TV}$ | Deflection angle of the thrust vectoring | deg. |
| $\varepsilon$ | Downwash angle | deg. |
| $\varepsilon_u$ | Upwash angle | deg. |
| $\frac{\partial \varepsilon}{\partial \alpha}$ | Rate of downwash | - |
| $\frac{\partial \varepsilon_u}{\partial \alpha}$ | Rate of upwash | - |
| $\rho$ | Air density | kg/m3 |
| $\lambda$ | Taper ratio | - |
| $\phi$ | Velocity potential | m/s |

## INTRODUCTION

the emphasis today is on technology that will allow fighters to survive and win in combat. There is great interest today in an area of technology that goes under the generic title of "Supermaneuverability".

Dr. Herbst, of West Germany's Messerchmitt-Bo1kow-Blohm **[Col. William, 1988]**, defined supermaneuverability as the capability to execute maneuvers with controlled sideslip at angles of attack well beyond those for maximum lift. The designer-general of the Sukhoi "Mikhail Simonov" defined the supermaneuverability **[Venik's Aviation, 2002]**, as a fighter's capacity to turn toward its target from any position in space with at least twice the rate of turn that the enemy fighter is capable of. One method to enhance maneuvering is to simply use all lift inherent in a particular design, or increasing the aerodynamic efficiency (Lift/Drag). Another way of obtaining unconventional maneuvering especially at slow speeds and at high angles of attack is the addition of Thrust Vectoring Flight Control (TVFC) at the rear (i.e. changing the direction of the thrust produced by an aircraft's engine(s) **(Fig. 1)**, and the foreplan (Canard) which provides substantial lift as well as longitudinal trim and control and the control canard which is used for longitudinal trim and control only **(Fig. 2)**. In the present paper, Depending on the flight condition requirements during pull-up maneuver and with assistance of panel method program and developed programs, a foreplane (canard) surface has been designed (geometry, position, permissible deflection angle) using the iterative process and added to the model for two purposes, as an aerodynamic surface and as a control surface with thrust vectoring technique. Studying the effect of the canard surface on the aerodynamic efficiency and total pitching moment of the whole configuration.

## COMUTATIONAL AERODYNAMIC ANALYSIS **[Mason, 1998]**

For small perturbations, the governing equation of the potential flow can be simplified greatly and solution of many problems becomes possible. The linearized three-dimensional potential equation is **[L. Morino, 1974]**:

$$\beta^2 \phi_{xx} + \phi_{yy} + \phi_{zz} = 0.0 \tag{1}$$

Where $\beta^2$ is the compressibility parameter and depends upon Mach number. Expect for the case of the transonic flow, Eq.1 is valid for both subsonic ($\beta^2 = (1 - M_\infty^2)$) and supersonic flows ($\beta^2 = (M_\infty^2 - 1)$).

The pressure coefficient is then calculated using the exact isentropic formula

$$C_{p_i} = \frac{-2}{\gamma M_\infty^2} \left\{ \left[ 1 + \frac{\gamma - 1}{2} M_\infty^2 \left( 1 - q_i^2 \right) \right]^{3.5} - 1 \right\} \qquad (2)$$

where $q_i^2 = u_i^2 + v_i^2 + w_i^2$ (3)

The forces and moments acting on the configuration can then be calculated by numerical integration.

$$N_i = -A_i C p_i \cos\theta_i \ \cos\delta_i \qquad (4)$$

$$T_i = A_i C p_i \sin\delta_i \qquad (5)$$

$$M_i = N_i x_i - T_i z_i \qquad (6)$$

The forces and moment coefficients acting on the configuration are obtained by summing the panel forces and moments on both side of the plane of symmetry.

$$C_N = \frac{1}{S} \sum_{i=1}^{N} 2 * N_i \qquad (7)$$

$$C_T = \frac{1}{S} \sum_{i=1}^{N} 2 * T_i \qquad (8)$$

$$C_M = \frac{1}{S\bar{c}} \sum_{i=1}^{N} 2 * M_i \qquad (9)$$

The lift and drag coefficients formulas are:-

$$C_L = C_N \cos\alpha - C_T \sin\alpha \quad \text{for (wing-body)} \qquad (10)$$

$$C_D = C_N \sin\alpha + C_T \cos\alpha \quad \text{for (wing-body-tail)} \qquad (11)$$

The maximum lift coefficient of lifting surfaces at subsonic speed is given by:

$$C_{L_{max}} = (C_{L_{max}})_{base} + \Delta C_{L_{max}} \qquad (12)$$

The value of $(C_{L_{max}})$ and $\Delta C_{L_{max}}$ can be estimated from **[(Hoak.),(Daniel, 1992)]**.

Taking into the considerations the contributions of the additional horizontal lifting and stabilizer surfaces on the aircraft total lift curve slope, to determine a horizontal tail contribution (the rate of downwash) **[Fink, 1975]**:-

$$\frac{\partial\varepsilon}{\partial\alpha} = \frac{21^{o} C_L^{\alpha}}{AR^{0.725}} \left( \frac{c_{avg}}{l_h} \right) \left( \frac{10 - 3\lambda}{7} \right) \left( 1 - \frac{z_h}{b} \right) \qquad (13)$$

Where $\frac{\partial\varepsilon}{\partial\alpha}$ is the rate of change of downwash in angle of attack.

$$\Delta C_L^{\alpha} (\text{due to horizontal tail}) = C_{L\,t}^{\alpha} \left( 1 - \frac{\partial\varepsilon}{\partial\alpha} \right) \frac{S_t}{S} \qquad (14)$$

While the contributions of the additional horizontal lifting surface (Canard) to the aircraft (the rate of upwash) is:-

$$\frac{\partial \varepsilon_u}{\partial \alpha} = \left(0.3AR^{0.3} - 0.33\right)\left(\frac{l_c}{c}\right)^{-\left(1.04+6AR^{-1.7}\right)} \tag{15}$$

Where $\frac{\partial \varepsilon_u}{\partial \alpha}$ is the rate of change of upwash in angle of attack.

$$\Delta C_L^{\alpha}\text{(due to canard)} = C_{L\,C}^{\alpha}\left(1+\frac{\partial \varepsilon_u}{\partial \alpha}\right)\frac{S_c}{S} \tag{16}$$

Once the contributions of canard and horizontal tail are estimated, the whole aircraft lift curve slope is given by:

$$\begin{aligned} C_L^{\alpha}(Total\ aircraft) = C_L^{\alpha}(wing+body+strake) &+ \\ \Delta C_L^{\alpha}(due\ to\ horizontal\ tail) &+ \\ \Delta C_L^{\alpha}(due\ to\ canard) & \end{aligned} \tag{17}$$

## TOTAL PITCHING MOMENT COEFFICIENT **[(F-15,2003),(Shaker,2000),(John,1997),( Perkins,1949),( B. Etkin,1996),( Nelson,1998)]**

For longitudinal static stability and pitch control, the total aircraft pitching moment curve is only considered. However, it is of interest to know the contribution of the wing, fuselage, tail, propulsion system, etc., to the pitching moment and longitudinal static stability characteristics of the aircraft. The aircraft pitching moment coefficient about the center of gravity due to the contribution of wing-fuselage, aft tail, canard and thrust vectoring is:-

$$C_{M_{cg}} = C_{M_0} + C_{M_\alpha}\alpha + C_{M_{\delta_S}}\delta_S + C_{M_{\delta_c}}\delta_c + C_{M_{TV}} \tag{18}$$

## g-LOADING **[Kotelnikov ,1973]**

In some cases to analyze the motion of the aircraft it is convenient to use the relative magnitudes of forces per unit of weight of the aircraft rather than the absolute ones. For this purpose the concept of the g-load is introduced. Aircraft load factor (g) or (g-loading) during a turn expresses the maneuvering (or acceleration due to lift) of an aircraft as a multiple of the standard acceleration due to gravity (g=9.81 m/s2). Therefore, it is related to turn. There are two important turns, "sustained" turn for some flight condition at which the thrust of the aircraft is just sufficient to maintain velocity and altitude in the turn i.e., thrust must equal the drag and lift equal g times the weight. Thus the maximum g for sustained turn can be expressed as **[Daniel, 1992]**:

$$g = \sqrt{\frac{0.5\rho V^2}{K(W/S)}\left(\frac{T}{W} - \frac{0.5\rho V^2 C_{D0}}{W/S}\right)} \tag{19}$$

where $K = 1/(\pi\, AR\, e)$, $e \approx 0.8 - 1.0$

The second turn is "instantaneous", if the aircraft turns at a quicker rate; the drag becomes greater than the available thrust, so the aircraft begins to slow down or loss altitude. Therefore, g will be limited by the maximum lift coefficient or structural strength of the aircraft and is equal to **[Daniel, 1992]**:

$$g = \frac{0.5\rho V^2 S C_{L\max}}{W} \tag{20}$$

## VERIFICATION TEST

For aerodynamic analysis, the verification test was used to confirm the validity of the computer program results with the flight data of supersonic aircraft model (Sukhoi Cy–20). Three-dimensional paneling of the symmetrical model contain three parts. 14 strips along the fuselage length and 6 strips along the half meridian have been used to represent the body fuselage by forming 84 panels. 12 strips along the span and 8 strips in each contour line at chordwise direction were used for wing, horizontal tail and vertical tail, which made 288 panels. Therefore, the total number of panels is 372 panels.

Using the above inputs with the assistance of theoretical approach computations for the lift and drag coefficients on the complete surface were made in three stages, wing-body, stabilizer-body and fin-body. **(Table 1)** gives the comparison results between the computer program and flight test **[AIRCRAFT,1972]**.

A good correlation was obtained although there was about +8% error in lift computations at supersonic speed. In fact, the present code shows a good performance in the subsonic region and an acceptable duration in the supersonic region. The maximum Mach number and angle of attack depends on the shape and dimension of the configuration, and should be within the linear aerodynamic zone.

## RESULTS AND DISCUSSION

Three-dimensional mesh and contours plotting were used to represent the pressure distribution over the complete selected aircraft configuration. **(Fig. 3)** represent these distributions at Mach number 0.8 and 1.6 with effective angles of attack of 10 and 15 degrees.

The maximum contour distribution as shown in **(Fig. 3(A))** at 0.8 Mach number is at the wing leading edge. It increases significantly when angle of attack is high. In **(Fig. 3(A))**, the Mach cone angle is approximately equal to the wing leading edge angle and covers the horizontal tail area when Mach number is 1.6 **(Fig. 3(B))**. The aircraft performance in cases of instantaneous and sustained maneuvers capability (load factor g) is shown in the form of contours (using the 3-dimensional Kriging Algorithm to represent the results **[Kotelnikov,1973]**. **(Figs. 4 and 5)** are used for specific flight conditions (constant combat weight = 12036.53 kg, different altitude = 0 m, 3048 m, 6069 m, 9144 m, 12192 m, 15240 m, Mach number up to 1.0, required angle of attack).

The maximum differences $\Delta C_{M\,c.g}$ between the two pitching moments generated from the two stabilator's deflection (positive and negative deflections $\pm 25^0$) is (0.1561) at an altitude of (6096 m) and Mach number (0.9) for (5g) in case of sustained maneuver, a (0.21452) was achieved at altitude (6096 m) and Mach number (0.9) for (7g). As for instantaneous maneuver, a (0.21452) was achieved at altitude (6096 m) and Mach number (0.9) for (7g). So, all the moving small foreplane (canard) surface, large and fast actuator and near to the aircraft nose with Thrust Vectoring Flight Control (TVFC) can be used to fix this problem.

Because both are sustained and instantaneous maneuvers $\Delta C_{M\,c.g\,\max}$ have the same altitude (6096 m) and Mach number (0.9), therefore, an intermediate value of $\Delta C_{M\,c.g\,\max}$

($\approx$0.18) will therefore be considered as an initial trail. Also to simplify the issue, the suggested canard will have the same airfoil section as for the wing and horizontal tail, i.e., NACA $64_A$-204, pitching moment about aerodynamic center $C_{M\,a.c.}$ about (–0.02) and the two-dimensional lift curve slope $c_l^{\alpha}$ is approximately 0.1/deg **[John,1997]**. The conventional design procedure (or the computerized iterative process) was used to solve the problem. Designing the proper area, lift and position of the canard was considered in the first step. Results of the iterative process are shown in **(Fig. 6)** for the first step. The minimum canard area is favorable because it ensures minimum interference with the fuselage and wing. From **(Fig. 6(A))**, the proper lift curve slope $C_{L\,C}^{\alpha}$ can be chosen. The canard longitudinal position **(Fig. 6(B))** is chosen to be as minimum as possible from aircraft nose to have a long arm for moment. Therefore, the required canard lift, area and position. At $\Delta C_{M\,c.g\,\max}$ $\approx$0.18 Canard Area $\approx$0.070$\rightarrow$0.072 of Wing Area $\approx$1.95$\rightarrow$2.0 $m^2$ ,Minimum required Canard Lift Curve Slope = 0.039/deg and the Longitudinal Canard Position from Aircraft Nose=3.7m. **(Table 2)** shows the initial canard layout which can be considered for the preliminary design.

The drag polar and lift-to-drag ratio of the isolated canard surface is plotted for different Mach numbers as shown in **(Fig. 7)**. The maximum lift curve slope of isolated canard $C_{L\,C}^{\alpha}$ is 0.00432 /deg at 1.2 Mach number **(Fig. 8)**. It appears as shown in **(Fig. 9)** that this model has enough moment and can support the horizontal tail (stabilator) during nose-down moment at high maneuvers capability. The effect of canard as an aerodynamic surface can be shown in **(Figs. 10,11 and 12)**. In general, a 5-6% increase in the lift curve slope and lift-to-drag ratio of the baseline configuration in both subsonic and supersonic regimes has been achieved when using small, all moving canard surface.

## CONCLUSIONS

- The pressure distributions over the upper surfaces of the configuration shows that the contour distribution increased significantly when the Mach number decreases and the pressure distribution shows a clear pattern of increasing peak pressure with angle of attack in agreement with the increasing the strength of the leading edge vortex.
- It appears that the selected supersonic aircraft was unstable in the subsonic aircraft regime (negative static margin) while, it was stable in the supersonic regime. Static margin is a measure of the aircraft stability, for stability criterion becomes when static margin > zero.

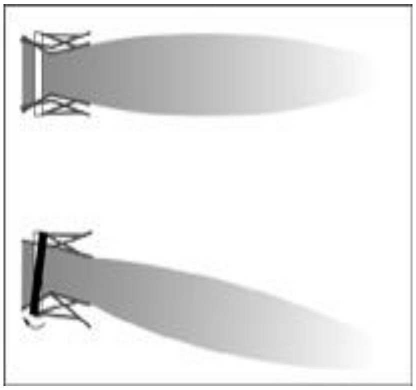

**Figure 1**
**Thrust Vectoring Flight Control**

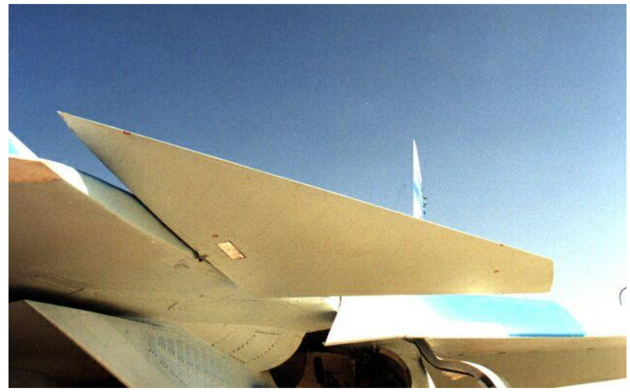

**Figure 2**
**Foreplane (Canard)**

**Table 1**
**Cy-20 Aerodynamic Characteristics**

| | *Mach* No. | Flight Data [15] | Wing-Body-Tail | | | | Error % |
|---|---|---|---|---|---|---|---|
| | | | Wing/Body | Horizontal Tail/Body | Vertical Tail/Body | Total | |
| $C_L^\alpha/\text{deg}$ | 0.8 | 0.0541 | 0.047346 | 0.007043 | - | 0.05052 | -6.60 |
| | 1.3 | 0.0607 | 0.054233 | 0.009251 | - | 0.05745 | -5.35 |
| | 1.6 | 0.05123 | 0.052063 | 0.009147 | - | 0.05537 | +8.09 |
| $C_{D0}$ | 0.8 | 0.0171 | 0.00867 | 0.00493 | 0.00256 | 0.01616 | -5.49 |
| | 1.3 | 0.0393 | 0.01859 | 0.01254 | 0.00708 | 0.03821 | -2.77 |
| | 1.6 | 0.0425 | 0.02625 | 0.01082 | 0.00584 | 0.04291 | +0.96 |

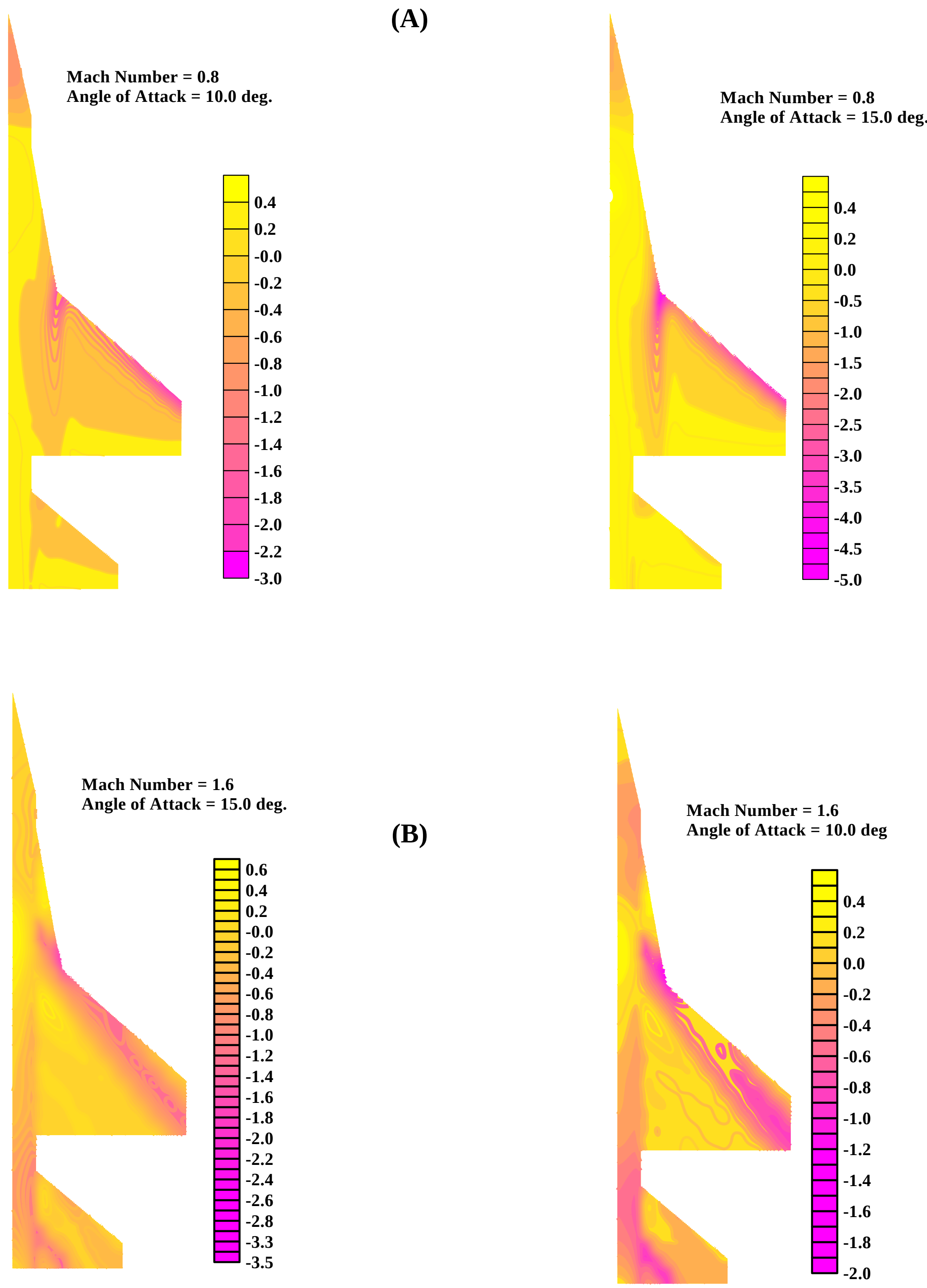


**Figure 3**
**Pressure Distribution Contours on the Upper Surface at(0.8 & 1.6) Mach number for (10 & 15) Angle of Attack**

Combat Take-off Weight = 12036.53 kg

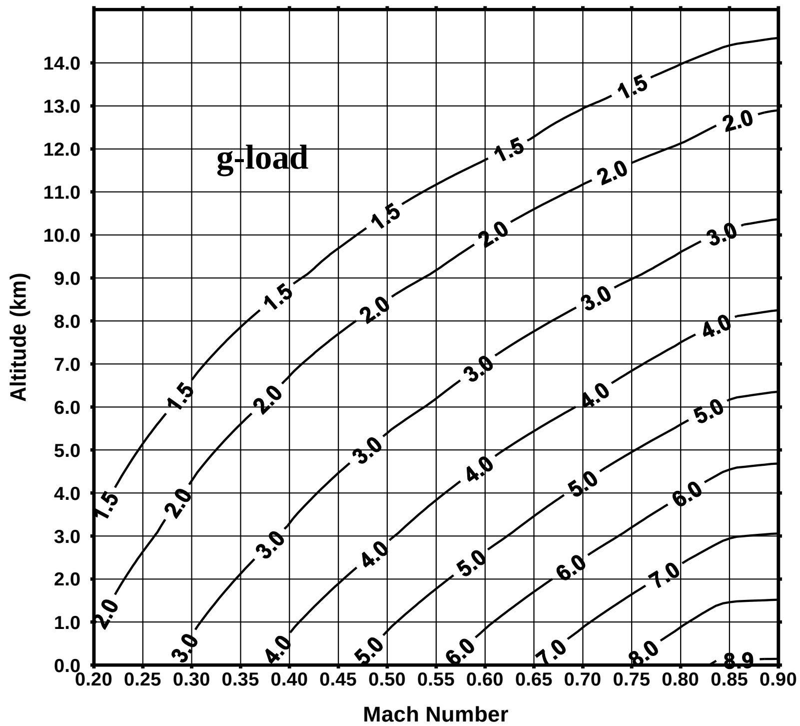


**Figure 4**
**Sustained Maneuvers Capability of the Selected Model in Subsonic Region**

Combat Take-off Weight = 12036.53 kg

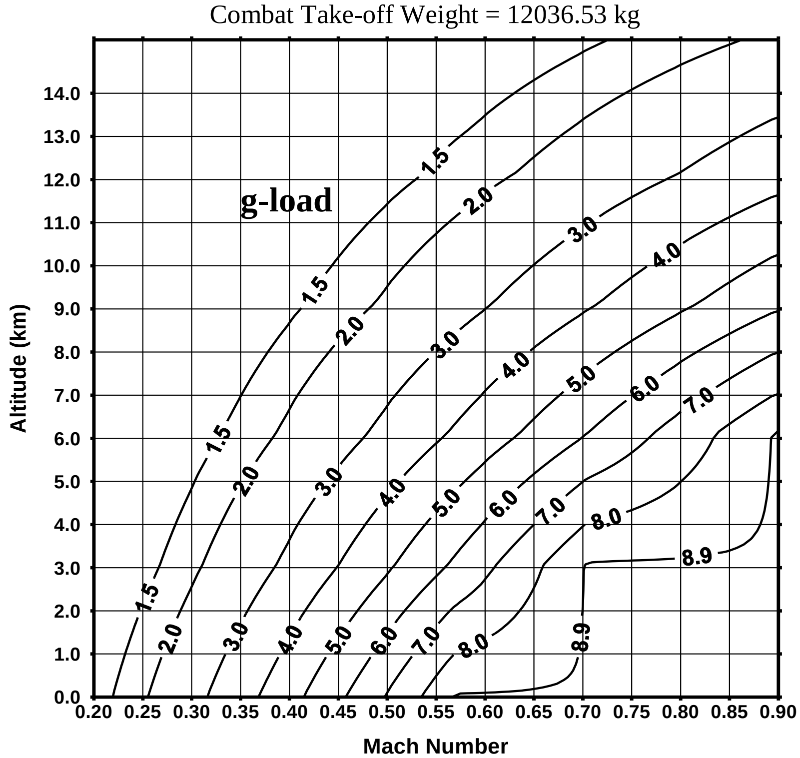


**Figure 5**
**Instantaneous Maneuvers Capability of the Selected Model in Subsonic Region**

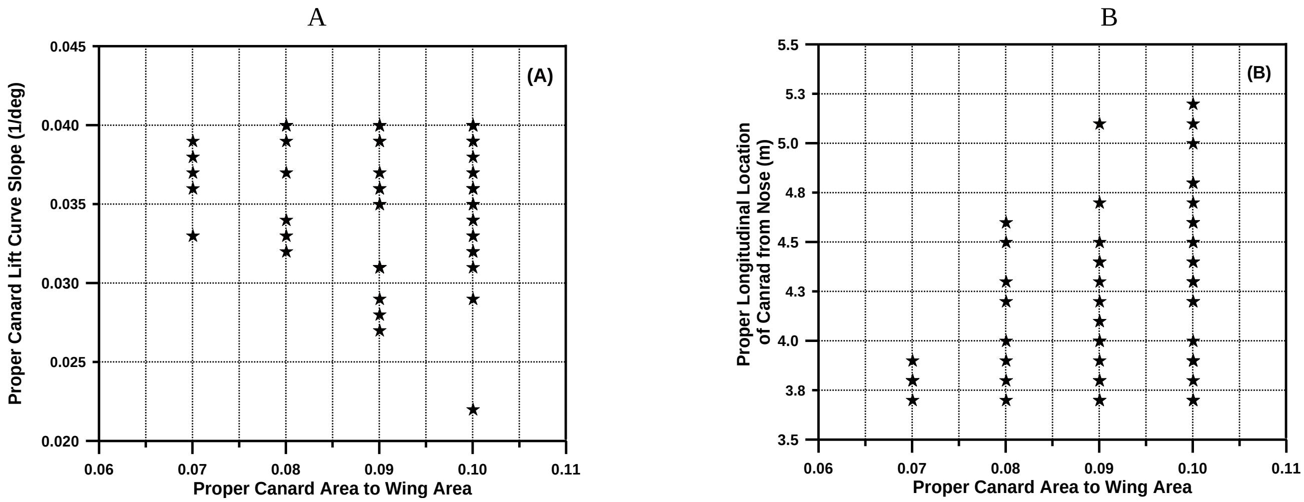


**Figure 6**
**Proper Canard Lift Curve Slope (1/deg) and its Longitudinal Location from the Aircraft Nose versus the Canard to Wing Area Ratio**

**Table 2**
**The Initial Canard Layout**

| | |
|---|---|
| Area ($m^2$) | 1.995 |
| Total Span (m) | 2.1 |
| Root Chord (m) | 1.6 |
| Tip Chord (m) | 0.3 |
| Aspect Ratio | 2.2105 |
| Taper Ratio | 0.1875 |
| Leading Edge Angle (deg.) | 57 |
| Trailing Edge Angle (deg.) | 73 |
| Maximum deflection (deg.) | $\pm 40$ |

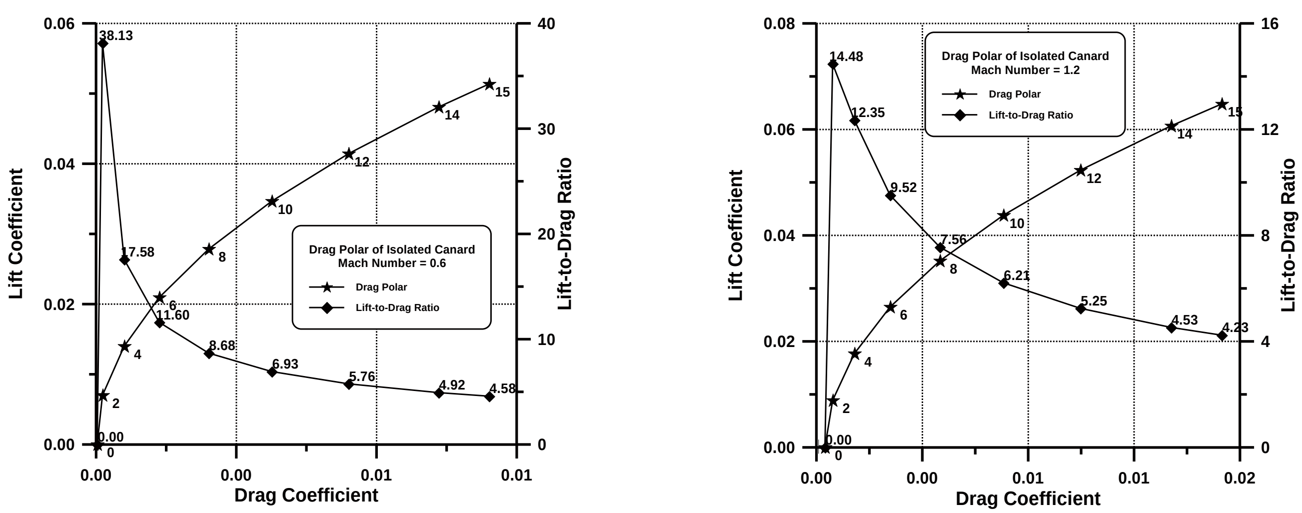


**Figure 7**
**Drag Polar and Lift-to-Drag Ratio of Isolated Canard Surface At Different Mach number**

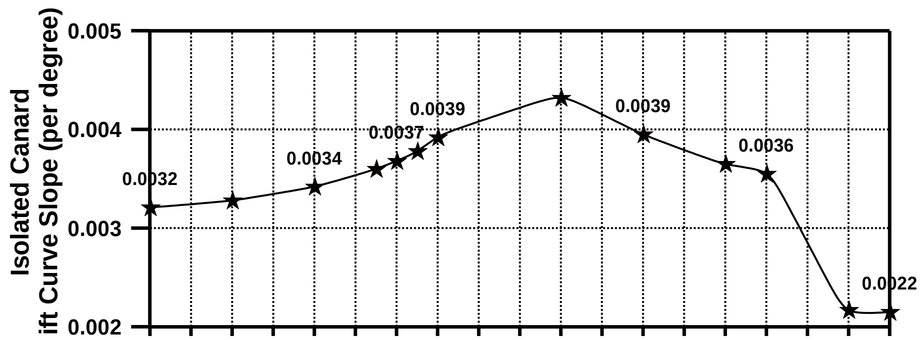


**Figure 8**
**Lift Curve Slope (per degree) of Isolated Canard Surface As a Function of Mach number**

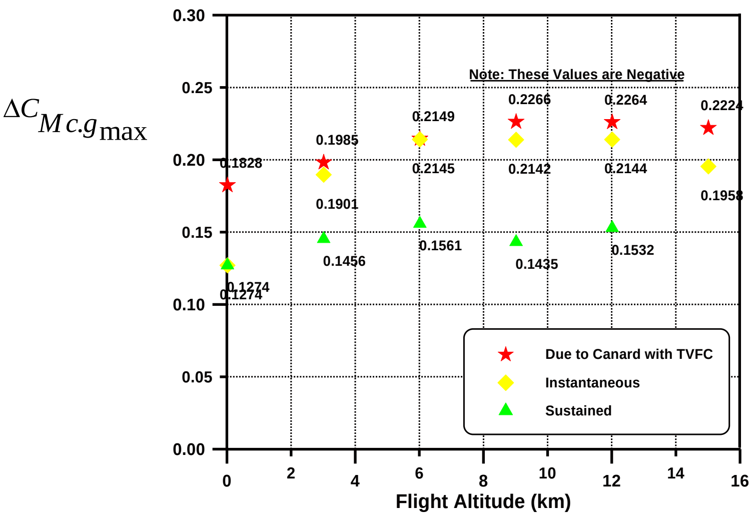


**Figure 9**
**Effect of Canard with TVFC Pitching Moment**

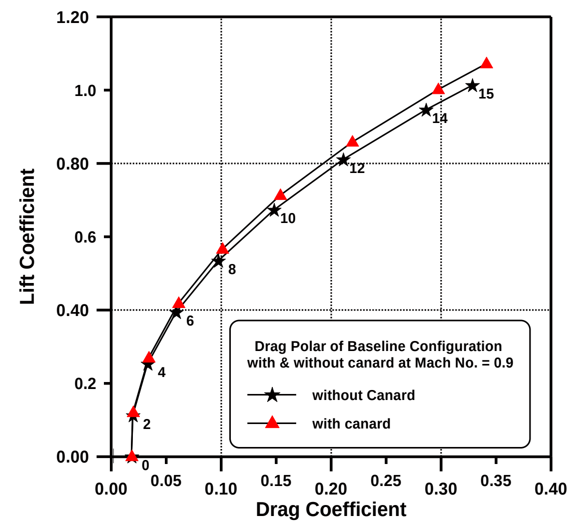


**Figure 10**
**Comparison Study of Drag Polar between the Baseline Configuration and Configuration with Canard Surface**

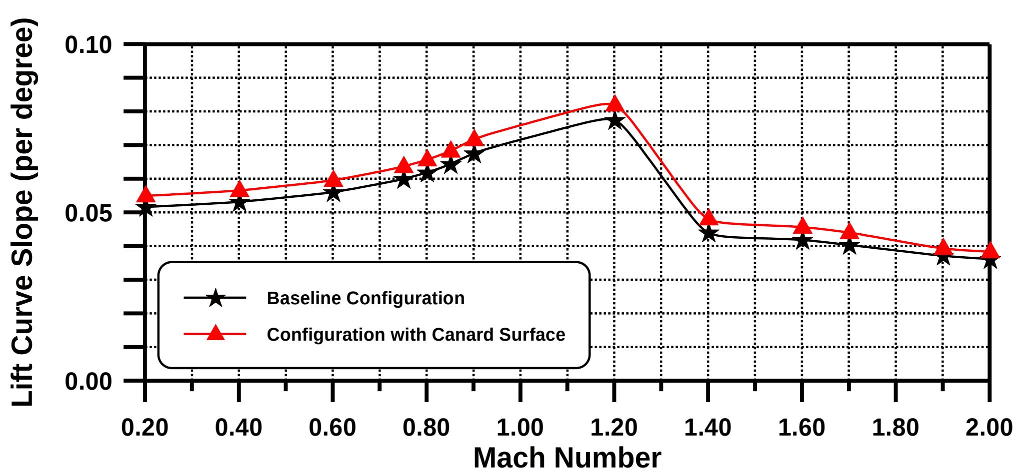


**Figure 11**
**Comparison Study of Lift Curve Slope between the Baseline Configuration and Configuration with Canard Surface**

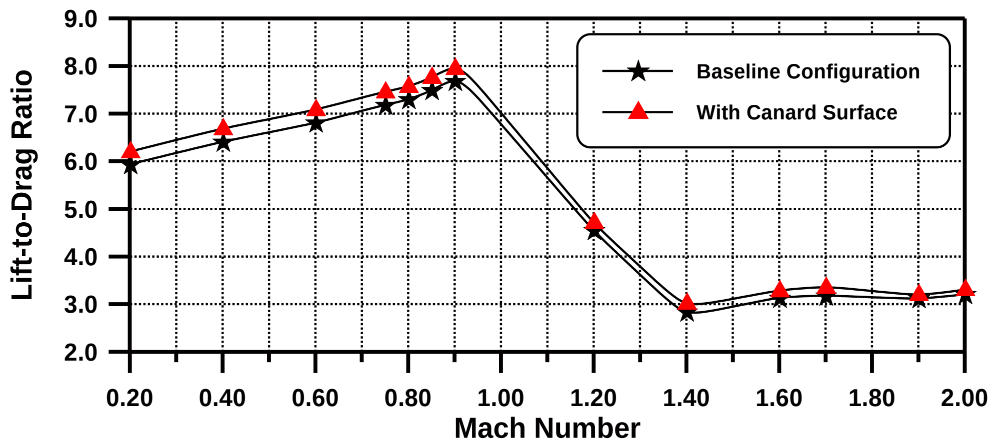


**Figure 12**
**Comparison Study of Lift –to-Drag between the Baseline Configuration and Configuration with Canard Surface**

## REFRENCES


- AIRCRAFT Cy-20, Technical Description, BOOK 1, "GENERAL INFORMATION AND FLIGHT PERFORMANCE", TOP SECRET, Copy No. 28, 1972.
- B. Etkin and L. D. Reid, "Dynamics of Flights: Stability and Control", John Wiley & Sons, New York, NY, third edition, 1996.
- Col. William D. Siuru, Jr., "Supermaneuverability", Aerospace Power Journal, Spring, 1988.
- Email: aspj@maxwell.af.mil
- Danie P. Raymer, "Aircraft Design: A Conceptual Design", AIAA, 1992.
- Fink, R.D., "USAF Stability and Control DATCOM", Wright-Patterson AFB, OH, 1975.
- "F-15 ACTIVE (Advanced Control Technology for Integrated Vehicles)- Research Program History and Technology", Document: EG-2003-01-001-DFRC, NASA Dryden Flight Research Center, 2003.
- Hoak, D., Ellison, D., et al., "USAF DATCOM", Air Force Flight Dynamics Lab., Wright-Patterson AFB, OH.
- John J. Bertin, Randall J. Stiles, and Steven A. Brandt, "Introduction to Aeronautics: A Design Perspective", American Institute of Aeronautics and Astronautics, January 1997.
- Kotelnikov, G. N., "Airplane Aerodynamics", Textbooks for Cadets of aircraft-Technician Officer Schools, Russia, 1973.
- L. Morino and C.C. Luo, " Subsonic Potential Aerodynamics for Complex Configurations. A General Theory", AIAA Journal, Vol. 12, No. 2, February 1974.
- Mason, W. H., "Applied Computational Aerodynamics", Internet Pages (a PDF File), April 1998.

- Nelson, R. C., “Flight Stability and Automatic Control”, WCB McGraw-Hill, New York, NY, second edition, 1998.
- Perkins, D. Courtland and Hage, E. Robert, “Airplane Performance Stability and Control”, John Wiley & Sons, New York, NY, 1949.
- Shaker M. Hussain, “Flight Performance Optimization of Supersonic General Aviation Design”, Ph.D. Thesis, Military College of Engineering, Baghdad, 2000.
- Venik’s Aviation, “Breakthrough in Supermaneuverability”, June 19,2002.
- Email: www.aeronautics.ru//venik.way.to

Number 3 Volume 16 September 2010 Journal of Engineering

# FLASH EVAPORATION ENHANCEMENT BY ELECTROLYSIS OF SATURATED WATER FLOWING UPWARDS IN VERTICAL PIPE

Dr. Akram. W. Izzat
Mechanical Engineering Department
University of Baghdad

Radwan Muhammad Addaiy
Mechanical Engineering Department
University of Baghdad

## ABSTRACT

An experimental system was designed and built to produce the flash evaporation of upward water flow in a (1.8 m) vertical mounted glass test section pipe. The water loses the static head as it moves up, accordingly flash evaporation occurs somewhere inside the test section, where the water local temperature reaches its saturation temperature at that position, which is dependent on the water inlet temperature and its mass flow rate. The steam quality in the test section exit was measured by collecting the steam generated in the test section outlet and condensed in the condenser at specified time.

The hydrogen bubbles are injected inside the two – phase mixture flow within the test section. These bubbles act as an exciter for steam generation inside saturated water.

Water electrolysis using (12 V) and ionization current (7 A), increases steam quality at test section outlet by (33%) when it is compared to that obtained without water electrolysis. A reduction of (42%) in non-equilibrium temperature difference is achieved using the same ionization settings. The effect of ionization process on flash inception point and temperature is investigated from the experiments.

The experimental results are compared to the theoretical results obtained using mathematical model based on solving the mass, momentum and energy equations for two –phase flow assuming separated flow model.

The effect of the electrical power used for water ionization is simply simulated in these calculations using mass and heat balance equation that covers the boundary conditions of the system.

## الخلاصة

تم تصميم منظومة تجريبية لغرض تحقيق ظاهرة الغليان التلقائي أثناء جريان الماء إلى الأعلى داخل أنبوب زجاجي بطول (1,8 م ) مخصص للقياسات , عمودي التثبيت . عند جريان الماء إلى الأعلى فانه يفقد جزءا من ضغطه الاستاتيكي , عند ذلك يحصل الغليان التلقائي عند نقطة ما داخل الأنبوب الزجاجي تكون فيها درجة حرارة الماء مساوية لدرجة حرارة الإشباع في تلك النقطة .

تم قياس النسبة الوزنية للبخار ( steam quality ) في مخرج الأنبوب الزجاجي من خلال تجميع البخار المتولد في الأنبوب الزجاجي والمتكثف في جهاز التكثيف خلال فترة زمنية محددة .
لقد تم حقن فقاعات الهيدروجين في داخل المزيج الثنائي الطور أثناء جريانه في الأنبوب الزجاجي. حيث تعمل فقاعات الهيدروجين كمحفز لتوليد البخار . لقد وجد إن نسبة البخار الوزنية ( steam quality) عند نهاية انبوبة الاختيار تزداد بنسبة ( 33 %) عما عليه بدون حقن تلك الفقاعات وذلك بتسليط فرق جهد قدره 12 فولت وتيار قيمته 7 أمبير, وانخفاض بنسبة (42%) من قيمة درجة الحرارة غير المتزنة عند نفس ظروف التأيين.
إن تأثير عملية التائيين على نقطة بداية الغليان التلقائي ودرجة حرارته تم دراستها خلال الجزء العملي .
النتائج العملية تم مقارنتها مع النتائج النظرية والتي حصلنا عليها باستخدام موديل رياضي يستند في حله على معادلات الكتلة والزخم والطاقة لجريان ثنائي الطور مع فرض نمط جريان أنفصال عند الحل .
إن تأثير الطاقة الكهربائية المستخدمة في عملية التائيين يكون مبسطا في عمليات الحساب باستخدام معادلة توازن الكتلة والحرارة والتي تغطي الظروف المحيطة بالمنظومة .

**KEYWORDS: Flash Evaporation, Electrolysis, Bubbles Injection, Steam Quality.**

## INTRODUCTION

Flow boiling is a boiling in a flowing stream of fluid, where the heating surface may be the channel wall confining the flow. The boiling flow is composed of a mixture of liquid and vapor. In this case individual dispersed bubbles are move independently up the vertical channel.

It is necessary to distinguish between boiling and flash evaporation. Boiling is a phase change accompanied by a supply of heat at constant pressure, while flashing is a phase change occurs due to reduction in pressure.

Boiling heat transfer is encountered in numerous engineering applications. One important field of application of boiling and evaporation is in desalination of sea water, which is becoming essential in some arid regions. That occurs by which the saline water is evaporated at reducing pressure. The vapor is taken to a condenser. The condensed steam is collected as fresh water; therefore, we need to enhance boiling.

There are several ways adopted for boiling enhancement. The main distinction is usually made between passive and active techniques. To augment boiling, passive techniques employ special boiling surface geometries, or fluid additive, such as roughening of the heat transfer surface, pitting the surface with corrosive chemical, integral fins or rolling, knurling integral finned tubes, coating the surface with a porous layer, etc. Active techniques need external power, such as electric or acoustic fields and surface vibration. The present research belongs to enhanced boiling by using electric field.

The process of water boiling enhancement using electric field is ensured by water ionization using electrical current. The ionization current breaks the bonds of water molecules casing generation of hydrogen and oxygen bubbles. These bubbles act as exciter for steam generation inside saturated water, (ZAGHOUDI, 2005).

The main target of the present research is to study the effect of saturated water electrolysis on the steam quality at the exit of vertically mounted test section and compare that with steam quality in the same test section without electrolysis.

W. NAKAYAMA, et a l, (1980) studied enhancement of nucleate boiling heat transfer with structure surfaces composed of internal cavities in the form of tunnels and small pores connecting the pool liquid and the tunnels. The authors dealt with porous surface which showed that wall superheat of a very small degree can start nucleate boiling. O. MIYATAKE , T.TOMIMURA, Y.ID, (1985) presented in their research an experimental study on the utilization of flash evaporation in power systems utilizing solar energy. They recognized that the spray flash evaporation were considerably faster than those of flowing liquid in conventional multistage flash evaporator and those of pool water exposed to sudden pressure drop in a container . They suggested that the best method of enhancement of flashing may be by injection of nucleation liquid through some nozzle configuration into a low- pressure vapor zone.

NOAM LIOR and ENJU NISHIYAMA, (1995) conducted experiments in a scale – down stage of flash evaporation at about (100 Cº) to examine the effect of the generated hydrogen bubbles on flash evaporation. They have shown that electrically generated hydrogen bubbles have indeed promoted ebullition in flash stage regions where the superheat was otherwise too low for flash evaporation, and thus have increased evaporation rates resulting in reduction of up to (15%) in the non-equilibrium temperature difference.

AKRAM W. IZZAT, (2003) studied experimentally the flash evaporation of upward water flow in a (1.8 m) vertical mounted glass test section pipe. Multi-diameter test section (3cm-10cm) was used both as divergent and convergent channel. The author has been concluded qualitatively that the hydrogen bubble injection inside the two–phase mixture increases the steam quality in the test section exit.

G. HETSRONI, et al, (2004)**,** investigated experimentally saturated and sub-cooled pool boiling of environmentally acceptable surfactant solution on horizontal tube. The kinetic of boiling (bubble nucleation, growth and departure) were investigated by high–speed video recording.

In the present experiments water is allowed to flow vertically upward in a vertical cross sectional area channel. When it reaches a certain distance in the test section and when the local pressure becomes equal to saturation pressure corresponding to the local temperature, water starts to evaporate due to the flashing. The experiments are conducted using low water velocities in order to observe the motion of bubbles along the test section.

The local pressure, local temperature is measured at three longitudinally distributed positions along the test section. The water flow rate, boiler pressure are measured.

Water temperature is measured using calibrated thermocouples, thermistors and digital thermometer, while the static pressure is measured using the water manometer and the local pressure gage. The water flow rate is measured using calibrated flow meter.

The results of these measurements are compared with those obtained from the theoretical analysis. The theoretical analysis adopted in the present work is based on separated flow model.

## EXPERIMENTAL APPROACH

The system arrangement shown in figure (1) is used to estimate the flow boiling enhancement by measuring the physical properties of the water during flashing process. The system consists of (1.8 m) length of the test section. The test section is manufactured from (PYREX) glass to ensure both clear visualization and good resistance to high temperature under maximum pressure of (1.2-1.6 bars). Test section diameter is constant (5cm).

Temperature and pressure measurement taps are distributed in the test section perimeter in three levels along the test section length. Four taps are specified for these measurements in each level. The first four taps are located at (15 cm) from the test section inlet. Each taps is a circular opening of (5 mm) inner diameter. The other four taps with the same inner diameter is located at (65 cm and 125 cm) distance from the test section inlet respectively.

These taps are specified for measurement purposes (static pressure and temperature measurements), also for the bubble air generation inside the test section during the ionization of water by the (electrolysis). The lower part of the test section is connected with the boiler, while the upper part is connected with enlarged glass test section part used for steam separation. This enlarged glass test section part is connected from its side to the horizontal glass pipe used to transport the water to the pump, while it is connected from the upper side to the condenser through flexible tube.

The water is circulated through the test section and the boiler using circulating pump located in perpendicular position to reduce the losses and any cavitation that could be anticipated during flash process. The boiler in the present experiments consists of electrically heated coil used to heat the water with heat capacity of (3kW). The body of the boiler is thermally insulated to reduce the heat losses to the environment .When the water passes through the boiler, its temperature rise above (100 $C^0$), as it is kept under the static pressure of the test section column (1.8m), then it enters the test section. The water velocity inside the test section is controlled by adjusting the water flow rate by the two valves (V1 and V2), while the water temperature during flashing is controlled by the cold water line valve (V5).

In order to ensure certain temperature difference between the boiler outlet and inlet , water flow rate inside the boiler is adjusted by mean of the same valves (V1 and V2) . The hot water circulation rate inside the test section is measured using flow meter (FM) of range (0.2-3 $m^3$/hr). In order to shorten the elapsed time required for the water to reach its steady state temperature, i.e constant temperature at test section inlet, the main parts of the experimental system are insulated with proper thermal insulation. Cold water at normal laboratory temperature (18 $C^0$) is added to the circulating water before the pump inlet by means of manually operated valve (V5) to balance the heat inside the system. For the purpose of mass balance, water is drained from the lower part of the test section by means of gravity action through valve (V4).

The fluid inside the test section is ionized by passing a (D.C) current across two electric poles at position (E1 and E2), see Fig. (1). The positive pole is fixed in position (1) ,while the negative pole is fixed in position (2) .The ionization current is measured at constant voltage by means of (12V – 10A ) D.C power supply type (PC-10A ) . These measurements are repeated at five different ionization currents, (3, 4.5, 5.5 and 7 A) using constant voltage power supply of (12V).

## THEORITICAL ANALYSIS

The assumptions and the formulation of mass, momentum and energy equations shown below, described in details by (IZZAT, 2003).

**Mass equation:**

$$\frac{\partial M}{\partial z}=0 \qquad (1)$$

Where:

$$M = \rho_f U_f As_f + \rho_g U_g As_g \qquad (2)$$

**Momentum equation:**

$$\rho_f U_f \frac{dU_f}{dz}=\frac{-dP}{dz}-\rho_f gCos\theta+\frac{F_{fg}-Fw_f}{(1-\alpha)d\forall}-\frac{1}{2}\frac{1}{(1-\alpha)}(Ug-U_f)G\frac{dx}{dz} \qquad (3)$$

$$\rho_g U_g \frac{dUg}{dz}=\frac{-dP}{dz}-\rho_g gCos\theta-\frac{F_{fg}}{\alpha d\forall}-\frac{1}{2\alpha}(U_g-U_f)G\frac{dx}{dz} \qquad (4)$$

Substitute for:

Cos θ = 1 since the flow in our case is in vertical direction pipe:

$$FW_f=\frac{fG_f^2}{2D\rho_f}=\frac{f\rho_f U_f^2(1-\alpha)}{2D} \qquad (5)$$

$$F_{fg}=\frac{12\pi\mu_f a(U_g-U_f)}{(1-\alpha)^2} \qquad (6)$$

$$\frac{dx}{dz}=\frac{\partial x}{\partial h}\frac{\partial h}{\partial z}+\frac{\partial x}{\partial p}\frac{\partial P}{\partial z} \qquad (7)$$

**Energy equation:**

$$\frac{\partial}{\partial t}\left[As\alpha\rho_g(e_g+\frac{U_g{}^2}{2})+As(1-\alpha)\rho_f(e_f+\frac{U_f^2}{2})\right]+$$
$$\frac{\partial}{\partial z}\left[\alpha As\rho_g U_g(h_g+U_g{}^2)+As(1-\alpha)\rho_f U_f(h_f+U_f^2)\right]= \qquad (8)$$
$$(qe+qm-ws-w\tau)As-((As\rho_g U_g+As\rho_f(1-\alpha)U_f)Cos\theta$$

After formulation of these equations the following final equations are used in the computer program to conduct the theoretical calculations:

$$\alpha=\frac{1}{1+\frac{1-x}{x}\frac{\rho_g}{\rho_f}s} \qquad (9)$$

Where:

s: is the slip ratio between the phases $s = \dfrac{U_g}{U_f}$ (10)

$$\rho_f U_f \frac{dU_f}{dz} = \frac{-d\rho}{dz} - \rho_{fg} + \left( \frac{12\pi\mu_f a\left(U_g - U_f\right)}{(1-\alpha)^2 \frac{\pi D^2}{4} Dz} - \frac{f\rho_f U_f^2}{2D} \right) \frac{1}{(1-\alpha)} - \frac{1}{2}$$
$$\frac{1}{(1-\alpha)}(U_g - U_f)\left[\alpha\rho_g U_g + (1-\alpha)\rho_f U_f\right]\left[\frac{Cp(T_{i+1}-T_i)}{h_{fg}\Delta z} + \frac{\partial x}{\partial P}\frac{\partial P}{\partial z}\right] \tag{11}$$

$$\rho_g U_g \frac{dU_g}{dz} = \frac{-dP}{dz} - \rho_g\, g - \frac{1}{\alpha}\left[\frac{12\pi\mu_f a\left(U_g - U_f\right)}{(1-\alpha)^2 \frac{\pi D^2}{4}\Delta z}\right]$$
$$-\frac{1}{2\alpha}(U_g - U_f)\left[\alpha\rho_g U_g + (1-\alpha)\rho_f U_f\right]*\left[\frac{Cp(T_{i+1}-T_i)}{h_{fg}\Delta z} + \frac{\partial x}{\partial P}\frac{\partial P}{\partial z}\right] \tag{12}$$

Where:

$$T_{i+1} = \frac{T^*_{i+1} - \frac{x_i}{Cp_i} h_{fgi}}{(1-x_i)} \tag{13}$$

$$T^*_{i+1} = \frac{\left[T_i \cdot \left(M_i\, Cp_i - \frac{hc_i Ac_i}{2}\right) + hc_i Ac_i Ta\right]}{\left(M_i Cp_i + \frac{Ac_i i\, hc_i}{2}\right)} \tag{14}$$

The first incremental value for the water temperature (Ti) at test section inlet is assumed to the initial value ($T_0$). The initial value is estimated using the following heat and balance equation:

$$T_0 = \left\{ QI + EP - hc*3.14*D*L*(Tout - Ta) + (Mi - Mout)*Cp*Tout + Mc*Cp*Tc \right\} / (Mi*Cp) \tag{15}$$

Where:

EP: is the electrolysis power.

$$EP = EV * EI \tag{16}$$

The mathematical calculations in this research take under consideration the mass and heat balance of the whole system which is realized by modifying the mathematical calculations performed by Akram.W.Izzat, using full theoretical equations based on postulated assumptions instead of incorporation of some measurement results in the computer program as input data.

Equation (16) simulates the effect of the electrolysis on the heat balance equation. This equation equals zero when the flow is without electrolysis after substitution the current input value equals to zero, while during electrolysis process steam quality is calculated based on different current values and constant ionization voltage.

**RESULTS AND DISCUSSION**

**- Fig. (2)** show steam quality at test section exit versus the ionization current used for hydrogen bubbles generation at water inlet temperature (101.2C$^0$). The figure clarifies the effects of the nuclei injection inside a saturated liquid on boiling enhancement. The curves plotted from the experimental and the theoretical results show that the steam quality in the exit of the test section increasing by increasing the amount of hydrogen nuclei generated inside the saturated water.

The effect of the non-equilibrium degree on the experimental results is clear when the saturated water flows in the test section without ionization. This makes a difference between the experimental and the theoretical results in such type of flow as shown in the figure. When water flows with electrolysis this difference becomes negligible as the electrolysis process eliminates the effect of the non-equilibrium on the experimental results. Accordingly the theoretical and the experimental results concur at certain ionization current.

**- Fig. (3)** show flash inception point versus the ionization current at water inlet temperature (101.2 C$^0$). The curves show that the flash inception point decreases by increasing the ionization current. The results obtained from the mathematical calculations coincide with those obtained from the measurements in the experiments without electrolysis while with electrolysis the experimental results show lower values than those obtained from theoretical due to the effect of hydrogen bubbles which initiates nucleate boiling earlier in the test section.

**- Fig. (4)** show water non-equilibrium degree, $^0$C versus the ionization current at water inlet temperature (101.2 $^0$C). From the curve it is clear that non – equilibrium degree decreases with increasing of the ionization current which in return decrease the distance of the flash inception point.

**- Fig. (5-A&B)** show the measured values of the local saturated water temperature and the saturation temperature based on local pressure versus test section length at constant mass flow rate and water inlet temperature. These figures show the position of the flash inception where the local water temperature equals to the saturation temperature. It is clear that this position is closer to the test section inlet when there is water electrolysis.

## CONCLUSIONS

- The steam quality in the test section exit increases (33%) proportionally with the injection rate of the hydrogen nuclei by using water electrolysis in the saturation water as the non-equilibrium degree decreases (42%) by increasing this percentage.
- The flash inception point decreases as the ionization current increases at constant water inlet temperature and constant mass flow rate as the hydrogen bubbles acts as exciter for steam generation inside saturated water.
- The behavior of the saturated water during flashing process as moving upward in a constant cross -section channel is similar to that induced in a multi- diameter divergent and convergent channel investigated by IZZAT, A. W. (2003), which means that the channel shape has a slight effect on the process in low water velocity.

## REFERENCES


- **EL-WAKEL, M. M. ,** Nuclear Power Engineering, McGraw-Hill, New York, 1962.

- **FURBERG, R**., Enhanced Boiling – Literature Survey, Royal Institute of Technology, Stockholm, Sweden, 2006.

- **G. HETSRONI,** Boiling with Environmentally acceptable Surfactants, International Journal of Heat and Fluid Flow, Vol. 25, pp 841-848, 2004.

- **IZZAT, A., W**., Investigation of Convergent and Divergent Flash Evaporation, Ph.D. Thesis Mechanical Department, Collage of Engineering – University of Baghdad, 2003.

- **NOIR LIOR,** Some Experiments of Flash Evaporation Enhancement by Electrically Generated Bubbles, Desalination, Vol. 100, pp. 71-76, 1995.

- **O. MIYATAK,** Dynamic Model of Enhancement Boiling Heat Transfer on Porous Surfaces, Journal of Heat Transfer Transaction of ASME, Vol. 102, pp. 445-450, 1980.

- **TONG, L. S.** , Boiling Heat Transfer and Two–Phase Flow, 2$^{nd}$ edition, 1966.

- **W. NAKAYAMA,** Dynamic Model of Enhancement Boiling Heat Transfer on Porous Surfaces, Journal of Heat Transfer Transaction of ASME, Vol. 102, pp.445-450, 1980.

- **ZAGHDOUDI, M. C. and LALLEMAND, M.**, Pool Boiling Heat Transfer Enhancement by Means of High DC Electric Field, The Arabian Journal for Science and Engineering, Vol. 30, No. 2B, 2005.

## NOMENCLATURE

| SYMBOL | DESCRIPTION | UNITS |
|---|---|---|
| Cp | Water heat capacity | J/kg $K^0$ |
| D | Diameter of the section | m |
| EI | Current of the electrolysis | A |
| EV | Voltage of the electrolysis | V |
| hc | Heat transfer coefficient between the test section wall and the surrounding | $W/m^2\ K^0$ |
| L | Test section length | m |
| $M_i$ | Initial water mass flow rate | kg/s |
| $M_e$ | Exit water mass flow rate | kg/s |
| QI | Heater power | W |
| Tc | Surrounding temperature | $K^0$ |
| $T_0$ | The initial value of the water temperature at test section inlet | $K^0$ |
| Te | The water temperature at test section exit | $K^0$ |

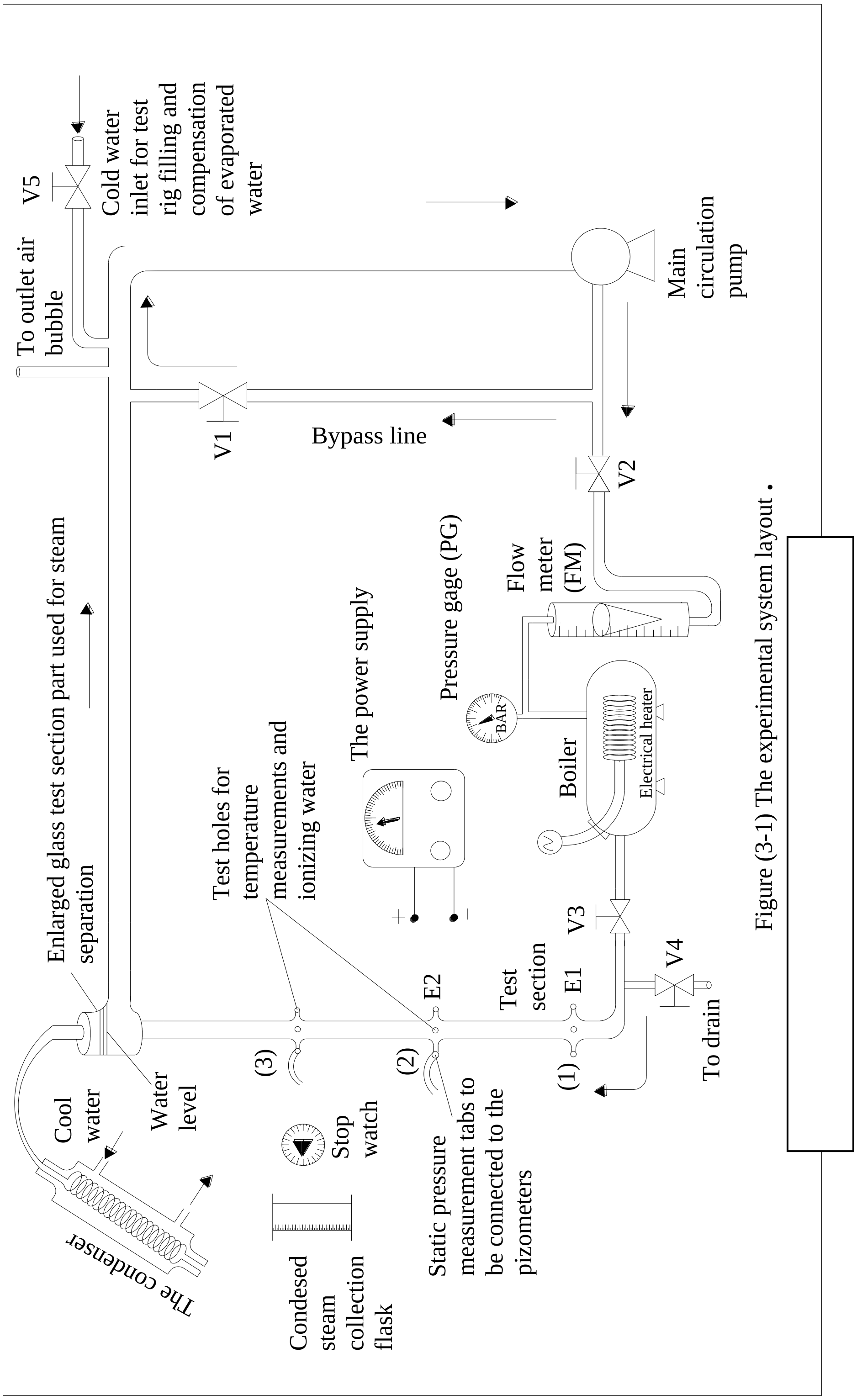


**Fig. (1): The experimental system layout**

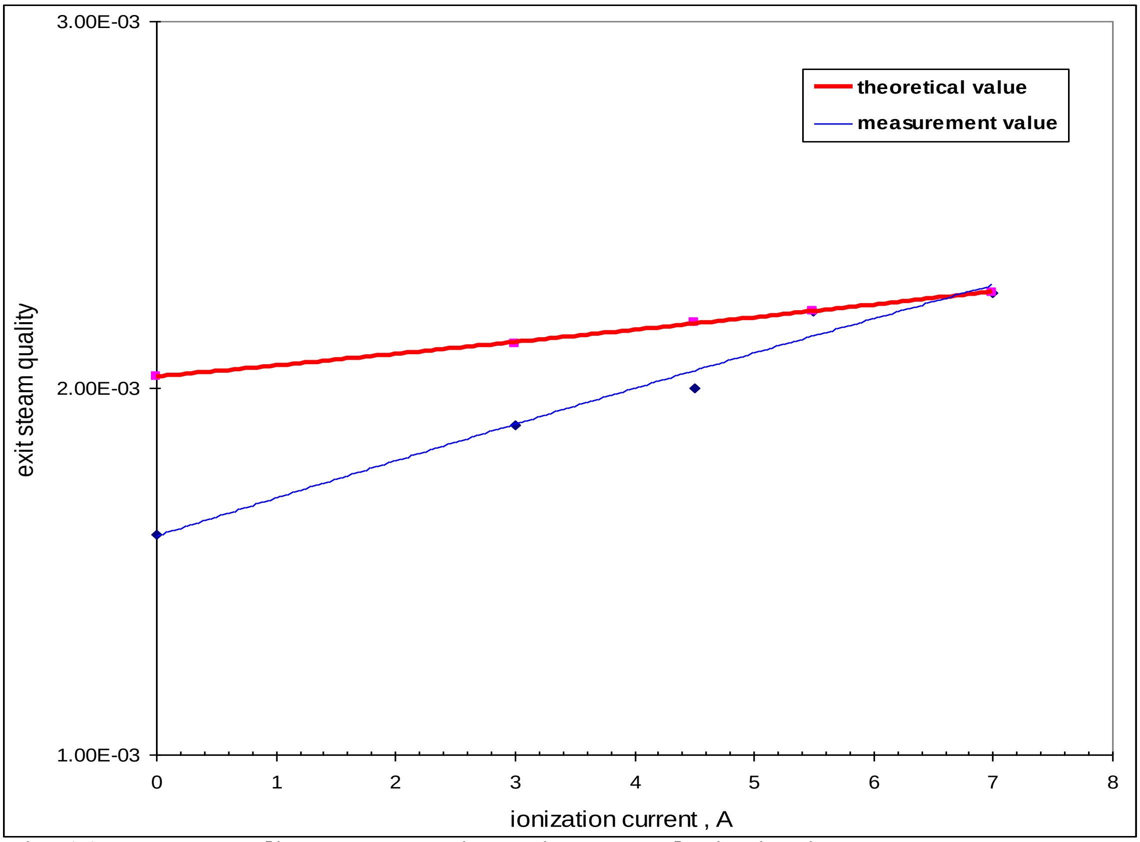


**Fig. (2): Steam quality at test section exit versus the ionization current at T1=101.2 C. mass flow rate=0.1722 kg/s.**

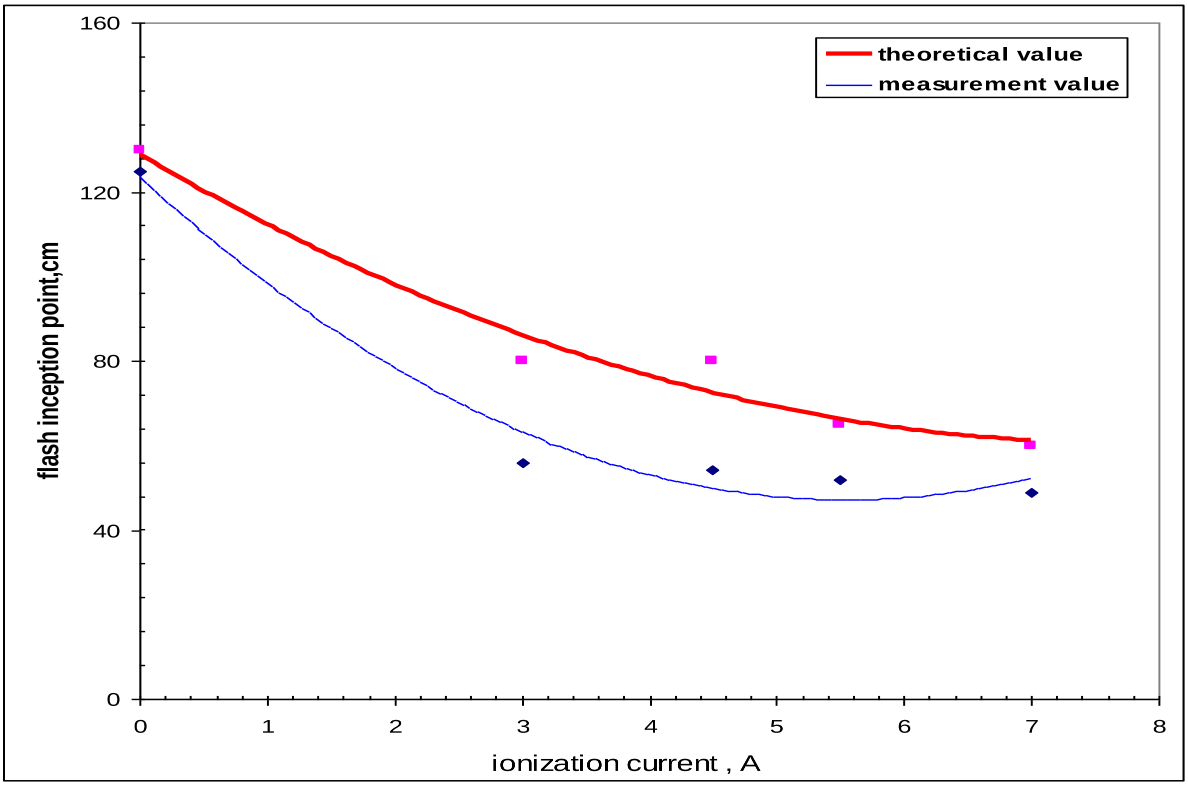


**Fig. (3): Flash inception point versus the ionization current at T1 =101.2 C, mass flow rate =0.1722 kg /s.**

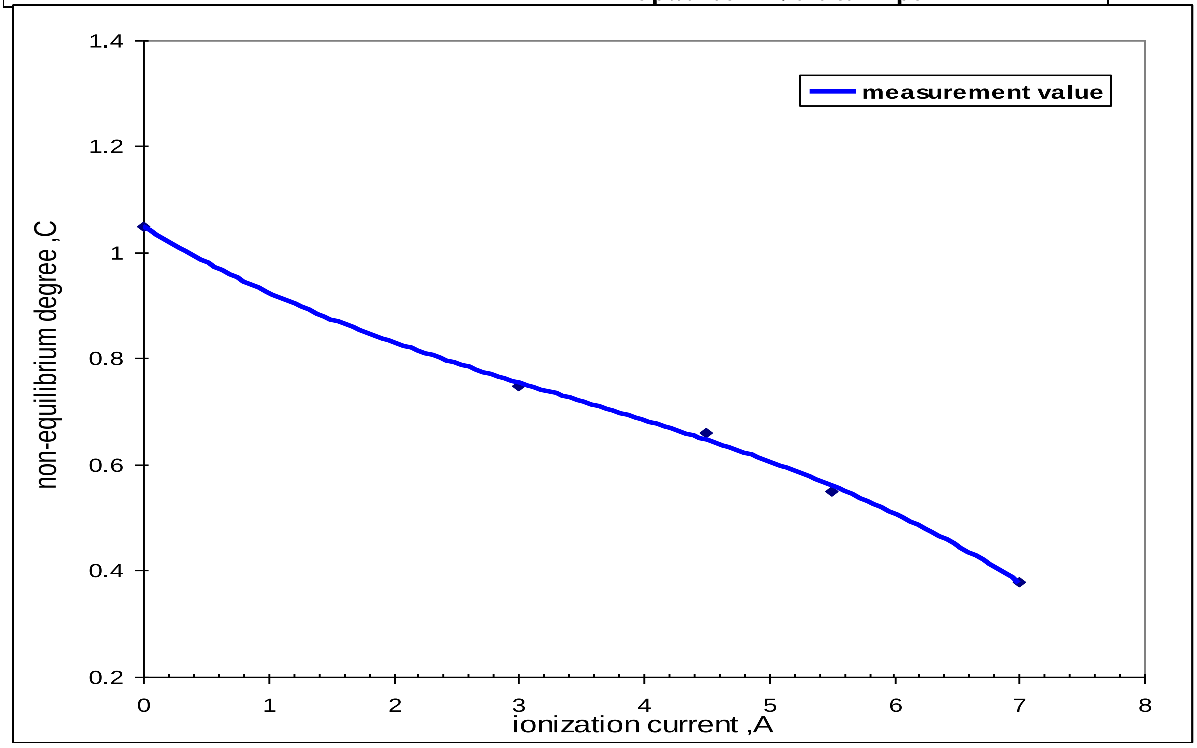


**Fig. (4): Measured value of the non-equilibrium degree in the flash inception point versus the ionization current at T1=101.2 C.**

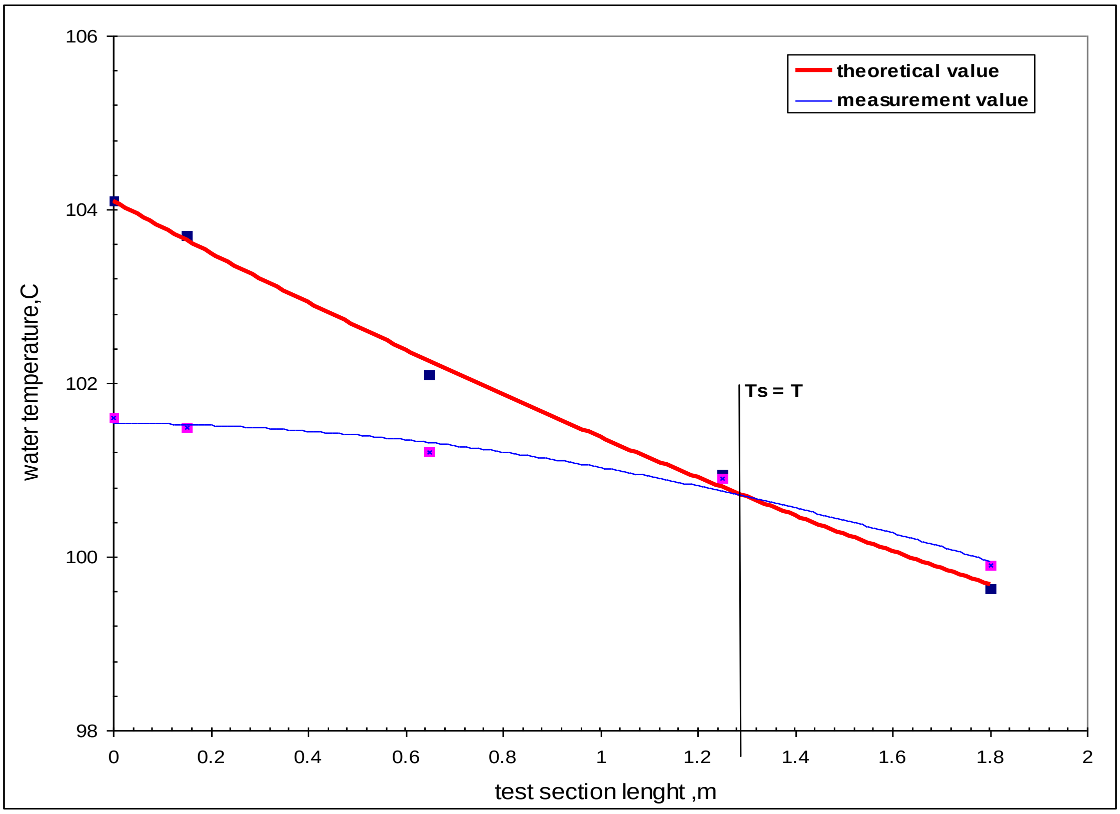


**Fig. (5A): Experimental and theoretical saturation water temperature distribution along test section length at T1=101.2C, mass flow rate =0.1722 kg/s (without water electrolysis).**

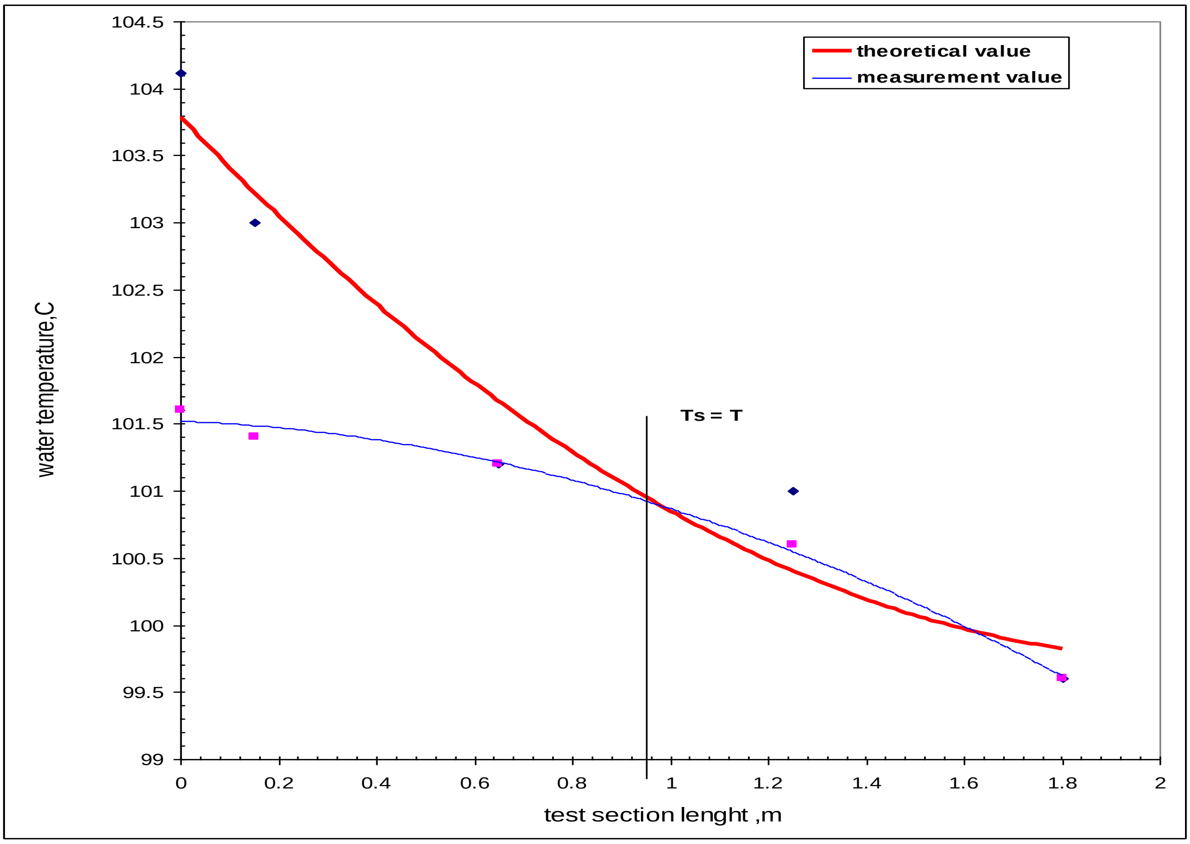


**Fig. (5B): Experimental and theoretical saturation water temperature distribution along test section length at T1=101.2C, mass flow rate =0.1722 kg/s (with water electrolysis), current=3A.**

# USE OF AVAILABILITY SIMULATION TO FIND OPTIMUM PERIOD OF TIME BETWEEN SCHEDULE MAINTENANCE

Dr. Z. I. AL-DAOUD
Assistant Professor
Collage of Engineering
University of Baghdad

HUSSAIN A. M. AL-BAWI
M.SC.Student
Collage of Engineering
University of Baghdad

**ABSTRACT**

This paper is concerned with the investigation of the optimum period of time between maintenance by the aid of Monte Carlo simulation technique of an old water tube boiler, double identical drums; its capacity is 70 ton/ hour of super heated steam. There are a multitude of failures that are caused by boiler operator's errors, boiler inspector, boiler maintainer and faults of boiler auxiliary equipments which lead to operation parameter deviations and boiler shut down. Changing maintenance plan to be based on optimum period of time between scheduled maintenance and inspection will achieve maximum boiler availability.

**الخلاصة**

يتعلق هذا البحث في دراسة وايجاد افضل فترة زمنية بين الصيانات المبرمجة بأستخدام اسلوب المحاكاة لمرجل بخاري قديم ذو وعائيين متناظرين علوي وسفلي طاقته الانتاجية 70 طن لكل ساعة من البخار المحمص. يتعرض هذا المرجل لحالات فشل عديدة نتيجة لاخطاء الكادر التشغيلي وكادر الصيانة والفحص لهذا المرجل اضافة الى فشل بعض المعدات الملحقة بالمرجل والتي تؤدي الى حدوث انحرافات في المتغيرات التشغيلية وبالتالي توقف المرجل. ان تغيير خطة الصيانة والفحص بحيث انها تعتمد على افضل زمن بين الصيانات والفحص المبرمجة سيؤدي الى تحقيق افضل توفرية ممكنة للمرجل البخاري.

**KEYWORDS: Availability, Simulation, Reliability, Optimum period between maintenance.**

## INTRODUCTION

Availability gives the probability of a unit being available - not broken and not undergoing repair when called upon for use, it combines the concepts of reliability and maintainability. Many studies are submitted to increase boiler reliability by describe the process design and control of boiler leak detection system **[marques j.2002]**, and improving boiler combustion efficiency **[david C. 2000]**. This paper is an attempt to increase boiler availability by changing the period of time between scheduled maintenance and inspection. System availability simulation process is based on Monte Carlo simulation method **[Kelton N. 2000]**, **[Sanders R. 2002],** availability simulation is performed based on analytical system reliability model to be as a simulation mathematical model. This would not be confused with the methodology of uses Monte Carlo simulation of individual components to estimate the overall system reliability **[reliability hotwire. 2006]**.

**SIMULATION METHODOLOGY**

The simulation method to estimate system's availability is employed. It includes the number of expected failures, number of expected maintenance actions and then expected mean time to repair. The estimation process involves synthesizing system performance over a given number of simulation runs or loops. Each loop simulates how the system might perform in real life based on the specified failure and downtime properties of the system. These properties consist of the interrelationships among the components, and the corresponding quantitative failure and repair for each component. The reliability block diagram determines how component failures can interact to cause system failures. The failure and repair determine how often components are likely to fail, how quickly they will be restored to service. By performing many simulation loops and recording a success or failure for each loop, a statistical picture of the system performance can be obtained. A simulation model of the system could be developed that simulates the random failures and repair times of the system, thus creating an overall picture of the up and down states for the system, as illustrated in **Fig. 1**

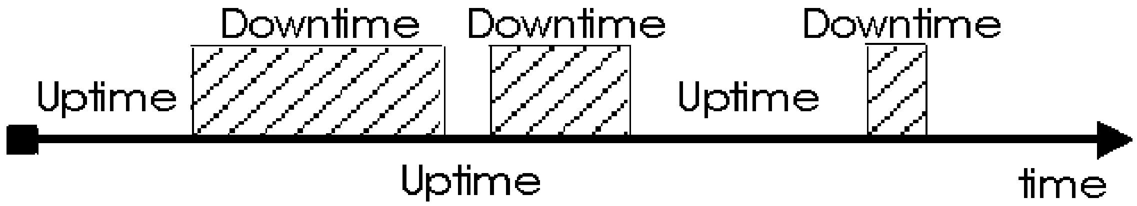


**Fig.1: Uptime and downtime of system**

## AVAILABILITY SIMULATION STEPS

Evaluation of system availability for a given operation time is performed by the following steps:
Random times-to-failure and times-to-repair are generated.

If the component or components that fail in that time period are vital to the operation of the system, the system is said to have failed.

This process is repeated for a specified number of iterations and the results are averaged to develop an overall model of system availability.

- The simulation program generates a random failure time for each component using Monte Carlo simulation, based on the analytical reliability model.
- This failure time is compared to the mission end time. If the failure time is greater than the mission end time, the loop is considered to be over and no downtime is logged for that loop.
- If the random failure time is less than the mission end time, a failure is logged against the system.
- At this point, a repair time is generated based on the system's repair distribution. This is logged as system downtime.
- The failed system has now accumulated life equivalent to the sum of the failure time and the repair time.
- If this sum, or elapsed time, is less than the mission end time, another random failure time is generated.
- If this new failure time is less than the remaining time (mission end time less elapsed time), another repair time is logged, and so on.
- This process repeats until enough failure and repair times have elapsed to meet or exceed the system mission end time, and the total downtime and number of failures for the loop are logged.
- This process is repeated for each loop, and the uptime for each loop (mission end time minus downtime) is calculated.
- At the end of all of the simulation loops, the downtime is averaged and divided by the mission

end time to determine the average availability.

- The point availability is determined by dividing the total number of times the system was operational at the end of each loop by the number of loops.

## MONTE CARLO SIMULATION MODELS

To illustrate how simulation data points are generated, it is important to demonstrate the availability simulation models by use of Monte carol simulation method:

**1-First Model:** generation of time to failure that based on boiler reliability model which consist of three subsystems in series connection, first and second subsystems consist of two components with parallel connection. The reliability model is calculated to be:

$$R_{system} = [1-(1-e^{-0.00035t})(1-e^{-0.000256t})]\times[1-(1-e^{-0.00037t})(1-e^{-0.0002t})]\times e^{-0.000189t} \quad (1)$$

Simulation is performed by generating a uniformly distributed random number *(Rnd)*, since $0 < R_{system}(t) < 1$, then let $U$ random number in the same interval $0 < U < 1$.

Substituting $U$ for $R_{system}(t)$ and solving for ($t$) as the following steps:

-At a selected desired mission time $(t_o)$, calculate boiler reliability $R_{system}(t_o)$ from **eq. 1**, then evaluate boiler failure rate from the equation:

$$\lambda_{system} = -\frac{t_o}{\ln R_{system}} \quad (2)$$

Where:

$\lambda_{system}$ = failure rate

$t_a$ = mission time

$R_{system}$ = boiler reliability

-Generating random number Rnd in the interval $0<Rnd<1$.

$$t_{simulation} = -\lambda_{system} \times \ln(U) \quad (3)$$

Where:

$U$ $= Rnd$

$t_{simulation}$ = *Simulated* mission time

$\lambda_{system}$ = failure rate

-Above step is repeated for 100 times, at each time the $t_{simulation}$ is recalculated.

-Average $t_{simulation}$ is calculated as below:

$$\text{Average } t_{simulation} = \frac{\sum_{i=1}^{100} t_{simulation}}{100} \quad (4)$$

-*Average* $t_{simulation}$ is compared with the mission time ($t_o$), if it is greater than ($t_o$), that's mean, the boiler is pass the mission time successfully and there is no failure, but if, it is less than ($t_o$), in this case, the boiler is failed and *Average* $t_{simulation}$ is represents the first time to failure.

*Average* $t_{simulation} \geq t_o$ = no failure

*Average* $t_{simulation} < t_o$ = failure

**SECOND MODEL**: generation of emergency repairing time, it is depends on the field data repairing times distribution, researcher considers the boiler as a one component, that because of, there is no recorded repairing time of boiler systems failures available to be collected in the boiler operation documents, just there are periods of boiler downtimes beyond consideration of which systems are failed and lead to boiler downtime. Although most of repairing times are conforming to the lognormal distribution **[Murphy E. 2002]**, but according to the natural of the collected field data of repairing times they are modeled by uniformly rectangular distributions, because of, the collected repairing times are not exact values, but they are in form of one day, two day,…….ect., in addition to there is no enough data base to be modeled, so that, their distribution are modeled by uniformly rectangular distributions, whereas, the x-axis is represents the probability of occurrence, and it is divided by the number of the collected data, y-axis is represents the number of day taken into repair (period of time). To introduce emergency repair time, program generates random number uniformly in the range {0-1}, and apply this random number on the x-axis of the distribution to find the corresponding emergency repairing time ($t_{repair}$) on y-axis, the distribution models are illustrated in **Fig. 2 (A, B, C, D, E, F, G, I, J, K, L, and M).** After generating time to failure and repairing time, the both values are subtracted from the mission time and the rest of the current mission time represents new mission time:

$$New\ mission\ time = t_o - (t_{simulated} + t_{repair}) \tag{5}$$

**THIRD MODEL**: generation of the second time to failure depends on the calculation of boiler reliability from **eq.1** too, but at new mission time of **eq. 5**. Before the calculation of new boiler failure rate, there is a fact has to be considered, since the emergency maintenance is a partial maintenance, which is performed just to repair the failed parts, the boiler restarts with reliability not equal to 100% at time equal to zero, that because it is pass a partial maintenance.

Researcher models this fact by the equation below:

$$\lambda_{system} = -\frac{t_o}{\ln(R_{system} - (d \times s))} \tag{6}$$

Where: d = the subtracted value to evaluate the real reliability when the boiler passes partial emergency maintenance,

S = number of the failures which were occurred, that (s) = 2 during calculation of the second time to failure, (s) = 3 during calculation of the third time to failure, the same order is applied for the other times to failure.

Researcher determines the value of (d) to be (0.025), this value is evaluated by validation of the historical field data base, and the validation is depends on the boiler data of the last three years as mentioned below:

- 1st year: the boiler was suffered of (9) times of emergency shutdown, that take (49) days as a repairing time.
- 2nd year: the boiler was suffered of (12) times of emergency shutdown, that take (58) days as a repairing time.
- 3rd year: the boiler was suffered of (10) times of emergency shutdown, that take (46) days as a repairing time.

The scheduled annual maintenance is approximately constant and equal to (35) days, the availabilities of the three years are determined according to equation **[Charles E. 1997]**:

$$\text{Availability} = \frac{\text{uptime}}{\text{uptime+downtime}} \tag{7}$$

Availability of 1st year = $\frac{8640-(49\times 24)}{8640+(35\times 24)} = 0.787\%$

Availability of 2nd year= $\frac{8640-(54\times 24)}{(8640+(35\times 24))} = 0.774\%$

Availability of 3rd year= $\frac{8640-(51\times 24)}{8640+(35\times 24)} = 0.7822\%$

Average availability= $\frac{0.787+0.774+0.7822}{3} = 0.78\%$

Researcher validate the outputs of the program with the average availability by making many try and error iterations to find the suitable value of (d).

The evaluation of the average second time to failure is evaluated randomly by the same procedure of evaluation of first time to failure, this average time to failure has to be compared with the new mission time in **eq. 5** as below:

-*Average second* $t_{simulation} > [\, t_o - (t_{simulated} + t_{repair})\,]$ = there is no second failure and simulation loop has to be stopped and the boiler pass the mission time *($t_o$)* with one failure.

-*Average second* $t_{simulation} < [\, t_o - (t_{simulated} + t_{repair})\,]$ = there is a second failure and simulation loop has to be continued checking for third time to failure.

**FOURTH MODEL**: is the evaluation of schedule repairing time, investigations show that the schedule maintenance time is consists of two parts:

- Primary time, it is the time takes into performing the preparation and fundamental jobs.
- Secondary time, it is the time takes into replacing the plugged and corroded boiler tubes.

Researcher studies the schedule repairing times of this boiler, it is planed to be (35) days, the primary time is about (15) day, and it is necessary for each scheduled shutdown, whatever the mission time, secondary time is then (20) day, it is depends on the planed boiler mission time.

Tube boiler corrosion rates are constant, and since (20) days are taking into repairing and replacing boiler failed tubes when the mission time is (12) months, so that researcher assumes that if boiler mission time is (11) month, the:

- For mission time of (11) month the schedule repairing time will be equal to $t_{schedule} = (\frac{11}{12}) \times 20$
- For mission time of (10) month the schedule repairing time will be equal to $t_{schedule} = (\frac{10}{12}) \times 20$
- For mission time of (9) month the schedule repairing time will be equal to $t_{schedule} = (\frac{9}{12}) \times 20$
- For mission time of (8) month the schedule repairing time will be equal to $t_{schedule} = (\frac{8}{12}) \times 20$

- For mission time of (7) month the schedule repairing time will be equal to $t_{schedule} = (\frac{7}{12}) \times 20$
- For mission time of (6) month the schedule repairing time will be equal to $t_{schedule} = (\frac{6}{12}) \times 20$
- For mission time of (5) month the schedule repairing time will be equal to $t_{schedule} = (\frac{5}{12}) \times 20$
- For mission time of (4) month the schedule repairing time will be equal to $t_{schedule} = (\frac{4}{12}) \times 20$
- For mission time of (3) month the schedule repairing time will be equal to $t_{schedule} = (\frac{3}{12}) \times 20$
- For mission time of (2) month the schedule repairing time will be equal to $t_{schedule} = (\frac{2}{12}) \times 20$
- For mission time of (1) month the schedule repairing time will be equal to $t_{schedule} = (\frac{1}{12}) \times 20$

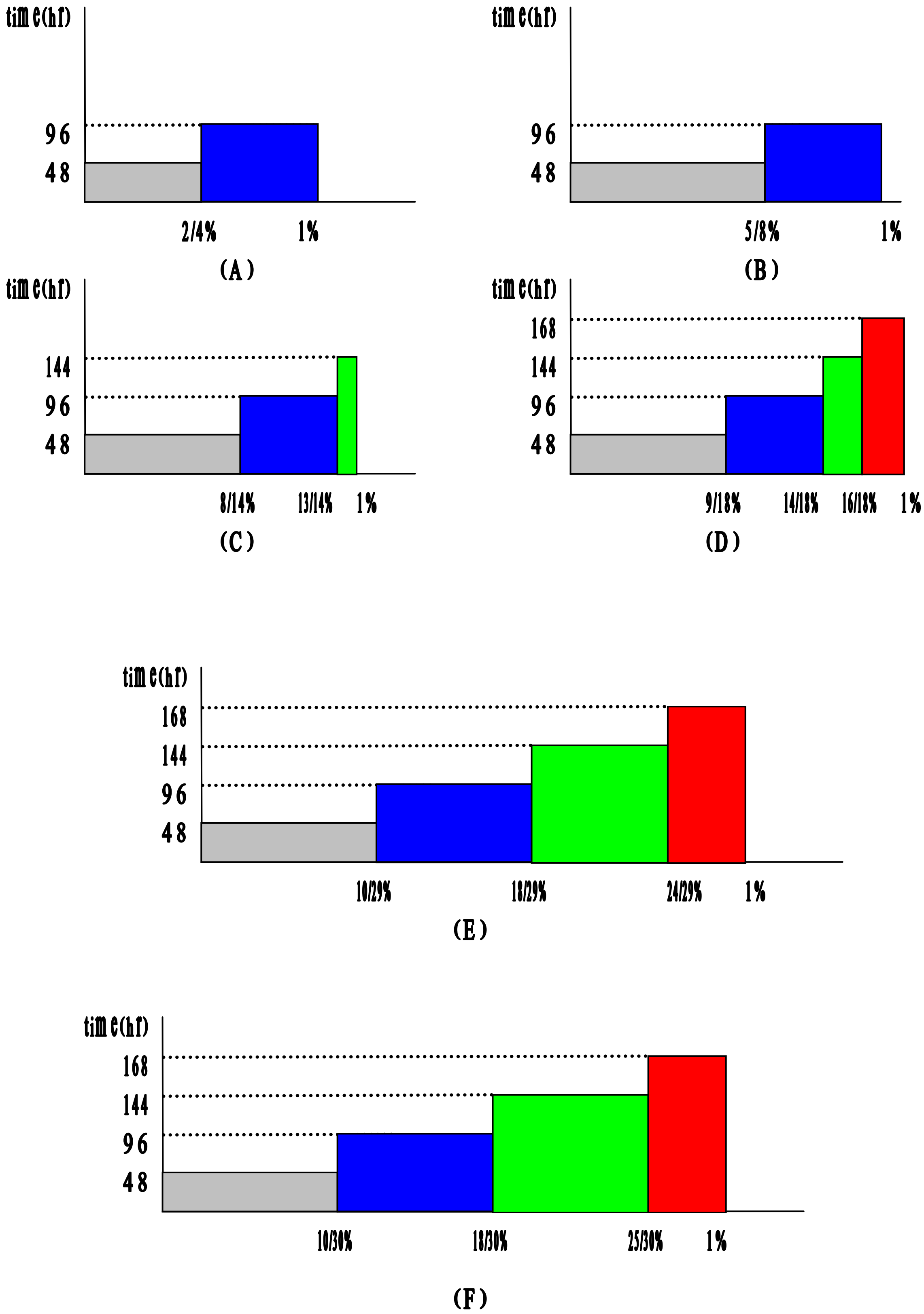


**Fig. 2: Boiler repairing time distribution for mission time as, (A) first month, (B) second month, (C) third month, (D) fourth month, (E) fifth month, (F) sixth month, (G) seventh month, (I) eighth month, (J) ninth month, (K) tenth month, (L) eleventh month, (M) twelfth month**

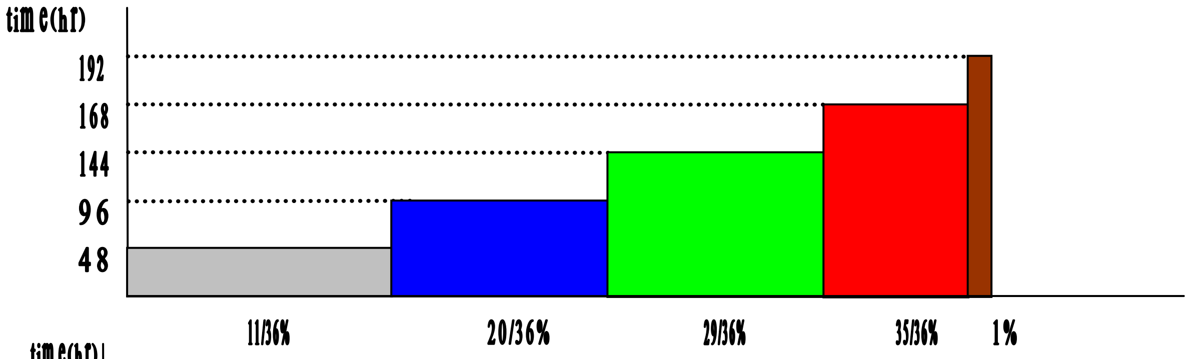


(G)

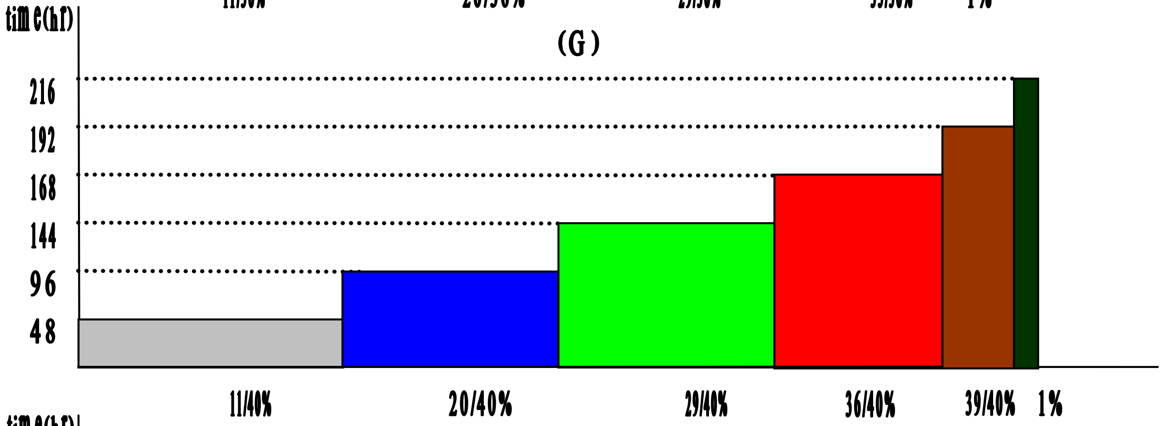


(I)

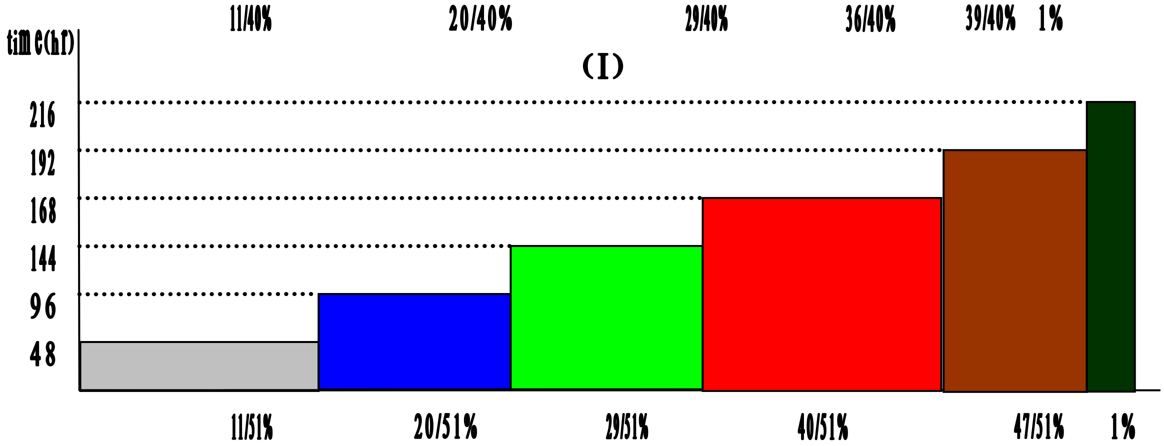


(J)

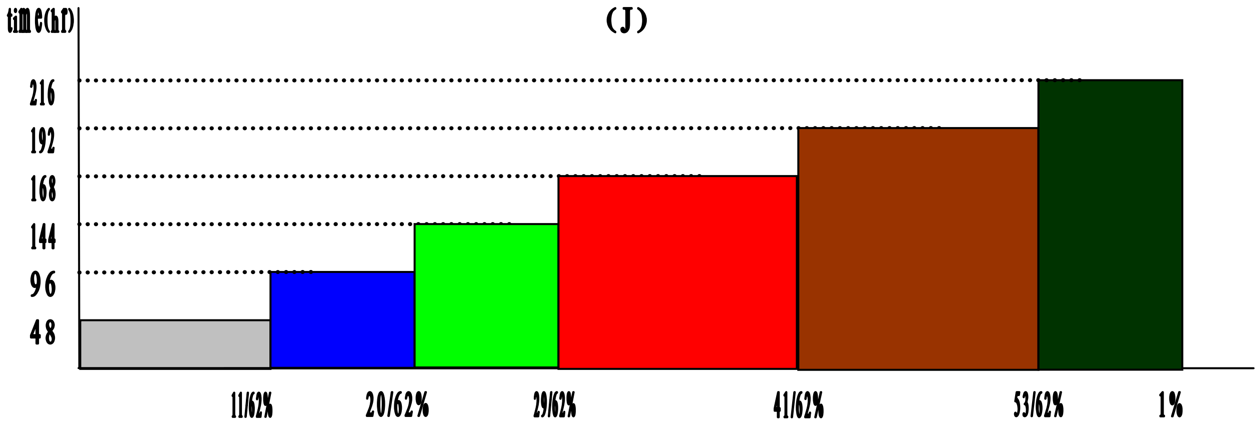


(K)

**Continued**

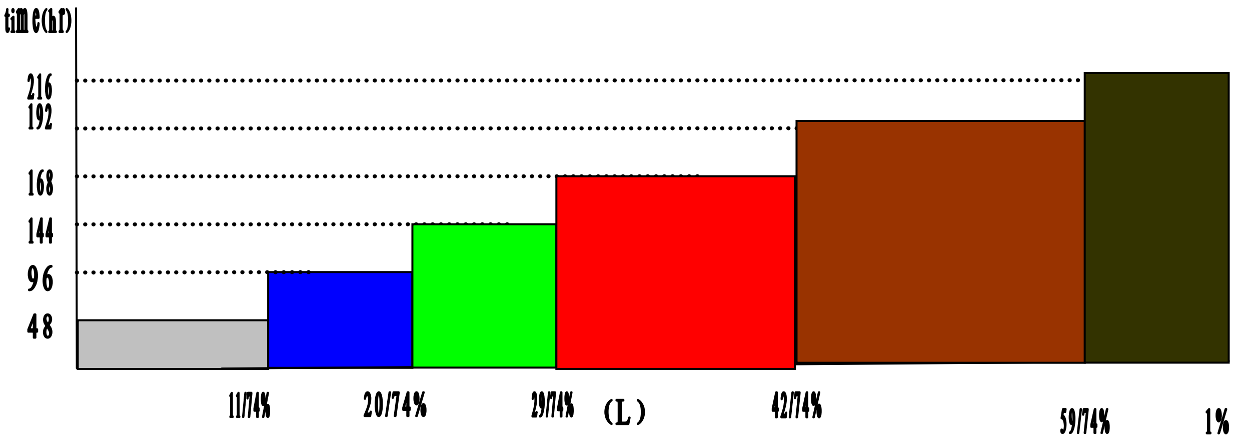


(L)

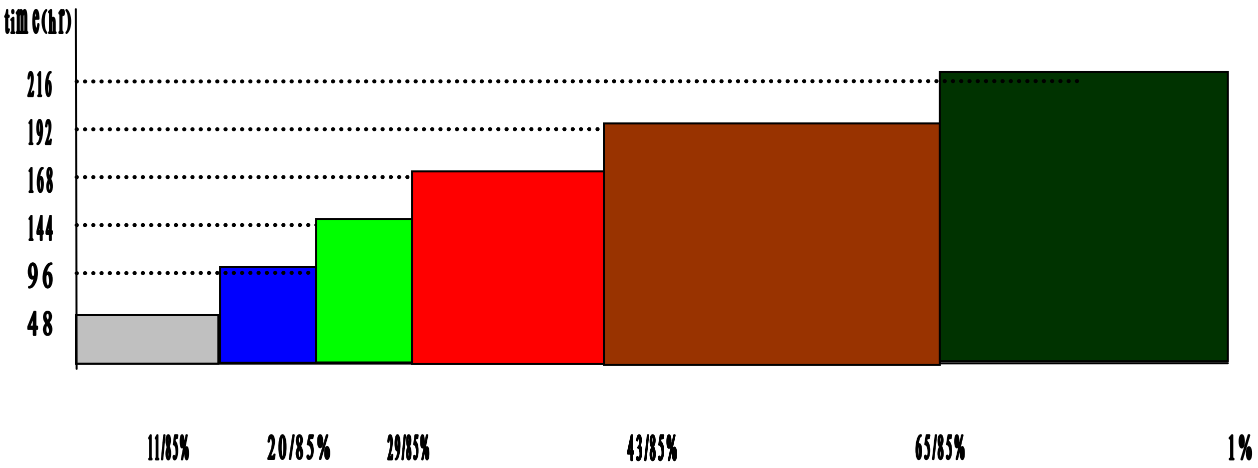


(M) Continued

## Results

**Fig. 3 represents the output (bar chart) of the computer program that used to perform the availability simulation after formulating all the simulation models based on visual basic language, each bar in the figure represents the availability of the boiler at its related mission time, first availability is simulated at mission time equal to one month, the others are simulated with increasing mission time by one month one each stage till the mission time reach its maximum value (twelve months).**

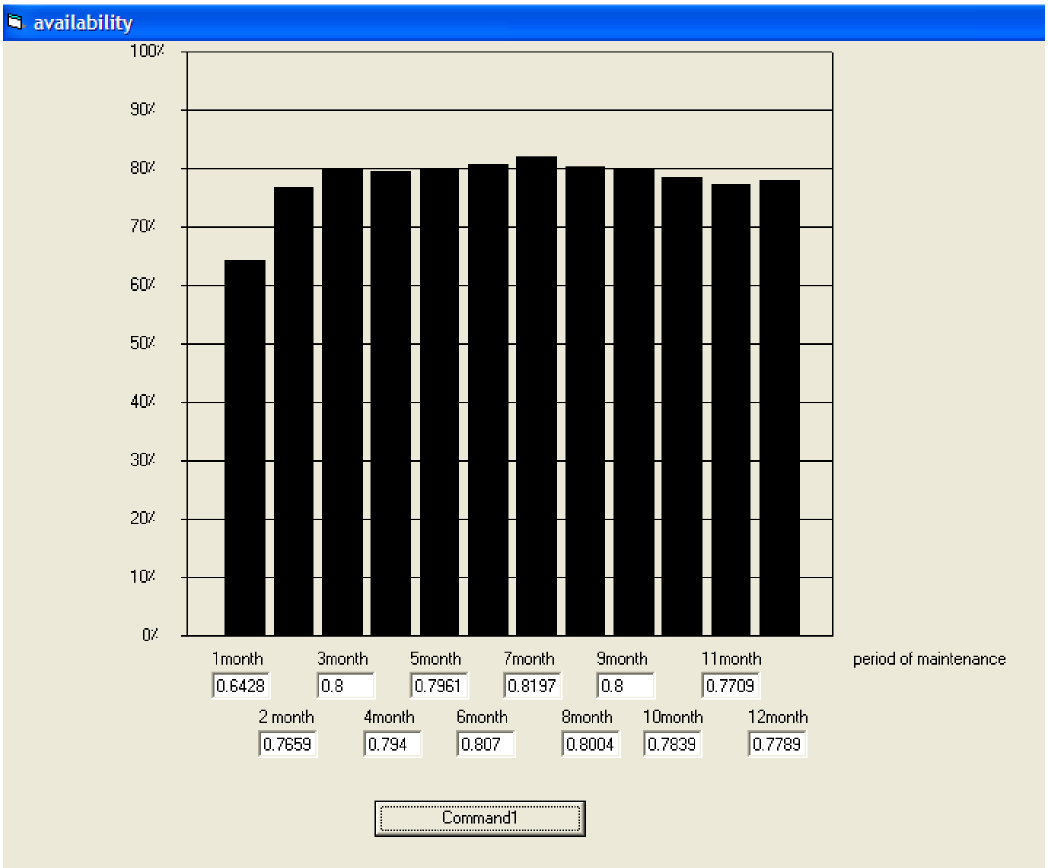


**Fig. 3: Simulated availability bar chart**

## CONCLUSION

In this work the boiler availability is investigated by changing boiler mission time, from one month to twelve month, in order to determine optimum period of time between scheduled maintenance that achieves as possible as maximum availability, from **Fig. 3** it is clear that maximum availability is achieved by use of seven month as a period of time between scheduled maintenance, so that, this period is represents the optimum period of time between maintenance.

## REFERENCES


- Xi Sun, Tongwen Chen, & Horacio J. Marquez, "**Boiler Leak Detection Using a System Identification Technique**", American chemical society, 2002

- C. David Farthing, "**improving boiler room efficiency**", Oklahoma City University, 2002.

- L. Averill, N. Kelton, W. David, "**simulation modeling and analysis**", New York, McGraw Hill, 2000

- R. Dan Red, Nada R. sanders, "**operation management**", John Wiley & sons, Inc. 2002.

- Reliability hotwire "**Estimating Availability through Simulation** ", http://www.weibull.com, the Magazine of reliability professional, issue 8, October, 2006.

- Kenneth E. Murphy," **The Exponential Distribution: the Good, the Bad and the Ugly. A Practical Guide to its Implementation",** IEEE RAMS Conference, 2002.

- Ebeling, Charles E., "**An Introduction to Reliability and Maintainability Engineering**", McGraw-Hill Companies, Inc., (1997).

# DEVELOPING LAMINAR MIXED CONVECTION HEAT TRANSFER THROUGH CONCENTRIC ANNULI

Asst. Prof. Dr. Ihsan Y. Hussain
Mechanical Engineering Department
University of Baghdad

Mohammed Abdul Raouf Nima Al-Safi
Mechanical Engineering Department
University of Baghdad

## ABSTRACT

Theoretical and experimental study has been conducted on developing laminar mixed convection heat transfer air flow through an annulus for both aiding and opposing flow with uniformly heated inner cylinder and adiabatic outer cylinder for the theoretical part and with uniformly heated inner cylinder while the outer cylinder is subjected to the ambient for the experimental part. In the theoretical investigation the energy equation was first solved using (ADI) method, and then the momentum equations and continuity equation were combined as the pressure correction formula and solved by the SIMPLE algorithm. The present theoretical work covers Ra range from $4.55*10^5$ to $5.649*10^6$ and Re range from 300 to 1000 with radius ratio of 0.555 and Pr=0.72. The velocity and temperature profile results have revealed that the secondary flow created by natural convection have significant effects on the heat transfer process and the results reveal an increase in the Nusselt number values as Ra increases. The experimental setup consists of an annulus which has a radius ratio of 0.555 and inner cylinder with a heated length 1.2m subjected to a constant heat flux while the outer cylinder is subjected to the ambient temperature. The investigation covers Reynolds number range from 154 to 724, heat flux varied from 93 $W/m^2$ to 857 $W/m^2$, and annulus angles of inclinations $\alpha$=0° (horizontal), $\alpha$=20°, 60° (inclined aiding flow), $\alpha$=-20,-60 (inclined opposing flow) and $\alpha$=90° (vertical). The experimental results show an increase in the local Nusselt number values as the heat flux increases and as the angle of the inclination moves from the positive angles (inclined aiding flow) to the horizontal position and from the negative angles (inclined opposing flow) to the horizontal position. The experimental results show that the local Nusselt number values of the aiding flow are higher than that of the opposing flow at the same Reynolds number and heat flux.

## الخلاصة

أُجريتْ دراسة نظرية و عملية لانتقال الحرارة بالحمل المختلط لجريان الهواء خلال تجويف حلقي ذو أسطوانتين متمركزتين (في حالة الجريان الثانوي باتجاه الجريان الرئيسي وفي حالة الجريان الثانوي عكس اتجاه الجريان الرئيسي)؛ الداخلية مسخنة تسخين منتظم و الخارجية معزولة في حالة الدراسة النظرية اما في حالة الدراسة العملية فان الاسطوانة الداخلية مسخنة تسخين منتظم والخارجية معرضة الى درجة حرارة الجو. في البحث النظري تم حل معادلة الطاقة اولا باستخدام طريقة (ADI) ثم تم ربط معادلات الزخم بمعادلة

الاستمرارية لانتاج معادلة تصحيح الضغط والتي تم حلها باستخدام خوارزمية (SIMPLE). رقم رينولدز Re المستخدم في هذا البحث النظري من 300 إلى 1000 أما رقم رالي Ra من $4.55*10^5$ الى $5.649*10^6$ مع نسبة نصف قطر تساوي 0.555 وهي نفسها المستخدمة في الجزء العملي من هذا البحث ورقم براندتل Pr=0.72. اظهرت نتائج توزيع السرعة و درجات الحرارة ان الجريان الثانوي الناتج من الحمل الحر(الطبيعي) له تاثير مهم على عملية انتقال الحرارة كما اظهرت النتائج زيادة في قيم رقم نسلت الموقعي عند زيادة رقم رالي Ra. البحث العملي تضمن اجراء تجارب عملية لدراسة انتقال الحرارة الموقعي و المعدّل بالحمل المختلط لجريان الهواء المشكّل تراكيباً ( أي تزامن التشكيل الحراري مع التشكيل الهيدروديناميكي) بتجويف حلقي بين اسطوانتين متحدتي المركز، نسبة نصف القطر لهما تعادل 0.555 و بطول كلي 1.2 m ، بالوضع الأفقي، المائل(في حالة الجريان الثانوي باتجاه الجريان الرئيسي وفي حالة الجريان الثانوي عكس اتجاه الجريان الرئيسي)، و العمودي. سخنت الاسطوانة الداخلية تحت فيض حراري ثابت ، بينما عرّضت الاسطوانة الخارجية إلى درجة حرارة الجو. يتراوح معدّل رقم رينولدز Re في هذا البحث من 154 إلى 724 أما الفيض الحراري فيتغير من $93\ W/m^2$ إلى $857\ W/m^2$ ، و زوايا ميل التجويف الحلقي هي 0° (أفقي)، 20° ، 60°، -20°، -60° ، 90° (عمودي). بينت النتائج المستخرجة من البحث العملي لكل زوايا الميلان ان رقم نسلت الموقعي يزداد كلما ازداد الفيض الحراري وكذلك يزداد رقم نسلت الموقعي عند تغير زاوية ميل الانبوب الحلقي من الزوايا الموجبة (الجريان الثانوي باتجاه الجريان الرئيسي) الى الموقع الافقي وعند تغير زاوية ميل الانبوب الحلقي من الزوايا السالبة (الجريان الثانوي عكس اتجاه الجريان الرئيسي) الى الموقع الافقي. كما بينت النتائج العملية ان قيم رقم نسلت الموقعي في حالة (الجريان الثانوي باتجاه الجريان الرئيسي) هي اكبر منها في حالة (الجريان الثانوي عكس اتجاه الجريان الرئيسي) عند نفس رقم رينولدز والفيض الحراري المسلط.

**KEYWORDS: Mixed Convection, Developing, Laminar, Concentric Annuli.**

## INTRODUCTION

Convection heat transfer involves the transfer of heat by the motion of a fluid. The term natural convection is used if this motion is caused by density variations resulting from temperature differences within the fluid. The term forced convection is used if this motion is caused by an outside force, such as a pump, blower fan and compressor. Mixed convection flow occurs when both natural and forced convection mechanisms simultaneously and significantly contribute to the heat transfer. **(Cony and El-Sharrawi 1975)**, presented the results of a finite difference analysis for incompressible laminar flow heat transfer in concentric annuli with a simultaneously developing hydrodynamic and thermal boundary layers with three radius ratios of (0.1, 0.5, and 0.9), the boundary conditions of one wall being isothermal and the outer wall adiabatic. Results show how much error can be introduced for the case of gases (Pr=0.7) if the heat transfer is calculated by assuming a fully developed profile from the entrance. This error decreases as the flow moves away from the duct entrance and approaches full development. Also results show that the local Nusselt number for the case of an isothermal inner wall and adiabatic outer wall is greater at the same dimensionless axial distance from entrance than for the case of an isothermal outer wall and adiabatic inner wall. Combined forced-free laminar convection with a flat velocity profile in the entrance region of vertical concentric annuli has been investigated by **(El-Sharrawi and Sarhan 1980)**, for three radius ratios of (0.5 , 0.8 and 0.9) and for two boundary conditions namely, the outer wall is isothermal while the inner wall is adiabatic under $-700 \leq Gr/Re \leq 1600$ and the inner wall is isothermal while the outer wall is adiabatic under $-200 \leq Gr/Re \leq 800$. The study show that when the free convection opposes the forced flow (i.e., heating with down flow or cooling with up flow) there exist a possibility of flow reversal near the heated boundary while such a flow reversal may occur near the insulated wall if the free convection is aiding the forced flow. **(Nazrul Islam , Gaitonde and Sharma 2001)**, performed a numerical as well as an experimental investigation of steady laminar mixed convection heat transfer in horizontal concentric annuli using air and water as the working fluid. The thermal boundary condition chosen is that of uniform heat flux at the inner wall and an adiabatic outer wall. The numerical investigations were carried out with $10^4<Ra<10^8$, $1.5 \le r_o/r_i \le 10$ , $0.7 \le Pr \le 5.42$ and $200 \le Re \le 1000$. It is observed that, depending on the value of Rayleigh number, the Nusselt numbers are considerably higher than the corresponding pure forced convection values over a significant portion of the annular duct.

The main aim of the present theoretical investigation is to determine the effect of Ra number, Re number and the flow direction (i.e., aiding and opposing flow) on the variation of surface temperature, Nusselt number, temperature profile and velocity profile along the annulus. The experimental study objectives are to determine the effect of the primary flow, heat flux, the effect of inclination angle and the direction of the main flow with respect to the secondary motion on the heat transfer process along the annulus for a specific range of inner cylinder heat flux and for laminar range of the air flow.

## MATHEMATICAL MODELING

For an air flow in a vertical annulus, both free and forced convection effect in axial and radial directions are presented. A two-dimensional model can be used to describe the mixed convection heat transfer in a vertical annulus with inner radius $r_i$ and outer radius $r_o$ which has a configuration shown in **Fig.(1)**.

## ASSUMPTIONS

The following assumptions are used in the modeling:

- Incompressible fluid.
- Two dimensional in (r,z) flow.
- Simultaneously developing hydrodynamic and thermal aiding flow.
- No internal heat generation and heat dissipation.
- Neglecting viscous dissipation.
- The physical properties are constant except the density in the buoyancy term of momentum equations which varies according to Boussinesq's approximation.

## GOVERNING EQUATIONS

$$\frac{\partial v}{\partial r}+\frac{v}{r}+\frac{\partial u}{\partial z}=0 \tag{1}$$

$$\rho\left(\frac{\partial u}{\partial t}+v\frac{\partial u}{\partial r}+u\frac{\partial u}{\partial z}\right)=-\frac{\partial p}{\partial z}+\mu\left(\frac{\partial^2 u}{\partial r^2}+\frac{1}{r}\frac{\partial u}{\partial r}+\frac{\partial^2 u}{\partial z^2}\right)+\rho g\beta(T-T_i) \tag{2}$$

$$\rho\left(\frac{\partial v}{\partial t}+v\frac{\partial v}{\partial r}+u\frac{\partial v}{\partial z}\right)=-\frac{\partial p}{\partial r}+\mu\left(\frac{\partial^2 v}{\partial r^2}+\frac{1}{r}\frac{\partial v}{\partial r}-\frac{v}{r^2}+\frac{\partial^2 v}{\partial z^2}\right) \tag{3}$$

$$\frac{\partial T}{\partial t}+v\frac{\partial T}{\partial r}+u\frac{\partial T}{\partial z}=\hat{\alpha}(\nabla^2 T) \tag{4}$$

## NONDIMENSIONALIZATION

To nondimensionalize the variables used in the governing equations, the following dimensionless variables are defined

$$R=\frac{r}{r_o},\quad Z=\frac{2z(1-N)}{r_o Re},\quad U=\frac{u}{u_i},\quad V=\frac{vr_o}{\upsilon},\quad P=\frac{p-p_i}{\rho_i u_i^{\,2}},\quad \Theta=\frac{(T-T_i)k}{q'' r_o},\quad \tau=\frac{\upsilon t}{r_o^2},$$

$$Re=\frac{u_i D_h}{\upsilon},\quad Gr=\frac{g\,\beta\,q'' r_o D_h^3}{\upsilon^2 k},\quad Pr=\frac{\mu c_p}{k}$$

## DIMENSIONLESS GOVERNING EQUATIONS

$$\frac{\partial V}{\partial R}+\frac{V}{R}+\frac{\partial U}{\partial Z}=0 \tag{5}$$

$$\frac{\partial U}{\partial \tau}+V\frac{\partial U}{\partial R}+U\frac{\partial U}{\partial Z}=-\frac{\partial P}{\partial Z}+\frac{\partial^2 U}{\partial R^2}+\frac{1}{R}\frac{\partial U}{\partial R}+\frac{4(1-N)^2}{Re^2}\frac{\partial^2 U}{\partial Z^2}+\frac{Gr}{Re}\frac{\Theta}{4(1-N)^2} \tag{6}$$

$$\frac{\partial V}{\partial \tau}+V\frac{\partial V}{\partial R}+U\frac{\partial V}{\partial Z}=-\frac{Re^2}{4(1-N)^2}\frac{\partial P}{\partial R}+\frac{\partial^2 V}{\partial R^2}+\frac{1}{R}\frac{\partial V}{\partial R}-\frac{V}{R^2}+\frac{4(1-N)^2}{Re^2}\frac{\partial^2 V}{\partial Z^2} \tag{7}$$

$$\frac{\partial \Theta}{\partial \tau}+V\frac{\partial \Theta}{\partial R}+U\frac{\partial \Theta}{\partial Z}=\frac{1}{Pr}\left(\frac{\partial^2 \Theta}{\partial R^2}+\frac{1}{R}\frac{\partial \Theta}{\partial R}+\frac{4(1-N)^2}{Re^2}\frac{\partial^2 \Theta}{\partial Z^2}\right) \tag{8}$$

**Entry Boundary Conditions** (see **Fig.(2)**)
At Z=0  $\Theta=0$ , U=1 , V=0 , P'=0 **(John D. Anderson, Jr. 1995)**

**Wall Boundary Conditions** (see **Fig.(2)**)
At R=N , $\partial\Theta/\partial R=-1$ (Constant heat flux). At R=1, $\partial\Theta/\partial R=0$ (Adiabatic wall)
At R=N & R=1  U=V=0 , $\partial P/\partial R=0$ **( John D. Anderson, Jr. 1995)**

**Exit Boundary Conditions (John D. Anderson, Jr. 1995)** (see **Fig.(2)**)
U & V (allowed to float, using zeroth-order extrapolation), P'=0

**Local and Average Nusselt Number**

The heat flux is computed from the following equation:

$$q_w=-k\left.\frac{\partial T}{\partial r}\right)_{r=ri} \tag{9}$$

The heat flux at inner wall surface equals the heat transferred by convection from this surface to the fluid that is represented by the following equation:

$$q_w=h(T_w-T_b) \tag{10}$$

By equating **eqs.(9)** and **(10)**, the heat transfer coefficient can be calculated as follows:

$$h(T_w-T_b)=-k\left.\frac{\partial T}{\partial r}\right)_{r=ri} \tag{11}$$

$$h=-k\left.\frac{\partial T}{\partial r}\right)_{r=ri}\frac{1}{(T_w-T_b)} \tag{12}$$

Hence, the Nusselt number becomes:

$$Nu_z = \frac{hD_h}{k} = -\frac{\partial T}{\partial r}\Big)_{r=ri} \frac{D_h}{(T_w - T_b)} \tag{13}$$

Or, in dimensionless form:

$$Nu_z = \frac{2(1-N)}{\Theta_w - \Theta_b} \tag{14}$$

Where;

$$\Theta_b = \frac{\int_N^1 \Theta\, U\, R\, dR}{\int_N^1 U\, R\, dR} \tag{15}$$

The average Nusselt number is defined as:

$$Nu_m = \frac{1}{L}\int_0^L Nu_z dz \tag{16}$$

## NUMERICAL SOLUTION

A rectangular grid was used for solving the energy equation while a staggered grid was used for solving the coupling of continuity and momentum equations to eliminate the possibility of a checkerboard pressure and velocity pattern. The pressure and temperature are calculated at the solid grid points and the velocities are calculated at the opened and crossed grid points as shown in **Fig.(3)**.

### Energy Equation

Using the Alternating Direction Implicit ADI method, the solution of the energy equation may be written as:

The implicit equation in R-direction;

$$a(j)\Theta^*_{(i,j-1)} + b(j)\Theta^*_{(i,j)} + c(j)\Theta^*_{(i,j+1)} = d(j) \tag{17}$$

Where;

$$a(j) = \left( \frac{\Delta\tau}{2\Pr(\Delta R)^2} - \frac{\Delta\tau}{\Pr R_{(j)}(4\Delta R)} + V_{(i,j)}\frac{\Delta\tau}{(4\Delta R)} \right) \tag{18}$$

$$b(j) = -1 - \left( \frac{\Delta\tau}{\Pr(\Delta R)^2} \right) \tag{19}$$

$$c(j)=\left(\frac{\Delta\tau}{2\Pr(\Delta R)^2}+\frac{\Delta\tau}{\Pr R_{(j)}(4\Delta R)}-V_{(i,j)}\frac{\Delta\tau}{(4\Delta R)}\right) \tag{20}$$

$$d(j)=-\Theta^n_{(i,j)}-\frac{2\,\Delta\tau\,(1-N)^2}{\Pr Re^2(\Delta Z)^2}\left(\Theta^n_{(i+1,j)}-2\Theta^n_{(i,j)}+\Theta^n_{(i-1,j)}\right)+\frac{\Delta\tau\,U_{(i,j)}}{(4\Delta Z)}\left(\Theta^n_{(i+1,j)}-\Theta^n_{(i-1,j)}\right) \tag{21}$$

The implicit equation in Z-direction;

$$a(i)\Theta^{n+1}_{(i-1,j)}+b(i)\Theta^{n+1}_{(i,j)}+c(i)\Theta^{n+1}_{(i+1,j)}=d(i) \tag{22}$$

Where;

$$a(i)=\left(\frac{2\,\Delta\tau\,(1-N)^2}{\Pr Re^2\,(\Delta Z)^2}+\frac{\Delta\tau\,U_{(i,j)}}{(4\Delta Z)}\right) \tag{23}$$

$$b(i)=-1-\left(\frac{4\,\Delta\tau\,(1-N)^2}{\Pr Re^2\,(\Delta Z)^2}\right) \tag{24}$$

$$c(i)=\left(\frac{2\,\Delta\tau\,(1-N)^2}{\Pr Re^2\,(\Delta Z)^2}-\frac{\Delta\tau\,U_{(i,j)}}{(4\Delta Z)}\right) \tag{25}$$

$$\begin{aligned}d(i)=&-\Theta^*_{(i,j)}-\frac{\Delta\tau}{2\Pr(\Delta R)^2}\left(\Theta^*_{(i,j+1)}-2\Theta^*_{(i,j)}+\Theta^*_{(i,j-1)}\right)\\&-\frac{\Delta\tau}{\Pr R_{(j)}\,(4\Delta R)}\left(\Theta^*_{(i,j+1)}-\Theta^*_{(i,j-1)}\right)+\frac{\Delta\tau\,V_{(i,j)}}{(4\Delta R)}\left(\Theta^*_{(i,j+1)}-\Theta^*_{(i,j-1)}\right)\end{aligned} \tag{26}$$

**Momentum Equation in Z-Direction**

Using forward difference in time and central difference in space around point (i+1/2,j) in **Fig.(3)**, **eq.(6)** becomes;

$$U^{n+1}_{(i+\frac{1}{2},j)}=U^{n}_{(i+\frac{1}{2},j)}+A\,\Delta\tau-\frac{\Delta\tau}{\Delta Z}\left(P^n_{(i+1,j)}-P^n_{(i,j)}\right) \tag{27}$$

Where;

$$\begin{aligned}A=&-\left(\frac{(U\overline{V})^n_{(i+\frac{1}{2},j+1)}-(UV)^n_{(i+\frac{1}{2},j-1)}}{(2\Delta R)}+\frac{(U^2)^n_{(i+\frac{3}{2},j)}-(U^2)^n_{(i-\frac{1}{2},j)}}{(2\Delta Z)}\right)+\frac{U^n_{(i+\frac{1}{2},j+1)}-2U^n_{(i+\frac{1}{2},j)}+U^n_{(i+\frac{1}{2},j-1)}}{(\Delta R)^2}\\&+\frac{1}{R_{(j)}}\frac{U^n_{(i+\frac{1}{2},j+1)}-U^n_{(i+\frac{1}{2},j-1)}}{(2\Delta R)}+\frac{4(1-N)^2}{Re^2}\frac{U^n_{(i+\frac{3}{2},j)}-2U^n_{(i+\frac{1}{2},j)}+U^n_{(i-\frac{1}{2},j)}}{(\Delta Z)^2}+\frac{Gr}{Re}\frac{\Theta^n_{(i,j)}}{4(1-N)^2}\end{aligned} \tag{28}$$

At the beginning of each new iteration, $P=P^*$. Thus **eq.(27)** becomes;

$$(U^*)^{n+1}_{(i+\frac{1}{2},j)}=(U^*)^{n}_{(i+\frac{1}{2},j)}+A^*\,\Delta\tau-\frac{\Delta\tau}{\Delta Z}\left(P^*_{(i+1,j)}-P^*_{(i,j)}\right) \tag{29}$$

Subtracting **eq.(29)** from **eq.(27)**, we have;

$$(U')^{n+1}_{(i+\frac{1}{2},j)} = (U')^{n}_{(i+\frac{1}{2},j)} + A'\,\Delta\tau - \frac{\Delta\tau}{\Delta Z}\left(P'_{(i+1,j)} - P'_{(i,j)}\right)^{n} \tag{30}$$

Where;

$$(U')^{n+1}_{(i+\frac{1}{2},j)} = U^{n+1}_{(i+\frac{1}{2},j)} - (U^{*})^{n+1}_{(i+\frac{1}{2},j)} \tag{31}$$

$$(U')^{n}_{(i+\frac{1}{2},j)} = U^{n}_{(i+\frac{1}{2},j)} - (U^{*})^{n}_{(i+\frac{1}{2},j)} \tag{32}$$

$$A' = A - A^{*} \tag{33}$$

$$P'_{(i,j)} = P_{(i,j)} - P^{*}_{(i,j)} \tag{34}$$

$$P'_{(i+1,j)} = P_{(i+1,j)} - P^{*}_{(i+1,j)} \tag{35}$$

Following the work of **(Suhas V. Patenkar 1980)**, let us arbitrary set $A'$ and $(U')^{n}$ equal to zero in **eq.(30)**, obtaining;

$$(U')^{n+1}_{(i+\frac{1}{2},j)} = -\frac{\Delta\tau}{\Delta Z}\left(P'_{(i+1,j)} - P'_{(i,j)}\right)^{n} \tag{36}$$

Substituting **eq.(31)** in **eq.(36)** gives;

$$(U)^{n+1}_{(i+\frac{1}{2},j)} = (U^{*})^{n+1}_{(i+\frac{1}{2},j)} - \frac{\Delta\tau}{\Delta Z}\left(P'_{(i+1,j)} - P'_{(i,j)}\right)^{n} \tag{37}$$

**Momentum Equation in R-Direction**

Using forward difference in time and central difference in space around point (i,j+1/2) in **Fig.(3)**, **eq.(7)** becomes;

$$V^{n+1}_{(i,j+\frac{1}{2})} = V^{n}_{(i,j+\frac{1}{2})} + B\,\Delta\tau - \frac{Re^{2}}{4(1-N)^{2}}\frac{\Delta\tau}{\Delta R}\left(P^{n}_{(i,j+1)} - P^{n}_{(i,j)}\right) \tag{38}$$

Where;

$$B = -\left(\frac{(V^{2})^{n}_{(i,j+\frac{3}{2})} - (V^{2})^{n}_{(i,j-\frac{1}{2})}}{(2\Delta R)} + \frac{(V\overline{U})^{n}_{(i+1,j+\frac{1}{2})} - (VU)^{n}_{(i-1,j+\frac{1}{2})}}{(2\Delta Z)}\right) + \frac{V^{n}_{(i,j+\frac{3}{2})} - 2V^{n}_{(i,j+\frac{1}{2})} + V^{n}_{(i,j-\frac{1}{2})}}{(\Delta R)^{2}} + \frac{1}{R_{(j+\frac{1}{2})}}\frac{V^{n}_{(i,j+\frac{3}{2})} - V^{n}_{(i,j-\frac{1}{2})}}{(2\Delta R)} - \frac{V^{n}_{(i,j+\frac{1}{2})}}{(R_{(j+\frac{1}{2})})^{2}} + \frac{4(1-N)^{2}}{Re^{2}}\frac{V^{n}_{(i+1,j+\frac{1}{2})} - 2V^{n}_{(i,j+\frac{1}{2})} + V^{n}_{(i-1,j+\frac{1}{2})}}{(\Delta Z)^{2}} \tag{39}$$

At the beginning of each new iteration, $P=P^*$. Thus **eq.(38)** becomes;

$$(V^*)^{n+1}_{(i,j+\frac{1}{2})} = (V^*)^{n}_{(i,j+\frac{1}{2})} + B^*\,\Delta\tau - \frac{Re^2}{4(1-N)^2}\frac{\Delta\tau}{\Delta R}\left(P^*_{(i,j+1)} - P^*_{(i,j)}\right) \tag{40}$$

Subtracting **eq.(40)** from **eq.(38)**, gives;

$$(V')^{n+1}_{(i,j+\frac{1}{2})} = (V')^{n}_{(i,j+\frac{1}{2})} + B'\,\Delta\tau - \frac{Re^2}{4(1-N)^2}\frac{\Delta\tau}{\Delta R}\left(P'_{(i,j+1)} - P'_{(i,j)}\right)^n \tag{41}$$

Where;

$$(V')^{n+1}_{(i,j+\frac{1}{2})} = (V)^{n+1}_{(i,j+\frac{1}{2})} - (V^*)^{n+1}_{(i,j+\frac{1}{2})} \tag{42}$$

$$(V')^{n}_{(i,j+\frac{1}{2})} = (V)^{n}_{(i,j+\frac{1}{2})} - (V^*)^{n}_{(i,j+\frac{1}{2})} \tag{43}$$

$$B' = B - B^* \tag{44}$$

$$P'_{(i,j)} = P_{(i,j)} - P^*_{(i,j)} \tag{45}$$

$$P'_{(i,j+1)} = P_{(i,j+1)} - P^*_{(i,j+1)} \tag{46}$$

Following the work of **(Suhas V. Patenkar 1980)**, let us arbitrary set $B'$ and $(V')^n$ equal to zero in **eq.(41)**, obtaining;

$$(V')^{n+1}_{(i,j+\frac{1}{2})} = -\frac{Re^2}{4(1-N)^2}\frac{\Delta\tau}{\Delta R}\left(P'_{(i,j+1)} - P'_{(i,j)}\right)^n \tag{47}$$

Substituting **eq.(42)** in **eq.(47)** gives;

$$(V)^{n+1}_{(i,j+\frac{1}{2})} = (V^*)^{n+1}_{(i,j+\frac{1}{2})} - \frac{Re^2}{4(1-N)^2}\frac{\Delta\tau}{\Delta R}\left(P'_{(i,j+1)} - P'_{(i,j)}\right)^n \tag{48}$$

**Continuity Equation**

Writing the continuity equation in the central difference form around (i,j);

$$\frac{V_{(i,j+\frac{1}{2})} - V_{(i,j-\frac{1}{2})}}{\Delta R} + \frac{V_{(i,j)}}{R_{(j)}} + \frac{U_{(i+\frac{1}{2},j)} - U_{(i-\frac{1}{2},j)}}{\Delta Z} = 0 \tag{49}$$

Substituting **eqs.(37) and (48)** in **eq.(49)** and dropping the subscript, we have;

$$P'_{(i,j)} = \frac{-1}{a}\left(bP'_{(i+1,j)} + bP'_{(i-1,j)} + cP'_{(i,j+1)} + cP'_{(i,j-1)} + d\right) \tag{50}$$

Where;

$$a = 2\left(\frac{\Delta\tau\,\Delta R}{\Delta Z} + \frac{Re^2}{4(1-N)^2}\frac{\Delta\tau\,\Delta Z}{\Delta R}\right) \tag{51}$$

$$b = -\frac{\Delta\tau\,\Delta R}{\Delta Z} \tag{52}$$

$$c = -\left(\frac{Re^2}{4(1-N)^2}\frac{\Delta\tau\,\Delta Z}{\Delta R}\right) \tag{53}$$

$$d = \Delta Z\left(V^*_{(i,j+\frac{1}{2})} - V^*_{(i,j-\frac{1}{2})}\right) + \frac{\Delta R\,\Delta Z}{R_{(j)}}V^*_{(i,j)} + \Delta R\left(U^*_{(i+\frac{1}{2},j)} - U^*_{(i-\frac{1}{2},j)}\right) \tag{54}$$

The local Nusselt number **eq.(14)** can be written as;

$$Nu_{(i)} = \frac{2(1-N)}{\Theta_{(i,1)} - \Theta_{b(i)}} \tag{55}$$

Applying Trapezoidal rule to integrate the average Nusselt number **eq.(16)**;

$$Nu_m = \frac{1}{Z}\left(Nu_{(2)} + 2\sum_{i=3}^{i=mt-1} Nu_{(i)} + Nu_{(mt)}\right)\frac{\Delta Z}{2} \tag{56}$$

**COMPUTATIONAL ALGORITHM**

- Solve **eqs.(17) and (22)** for temperature $\Theta^{n+1}_{(i,j)}$.
- Guess values of $(P^*)^n$ at all the pressure grid points (the filled points in **Fig.(3)**). Also arbitrary set values of $(U^*)^n$ and $(V^*)^n$ at the proper velocity grid points (the open and crossed points in **Fig.(3)**).
- Solve for $(U^*)^{n+1}$ and $(V^*)^{n+1}$ from **eqs.(29) and (40)** respectively at all appropriate interior grid points.
- Using the values of $(U^*)^{n+1}$ and $(V^*)^{n+1}$ obtained in steps 3, solve for (P') from the pressure correction formula, **eq.(50)** by the relaxation technique.
- Calculate $(P)^{n+1}$ at all internal grid points from the following equation;
- $P^{n+1}_{(i,j)} = (P^*)^n_{(i,j)} + \alpha_p P'$
  (57)
    - Where $\alpha_p$ is underrelaxation factor. In the present work, the value of $\alpha_p$ was set as 0.2.
- Calculate (U') and (V') from **eqs.(36) and (47)** respectively.
- The new values of $(U^*)^n$ and $(V^*)^n$ for the next iteration will be obtained by underrelaxate $(U^*)^{n+1}$ and $(V^*)^{n+1}$ obtained in step 3, as follows ;

- $$(U^*)^n = (U^*)^{n+1} + \alpha_p U'$$
  (58)
- $$(V^*)^n = (V^*)^{n+1} + \alpha_p V'$$
  (59)
- Calculate the average Nusselt Number using **eq.(56)**.
- Repeat steps 1 to 8 until convergence is reached by setting the summation of the mass source term (d) for the entire domain in **eq.(54)** equal to $10^{-4}$ and by setting the difference in the average Nusselt number $Nu_m$ between the present iteration and the previous iteration equal to $10^{-4}$.

## EXPERIMENTAL APPARATUS AND PROCEDURES

An experimental rig was designed and constructed by **(Akeel Al−Sudani, 2005)** in the University of Technology and it was used in the present work to study the heat transfer process by mixed convection to a simultaneously hydrodynamic and thermal developing air flow in an inclined annulus. The experimental apparatus is shown in **Fig.(4)**. The present study including the opposing flow position in addition to the aiding flow position with a different inclination angles to those covered by **(Akeel Al−Sudani, 2005)**. The purpose of using this rig was to deduce an empirical equation of average Nusselt number as a function of Reynolds number, Raylieh number, and to compare the theoretical results with the experimental ones.

### Experimental Procedure

- The inclination angle of the annulus was adjusted as required.
- The centrifugal fan was then switched on to circulate the air, through the open loop. A regulating valve was used for adjusting the required mass flow rate.
- The electrical heater was switched on and the heater input power then adjusted to give the required heat flux.
- The apparatus was left at least three hours to establish steady state condition. The thermocouples readings were measured every half an hour by means of the digital electronic thermometer until the reading became constant, a final reading was recorded.
- During each test run, the angle of inclination of the annulus in degree, the reading of the manometer (air flow rate) in mm $H_2o$, the readings of the thermocouples in ˚C, the heater current in amperes and the heater voltage in volts were recorded.

## RESULTS AND DISCUSSION

### Experimental Results

A total of 51 test runs were carried out to cover annulus inclination angles, horizontal ( $\alpha=0^o$ ), aiding flow ( $\alpha=20^o$, $60^o$ and $90^o$ ) and opposing flow ($\alpha=-20^o$ and $-60^o$). The heat flux varied from 93 W/m$^2$ to 857 W/m$^2$ and Reynolds number varied from 154 to 724.

### Heat Flux and Reynolds Number Effect on the Surface Temperature & $Nu_z$ Distribution

**Figs.(5) and (6)** show the variation of the surface temperature and the local Nusselt number along the inner cylinder for different heat flux and for Re=218. Figures show that the surface temperature and the local Nusselt number increase as the heat flux increase with constant Reynolds number. This can be attributed to the increasing of the thermal boundary layer faster due to buoyancy effect as the heat flux increases for the same Reynolds number.

**Figs.(7) and (8)** show the variation of the surface temperature and the local Nusselt number along the inner cylinder for different Reynolds number and for heat flux (258 W/m$^2$). Figures show that the surface temperature decrease and the local Nusselt number increase as the Re number increase with constant heat flux**.** It is necessary to mention that as heat flux increases the inner tube surface temperature increases because the free convection is the dominating factor in the heat transfer process.

**Angle of Inclination Effect on the Surface Temperature & Nu$_z$ Distribution**

**Figs.(9) and (10)** show the influence of inclination angle for aiding flow on the inner cylinder surface temperature and the local Nusselt number distribution for (Re=378, q=379 W/m$^2$). Figures show a reduction in surface temperature and increasing in the local Nusselt number as the angle of inclination changes from vertical to horizontal position (aiding flow); this can be attributed to the large buoyancy effect in a horizontal annulus compared with the other annulus angle of inclination. The same behavior is found as the angle of inclination changes from negative angles (opposing flow) to horizontal position.

**Flow Direction Effect on the Surface Temperature & Nu$_z$ Distribution**

**Figs.(11) and (12)** show the influence of flow direction (i.e., aiding & opposing flow) on the inner cylinder surface temperature and the local Nusselt number distribution for (Re=154, q=258 W/m$^2$) for ($\alpha$=20$^o$ and $\alpha$=-20$^o$). Figures show a reduction in surface temperature and increasing in the local Nusselt number as the angle of inclination changes from negative angles (opposing flow) to the positive angles ( aiding flow); this can be attributed to the large buoyancy effect in the positive angles ( aiding flow) compared with the negative angles (opposing flow).

**Angle of Inclination Effect on Average Nusselt Number**

The influence of inclination angle on Nu$_m$ is plotted for both aiding and opposing flow in **Figs.(13) and (14)** for (q=676 W/m$^2$, Re=308) and (q=517 W/m$^2$, Re=218); respectively. Figures show that ($\zeta$) decrease as the angle of inclination changes from horizontal position to the positive angles (aiding flow) and from horizontal position to negative angles (opposing flow) due to the decreasing of buoyancy effect as the angle changes from the horizontal position to the inclined position.

**Average Nusselt Number versus Reynolds Number and Rayleigah Number**

The relationship between average Nusselt number and Reynolds number are plotted in **Figs.(15) and (16)** for ($\alpha$=0$^o$, q=258 W/m$^2$), ($\alpha$=$\pm$60$^o$, q=676 W/m$^2$), respectively. Figures show that an increase in the average Nusselt number as Reynolds number increase and the values of the average Nusselt number for aiding flow are greater than that for opposing flow at the same Reynolds number. This can be attributed to the increase of the bouncy effect in the case of aiding flow which improves the heat transfer process.

The relationship between average Nusselt number and Rayleigh number are plotted in **Figs.(17) and (18)** for ($\alpha=0^o$, Re=218), ($\alpha=\pm60^o$, Re=378), respectively. Figures show an increase in the average Nusselt number as Rayleigh number increase and that the values the average Nusselt number for aiding flow are greater than that for opposing flow at the same Rayleigh number. This can be attributed to the increase of the bouncy effect in the case of aiding flow which improves the heat transfer process.

## THEORETICAL RESULTS

### Temperature Profile

The variation of temperature profiles along the vertical annulus are shown in **Fig.(19)**, for (q=150 W/$m^2$, Re=1000). Figure shows a steep temperature gradient near the heated surface and the thickness of the thermal boundary layer gradually increases as the flow moves from annulus inlet towards annulus exit.

### Velocity Profile

The velocity Profiles show the limitation of the buoyancy effect in the case of Gr/Re=0 see **Fig.(20)**, as all the profiles show approximately similar distribution about the middle of the annular space which is similar to pure forced convection behavior **(Cony and El-Sharrawi 1975)**. **Fig.(21)** shows the development of the axial velocity profiles along the annulus axis for (q=150 W/$m^2$, Re=1000). It can be seen that the profiles bias slightly towards the heated surface. That can be attributed to the decreasing in the air density near the heated surface which will cause a decrease in the effect of the gravitational body force, which is proportional to the density. **Fig.(22)** shows the effect of the parameter Gr/Re on the axial velocity profile at z=0.603m for Gr/Re=±1898 with Gr/Re=0. It is clear from the this figure that when the free convection opposes the forced flow the buoyancy force tends to retard the fluid near the heated boundary and accelerates it near the opposite adiabatic wall and vice versa, which have the same behavior that found by **(El-Sharrawi and Sarhan 1980)**.

### Surface Temperature & Local Nusselt Number

The effect of heat flux and Reynolds number on the surface temperature and the local Nusselt number obtained in the theoretical study is similar to that obtained in the experimental study. **Fig.(23)** shows the effect of the parameter Gr/Re on the local Nusselt number values for Gr/Re=±633 and Gr/Re=±1898 with Gr/Re=0, respectively. It is clear from this figure that with positive values of Gr/Re, the values of local Nusselt number are higher for the same dimensionless axial distance than their corresponding values of the purely forced convection case (Gr/Re=0) and vice versa with the negative values of Gr/Re. This is attributed to the higher velocities near the heated surface, and hence the decrease in the thickness of the developing boundary layer on that boundary, in case of an aiding free convection, which have the same behavior that found by **(El-Sharrawi and Sarhan 1980)**.

### Comparison with the Present Theoretical Results

The experimental local Nusselt number results for Re=378, q=258 W/$m^2$ is compared with the present theoretical results, as shown in **Fig.(24)**. Figure reveals that the experimental local Nusselt number follows the same trend as the present theoretical results but is approximately higher with maximum difference of 29.47%, minimum difference of 6.46% and mean difference of 17.96%.

## CONCLUSIONS

The experimental investigation show that the inner tube surface temperature in the case of aiding flow is lower than that in the case of opposing flow, while the $Nu_z$ value in the case of aiding flow is higher than that in the case of opposing flow (the maximum value occurs in the horizontal position) at the same Reynolds number and heat flux. For the same Reynolds number and annulus orientation, the inner tube surface temperature and the $Nu_z$ increases as the heat flux increases. For the same heat flux and annulus orientation, the inner tube surface temperature increases as the Reynolds number decreases. The theoretical investigation show that The temperature profile along the annulus shows a steep profile near the heated surface with the thermal boundary thickness increases as the heat flux increases, Reynolds number decreases for the same axial position. When the free convection opposes the forced flow the buoyancy force tends to retard the fluid near the heated boundary and accelerates it near the opposite adiabatic wall. But when the free convection aids the forced flow the fluid accelerates near the heated wall and decelerates near the opposite adiabatic boundary, while in the case of Gr/Re=0 (pure forced convection) the maximum velocity occurs at the annular gap centerline (fully developed velocity profile). For constant heat flux the $Nu_z$ value increases at the annulus entrance as Reynolds number increases because of forced convection is dominant, while the $Nu_z$ value increases in the annulus downstream as the Reynolds number decreases due to free convection is dominant. With positive values of Gr/Re the values of $Nu_z$ are higher for the same logarithmic dimensionless axial distance (ZZ) than their corresponding values of the purely forced convection case (Gr/Re=0) and vice versa with the negative values of Gr/Re. The buoyancy effect can be neglected at the annulus entrance for all Reynolds number and heat flux covered in this study.

## REFERENCES


- **Akeel A. M. Al−Sudani,** "An investigation into laminar combined convection heat transfer through concentric annuli", PhD. Thesis, University of Technology, Mechanical Engineering Department, September 2005.

- **Cony J. E. R. and El-Shaarawi M. A. I. ,**"Finite difference analysis for laminar flow heat transfer in concentric annuli with simultaneously developing hydrodynamic and thermal boundary layers " , Int. Journal for Numerical Method in Engineering, Vol. 9, pp. 17-38, 1975.

- **El-Shaarawi M. A. and Sarhan A.,** "Free convection effects on the developing laminar flow in vertical concentric annuli ,"J. Heat Transfer, Vol. 102, pp.617-622, November, 1980.

- **John D. Anderson, Jr.,**" Computational Fluid Dynamics"**,** Mc Graw-Hill, New York, 1995**.**

- **Nazrul Islam, Gaitonde U.N. and Sharma G.K.,**" Mixed convection heat transfer in the entrance region of horizontal annuli", Int. J. Heat Mass Transfer. Vol.44, No.11, pp. 2107- 2120, 2001.

- **Suhas V. Patenkar,**"Numerical Heat Transfer and Fluid Flow", Hemisphere, New York, 1980.


## NOMENCLATURE

### Latin Symbols

| SYMBOL | DESCRIPTION | UNITS |
|---|---|---|
| $D_h$ | Hydraulic diameter=$2(r_o\text{-}r_i)$ | m |
| h | Heat transfer coefficient | $W/m^2.\,^oC$ |
| k | Thermal conductivity | $W/m.\,^oC$ |
| L | Length | m |
| N | Radius ratio=$r_i/r_o$ | – |
| p | Pressure | $N/m^2$ |
| q | Heat flux | $W/m^2$ |
| r | Radial coordinate | m |
| $r_o$ | Outer radius of inner cylinder | m |
| $r_i$ | Inner radius of outer cylinder | m |
| t | Time | s |
| T | Temperature | $^oC$ |
| u | Axial velocity | m/s |
| v | Radial velocity | m/s |
| z | Axial coordinate | m |

### Creak Symbols

| | | |
|---|---|---|
| $\alpha_p$ | Relaxation factor | – |
| $\alpha$ | Angle of inclination | degree |
| $\hat{\alpha}$ | Thermal diffusivity | $m^2/s$ |
| $\beta$ | Coefficient of volume expansion | 1/K |
| $\zeta$ | Average Nusselt number ratio for inclined to horizontal position | – |
| $\mu$ | Dynamic viscosity | kg/m.s |
| $\upsilon$ | Kinematic viscosity | $m^2/s$ |
| $\rho$ | Density | $kg/m^3$ |

### Dimensionless Groups

| | | |
|---|---|---|
| Gr | Grashof number | $g\,\beta\,q\,r_o D_h^3 / \upsilon^2 k$ |
| Nu | Nusselt number | $h\,D_h/k$ |
| P | Pressure at any cross section | $p\text{–}p_i/\,\rho_i.u_i^2$ |
| Pr | Prandtl number | $\mu.C_p/k$ |
| R | Radial coordinate | $r/r_o$ |
| Ra | Rayligh number | Gr.Pr |
| Re | Reynolds number | $u_{i.}D_h/\upsilon$ |
| $\Theta$ | Temperature | $(T\text{-}T_i)\,k/q''\,r_o$ |

| | | |
|---|---|---|
| $\tau$ | Time | $\upsilon t/r_o$ |
| U | Axial velocity component | $u/u_i$ |
| V | Radial velocity component | $v.r_o/\upsilon$ |
| Z | Axial coordinate | $2z(1-N)/\ r_oRe$ |
| ZZ | Inverse Graetz number | $z/Re.Pr.D_h$ |

**Superscript**

| | |
|---|---|
| * | Intermediate time step |
| n+1 | forward time step |
| – | average |
| * | Initial guessed value |
| ' | Difference between two values |

**Subscript**

| | |
|---|---|
| B | BULK |
| i | Axial mesh point |
| j | Radial mesh point |
| m | Mean |
| w | Wall |
| z | Local in axial direction |

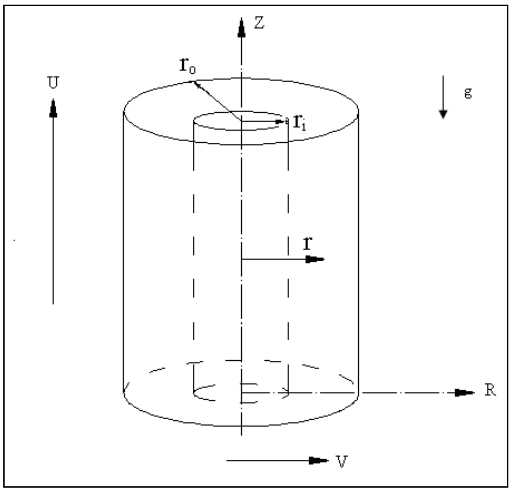


**Fig.1: Two-Dimensional Annular Geometry.**

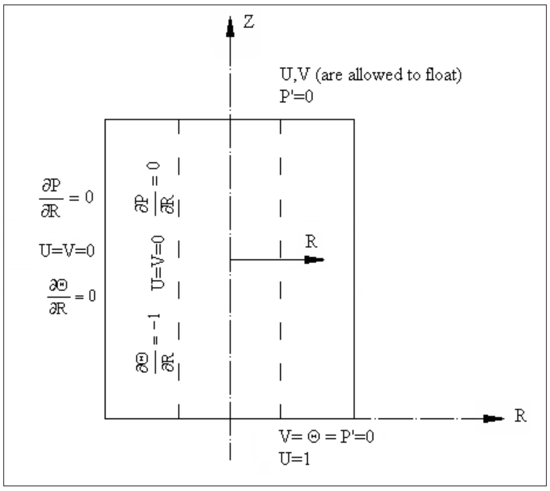


**Fig.2: Boundary Conditions**

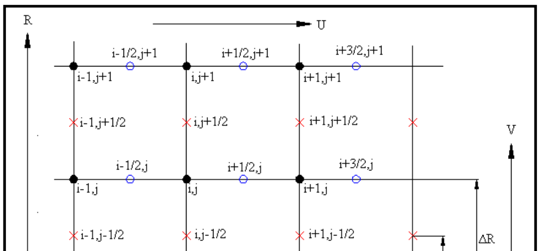




**Fig.3: Staggered Mesh Network.**

**Fig.4: A Photograph of Apparatus.**

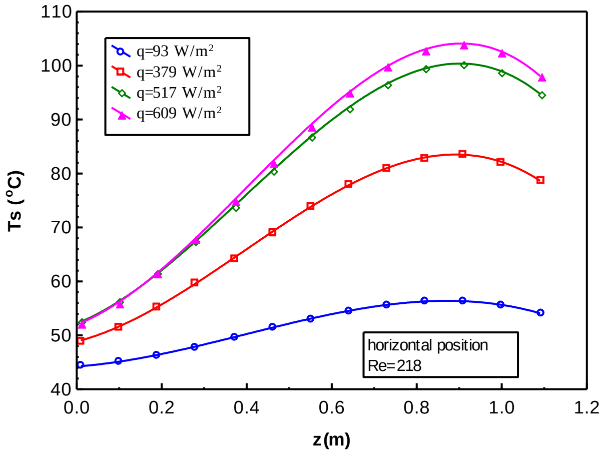


**Fig.5: Experimental Variation of the Surface Temperature with the Axial Distance, Re=218, $\alpha=0^o$.**

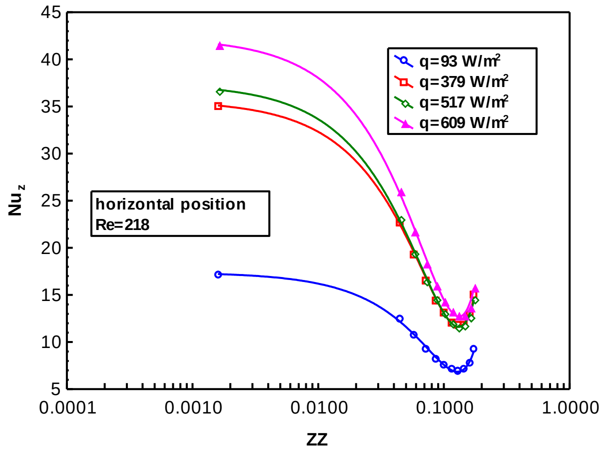


**Fig.6: Experimental Local Nusselt Number Versus Dimensionless Axial Distance, Re=218, $\alpha=0^o$.**

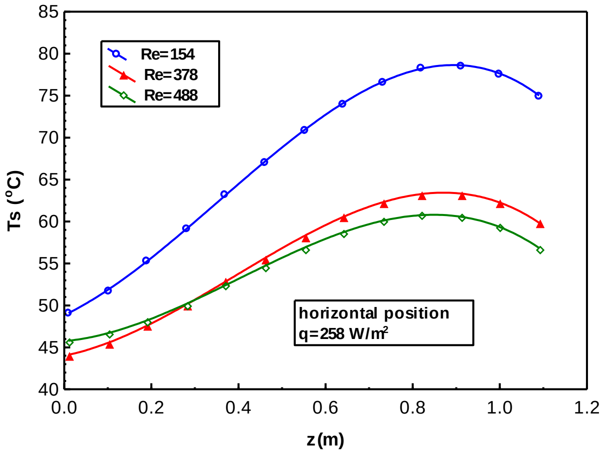


**Fig.7: Experimental Variation of the Surface Temperature with the Axial Distance, q=258 W/m$^2$, $\alpha=0^o$.**

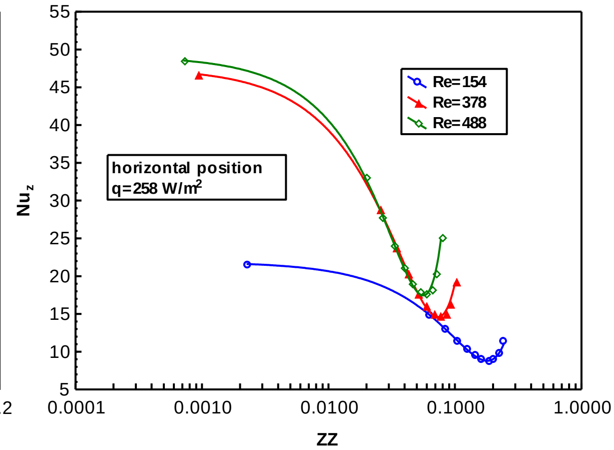


**Fig.8: Experimental Local Nusselt Number Versus Dimensionless Axial Distance q=258 W/m$^2$, $\alpha=0^o$.**

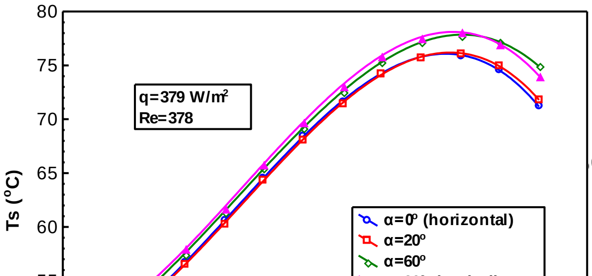


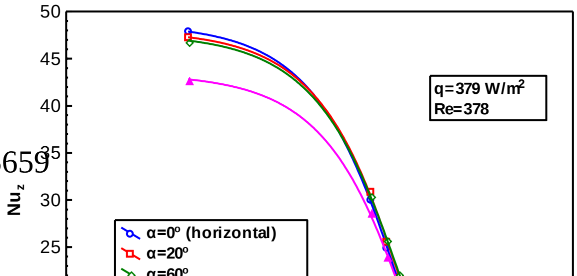

**Fig.9: Experimental Variation of the Surface Temperature with the Axial Distance for Various Angles, q=379 W/m$^2$, Re=378.**

**Fig.10: Experimental Local Nusselt Number Versus Dimensionless Axial Distance for Various Angles, q=379 W/m$^2$, Re=378.**

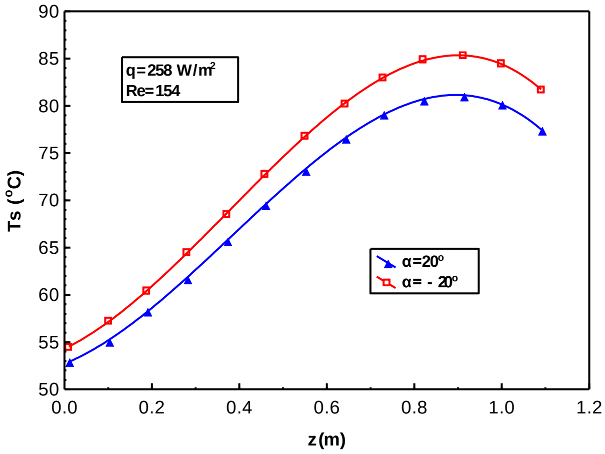


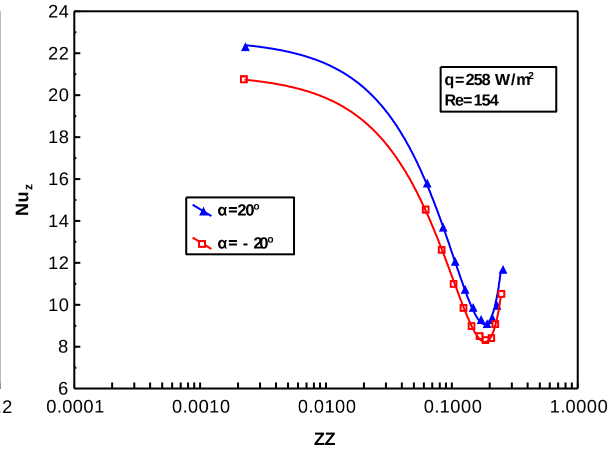


**Fig.11: Experimental Variation of the Surface Temperature with the Axial Distance for Various Angles, q=258 W/m$^2$, Re=154.**

**Fig.12: Experimental Local Nusselt Number Versus Dimensionless Axial Distance for Various Angles, q=258 W/m$^2$, Re=154.**

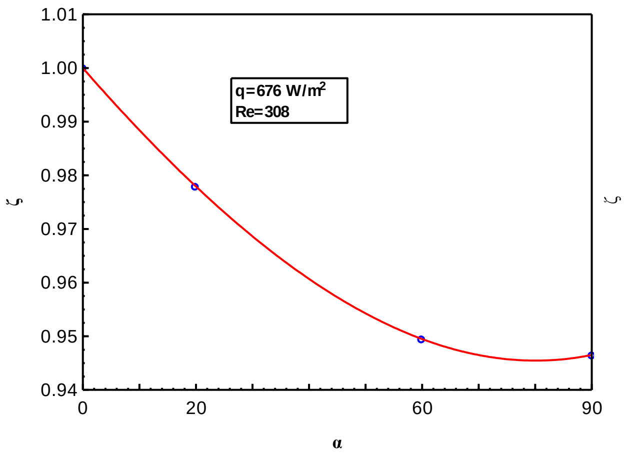


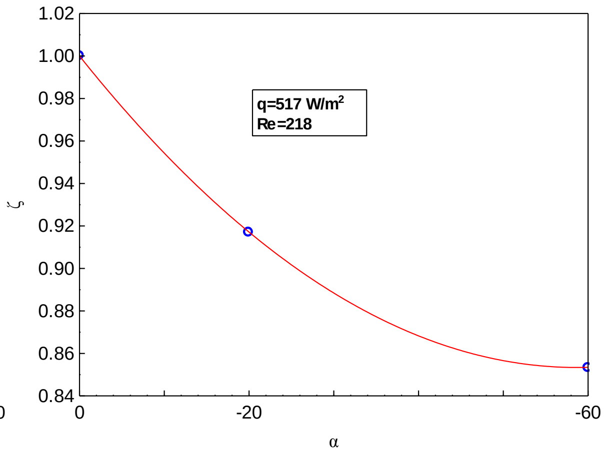


**Fig.13: Experimental $\zeta=(Nu_m)_{inc.}/(Nu_m)_{hor}$ as a Function of Inclination Angle for q=676 W/m$^2$, Re=308 (Aiding Flow).**

**Fig.14: Experimental $\zeta=(Nu_m)_{inc.}/(Nu_m)_{hor}$ as a Function of Inclination Angle for q=517 W/m$^2$, Re=218 (Opposing Flow).**

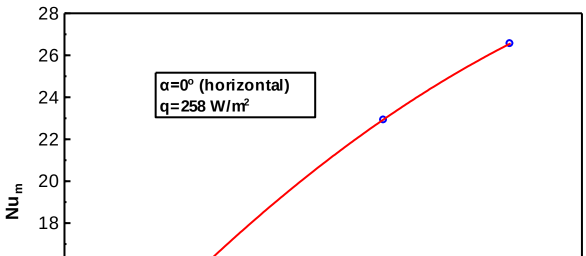


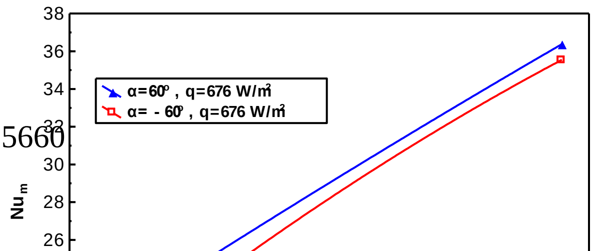

**Fig.15: Experimental Average Nusselt Number Versus Reynolds Number for q=258 W/m$^2$ , α=0$^o$ (Horizontal).**

**Fig.16: Experimental Average Nusselt Number Versus Reynolds Number for Various Angles, q=676 W/m$^2$ .**

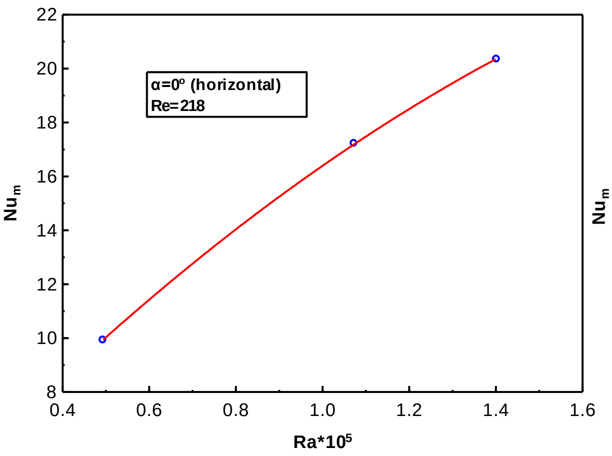


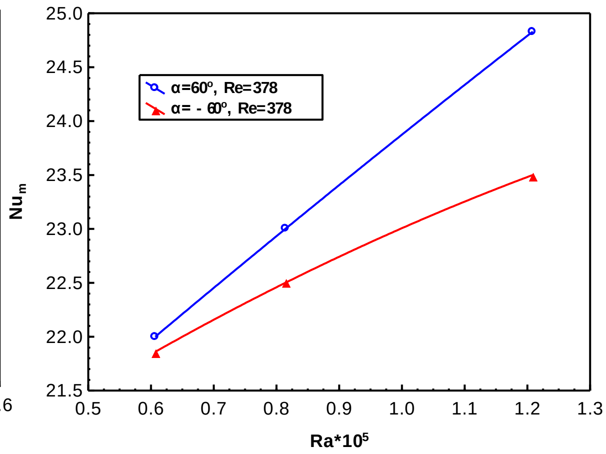


**Fig.17: Experimental Average Nusselt Number Versus Rayleigh Number for Re=218, α=0$^o$ (Horizontal).**

**Fig.18: Experimental Average Nusselt Number Versus Rayleigh Number for Various Angles,** Re=378.

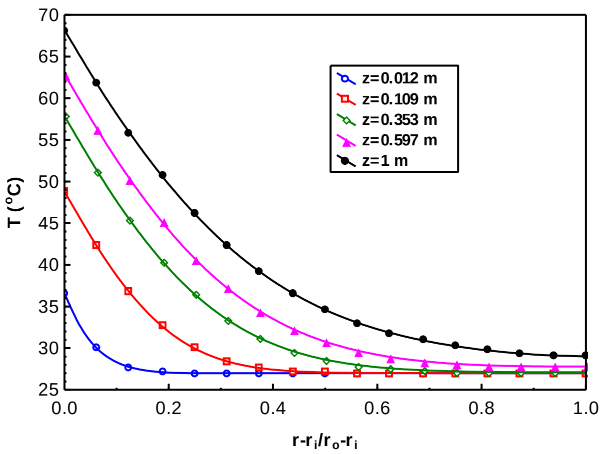


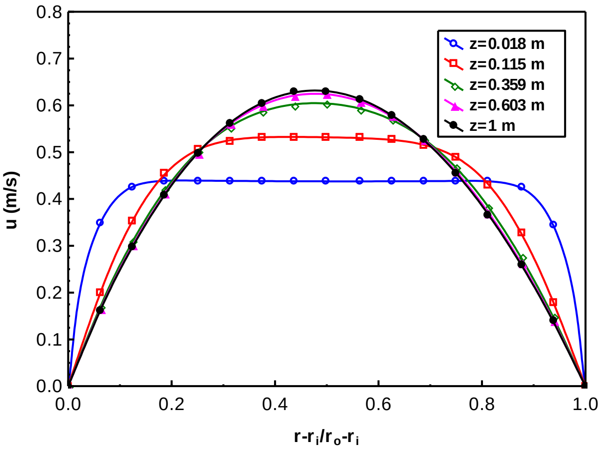


**Fig.19: Theoretical Development of the Temperature Profiles Along the Annulus for q=150 W/m$^2$ , Re=1000.**

**Fig.20: Theoretical Development of the Axial Velocity Profiles Along the Annulus for Gr/Re=0.**

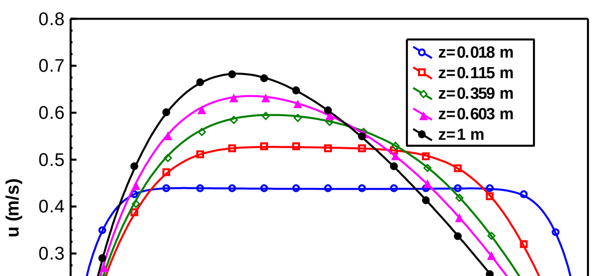


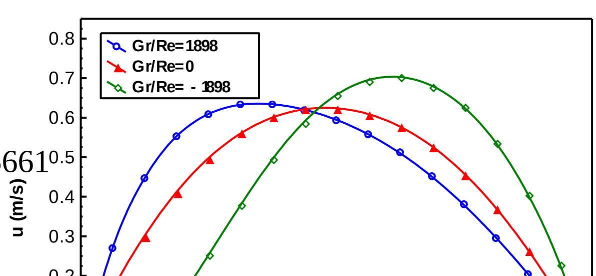

Fig.21: Theoretical Development of the Axial Velocity Profiles Along the Annulus for q=150 W/m$^2$ , Re=1000.

Fig.22: Theoretical Development of the Axial Velocity Profiles at z=0.603m for Various Values of Gr/Re.

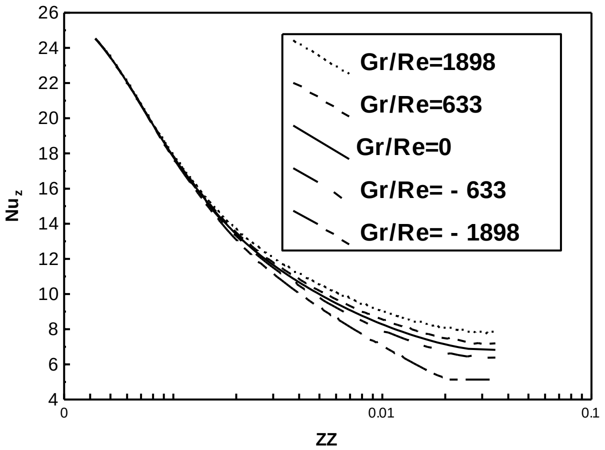


Fig.23: Theoretical Local Nusselt Number Versus Dimensionless Axial Distance for Various Values of Gr/Re.

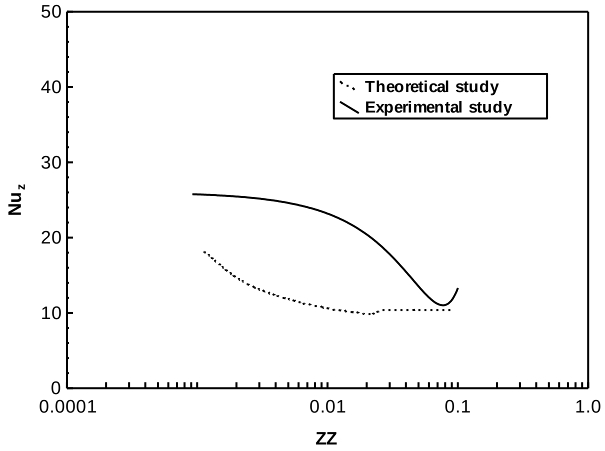


Fig.24: Comparison of Experimental Nu$_z$ with the Theoretical Result for Vertical Position, q=258 W/m$^2$ Re=378 .

# FLOW SEPARATION OF AXIAL COMPRESSOR CASCADE BLADES

Dr. Arkan Kh. Al-Taie
(Assist. Prof.) Mech. Eng. Dept., UOT
Baghdad - Iraq

Sabah Faleh Habeeb
(M.Sc. Student), Mech. Eng. Dept., UOT
Baghdad - Iraq

## ABSTRACT

An experimental and theoretical investigation of the effect of flow separation on the performance of a cascade NACA 65_(12)10 axial compressor blade has been carried out. The experimental work includes the fabrication of three blades from wood, each having a chord (100mm) but one of these blades having a span of (90mm) for smoke tunnel testing and the other two blades having a span of (380mm) for wind tunnel testing.The two blades were connected by suitable mechanism in order to be fixed in the wind tunnel protractor and rotated in the required stagger angle. The cascade was tested in an open type low-speed subsonic (Mach number=0.117) wind tunnel, for Reynolds number (Re=239605) based on maximum velocity (35 m/s) and airfoil chord length. The total and static pressures were measured in selected points between the two blades for stagger angles of ($4^0$, $0^0$ ,-$4^0$,-$8^0$ and -$12^0$) by using a multi-tube manometer and a pitot static tube. The small blade (90mm span) is tested in the smoke tunnel to visualize the real behavior of flow separation. The theoretical work includes using the software FLUENT (V6.2) to simulate the flow between the two blades. The study shows that the flow separation begins when the cascade are inclined at a stagger angle of (-$4^0$) on the suction side of the lower blade at a position (96%chord experimentally and 98%chord theoretically). Then, the separation zone increases with increased stagger angle (in clockwise direction) and reach to the position (61%chord experimentally and 63%chord theoretically) at a stagger angle (-$12^0$).These results are validated by a smoke tunnel tests.This separation affects the performance of the compressor, where the static pressure ratio ($p_{s_e}/p_{s_i}$) decreases as the separation zone gets bigger. The range of working stagger angle is then calculated. It was found in the range (-$18^0$ to $36^0$). The flow behavior between the two blades shows that the blade-to-blade configuration works as nozzle-diffuser. The theoretical results were compared with the experimental results and good agreement was obtained.

**الخلاصة:**

تم في هذا البحث اجراء دراسة عملية ونظرية لتاثير انفصال الجريان على اداء الريشتين المتعاقبتين للضاغطة المحورية من نوع [NACA 65_ (12)10] . الجزء العملي يتضمن تصنيع ثلاث ريش من مادة الخشب, وتر كل ريشة (100ملم) لكن احدى الريش ذات عرض(90 ملم) لاختبارات النفق الدخاني والريشتين المتبقتين ذواتا عرض(380ملم)لاختبارات النفق الهوائي. تربط الريشتيين المستخدمتين لاختبارات النفق الهوائي بآليه مناسبة لكي تثتبت بمنقلة النفق وبالتالي يمكن تدويرها بالزاوية المطلوبة. تم اختبار متعاقبة الريشتين في نفق هوائي تحت صوتي واطى السرعة لعدد رينولد(Re=239605) المحسوب على اساس السرعة القصوى (35م\ثا) وطول وتر الريشة. لقد تم قياس الضغط الكلي والضغط الاستاتيكي للنقاط المختاره بين ريشتي الضاغطة

لخمس زوايا أنحراف هي (4,0,4-,8- و12-) باستخدام مانوميترمتعدد الانابيب وأنبوب بيتوت-أستاتي. تم أختبار الريشة الصغيرة (ذات عرض90 ملم) بأستخدام النفق الدخاني لرؤية السلوك الحقيقي لأنفصال الجريان. الدراسة النظرية تتضمن استخدام البرنامج الجاهز (FLUENT V6.2) لمحاكات الجريان بين الريشتين. أظهرت الدراسة بأن الأنفصال يبدأ عندما تكون زاوية الأنحراف (4-) حيث يحدث على السطح العلوي للريشة السفلى وبمسافة (96% من الوتر عمليا" و98 % من الوتر نظريا") من الدخول الى الخروج للمتعاقبة‘. وبعد ذلك تزداد منطقة الأنفصال بأزدياد زاوية الأنحراف(stagger angle)(بأتجاه عقرب الساعة) حتى تصل الى (61% من الوتر عمليا" و63% من الوتر نظريا") من الدخول الى الخروج عند زاوية أنحراف (12-) وهذا ما يوضحه أختبار النفق الدخاني. يؤثر الأنفصال على أداء الريشتين المتعاقبتين حيث تقل نسبة الضغط (الضغط الستاتيكي الخارج الى الضغط الستاتيكي الداخل) بأزدياد منطقة الانفصال. وبعد ذلك تم حساب المدى الشغال لزوايا الأنحراف . الذي وجد ضمن المدى (من-18 الى 36) . أن سلوك الجريان بين الريشتين يبين بأن الريشتين المتعاقبتين تعملان كبوق متقارب- متباعد. تمت مقارنة النتائج النظرية مع النتائج العملية وجد تقارب جيد بين تلك النتائج.

**KEYWORDS: Axial Compressor Cascade, Viscous Flow, Separation, FLUENT, Visualization**

## INTRODUCTION:

The compressor, which is the important part of gas turbine engines, has to be given special attention during operation. The main task of the axial-flow compressor is to increase the pressure of air by converting air kinetic energy through a series of rotating and stationary blades. One of the most important problems that affect performance is the flow separation. Separation starts by deviation of fluid particles away from blade surface in the boundary layer. This causes a drop in kinetic energy, and cause the flow to re circulate [You D. AND Moin, P., 2006]. After stall region the fluid particles velocity reaches to zero in boundary layer near to blade surface and this deceleration causes increasing in boundary layer thickness and at a small distance after stall region the particles stop and reverse in direction due to positive pressure gradient. The low Reynolds number in conjunction with the local adverse pressure gradient makes it susceptible to flow separation [Meinhard T. Schobeiri etal, 2003]. This study consists of two major parts: the experimental part a cascade tested in an open jet low speed wind tunnel. The total and static pressure between two axial compressor blades were measured using a Pitot - static tube and a manometer. To visualize the flow a smoke tunnel was used. The stagger angle was taken equals ($4^0$, $0^0$,$-4^0$,$-8^0$, and$-12^0$). Secondary, in the theoretical part that depends on simulation the flow between the two blades by using a software **FLUENT**. The objectives of this paper are:

1. Study the effect of viscous flow separation (through the cascade of an axial compressor) on the flow variables (velocity, static pressure, total pressure…etc) by utilizing FLUENT (V6.2) software.

- Investigate the effect of stagger angle on flow separation.
- Comparison of the experimental results with the theoretical results.

## THEORITICAL PART:

**Assumptions**:

The flow is steady, two-dimensional, incompressible , turbulent, Newtonian, isotropicand isothermal.

**Governing Equations:**

The domain for which the model is build is shown in fig.(1) since the flow through a compressor is three-dimensional and quite complex, a simplified approach is adopted to analyze the fluid flow through cascade passage in two dimensions. Figs.(1) and (2) show the cascade and the physical domain. The equations of continuity, momentum and turbulence model are [Hill, P. G., 1965]:

1- Continuity Equation:

$$\frac{\partial u}{\partial x}+\frac{\partial v}{\partial y}=0 \qquad (a).$$

X-Momentum Equation:

$$\rho\frac{\partial u^2}{\partial x}+\rho\frac{\partial uv}{\partial y}-\frac{\partial}{\partial x}\left[\mu_e\frac{\partial u}{\partial x}\right]-\frac{\partial}{\partial y}\left[\mu_e\frac{\partial u}{\partial y}\right]=-\frac{\partial p}{\partial x}+\frac{\partial}{\partial x}\left[\mu_e\frac{\partial u}{\partial x}\right]+\frac{\partial}{\partial y}\left[\mu_e\frac{\partial v}{\partial x}\right] \quad \text{(b).}$$

Y-Momentum Equation:

$$\rho\frac{\partial uv}{\partial x}+\rho\frac{\partial v^2}{\partial y}-\frac{\partial}{\partial x}\left[\mu_e\frac{\partial v}{\partial x}\right]-\frac{\partial}{\partial y}\left[\mu_e\frac{\partial v}{\partial y}\right]=-\frac{\partial p}{\partial y}+\frac{\partial}{\partial x}\left[\mu_e\frac{\partial u}{\partial y}\right]+\frac{\partial}{\partial y}\left[\mu_e\frac{\partial v}{\partial y}\right] \quad \text{(c).}$$

The turbulence kinetic energy – dissipation model at high Reynolds number is used [Moult, A. etal,1977].

A-Turbulence kinetic energy: $K=0.5\left(u'^2+v'^2+w'^2\right)$

$$\rho\left[\frac{\partial Ku}{\partial x}+\frac{\partial Kv}{\partial y}\right]=\frac{\partial}{\partial x}\left[\frac{\mu_e}{\sigma_k}\frac{\partial K}{\partial x}\right]+\frac{\partial}{\partial y}\left[\frac{\mu_e}{\sigma_k}\frac{\partial K}{\partial y}\right]+G_k-\rho\varepsilon \quad \text{(d).}$$

The quantity $G_k$ is the generation term for the kinetic energy of turbulence given by:

$$G_k=\mu_t\left\{2\left[\left(\frac{\partial u}{\partial x}\right)^2+\left(\frac{\partial v}{\partial y}\right)^2+\left(\frac{\partial u}{\partial y}+\frac{\partial v}{\partial x}\right)^2\right]\right\} \quad \text{(e).}$$

B-Dissipation: $\left[\varepsilon=v\left(\frac{\partial u'}{\partial y}+\frac{\partial v'}{\partial x}\right)^2\right]$

$$\rho\left[\frac{\partial \varepsilon u}{\partial x}+\frac{\partial \varepsilon v}{\partial y}\right]=\frac{\partial}{\partial x}\left[\frac{\mu_e}{\sigma_\varepsilon}\frac{\partial \varepsilon}{\partial x}\right]+\frac{\partial}{\partial y}\left[\frac{\mu_e}{\sigma_\varepsilon}\frac{\partial \varepsilon}{\partial y}\right]+{\left(C_1G_k-C_2\rho\varepsilon\right)\varepsilon}/{K} \quad \text{(f).}$$

The $K-\varepsilon$ turbulence model was extended by ref**.** [Jones, W. P. and Launder, B. E., 1972] to low-Reynolds number flow as follows:

$$\rho\left[\frac{\partial Ku}{\partial x}+\frac{\partial Kv}{\partial y}\right]=\frac{\partial}{\partial x}\left[\left(\frac{\mu_t}{\sigma_k}+\mu\right)\frac{\partial K}{\partial x}\right]+\frac{\partial}{\partial y}\left[\left(\frac{\mu_t}{\sigma_k}+\mu\right)\frac{\partial K}{\partial y}\right]+\mu_t\left[2\left(\frac{\partial u}{\partial x}\right)^2+2\left(\frac{\partial v}{\partial y}\right)^2+\left(\frac{\partial u}{\partial y}+\frac{\partial v}{\partial x}\right)^2\right]-2\mu\left[\frac{\partial K^{0.5}}{\partial x}+\frac{\partial K^{0.5}}{\partial y}\right]^2-\rho\varepsilon \quad \text{(g).}$$

$$\rho\left[\frac{\partial \varepsilon u}{\partial x}+\frac{\partial \varepsilon v}{\partial y}\right]=\frac{\partial}{\partial x}\left[\left(\frac{\mu_t}{\sigma_\varepsilon}+\mu\right)\frac{\partial \varepsilon}{\partial x}\right]+\frac{\partial}{\partial y}\left[\left(\frac{\mu_t}{\sigma_\varepsilon}+\mu\right)\frac{\partial \varepsilon}{\partial y}\right]+\frac{C_1\mu_t}{K}\varepsilon\left[2\left(\frac{\partial u}{\partial x}\right)^2+2\left(\frac{\partial v}{\partial y}\right)^2+\left(\frac{\partial u}{\partial y}+\frac{\partial v}{\partial x}\right)^2\right]-\frac{\rho C_2\varepsilon^2}{K}-2\upsilon\mu_t\left[\frac{\partial^2 u}{\partial x^2}+\frac{\partial^2 u}{\partial x\partial y}+\frac{\partial^2 v}{\partial x\partial y}+\frac{\partial^2 v}{\partial y^2}\right] \qquad \text{(h).}$$

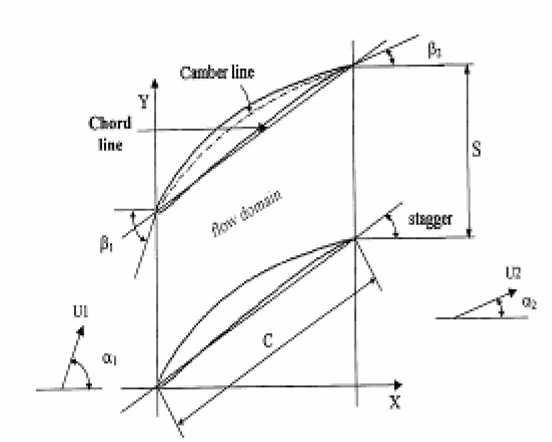


**Fig. (1): Compressor Cascade Geometry.**

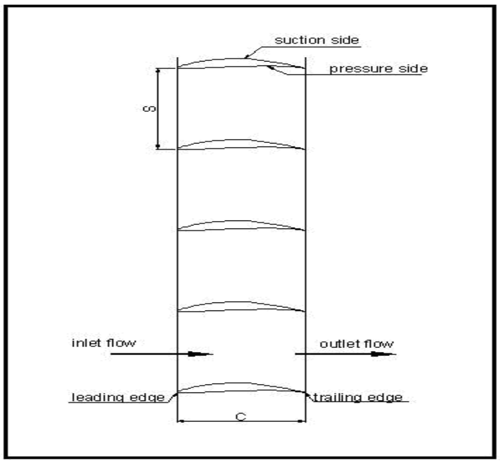


**Fig.(2): General View of the Cascade.**

**FLUENT Code:**

**<u>Analysis Steps:</u>**

There are two processors used to solve the flow equations:

A. preprocessor is a program that structure creates the geometry and grid by using GAMBIT as follows:

- Modeling of geometry, fig.(3) and fig.(4).
- Mesh generation (Discitization), fig.(5).
- Boundary conditions. There are three type of boundary conditions:
  a. Inlet boundary conditions(velocity and pressure inlet).
  b. Outlet flow boundary conditions.
  c. Solid surface(wall) boundary conditions.
  d. Periodic boundary condition(flow regions before and after two blades).

B. Postprocessor: is:

- Solving Navier-Stokes equations (which includes continuity and momentum equations) as wall as turbulent flow model by using FLUENT software with ().
- Plotting the results.

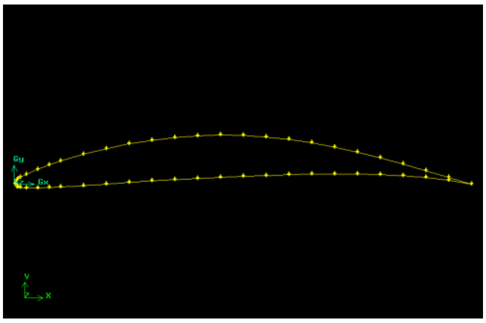

**Fig.(3):Axial compressor Blade by Points and Edges.**

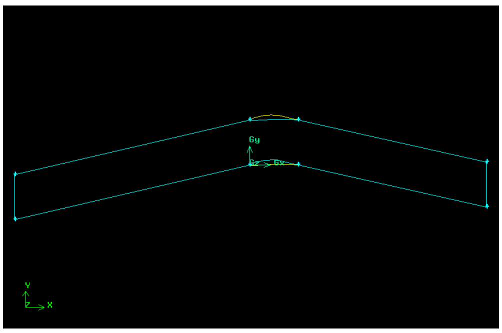

**Fig.(4):Axial Compressor Blade as a face.**

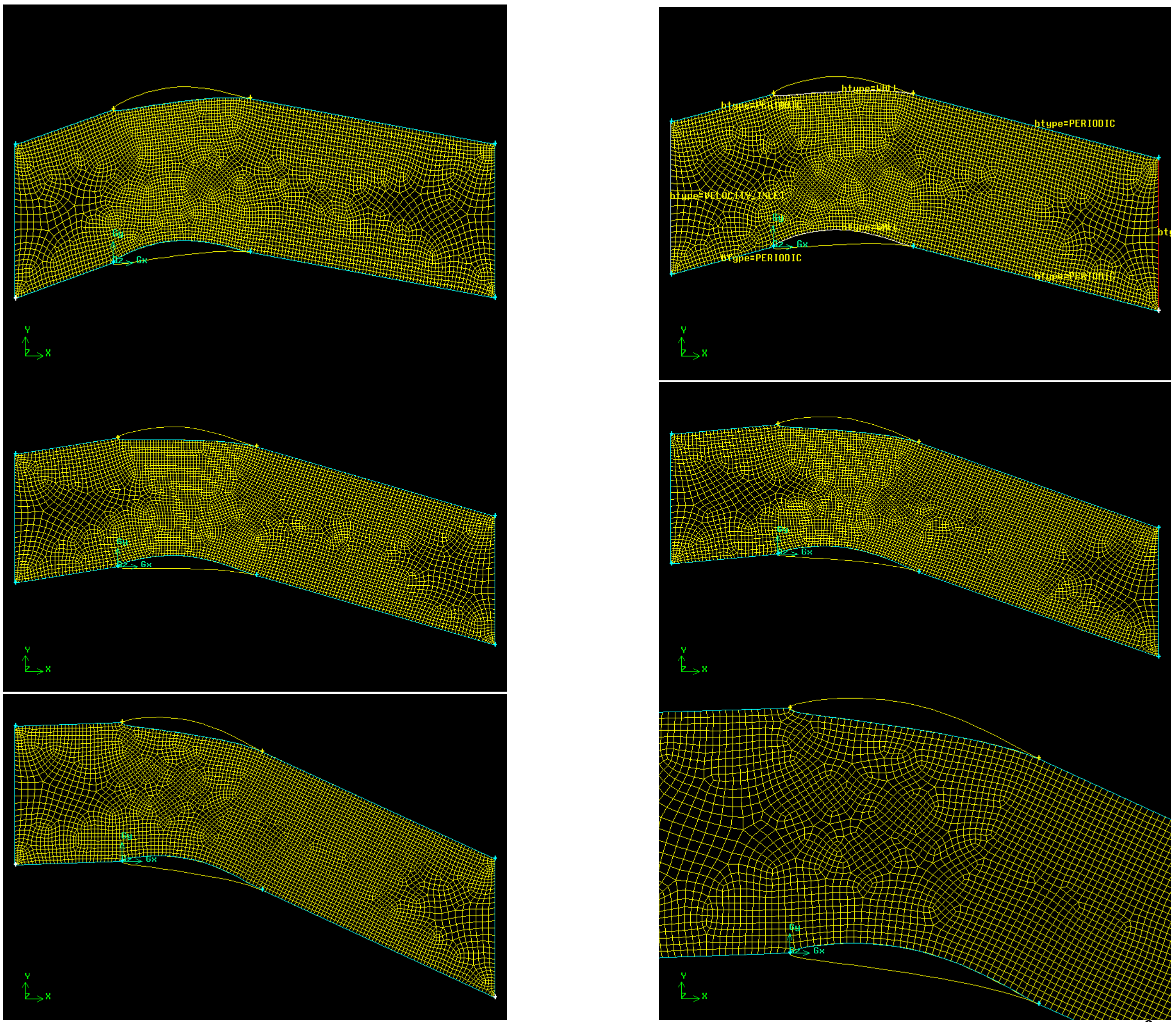

**Fig. (5): Grid (Mesh) generation of axial compressor vanes passage for (stagger angle =$4^0$,$0^0$,-$4^0$,-$8^0$ and -$12^0$).**

## EXPERIMENTAL WORK:

### Blade to Blade Configuration:

In the present work a cascade consists of two blades, each having a chord of (100mm) but one of these blades has a span of (90mm) and the other two blades have a span of (380mm) were made from wood fig.(6). The two blades of (380mm in span) are connected by suitable mechanism, as shown in fig.(7) in order to be fixed in wind tunnel protractor and achieved on required stagger angle. The two blates are fixed by aluminum plates, fig.(7).

**Fig.(6): Axial Compressor Blades NACA 65_ (12)10.**

**Fig.(7): Blade to Blade Configuration.**

## Apparatus:

### Subsonic Wind Tunnel:

Low- speed subsonic (Mach number=0.117) open type wind tunnel is used in this work of cross section of (305mm* 305mm). Wind speed of (35m/s) is achievable allowing experiments on many aspects of incompressible air flow and subsonic aerodynamics to be performed at satisfactory Reynolds number. Reynolds number is (Re=239605) based on inlet velocity and blade chord. The tunnel has a smooth contraction fitted with the protective screen. The test section is constructed of clear Perspex, to see the blade to blade configuration clearly with a square cross section of ($305mm \times 305mm$) and a length of (610mm). The blade to blade configuration was put inside the test section parallel to flow direction and connect by protractor to limit stagger angle. The control of the stagger angle of the blade to blade configuration was made by a suitable mechanism, fig.(9). The upper surface of the test section has a slot used to fix the pitot-static tube to measure the static pressure and total pressure. Fig.(8) is a photo of the wind tunnel and the working section. Downstream of the test section is a diffuser which leads to an axial flow fan driven by a (5.6kW three phase A.C motor). The flow is controlled by a butterfly valve before exhaust to atmosphere through exhaust section. The air enters the tunnel through a carefully shaped diffuser. The test section gives a full visibility of flow field.

**Fig.(8): Wind Tunnel Device (Open Circuit) and Multi-Tube Manometer.**

**Fig.(9): Protractor of Subsonic Low Speed Wind Tunnel.**

### Multi Tube Manometer:

A water multi tube manometer was used to measure total and static pressure between the two axial flow compressor blades, fig.(10). The manometer holes are connected to the Pitot - static tube by suitable connection pipes.

### Pitot – Static Tube:

The purpose of using pitot – static tube is to measure air static pressure, total pressure and then velocity inside test section. The external dimensions are (5mm) diameter, (200mm) arm length. Tube reading were corrected according to reference [Omran, K. J.,2003] as following:

$$\Delta p = p_d = p_t - p_s = \rho_{water} * g * \Delta H_{water} \qquad \text{(i).}$$

$$p_d = \frac{1}{2} * E * \rho_{air} * U^2{}_{\infty} \qquad \text{(j).}$$

$$\Delta p = \rho_{water} * g * \Delta H_{water} = \frac{1}{2} * E * \rho_{air} * U^2 \qquad \text{(k).}$$

$$E = E_0 + \omega + \Omega \qquad \text{(l).}$$

Where: E=Correction coefficient, $\omega$ =Viscosity coefficients, its value(0), $\Omega$ =Effect of distance from tube to wall which is found from fig.(11), $E_0$ =Effect of static pressure holes distance of (0.9976) value.

**Fig.(10): Multi Tube Manometer.**

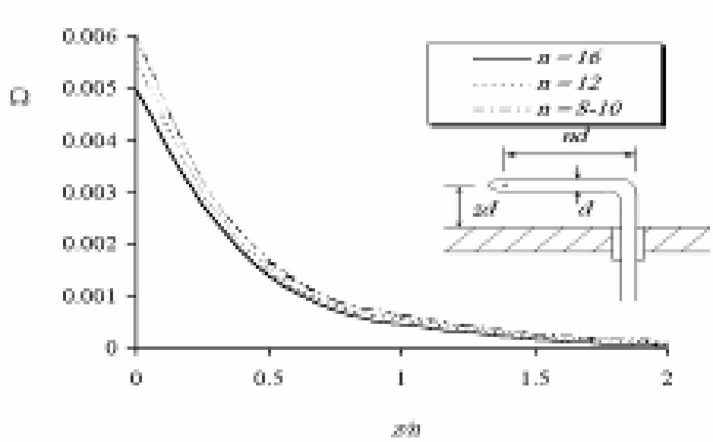


**Fig.(11): Correction of Pitot - static tube Distance. [Omran, K. J., 2003].**

**<u>Smoke Tunnel:</u>**

To illustrate a real view of flow development and separation, a smoke tunnel was used as shown in fig.(12). The air is drawn by a fan which is rotated by an electrical motor of variable velocity at the top of the tunnel. The air enters to the tunnel at the base. The test section has dimensions of (180mm) width, (240mm) height and (100mm) deep. The models installed in the back wall of the test section, the front wall of the test section are easy to remove. It is made of clear Perspex. Smoke generation is controlled at the bottom of the tunnel. The section has (23) holes from it smoke enter. The space between any two adjacent holes is (7mm). A high light source is put in the sides of the test section to see smoke clearly. The smoke generated by a smoke generator which evaporates kerosene in class evaporator carried on the front wall of the smoke generator. The smoke generated is dragged by the fan at the top of the tunnel through the test section. Flow Photo is taken using a digital Camera.

**Fig.(12): Smoke Tunnel.**

**Procedure of Experiments:**

The flow between two axial flow compressor blades was tested by wind tunnel as described in the following steps:

- Measure the atmospheric pressure and temperature before carrying out the experiments to calculate the air density accurately.
- Fix the blade to blade configuration in the test section with the required stagger angle.

- Prepare the multi tube manometer, controlling speed valve, and pitot static tube.
- Operating the wind tunnel for (15min) to reach steady state conditions.
- Reading the dynamic head by using pitot static-tube which is connected to multi tube manometer by suitable connection tubes.
- Repeating the previous procedure for other stagger angles ranges from( $4^0$ to $-12^0$ ).
- The experiments carried out in smoke tunnel were as following:
  - Fill the bottle with Kerosene to the required limit.
  - Put the model inside smoke tunnel test section and fixed at a certain angle indicated by protractor.
  - Turn on the smoke generator.
  - After about (3minutes) the smoke begins to formulate.
  - After smoke formulation the fan is turned on and controlled by the speed controller.
  - A high resolution digital camera was then used to photograph the models and flow.

## RESULTS AND DISCUSION:

### Experimental Results:

The experimental results are presented for three different curve lines located at (0.125,0.5 and 0.875) of (S) as shown in fig.(13). The operating and boundary conditions of the blades and flow passage are listed in table(1).

**Table (1): Operating and Boundary Conditions.**

| Case | Stagger Angle in (degree) | Inlet Velocity (m/s) | Number of grid points | Static Pressure Ratio |
|---|---|---|---|---|
| 1 | 4 | 35 | 63 | 1.08 |
| 2 | 0 | 35 | 63 | 1.12 |
| 3 | -4 | 35 | 63 | 1.1 |
| 4 | -8 | 35 | 63 | 1.07 |
| 5 | -12 | 35 | 63 | 1.04 |

The velocity and static pressure distribution (for the three sections) of flow between the two blades for stagger angle ($4^0$, $0^0$,$-4^0$, $-8^0$ and $-12^0$) are presented in fig.(14)and(15). These figures show that the flow is accelerated along section 1 (0.125S) up to a certain position,( refer to third column of table(2). Then the flow decelerates to the exit for stagger angles ($4^0$ and $0^0$) up to a certain position, see the fourth column of table (2) for stagger angles ($-4^0$, $-8^0$ and$-12^0$) where the flow is separated. The flow decelerates along section 3 (0.875S) from the inlet to the exit for all taken stagger angles. The velocity and static pressure remains constant along the section 2(0.5S) from the inlet to the exit for stagger angles ($-8^0$ and $-12^0$) and to a certain position for stagger angles ($4^0$, $0^0$ and $-4^0$), the fifth column of table (2). Then the flow decelerates to the exit. The pressure ratio is the exit static pressure from blade to blade passage divided by inlet static pressure. The pressure ratio for all cases is shown in table (2).

The reason behind such behavior is the effect of stagger angle. Within a certain range of stagger angles (from $4^0$ to $-4^0$) the flow remains in contact with the blade surface. As the stagger angle is increased, the blade profile forces the flow a way from its surface, hence, the flow starts to separate. Separation starts close to the trailing edge and progresses upwards as the stagger angle is changed (from $-4^0$ to $-12^0$). This effect is not clear in the middle section of the passage as the profile effects on flow behavior diminishes. The behavior of static pressure distribution is complimentary to the behavior of velocity. The flow separate from the suction side of the lower blade of cascade for stagger angle (from $-4^0$ to $-12^0$) because of adverse pressure gradient.

**Table (2): Experimental properties and behavior of flow between two blades in wind tunnel.**

| Case | Stagger angles in (degrees) | Location of maximum velocity and minimum static pressure along section 1 (%chord) | Location of separation point along section 1 (%chord) | Location of flow deceleration along section 2 (%chord) | Pressure ratio |
|---|---|---|---|---|---|
| 1 | 4 | 43 | - | 87.3 | 1.08 |
| 2 | 0 | 37.5 | - | 75 | 1.12 |
| 3 | -4 | 36 | 96 | 73 | 1.1 |
| 4 | -8 | 25 | 64 | - | 1.07 |
| 5 | -12 | 12 | 61 | - | 1.04 |

The total pressure distribution of flow between two axial compressor blades for different stagger angle is presented in figure (16) .This figure show that the fluid total pressure decreases as it passage from the inlet to the exit due to friction losses. The total pressure losses increases when the stagger angle increases (in clockwise direction) and the maximum total pressure losses occurs for stagger angle ($-12^0$) in separation region.

Figure (17) presents the pressure ratio distribution for stagger angles ($4^0$, $0^0$,$-4^0$, $-8^0$ and $-12^0$). The pressure ratio decreases when the stagger angle increases and separation zone increases, see table (2). By using curve fitting method for this polynomial distribution, the concluded mathematical relationship between this pressure ratio and stagger angle for NACA 65_(12)10 axial compressor cascade is:

$$\frac{p_{s_e}}{p_{s_i}} = 1.1057 - 0.0021\theta - 0.0007\theta^2 \qquad \text{(m).}$$

Where: θ: Stagger angle in (degrees). $\frac{p_{s_e}}{p_{s_i}}$ : Pressure ratio.

By equating equation (m) to one, the range of stagger angle for NACA 65_(12) 10 axial compressor blade aerofoil is (from $-18^0$ to $36^0$).

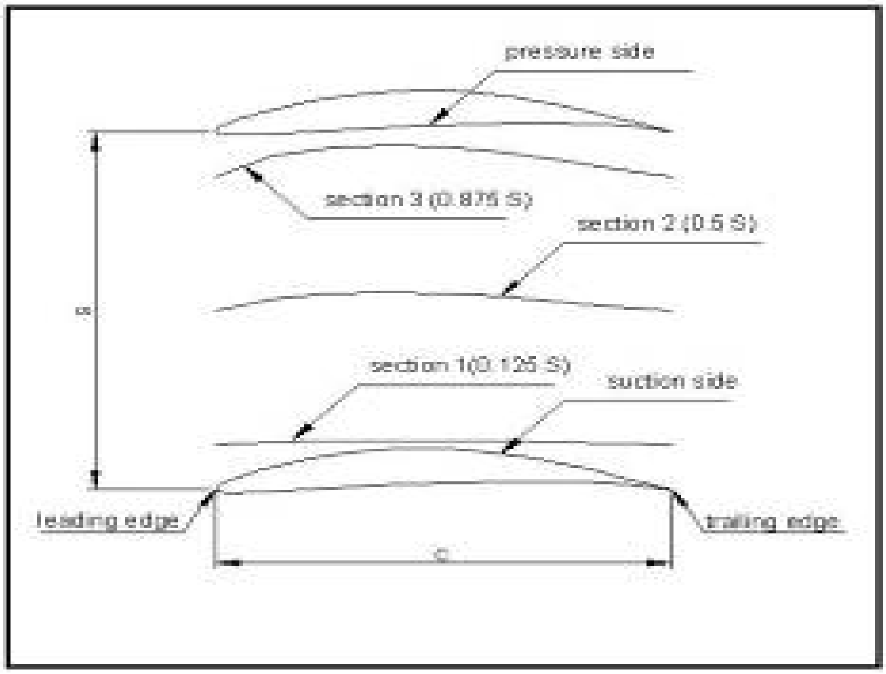


**Fig.(13): Blade to blade configuration with taken three sections in flow passage.**

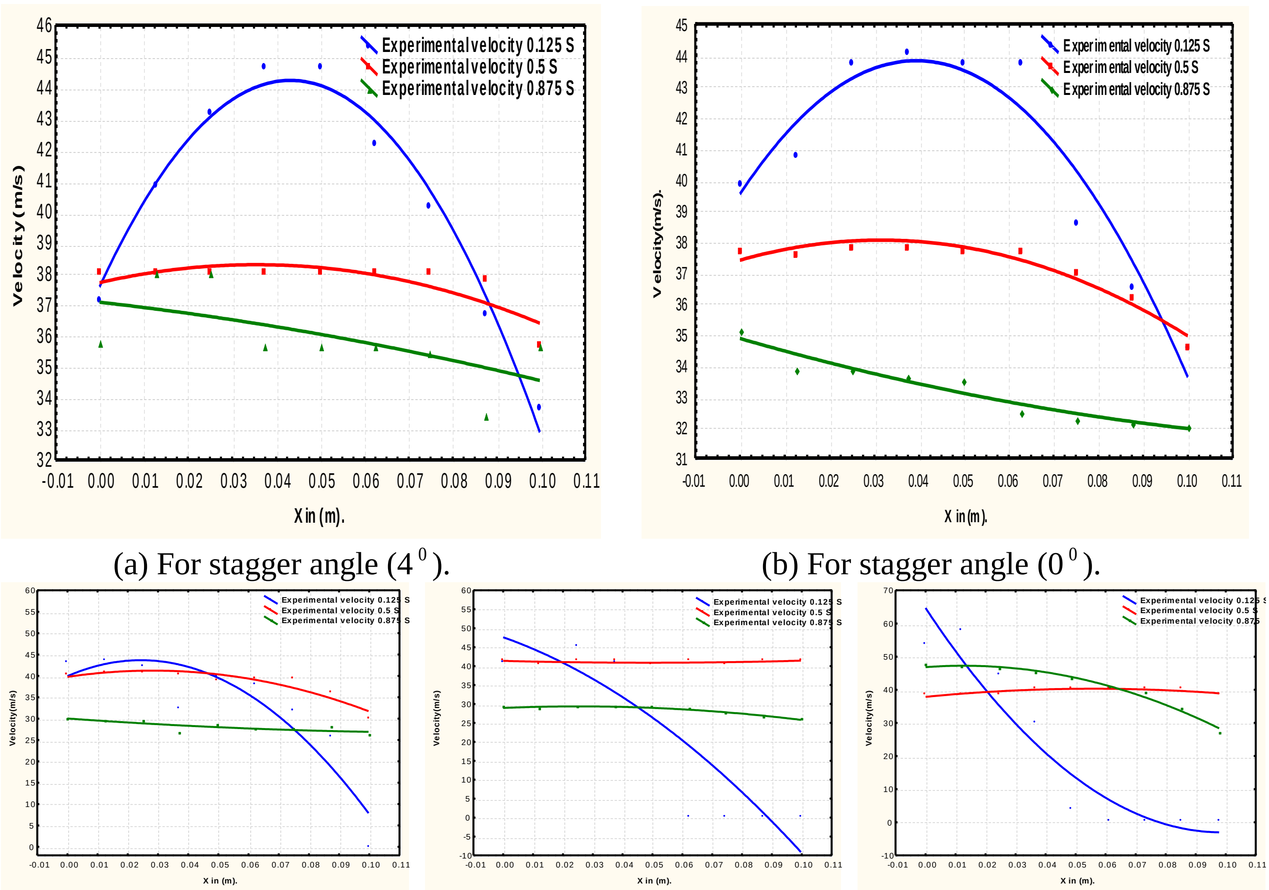


(a) For stagger angle ($4^0$). (b) For stagger angle ($0^0$).

(c) For stagger angle=-4. (d) For stagger angle=-8. (e) For stagger angle=-12.

**Fig.(14): Velocity distribution for (0.125S, 0.5S and 0.875S).**

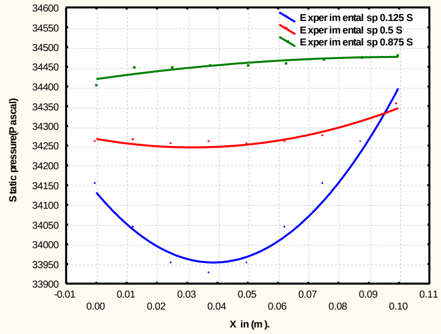


(a) For stagger angle=4.

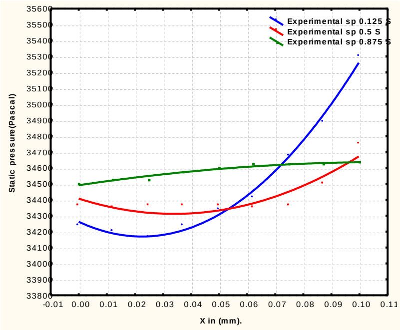


(b) For stagger angle=0.

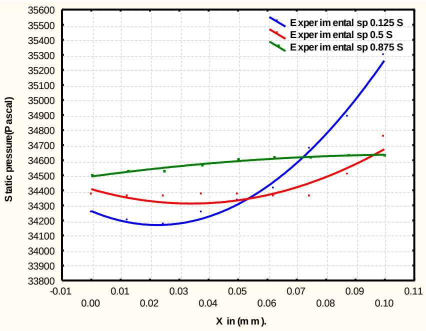


(c) For stagger angle=-4

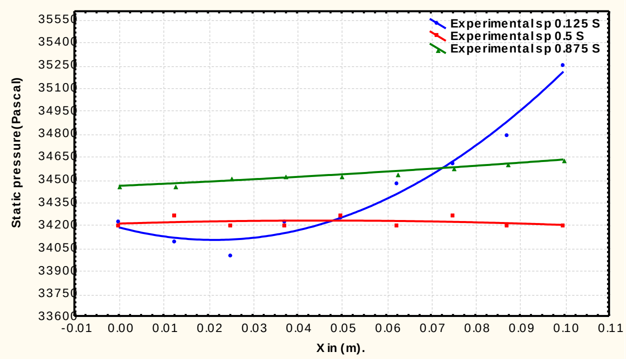


(d) For stagger angle=-8.

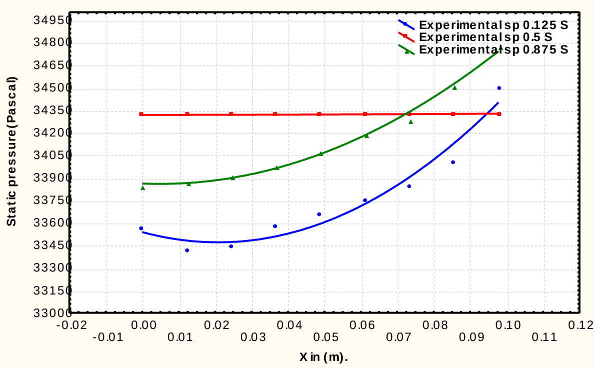


(e) For stagger angle=-12.

**Fig.(15): Static pressure distribution for (0.125S, 0.5S and 0.875S).**

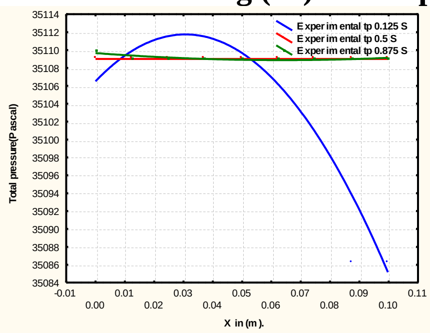


(a) For stagger angle=4.

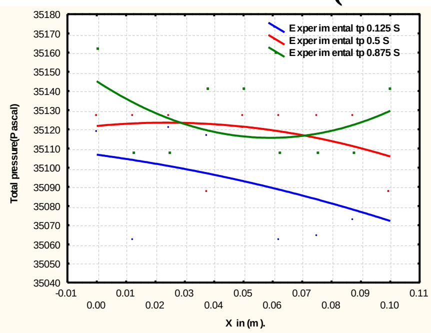


(b) For stagger angle=0.

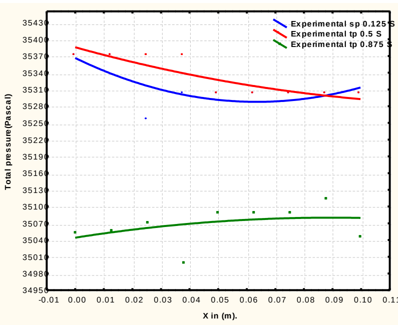


(c) For stagger angle=-4.

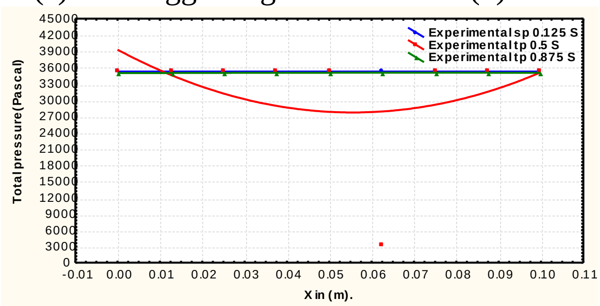


(d) For stagger angle=-8.

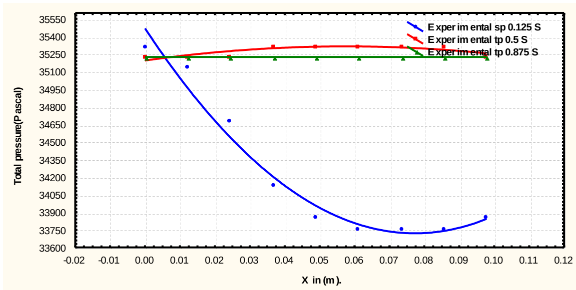


(e) For stagger angle=-12.

**Fig.(16): Total pressure distribution for (0.125S, 0.5S and 0.875S).**

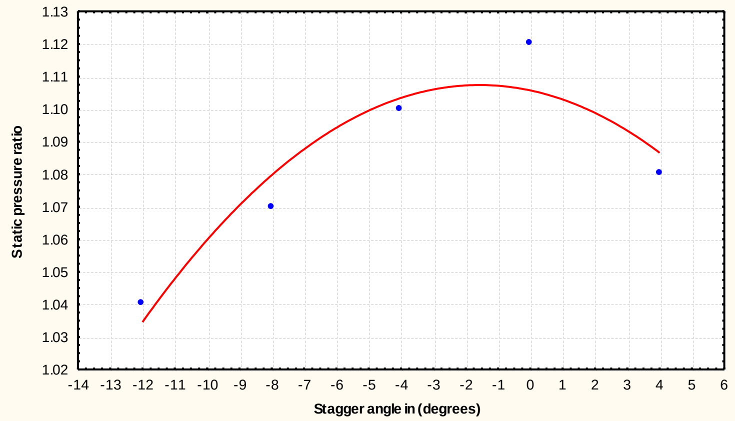


**Fig.(17): Correlation of pressure ratio with stagger angles.**

**Smoke Tunnel Results:**

To see the real view and stream lines of flow separation on blade surface, the blade tests in smoke tunnel for stagger angle ($4^0$,$0^0$,$-4^0$,$-8^0$ and $-12^0$) are shown in fig.(18). The flow separation begins from the upper surface in stagger angle ($-4^0$).As the stagger angle increases, separation propagates towards the leading edge.

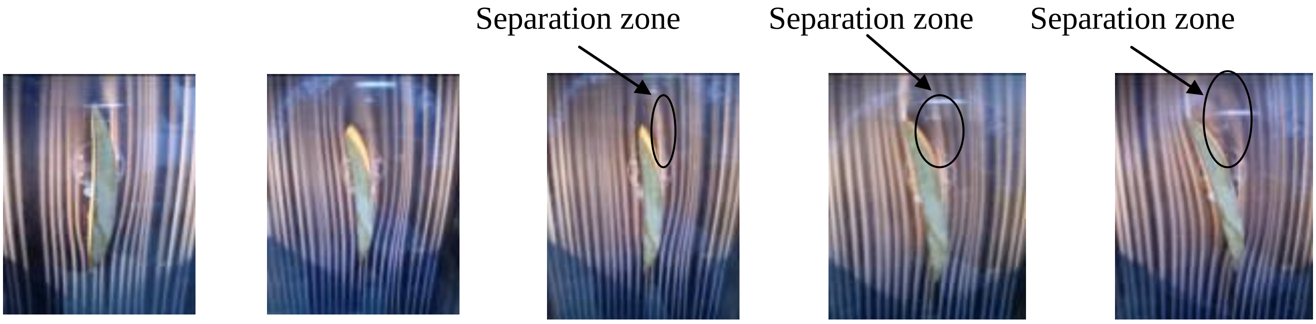


(A) (B) (C) (D) (E)

**Fig.(18): Stream line distribution on surface of axial compressor blade section NACA 65_(12)10: (A) Stagger angle =4. (B) Stagger angle =0. (C) Stagger angle =-4. (D) Stagger angle =-8. (E) Stagger angle =-12.**

## COMPUTATIONAL RESULTS:

The operating and boundary conditions for the flow passage between two axial compressor blades are listed in Table (3).

**Table (3): Operating and Boundary Conditions.**

| Case | Stagger Angle in (degree) | Inlet Velocity (m/s) | Number of grid points | Number of iterations to convergence | CPU time in (min). |
|---|---|---|---|---|---|
| 1 | 4 | 35 | 5473 | 8398 | 73 |
| 2 | 0 | 35 | 5573 | 7492 | 62 |
| 3 | -4 | 35 | 5528 | 8403 | 74 |
| 4 | -8 | 35 | 5440 | 8881 | 86 |
| 5 | -12 | 35 | 4888 | 1019 | 93 |

The velocity and static pressure contours of flow between two axial compressor blades for stagger angles ($4^0$, $0^0$,$-4^0$, $-8^0$ and $-12^0$) are presented in fig.(19) and (20). These figures show that the fluid flow being accelerated near and along suction side (upper surface of lower blade) up to a certain position, see the third column of tables (4). Then the flow decelerates to the exit for stagger angles ($4^0$ and $0^0$) and to a certain position for stagger angles ($-4^0$, $-8^0$ and $-12^0$), see the fourth column of table (4), where the flow separates from the blade surface. The flow decelerates near and along the pressure side (lower surface of upper blade) from the leading edge to the tailing edge along the chord line for all cases. The velocity and static pressure remains constant in the mid-space between the two blades from the inlet to the exit for stagger angles ($-8^0$ and $-12^0$) and to the certain position for stagger angles ($4^0$, $0^0$ and $-4^0$), see the fifth column of tables (4). Then the flow decelerates to the exit. The fluid flow being accelerated as it passes through the contracting flow area after that the flow being decelerated to the trailing edge. These phenomena prove that the suction side works as a nozzle-diffuser, the pressure side works as a diffuser and the blade to blade configuration works as a nozzle-diffuser.

**Table (4): Theoretical properties and behavior of flow between two blades in FLUENT.**

| No. | Stagger angles in (degrees) | Location of maximum velocity and minimum static pressure near and along the suction side (%chord) | Location of separation point near and along suction side (%chord) | Location of flow deceleration along mid-space between blades (0.5S)(%chord) |
|---|---|---|---|---|
| 1 | 4 | 45 | - | 84 |
| 2 | 0 | 36 | - | 81 |
| 3 | -4 | 35 | 98 | 74 |
| 4 | -8 | 22 | 65 | - |
| 5 | -12 | 12 | 63 | - |

The total pressure contours of flow between the two blades for stagger angle ($4^0$, $0^0$, $-4^0$, $-8^0$ and $-12^0$) are presented in fig.(21) .This figure shows that the total pressure decreases as it passes from the inlet to the exit due to friction losses. The total pressure losses increases when the stagger angle increases (in clockwise direction) and the maximum total pressure losses occurs when stagger angle ($-12^0$) in separation region due to increased friction losses and adverse pressure gradient.

The flow separation affects the performance of a cascade and hence, affects the compressor performance where the pressure ratio decreases when the separation zone increases.

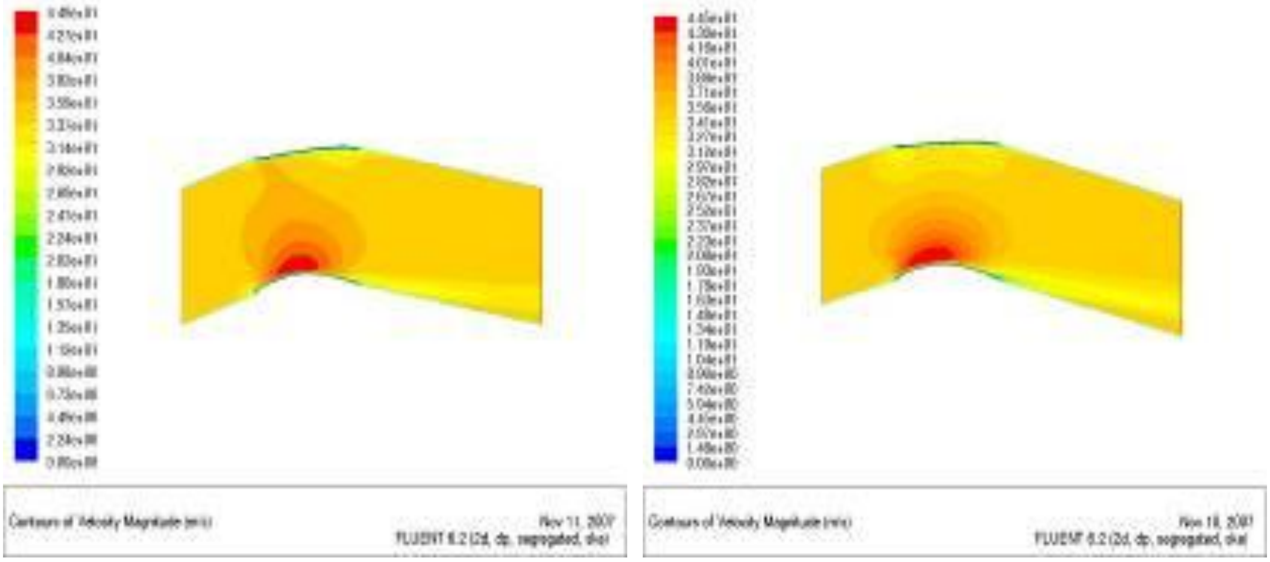


(a) (b)

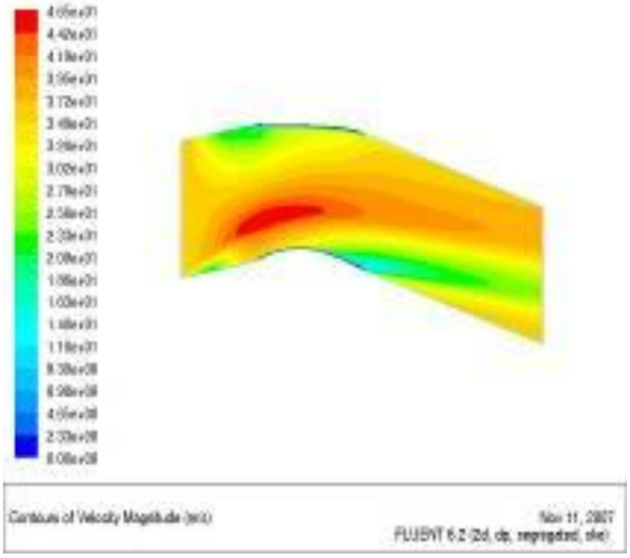


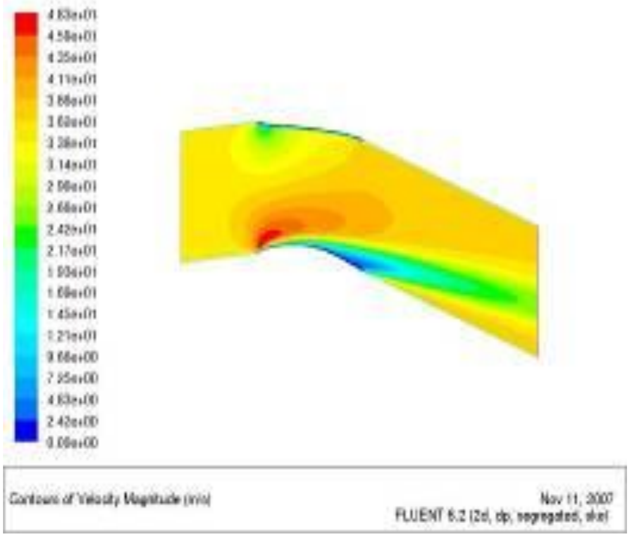


(c)

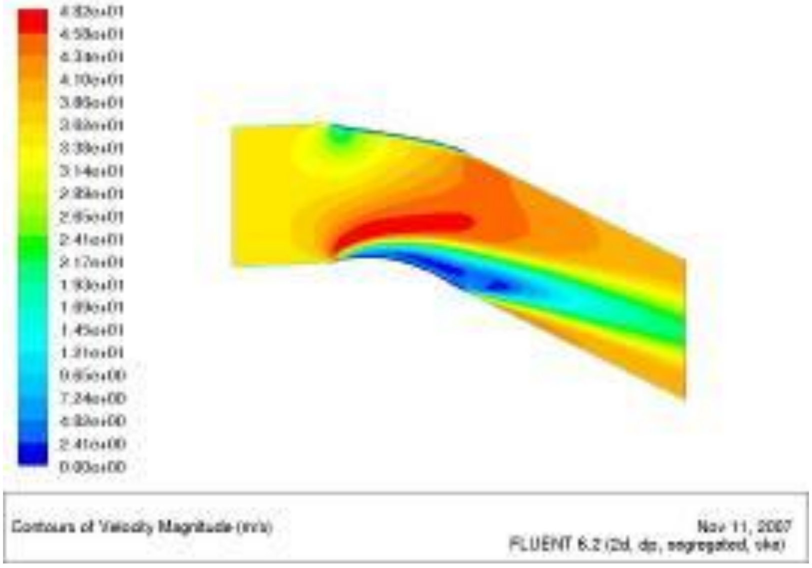


(e)

**Fig.(19):Contours of velocity:(a) Stagger angle=4$^0$. (b) Stagger angle=0$^0$. (c) Stagger angle=-4$^0$. (d) Stagger angle=-8$^0$. (e) Stagger angle=-12$^0$.**

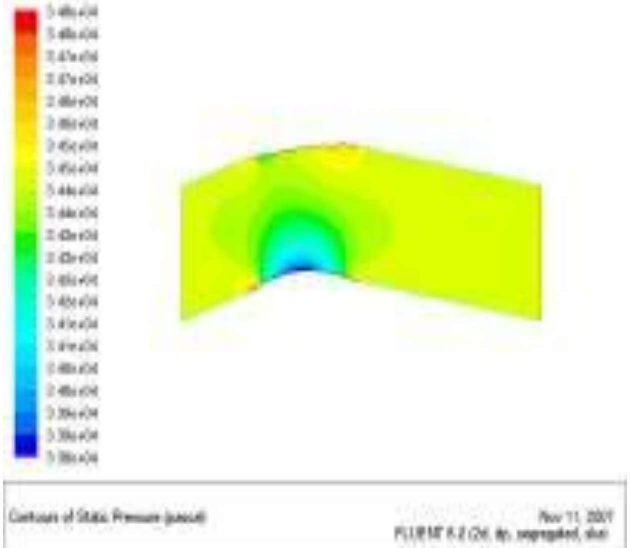


(a)

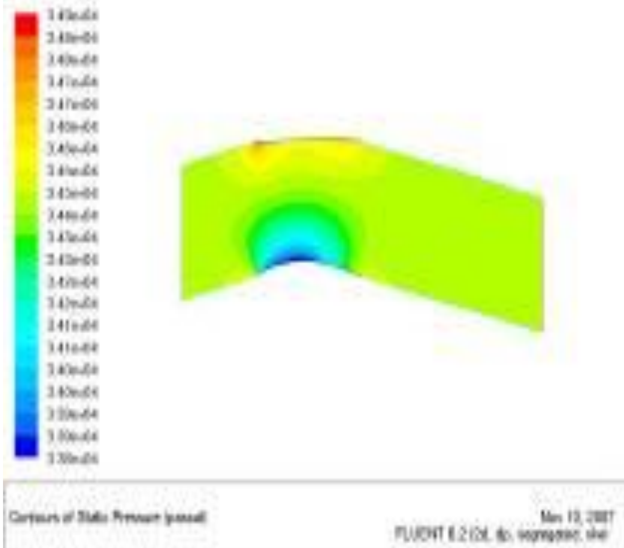


(b)

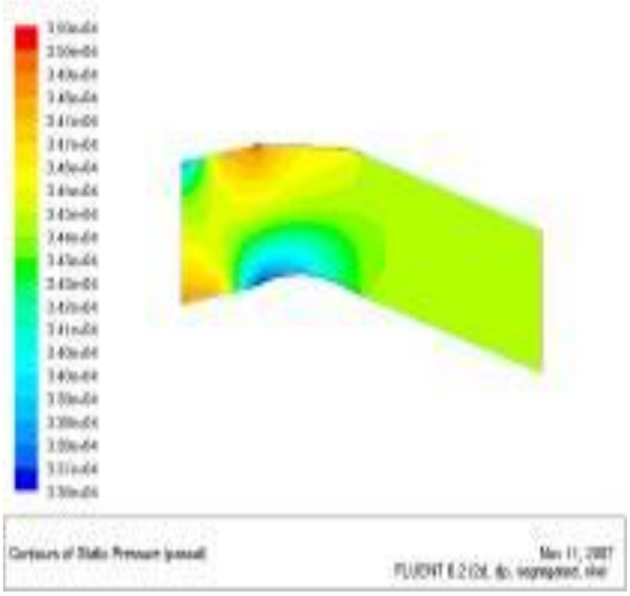


(c)

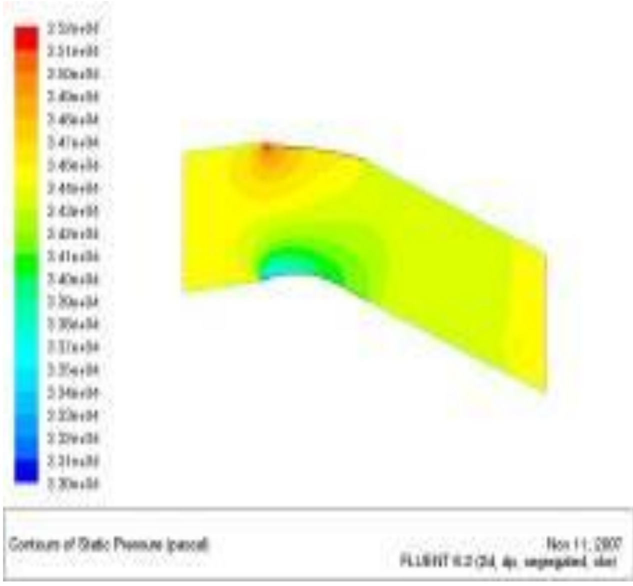


(d)

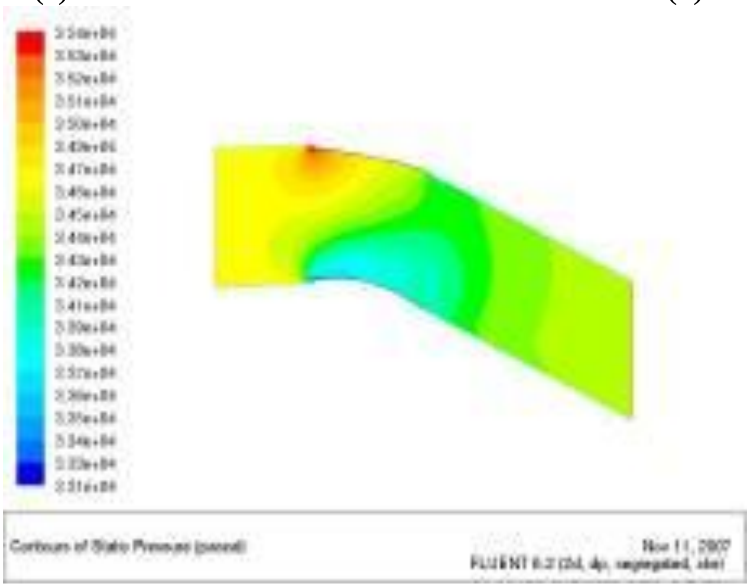


(e)

**Fig.(20): Contours of static pressure: (a) Stagger angle=4$^0$. (b) Stagger angle=0$^0$. (c) Stagger angle=-4$^0$. (d) Stagger angle=-8$^0$. (e) Stagger angle=-12$^0$.**

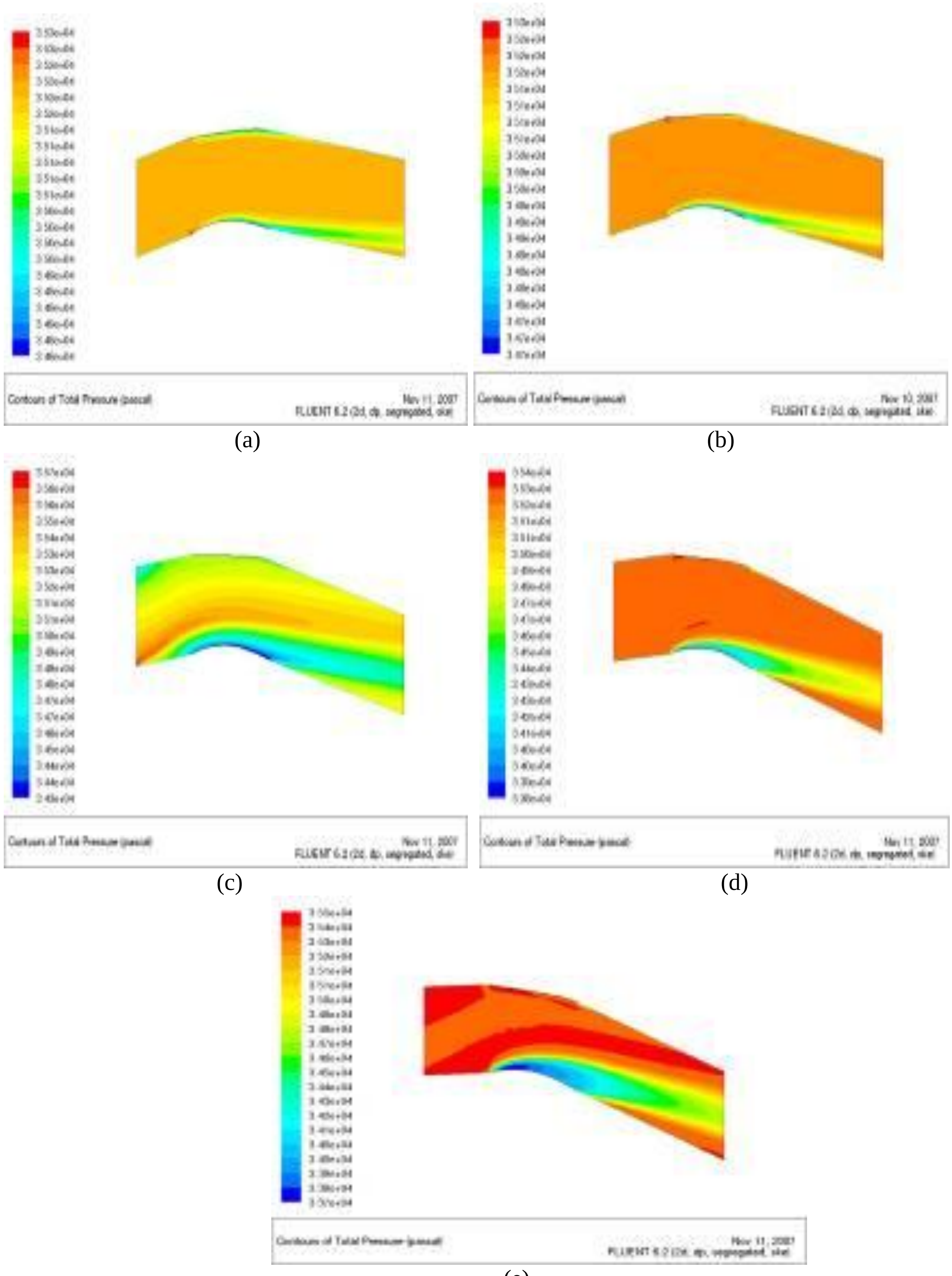


**Fig.(21): Contours of total pressure: (a) For stagger angle=4$^0$. (b) For stagger angle=0$^0$. (c) For stagger angle=-4$^0$. (d) For stagger angle=-8$^0$. (e) For stagger angle=-12$^0$.**

**ACCURACY OF SOLUTION:**

The FLUENT (V6.2) code is considered as a high accuracy computational fluid dynamics software package. Fig.(22) presents the distribution of residual and number of iterations for continuity, momentum and k-ε model equations and for stagger angle ($0^0$ and $-8^0$). As the stagger angle increases, the number of iterations to convergence increases because the problem gets complicated when the flow separation occurs, see table (3).

**THE COMPARISON BETWEEN THE EXPERIMENTAL AND THEORICAL RESULTS:**

The theoretical results obtained in this study by using FLUENT (V6.2) were compared with those obtained experimentally using the wind tunnel. Fig.(23) shows this comparison for the velocity in the three locations of interest for stagger angle ($0^0$).This figure shows good agreement between the theoretical and experimental results, where the flow behavior similar between these results and the range of different velocity between these results is(1-3)m/s.

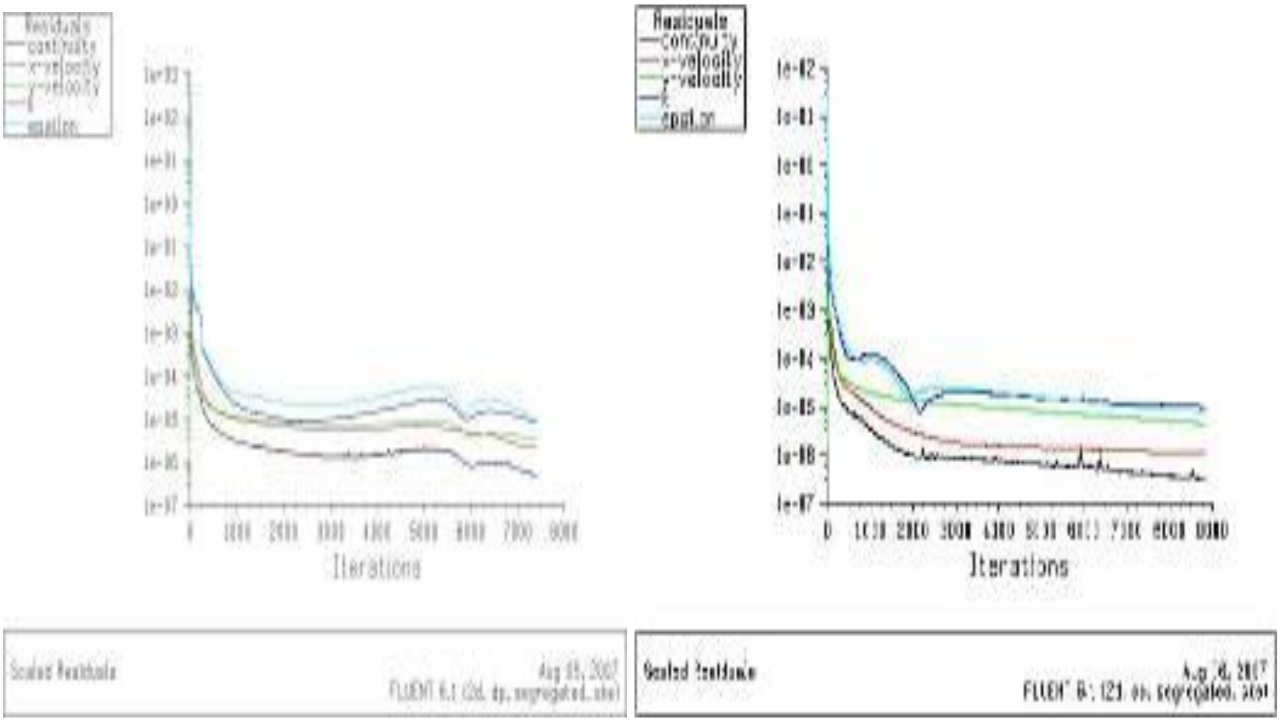


**(a)** For stagger angle=0. **(D)** For stagger angle=-8.

**Fig.(22): Distribution of number of Iterations to convergence and Residuals for stagger angle ($4^0$ and $-8^0$)**

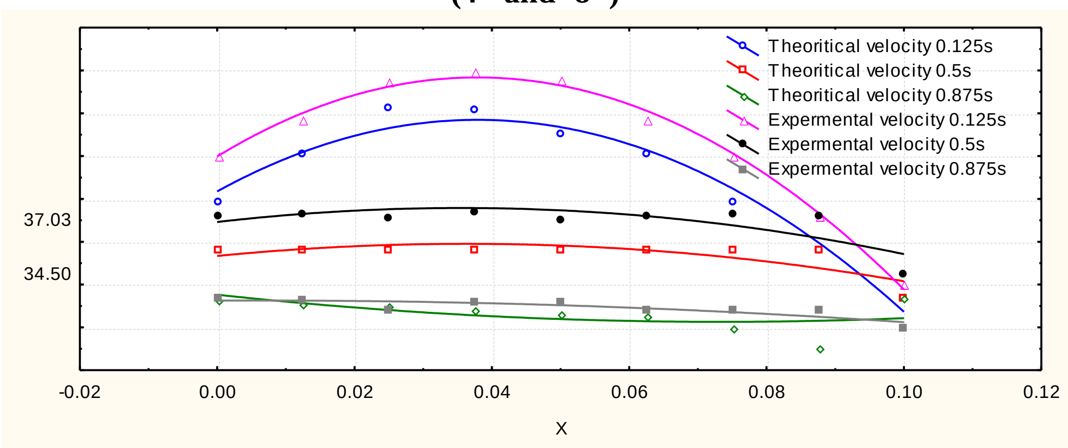


**Fig.(23): The comparison of velocity distribution between the experimental results and the theoretical results.**

**CONCLUSIONS:**

- The area between two axial compressor blades for NACA 65_ (12)10 works as a nozzle-diffuser.
- Smoke tunnel was successfully used to show separation of flow from upper blade surface.
- The flow separation was seen to start at a stagger angle of ($-4^0$) experimentally and theoretically.
- The mathematical relationship between the static pressure ratio and stagger angle for NACA 65_ (12)10 axial compressor cascade is concluded by using curve fitting method for polynomial distribution.

$$\frac{p_{s_e}}{p_{s_i}}=1.1057-0.0021\theta-0.0007\theta^2 \qquad (n).$$

The range of stagger angle for NACA 65_ (12) 10 axial compressor blade aerofoil is calculated from this relationship. It was found in the range ($-18^0$ to $36^0$).

Total pressure was seen to reduce through the blade passage. It drops sharply for the separation zone.

FLUENT (V6.2) was used successfully to predict separation as compared to the experimental measurements in the wind tunnel and as compared with other works.

**NOMENCLATURE**

**English Symbols**

| Symbol | Description | Units |
|---|---|---|
| C | Blade chord line. | m |
| $C_1, C_2$ | Constants in turbulence model. | m |
| d, nd, zd | Dimension of pitot static tube. | m |
| E | Correction coefficient. | |
| $E_0$ | Effect of static pressure holes distance. | - |
| $G_k$ | Production term of kinetic energy. | kJ |
| g | Acceleration of gravity. | $m/s^2$ |
| K | Kinetic energy of turbulence. | $m^2/s^2$ |
| P | Pressure. | Pascal |
| n | Local coordinate normal to the wall. | m |
| Re | Reynolds number. | - |
| S | Space between two blades. | mm |
| x, y | Coordinates in X and Y- directions. | m |
| U | Velocity of air. | m/s |
| u, v, w | Velocity components in x, y and z directions | m/s |

**Greek Symbol**

| Symbol | Description | Units |
|---|---|---|
| $\alpha$ | Flow angle. | degree |
| $\beta$ | Blade angle. | degree |
| $\varepsilon$ | Dissipation rate of turbulent kinetic energy. | $m^2/s^2$ |
| $\mu$ | Laminar viscosity. | kg/m.s |
| $\mu_e$ | Effective viscosity. | kg/m.s |
| $\mu_t$ | Turbulence viscosity. | kg/m.s |

| | | |
|---|---|---|
| $\upsilon$ | Kinematic viscosity. | $m^2/s$ |
| $\omega$ | Viscosity coefficients value. | - |
| $\theta$ | Stagger angle. | degree |
| $\rho$ | Density. | $kg/m^3$ |
| $\sigma_k, \sigma_\varepsilon$ | Effective prandtl numbers. | - |
| $\Omega$ | Distance action from tube to wall. | - |
| $H\Delta$ | Tube head in manometer. | o $_2$ cmH |
| $P\Delta$ | Change in pressure. | Pascal |

**Superscripts**

| Symbol | Description |
|---|---|
| ' | Fluctuating quantity. |

**Subscripts**

| Symbol | Description |
|---|---|
| air | Air. |
| d | Dynamic. |
| s | Static. |
| $s_e$ | Static exit. |
| $s_i$ | Static inlet. |
| t | Total. |
| water | Water. |
| 1 | Inlet conditions. |
| 2 | Outlet conditions. |

**Abbreviations**

| Symbol | Description |
|---|---|
| A.C motor | Alternating Current Motor. |
| CFD | Computational Fluid Dynamics. |
| Fig. | Figure. |
| NACA | National Advisory Committee for Aeronautics. |
| NASA | National Aeronautics and Space Administration. |
| SIMPLE | Simi – implicit method for pressure linked equations. |
| SIMPLEST | SIMPLE – Specially Treated (Newly developed). |

## REFERENCES


- Chittiappa Muthanna, "Flow field Downstream of a Compressor Cascade with Tip Leakage", Ph.D. thesis, Virginia Polytechnic Institute and State University, Aerospace Engineering Department, November, 1998.

- Hill, P. G., and Peterson, C. R., "Mechanics and thermodynamics of propulsion", Addison-Wesley publishing Company, Inc. 1965.

- Jones, W. P. and Launder, B. E., "The Predication of Laminariztion With a Two-Equation Model of Turbulence", Journal of Heat and Mass Transfer, Vol.15, pp.301-314, 1972.

- Meinhard T. Schobeiri, Burak Öztürk and David E. Ashpis, "On the Physics of Flow Separation A long a Low Pressure Turbine Blade Under Unsteady Flow Conditions", Texas A&M University, Turbomachinery Performance and Flow Research Laboratory, College Station, Texas 77843, Available from: NASA Center for Aerospace Information 7121 Standard Drive Hanover, MD 21076, http://gltrs.grc.nasa.gov and National Technical Information Service 5285 Port Royal Road Springfield, VA 22100,June, 2003.

- Moult, A., and Srivatsa, S. K.,”CORA-2 A computer program Code for Axi-Symmetrical Combustion chambers”, CHAM Computer Code 201, 1977.

- Omran, K. J., "An Experimental Study of Backward Facing Step's Effect on The Aerodynamic Characteristics of Airfoil at Low Flight Speeds", M.Sc. Thesis, Aeronautical Specialization, Department of Machines and equipments, University of Technology, 2003

- You D. AND Moin, P., "Large-eddy simulation of flow separation over an airfoil with synthetic jet control", Center for Turbulence Research, Annual Research Briefs, 2006.

# MATHEMATICAL MODEL TO INVESTIGATE THE TEMPERATURE AND HARDNESS DISTRIBUTIONS DURING THE ANNEALING AND NORMALIZING TREATMENT

B. Shaheen. Bachy
Mechanical Department, College Of Engineering, Baghdad University

**ABSTRACT**

**A**nnealing and normalizing treatment are one of the most important heat treatment for the steel and its alloys. In the present work a mathematical model has been used to simulate this process, this model taken in account the variation in the physical material properties and heat transfer coefficient for the surface of metal. A numerical scheme based on control finite volume method has been used. A computer program with C++ language was constricted to found the final solution of the numerical equations.

The model was used to estimate the temperatures distribution and the hardness value at each point of the workpiece. Good agreement has been obtained when compared the result of the present model with other experimental published data.

**KEYWORD**: annealing and normalizing heat treatment, mathematical model, hardness predications

**الخلاصة**:

التخمير والتطبيع يعدا من المعاملات الحرارية المهمة للفولاذ وسبائكه، في هذا البحث تم اقتراح انموذج رياضي لوصف عملية الانتقال الحراري الذي يحدث خلال هذه المعاملات، هذا الانموذج المقترح ياخذ بنظر الاعتبار التغير في الخواص الفيزيائية للمعدن مع تغير درجات الحرارة خلال المعاملات الحرارية وكذلك التغير في معامل الانتقال الحراري لسطح المعدن. تم استخدام طريقة عددية لايجاد الحلول لهذا الانموذج وكذلك تم بناء برنامج حاسوب بالاستعانة بلغة البرمجة سي ++ لايجاد الحلول النهائية للمعادلات الخاصة بالانموذج.

استخدم هذا الانموذج لمعرفة توزيع درجات الحرارة على طول مساحة مقطع القطع المعاملة حرارية وكذلك حساب مقدار الصلادة في كل نقطة من المعدن للقطعة ، ايضا استخدم الانموذج لدراسة تاثير مساحة المقطع في هذه المعاملات الحرارية. تم الحصول على تطابق جيد عند المقارنة بين نتائج الانموذج مع نتائج عملية سابقة منشورة.

## INTRODUCTION

It is well known that the heat treatment process of the steel is very old process technology of materials. In this process we can improve the mechanical properties of the steel. It's involved a cycle of heating and cooling process in all heat treatment types. The mean difference between the types of this process is the cooling rate, for example high cooling rate used in quenching treatment while very slow in annealing treatment. During the heat treatment process there are coupled phenomena, such as thermal-mechanical coupled effect, temperature-microstructure coupled effect. So that it's very important to study the temperature distributions in this process from this distribution we can expect the phase transformation and the microstructure as well as the thermal stress which is may occur in the workpiece during the heat treatment process.

In the recent years, the mathematical modeling of heat treatment process has been used in the world to reduce the offers in this process and to make the effective parameters for this process under the control.

[B.Shaheen.B.2010] developed a mathematical model to simulate the quenching treatment of viruses steel types. In this work a computer program was constricted to evaluate the temperatures distribution and to study the important parameters in the quenching treatment of steel with different quenching media and workpiece dimension.

[B.Smoljam etal 2006] a numerical simulation the quenching process have been carried out in this work, the relationship between the time from 800 $^{o}$C to 500 $^{o}$C and the distance from quenching end of Jumine- specimant have been studies to estimate the hardness distribution depending on the cooling rate or cooling curve for the workpiece.

[B.Smoljam etal 2009] a heat transfer model was used in this work to simulate the quenching treatment. The hardness distribution have been estimated based on the relationship between the cooling time from 800 to 500 and the Jumine- specimant.

[Haji Badrul etal 2009] in this work a heat transfer simulation to the quenching treatment using finite element software ANSYS workbench have been carried out to investigate the temperatures distribution. The hardness distribution have been predicated by using method based on the relationship between the Juminy distance versus cooling time to 500 $^{o}$C and hardness versus Jominy distance.

A further work was carried out by [B. Liscic etal ] to simulate the heat treatment process (quenching treatment). The temperatures distribution have been investigated, the hardness distribution also investigated by method based on the relationship Continuous-Cooling-Transformation (CCT) diagram of steel and the phase structure versus hardness diagram depending on the time to 500 $^{o}$C .

In the present work a mathematical heat transfer model based on a computer program with C++ language have been carried out to simulate two kinds of the most important heat treatment process which is annealing and normalizing treatments. This work taken in account the variations in the physical properties for the workpiece metal which is occur during the treatment (increasing in the temperature of the workpiece) as well as the relationship between surface temperature and the heat transfer coefficient of the workpiece during the treatment.

## MATHEMATICAL MODEL

The heat conduction equation in the middle of workpiece taken as in equation (1)

$$\frac{\partial}{\partial x}\left(K\frac{\partial T}{\partial x}\right)+\frac{\partial}{\partial y}\left(K\frac{\partial T}{\partial y}\right)=\rho C_p\frac{\partial T}{\partial t} \qquad (1)$$

Where **k** is the thermal conductivity and $\mathbf{C_p}$ the specific heat and **ρ** the density of the metal workpiece. From above model we can see that the temperature variation is with time and the coordinate x and y, also we assume that the maximum variation in workpiece temperature is taking place across the cross sectional area (X-Y) plane [B.Shaheen.B.2010] . The all thermal material properties i.e. thermal conductivity, specific heat, density are temperature dependent [ASM Handbook, Volume 1, 2005]

By using numerical scheme based on control volume method the nonlinear heat conduction equation eq. (1) will be discreted and we will obtain

$$a_p T_p = a_E T_E + a_W T_W + a_N T_N + a_S T_S + a_P^o T_P^o$$

Where

$$a_E = \frac{k_e \, \Delta y}{(\delta_x)_e} \qquad a_W = \frac{k_w \, \Delta y}{(\delta_x)_w} \qquad a_N = \frac{k_n \, \Delta x}{(\delta_y)_n} \qquad a_S = \frac{k_s \, \Delta x}{(\delta_y)_s}$$

$$a_{p^o} = \frac{\rho c_p \Delta x \Delta y}{\Delta t} \qquad a_p = a_E + a_W + a_N + a_S + a_{p^o}$$

**Boundary Conditions**

We can describe the boundary conditions in the present work a follows (see figure 1)

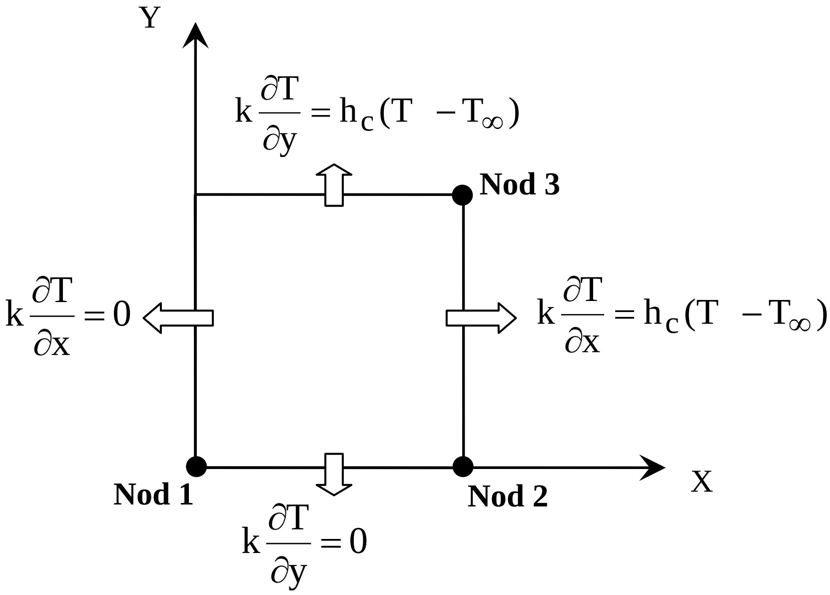


**Figure (1). Geometry and the boundary conditions.**

Where $h_c$ The value of heat transfer coefficient and T is the surface temperature of the workpiece and T∞ is the cooling media temperature where this value in case of annealing treatment equal to the temperature of furnace and in case of normalizing treatment equal to air temperature.

The value of heat transfer coefficient ($h_c$) is taken as temperatures dependent. Table (1) shows these values for the two cases annealing and normalizing treatment [Brandon Elliott B. and Christoph Beckerman 2007].

**Table (1) The heat transfer coefficient for the annealing and normalizing treatment**

| T °C | 30 | 100 | 200 | 300 | 400 | 500 | 600 | 700 | 800 | 900 | 1000 |
|---|---|---|---|---|---|---|---|---|---|---|---|
| $h_c$ (w/m$^2$.C) Annealing | 500 | 550 | 850 | 900 | 1054 | 1210 | 1300 | 1540 | 1650 | 1800 | 2000 |
| $h_c$ (w/m$^2$.C) Normalizing | 500 | 500 | 600 | 650 | 700 | 725 | 800 | 850 | 950 | 980 | 1000 |

In the previous section we described the mathematical model and the numerical data needed, after this step we will used numerical scheme based on control volume method and iterative method known as (TDMA) also used to solve the system of equations which is consist of the boundaries equations and the medal equation finally computer program was constructed in this work based on C++ language to found the final solution for the proposed model and the out put of this program used in others computers program to show the results of the program.

## HARDNESS VERIFICATION

It's very important to verify the result of the present model, so that a comparison between the values of hardness calculated in the present work and experimental published data [B.Smoljam etal 2006] [B.Smoljam etal 2009] as show in table (2) below:

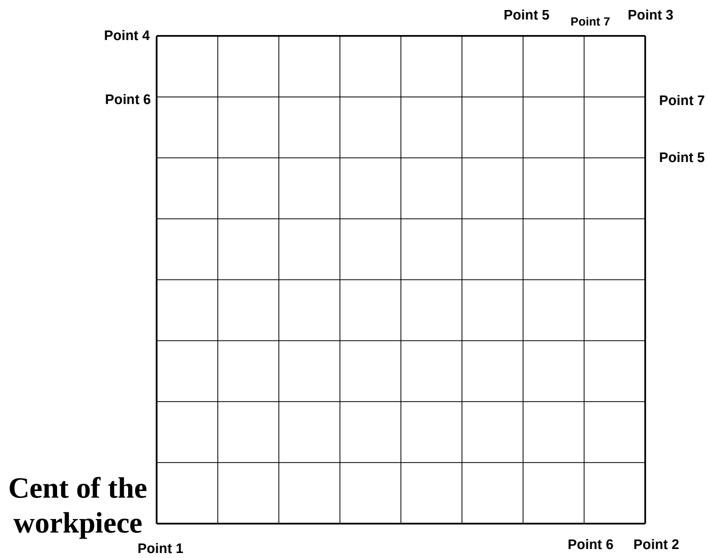


**Figure (2) the nod points as described in the table (2).**

**Table (2) a comparison between the hardness calculated in the present work and [B.Smoljam etal 2006] [B.Smoljam etal 2009]**

| Point Node No | Point 1 | Point 2 | Point 3 | Point 4 | Point 5 | Point 6 | Point 7 |
|---|---|---|---|---|---|---|---|
| **Present work** | **290** | **330** | **324** | **330** | **350** | **310** | **340** |
| **[B.Smoljam etal 2006] [B.Smoljam etal 2009]** | **311** | **349** | **340** | **349** | **368** | **324** | **379** |

A further comparison has been made with [B.Smoljam etal 2009] to the point node no 2 which is equal to point 4 as show in table (3) below:

**Table (3) a comparison between the hardness calculated in the present work and [B.Smoljam etal 2009]**

| | % F | % P | % B | % M | H. No |
|---|---|---|---|---|---|
| **Present work** | **5.2** | **8.5** | **73.8** | **12.5** | **330** |
| **[B.Smoljam etal 2009]** | **% F+ P** | | **42-74** | **5-36** | **290-349** |
| | **0-12** | | | | |

## RESULTS AND DISCUSSIONS

Different cases have been study in this work by the proposed model, figure (3) below shows a flow chart for these cases.

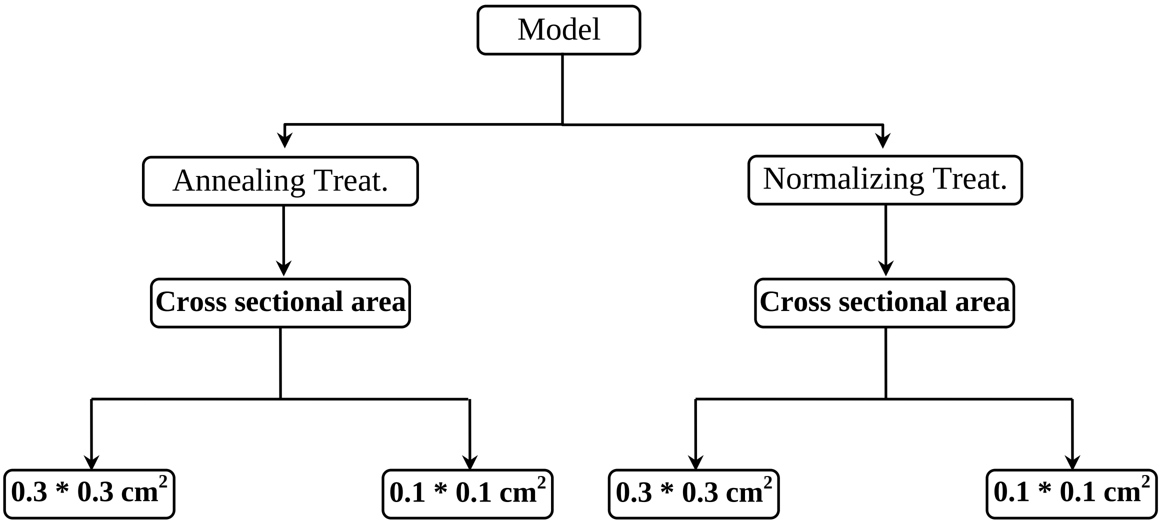


**Figure(3). Case study by the proposed model in the present work for the steel type DIN 41Cr4.**

The above cases were study to the steel **DIN 41Cr4** which have the chemical composition shown in table (4) [ASM Handbook, Volume 1, 2005]

**Table (4) Chemical Composition to the Steel DIN 41Cr4**

| **Chemical Composition** | C | Si | Mn | P | S | Cr | Cu | Mo | Ni | V |
|---|---|---|---|---|---|---|---|---|---|---|
| | 0.44 | 0.22 | 0.80 | 0.030 | 0.023 | 1.04 | 0.17 | 0.04 | 0.26 | <0.01 |

Figure (4) A, B shows the temperatures variation with time for the three points (points nod 1, points nod 2 and points nod3 see figure (1)) for the two cases which is annealing and normalizing treatment and when the cross sectional area is **(30 * 30) cm$^2$ , (10 * 10) cm$^2$ .**

In case of the annealing treatment fig (4)-A, we can see that the difference in temperatures between the described points is not high especially when the cross sectional area is **(10 * 10) cm$^2$**. The difference will increase with cross sectional area increasing. In general there is no high temperatures difference between the two cases of cross sectional area in the annealing treatment.

But these behavior is different in the normalizing treatment see figure(4)-B, where this figure shows that the temperatures difference between these points is increasing especially in case of (**30 * 30) cm$^2$** cross sectional area

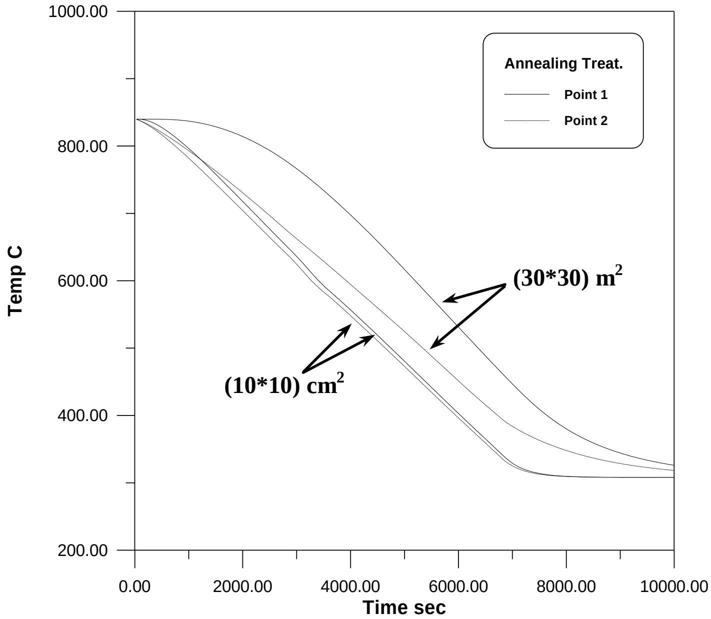


**A-Annealing Treatment**

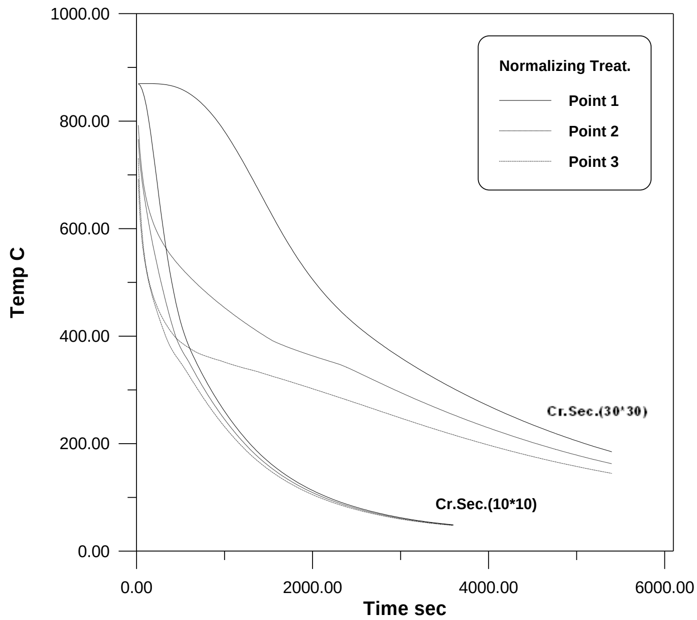


**A- Normalizing treatment**

**Figure (4) Temperatures variations vs. time for at two cross sectional area with two cases, A-Annealing treatment** and **B- Normalizing treatment.**

Figure (5) A, B shows a comparison between the annealing and normalizing treatment for three points in the workpiece and when the cross sectional area are (**10*10) cm$^2$** and (**30*30) cm$^2$**. It's very important to note that the thermal gradient in the normalizing treatment is more than in the annealing treatment, actually its come from the value of heat transfer coefficient and the environment temperature or the cooling media temperature which is different in the two treatment process (annealing and normalizing) as we described before.

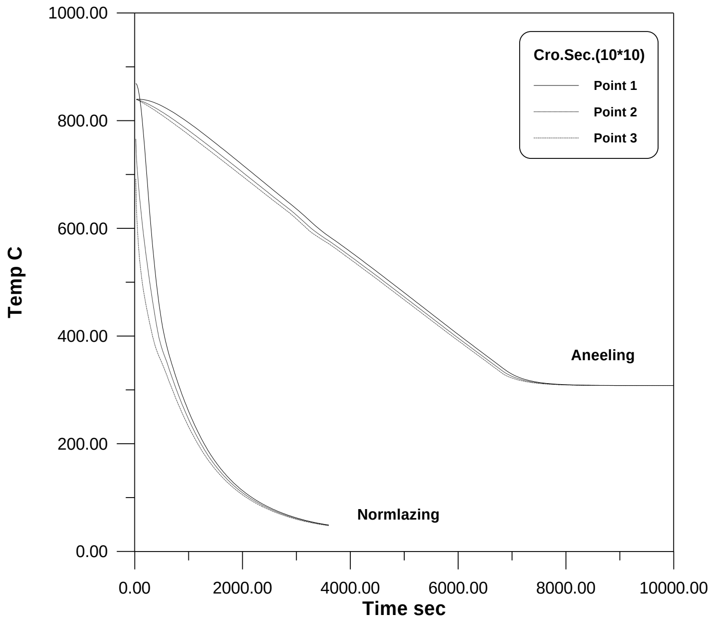


**A-Cross sectional area (10*10) $cm^2$.**

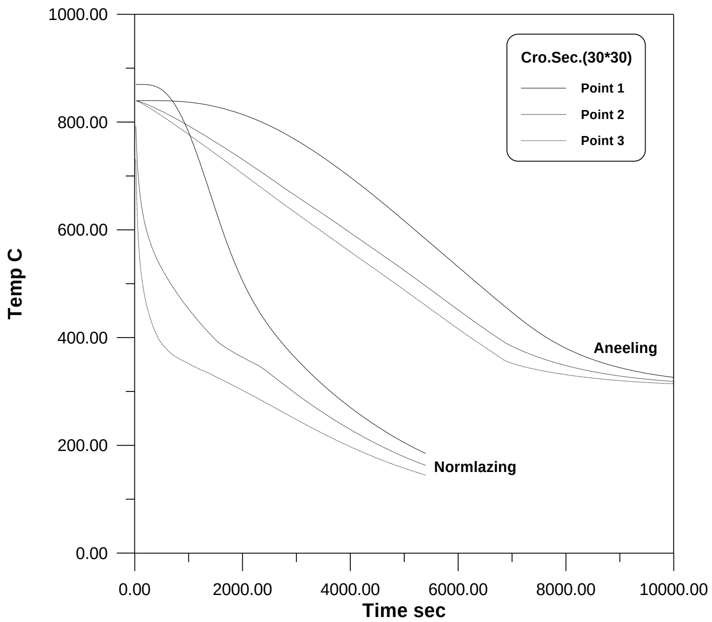


**B- Cross sectional area (30*30) $cm^2$**

**Figure (5) Temperatures vs. time in a comparison between annealing and normalizing treatment for three points at two cases A-Cross sectional area (10 * 10) $cm^2$, B- Cross sectional area (30*30) $cm^2$**

Figure (6)-A,B,C show the temperature distribution for the annealing (0.3*0.3 $m^2$) at different time 30, 1832,7032 and 1000 sec, from this figure we can se that the thermal gradient throe the cross sectional area is changing with time, in the first time step the thermal gradient not high but with increasing time this gradient increase until reach same point (specific time) then this gradient will decreasing with time increase this mean there is a specific critical time point before which the gradient increase with time and after which the gradient decreasing with time increase.

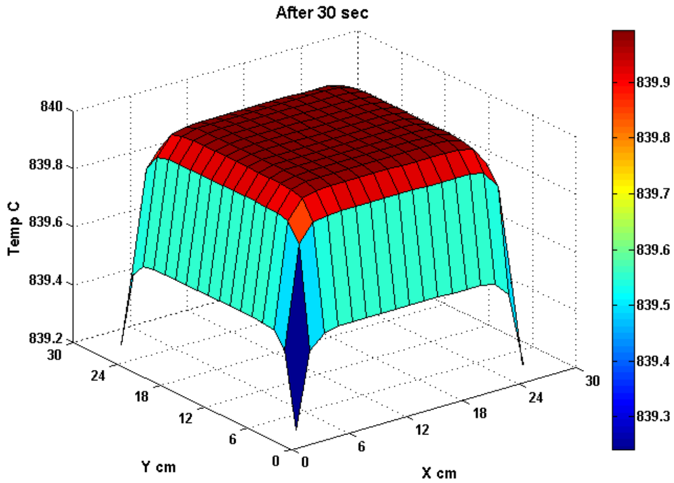


**A- After 30 sec**

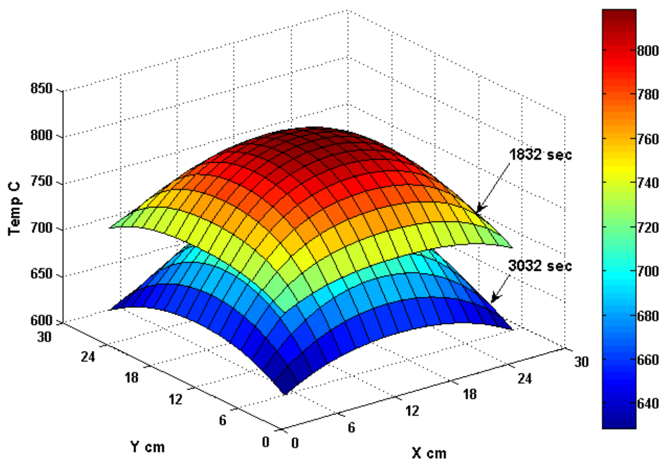


**B- After 1832 and 3032 sec**

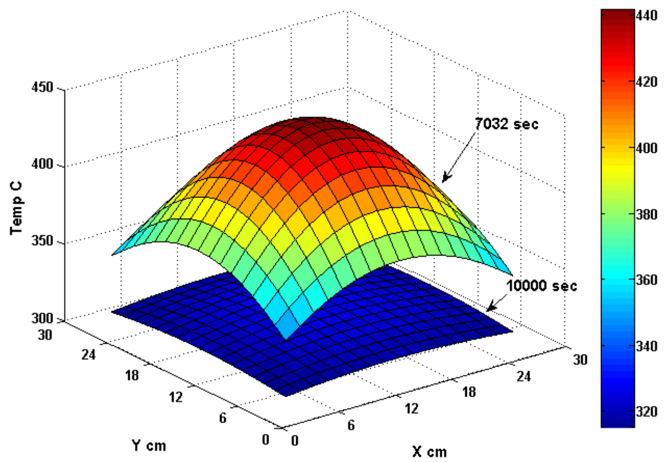


**C- After 7032 and 10000 sec**

**Figure (6)-A,B,C The temperature distribution for the annealing for (0.3*0.3 m$^2$)**

Another case shows in figure (7), which described a comparison between temperatures distribution for the normalizing treatment when the cross sectional area is ($0.3*0.3$ $m^2$) at different time (30, 330, 1832 and 3032) sec. From this figure we can see that the thermal gradient increase with time increase from 30 to 330 sec after this time the thermal gradient will be decrease with time increase.

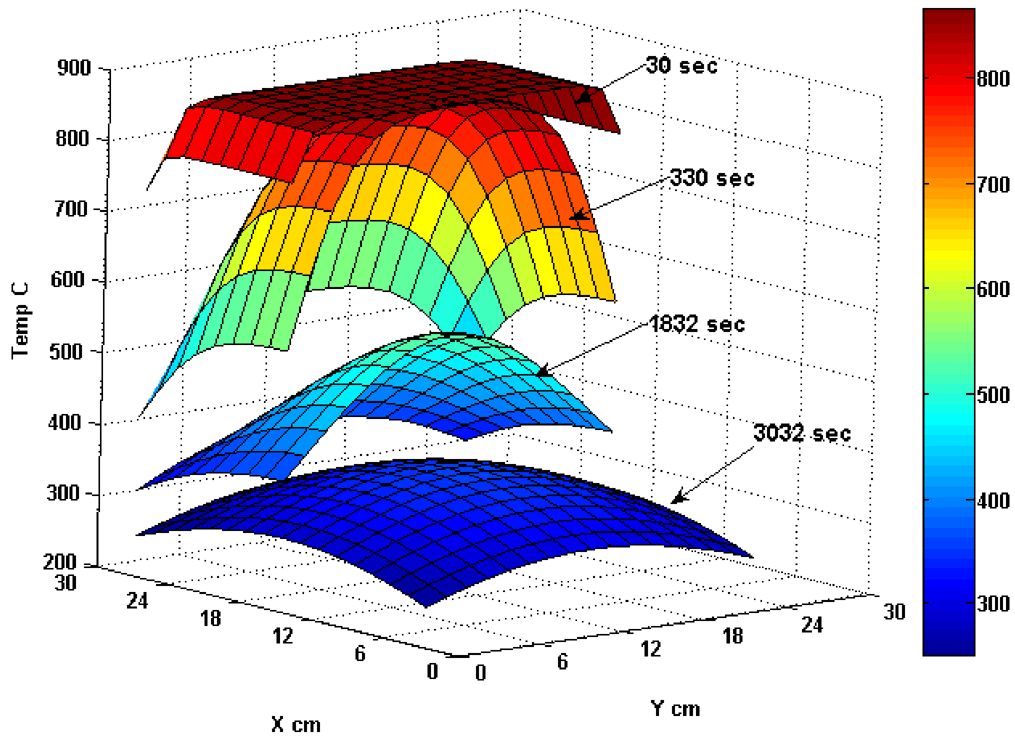


**Figure (7) - The temperature distribution for the normalizing treatment for ($0.3*0.3$ $m^2$)**

Actually there is a specific time point at which the thermal gradient is maximum, before this point (this time) the thermal gradient is increase with time increase and after this point the gradient is decrease with time increasing as we mention that before.

We can described this point as (**Time of Maximum Thermal Gradient**) (**$T_{M.T.G}$** ). Value of **$T_{M.T.G}$** is effected by many parameters such as the cross sectional area, temperature of heat treatment and heat treatment type. Thermal stress or crack may be occurring due to high thermal gradient so that it's very important to specify this point in the heat treatment process to avoid these defects. A special cooling process can be used to eliminate the effect of this phenomenon.

Another comparison shows in figure (8)-A, B, where figure (8)-A shows a comparison between the temperatures distribution for the annealing and normalizing treatment process at different time (30, 1832, 3032 ) sec, when the cross sectional area ($0.1*0.1$ $m^2$) while figure (8)-B shows the same case but for the cross sectional area ($0.3*0.3$ $m^2$). It's very important to noted that there is many differences between the temperatures distribution for the annealing and normalizing we can see that from the contours line of temperatures distribution and the temperature bar, this difference is increasing with time increase and with cross sectional area decrease. This is due to the value of heat transfer coefficient and the cooling process in the heat treatment process type.

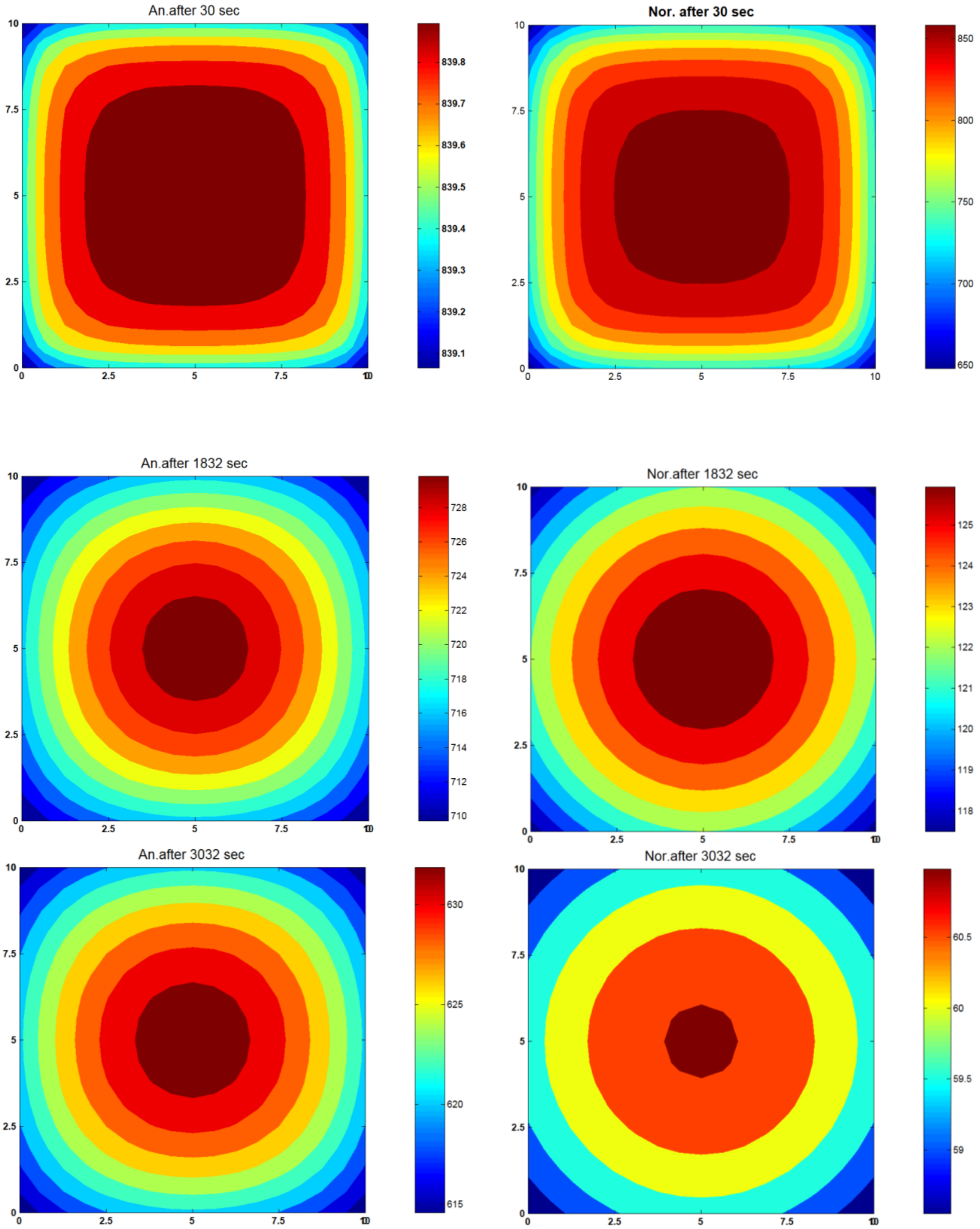


**A-(10*10) $cm^2$ Cross Sectional Area**

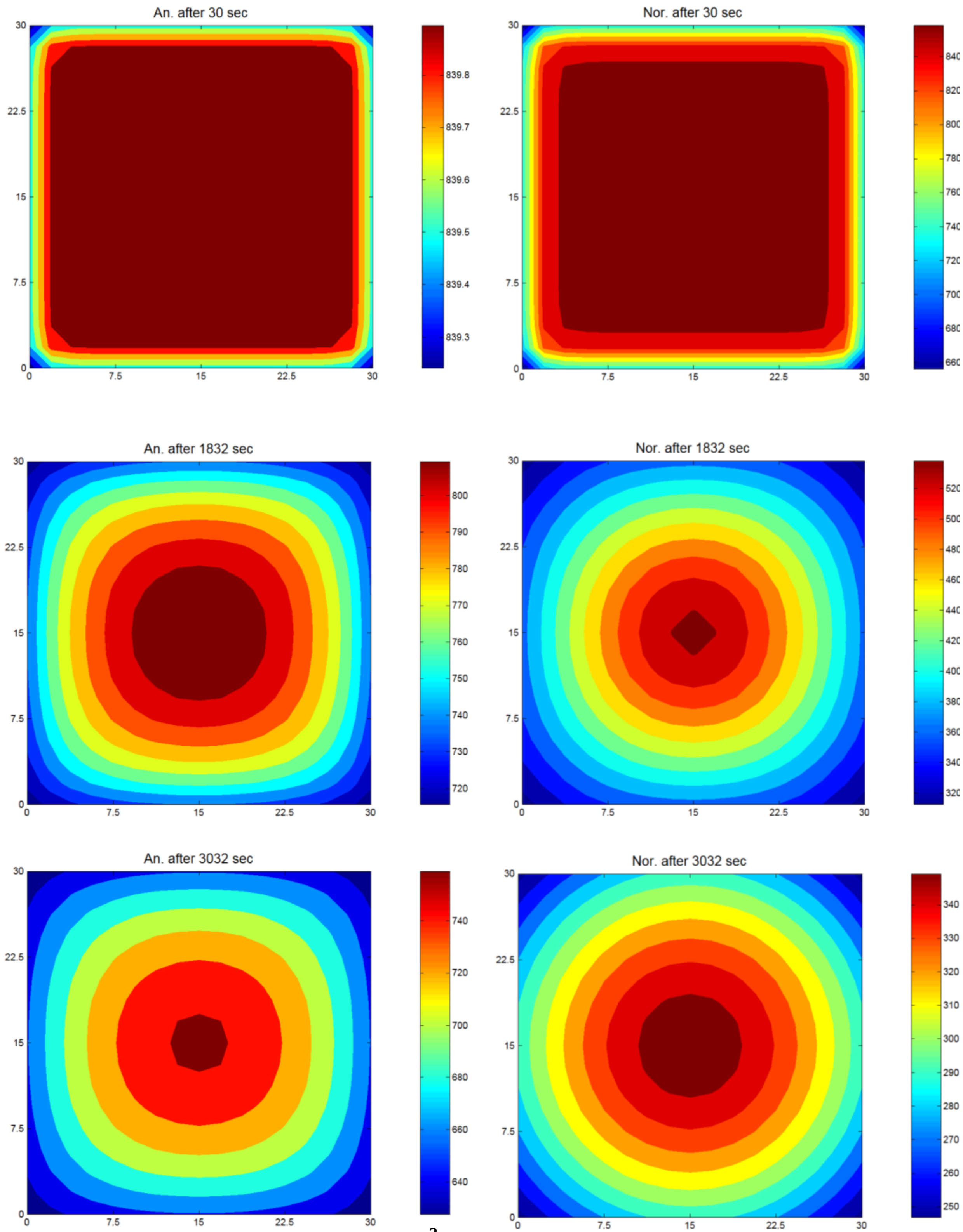


**B-(30*30) $cm^2$ Cross Sectional Area**

Figure (8)-A, B, comparison between the temperatures distribution for the annealing and normalizing treatment

## THE HARDNESS PREDICATION

After we calculate the temperature distribution in the previous section we will used this data to investigate the phase transformation and the value of the hardness in each point in the workpiece by using a method consist of the below steps.

By using the continuous-cooling-transformation (CCT) diagram we can determined time required to reach the temperature 500 $^oC$ (by intersection with the isothermal line 500 $^oC$), this step will be use to examination each point in the workpiece and determined the required time to reach the temperature 500 $^oC$ for each point.

For example figure (9) A, B shows the cooling curve for the three point (point nod 1, point nod2 and point node 3 see figure 1) for the normalizing and annealing treatment respectively and when the cross sectional area is **(30*30) cm$^2$** , from figure (9)-A we can see the time required to reach the isothermal line 500 $^oC$ (to the three points) this time can be noted as 1, 2 and 3, from these value we can see that the time required to each point is different from point to other this lead to different phase structure and mechanical properties. Figure (9)-B shows the same case but for the annealing treatment. It's very important to noted that the different between time required to reach the isothermal line 500 $^oC$ for the three point (point nod 1, point nod2 and point node 3) in the annealing case are less than that for the normalizing treatment, this case lead to uniform phase structure in the annealing treatment more that that for the normalizing treatment.

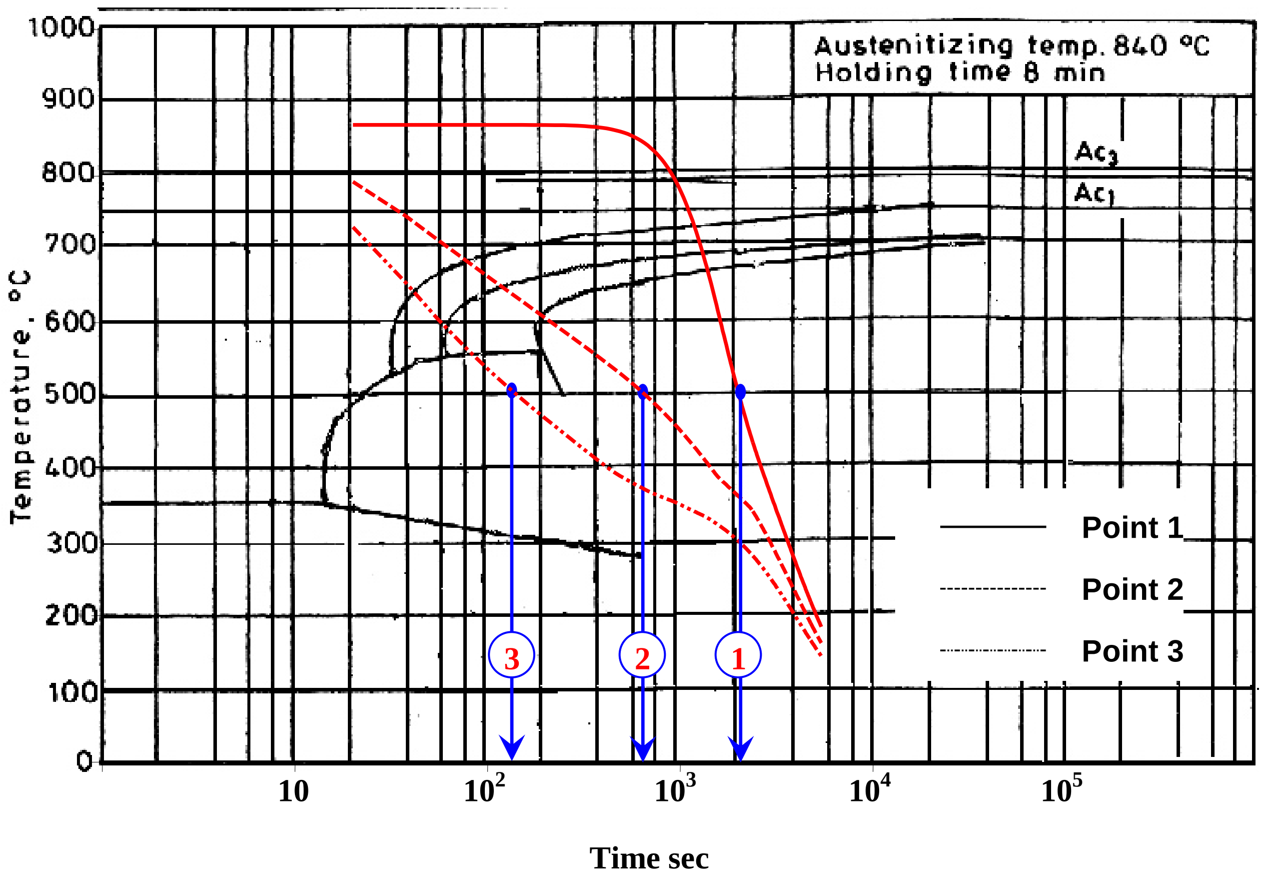


**A-Normalizing Treatment**

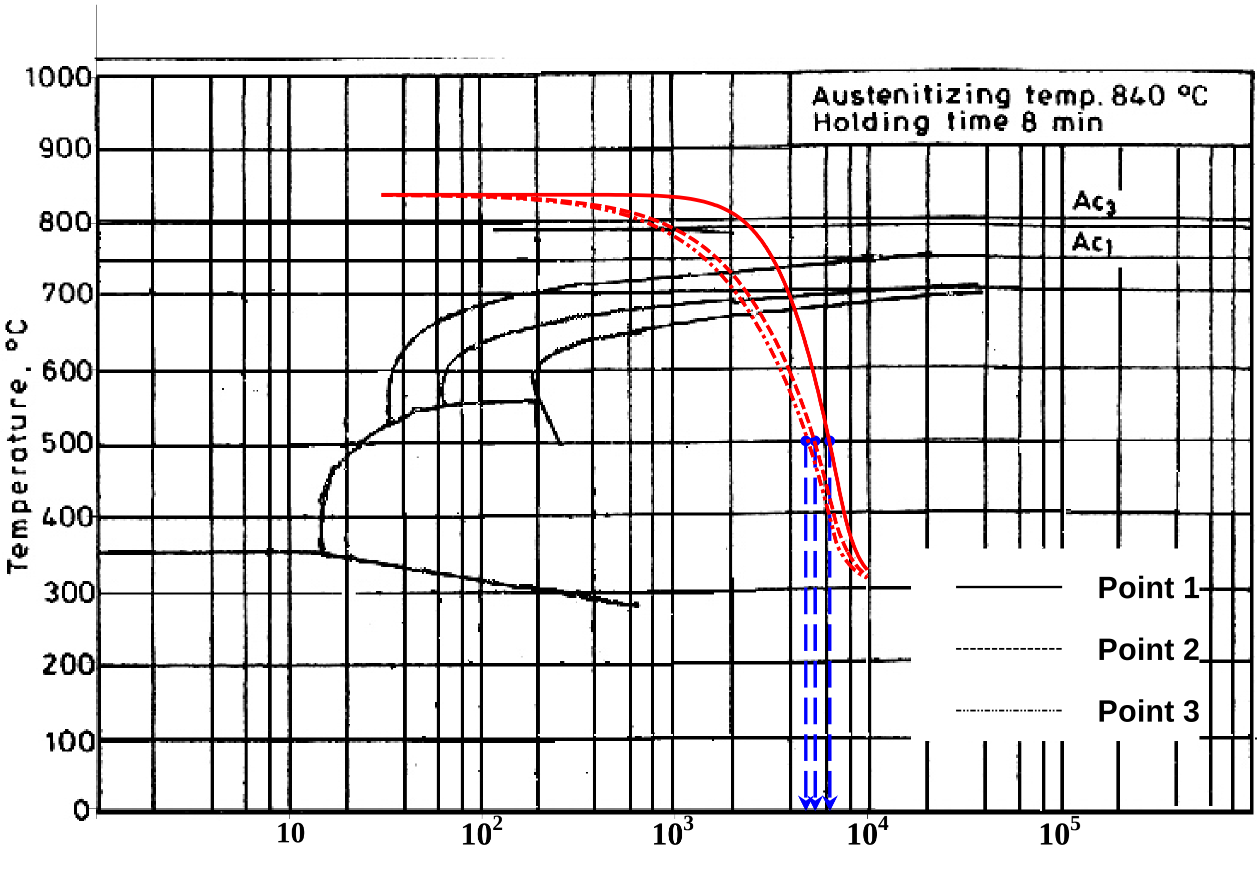


**B-Annealing Treatment**

**Figure (9)** Continuous-Cooling-Transformation (CCT) Diagram and steps to determined the required time to reach the isothermal line 500 $^{o}$C for the two cases

**A-Normalizing, B-Annealing**

After we determined the time for each point in the workpiece we will use this value to determine the phase structure and the hardness at each point by using figure (10), which shows the relationship between the time and the phase structure and the hardness value in HRC.

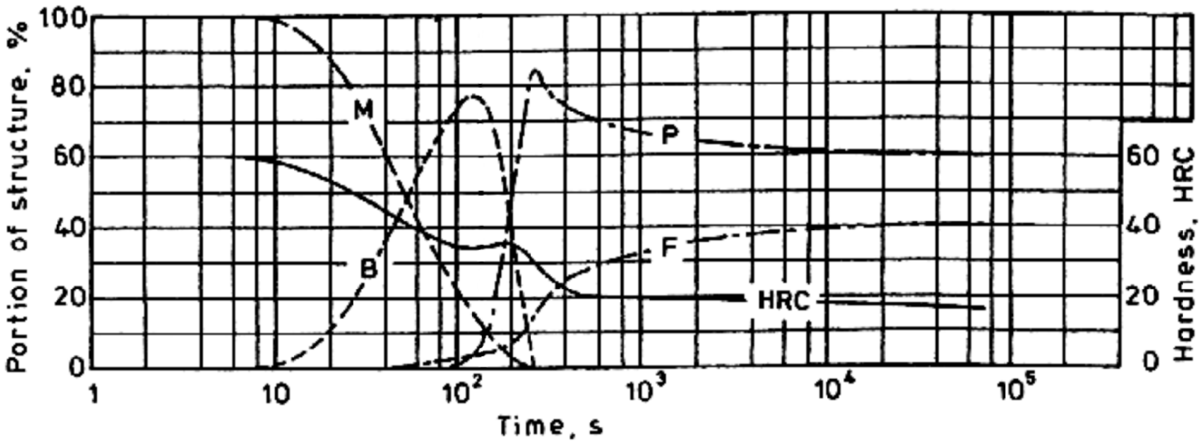


Figure (10) The relationship between the time and phase fraction and hardness in HRC [ 5 ].

Table (5) shows the phase structure and the hardness no in HRC for same point for the annealing and normalizing treatment and with two cross sectional area which are **(10*10) cm$^2$** and **(30*30) cm$^2$** .

**Table (5) The phase structure and the hardness no in HRC**

| Treatment Type | Nod Point | %F | %P | %B | %M | HRC |
|---|---|---|---|---|---|---|
| **Annealing Treatment (10*10) cm$^2$** | Nod 1 | 38 | 62 | | | 19 |
| | Nod 2 | 37.2 | 62.8 | | | 19.5 |
| | Nod 3 | 37 | 63 | | | 19.7 |
| **Annealing Treatment (30*30) cm$^2$** | Nod 1 | 39 | 61 | | | 18 |
| | Nod 2 | 37 | 63 | | | 19.7 |
| | Nod 3 | 36.6 | 63.4 | | | 19.8 |
| **Normalizing Treatment (10*10) cm$^2$** | Nod 1 | 25 | 75 | | | 24.1 |
| | Nod 2 | 12 | 78.5 | 9.5 | | 33 |
| | Nod 3 | 5.2 | 8.5 | 73.8 | 12.5 | 31.9 |
| **Normalizing Treatment (30*30) cm$^2$** | Nod 1 | 36.6 | 63.4 | | | 19.8 |
| | Nod 2 | 31 | 69 | | | 20 |
| | Nod 3 | 6 | 9.5 | 72.5 | 12 | 32.5 |

After we used the above methods to determined or predicate the hardness distribution for the workpiece for the two cases of heat treatment process these hardness value show in figure (11)-A,B,C and D, where this figure show the hardness distribution in HRC for the annealing and normalizing treatment process with (10*10 cm$^2$) and (30*30 cm$^2$), from this figure we can see there is a hardness difference between each point in workpiece, in fact this is duo to differences in the microstructure or phase structure which is depending on the cooling rate of each points from the workpiece, from figure(11)-A, we can see that the difference is not high between the inner and the boundary of the workpiece, these difference is increase with cross sectional area increasing see figure (11)-B, figure (11)-C shows the hardness value and distribution which is more that that for annealing treatment , and the hardness increment when the cross sectional area increase is more than that in the annealing treatment see figure (1).

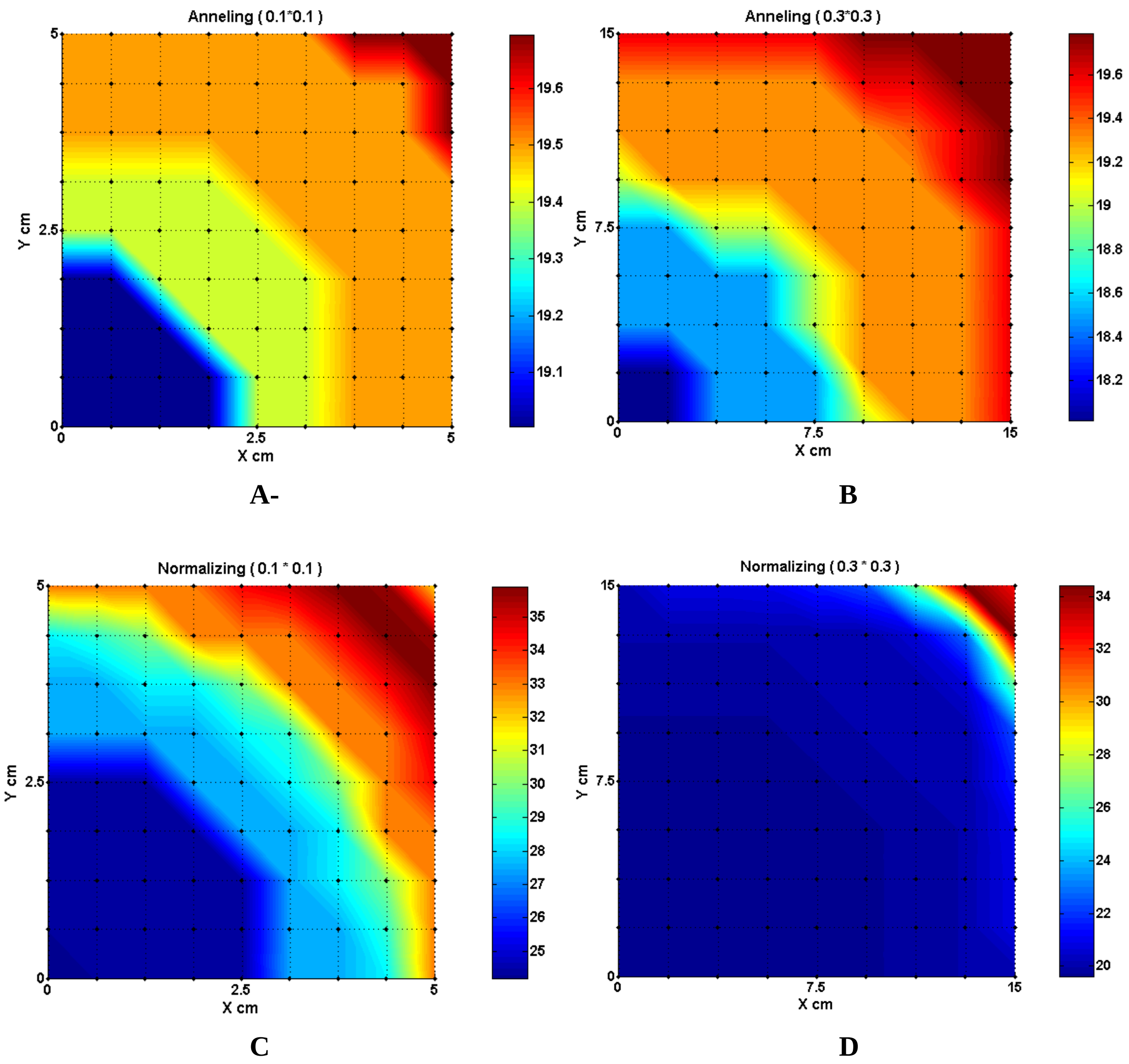


Figure (11) the hardness distribution for the workpiece

## CONCLUSIONS

1-During the cooling process in the heat treatment there is a specific time at which the thermal gradient through the cross sectional area is maximum we can note it as ($T_{M.T.G}$ ) (**Time of Maximum Thermal Gradient**), before this time ($T_{M.T.G}$ ) the thermal gradient is increase with time increase and after this time the gradient is decrease with time increasing. Thermal stress or crack may be occurring duo to high thermal gradient (which is occurs at this point) so that it's very important to specify this point in the heat treatment process.

2-The possibility of thermal stress and crack during the normalizing treatment is more than that in the annealing treatment also the high cross sectional area tend to this defect more than the small cross sectional area.

3-Generally the hardness is a function for (phase type and phase percent), and this hardness value decrease when the cooling time increase, but this behavior is change between the times from (120 to 200) sec where the hardness value at this cooling time range will increase with time increasing, even with phase portion change so that the hardness of point nod 3 (P3) is less than the hardness of point 5, point 4, and point 7. Also in the cooling time range (440 to 3100) sec there is no effect to the cooling time on the hardness even with increasing the %F phase and decreasing the %P phase.

## REFERENCES

ASM Handbook, Volume 1, "**Properties and Selection: Irons, Steels, and High Performance Alloys**" 2005

Brandon Elliott Brooks and Christoph Beckerman " **Prediction Of Heat Treatment Distortion Of Cast Steel C-Rings** "In proceedings of the 61st Technical and Operating conference. SFSA, Chicago, IL. 2007.

B. Shaheen. Bachy "**Simulation of Heat Treatment Process by Numerical Heat Transfer Mode**l" 2010

B. Smoljan a, N. Tomašić , D. Iljkić , I. Felde , T. Reti "**Application of JM®-Test in 3D simulation of quenching** " Journal of Achievements in Materials and Manufacturing Engineering, VOLUME 17 ISSUE 1-2 July-August 2006

B. Smoljan, D. Iljkić, S. Smokvina Hanza "**Computer simulation of working stress of heat treated steel specimen**" Journal of Achievements in Materials and Manufacturing Engineering, VOLUME 34 ISSUE 2 June 2009

Božidar Liščić1 – Saša Singer2 – Božo Smoljan3 "**Prediction of Quench-Hardness Within The Whole Volume of Axially-Symmetric Workpieces of Any Shape"**

Prof. Dr. Haji Badrul Bin Omar , Prof. Dr. Mohamed Elshayeb and Abdlmanam. S.A. Elmaryami "**Unsteady State Thermal Behavior of Industrial Quenched Steel Bar"** 18th World IMACS / MODSIM Congress, Cairns, Australia 13-17 July 2009.

Number 3 Volume 16 September 2010 Journal of Engineering

# THREE-DIMENSIONAL FINITE ELEMENT ANALYSES OF A SINGLE PILE IN AN ELASTOPLASTIC CLAYEY SOIL

Omar al-Farouk Salem al-Damluji,
Department of Civil Enginering,
University of Baghdad.

Usama Saeed Al-Anbaki,
Former Postgraduate Student,
Department of Civil Engineering,
University of Baghdad.

## ABSTRACT

A three-dimensional coupled finite element analysis algorithm is developed to predict the behaviour of single piles in clay. Three dimensional 20-noded brick elements are used in the analyses carried out on three documented field studies. Each node carries four degrees of freedom, three being for displacements in the three perpendicular space dimensions while the fourth is allocated for pore water pressure. The behaviour of the material of the pile is idealized through a linear elastic constitutive relationship while that for the soil by the Modified Cam-Clay model both extended to cover three-dimensional characteristics. The load-displacement results from the developed algorithm on the three selected problems from literature show a very good agreement with the observations. Moreover, the build-up of pore fluid pressures and their dissipations were found to be consistent with field measurements also.

## الخلاصة

لقد تم تطوير حسابات تحليل باستخدام طريقة العناصر المحددة المزدوجة بالاتجاهات الثلاثة لتوقع تصرف الركائز المنفردة في الترب الطينية. لقد تم استخدام عناصر طابوقية ذات 20 عقدة بالابعاد الثلاثة لتحليل ثلاثة دراسات حقلية موثقة. تحمل كل عقدة في العنصر المحدد اربعة درجات للحرية, ثلاثة منها للازاحات بالابعاد الثلاثة المتعامدة و الرابعة لضغط ماء المسام. يتم تمثيل التصرف التكويني لمادة الركيزة باستخدام العلاقة الخطية في حين للتربة الطينية بنظرية طين كام المعدلة بعدما تم توسيعها لتشتمل على التصرف بالابعاد الثلاثة. تظهر نتائج الثقل-الازاحة من الحسابات المطورة توافقاً جيداً مع المشاهدات الحقلية. كما تم التوصل على ان النتائج المستحصلة من التحليل لضغط ماء المسام متوافقة مع القياسات الحقلية ايضاً.

**KEYWORDS:** coupled analysis, finite element, Cam-clay, three dimensional brick elements, load-settlement, pore-water pressure

## - PREVIOUS WORKS

As an introduction, a review of literature is made for the behaviour of a single pile in clayey soils and under static loading.

**- <u>Analysis of Piles by the Finite Element Method</u>:- Randolph and Wroth** *(1978)* used the finite element method to model the manner in which a pile transfers load to the soil for analysis of deformation of vertically loaded piles. Good agreement was obtained between the results of the analysis and solutions obtained from available numerical methods and noticed that the shear stress around the pile decreases in an inverse proportion to the radius. **Desai** *(1978)* studied the effects and simulation of driving of piles into saturated soil media. A procedure for numerical simulation of driving is proposed. Consolidation caused by changes in stress and in pore water pressures, which are obtained on the basis of the *cavity expansion approach*, in the soil mass due to driving was solved using a finite element procedure. **Kuhlemeyer** *(1979)* presented a formulation for an approximation to bending of beams of circular cross sections by the use of the finite element method. The three-degree of freedom characteristic of the element permits an efficient solution to the three dimensional problem of lateral displacement and rotation of transversely loaded circular beams. The high accuracy of the element was confirmed by studying the deflection of cantilever beams subjected to lateral loads. **Kirby and Esrig** *(1979)* used an elastic finite element analysis for pile loading and suggested that the changes in pore pressure associated with changes in mean normal total stress are small and probably in the order of (5-10%) of the undrained shear strength of the soil. Measured pore pressures due to pile loading are typically (0-25%) of the undrained shear strength. **Cooke et al.** *(1979)* described a series of tests made on instrumented tubular steel piles in the field to examine the mechanism of load transfer from piles in stiff clay. During installation of the first pile, loading tests were made to piles in stiff clay. During installation of the first pile, loading tests were made so that the variation of the soil properties and the effect of pile length on settlements at corresponding working loads could be examined. **Ottaviani and Marchetti** *(1979)* compared results obtained from a loading test on cast-in-place piles with those obtained from a non-linear finite element analysis based on geotechnical parameters of cohesive soils. The comparison found a good agreement for the loads before failure (allowable) but, there are differences in the loads close to failure (ultimate). **Grande and Nordal** *(1979)* used the finite element method to deal with long term pile head loads. Formulae concerning the ultimate and service load components were derived. In addition to these, equations describing deformations and soil reaction coefficients were introduced. **Randolph et al.** *(1979)* made a numerical analysis of an installation of a single pile driven into clay and the effects on the distribution of stresses and displacements in the soil near the piles immediately after driving and during subsequent consolidation of the clay. The installation of driven piles with the expansion of a *cylindrical cavity* was modelled. The path applied to elements of soil in this process, a strain controlled path, consists, for a typical clay deposit of large lateral extent, of one-dimensional consolidation followed by plane strain constant volume shearing with the plane of shearing being perpendicular to the previous direction of consolidation (rapid installation of the pile). The consolidation of the soil was studied using a work-hardening elasto-plastic soil model, namely, *the Cam-clay model*. **Pal and Parikh** *(1980)* used a finite element analysis for an axially loaded pile-clay system in the elastic region with a computer program capable to handle non-homogeneous and homogeneous clays as well as different pile geometries and different pile penetrations. It was seen that as **L/H** (which is the ratio of the pile length to the total depth of the soil) ranges between **0.75** to **1.00**, there would be an increase in the rate of settlement for a specific slenderness ratio of pile. Morever, it was observed that in the case of full penetration, the amount of load transferred at the base shows a tremendous increase.

**Bhowmik and Long** *(1990)* presented results of *nonlinear finite element analyses* of an axial pile load test using a *bounding surface plasticity model* to simulate the soil behaviour. The interface between the pile and the surrounding soil is modelled by using thin isoparametric elements. The comparison between observed and predicted pile behaviour is presented and the sensitivity of the analytical solutions to the properties of interface elements is investigated and discussed. The soil-interface-pile model used in this analysis provides a good simulation of the load test analyzed. **Phoon et al.** *(1990)* used the finite element method to study the effect of a spatially varying soil medium on the settlement of single-pile foundations. The soil is assumed to be linear-elastic and it is modelled as a homogeneous field. Using a first-order second-moment technique, the mean and coefficient of variation of the pile head settlement were determined. It is found that the uncertainty of the pile head settlement is dependent on both deterministic and stochastic parameters. Analysis is then performed to compute the reliability index and the corresponding probability of unserviceable behaviour. **Yasser and Hassiotis** *(2001)* developed a three-dimensional, nonlinear finite element model. It is used to study stresses on piles and pile-soils. The model consists of soil continuum elements according to a *Mohr-Coloumb failure criterion* with material nonlinearities for the piles and soil, respectively. The objective of that investigation was to study the mechanism of pile-soil interaction. **Al-Marsumi** *(2003)* developed four algorithms to calculate the total stress, pore water pressure in addition to inclusion of earthquake effects. A three dimensional finite element method was used to analyze the pile-soil system. A single pile with cap and a group of piles with cap were studied while the soil was represented as a homogeneous isotropic and non-homogeneous anisotropic material using the *Modified Cam-Clay model*. **Maharaj et al.** *(2004)* analyzed piles of varying cross-sections by a nonlinear finite element method under plane strain conditions. The soil was modelled by an elasto-plastic medium incorporating *Drucker-Prager* yield criterion. It was found that the load carrying capacity of a single pile is more than that of a pile in a group in case of piles under uplift load and of varying cross-section. **Raheem** *(2005)* used the finite element method to study the behaviour of axially loaded piles embedded in a clayey soil and studying the pore water pressure developed with a thin layer interface element using the *Cam-Clay* model. It was concluded that during undrained loading conditions, the vertical settlement values at the tip of the pile increased in the order of 22.5% when slip elements are used. **Al-Baghdadi** *(2006)* developed a three-dimensional, nonlinear finite element computer program to model soil-pile-raft systems with interface elements between the pile and the surrounding soil. A twenty-noded isoparametric brick element was used. The behaviour of the piled raft material is simulated by using a linear elastic model. However, the behaviour of soil and interface materials is simulated by an elasto-plastic model using the *Mohr-Coulomb failure criterion.*

In this paper, a solution to the problem is proposed by using the *Modified Cam-Clay model* for the soil and the *linear elastic model* for the material of the pile both extended to cover three dimensional conditions.

## - DIFFERENTIAL EQUATIONS GOVERNING THE PROBLEM:-

Biot, (1941) developed a three-dimensional consolidation theory based on elastic theory. The assumptions of *Terzaghi-Rendulic* theory are adopted here except that the total stress is allowed to vary within the soil mass although the applied load remains constant. *Biot*'s theory includes the compressibility of the fluid and the soil skeleton and it also deals with partly saturated soils. For saturated soils, *Biot*'s theory for general three-dimensional problems may be expressed as (Biot 1955, 1956):-

**- Equilibrium Equation:-** For static analysis, the equilibrium equation is (Smith and Griffiths, 1988):-

$$K\frac{d\bar{u}}{dt} + L\frac{d\bar{p}}{dt} - C - \frac{df}{dt} = 0 \quad (1)$$

When encountering a non-porous material like concrete, the above equation reduces to:

$$\{F\} = [K].\{\delta\} \quad (2)$$

where:- {F}= vector of nodal forces,
[K] = stiffness matrix, and
{δ}= vector of nodal displacements.

The element stiffness matrix for Equation (1) is given by (Smith and Griffiths, 1998):-

$$K = \int_{\Omega} [B]^T [D][B] d\Omega \quad (3)$$

where:- [D]= the stress-strain (constitutive) matrix,
[B]= the strain-displacement matrix,
dΩ= the domain of the integration, and
the superscript ( $^{\mathbf{T}}$ ) represents the transpose of the matrix.

Equation (3) can be rewritten in a three-dimensional *local form* as follows:-

$$K = \int_{-1}^{+1}\int_{-1}^{+1}\int_{-1}^{+1} [B]^T [D][B].\det J.d\xi\, d\eta\, d\zeta \quad (4)$$

**- Fluid Flow Equation:-** This equation is applied onto flow of water in porous materials like soils only. It can be written as (Lewis and Schrefler, 1987):-

$$H\bar{p} + S\frac{d\bar{p}}{dt} + L^T\frac{d\bar{u}}{dt} - \bar{f} = 0 \quad (5)$$

**- Governing Element Matrix Equation:-** By augmenting equations (1) and (5), the following matrix equation is obtained (Lewis and Schrefler, 1987):

$$\begin{bmatrix} K & L \\ L^T & S+\alpha H\Delta t_k \end{bmatrix}_{k,\alpha} \begin{Bmatrix} \bar{u} \\ \bar{p} \end{Bmatrix}_{t_k+\Delta t_k} = \begin{bmatrix} K & L \\ L^T & S-(1-\alpha)H\Delta t_k \end{bmatrix}_{k,\alpha} \begin{Bmatrix} \bar{u} \\ \bar{p} \end{Bmatrix}_{t_k} + \begin{Bmatrix} \frac{df}{dt}+C \\ \bar{f} \end{Bmatrix}_{k,\alpha} \Delta t_k \quad (6)$$

The above equation represents the equation governing the soil medium surrounding the pile.

## THREE-DIMENSIONAL BRICK ELEMENT:-

In this paper, the problems under consideration are discretized into three-dimensional twenty-node brick elements. Each node in this element has three degrees of freedom representing displacements in the **x**, **y**, and **z**-directions, as well as an additional fourth degree of freedom for pore water pressure.

For the derivation of the required matrices and vectors, the coordinates and local displacement fields of an element are interpolated using polynomials as follows (Owen and Hinton 1980):-

For the three displacement components **u**, **v**, and **w**:-

$$\begin{Bmatrix} u \\ v \\ w \end{Bmatrix} = \begin{bmatrix} [N] & 0 & 0 \\ 0 & [N] & 0 \\ 0 & 0 & [N] \end{bmatrix} \begin{Bmatrix} \delta_i \\ \delta_i \\ \delta_i \end{Bmatrix} \quad \ldots\ldots (7)$$

Also for three coordinates **x**, **y**, and **z**:-

$$\begin{Bmatrix} x \\ y \\ z \end{Bmatrix} = \begin{bmatrix} [N] & 0 & 0 \\ 0 & [N] & 0 \\ 0 & 0 & [N] \end{bmatrix} \begin{Bmatrix} x_i \\ y_i \\ z_i \end{Bmatrix} \quad \ldots\ldots (8)$$

where:- $\{u\} = \{u \quad v \quad w\}^T$, vector of global displacements in the **x**, **y**, and **z**-directions, respectively,

m = number of nodes per element,

$\{\delta_i\}$ = nodal global displacements of node (i),

$\{x\} = \{x \quad y \quad z\}^T$ vector of global coordinates at any point,

$\{X_i\}$ = vector of global coordinates of nodal point (i), and

$\{N_i\}$ = interpolation function of nodal point (i) (as functions of local coordinates **ξ**, **η**, and **ζ**).

For *small strain theory*, the strain vector for a three-dimensional stress analysis can be written as (Reddy, 1984): -

$$\{\varepsilon\} = \begin{Bmatrix} \varepsilon_x \\ \varepsilon_y \\ \varepsilon_z \\ \gamma_{xy} \\ \gamma_{yz} \\ \gamma_{zx} \end{Bmatrix} = \begin{Bmatrix} \frac{\partial u}{\partial x} \\ \frac{\partial v}{\partial y} \\ \frac{\partial w}{\partial z} \\ \frac{\partial u}{\partial y} + \frac{\partial v}{\partial x} \\ \frac{\partial v}{\partial z} + \frac{\partial w}{\partial y} \\ \frac{\partial w}{\partial x} + \frac{\partial u}{\partial z} \end{Bmatrix} \quad \ldots\ldots (9)$$

The evaluation of the strain vector requires the evaluation of the derivatives given in Equation (7). The derivatives are calculated by using a *Jacobian transformation matrix*, which relates global coordinates **x**, **y** and **z** derivatives to local coordinate **ξ**, **η**, and **ζ** derivatives (Bathe, 1996):-

$$\begin{Bmatrix} \frac{\partial}{\partial \xi} \\ \frac{\partial}{\partial \eta} \\ \frac{\partial}{\partial \zeta} \end{Bmatrix} = [J]^e \begin{Bmatrix} \frac{\partial}{\partial x} \\ \frac{\partial}{\partial y} \\ \frac{\partial}{\partial z} \end{Bmatrix} \quad \ldots\ldots (10)$$

where:-

$[J]^e$= the Jacobian matrix in Cartesian coordinates.

The *strain-displacement relation* is given as:-

$$\{\varepsilon\} = \sum_{i=1}^{m} [B_i]\{\delta_i\} \quad \ldots\ldots (11)$$

where:-

$[B_i]$= The strain-nodal displacement matrix described by:-

$$[B_i]=\begin{bmatrix} N_{1,1} & 0 & 0 & N_{2,1} & \dots & 0 \\ 0 & N_{1,2} & 0 & 0 & \dots & 0 \\ 0 & 0 & N_{1,3} & 0 & \dots & N_{m,3} \\ N_{1,2} & N_{1,1} & 0 & N_{2,2} & \dots & N_{m,1} \\ N_{1,3} & 0 & N_{1,1} & N_{2,3} & \dots & N_{m,1} \\ 0 & N_{1,3} & N_{1,2} & 0 & \dots & N_{m,2} \end{bmatrix} \quad \dots\dots (12)$$

In the above:-

$$N_{i,j}=\frac{\partial N_i}{\partial x_j}$$ (the first derivative of the shape function).

The three normal and the three shearing stresses are related to the corresponding strains through the stress-strain constitutive matrix **[D]**:-

$$\{\sigma\}=[D]\{\varepsilon\} \quad \dots\dots (13)$$

## CONSTITUTIVE RELATIONSHIPS:-

- **Elastic Model:-** Elastic behaviour of a material occurs when no residual strains are retained after unloading, and the material returns to its original shape (Atkinson and Bransby, 1978). In the case of a three-dimensional continuum, it may be expressed in terms of two constants **(K)** and **(G)** as follows (Saada, 1974):-

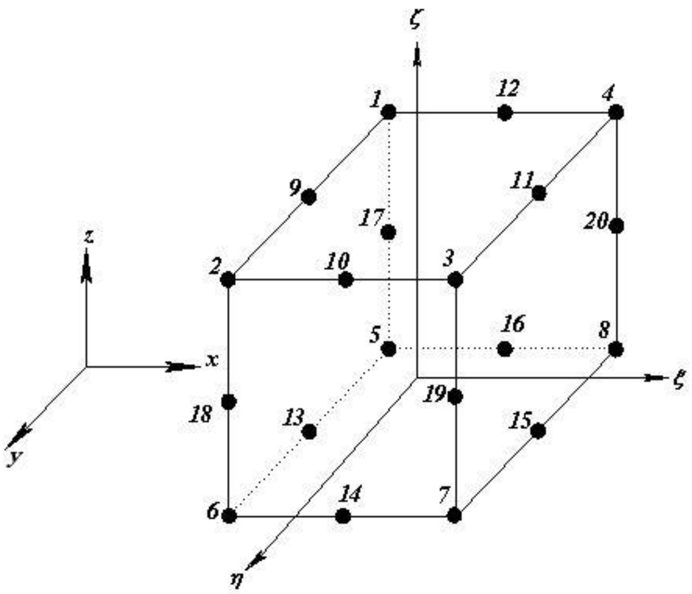


| Local Node Number | ξ | η | ζ |
|---|---|---|---|
| 1 | -1 | -1 | 1 |
| 2 | -1 | 1 | 1 |
| 3 | 1 | 1 | 1 |
| 4 | 1 | -1 | 1 |
| 5 | -1 | -1 | -1 |
| 6 | -1 | 1 | -1 |
| 7 | 1 | 1 | -1 |
| 8 | 1 | -1 | -1 |
| 9 | -1 | 0 | 1 |
| 10 | 0 | 1 | 1 |
| 11 | 1 | 0 | 1 |
| 12 | 0 | -1 | 1 |
| 13 | -1 | 0 | -1 |
| 14 | 0 | 1 | -1 |
| 15 | 1 | 0 | -1 |
| 16 | 0 | -1 | -1 |

| | | | |
|---|---|---|---|
| 17 | -1 | -1 | 0 |
| 18 | -1 | 1 | 0 |
| 19 | 1 | 1 | 0 |
| 20 | 1 | -1 | 0 |

**Figure (1) Twenty-node brick element.**

$$D=\begin{bmatrix} K+\frac{4}{3}G & K-\frac{2}{3}G & K-\frac{2}{3}G & 0 & 0 & 0 \\ K-\frac{2}{3}G & K+\frac{4}{3}G & K-\frac{2}{3}G & 0 & 0 & 0 \\ K-\frac{2}{3}G & K-\frac{2}{3}G & K+\frac{4}{3}G & 0 & 0 & 0 \\ 0 & 0 & 0 & 2G & 0 & 0 \\ 0 & 0 & 0 & 0 & 2G & 0 \\ 0 & 0 & 0 & 0 & 0 & 2G \end{bmatrix} \qquad \ldots\ldots\ldots\ldots(14)$$

where:- K= Bulk modulus = $\frac{E}{3(1-2\nu)}$ ……………………………………………..... (15)

G= Shear modulus = $\frac{E}{2(1+\nu)}$ …………………………………………… (16)

In all analyses considered in this paper, the material of the pile, which is concrete, is assumed to follow the constitutive relation described by equation (14).

**- <u>Elasto-Plastic Analysis</u>:-** The relationship between increments of stress and increments of strain for elasto-plastic materials is given by the following equation (Desai and Siriwardane, 1984):-

$$\delta\varepsilon = D^{ep}\delta\sigma' \ldots\ldots\ldots\ldots\ldots\ldots\ldots\ldots\ldots\ldots\ldots\ldots\ldots\ldots (17)$$

where **δσ'** and **δε** are increments of effective stress and total strain (elastic and plastic), respectively and **($D^{ep}$)** is the elasto-plastic constitutive matrix. In this study, the critical state model is applied. Since this model requires an *associative flow rule*, where the plastic potential surface is equal to the yield surface (**Q≡F**), the following equation is derived (Al-Damluji, 1981):-

$$d\sigma' = \left[ D^e - \frac{D^e \frac{\partial F}{\partial \sigma'} \left\{ \frac{\partial F}{\partial \sigma'} \right\}^T D^e}{\left[ -\left\{ \frac{\partial F}{\partial \varepsilon^p} \right\}^T \frac{\partial F}{\partial \sigma'} + \left\{ \frac{\partial F}{\partial \sigma'} \right\}^T D^e \frac{\partial F}{\partial \sigma'} \right]} \right] d\varepsilon \qquad \ldots\ldots\ldots\ldots\ldots (18)$$

- **<u>Modified Cam-Clay Model</u>:-** The *Modified Cam-clay model* addresses the much particular dissatisfaction with the original *Cam-Clay* one. Its yield surface is an ellipse in the meridional plane, shown in Figure (2), and is defined by the equation (Lewis and Schrefler, 1987):-

$$F = \frac{q'^2}{M_{cs}^2} - 2p'p'_c\left(\varepsilon_v^p\right) + p'^2 = 0 \quad (19)$$

in which $\mathbf{M_{cs}}$ is the slope of the critical state line in the ($\mathbf{p'}$, $\mathbf{q}$) plot, $\mathbf{p'_c}\left(\boldsymbol{\varepsilon}_v^p\right)$ is the preconsolidation pressure to which the soil has previously been subjected to during its past history. It represents the current semi-diameter of the ellipse in the p′-direction.

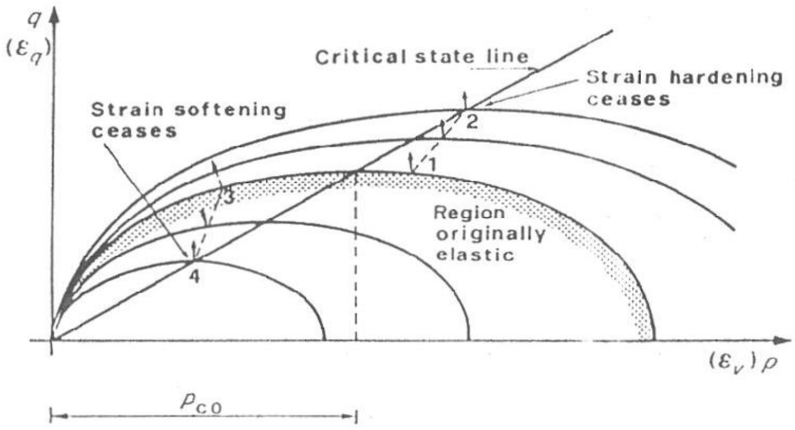


**Figure (2) Modified Cam-clay model in the space of two stress invariants q and p.**

**(after Lewis and Schrefler, 1987)**

Clays surrounding piles in the problems solved in this paper are assumed to obey equations (18) and (19). Al-Anbaki (2006) presented all the necessary extensions of the derivations to cover three-dimensional behaviour.

## PRESENTATION OF RESULTS:-

After checking the validity of the elastic and elasto-plastic consolidation schemes and the ability of the developed computer program, which was given the name DARC3 (Al-Anbaki, 2006), the present section will discuss the observation results for three field problems documented in literature and compare them with the proposed algorithm output predictions.

**<u>-Properties, Geometry and Boundary Conditions</u>:-** The pile material used through the following three problems is concrete obeying a linear elastic constitutive relationship as depicted by Equation 14. While for soil, the type of clay involved is modelled by an elasto-plastic *Modified Cam-clay* constitutive relationship as presented by Equation 18. The soil is assumed to be homogeneous and isotropic. The water table is assumed to be at ground level. As the pile section is circular, the meshes used are for a quarter of a cylinder medium. The boundary conditions for the problems are restrained from lateral movement for all nodes while they are free in vertical movements except at the bottom of the mesh. For pore water pressures, they are restrained only at the bottom of the mesh at the circumference.

- **<u>Case Study Number One-Single Pile Analysis (After Desai, 1978)</u>:-** This problem is analyzed according to the research presented by Desai (1978) in which a simulation of driving a pile in a saturated clayey soil is proposed. A discussion of the consolidation process in the soil mass due to changes in stresses and pore water pressures employing dissipations during driving and after subsequent loadings is presented through a nonlinear finite element solution.

- **<u>Mesh and Geometry</u>:-** Figure (3) shows the three-dimensional finite element mesh for a quadrant of a single pile medium with a diameter of (0.4066m) and length of embedment of (15.25m). The depth of the clay layer is (27.452m). It is assumed to extend in the x and y directions about (3.352m) away from the centre of the pile. The total number of three dimensional brick elements employed is (324) and the total number of nodes is (895). Figure (4) shows the x-z plane of the problem while Figure (5) shows the x-y plane.

**- <u>Problem Properties</u>:-** The material properties adopted for this problem are presented in Table (1).

**- <u>Loading</u>:-** The total uniformly distributed load (working load) applied vertically on the top of the pile is (1700) $kN/m^2$ which is equal to (45%) of the ultimate bearing capacity of the pile of (3800) $kN/m^2$. The load is applied after (31.1) days from driving of the pile. Through the results presented in this work, the load is assumed to be applied immediately after the installation of the pile.

**- <u>Results</u>:-**

**a. <u>Load-Settlement Curve</u>**:-

The load-settlement comparison curves at the tip of the pile between the results obtained from the Desai (1978) and these obtained through the current work are shown in Figure (6). It can be seen from the figure that the curves seem to be similar in shape and the difference ratio between the results at the end of loading stage is about (**15%**). Generally, the load-settlement curve seems to be very close to the linear relation behaviour at the

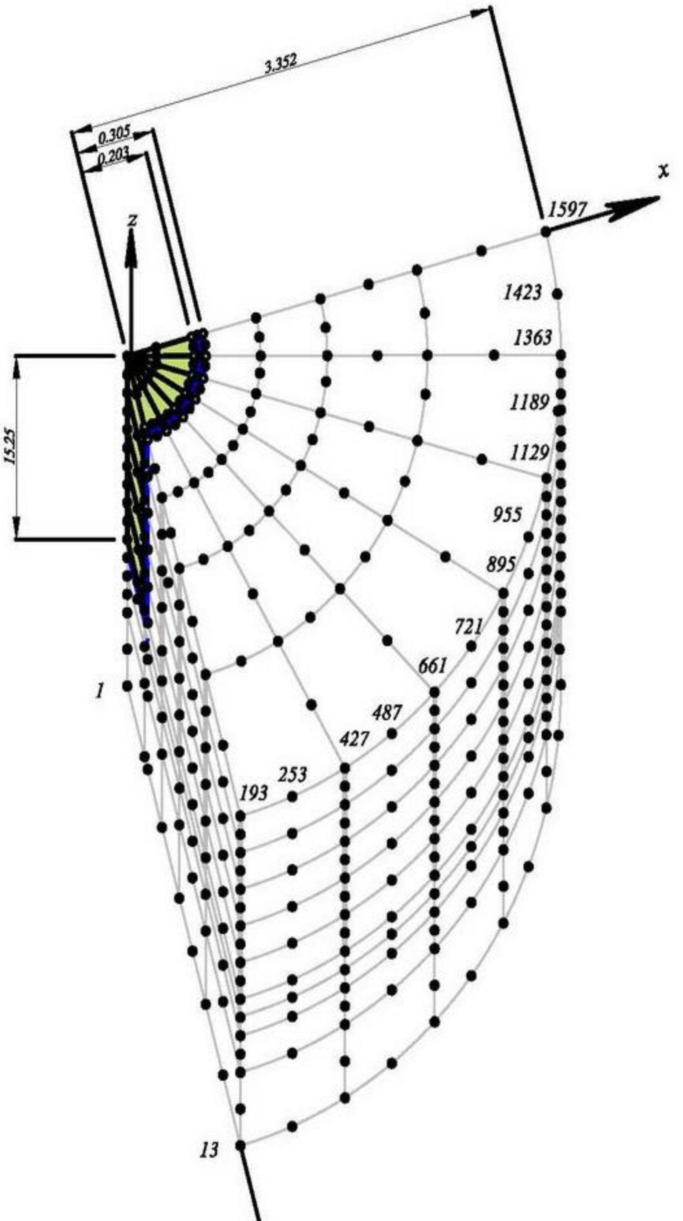


**Figure (3) Three- Dimensional finite element mesh for a pile- soil quadrant**

initial stage. This may be attributed to the very small pile displacements due to small load increments. As the loading level is increased, the curve tends to show a non-linear relation with smaller slopes (higher settlement values).

**b. <u>Pore Water Pressure Dissipation</u>**:- Figure (7) shows the pore water pressure dissipation behaviour around the pile at location surface **A-A** shown in Figure (4) for different time steps. The distribution of the excess pore water pressure becomes uniform after considerable time. This may be attributed to the concentration of stresses and strains close to the pile tip. Figure (8) shows the pore water pressure dissipation obtained by Desai (1978). It can be noticed that there is a similarity in the shapes of the pore water pressure curves between these obtained from the current study and the ones concluded by Desai (1978) for time steps greater than (31.1) days. The difference may be attributed to the load which has been applied (31.1) days after installation by Desai (1978) while it is assumed to be applied immediately in the current study.

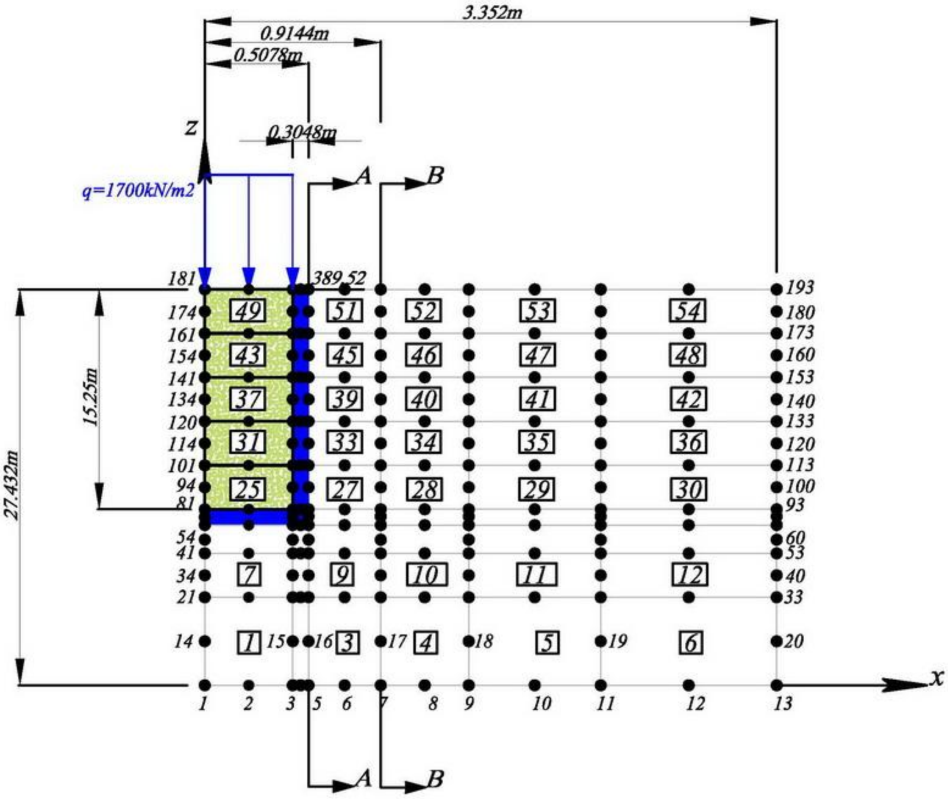


**Figure (4) x-z Plane of the Problem**

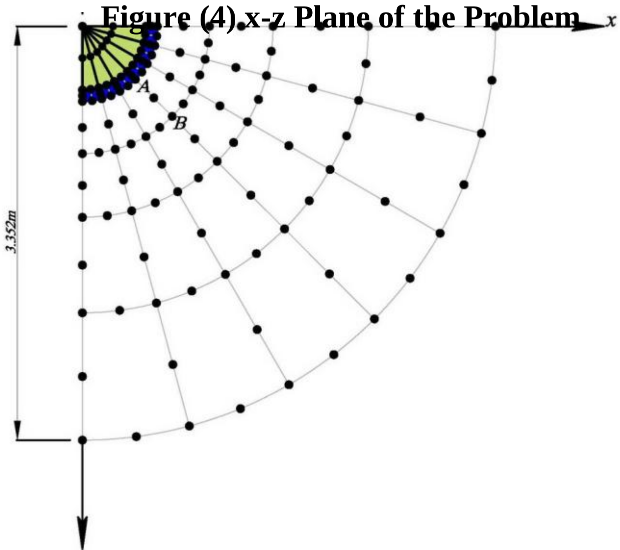

*y*

**Figure (5) x-y plane for problem number one.**

**Table (1) Material properties for case study number one (from Desai, 1978).**

| | |
|---|---|
| **Soil Properties** | |
| **Property** | **Value** |
| Undrained strength, $\mathbf{c_u}$ | 490 lb/ft$^2$ (23.9 kN/m$^2$) |
| Modulus of elasticity of the soil, $\mathbf{E_{soil}}$ | 44100 lb/ft$^2$ (2150 kN/m$^2$) |
| Poisson's ratio of the soil, $\boldsymbol{\nu_{soil}}$ | 0.35 |
| The adhesion factor, $\boldsymbol{\alpha}$ | 1.0 |
| Normal consolidation line slope, $\boldsymbol{\lambda}$ | 0.17 |
| Shear modulus, **G** | 15200 lb/ft$^2$ (725 kN/m$^2$) |
| Pore water pressure parameter in the triaxial state of stress, **A** | 1 |
| Unit weight of the soil, $\boldsymbol{\gamma_{soil}}$ | 110 lb/ft$^3$ (17.5 kN/m$^3$) |
| Permeability coefficient, $\mathbf{k_x=k_y=k_z}$ | 0.638×10$^{-4}$ ft/day (20×10$^{-6}$ m/day) |
| **Pile Properties** | |
| **Property** | **Value** |
| Modulus of elasticity of the pile, $\mathbf{E_{pile}}$ | 4.32×10$^8$ lb/ft$^2$ (21×10$^6$ kN/m$^2$) |
| Poisson's ratio of the pile, $\boldsymbol{\nu_{pile}}$ | 0.2 |
| Unit weight of the pile, $\boldsymbol{\gamma_{pile}}$ | 150 lb/ft$^3$ (24.0 kN/m$^3$) |
| **Interface Element Properties** | |
| **Property** | **Value** |
| Modulus of elasticity of the interface, $\mathbf{E_{interface}}$ | 44100 lb/ft$^2$ (2150 kN/m$^2$) |
| Poisson's ratio of the interface, $\boldsymbol{\nu_{interface}}$ | 0.41 |
| Unit weight of the interface, $\boldsymbol{\gamma_{interface}}$ | 110 lb/ft$^3$ (17.5 kN/m$^3$) |
| Adhesion, $\mathbf{c_a}$ | 0.3 (kPa) |
| Wall friction angle, $\boldsymbol{\delta}$ | 30$^o$ |

In Figure (9), the pore water pressure dissipation is calculated at location surface B-B shown in Figure (4). It is evident that values of the pore water pressures in section B-B are not much different from those obtained at section A-A. This may be attributed to the boundary conditions governing the problem and the small distance between the two sections.

**c. <u>Load Distribution Around The Pile</u>**:- Figure (10) shows the distribution of the load around the pile and at the tip for different depths and for several values of the load applied at the head of the pile.

**- <u>Case Study Number Two-Single Pile Analysis (After Ottaviani and Marchetti, 1977)</u>:-** A three-dimensional finite element mesh is used similar to Ottaviani and Marchetti's (1977) two-dimensional discretization. In that paper, results are compared between field data and those obtained from the finite element analysis conducted on the same problem. Analysis by the procedure proposed herein will be presented below.

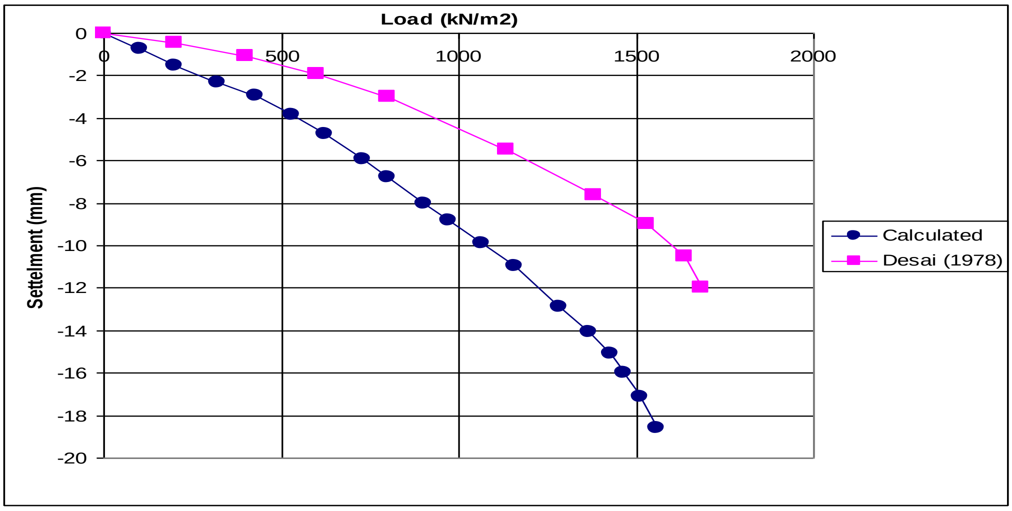


**Figure (6) Load-settlement curve.**

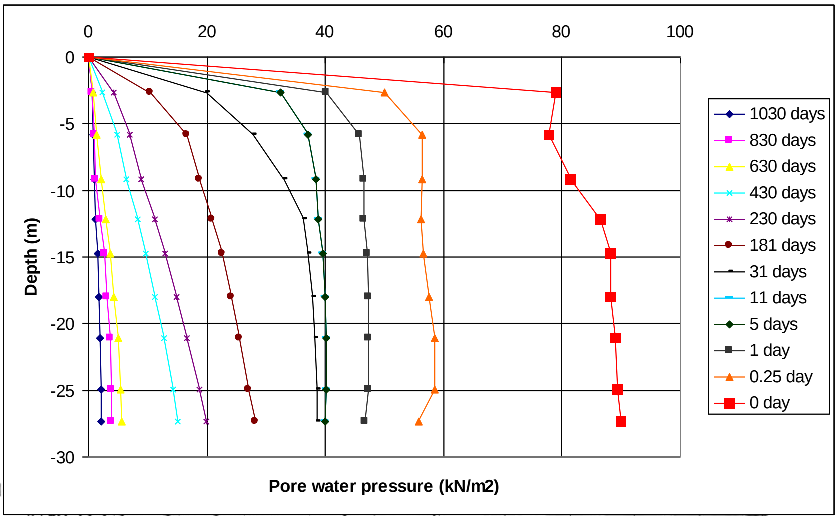


**Figure (7) Excess pore water pressure for section A-A.**

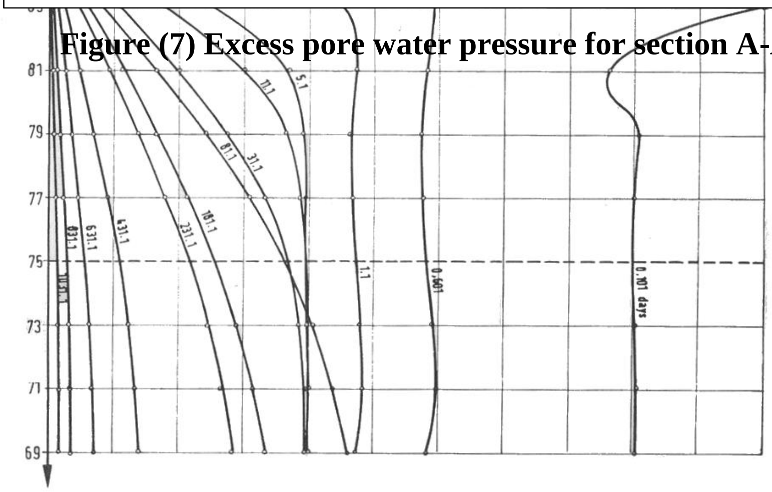

**Figure (8) Excess pore water pressures for section A-A (after Desai, 1978), ($1kN/m^2=0.04788LB/FT^2$).**

- **Mesh and Geometry:-** Figure (11) shows the three-dimensional finite element mesh for the single pile in clay with a diameter of (0.6)m and length of embedment of (23.5)m. The depth of the clay layer is (32)m. It is assumed to extend in the x and y directions about (4.5)m. The total number of three-dimensional brick elements employed in the current analysis is (1584) and the total number of nodes is (9993).

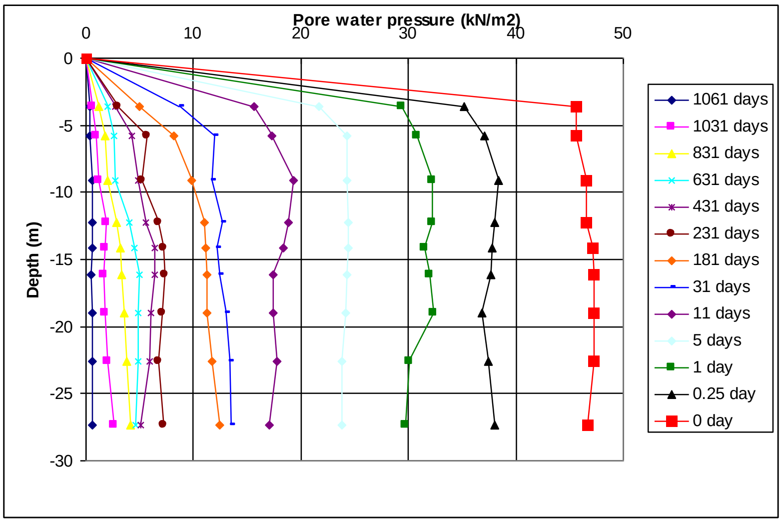


**Figure (9) Excess pore water pressure for section B-B.**

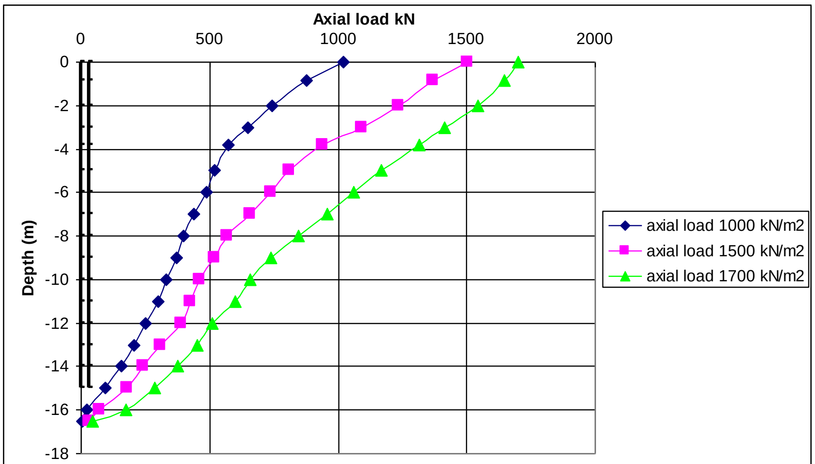


**Figure (10) Load distribution in the pile.**

- **Soil and Pile Properties:-** The material properties for this problem are presented in Table (2). Figure (12) shows the geotechnical properties of the soil at the location of the pile. It should be noted that during this study, the soil is assumed to be a homogeneous layer of a clayey deposit and that the properties of the thin layers of sand and the silt are neglected.

**- Loading:-** The total load applied vertically on the top of the pile is (3400) kN which is the ultimate load applied onto the pile.

**- Results:-**

**a. Load-Settlement Curve**:- Figure (13) shows a comparison between the load-settlement curve for the tip of the pile obtained from the current analysis and that predicted from strain cells at site. It shows a good agreement between the developed algorithm and the measured results. The percentage of differences between the two curves is about (8%) at ultimate load.

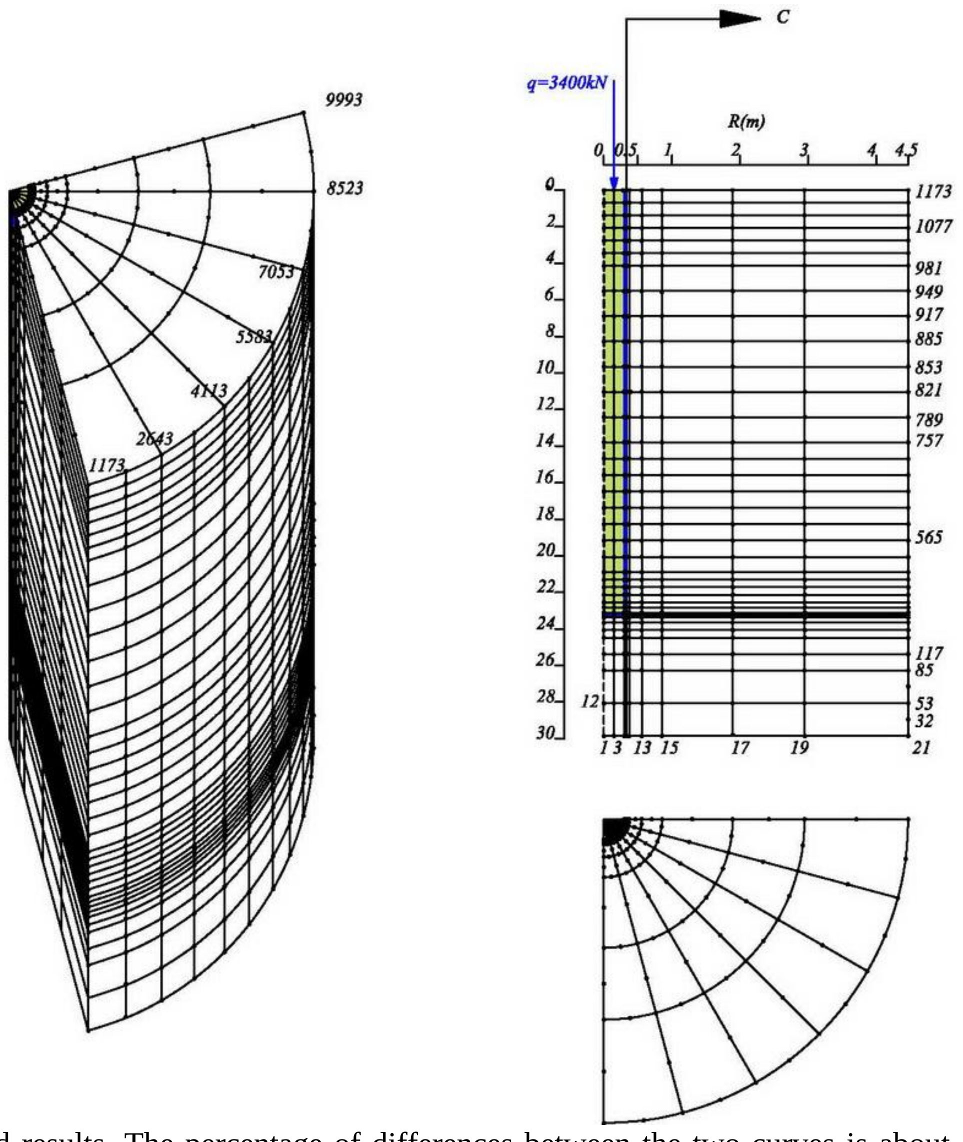


**Figure (11) Finite element mesh for the single pile in clay after Ottaviani and Marchetti, 1979.**

**b. Pore Water Pressure Dissipation**:- Figure (14) shows the pore water pressure dissipation at section C-C near the pile for different time steps. The curves seemed uniform and this may be attributed to the concentration of stresses and strains near the pile.

**c. Load Distribution Around the Pile**:- Figure (15a-d) shows a comparison of the distribution of the load around the pile between the observed and calculated at different depths for several values applied at the head of the pile. As can be noticed, a good agreement between the observed and the calculated bearing capacities is obtained for small load values while there are some differences under high loads.

**Table (2) Material properties for case study number two**

**(after Ottaviani and Marchetti, 1977).**

| **Soil Properties** | |
|---|---|
| **Property** | **Value** |
| Undrained strength, $\mathbf{c_u}$ | 120 $kN/m^2$ |
| Modulus of elasticity of the soil, $\mathbf{E_{soil}}$ | 1700 $kN/m^2$ |
| Poisson's ratio of the soil, $\boldsymbol{\nu}_{\mathbf{soil}}$ | 0.35 |
| The adhesion factor, $\boldsymbol{\alpha}$ | 1.0 |
| Normal consolidation line slope, $\boldsymbol{\lambda}$ | 0.15 |
| Unit weight of the soil, $\boldsymbol{\gamma}_{\mathbf{soil}}$ | 18.5 $kN/m^3$ |
| Permeability coefficient, $\mathbf{k_h=k_v}$ | $0.2\times10^{-4}$ m/day |
| **Pile Properties** | |
| **Property** | **Value** |
| Modulus of elasticity of the pile, $\mathbf{E_{pile}}$ | $2.2\times10^{7}$ $kN/m^2$ |
| Poisson's ratio of the pile, $\boldsymbol{\nu}_{\mathbf{pile}}$ | 0.25 |
| Unit weight of the pile, $\boldsymbol{\gamma}_{\mathbf{pile}}$ | 23.5 $kN/m^3$ |
| **Interface Element Properties** | |
| **Property** | **Value** |
| Modulus of elasticity of the interface, $\mathbf{E_{interface}}$ | 2000 $kN/m^2$ |
| Poisson's ratio of the interface, $\boldsymbol{\nu}_{\mathbf{interface}}$ | 0.45 |
| Unit weight of the interface, $\boldsymbol{\gamma}_{\mathbf{interface}}$ | 18.5 $kN/m^3$ |
| Adhesion, $\mathbf{c_a}$ | 92 (kPa) |
| Wall friction angle, $\boldsymbol{\delta}$ | $32^o$ |

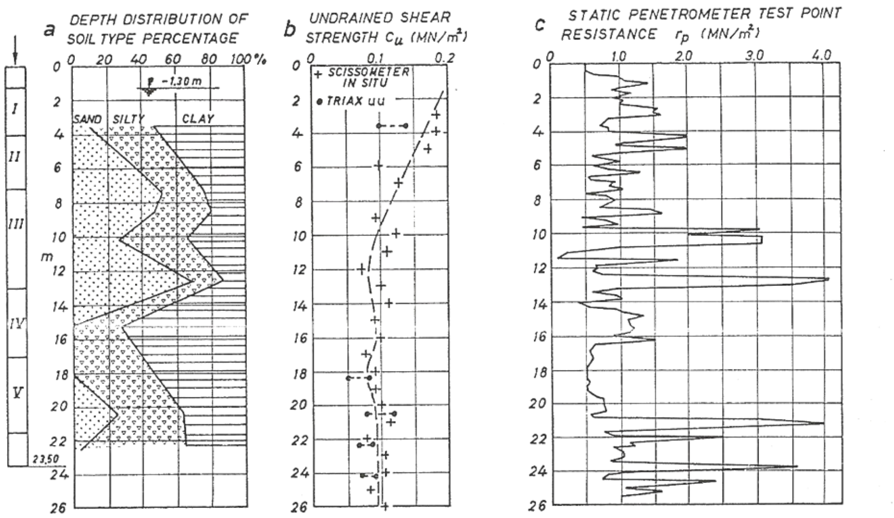

Figure (12) Geotechnical properties of case study number two after Ottaviani and Marchetti, (1979).

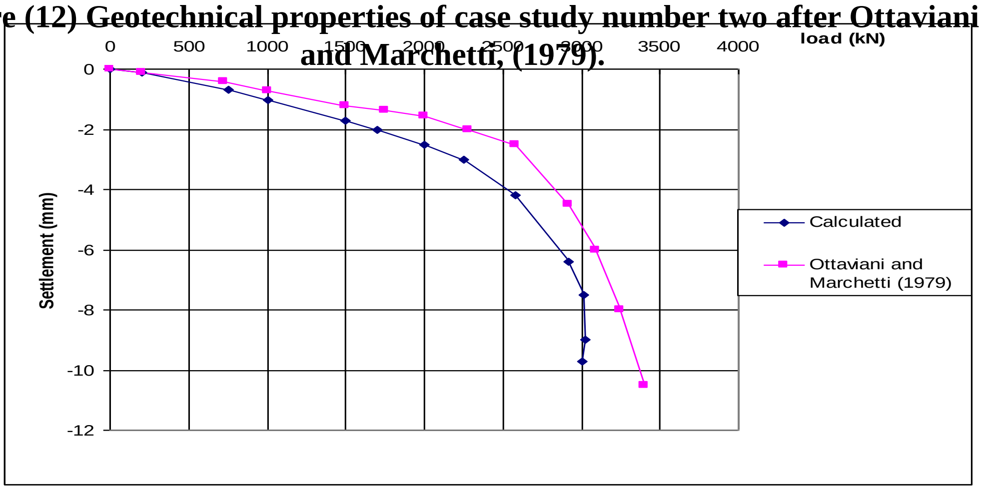


Figure (13) Load-settlement curve.

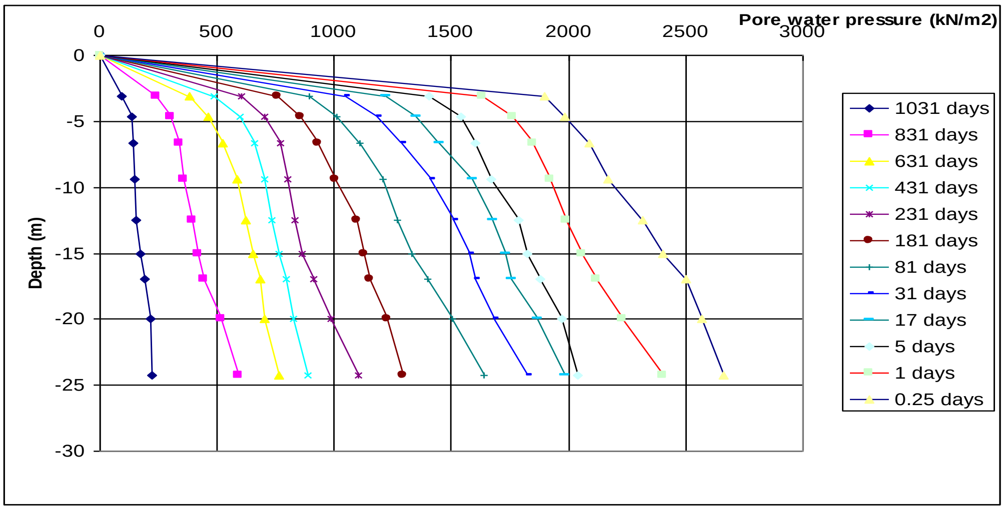


Figure (14) Pore water pressure dissipation.

**- <u>Case Study Number Three-Single Pile Analysis (After Seed and Reese, 1955)</u>:-** This problem is analyzed according to the research conducted by H. Bolton Seed and Lymon C. Reese (1955).

**- <u>Mesh and Geometry</u>:-** Figure (16) shows the three-dimensional finite element mesh for a single pile in clay with a diameter of (0.1524 m) and length of embedment of (22m).

**- <u>Soil and Pile Properties</u>:-** The material properties for this problem are presented in Table (3).

**- <u>Loading</u>:-** The total load applied vertically at the top of the pile is (8000) kN which is the ultimate applied load onto the pile.

**- <u>Results</u>:-**

**a. <u>Load-Settlement Curve</u>**:- Figure (17) shows a comparison among the load-settlement curve for the tip of the pile obtained from the present study and those predicted from the strain cells at site in addition to the finite element analysis results presented by the authors. A good agreement shows among these curves. The difference ratio between the curve obtained from the current finite element analysis and the observed values at end of loading is about (25%).

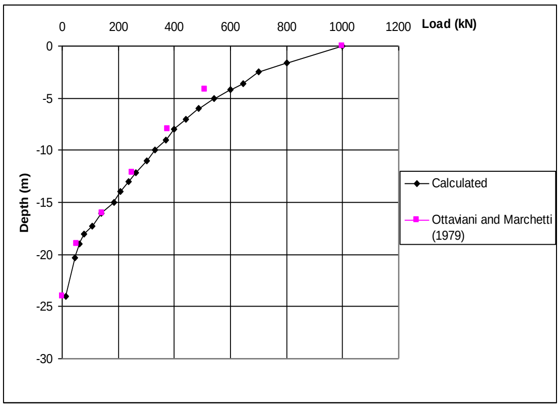


**-A-**

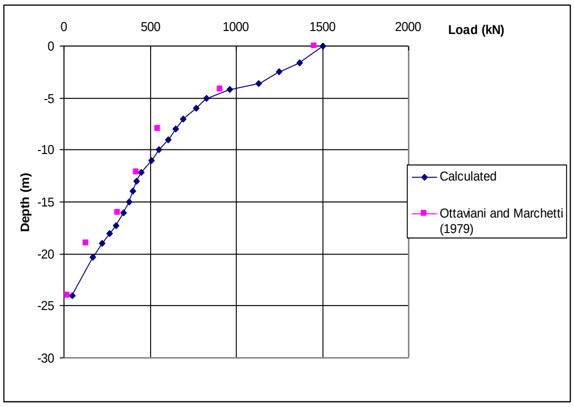


**-B-**

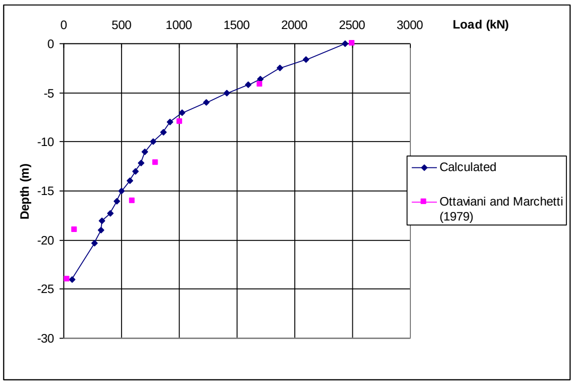


**-C-**

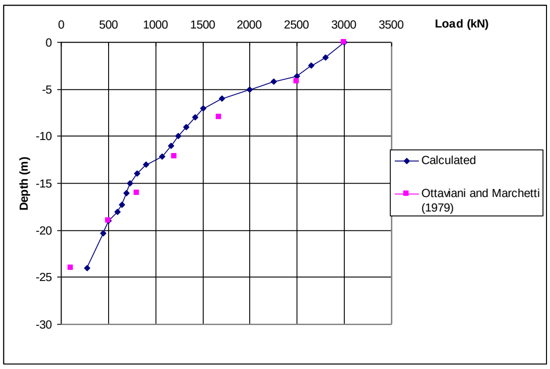


**-D-**

**Figure (15) Load distribution in the pile.**

**b. <u>Pore Water Pressure Dissipation</u>**:- Figure (18) shows the pore water pressure dissipation at section C-C near the pile for different time steps. The study conducted by Seed and Reese did not include pore water pressure measurements.

**c. <u>Load Distribution Around The Pile</u>**:- Figure (19) shows the distribution of the load in the pile at different depths for several values of the load applied at the head of the pile. The load-distribution curves for the pile showed that most of the load was removed from the pile by shaft resistance while only approximately 10% of the load reached the pile tip. The increased rate of load transfer was exhibited by soil strata at all depths. The load-distribution curves for all loadings showed a general increase in the rate of load transfer with depth with no load being removed by the soil near the ground surface.

## CONCLUSIONS:-

The following conclusions can be drawn herein with regard to the results obtained for the analysis of a single pile in elastoplastic clayey soils in three dimensions:

***1.*** For the single pile driven in clay analyzed by Desai (1978), when applying the developed algorithm based on ACED3 program herein, the following results have been obtained:-

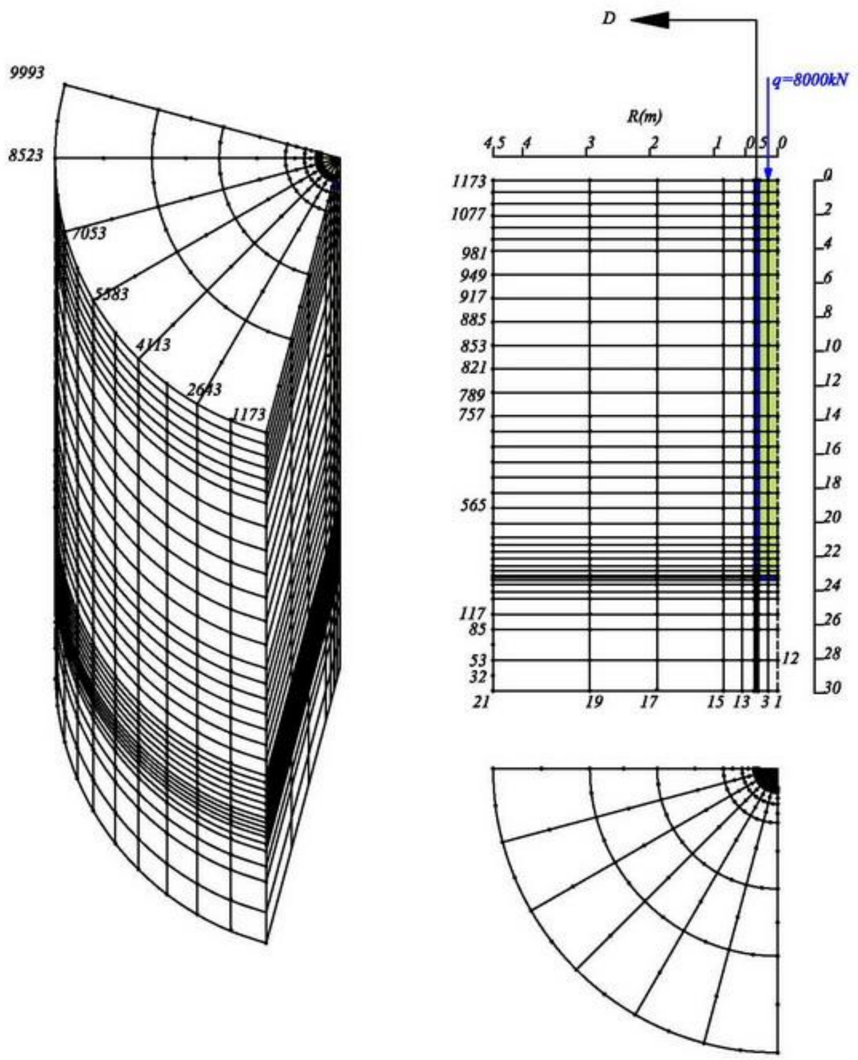


**Figure (16) Finite element mesh for the single pile in clay after Seed and Reese, 1955.**

**i.** For displacements at the tip of the pile, the maximum difference obtained at the end of loading is about 15%.

**ii.** For pore water pressure at a plane adjacent to and slightly away from the pile, the shapes of the dissipation curves of the pore water pressure isochrones were found similar to those obtained by Desai (1978).

***2.*** A single pile driven in a clayey soil was analyzed by Ottaviani and Marchetti (1977). When applying the developed algorithm onto the problem, the following conclusions are reached:-

**i.** For displacements at the tip of the pile, the maximum difference obtained at the end of loading is about 8%.

**ii.** For pore water pressure at a plane adjacent to and slightly away from the pile, the trend of the dissipation of the pore water pressure is found comprehensible.

| **Soil Properties** | |
|---|---|
| **Property** | **Value** |
| Undrained strength, $\mathbf{c_u}$ | 490 lb/ft$^2$ (23.5 kN/m$^2$) |
| Modulus of elasticity of the soil, $\mathbf{E_{soil}}$ | 44100 lb/ft$^2$ (2110 kN/m$^2$) |
| Poisson's ratio of the soil, $\boldsymbol{\nu_{soil}}$ | 0.35 |
| The adhesion factor, $\boldsymbol{\alpha}$ | 1.0 |
| Normal consolidation line slope, $\boldsymbol{\lambda}$ | 0.2 |
| Shear modulus, **G** | 15200 lb/ft$^2$ (725 kN/m$^2$) |
| Unit weight of the soil, $\boldsymbol{\gamma_{soil}}$ | 110 lb/ft$^3$ (17.0 kN/m$^3$) |
| Permeability coefficient, $\mathbf{k_h=k_v}$ | $0.638\times10^{-4}$ ft/day ($0.2\times10^{-4}$ m/day) |
| **Pile Properties** | |
| **Property** | **Value** |
| Modulus of elasticity of the pile, $\mathbf{E_{pile}}$ | $4.32\times10^8$ lb/ft$^2$ ($2.1\times10^7$ kN/m$^2$) |
| Poisson's ratio of the pile, $\boldsymbol{\nu_{pile}}$ | 0.25 |
| Unit weight of the pile, $\boldsymbol{\gamma_{pile}}$ | 150 lb/ft$^3$ (23.5 kN/m$^3$) |
| **Interface Element Properties** | |
| **Property** | **Value** |
| Modulus of elasticity of the interface, $\mathbf{E_{interface}}$ | 44100 lb/ft$^2$ (2110 kN/m$^2$) |
| Poisson's ratio of the interface, $\boldsymbol{\nu_{interface}}$ | 0.45 |
| Unit weight of the interface, $\boldsymbol{\gamma_{interface}}$ | 110 lb/ft$^3$ (17.0 kN/m$^3$) |

| | |
|---|---|
| Adhesion, $c_a$ | 0.3 (kPa) |
| Wall friction angle, $\delta$ | $30^o$ |

**Table (3) Material properties for case study number three**

**(after Seed and Reese, 1955).**

**iii.** The bearing resistance along the pile shaft and at the tip, and for different loading steps is found to be similar to those obtained by Ottaviani and Marchetti (1977).

***3.*** Finally, a problem of a prototype pile in a clay soil tested by Seed and Reese (1955) is considered. When the same pile is analyzed by the algorithm developed in this research, namely ACED3, the following conclusions are reached:-

**i.** For displacements at the tip of the pile, the maximum difference at the end of loading is about 25%.

**ii.** For pore water pressure at a plane adjacent to and slightly away from the pile, the trend of the dissipation of the pore water pressure is found to be in line with respect to similar patterns of geometry, boundary and loading conditions.

**iii.** The bearing resistance along the pile shaft and at the tip, and for different loading steps, is found to be similar to those obtained by Seed and Reese (1955).

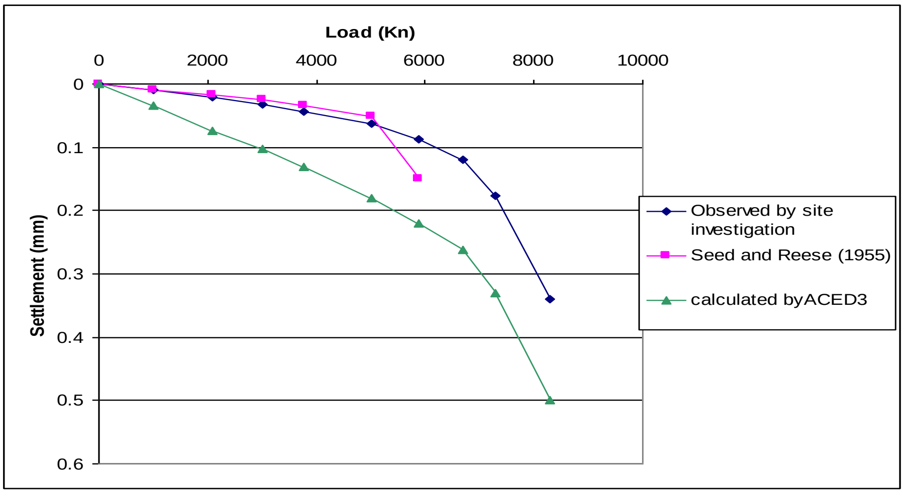


**Figure (17) Load-settlement curve.**

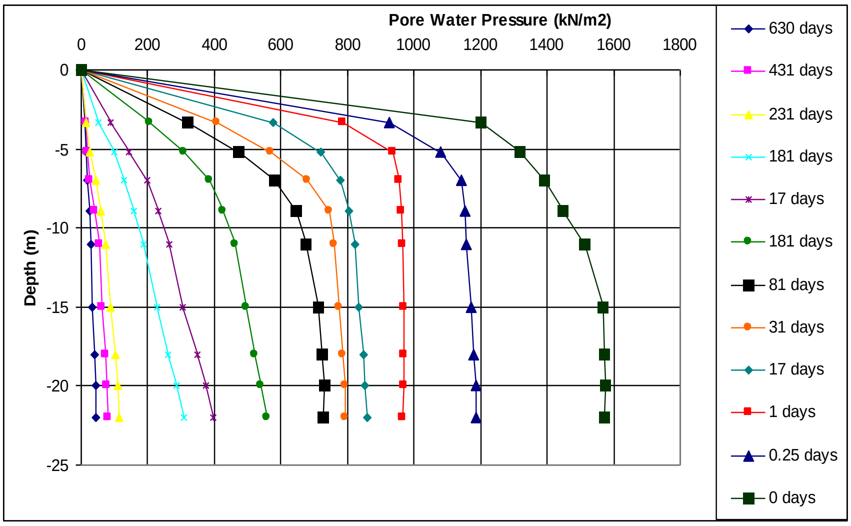


**Figure (18) Pore water pressure dissipation.**

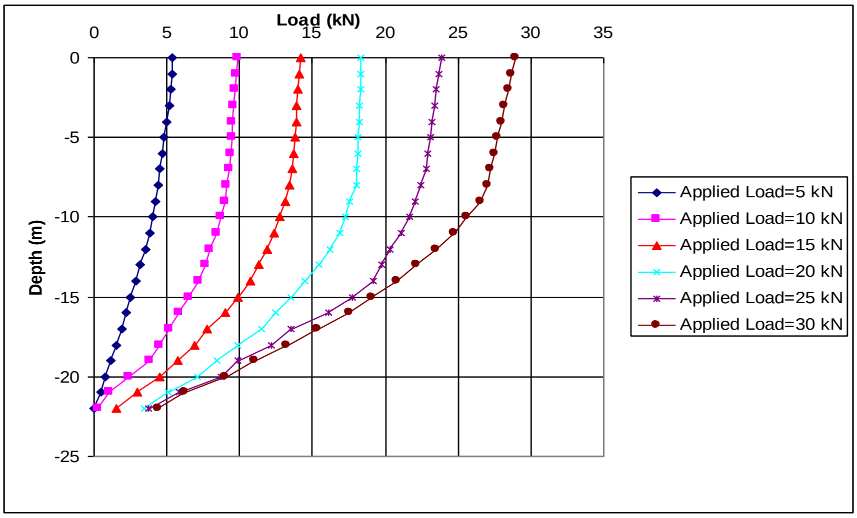


**Figure (19) Load around the pile.**

## REFERENCES:


- Al-Anbaki, "**Three-Dimensional Analysis of Single Pile in Clay By The Finite Element Method**", A thesis submitted to the Department of Civil Engineering of the University of Baghdad for the degree of Master of Science, 2006.

- Al-Baghdadi, N. H., (2006), "**Soil-Pile Analysis by the Finite Element Method**", A thesis submitted to the Civil Eng. Dept. of the University of Kufa for the partial fulfillment of the degree of Masters of Science.

- Al-Damluji, O. F., (1981),"**Non-Linear Soil Behaviour by Finite Element Method**", M.Sc. Thesis, College of Engineering, University of Baghdad, Iraq.

- Al-Damluji, O. F. S., (1994), "**Dynamic Penetration Contact Problems with Particular Reference to Porous Media**", Ph.D. Thesis, College of Engineering, University of Baghdad.

- Al-Marsumi, M. R., (2003), "**The Effect of Time on Concrete Piles by Three-Dimensional Finite Element Analysis**", A thesis submitted to the Building and Construction Engineering Dept. of the University of Technology, Baghdad, for the partial fulfillment of the degree of Doctorate of Science.

- Atkinson J. H. and Bransby P.L., (1978); "**The Mechanics of Soils, An Introduction to Critical State Soil Mechanics**", McGraw-Hill Book Company, London, UK.

- Bathe, K. J., (1996), "**Finite Element Procedures**", Prentice-Hall International.

- Bhowmilk, S., and Long, J. H., (1990); "**Application of a Bounding Surface Plasticity Model in the Analysis of Axially Loaded Piles**", Proceedings of the Third International Conference on Numerical Methods in Engineering: Theory and Applications (NUMETA 90), 7-11 January, 1990, University College of Swansea, Swansea, Wales, U.K.

- Biot, M. A., (1955), "**Theory of Elasticity and Consolidation for a Porous Anisotropic Solid**", Journal of Applied Physics, Volume 26, pp. 182-185.
- Biot, M. A., (1956), "**Theory of Propagation of Elastic Waves in a Fluid Saturated Porous Solid**". Journal of the Acoustical Society of America, Volume 28, No. 2, March, pp.168-191.

- Cooke R. W., Price G. and Tarr K., (1979); "**Jacked Piles in London Clay: A Study of Load Transfer and Settlement under Working Conditions**", Geotechnique, Volume 29, No.2, P.P. 113-147.

- Desai, C. S., (1978). "**Effects of Driven and Subsequent Consolidation on Behaviour of Driven Piles**", International Journal for Numerical and Analytical Methods in Geomechanics, Vol. 2, pp.283-301.

- Desai, C. S., and Siriwardane, H. J. (1984), "Constitutive Laws for Engineering Materials with Emphasis on Geologic Materials", Prentice-Hall, Inc., Englewood Cliffs, New Jersey.

- Grande L. and Nordal S., (1979); "**Pile-Soil Interaction Analysis on Effective Stress Basis**", Recent Developments in the Design and Construction of Piles, ICE, London.

- Kirby R.C. and Esrig M.I., (1979); "**Further Development of a General Effective Stress Method for Prediction of Axial Capacity for Driven Piles in Clay**", Recent Developments in the Design and Construction of Piles, ICE, London.

- Kuhlemeyer, R., (1979), "**Bending Element for Circular Beams and Piles**", ASCE Journal of the Geotechnical Engineering Div, Volume: 105 Number: GT2, pp 325-330.

- Lewis, R. W. and Schrefler, B. A., (1987), "**The Finite Element Method in the Deformation and Consolidation of Porous Media**", John Wiley and Sons Ltd., London.

- Maharaj D. K., Gayatri J. and Jayanthi D., (2004); "**Uplift Capacity of Pile by the Finite Element Method**", Electronic Journal of Geotechnical Engineering, Vol. 8, P.P.414-420.

- Ottaviani, M., and Marchetti, S., (1979), "**Observed and Predicted Test Pile Behaviour**", International Journal for Numerical Methods in Geomechanics, Vol. 3, pp. 131-143.

- Owen, D. R. J., and Hinton, E., (1980), "**Finite Elements in Plasticity-Theory and Practice**", Pineridge Press Ltd., Swansea.

- Pal S.C and Parikh S. K., (1980); "**Linear Axi-Symmetric Finite Element Analysis of Concrete Piles in Nonhomogenous Clay Soil**", Journal of Indian Geotehnique, No.3, vol.10, P.P. 185-202.

- Phoon, K. K., Quek, S. T., Chow, Y. K., and Lee, S. L., (1990) "**Reliability Analysis of Pile Settlement**", Journal of Geotechnical Engineering, ASCE, Vol. 116, No. 11, November 1990, pp. 1717-1735.

- Raheem, A. M., (2005), "**Pile-Soil Interaction Analysis on Effective Stress Basis**", a thesis submitted to Civil Eng. Dept. of the University of Baghdad for the partial fulfillment of the degree of Masters of Science.

- Randolph M. F. and Wroth C. P., (1978); "**Analysis of Deformation of Vertically Loaded Piles**", Geotechnique, Vol. 104, No. 12, P.P. 1465-1488.

- Randolph M.F., Carter J.P. and Wroth, (1979); "**Driven Piles in Clay-The Effects of Installation and Subsequent Consolidation**", Geotechnique, Vol. 29, No.4, P.P. 361-393.

- Reddy, J. N., (1984), "**An Introduction to the Finite Element Method**", McGraw-Hill International Editions.

- Saada, A. S., (1974), "**Elasticity, Theory and Application**", Pergamon Press Inc.

- Seed, H. B., and Reese, L. C., (1955), "**The Action of Soft Clay along Friction Piles**", Transactions of the ASCE, Vol. 23, No. 122, P.P. 731-754.

- Smith, I. M. and Griffiths, D. V., (1988), "**Programming the Finite Element Method**", 2nd Edition, John Wiley and Sons. Inc.

- Yasser, A. K. and Hassiotis, S., (2001); "**Analysis of Pile Soil Interaction**", Geotechnique, Vol. 22, No. 4, P.P. 103-115.


## LIST OF SYMBOLS:

$\alpha$ : time integration constant.

**$\alpha$:** adhesion factor.
**$\gamma_{interface}$** : Unit weight of the interface.
**$\gamma_{pile:}$** Unit weight of the pile.
**$\gamma_{soil:}$** Unit weight of the soil.
$\Delta t_k$: length of the k-th time step.
**$\delta$** : Wall friction angle.
$\delta\varepsilon$: small changes in strain.
$\delta\sigma'$: small changes in effective stress.
$\delta\lambda$: a positive scalar factor of proportionality dependent on the state of stress and loading history.
$\{\delta_i\}$: vector of nodal displacements of node (i).
$\lambda$: normal consolidation line slope.
$\xi$, , $\eta$ and $\zeta$ are the finite element local coordinates as defined by Figure (1).
$\nu$: Poisson's ratio.
**$\nu_{interface}$** : Poisson's ratio of the interface.
**$\nu_{pile:}$** Poisson's ratio of the pile,
**$\nu_{soil:}$** Poisson's ratio of the soil.
$\sigma_n$, $\sigma$, $\sigma_{nn}$: normal stress.
$\sigma'_{mo}$: isotropic effective stress.
$\sigma'_x$ , $\sigma'_y$, $\sigma'_z$: effective stresses in the x, y and z directions, respectively.
$\sigma_x$, $\sigma_y$, $\sigma_z$: total stress increments in x, y ,z directions, respectively.
$\sigma_1$, $\sigma_2$, $\sigma_3$: principal stresses acting on right angles to each other.
$\Omega$: total domain of the continuum.
[B]: strain-nodal displacement matrix (transformation matrix).
B: bulk modulus
C: creep function.
**$c_a$** : Adhesion.
**$c_u$** : Undrained strength.
[D]: stress-strain (constitutive) matrix.
$d\Omega$: domain of the integration.
$d\varepsilon$: total strain of the skeleton.
**$E_{interface:}$** Modulus of elasticity of the interface.
**$E_{pile:}$** Modulus of elasticity of the pile.
**$E_{soil:}$** Modulus of elasticity of the soil.
$d\varepsilon_c$: creep strain.
$d\varepsilon_p$: overall volumetric strains caused by uniform compression of the particles by the pressure of the pore fluid.
$d\hat{f}$ : change in external force due to boundary and body force loadings.
df: load vector equivalent to the body force, surface traction and autogenous strain, respectively.
E: modulus of elasticity of soil skeleton.
$f$: yield criterion.
$\bar{f}$ : load vector equivalent to fluid flow of source elements, creep function and gravity load, respectively.
{F}: vector of nodal forces,

G: shear modulus.
H: spatial flow (or seepage) matrix applied in three dimension form.
[J], $[J]^e$: Jacobian matrix in Cartesian coordinates.
K: Bulk modulus.
$K_0$: earth pressure coefficient at rest.
[K] : stiffness matrix.
$\mathbf{k_h}$,$\mathbf{k_v}$: horizontal and vertical permeability coefficients, respectively.
L: coupling matrix representing the influence of pore pressure in force equilibrium.
m: number of nodes per element.
$\mathbf{M_{cs}}$ : the slope of the critical state line.
$\{N_i\}$ = interpolation function of nodal point (i).
$\bar{\mathbf{p}}$ : pore pressures.
p: pore water pressure.
**p′:** mean effective stress.
$\mathbf{p'_c}(\boldsymbol{\varepsilon}^{\mathbf{p}}_{\mathbf{v}})$ is the preconsolidation pressure to which the soil has previously been subjected to during its past history. The superscript p for volumetric strain is for plastic.
**q:** deviatoric stress.
S: compressibility matrix.
t: time of consolidation.
u: displacement vector.
ū: displacements.
$\{X_i\}$: vector of coordinates of nodal point (i).
the superscript ( $^{\mathbf{T}}$ ) represents the transpose of the matrix.

Number 3 Volume 16 September 2010 Journal of Engineering

# PCCC MC-CDMA COMBINATION PERFORMANCE OVER MULTIPATH RAYLEIGH FADING CHANNEL

Husam Abduldaem. Mohammed
Assistant Lecturer \ Baghdad University\ College of Engineering\ Elec. & Comm. Dep.

**الخلاصة:**

هذا العمل يقدم محاكاة ل Parallel Concatenation Convolution Coding PCCC مع رمز الناقل المتعدد الوصول (MC-CDMA) عبر قناه الخفوت متعدد المسار multipath fading channel مع مقارنة لحالة المعلومات الغير المشفرة و المعلومات التي تستخدم Serial Concatenation Convolution Coding SCCC. تقنية فك الشفرة المستخدمة في المحاكاة كانت فك الشفرة المتكررة حيث تعطي اقصى كفاءة مع ان هناك تحسين بالاست تكرارات . تم استخدام تضمين phase shift keying مع M = 2, 4, 8 and 16 مع مزج تقسيمات التردد المتعامده OFDM. نموذج القناة المتستخدم هو نفسه المخصص 3GPP مع مواصفات تقنية TS 25.101 v2.10 وعرض نطاق قناة قدره 5MHz.
من خلال العمل لوحظ ان هناك تحسين بالاداء بالنسبة لل PCCC نسبة الى SCCC و المعلومات غير المشفرة بدلالة ال Signal to Noise Ratio (SNR) بمقدار عدة dBs كما موضح بالجدول رقم (2).

**ABSTRACT**

This work presents the simulation of a Parallel Concatenation Convolution Coding PCCC with Multi-Carrier Code Division Multiple Access (MC-CDMA) system over multipath fading channels with a comparison with the uncoded data and that uses Serial Concatenated Convolutional Coding SCCC. The decoding technique used in the simulation was iterative decoding since it gives maximum efficiency with six iteration. Modulation schemes that used are Phase Shift Keying (BPSK, QPSK and 16 PSK), along with the Orthogonal Frequency Division Multiplexing (OFDM). The channel models used are as specified in the Third Generation Partnership Project (3GPP) Technical Specification TS 25.101v2.10 with a channel bandwidth of 5 MHz.
It was noticed that there is an improvement in the performance of the use of the PCCC data over the SCCC and uncoded data of SNR by many dBs as summarized in table [2] but with 8 and 16 PSK modulation schemes with the multipath fading channel a convergence of the BER to $10^{-4}$ cannot be obtained and it remains fluctuating around BER of $10^{-2}$.

## INTRODUCTION

Future wireless systems such as fourth generation (4G) cellular will need flexibility to provide subscribers with a variety of services such as voice, data, images, and video. Meanwhile, multicarrier CDMA (MC-CDMA) has emerged as a powerful alternative to conventional direct sequence CDMA (DS-CDMA) in mobile wireless communications [1, 2], that has been shown to have superior performance to single carrier CDMA in multipath fading. The attractive features derived from the CDMA-OFDM combination makes MC-CDMA a firm candidate for the next generation of wireless system [3, 4]. Since 1993, MC-CDMA rapidly has become a topic of research. Wireless mobile communication systems present several design challenges resulting from the mobility of users throughout the system and the time-varying channel (Multi-path fading). There has been an increasing demand for efficient and reliable digital communication systems. To tackle these problems effectively, an efficient design of forward error coding (FEC) scheme is required for providing high coding gain. To obtain high coding gains with moderate decoding complexity, concatenation of codes with iterative decoding algorithms has proved to be an attractive scheme.

In iterative decoding, instead of extracting all information from the received symbols and the knowledge about the code in a single run, it is done during several iterations with successively better reliability of the result. On the contrary, iterative decoders only extract little new information during every iteration which is added to the previously extracted information.

## MC-CDMA SYSTEM DESCRIPTION

The generation of an MC-CDMA signal can be described as shown in Figures 1 and 2, a single data symbol is replicated into N parallel copies. Each branch of the parallel stream is multiplied by one chip of a spreading code of length N [5]. The resulting chips are then fed to a bank of orthogonal subcarriers. As is commonly done in MC-CDMA, it is assumed that the spreading sequence length N equals the number of subcarriers. However, this scheme can be generalized to the case where the number of carriers is a multiple of the spreading sequence length allowing in this way the simultaneous transmission of several symbols from the same user. Carrier modulation is efficiently implemented using the inverse fast Fourier transform (IFFT) [3].

After parallel-to-serial (P/S) conversion, a cyclic prefix (CP) is appended to the resulting signal to minimize the effects of the channel dispersion. It is assumed that the CP length exceeds the maximum channel delay spread and therefore, there is no interference among successively transmitted symbols (i.e. there is no interblock interference).

The transmitted signal corresponding to the $k^{th}$ data bit of the $m^{th}$ user ($a_m[k]$) is given by [5]

$$S_m = \sum_{i=0}^{N-1} c_m[i]\, a_m[k] \cos(2\pi f_c t + 2\pi i \frac{F}{T_b} t)\, p_{T_b}(t - kT_b) \qquad [1]$$

$$c_m[i] \in \{-1, 1\}$$

where $c_m[0]$, $c_m[1]$, ... , $c_m[N-1]$ represents the spreading code of the $m^{th}$ user and $p_{Tb}(t)$ is defined to be an unit amplitude pulse that is non-zero in the interval of [0, Tb]. The input data symbols, $a_m[k]$, are assumed to takes on values of -1 and 1 with equal probability.

At the receiver side, opposite operation to that done at the transmitter are done. These operations are the OFDM demodulation, dispreading, MPSK demodulation, demapping and the PCCC decoding.

## Parallel and Serial Concatenated Convolutional (PCCC and SCCC) Encoding

The convolutional turbo coder consists of a parallel concatenation of recursive systematic convolutional RSC encoders separated by a pseudo-random interleaver [6]. The main aim of RSC is to produce more high weight codes even though input contains more number of zeros [7]. The stream of input bits is fed to the first encoder without any modification and is randomly interleaved for the second encoder. A natural rate for such a code is 1/3 (one systematic bit and two parity bits for one data bit). The rate can be relatively easy increased by puncturing the parity bits but reducing the rate below 1/3 is more difficult and may involve repetition of some bits [6]. The structure of such a parallel concatenated convolutional code (PCCC) is shown in Figure (3).

One important feature of turbo codes is the iterative decoding which uses a soft-in/soft-out (SISO) like MAP (Maximum A Posteriori) decoding algorithm which was first applied to convolution

codes by Bahl Cocke, Jelink and Raviv also known as (BCJR) algorithm [8]. In iterative decoding, there are two SISO decoders where the extrinsic information obtained from decoding process is exchanged between them [6]. MAP algorithm gives optimal estimate of information symbols given the received data sequence. In MAP decoding scheme the fact that it gives the maximum MAP estimate of each individual information bit is crucial in allowing the iterative decoding procedure to converge at very low SNR's although soft output Viterbie algorithm SOVA can also be used to decode turbo codes but a significant improvements can be obtained with MAP algorithm. This algorithm requires a forward and backward recursion and is therefore suitable for block oriented processing since turbo code is a block oriented process this algorithm. The MAP algorithm calculates the posterior probability (APP) of each state transition massage bit. The log-MAP algorithm is the most complex of the algorithms used when implemented in software, but generally offers the best bit error rate (BER) performance. The max-log-APP decoding scheme is an approximation of the log-APP decoding and is widely used in practice because of its reduced computational complexity [8].
The Max-Log-MAP (MLMAP) algorithm is a good compromise between performance and complexity [9]. It is very simple and, with the correction operation, also very effective [10]. Compared to the MAP/Log-MAP algorithm no SNR-information is necessary and the critical path within the add-compare-select (ACS) unit is shorter because of the maximum operation without the correction term [11]. The performance is better than the standard SOVA algorithm and reaches nearly the optimal performance results of the MAP/Log-MAP algorithm.
The decoding is done for each inner code vector. The decoded bits are then decoded again according to the outer code used [12]. It consists of two soft input soft output SISO [14] modules connected in a ring.
The Turbo decoding process is done in an iterative manner. SISO decoding of the convolutional subcodes is done with the use of a-priori information of previous decoding steps. Here only relevant formulas of the used Max-Log-APP MLMAP algorithm are given.

Like other methods max-log-APP algorithm calculates approximate log-likelihood ratios LLR's for each input sample as an estimate of which possible information bit was transmitted at each sample time[10].They are calculated according to[10,11]

$$L_i = \max_m [A_i^m + D_i^{0,m} + B_{i+1}^{f(0,m)}] - \max_m [A_i^m + D_i^{1,m} + B_{i+1}^{f(1,m)}] \qquad [2]$$

where i is the sample time index, m $\in\{0, \dots, N_s-1\}$ is the present state, $N_s$ is the number of encoder states, f(d, m) is the next state given present state m and input bit d $\in \{0,1\}$, $A_i^m$ is the forward state metric for state m at time i, $B_i^m$ is the reverse or backward state metric for state m at time i, and $D_i^{d,m}$ is the branch metric at time i given present state m and input bit d$\in\{0,1\}$. The forward state metrics are calculated starting at the first sample received in the block and moving forward in time to the last sample received. The reverse state metrics are calculated starting at the last sample received and moving backward in time to the first sample received. More formally, the state and branch metrics are given by

$$A_i^m = \max [A_{i-1}^{b(0,m)} + D_{i-1}^{0,b(0,m)}, A_{i-1}^{b(1,m)} + D_{i-1}^{1.b(1,m)}] \qquad [3]$$

$$B_i^m = \max [D_i^{0,m} + B_{i+1}^{f(0,m)}, D_i^{1.m} + B_{i+1}^{f(1,m)}] \qquad [4]$$

$$D_i^{d,m} = \frac{1}{2}(x_i d' + y_i c'^{d,m}) \qquad [5]$$

where b(d,m) is the previous state given present state m and previous input bit d∈{0,1}, $x_i$ is the $i^{th}$ systematic sample, $y_i$ is the $i^{th}$ parity sample, d is a systematic bit, $c^{d,m}$ is the corresponding coded bit given state m and bit d, $d'^{d,m}$ =1-2d , and $c'^{d,m} = 1-2c^{d,m}$. The state metrics provide a measure of the probability that state m is the correct one at time i, while the branch metrics are a measure of the probability that each possible combination of encoder outputs is the correct one given the channel outputs $x_i$ and $y_i$.

Note that in contrast to the true-APP or log-APP algorithms, no estimate of the channel signal-to-noise ratio (SNR) is required. It is apparent that metric combining involves adding up all of the metrics associated with a given branch in the trellis, with each sum being an input to one of the max[.] operations in (2).

The calculations in (3) and (4) are exactly the Viterbi algorithm without history and will therefore find the same winning path through the decoding trellis given the same inputs and initial conditions. The max-log-APP algorithm is sub-optimum due to the approximations involved. However, most of the performance loss associated with this suboptimality can be recovered by applying a simple scale f onstituent decoder. The so-called extrinsic information may l

$$L_{ex}^{n} = sf \cdot \left(L_{out}^{n} - L_{in}^{n}\right) \qquad [6]$$

where $n \in \{1,2\}$ denotes one of the constituent decoders, $L_{out}^{n}$ represents the set of LLRs produced by the max-log-MAP decoder, $L_{in}^{n}$ represents the set of input LLRs, and *sf* is an appropriate scale factor. Corrected LLRs are then calculated according to

$$L_{cor}^{n} = L_{in}^{n} + L_{ex}^{n} \qquad [7]$$

These corrected LLRs are the systematic input to the next constituent decoder, while the extrinsic information $L_{ex}^{n}$ is fed back to be subtracted off on the next iteration. It has been found that setting *sf* = 5/8 = 0.625 typically yields performance within 0.1 dB to 0.2 dB of a true-APP decoder given the same number of iterations. At the same time, using this method vastly reduces the amount of computation required.

While in SCCC, only the inner code must be recursive systematic convolutional RSC. The information bits are encoded by the outer encoder and the resulting code bits are interleaved by the bit wise random interleaver and become the information bits of the inner encoder. The outer code with a rate $R_o = k/p$ and the inner code with rate $R_i = p/n$ joined by an interleaver of length N bits, generating an SCCC with rate $R_c = k/n$. Note that N must be an integer multiple of p [14]. For more details about the SCCC decoding refer to [15].

## SIMULATION RESULTS

The proposed system is illustrated in Figure [5]. A 20 Mbps was transmitted over the system. Since the channel for the $4^{th}$ generation is not developed yet, therefore, the 3.5 G channel specifications was used in the simulation process. These channels are AWGN and frequency selective fading channels. The modulation schemes are the MPSK with M=2, 4 and 16. The simulation was performed using Matlab program version R2008b.

First, a simulation of MC-CDMA system that utilized the parallel concatenated coded data PCCC was achieved with AWGN channel and for multipath fading channel. First, the input binary data generated at the transmitter side is encoded with the parallel concatenated convolutional coder with both the upper and lower coder of a generator polynomial of [1 0 1 1; 1 1 0 1] ) polynomial generators and a constraint length of (4). With the MAP decoding algorithm which is an iterative decoding algorithm. The performance of the concatenated convolutional code system depends upon the number of iteration of the decoder.
The same work was repeated with the serially concatenated convolutional code with the outer coder of a generator polynomial in octal of (3, [7 5], 7) while the inner one has a ([3 3], [7 0 5; 0 7 6], [7 7]) generator polynomial. The random interleaver length was 1024 in both cases.

Table [1] summaries the system specifications for the AWGN and frequency selective fading channels [16] while figure (6) shows the flow chart of the proposed system.

The performance characteristics of the proposed system shown in figures (7, 8, 9 and 10) for binary, 4, 8 and 16 PSK modulation techniques respectively. The figures also contain comparison of the system with the PCCC data with that uses serially concatenated code and uncoded data.

**Table 1-Simulation parameters for the AWGN channel**

| Available bandwidth | 5 MHz |
|---|---|
| FFT sampling rate | 5 MHz |
| Spreading code | Hadamard Walsh |
| Spreading factor | 32 |
| FFT size | 512 |
| Subcarrier spacing | 2.4414 kHz |
| Effective symbol duration | 409.6 μs |
| Guard time duration | 102.4 μs |
| MC-CDMA symbol duration | 128 μs |
| Modulation technique | BPSK, QPSK, 8PSK & 16PSK |
| No. of iterations | 6 |

Figures (11, 12 and 13) show a comparison of the BER versus symbol signal power to the noise power) $E_s/N_o$ for MC-CDMA system with PCCC, SCCC and uncoded data with multipath fading channel and 2,4,and 8 PSK modulation techniques respectively.

Table [2] summarizes the obtained results as a comparison of SNR in dB for the selected channels; AWGN channel, Multipath fading channel for modulation techniques of BPSK, 4 PSK and 16 PSK with uncoded, serially concatenated convolutional coded (SCCC) data and parallel concatenated convolutional coded (PCCC) data.

**Table [2]: A comparison of SNR in dB for Uncoded, SCCC and PCCC data for BER of $10^{-4}$.**

| MPSK | SNR/dB for AWGN channel | | | SNR/dB for multipath fading channel | | |
|---|---|---|---|---|---|---|
| | Uncoded | SCCC | PCCC | Uncoded | SCCC | PCCC |
| 2 PSK | 21 | 16.5 | 12 | 24 | 15 | 8 |
| 4 PSK | 25 | 18.1 | 16 | 28 | 21.5 | 11.2 |
| 8 PSK | 29 | 23 | 17 | - | - | - |
| 16 PSK | 34 | 27 | 22.5 | - | - | - |

## CONCLUSION:

The use of the parallel concatenated convolutional coded (PCCC) technique in conjunction with the MC-CDMA system improved the performance of the system over that which uses the uncoded or serially concatenated convolutional coded (SCCC) data. It can be noticed that there is an improvement in the results of the use of the PCCC data over the others as summarized in table 3.
It can be noticed that with 8 and 16 PSK modulation schemes with the multipath fading channel a convergence of the BER to $10^{-4}$ cannot be obtained and it remains fluctuating around BER of $10^{-2}$.

## REFERENCES


- J. G. Andrews and T. H. Meng, “Performance of multicarrier CDMA with successive interference cancellation in a multipath fading channel,” IEEE Transactions on Communications, vol. 52, pp. 811–822, May 2004.

- L. L. Yang and L. Hanzo, “Multicarrier DS-CDMA: a multiple access scheme for ubiquitous broadband wireless communications,” IEEE Communications Magazine, vol. 41, pp. 116–124, October 2003.

- Felip Riera-Palou, Guillem Femenias & Jaume Ramism, Performance Analysis of Multiuser Detectors for Uplink Quasi-synchronous MC-CDMA Systems Wireless Personal Communications Volume 43, Number 4, 2007.

- Fazel, K., & Kaiser, S. (2005). Multi-carrier and spread spectrum systems. New york: Wiley.

- Nathan Yee, Jean-Paul Linnartz and Gerhard Fettweis, "Multi-carrier CDMA in indoor wireless radio networks", IEICE Transaction on Communications, Japan, Vol. E77-B, No. 7, July 1994, pp. 900-904.

- Ramasmay K., Mohammed U. S., mohammed Y. A. and A. Arunagiri, " Performance comparison of convolutional and block codes",IEICE Electronic Express, V. 3, N. 13, pp, 322-327, 2006.

- Shanmugam A., A. R. Abdul Rajak, "Optimal design of forward error correcting codes for wireless communication", Academic open Internet journal, V. 14, 2005, http://www.acadjournal.com/.

- Bahl, J. L. Cocke, F. Jelinek, and J. Raviv, “Optimal decoding of linear codes for minimizing symbol error rate,” *IEEE Trans. Inform. Theory*, vol. IT-20, pp. 284–287, Mar. 1974.

- Vogt J., K. KOORA, A. FINGER and G. FETTWEIS: "Comparison of Different Turbo Decoder Realizations for IMT-2000", in Proc. of the IEEE GLOBECOM '99, Rio de Janeiro, Dec. 1999, pp. 2704-2708.

- Robertson P., E. Villebrun, and P. Hoeher, “A Comparison of Optimal and Sub-Optimal MAP Decoding Algorithms Operating in the Log Domain”, Proceedings of the 1995 International Conference on Communications (ICC’95), Seattle, WA, USA, pp. 1009-1013, June 1995.

- Robertson, P. Hoeher, and E. Villebrun, “Optimal and Sub-Optimal Maximum a Posteriori Algorithms Suitable for Turbo Decoding”, *IEEE Communications Theory*, Vol. 8, No. 2, pp. 119-125, March-April 1997.

- G. D. Forney Jr., Concatenated Codes, MIT Press, Cambridge, Mass,1966.

- Yang L. L. and L. Hanzo, “Multicarrier DS-CDMA: a multiple access scheme for ubiquitous broadband wireless communications,” *IEEE Communications Magazine*, vol. 41, pp. 116–124, October 2003.

- Sergio, Dariush Divsalar, Guido Montorsi and Fabrizio Pollara, "Serial concatenation of Interleaved Codes: Performance Analysis, Design, and Iterative Decoding", IEEE Transactions on information theory, V. 44, No. 3, May 1998.

- Aqiel N. Almaamory, Husam A. Mohammed, " SCCC-MCCDMA combination performance over multipath Rayleigh fading channel", to be published Kerbalaa university.

- Minh-Quang Nguyen, Paul Fortier and Sébastien Roy, "Simulation of MC-CDMA systems", Defence R&D Canada – Ottawa, November 200


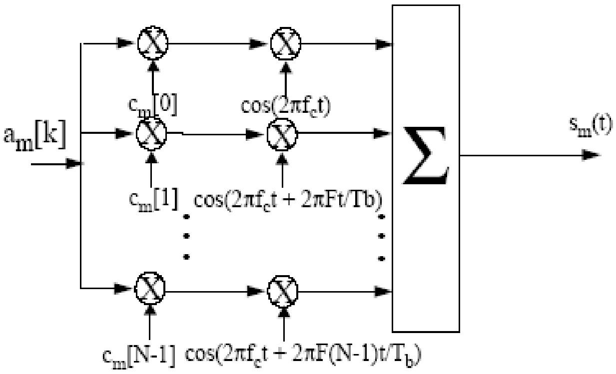


**Figure (1) MC-CDMA transmitter**

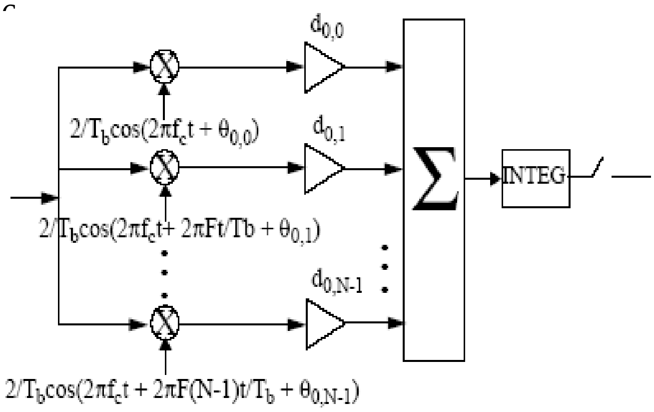


**Figure (2) MC-CDMA receiver**

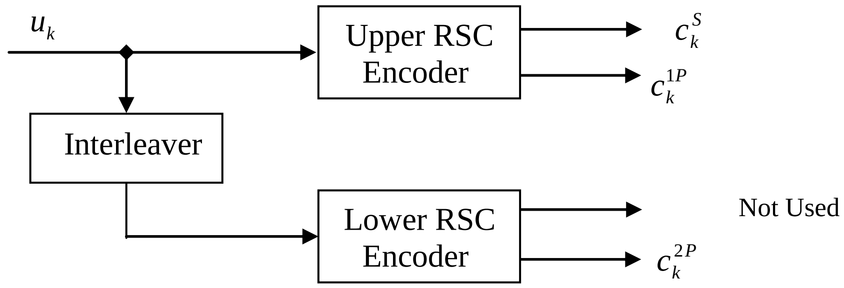


**Figure (3) Parallel concatenation convolutional code (PCCC) Encoder**

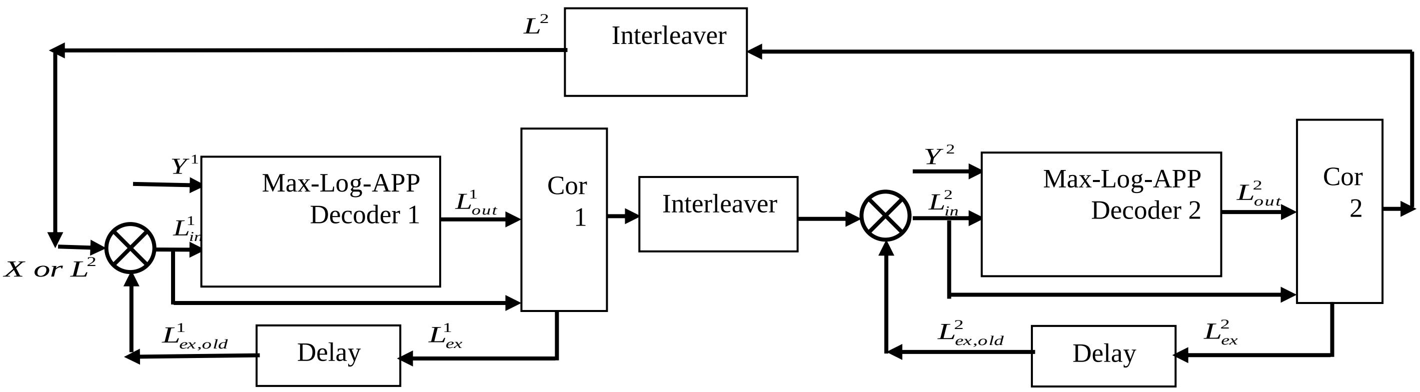


Figure (4): block diagram of the Max-Log-MAP decoding for the PCCC scheme and scale factor correction.

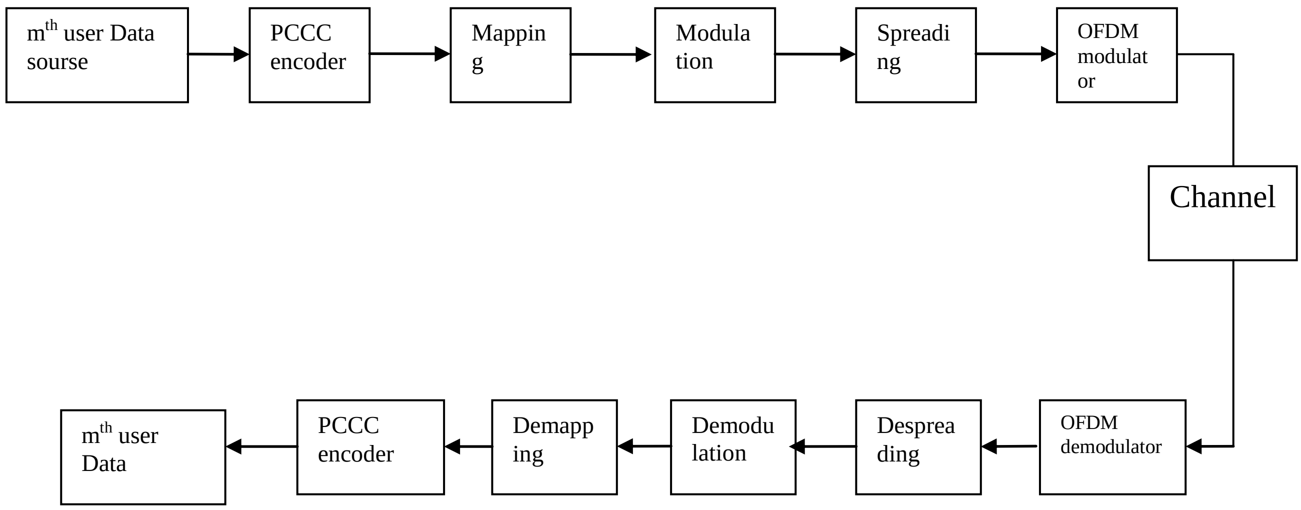


**Figure (5) block diagram of the serially convolutional coded MC-CDMA system.**

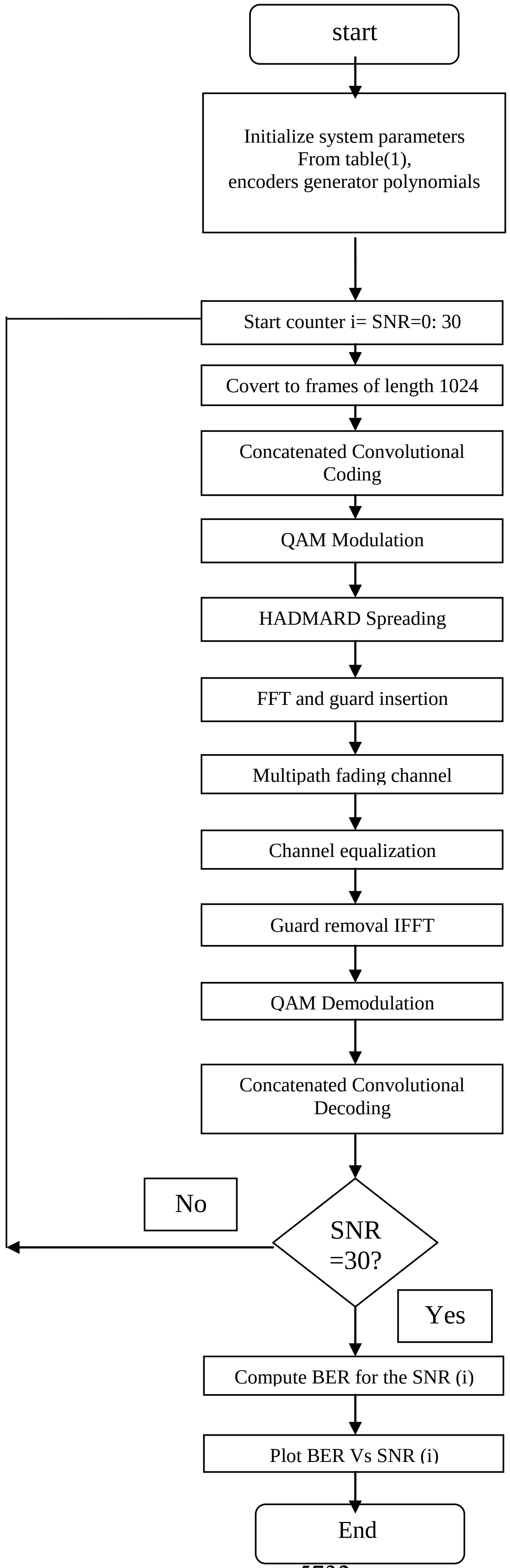




**Figure (6): flow chart of the proposed system**

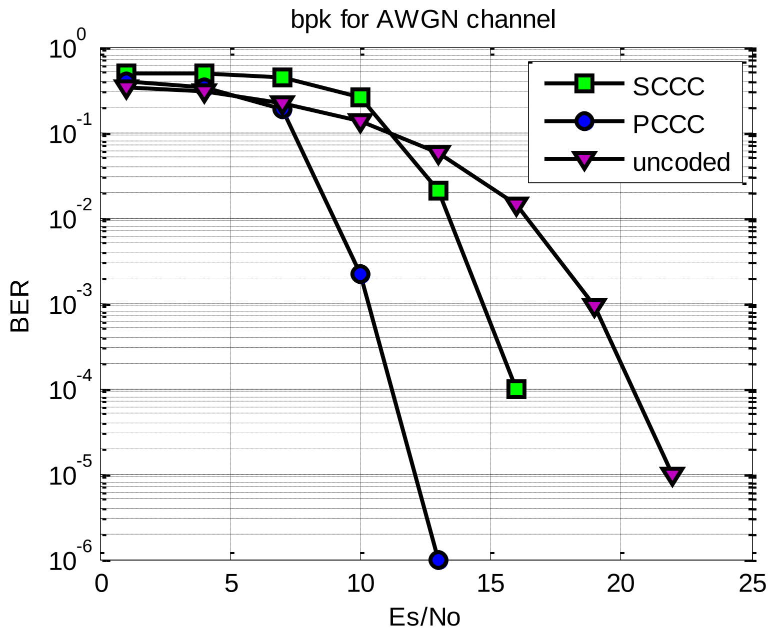


**Figure (7) BER Vs SNR for AWGN channel with M=2**

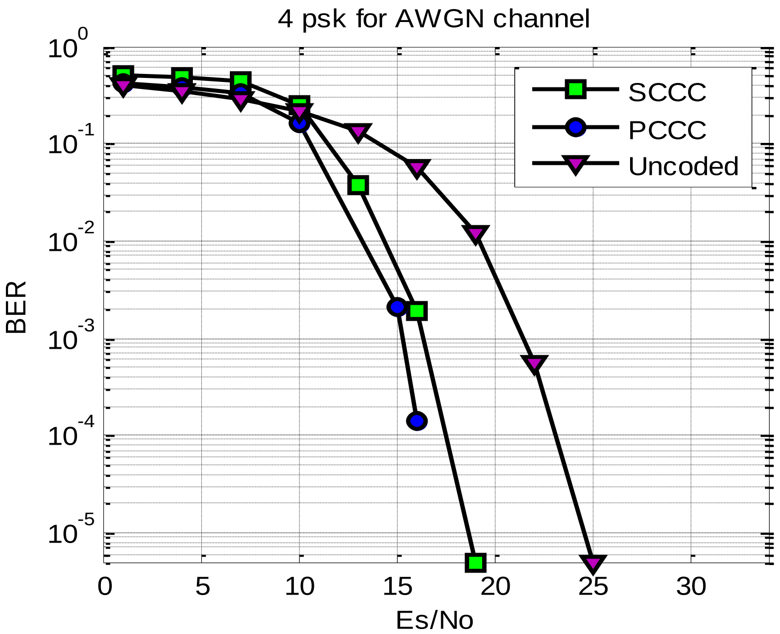


**Figure (8) BER Vs SNR for AWGN channel with M=4**

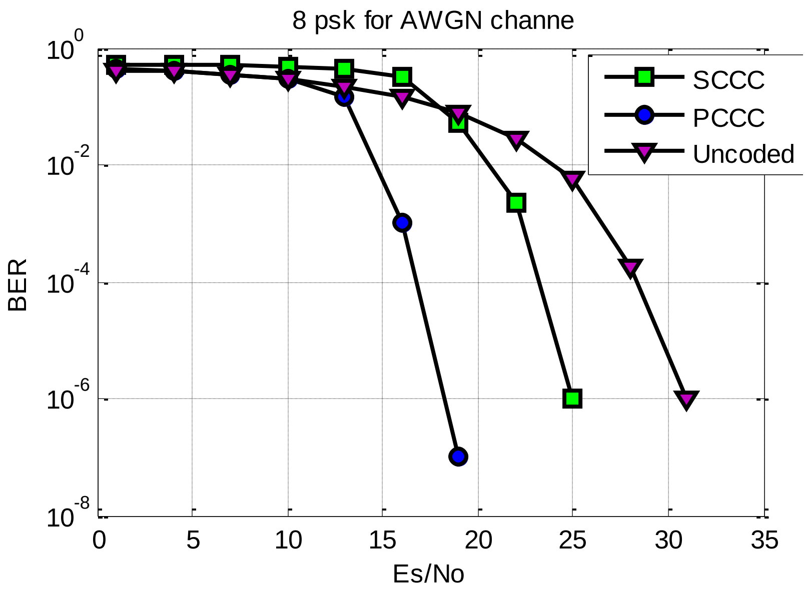


**Figure (9) BER Vs SNR for AWGN channel with M=8**

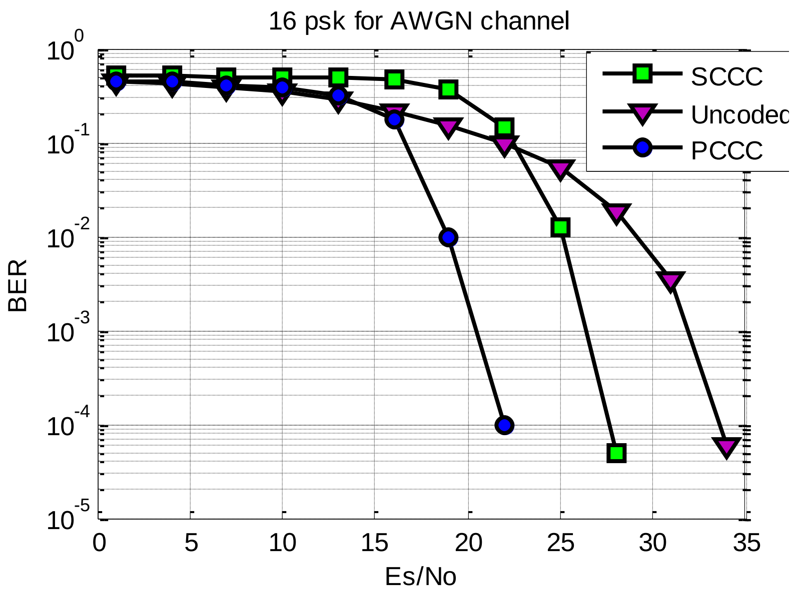


**Figure (10) BER Vs SNR for AWGNchannel with M=16**

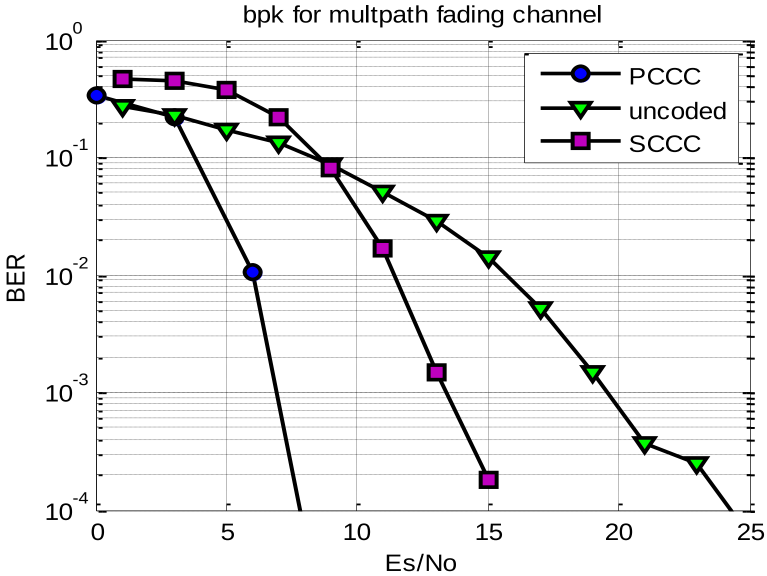


Figure (11) BER Vs SNR for multipath fading channel with M=2

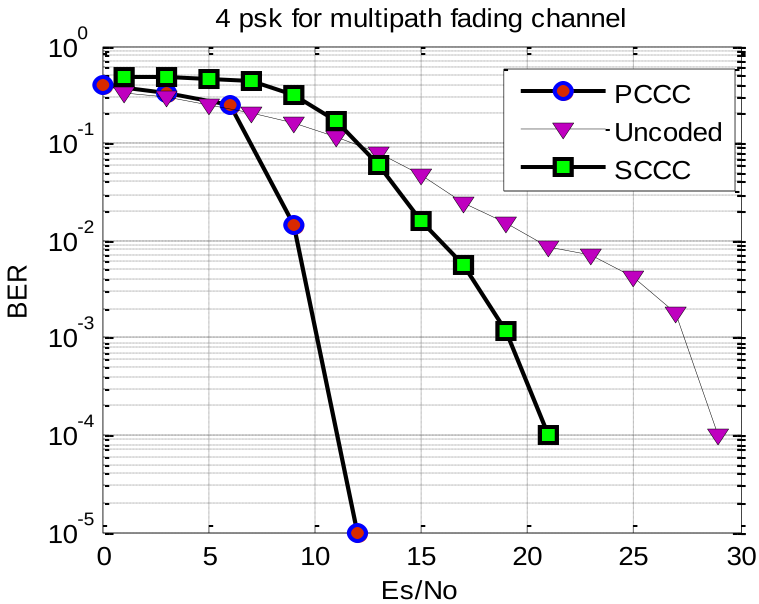


Figure (12) BER Vs SNR for multipath fading

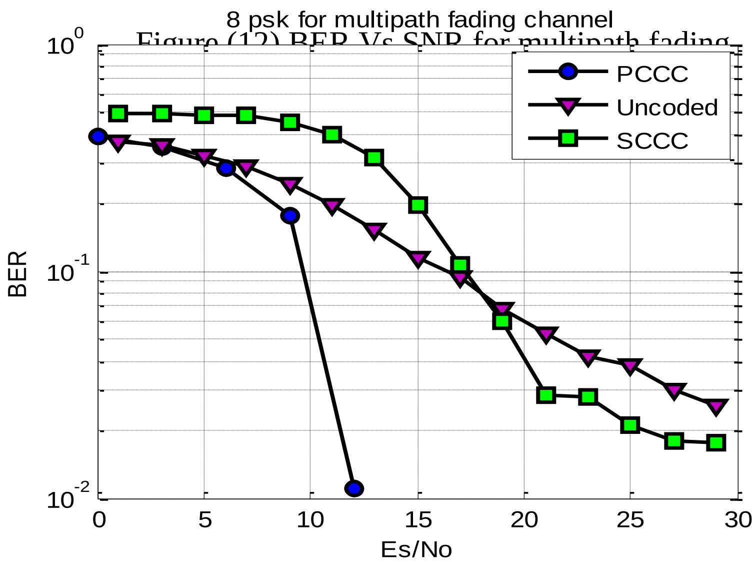


Figure (13) BER Vs SNR for multipath fading channel with M =8.

# VOLTAGE STABILITY ENHANCEMENT AND LOSS REDUCTION VIA OPTIMUM LOCATION OF A SERIES CAPACITOR

Dr. Firas Mohammed Tuaimah
Electrical Engineering Department
University of Baghdad

**ABSTRACT**

Series compensation is frequently found on long transmission lines used to improve voltage stability. Due to the long transmission lines, voltage begins to decay as the line moves further from the source. Series compensation devices placed strategically on the line to increase the voltage profile of the line to levels near 1.0 p.u.. This paper presents a novel optimum location and optimum percentage compensation value of a series capacitor as a compensation method to enhance the voltage stability and loss reduction. The proposed method is applied to a 11-bus power system.

The load flow analysis using Newton-Raphson approach for the 11-bus test system was designed and tested using MATLAB 7 programming language.

# تحسين استقرارية الفولتية وتقليل الخسائر عبر تحديد مكان امثل لوضع متسعة على التوالي

**الخلاصة**

غالبا ما يتم استخدام التعزيز المربوط على التوالي عبر استخدام المتسعة في خطوط النقل وذلك لتحسين الفولتية. بسب المسافات الطويلة لخطوط النقل, فأن الفولتية تبدأ بالأنخفاض كلما ابتعدنا عن المصدر. ولأجل هذا يتم استخدام متسعات موزعة وفق حسابات لتحافض على الفولتية بمستوى 1 للوحدة الثابتة (p.u.). تم في هذا البحث استخدام الية مثلى لوضع او استخدام المتسعة لتحسين الفولتية ولتقليل الخسائر. حيث تم تطبيق الطريقة على منظومة أفتراضية عالمية ذات 11 عقدة (IEEE-11BUS) .

تم استخدام طريقة الجريان نيوتن- رافسون على هذه المنظومة وأستخدمت اللغة البرمجية **MATLAB 7.**

**KEYWORDS: voltage stability, loss reduction, series capacitor, load flow**

## INTRODUCTION

When exist the need to transmit large amount of electric power over transmission lines, it is necessary to consider a group of factors that limit the electrical energy transmission capacity. Some of these factors are: the voltage drop, the stability problem, the thermal effect on the conductors, etc. The constraints imposed by these factors may be overcome by means the construction of new transmission lines or by a transmission upgrade. These alternatives are commonly very expensive, especially in the case of long transmission lines. A more economic alternative in these cases is the series compensation.

Transmission line compensation implies a modification in the electric characteristic of the transmission line with the objective of increase power transfer capability. In the case of series compensation, the objective is to cancel part of the reactance of the line by means of series capacitors. The result is an enhanced system stability, which is evidenced with an increased power transfer capability of the line, a reduction in the transmission angle at a given level of power transfer and an increased virtual natural load.

Series compensation has been in use since the early part of the 20th century. The first series capacitor for EHV power transmission application was installed in a 245 kV line back in 1951 in Sweden [1, 2].

M. Ghandhari et.al. [3] have been proved that a controllable series capacitor with a suitable control scheme can improve transient stability and help to damp electromechanical oscillations in a multi-machine power system based on Lyapunov theory**.**

Maurício Aredes et.al. [4]discusses the possibility of using FACTS devices like small series compensation to control large quantities of active power transmitted by half-wave length transmission lines, which proves to be efficient, simple and robust.

Belkacem Mahdad et.al. [5] describes a simple approach based on logic concept. Fuzzy logic approach is described, which achieves a logical and feasible economic cost of operation without the need of exact mathematical formulation.

K. Narasimha Rao et.al. [6] presents the aspects of enhancement of ATC limited by the voltage with and without contingency by simple and efficient models of FACTS devices. The effectiveness of the proposed methods is demonstrated on IEEE-14 bus and IEEE-30 bus system and the results are compared.

Héctor J. Altuve et.al. [7] presents modern solutions to improve directional, distance, and differential element operation on series-compensated lines.

J. Miguel Gonz´alez et.al. [8] present a Complete stability analyses, including voltage, small perturbation and transient stability studies, and the associated models and controls of a Series Vectorial Compensator (SVeC).

## SERIES CAPACITORS (SC)

A series capacitor is not just a capacitor in series with the line. For proper functioning, series compensation requires control, protection and supervision facilities to enable it to perform as an integrated part of a power system. Also, since the series capacitor is working at the same voltage level as the rest of the system, it needs to be fully insulated to ground.

The main circuit diagram of a series capacitor is shown in Fig.1. The main protective device is a varistor, usually of $Z_nO$ type, limiting the voltage across the capacitor to safe values in conjunction with system faults giving rise to large short circuit currents flowing through the line.

A spark gap is utilized in many cases, to enable by-pass of the series capacitor in situations where the varistor is not sufficient to absorb the excess current during a fault sequence. There are various bypass solutions available today like spark gap, high power plasma switch, power electronic device, etc. [9]

Finally, a circuit breaker is incorporated in the scheme to enable bypassing of the series capacitor for more extended periods of time as need may be. It is also needed for extinguishing the spark gap, or, in the absence of a spark gap, for by-passing the varistor in conjunction with faults close to the series capacitor (so-called internal faults).

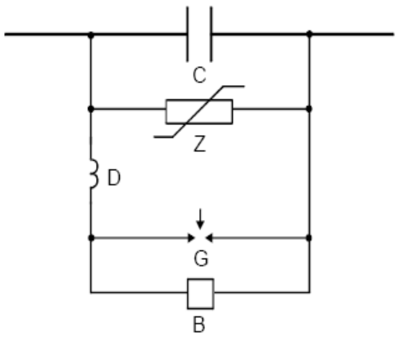


**C Capacitor**
**Z Metal oxide**
**D Discharge damping**
**G Forced triggered spark**
**B By-pass**

**Fig.1 Main Configuration of a Series Capacitor**

Series capacitors may be installed at one or both line ends. Line ends are typical capacitor locations, because it is generally possible to use space available in the substation. In turn, this reduces installation cost. Another possibility is to install the series capacitors at some central location on the line. Series capacitors located at the line ends create more complex protection problems than those installed at the center of the line. The principal applications of series compensations are [9]:

- Improves voltage regulation
- Increase power transmission capability.
- Improve system stability.
- Reduce system losses.
- Optimize power flow between parallel lines.

## DEGREE OF SERIES COMPENSATION

The degree of series compensation is defined as the relation between the capacitive reactance of the series capacitor and the inductive reactance of the transmission line.

$$\text{Degree of Compensation } = \frac{X_C}{X_L} \times 100\% \qquad (1)$$

Theoretically, the degree of compensation could be 100%, however this degree of compensation may produce large currents flows in the presence of small disturbances or faults. The circuit would also series resonant at the fundamental frequency, and it would be difficult to control transient voltages and currents during the disturbance. In the other hand a high level of compensation highlight the problems in protective relays and in the voltage profile during fault conditions. A practical limitation of compensation is between 25-75%. [2]

Decreasing line reactance increases maximum active power demand, which in turn enhances the voltages at the busses as shown in Fig.2.

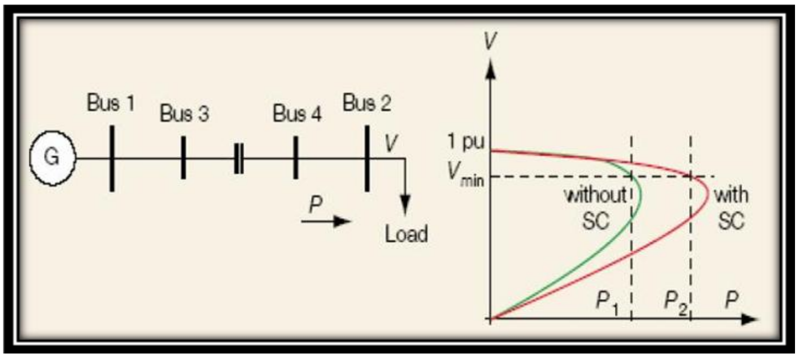


**Fig.2 Series capacitor effect on voltage**

Dynamically, the power transfer between two interconnected systems, as shown in Fig. 3, is defined by:

$$P = \frac{V_S V_R}{X_L} \sin\delta, \qquad \delta = \delta_1 - \delta_2 \tag{2}$$

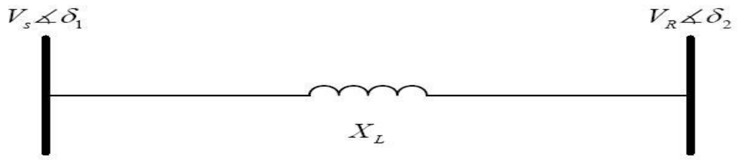


**Fig.3 Equivalent network configuration for two interconnected systems**

**PROPOSED METHOD**

The proposed method is to obtain optimal location and amount of series compensation which is used to reduce the total reactance of the transmission line, which is often the main reason for their application. This improves power system stability, reduces reactive power losses and improves voltage regulation of the transmission line. The power system is modeled using MATLAB 7 programming language and comprised of the following steps:

(i) Input all possible data of the 11-bus test system shown in Fig.4, from the line resistances, reactance's, line charging reactance's, bus voltages, active power, reactive power, angles etc.

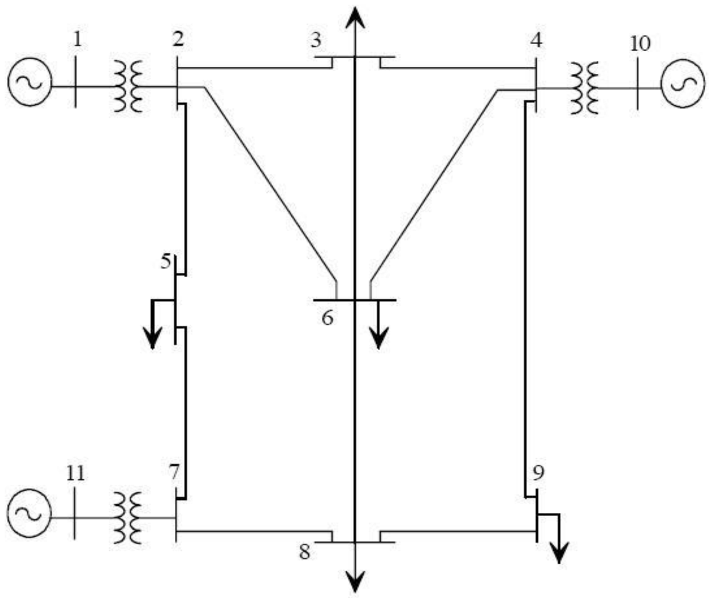


**Fig.4 IEEE-11 bus test system**

(ii) Perform load flow calculation using Newtom-Raphson method without using the series capacitor, then obtaining the buses voltages.

(iii)Perform load flow calculation using Newtom-Raphson method with the use of the series capacitor at each line of the system. The power flow along the transmission line is directly proportional to the difference of the phase angle and inversely proportional to the magnitude of the reactance. This concept can be demonstrated by using simple two bus lossless system as shown in Fig.5. The degree of compensation is chosen in this paper from 10% to 70% in suitable steps and then obtaining the new bus voltages. If the line is 100% compensated, it will behave as a purely resistive element and would cause series resonance even at fundamental frequency

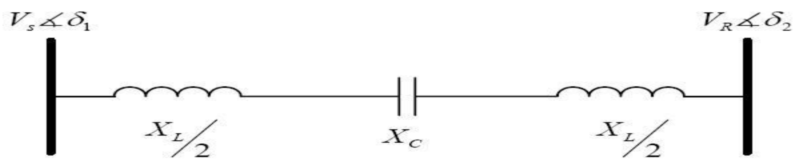


**Fig.5 Equivalent system with series compensation**

and hence power transferred across the transmission line is increased to:

$$P = \frac{V_S V_R}{X_L - X_C} \sin \delta \tag{3}$$

(iv)For each compensation recalculate the active power loss and reactive power loss according to the

$$\mathrm{Re}\,active - Loss = \sum_{i=1}^{n} \left| I(i) \right|^2 X(i) \tag{4}$$

$$Active - Loss = \sum_{i=1}^{n} |I(i)|^2 R(i) \tag{5}$$

## SIMULATION RESULTS

The following steps where performed:

- The 11-buses voltages before inserting any capacitor as a compensator in any line will be as shown in Fig.6, in which the maximum value is 1.0702 and the minimum value is 1.0252.

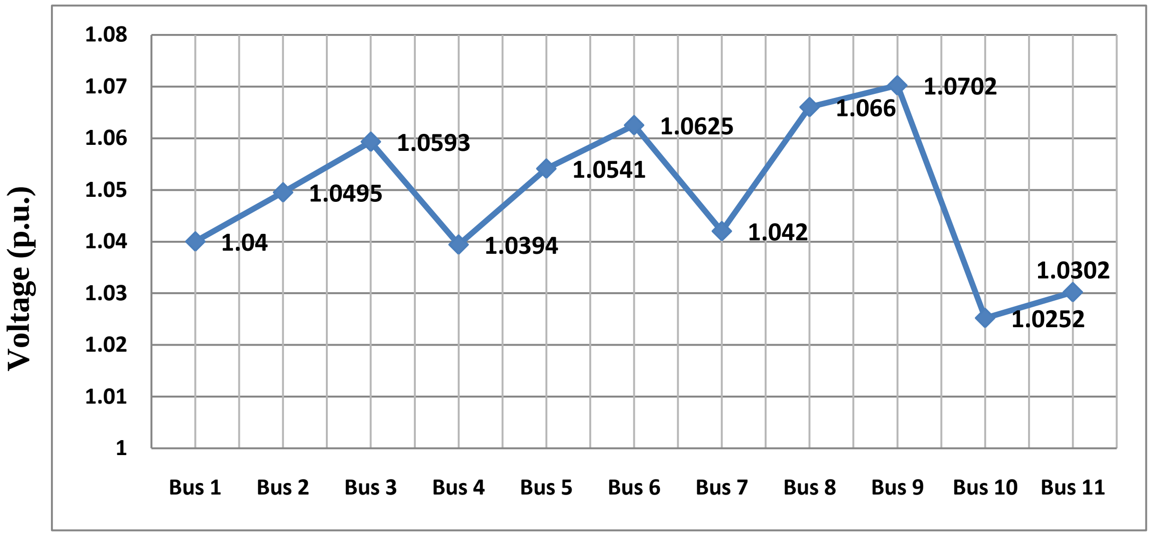


**Fig.6 The 11-buses voltages before inserting a series capacitor**

- A series capacitor will be inserted in the lines 1-2, 2-3, 2-5, 2-6, 3-4, 3-6, 4-9, 4-6, 4-10, 5-7, 6-8, 7-8, 7-11 and 8-9. In This paper the value of the inserted capacitor will be chosen as 10%, 30%, 50% and 70% of each line reactance.
- The proposed steps of a series capacitor will be applied on all the given lines. Next figures will show the busses voltages for each capacitor value.

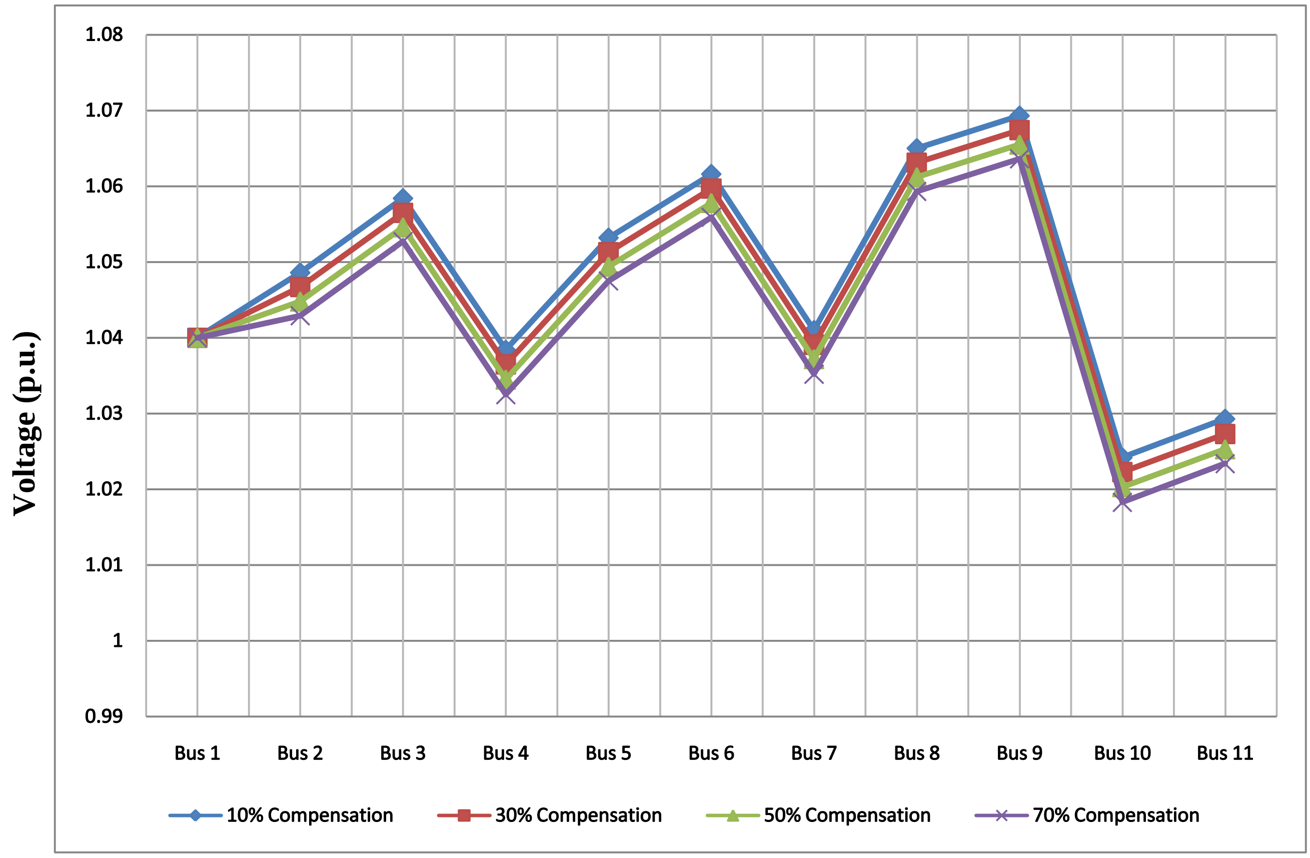


**Fig.7 The effect of inserting series capacitor between bus 1 and 2 on buses voltages**

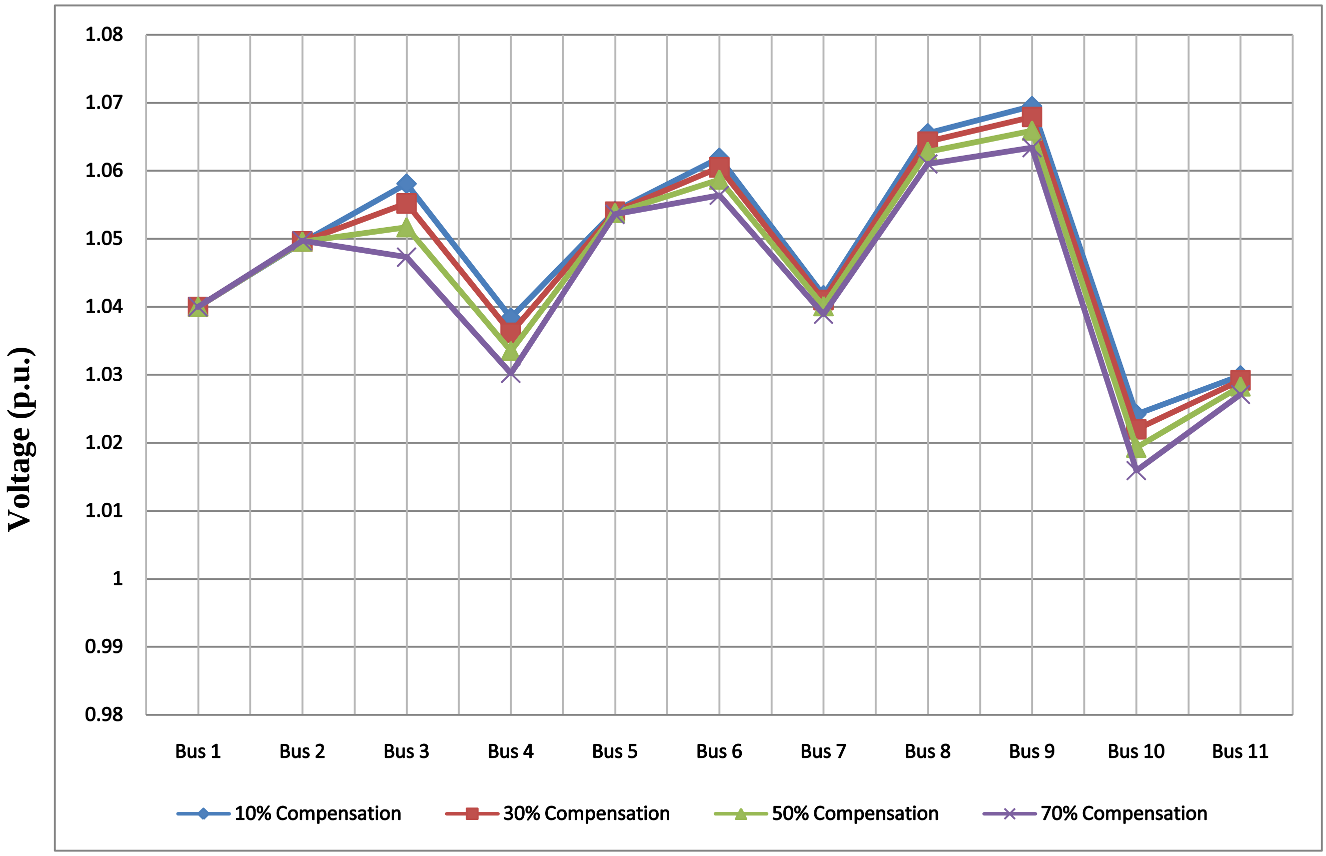


**Fig.8 The effect of inserting series capacitor between bus 2 and 3 on buses voltages**

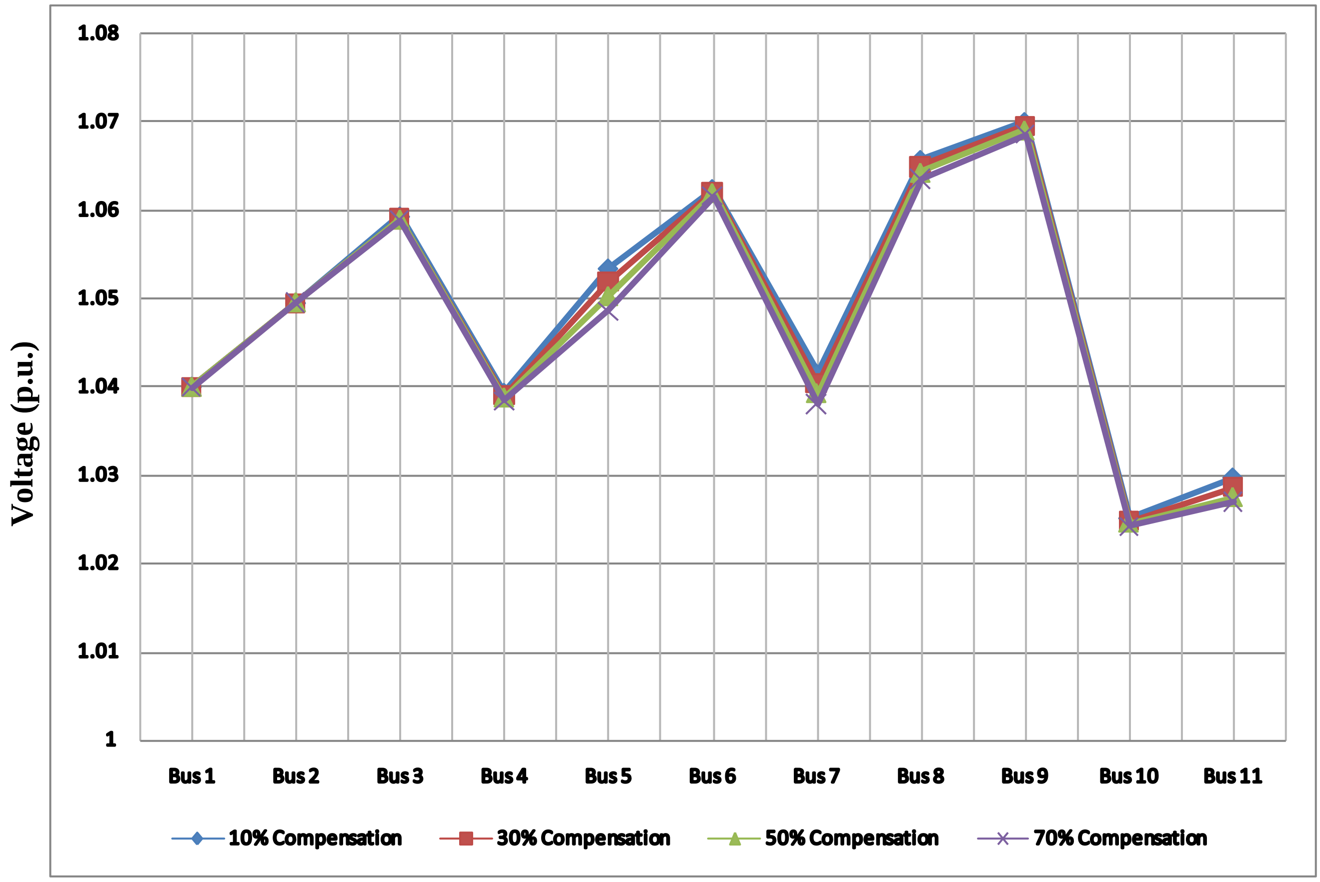


**Fig.9 The effect of inserting series capacitor between bus 2 and 5 on buses voltages**

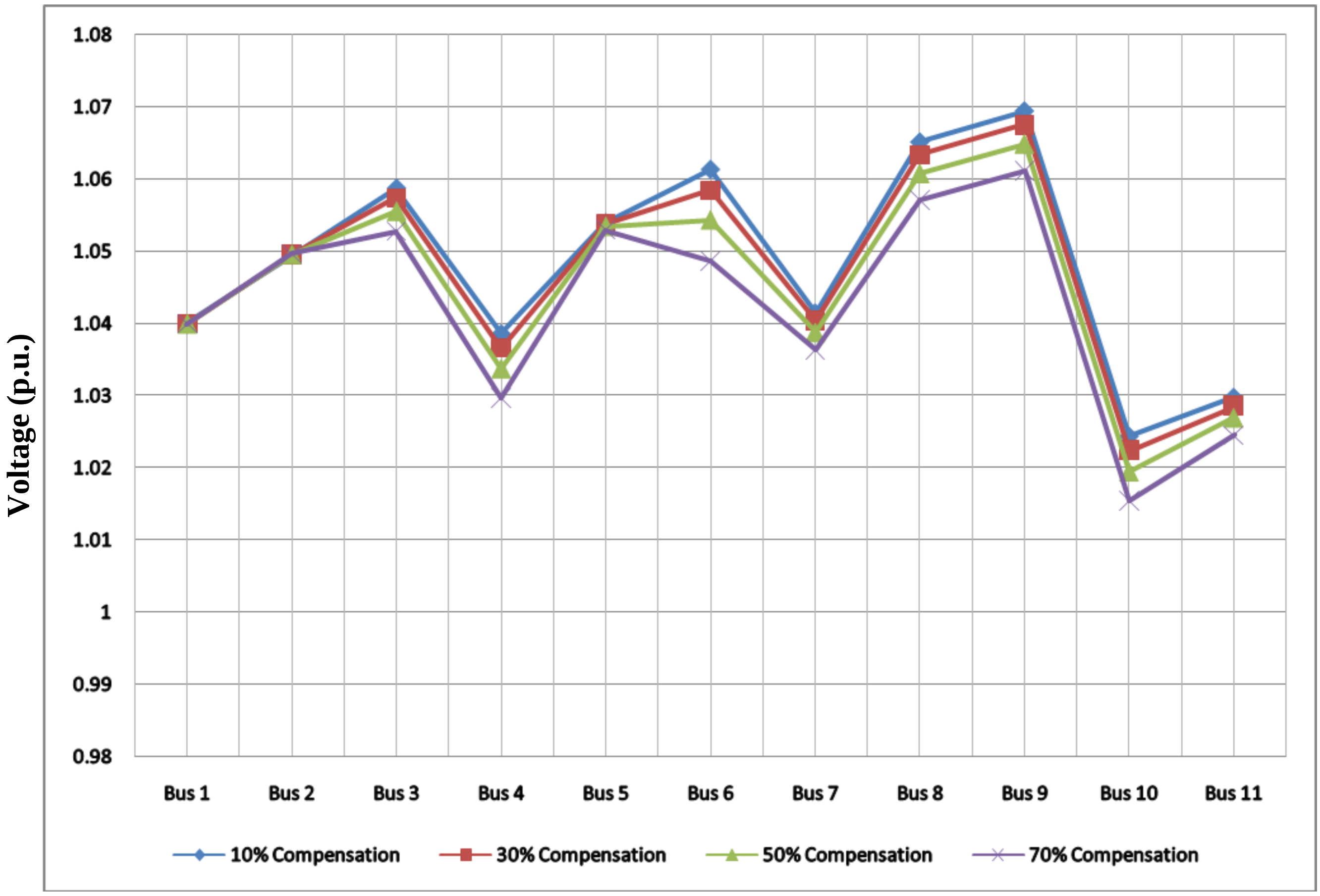


**Fig.10 The effect of inserting series capacitor between bus 2 and 6 on buses voltages**

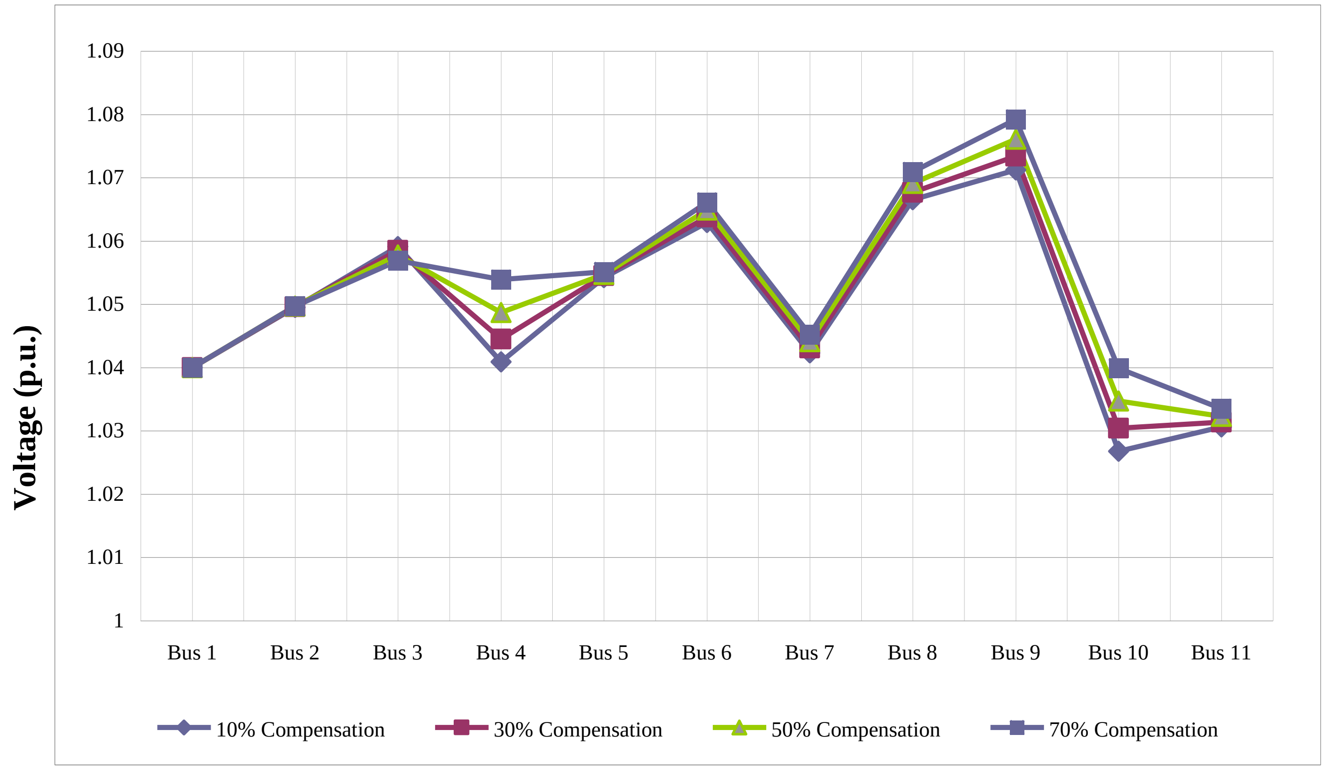


**Fig.11 The effect of inserting series capacitor between bus 3 and 4 on buses voltages**

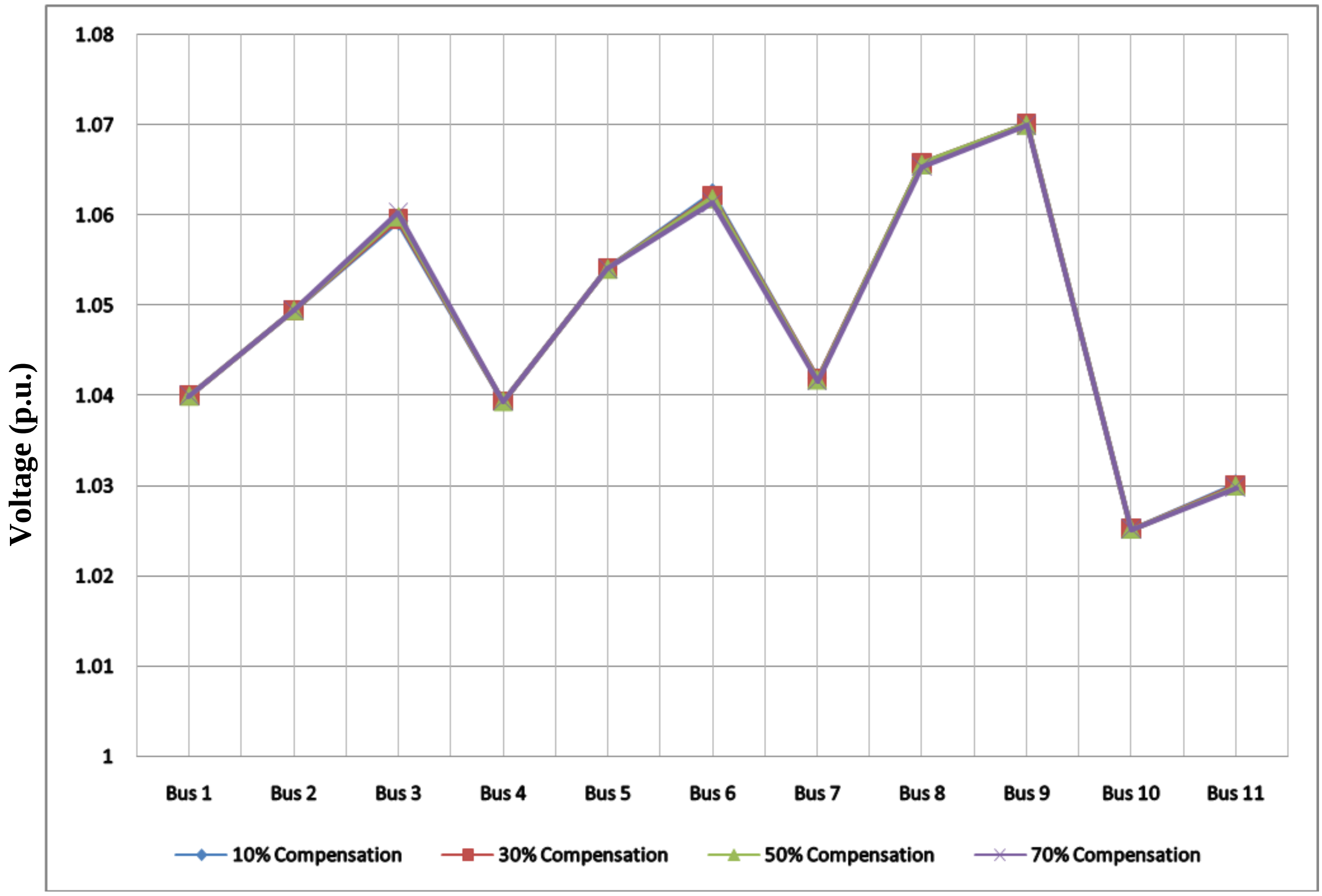


**Fig.12 The effect of inserting series capacitor between bus 3 and 6 on buses voltages**

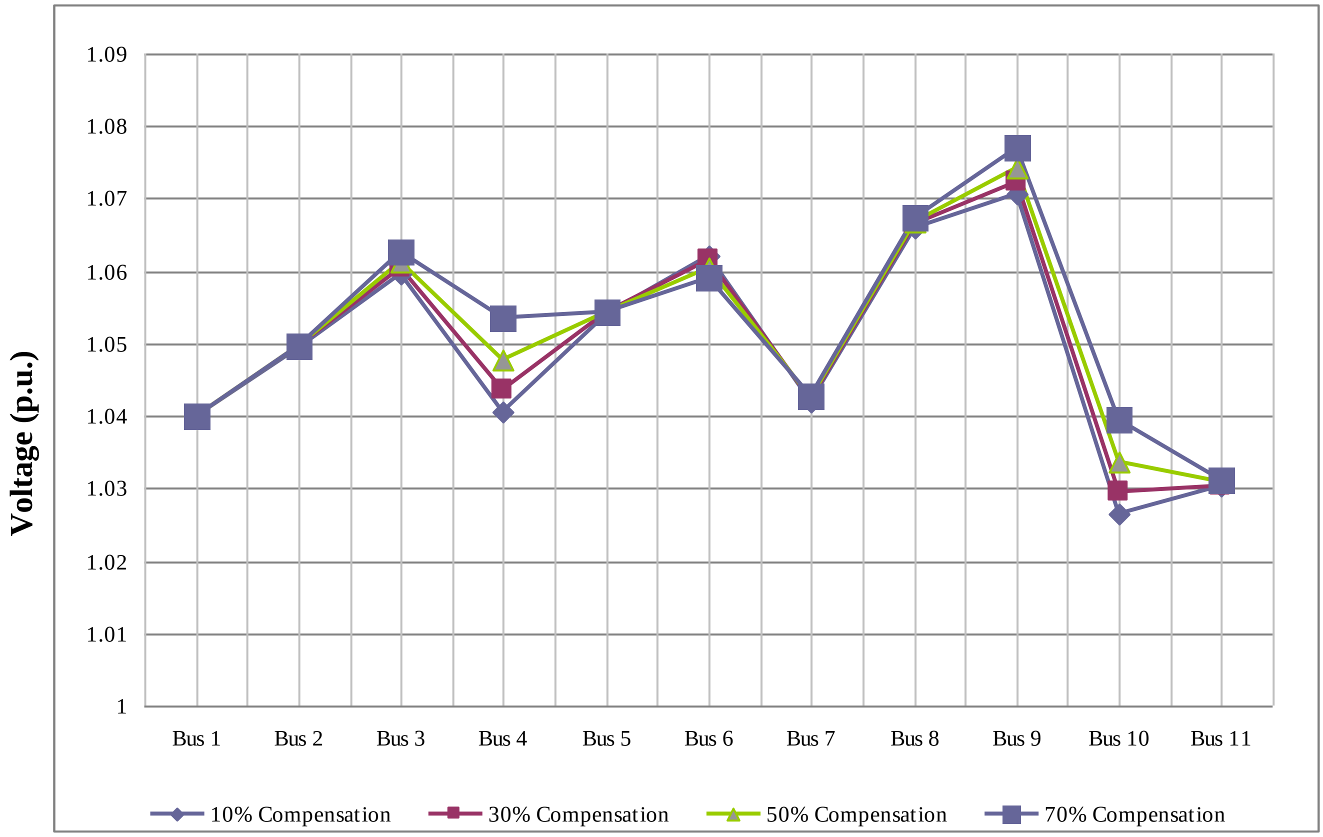


**Fig.13 The effect of inserting series capacitor between bus 4 and 6 on buses voltages**

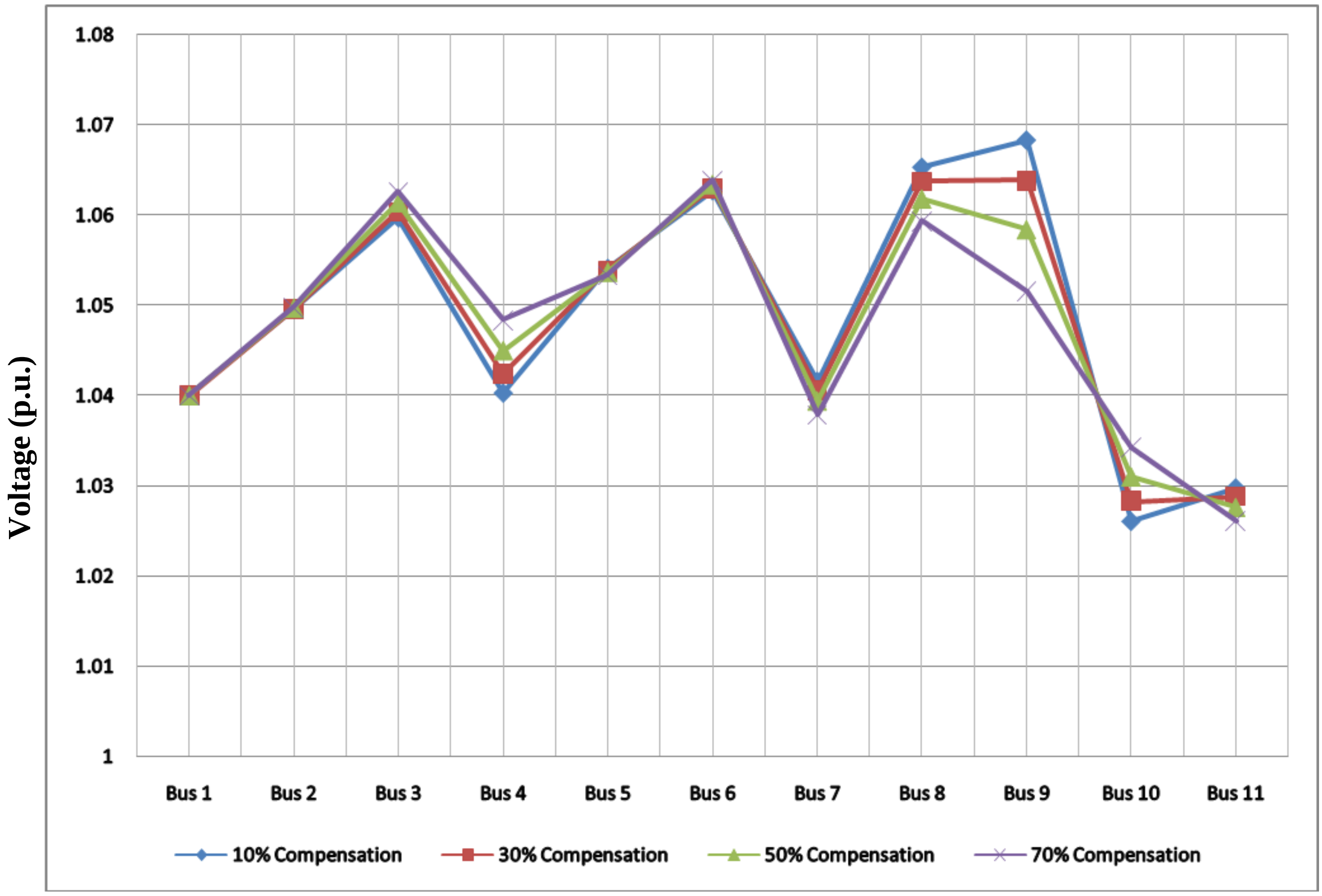


**Fig.14 The effect of inserting series capacitor between bus 4 and 9 on buses voltages**

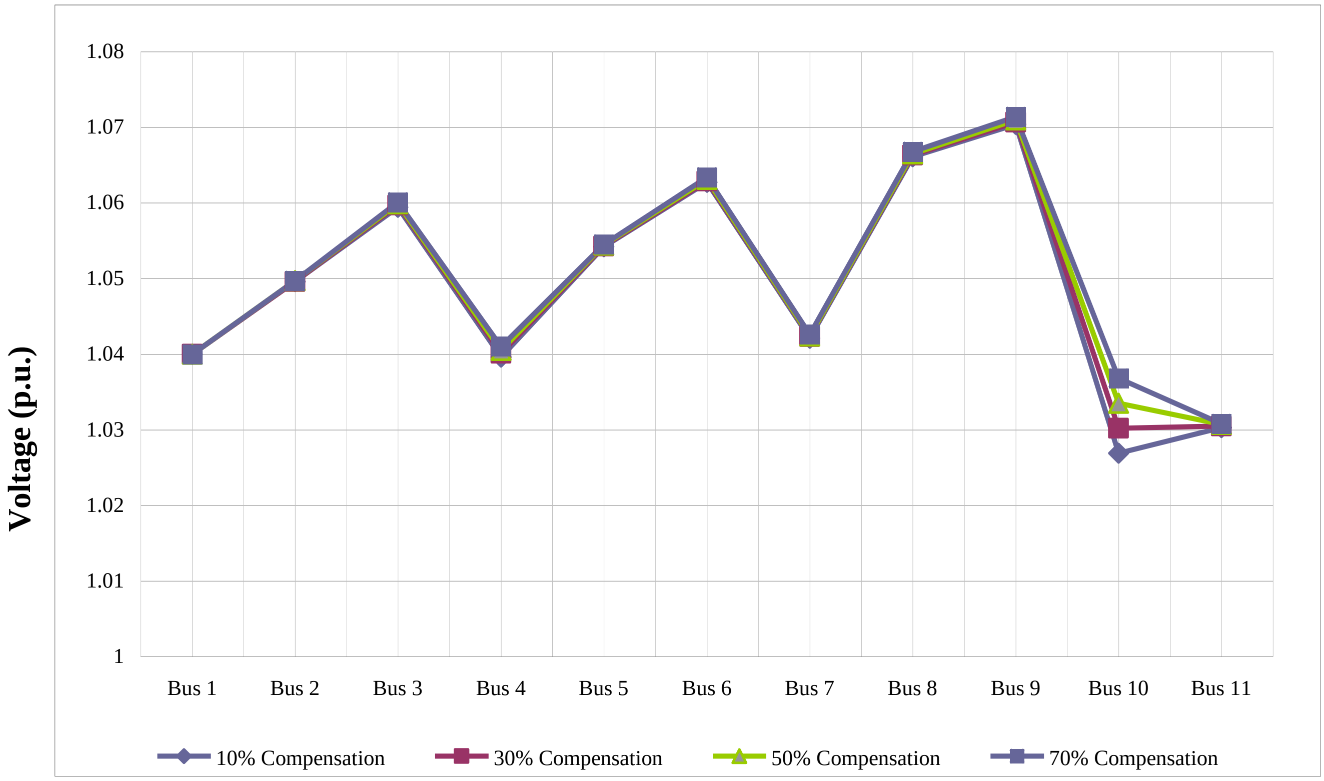


**Fig.15 The effect of inserting series capacitor between bus 4 and 10 on buses voltages**

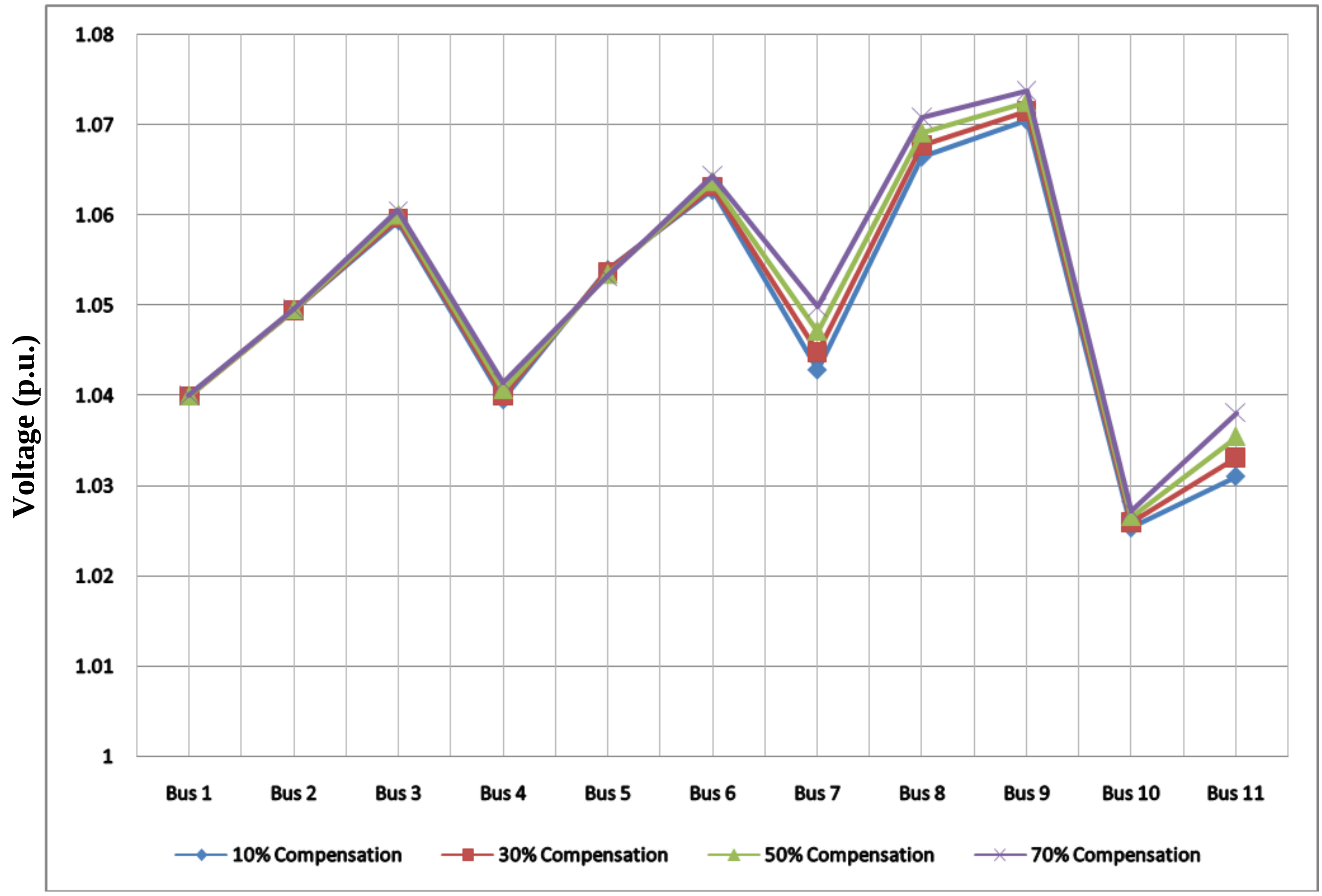


**Fig.16 The effect of inserting series capacitor between bus 5 and 7 on buses voltages**

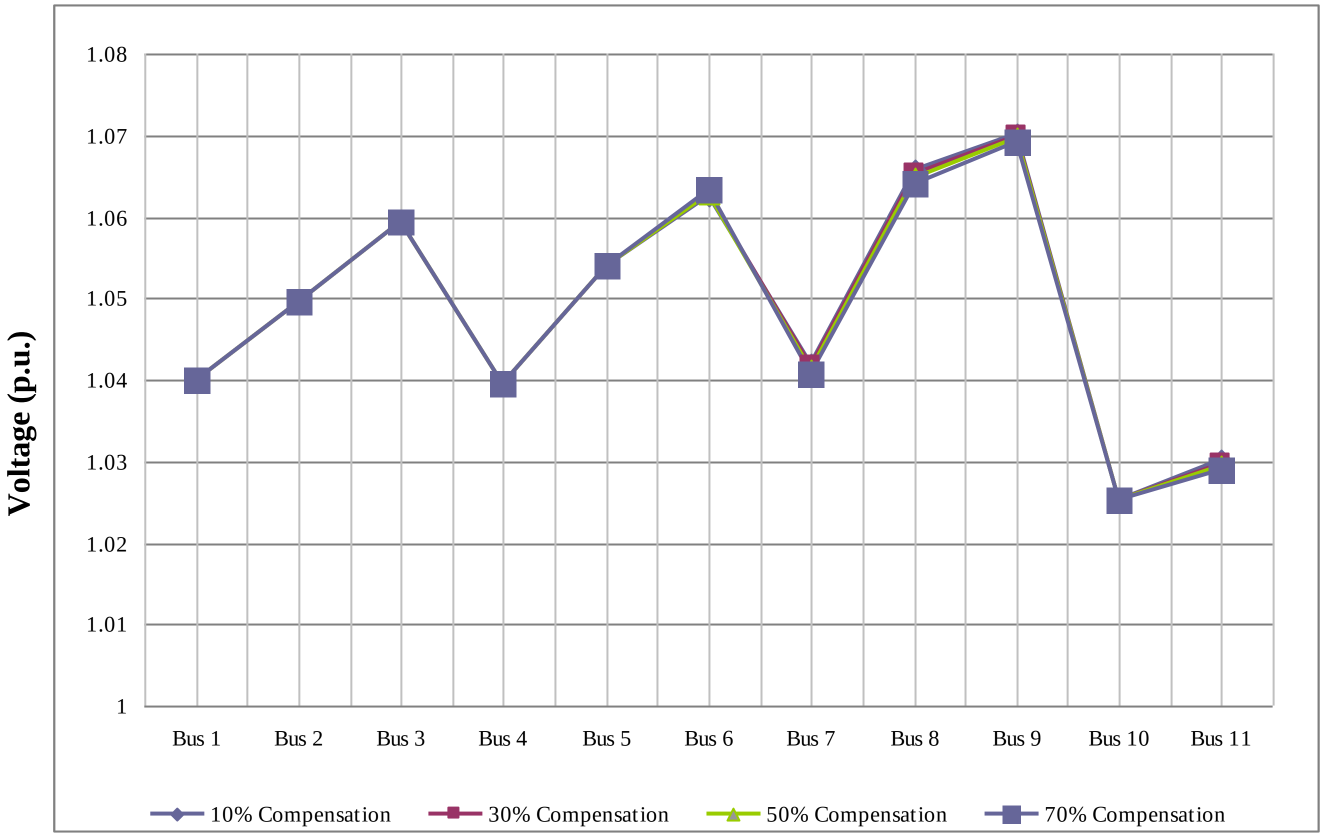


**Fig.17 The effect of inserting series capacitor between bus 6 and 8 on buses voltages**

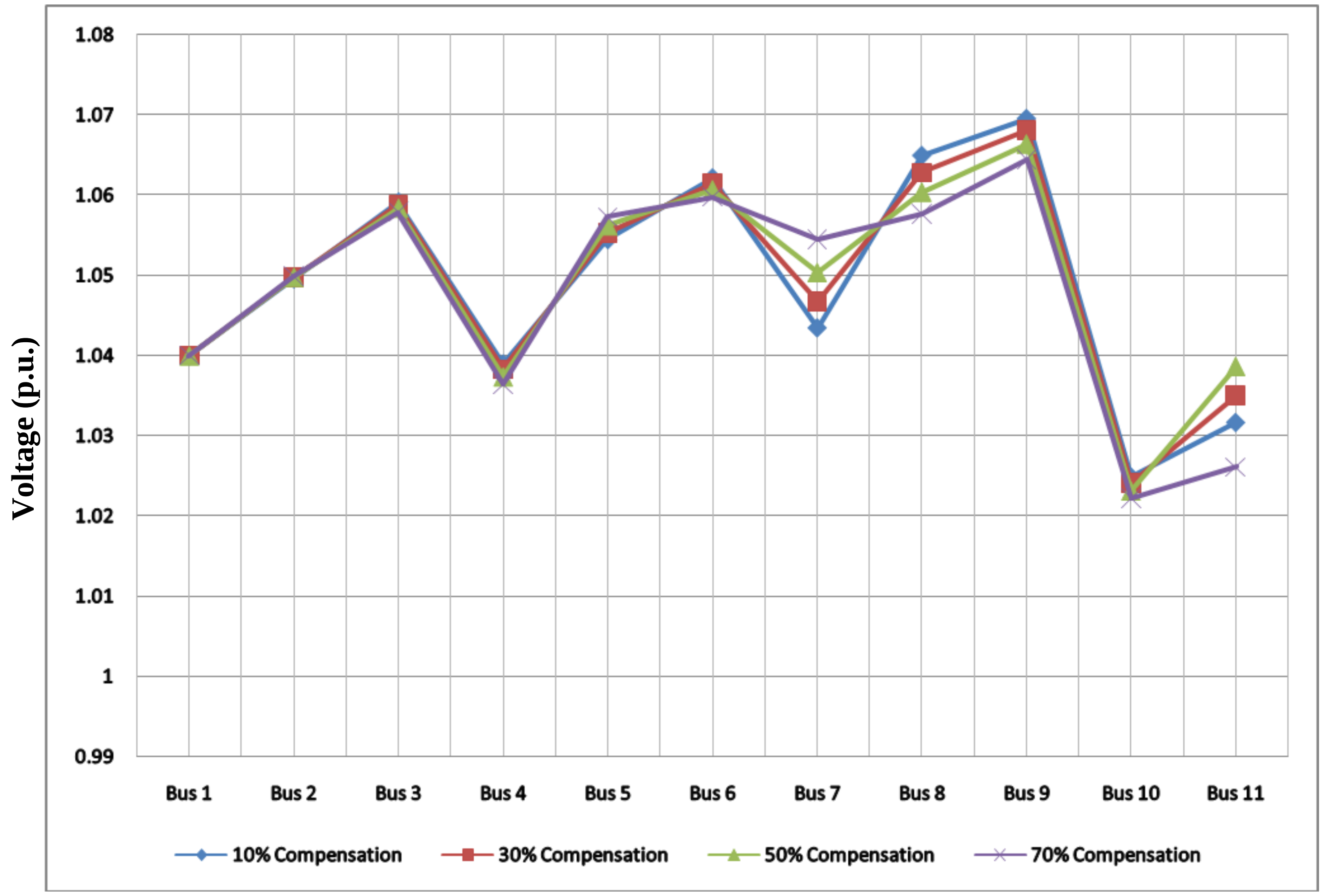


**Fig.18 The effect of inserting series capacitor between bus 7 and 8 on buses voltages**

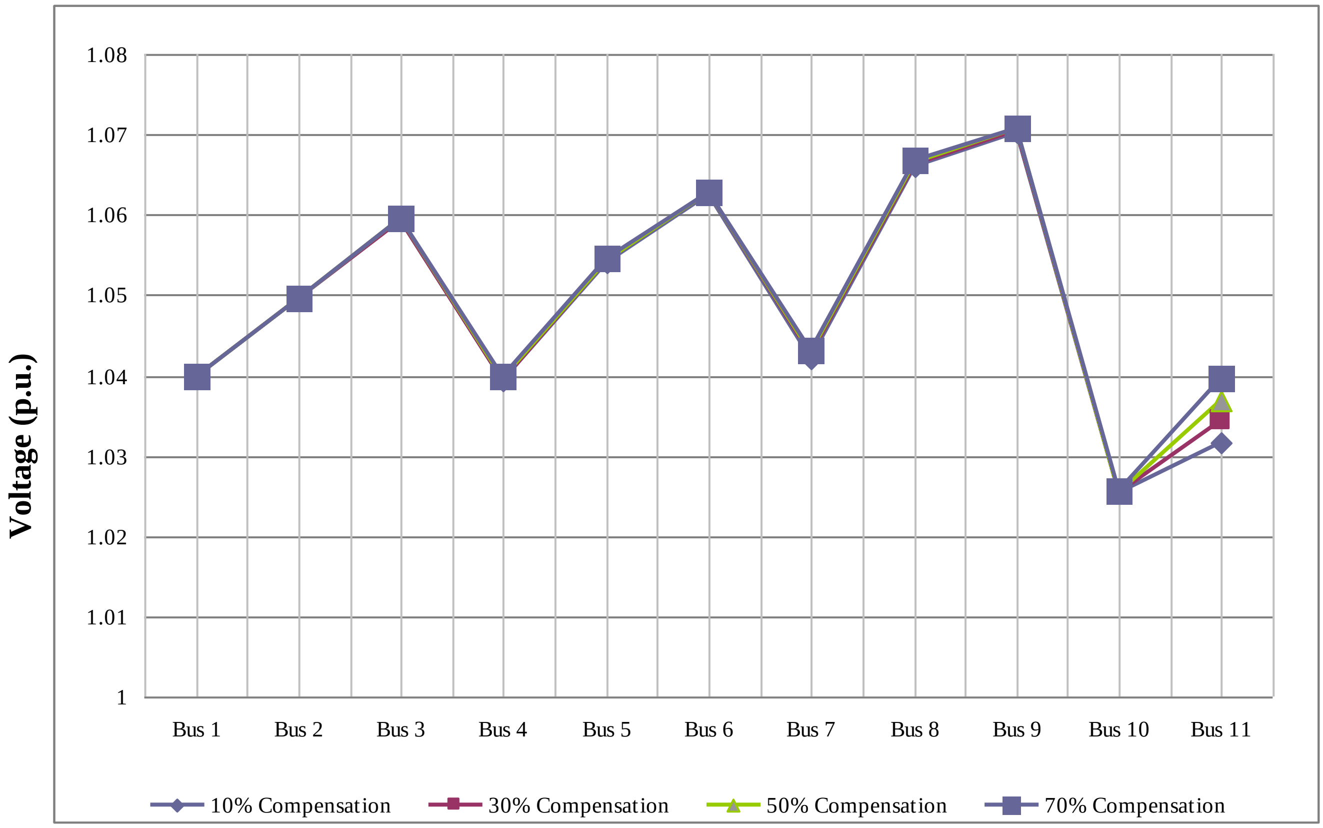


**Fig.19 The effect of inserting series capacitor between bus 7 and 11 on buses voltages**

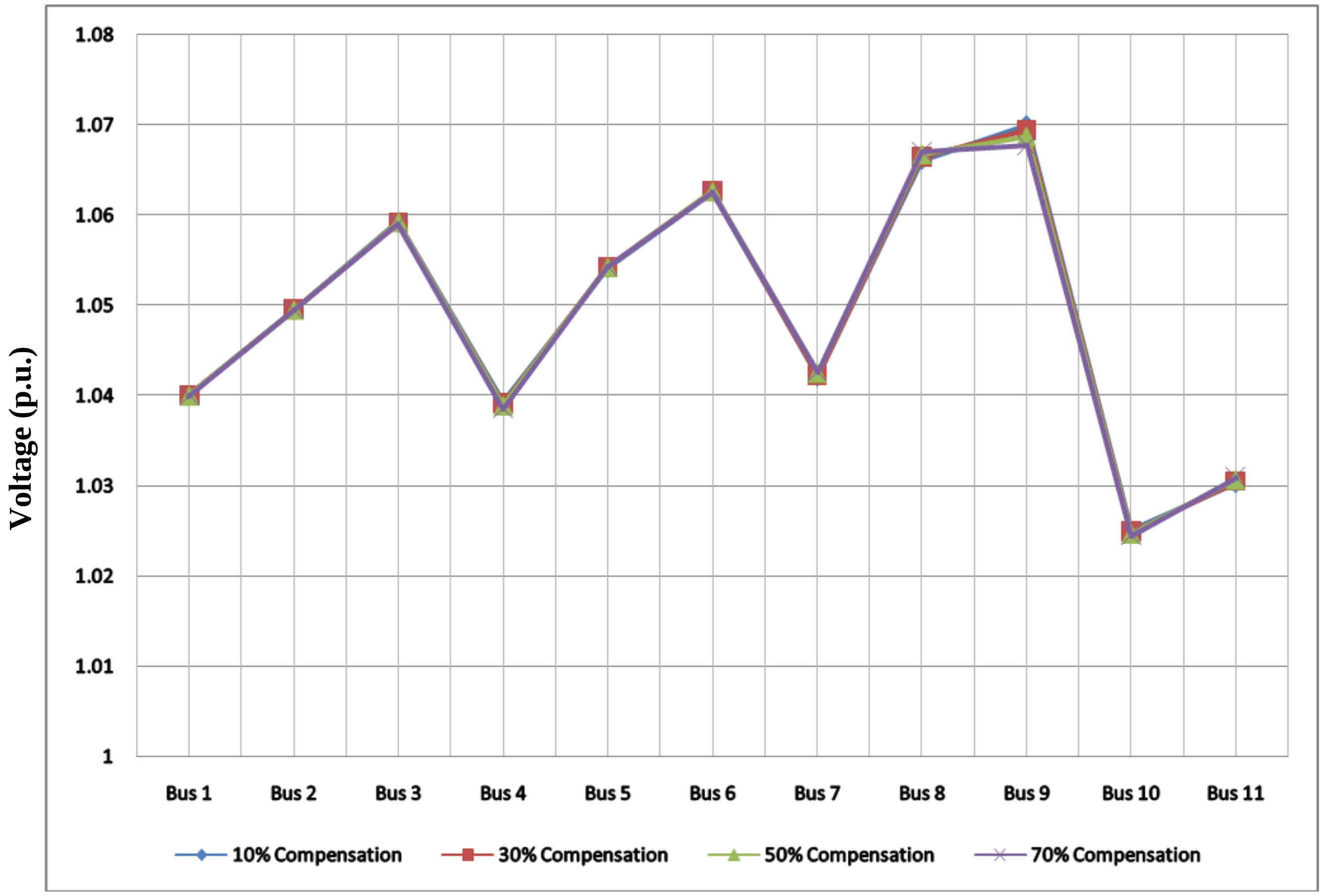


**Fig.20 The effect of inserting series capacitor between bus 8 and 9 on buses voltages**

- The reactive power losses and active power losses according to eq. (4) and eq. (5) can be given as shown in Fig.21 and Fig.22 respectively for 70% compensation.

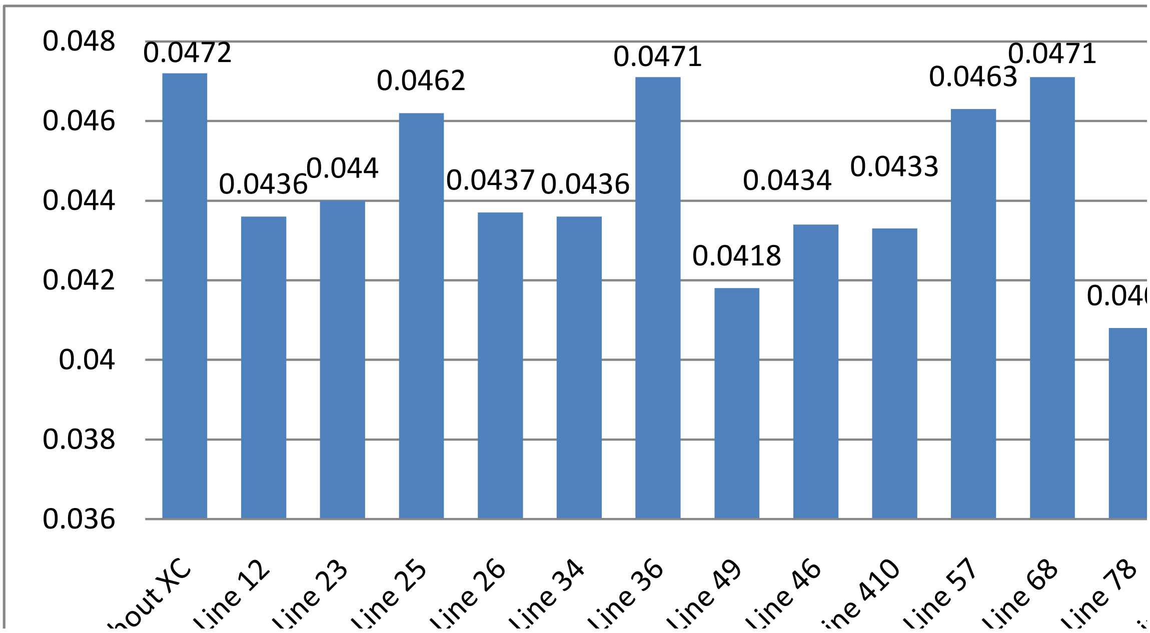


**Fig.21 The reactive power losses at each line depending on 70% compensation**

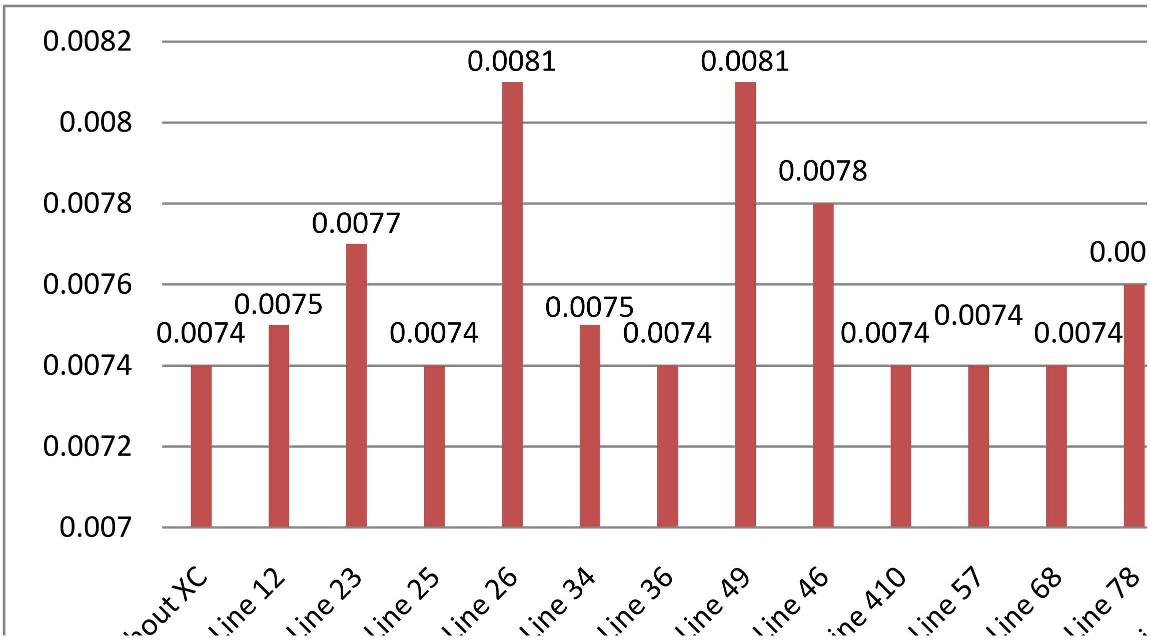


**Fig.22 The active power losses at each line depending on 70% compensation**

## CONCLUSIONS

- It is obvious shown from Fig.7 to Fig.20 that the 70% compensation give best results for the large number of these cases. Fig.23 gives all the buses voltages cases for 70% compensation.

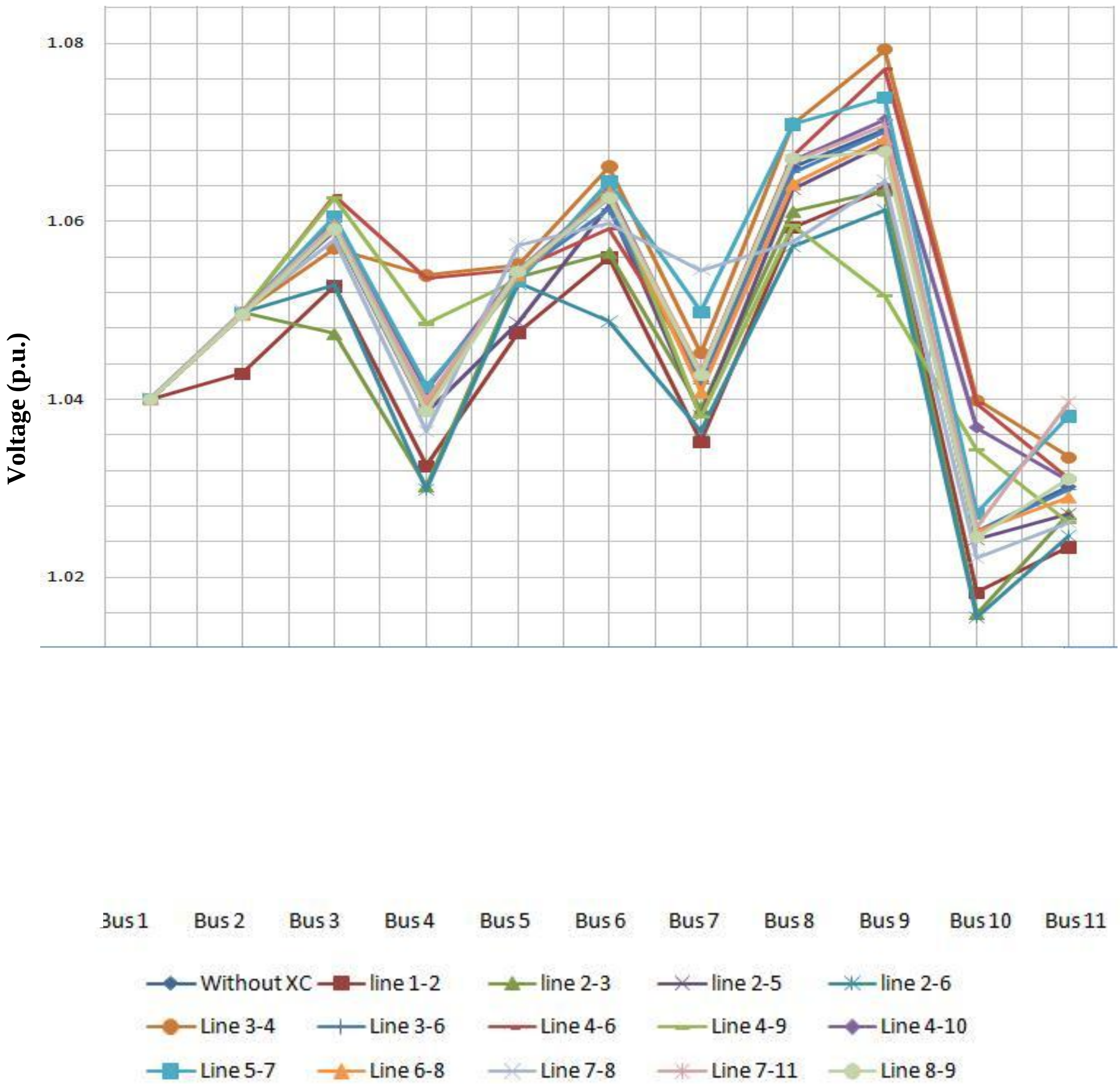


**Fig.23 The 70% compensation buses voltages for all 11-bus system lines**

- From Fig.23, when inserting the 70% capacitor, the best results for buses voltages exist at the lines 1-2, 2-3 and 2-6.
- One of the important results of a series capacitor application is the reduction of the reactive power losses in the system especially in the compensated line, as shown in Fig.21. Whereas there is no affective change with the active power loss, as shown in Fig.22.
- The busses voltages for the three pre mentioned cases (XC at Line 1-2, XC at Line 2-3, XC at Line 2-6), with the case of no XC and for 70% compensation can be drawn as in Fig.24.

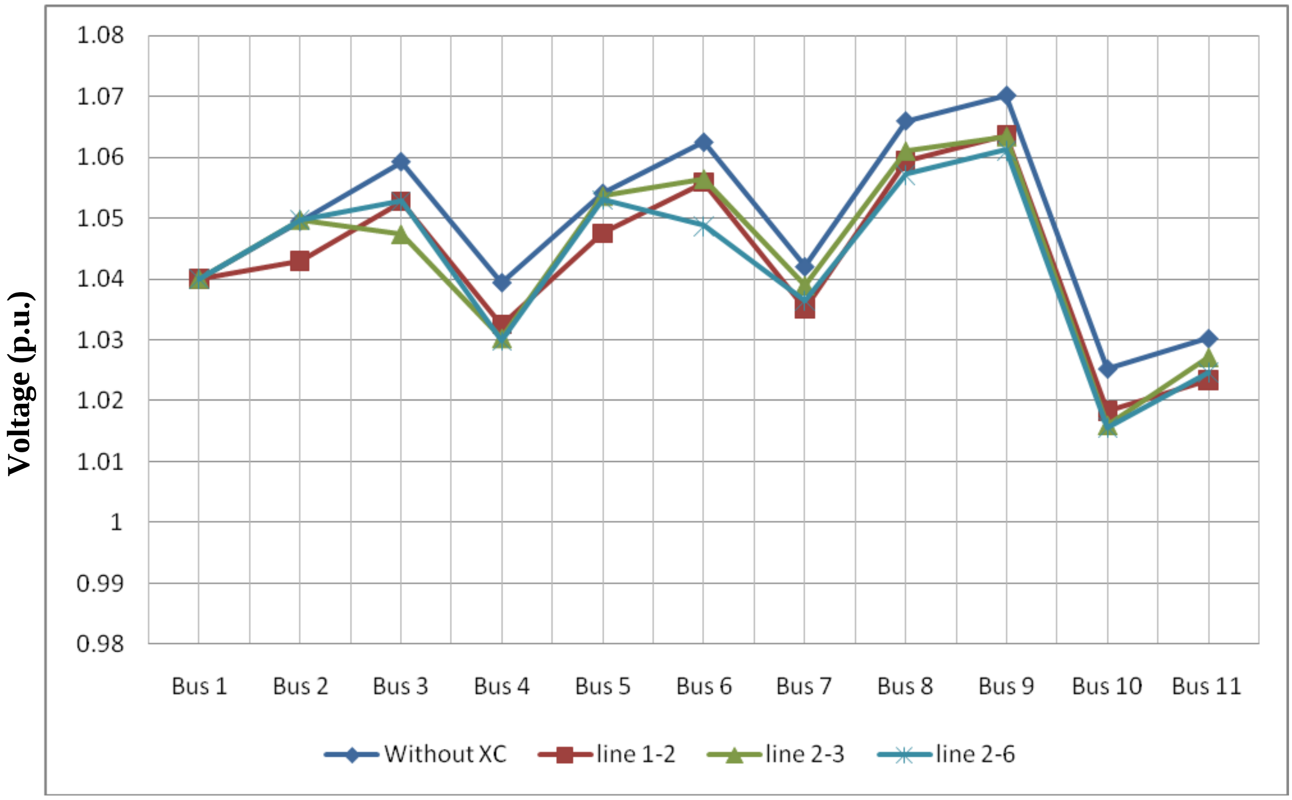


**Fig.24 70% compensation for Line 1-2, Line 2-3 and 2-6**

- There is no change or slight change in busses voltages when inserting a capacitor, like line 2-5, 3-6, 4-10, 6-8, 7-11 and 8-9.
- To get the optimum insertion of capacitor for the three lines (1-2, 2-3 and 2-6) the mean value of the busses voltages, which is the sum of all busses voltages over the number of busses, can be used as a criteria, as well as the minimum reactive power losses, as given in Table 1.

**Table 1 Comparison for mean voltage value and reactive power loss for each line**

| Line | Mean Voltage Value | Reactive Power Losses |
|---|---|---|
| Without XC | 1.0490 | 0.0472 |
| XC at Line 1-2 | 1.0428 | 0.0436 |
| XC at Line 2-3 | 1.0440 | 0.0440 |
| XC at Line 2-6 | 1.0426 | 0.0437 |

- It is clearly shown from Table 1 that inserting a capacitor as a compensator in 11-bus test system, gives the optimum results for voltage enhancement and reactive power reduction, if the insertion was at **Line 1-2** or **Line 2-6**.

## REFERENCES


- P. Kundur, *Power System Stability and Control*. New York: Mc-Graw Hill, 1994.

- Alfredo A. Cuello-Reyna et. al.:Transient Performance for a Series-Compensation in a High Voltage Transmission System, Department of Electrical and Computer Engineering, University of Puerto Rico at Mayagüez, Mayagüez, Puerto Rico, 00682 (email: alfredo.cuello@ece.uprm.edu), 2006, pp.1-10

- M. Ghandhari et. al.: A control strategy for controllable series capacitor in electric power Systems, Elsevier Science Ltd. 2001, pp. 1575-1583

- Maurício Aredes et. al.: The GTO-Controlled Series Capacitor Applied to Half-Wave Length Transmission-Lines, International Conference on Power Systems Transients – IPST 2003, pp.1-6

- Belkacem Mahdad et.al.: Dynamic compensation of the Reactive energy using a fuzzy controller, Leonardo Electronic Journal of Practices and Technologies, Issue 7, July-December 2005, pp.1-16

- K. Narasimha Rao et. al.: Voltage constrained available transfer capability enhancement with facts devices, ARPN Journal of Engineering and Applied Sciences, Vol. 2, No. 6, December 2007, pp.1-9

- Héctor J. Altuve et. al.: Advances in Series-Compensated Line Protection, Schweitzer Engineering Laboratories, Inc., 2008, pp.1-13

- J. Miguel Gonz´alez et. al.: Stability Modeling and Comparative Study of Series Vectorial Compensators, IEEE Transactions On Power Delivery, May 2009, pp.1-11

- S. Meikandasivam et. al.: Behavioral Study of TCSC Device – A MATLAB/Simulink Implementation, World Academy of Science, Engineering and Technology, 2008, pp.694-699


## LIST OF SYMBOLS

$V_S$ Sending voltage (volt)
$V_R$ Receiving voltage (volt)
P Active power (watt)
$\delta$ Rotor angle (degree)
$X_L$ Transmission line reactance (ohm)
$X_C$ Capacitance (ohm)

# STRENGTHENING OF CRACKED REINFORCED CONCRETE T-BEAM BY JACKETING

Dr. ADNAN SADIQ AL-KUAITY
LecturerOf Civil Engineering,
Engineering Faculty, University of Kufa

## ABSTRACT

This investigation presents an extensive experimental study on the behaviour and strength of reinforced concrete T-beams before and after strengthening by using reinforced concrete jacket. Four full scale beams were first loaded to certain levels of ultimate capacity (0, 60%, 77%, 100% of failure load). Then, after formation of cracks or failure, they were repaired by reinforced concrete jacketing method and tested again up to failure.

The main objective of this study is to restore the full ultimate capacity beams failed by flexure and to strengthen the cracked beam. Also, it is aimed to investigate the effect of loadig condition on beam before repair on the ultimate capacity after repair. Extensive measurements of deformations, cracking and strength were made before and after repair throughout all stages of loading.

Test results showed that the repairing by reinforced jacketing can effectively restore more than 150% of the full flexural capacity of the original beam. Also reinforced jacket can effectively increase the ultimate capacity of cracked T-beam after repair up to 250%. Furthermore, the use of reinforced jacket for the cracked or failed beams is greatly improved serviceability, deformation behaviour, cracking behaviour as well as ductility of T- beams compared to those of the original beams.The ultimate flexural strength of T-beams failed by flexure and repaired by reinforced concrete jacket can accurately be predicted using conventional ultimate strength method of reinforced concrete .

**KEYWORD**: **cracks,flexure, jacketing, reinforced concrete, repair, strengthening,T-beam**.

**الخلاصة:**

يقدم هذا البحث دراسة عملية شاملة لسلوك و مقاومة الروافد الخرسانية المسلحة بمقطع نوع T قبل وبعد تقويتها باستخدام الغلاف الخرساني المسلح .تم تحميل اربعة نماذج من الروافد الخرسانية الى مستويات متفاوتة من التحميل وهي:
0%،60%،77%،100% من التحمل الاقصى لهذه الروافد و بعد حدوث التشققات او حدوث الفشل في هذه الروافد تم إصلاحها بإحاطتها بالغلاف الخرساني المسلح ومن ثم أعيد فحصها لغاية الفشل.

ان الغرض الاساسي من هذه الدراسة هي بحث امكانية استرجاع مقاومة الروافد الفاشلة او المتشققة. و تهدف هذه الدراسة كذلك الى بحث تاثير التحميل المسبق قبل الاصلاح على قابيلية تحملها بعد الاصلاح.

أجريت قياسات مكثفة للتشوهات و التشققات اثناء كافة مراحل التحميل قبل و بعد عملية الاصلاح.

اظهرت نتائج البحث ان الغلاف الخرساني المسلح كان فعالاً في استرجاع المقاومة القصوى بنسب تصل الى 150% من مقاومة الثني لهذه الروافد.

لقد اظهرت النتائج كذلك بان الغلاف الخرساني المسلح قد ادى الى زيادة المقاومة القصوى في الروافد المتشققة بنسب تصل الى اكثر من 250% من اقاومتها الاصلية.

اضافة الى ذلك فان استخدام الاغلفة الخرسانية المسلحة في تقوية الروافد المتشققة قد حسنت بصورة كبيرة قابلية الخدمة في هذه الروافد وادت الى زيادة في اللدونة مقارنة الى حالتها الاصلية.
من الممكن ايجاد قابلية تحمل هذه الروافد التي صلحت بالاغلفة الخرسانية المسلحة بالاعتماد على الطريقة المالوفة في الكود الامريكي الخاص بحساب المقاومة القصوى للروافد الاعتيادية.

## CONTENTS



## -INTRODUCTION

In recent years, the repair of existing structures is rapidly emerging as new sector in structural engineering. Sometimes, repair of deteriorated concrete structures (strengthening, rehabilitation and retrofitting) becomes more economical than building new one, if by repairing a safe and serviceable structure can be achieved. The success of a rpair or rehabilitaion projet will depend upon the degree to which the work is excuted in conformance with plans and specifications.

Due to the importance of the problem, many international conference are currently been held (7th International Conference,2001) to investigate the problems and to suggest the solutions involving the repair of damage structures or unserviceable structures.Guidance manuals are also presnted for evaluation and repair of concrete structures (U.S.Army Corps of Eng.,2002). In fact, the repair involves many uncertain factors, which has not yet been fully investigated.

One of the main problem related to repair is the bond between the surface of the damaged concrete and the material of repair. The short-term properties (shrinkage and creep) of both the damage concrete and the material of repair would significantly affect the performance of the structure after repair.It is important that the design engineer reponsible for the investigation of the distress and selection of repair materials and construction techniques.

In certain cases, reinforced concrete structures may require to increase its own ultimate capacity by strengthening some main structural members like beams and columns.Strengthening may also used to stop the deterioration of the structures by repairing the harmful cracks and preventing the excessive deflection.

The reduction in the strength of reinforced concrete members can be resulted from different reasons. These may be due to natural disasters (earthquake), wars, successive deflection, cracking due to misuse of the structures and corrosion of steel reinforcement, especially, at offshore structures.... etc.

Repair and strengthening of reinforced concrete beam is commonly carried out by “Jacketing” . Jacketing is casting new reinforced concrete shell around the damage member. There are several methods and materials for concrete repair [ Emmons,1993].

The concrete used in the jacket may be pre-replaced aggregate concrete with compressive strength higher than that for the old concrete. The bond strength between the new concrete and the old concrete can be assessed by slant shear tests [Ersoy,1993].

In other cases of repairing of damaged beam, additional steel is required. Full anchorage of the additional steel is necessary and should be located at the region of minimum flexural stresses. Anchorage of the additional links at the top of the beam is also necessary. However,, jacketing may be one of[Johnson,1965] more reliable method of strengthening than externally bonded plate, but, it would increase the size of the original beam. On the other hand, externally bonded plate method, may be easier than jacketing method.

Very few research works have been done on experimental behaviour of jacketed reinforced concrete beams. Cheong and MacAlevey, [2000] carried static and dynamic load tests to failure on 61 slant shear prisms and 13 jacketed reinforced concrete T-beams. The concrete used in the jacket was replaced aggregate concrete. The strength of the bond between preplaced aggregate concrete and plain concrete was assessed by slant shear tests and a Mohr-coulomb type failure envelope was derived. Static failure of the beam specimens was related to this failure envelope. Test results showed the importance of adequate reinforcement detailing on the beam strength (i.e. that full anchorage of the additional steel at simple supports and points of counter flexure and anchorage of the additional links at the top of the beam was necessary).However, they concluded that good reinforcement detailing in beams was fully contributing to the strength of the jacketed beams. Furthermore, moderate dynamic loading of jacketed beam does not seem to result in significant reduction in the load capacity.

Cracks can form in reinforced concrete members due to several reasons .Errors in design and detailing that may result in unacceptable cracking include use of poorly detailed corners in walls, precast members and slabs. The use of an inadequate amount of reinforcing may result in excessive cracking.

Generally, deterioration of concrete structures is mainly due to formation of cracks as aresult of many reasons. Inadequate detailing of reinforcement, expansion, and construction joints, creep and shrinkage and unexpected loads may cause cracks in concrete.

Crack width increases with increasing steel stress, cover thickness, and area of concrete surrounding each reinforcing bar. The width of a bottom crack increases with an increasing strain gradient between the steel and the tension face of the beam.However, jacketing method of repair for T-beam is adopted in this study ,since, it can provide new reliable hollow sectins around the existing damage member. The research work is aimed to investigate the following objectives:

-To restore the capacity of partially and totally failed reinforced concrete T-beams by flexural.

-To increase the flexural capacity of existing reinforced concrete T-beam
-To investigate the behaviour of T-beam repaired by jacketing using ordinary reinforced concrete .
The main variables considered in this research are the effect of working loads before strengthening on the behaviour and strength of reinforced concrete beams after repair.

## EXPERIMENTAL INVESTIGATION

The test program reported in this study is intended to investigate the possibility of restoring the capacity of reinforced concrete T-beam which was failed by flexure. Four reinforced concrete T-beams were subjected to two point load which was increased up to certain level of failure load. The behavior and strength of repaired T-beam under two point loads were observed at all stages of loading. The method of repair used here was the reinforced concrete jacketing. Jacketing is generally used where there is no limitation for the increase in the size of the member.
The main variables considered in the test beams are the effect of cracking condition caused by applied loads (preloading) on their strength after repairing or strengthening. The preloading is defined here to be the ratio of applied load on the member before repair to its own ultimate load. It is well known that the applied load is variable during the useful life of the member. It could be less or more than the maximum service load.
Therefore, it may causes instantaneous deformation or long term deformation in addition to invisible cracks. The intensity of the deformation and cracks depend mainly on the amount and the period of application of the applied load. Test programme involves four beams given in Table 1.

**Table (1) Test Beams**

| Beam | Stage-One Loading condition | | Stage-Two Test after jacketing | |
|---|---|---|---|---|
| | Applied load as % of ultimate load ($\lambda$) | Cracking condition | Repairing details | Applied load |
| B0 | 0 | No cracks | Fig.1 | up to failure |
| B60 | 60 | Flexural cracks | Fig. 1 | “ |
| B77 | 77 | Flexural cracks | Fig.1 | “ |
| B100 | 100 | Flexural failure | Fig.1 | “ |

## Test beams

Series BO beams is designed to investigate the effect of preloading ($\lambda$=0 %, 60%, 77% and 100%) on the strength and behaviour of beams B0, B60, B77, B100 ) after repair .Beam B100 is loaded first to failure ,then repaired by jacketing method (see Figure (1)) and tested again up to failure. This beam was designed to study the possibility of restoring the flexural capacity by using jacketing method. Beam B0 was not loaded at first stage and therefore has no cracks whereas the other (B60,B77) were loaded at first stage up to 60% and 77% of failure load which produced flexural hair cracks at first stage.All beams have same flexural capacity. Then, all these beams were strengthening by jacketing as shown Figure(1) and Figure(2).
The main tensile reinforcement (bottom reinforcement) is kept constant (2¢12) .Minimum stirrups of ¢6@100mm cc was used in the original beams and same amount was used again at jacketing to prevent shear failure. The new stirrups added to the beams during repair are welded from the top by overlapping the bar's end at a distance 4 times diameter of bars [BS, 1990]. The original beams (B60,B77,B100) were loaded first up to the degree of loading $\lambda$ mentioned above (60%,77%,100%), then, they were repaired as shown in Figure(1) and (2).Then, all beams retested again up to failure.

## Strengthening of beams by jacketing

- Remove all the concrete which has been cracked or crushed at compression zone and else
- where due to failure of beams (B100)
- Remove the concrete covers of the sides and bottom reinforcement for beams (B0, B60,
- B77), which are prepared for strengthening.
- Clean concrete surface by washing with water for all beams.
- Fix the new main steel reinforcement for beam (B0, B60, B77, B100) as shwn in Figure (1)
- and (2).
- Prepare concrete mix in same quantities of materials used for the original beams.
- Before casting the new concrete, all concrete surface should be covered with 1:1 water :
- cement liquid.
- Concrete was compacted by using damping rod and vibrators.
- Beams were cured again for 28 day before testing.

•

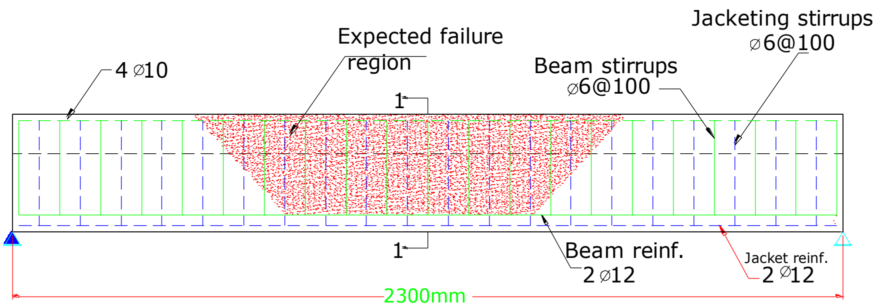


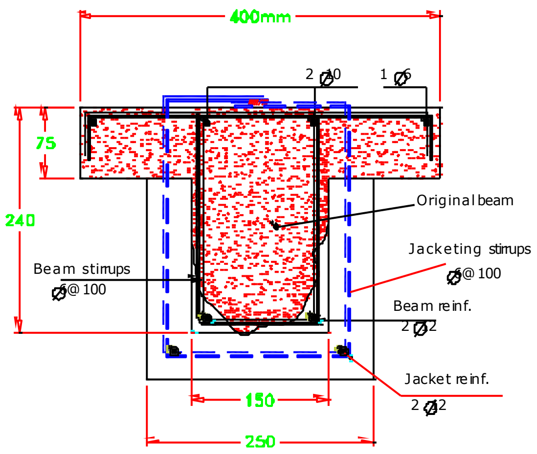


Sec. 1-1

**Figure ( 1 ) Typical jacketing of test beams**

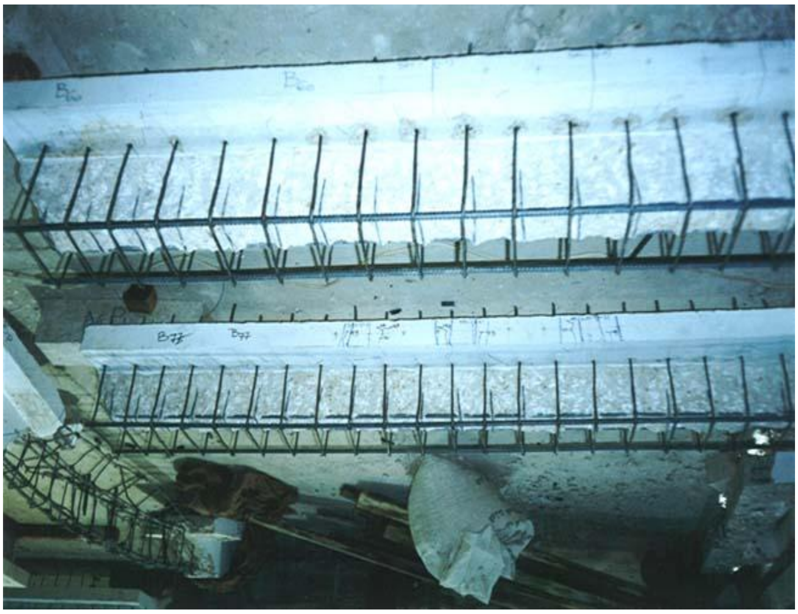

**Figure (2 ) Preparing of beams B60 B77 B100 for jacketing**

## Concrete

In this research the mix proportion of concrete used was 1 : 2 : 4 by weight ( cement : sand : coarse aggregate) with 0.55 w/c ratio.This mix was aimed to obtain about 30N/mm2 cube compressive strength at age 28-days.
The concrete mix used for repairing was same as that used for beams except the w/c ratio was reduced to 0.5 to get the target compressive strength of about 35 N/mm2 at age 28-days. The concrete mix was found to be workable with slump of about 70mm which suitable for casting and repairing of test specimens.

## Steel reinforcement

The steel reinforcement used are 6mm, 10mm, 12mm, and 16mm dia. deformed bars which are free from harmful defects, seams, porosity, segregation, non-metallic inclusions.
In this research the samples of steel bars are tested in tension according to BS4449:1988 .The test results are given in Table (2). All samples tested are satisfying the BS4449:1988 standards.
All stirrups used for beams before repair are 6mm diameter. Same diameter are used for beams after repair which are welded by E43 electrode according to BS5950 part 1:1990. The overlap is about 50mm. Tensile tests were carried on this type of welding. Results have shown that the strength of weld is greater than the strength of the original reinforcement. The yield stress and ultimate stress of bars tested are summarised in Table (2).

**Table (2) tensile strength of bars reinforcement**

| Bar dia. (mm) | 6 | 10 | 12 |
|---|---|---|---|
| Yield stress (N/mm2) | 255 | 287 | 361 |
| Ultimat stress (N/mm2) | 368 | 431 | 595 |

## Test procedure

The test procedure was carried out as follows:-
- The sample was put under the test instrument type FM 2750 machine Nr. 613 wolpert
- ch-8232 Merishausen where the hydraulic jack is used to exert load on the specimen
- (See Figure (3).
- The load capacity of the testing machine used is 30 tons and its sensitivity is 0.1 KN
- The specimen was put on supported roller to be simply supported.
- A steel beam with a dimension of 1000 x 240 x 120 mm was used to transfer the single load from the testing machine to two points loads on the tests specimen. The said steel beam would change the concentrated loads in to two equal loads.
- The initial readings were taken before loading, for all deflection points and concrete strain gauges.

The loading was exerted on the specimen at increment which was 4 KN. until the appearance of the first cracking load. All cracks were marked on the concrete surfaces of the specimen during all loading stages. The deflection and concrete strain gauge readings were taken at each stage of the loading until the concrete failure occurs.

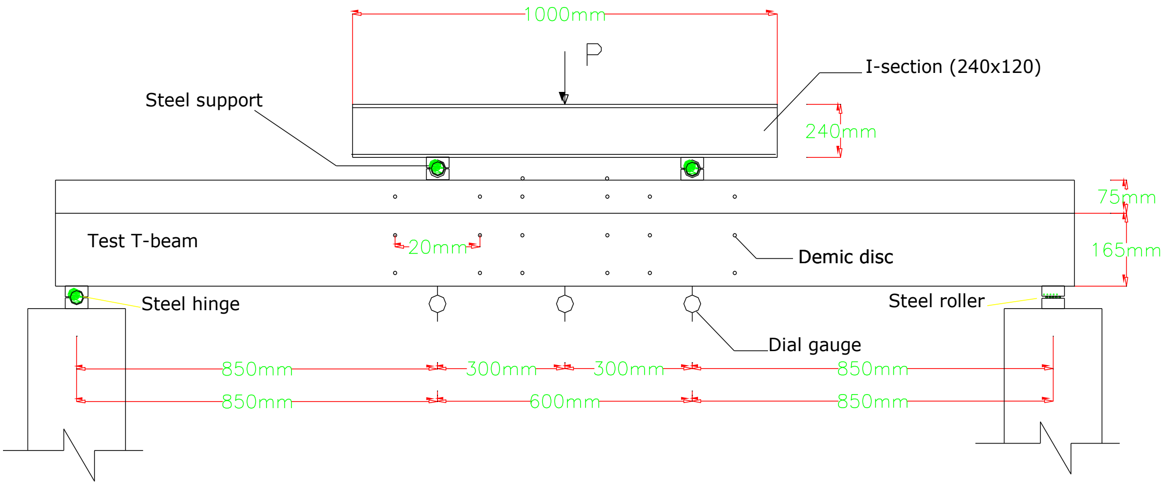


**Figure ( 3 ) Typical instrumentation of test beams**

## TEST RESULTS

The behaviour of reinforced concrete beams is well established by research workers but it its behaviour after repair has not yet been fully investigated. However, one of the objective of this study is to investigate the behaviour of repaired beam under flexure.
The beams must be safe and serviceable. A beam is safe if it is able to resist all forces which will act on it during its life time. Serviceability implies that deflections and other distortions under load shall be unobjectionable small.

## Load- deflection behaviour

The deflections along the spans of the test beam before and after repair were measured at all stages of loading. The maximum centre deflections for these beams were plotted in Figure (4). as a function of the total applied load. All beams have shown similar behavior before and after repair. These curves are composed of three distinguished regions namely, pre-cracking stage, post cracking stage and post serviceability cracking stage.
At pre-cracking stage, the applied loads are directly proportional to the centre deflections for beams before and after repair. This means that the entire concrete section is effective in resisting deflection, which caused by applied load. The pre-cracking segment of load deflection curve is, therefore, defining full elastic behaviour for all beams tested here. The theoretical deflections shown on the figures, are based on moment of inertia of the un cracked reinforced concrete section which agreed well with those obtained from test results. The theoretical deflections are slightly lower than those observed from tests. This may be due to approximate evaluation of modulus of elasticity by ACI expression:

$$EC = W_c^{1.5} \times 0.043 \sqrt{f_c'}$$

However, the elastic behaviour of beams after repair are similar to those before repair irrespective to the loading condition before repair.

When the load on the test beams is gradually increased beyond the first crack to the service load, the behaviour of beams changed slightly in to a post-cracking stage. Figure (4) showed that the relationship between load and deflection at post-cracking stage are approximately linear defining semi-elastic behaviour.
At post-cracking service load stage, the formation of flexural cracks in beams before repair reduced the flexural stiffness of the beam section making the load-deflection curve less steep in this region than in the pre-cracking stage segment. Similar behaviour was observed for the beams after repairs.The theoretical deflections on these figuress are calculated based on the procedure specified by ACI code,2005, art 9-5-2-2. ACI code methods is slightly underestimated the deflection especially for beams before repairs.This may be due evaluation of cracking moment capacity Mcr in ACI-method which related to approximate value of modulus of rapture

$$(M_{cr} = \frac{f_r\ I_g}{y_t})$$

However, Fig (4) shows that the beams repaired by jacketing gave higher flexural stiffness than their original flexural stiffness, in spite, of the existing cracks in the original concrete. This means the jacketing is significantly increased the flexural stiffness and hence would improve the serviceability.
When the load is further increased beyond the service load, the beams showed substantial loss in their stiffness because of the extensive cracking penetrating to the compression zone. In the region (post serviceability cracking stage), the load deflection curve tend to be flatter. The small increase in the applied load resulted in large amount of deflection.

However, the repaired beams have shown similar or even better load deflection behaviour than the original beams. Jacketing method enhanced the serviceability compared to the original beam. On the other hand, the loading condition and crack condition of the beams before repairs have no significant effect on the load deflection behaviour of the beams after repair. Repair by jacketing resulted in reduction in the deflection under service load to about 40% of the original deflection before repair. The jacketing method has given the best result in improving the load deflection behaviour of beams.

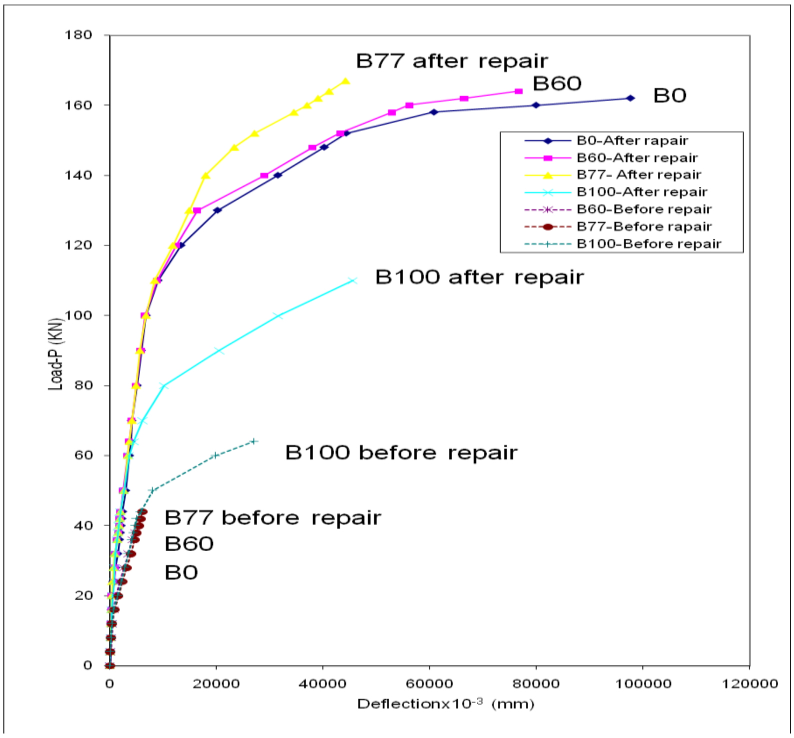


**Figure (4 ) Load-deflection curves of beams before and after jacketing**

## Load-steel strain curves

The steel strains were measured at three sections along the span (under two points load and at the middle sections). Mechanical strain gauge was used with 200mm gauge length, which measured the concrete surface strain at steel level.

It is assumed that the concrete surface adjacent to the steel will have same strain as the steel. However, this is the best available technique in the laboratory.

The load-tensile steel strain curves at mid-span were plotted for all beams before and after repair as shown in Figure (5). Three different stages of behaviour can be clearly distinguished.

At low load, it can be seen that the steel strain is directly proportional with the applied load following the elastic behaviour (elastic stage). After formation the first crack, the steel strain is changed to be flatter than that before crack. Then it increases steadily and linearly up to the yielding strain.

In the cracking region, the stresses are still proportional to strains. Further increase in the applied load beyond the service load resulted in a large and non-linear increase in the tensile strain of beams before and after repair.

Test results show that the repair by jacketing causes a great decrease in the tensile strain of the original beams. This means that the reinforcement of the jacketing is significantly contributing in resisting the applied load besides the original reinforcement. The percentage of decrease is ranging between about 90% in beam B77 to about 70% in beam B100 at service load.

On the other hand, the top steel plate reduced the steel strain in beams before repairs as shown in Fig. (5).

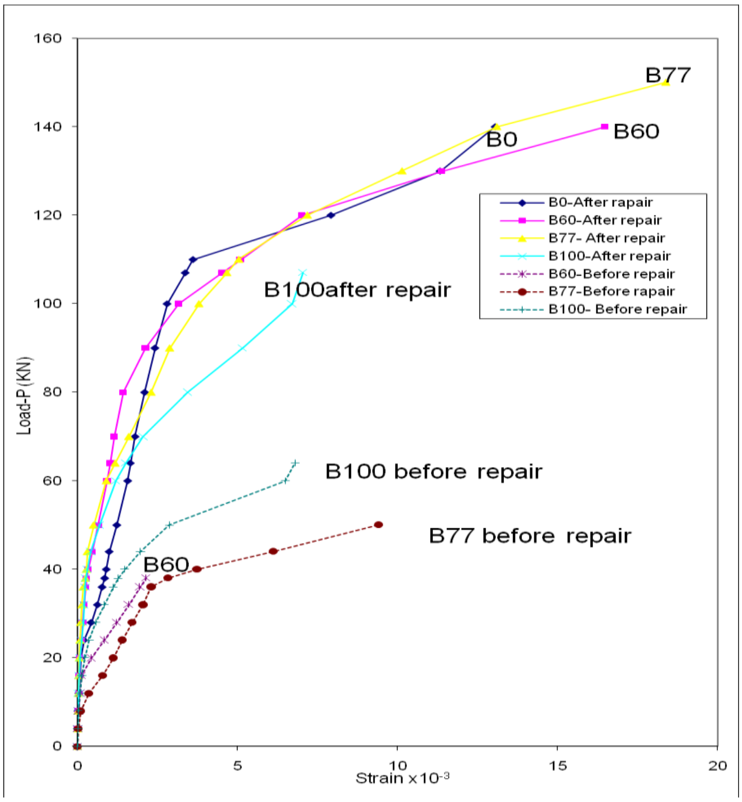


**Figure ( 5 ) Load-steel stain curves for beams before and after repair by jacketing**

## Load-Concrete Strain Behaviour

Concrete compressive strains at top fibre of the mid-span section of each beam were measured. Compressive strains under the point loads are also measured. The compressive strains at the mid-span are plotted with applied load for all test beams as shown in Figure(6). The load compressive strain behaviours are similar to the load-tensile strain behaviour discussed elsewhere. Therefore, there is a consistency between the tensile and compressive strain under loading. This should be existing to agree with the rational theory of ultimate bending strength of the beam (strain distribution across any section of the beam is assumed to be linear).

Reinforced jacket acted to redistribute the compressive strain between the original and new concrete. Therefore, the compressive strains are reduced in compression zone of repaired concrete compared to the original strains as shown in Figure (6). The percentage of reduction was observed to be between about 30% in beam B60, Fig. (5.35) to 60% in B100 Fig. (5.39). This behaviour is consistent with the original behaviour . All repaired beams have reached to the specified yield strain of concrete or slightly higher than that. The observed yield strain was ranging between about 0.0035 to 0.0060. The concrete strain in the original beam has reached to about 0.003. This indicates that the jacketing increased the ductility of concrete.

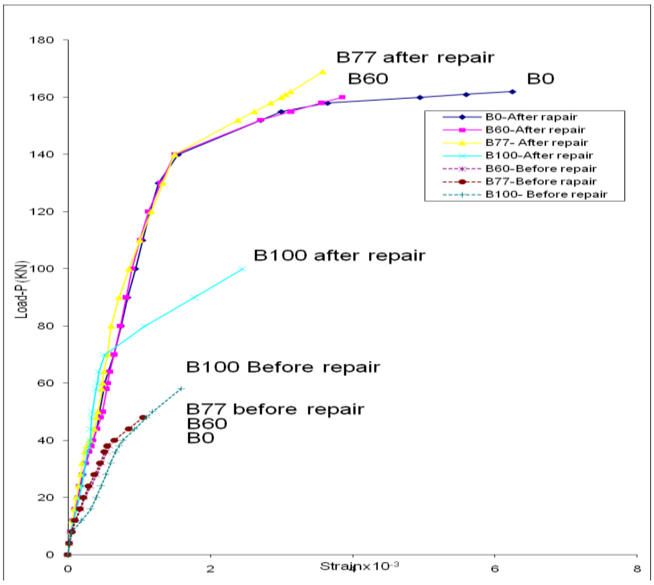


**Figure ( 6 ) Load-compressive stain curves for beams before and after repair by jacketing**

## CRACKING BEHAVIOUR

The formation of cracks at every stage of loading is marked on the test beams as shown in Figures (7) and (8). Concrete cracks at an early stage of its loading history will crack first because its weak in tension. Consequently, it is necessary to study its cracking behaviour and control the width of the flexural cracks. Cracking contributes to the corrosion of the reinforcement, surface deterioration and its long-term deterioration effects. The problem of cracking becomes much more important in retrofitting the deteriorated beams, because, the existing uncontrolled cracks may reduce the load carrying capacity of the beams and will increase the deflections beyond the permitted limits.
Hence, the prediction and control of cracking and crack widths are essential for reliable serviceability performance under long-term loading.
As a beam is subjected to bending moment resulting from applied loads, tension stresses will occur in one side of neutral axis and compression stresses developed in the other side. When the tension stress exceeds the modulus of rapture, cracks form. If the concrete compression stress is less than approximately half compressive concrete strength and the steel stress has not yet reached the yield point, both materials continue to behave elastically or very nearly so. At this stage, it is assumed that tension cracks have progressed all the way to the neutral axis, and that sections plane before bending are plane in the bent member.

### <u>Beams before repair</u>

The initial flexural cracks have first developed in all beams tested except beams B0, which was not loaded before repair. The typical cracking condition of B100 is shown in Figure (7). All beams have shown that the first crackform at about same load, which was about 16 KN because these beams were identical. The flexural cracks developed at bottom fibre in the region of maximum bending moment (between points loads). These cracks penetrated upward as the load increased and new cracks spread toward the points load. Then, the load was removed when it reached to 60% of the ultimate load (B60) whereas the applied load continued, untill 77% of the ultimate load in beam B77 . In this beam, the flexural cracks penetrate deeper in the flange of the beam (compression zone) and some cracks separated

into two branches. Beam B100 has nearly similar cracking behaviour at this stage (77% Pu). Then, the loading continued for beam B100 up to failure.
As the loaded increases above 77% of the ultimate load in beam B100, the cracks, under the left point load have deeply penetrated to the compression zone resulting in complete failure by crushing the flange under the point load resulting a complete flexural failure.

**Beams after repair**

The objective of B0 was to investigate the possibility of increasing the ultimate capacity of non-cracked section by jacketing method. Beams B60, B77 were tested to investigate the strengthening of cracked sections using jacketing method. To retrofit the failed beam by jacketing, B100 was investigated. The cracking behaviour of B0 after strengthening, is similar to the cracking behaviour of beams B60, B77, B100 before repair. This means, the strengthening by jacketing would result in similar cracking behaviour to that of the original beams.
Therefore, same principle of the original beam may be used to predict crack width of the beams strengthened by jacketing. The mode of failure of beam B0 is a pure flexural failure which crushed the compression zone, (top flange) between points load. So, the ultimate strength theory can also be used to predict the moment carrying capacity of strengthened beam by jacketing.
After repairing beams B60, B77, B100 by jacketing, the cracking behaviour were approximately similar to those observed before repair . A typical cracking condition of beam after repair is shown in Figure(8). Then, the mode of failure of beam B100 after repair Figure (10) was exactly in similar type and in same location as that of the original beam before repair Figure (9). Beams B60, B77 showed similar mode of failure after repair as in beam B100 but with improved ductility (large deflection before failure). This indicates that the behaviour of strengthened beams (B77, B60) are more ductile than the retrofitted beam (B100).

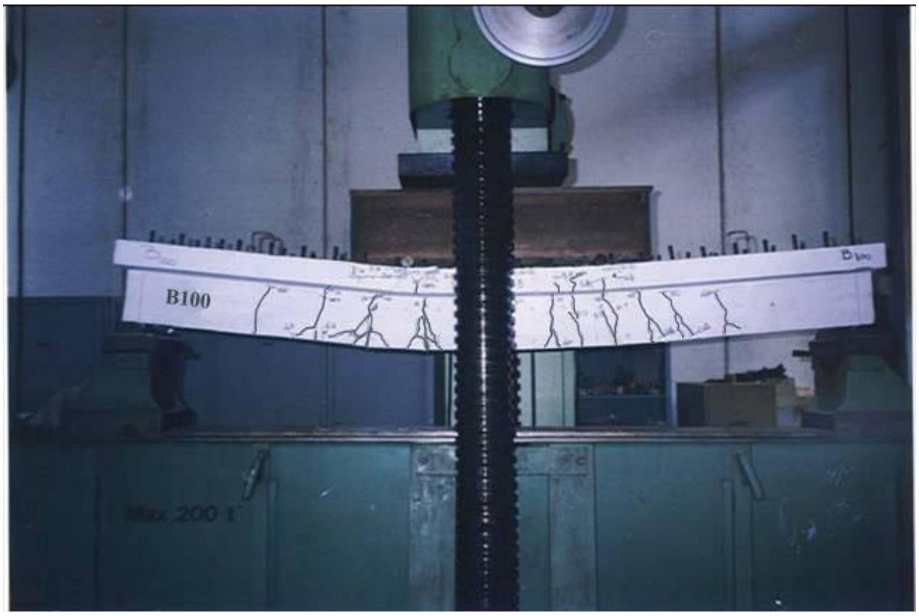


**Figure ( 7 ) Cracking of Beam B100 (before repair)**

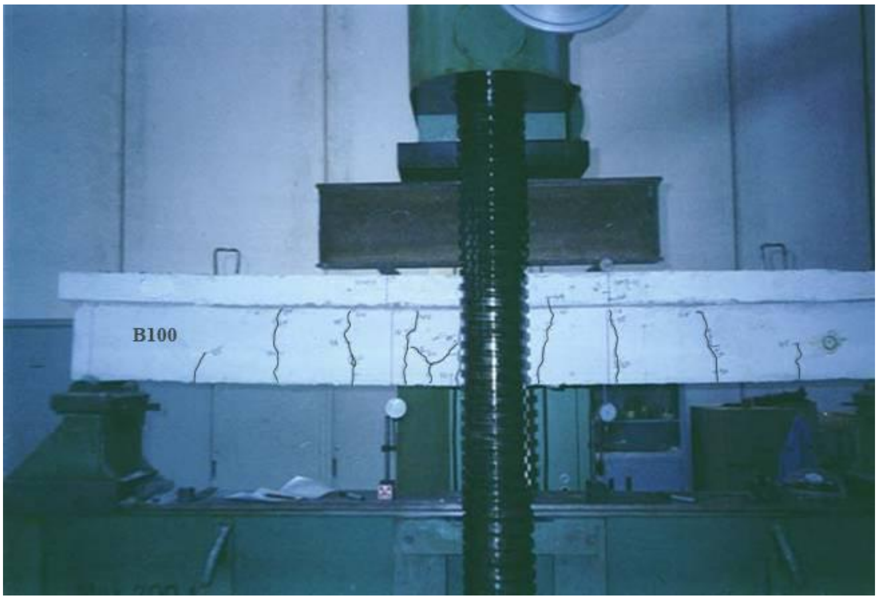


**Figure ( 8 ) Cracking of Beam B100 (after repair)**

## FAILURE LOAD OF TEST BEAMS

Experimental and theoretical failure loads are given in Table (3). Based on this table, the strength and the efficiency of repair are presented here.
As mensioned elswhere,all beams have same steel reinforcement, size and concrete properties. They were designed to have flexural failure before repair at ultimate load of about 38KN according to ACI method.
Beam B0 was strengthened by reinforced jacket without any flexural cracks in the original concrete, (unloaded before repair). To show the efficiency of jacketing method in non-cracked section.
Beams B60 , B77 were loaded to 60% and 77% of the failure load obtained from test. Such loading produced flexural cracks with intensity related to the applied load .In fact, the higher the load the more cracks will produce. Then, these beams were repaired by reinforced jacket as mentioned elsewhere. After curing, the beams were tested again to gradually up to failure. Observations were made for surface strain and deflection during the loading. Cracks were also marked on concrete surfaces. Beam B100 was first loaded to flexural failure. then, the crushed concrete was removed and replaced by new concrete in addition to the reinforced jacket. The main aim of this beam was to investigate the possibility of restoring the flexural strength of failed beam using reinforced jacket.

Referring to Table (3), the use reinforced jacket with (2$\phi$ 12) increased the failure load of beam B0, B60, B77 from 64KN to about 165KN. This means the failure load after strengthening increased to about 150% as much as the original failure load irrespective to the condition of cracks before repair. Therefore, the existing flexural cracks have no significant effect on the flexural strength after repair.
The high flexural strength of beams may be attributed to the confinment of cracked beam by new jacket with very high bond strength between the original and jacket concrete,These will make the beam to act as one unit. In fact, the removing of the concrete cover of these beams before jacketing provided a very rough surface for good bond between cracked concrete and new concrete. The ratio between theoretical failure load to the experimental value is about 0.82. The theoretical procedure followed here has taken in consideration the increase in

effective deth after jacketing as weel as the exiting reinforcement in the original beam. On the other hand, the theoretical failure load is very closed to the experimental failure load of the original beam (before jacketing). The ratio between the theoretical to the experimental is about 0.91.

For beam B100, the jacketing was restored about 167% of the original ultimate capacity of the beam. The original reinforcement in this beam was useless since it was ruptured by the first test before jacketing. The ratio between the theoretical and the experimental failure load was about 0.73. this means, that the existing reptured steel contribute in resisting applied load. However, the yield reinforcement may carried about 27% of the failure load in the second test (after jacketing).

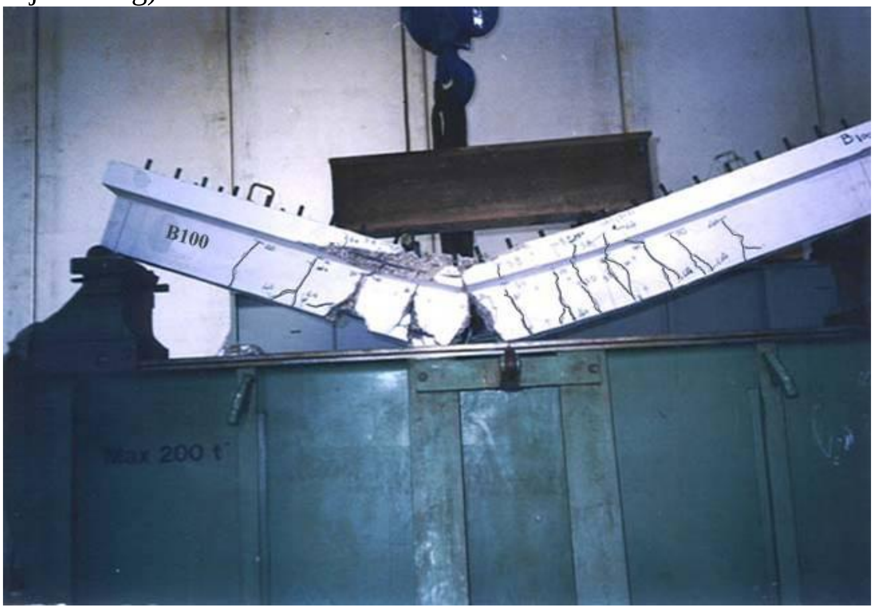


**Figure ( 9 ) Flexural failure mode of Beam B100 (before repair)**


**Figure (10 ) Failure mode of Beam B100 (after repair)**

**Table (3) Ultimate experimental loads of beams repaired by jacketing**

| Beam | 1st cracking load | | | | Failure load (Pu) | | | | Mode of failure |
|---|---|---|---|---|---|---|---|---|---|
| | Original beam | | After repair | | Original beam | | After repair | | |
| | Exp. (KN) | Theo. (KN) | Exp. (KN) | Theo. (KN) | Exp. (KN) | Theo. (KN) | Exp. (KN) | Theo. (KN) | |
| B0 | 16 | 18.5 | 20 | 41.6 | 64 | 62 | 162 | 135 | Flexure |
| B60 | 16 | 18.30 | 22 | 33.9 | 64 | 62 | 164 | 135 | Flexure |
| B77 | 16 | 18.30 | 20 | 34.2 | 64 | 62 | 169 | 135 | Flexure |
| B100 | 18 | 18.50 | 22 | 41.6 | 64 | 62 | 107 | 78 | Flexure |

## EFFECT OF LOADING ON THE STRENGTH OF REPAIRED BEAM

The failure loads of beams B0, B60, B77, B100 were plotted against the first load test $\left(P/P_u \times 100\right)$, which corresponded to crack condition of the original beams before repair as shown in Figure (11). All beams have same failure load because they are identical. The conditions of cracks at the original beams were marked on the axis.
Figure (11) shows that, the existing flexural cracks in the original beam up to load level of 77% has no significant effect on the strength after jacketing. The strength of beams after jacketing is mainly affected by the amount both the existing reinforcement and the reinforcement of jacketing. The reduction in the strength of beam failed in flexural before jacketing, (Beam B100) compared to other, (B0, B60 and B77), was mainly due to lost of original reinforcement by rupture during the first test.

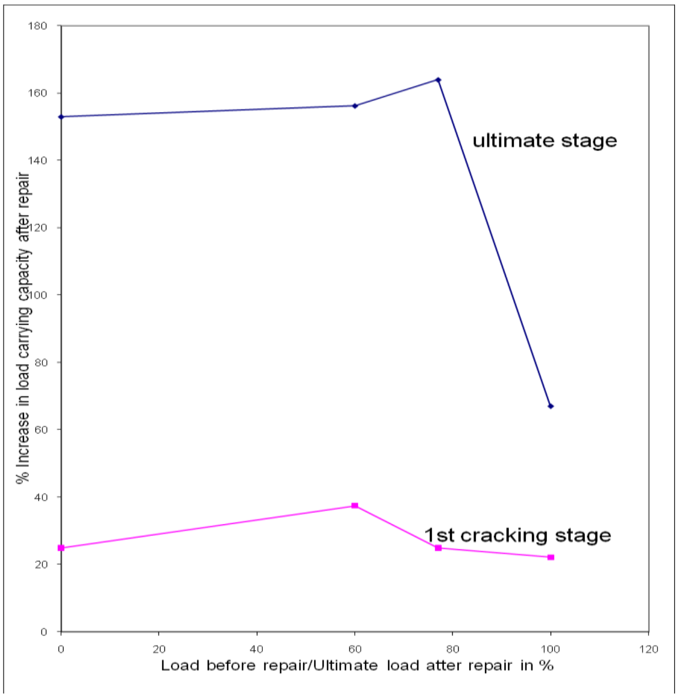


**Fig. (11) Effect of loadig before repair on the strength of beams repaired by jacketing**

**THEORETICAL FAILURE LOAD**

Based on ACI-318M-2005 the ultimate moment capacity of the beam (B0, B60, B77, B100), were calculated using the actual dimensions in Figures (1),(3) and material strengths Table (2).The notations used here are same as that given in ACI Code.

**Beam before repair**

$F_{cu}$ = 35.6 N/mm2 , $f_{c'}$ = 30 N/mm2 , $f_{su}$ = 595 N/mm2 ,

Main reinforcement 2 Ø 12

$A_s$ = 113X2 =226 mm2

Effective depth = 240 - (25 + 12) = 203 mm

As $_{min}$ = 0.005 x b x d

As $_{min}$ = 0.005 x 150 x 203 =152.25 mm2

$$a = \frac{As \times f_y}{0.85 \times f_{c'} \times b} = \frac{226 \times 595}{o.85 \times 30 \times 400} = 13.2 \text{ mm} < t \quad (\text{Sec. rectangular with } b = 400)$$

$$\rho_b = \frac{0.85B \times f_c'}{f_y}\left(\frac{600}{600 \times f_y}\right)$$

$$B_1 = 0.85,\ f_y = 361\,N/mm^2,\ f_c' = 30\,N/mm^2$$

$$\rho_b = \frac{0.85 \times 0.85 \times 30}{361}\left(\frac{600}{600 \times 361}\right) = 0.037487$$

$$A_{s_{max}} = 0.75\,\rho_b\,bd$$

$$= 0.75 \times 0.037487 \times 150 \times 203 = 856.106\,mm^2$$

As prov.< As max. O.K. $\therefore$ beam under reinforced.

Mu = $A_s$ $f_u$ ( d – a/2) Ø = 1 (actual moment capacity without factor of safety)

Mu = 226 x 595 ( 203 – 13.2/2 ) = 26409908 N.mm = 26.4 kN.m

Total failure load ($P_u$) = 2 x 26.4/.85 = 62 kN.m

**Beam with jacket B 100**

$F_{cu}$ = 35.6 N/mm2 , $f_{c'}$ = 30 N/mm2 , $f_{su}$ = 595 N/mm2 ,

Main reinforcement 2 Ø 12

$A_s$ = 113X2 =226 mm2

Effective depth = 240 + 50 - (25 + 12) = 253 mm

As $_{min}$ = 0.005 x b x d

As $_{min}$ = 0.005 x 150 x 253 =189.75 mm2

$$a = \frac{As \times f_y}{0.85 \times f_{c'} \times b} = \frac{226 \times 595}{0.85 \times 30 \times 400} = 13.2 \text{ mm} < t$$

( Sec. rectangular with b =400)

$$\rho_b = \frac{0.85B \times f_c'}{f_y}\left(\frac{600}{600 \times f_y}\right)$$

$$B_1 = 0.85,\ f_y = 361 N/mm^2,\ f_c' = 30 N/mm^2$$

$$\rho_b = \frac{0.85 \times 0.85 \times 30}{361}\left(\frac{600}{600 \times 361}\right) = 0.037487$$

$$A_{s_{max}} = 0.75 \rho_b bd$$

$$= 0.75 \times 0.037487 \times 150 \times 203 = 856.106 mm^2$$

As prov.< As max. O.K. $\therefore$ beam under reinforced.

Mu = $A_s f_u$ ( d – a/2) Ø = 1 (actual moment capacity without factor of safety)

Mu = 226 x 595 ( 253 – 13.2/2 ) = 33133408 N.mm = 33.13 kN.m

Total failure load ($P_u$) = 2 x 33.13/.85 = 78 kN.m

## CONCLUSIONS

The main factor considered here is the effect of the level of loading in percentage of ultimate load before repair on the strength and behaviours of the beam after repair. However, this investigation can not be considered to have given a complete study of problems related to repairing and retrofitting of T-beams but it is hoped that the present investigation show the effectiveness of jacketing method in restoring the flexural strength of T-beams. The test results have led to make some useful contribution towards better understanding of strength and behaviour of reinforced concrete T-beams repaired by jacketing method. The major overall conclusions drawn from the test results are summarized as follows:

- Reinforced concrete jacket has greatly increased the flexural capacity of beams cracked in flexural. The flexural capacity of jacketed beams was about 2.5 times its capacity before jacketing.
- Reinforced jacket was very effective in restoring the flexural capacity of beam failing in flexure. The repairing by reinforced jacketing resulted in increase in the capacity of failed beam into about 167% of the original strength of the beam.
- It was observed that the effect of loading condition of the beam before repair has only slight influence on the flexural capacity of beam after repair by jacketing. That effect

becomes very significant when there is a a complete flexural failure in the beam before repair.

- First flexural cracking load of beams strengthening by jacketing is increased by amount of 25% resulting in an improvement in workability.
- Test results showed that the yielded reinforcement before repair contribute in increasing the flexural capacity of beam after jacketing by amount of 27% of the failure load.
- Reinforced jacket increased, significantly, the flexural stiffness of the original beams resulting in less deflection under service load. The percentage of reduction in deflection was about 40%.
- Tensile steel strain was, considerably, reduced by reinforced jacketing. The percentage of decrease was ranging between 70% to 90% .
- Reinforced jacketing has led to considerable increase in concrete compressive strain at ultimate stage of loading in a very ductile mode of failure.
- Reinforced concrete jacketing has greatly improved the cracking behaviour of beams irrespetive to cracking condition before repair.
- Test results showed that the addition of steel reinforcement at the compression zone increased both the ultimate capacity (22%) and ductility.
- A safe and reliable prediction of failure load of beams repaired by reinforced jacket can be obtained using stress-strain relationship of steel reinforcement. Neglecting the existing yield reinforcement, the average ratio of predicted failure load to that obtained from test beam was about 0.75.

## REFERENCECS


- ACI-318M-2005 “Building Code Requirement Concrete: American Concrete Institute, 2005.
- British Standard Specifications,Table 32, BS5950part1:1990.
- British Standard Specifications for steel tension(BS4449:19888).
- Department of th army U.S.Army Corps of Engineers "Evaluation and Repair of Concrete Structures"Manual No.1110-2-2002.
- Emmons,P. H.,Vaysburd,Alexander M,and McDonald,James E."Arational Approach to Durable Concrete Repairs,"Concrete International,Vol. 15, No.9, pp40-45.
- Ersoy, U, Tankut, T and Suleiman, R. “Behavior of Jacketed columns” ACI Jr. May-June 1993 pp. 288-293.
- H.K. Cheong W. MacAlevey, "Experimental behavior of jackted reinforced concrete beams" (2000).
- Johnson,S. M. "Detterioration Maintenance, and Repair of Structures"McGraw-Hill, New York.
- 7th International Conference on inspection ,Appraisal repair and maintenance of buildings and Structures 11-13 September 2001, Nottingham Trent University compus, Nottingham, UK.

# COPPER ETCHING IN AIR REGENERATED CUPRIC CHLORIDE SOLUTION

Baseem H. Fadhil
Chemical Engineering Department – College of Engineering – University of Baghdad – Iraq
baseemee@yahoo.com

**ABSTRACT**

One of the most important steps in the world of printed circuit board manufacturing (PCB) is the copper etching process. Because of its low cost, environment aspects, and simple regeneration techniques, cupric chloride was chosen to be the most attractive etchant.

Etching of copper from standard single-sided copper boards used usually for printed circuit board fabrication was conducted in a cell containing cupric chloride solution. Average etching rates were recorded as a function of time, etchant specific gravity, free acid concentration, and temperature. Air was injected continuously in the etching cell during the process enabling mixing and solution regeneration. It is found that best operating conditions to obtain maximum etching rate is at 45-55°C, specific gravity of 1.3-1.4, and free acid concentration of 1.3-1.4 M.

**KEYWORDS**

**Etching, chemical machining, cupric chloride, regeneration, PCB**.

**الخلاصة**

ان التأكل الموجّه للنحاس يعد احد العمليات المهمة في عالم صناعة الدوائر الالكترونية المطبوعة (PCB). وانتخب محلول كلوريد النحاس ليكون احد اهم المحاليل المسببة لعملية التأكل الموجه نظراً لرخص ثمنه، وسهولة استرجاع فعاليته بعد استعماله، ولاعتبارات بيئية.

دُرس تأكل النحاس عبر عينات قياسية لالواح نحاس ذات وجه واحد تستخدم عادةً للطباعة الالكترونية في خلية تحوي محلول كلوريد النحاس، وسُجلت معدلات التأكل للعينات بالنسبة للزمن، ولدرجة الحرارة، وكثافة المحلول، وتركيز الحامض الحر. حُقن هواء بشكل مستمر في داخل الخلية بهدف مزج المحلول واسترجاع فعاليته. وجد ان افضل الظروف لتحقيق اعلى المعدلات للتاكل تكون بدرجة حرارة 45–55°م، وكثافة نوعية بحدود 1.3–1.4، وتركيز الحامض الحر بحدود 1.3–1.4 مولاري.

## INTRODUCTION

Etching can be defined as a machining technique, in which, controlled corrosion process was applied on selected areas of the metal part. This is usually occurring in the presence of a corrosive media, called *etchant*. The process was used by ancient Egyptians to make copper jewelries when they etched copper with citric acid around 2500 BC. Etching, nowadays, is extensively used to manufacture geometry complex and precision parts for electronic, aerospace, automotive, medical, decorative, and microcomponent production industries (O. Cakir *et al*, 2007; O. Cakir, 2007).

One of the most important steps in the world of printed circuit boards fabrication is the copper etching step from circuit boards. Circuit boards are usually fabricated from glass fiber reinforced epoxy

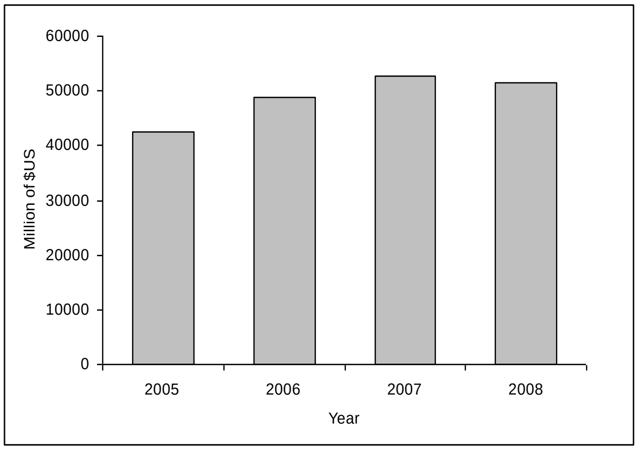


Fig.1 World PCB production (WECC reports)

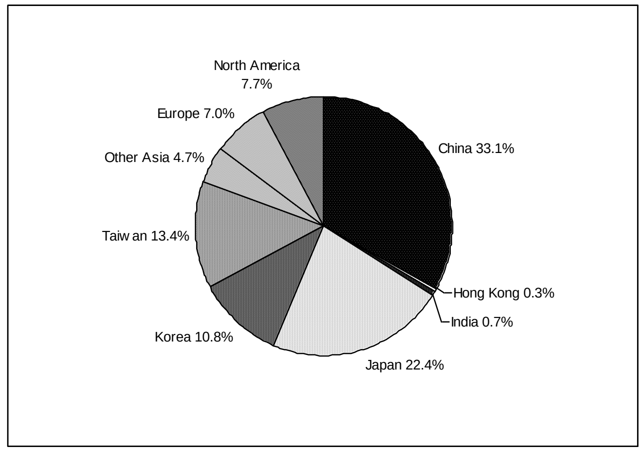


Fig. 2 Countries sharing PCB production for the year 2008 (WECC report)

with copper layers of 25 to 50 μm thick (Xingsheng Liu, 2001). There are three basic varieties of printed circuit boards: single-sided, double-sided, and multi-layered. The spatial and density requirement and circuitry complexity determine the type of board produced. **Fig. 1** Show the world PCB production estimates from 2005 till 2008, and **Fig. 2** show the major countries that share the production for the year 2008 (WECC – World Electronic Circuits Council, 2009).

Copper was commonly etched with alkaline ammonia and cupric chloride (continuous operation). Less common etchants include peroxide-sulfuric acid, persulfates, and ferric chloride (batch operation). The selection of etchant has been limited by economic, operational, and environmental concerns (Clyde F. Coombs, Jr, 2008). For single-sided boards, cupric chloride is the most suitable etchant even for large scale production lines (O. Cakir, 2006). It offers some distinct advantages like: simple regeneration of spent solution, no waste disposal problems, low cost, simple process control, and no sludging problem (Stephen D. Kasten, 1983).

## Chemistry of Copper Etching with Cupric Chloride and the Regeneration Process

Cupric chloride is a yellow-brown solid with the formula $CuCl_2$ in its dehydrated state. It is sold usually in its hydrated state ($CuCl_2.2H_2O$) with a blue-green color as it absorbs moisture from the ambient. Cupric chloride reacts with copper to form cuprous chloride:

$$Cu + CuCl_2 \rightarrow 2CuCl \qquad (1)$$

As the reaction proceeds, cupric ions will deplete and the reaction goes to slowdown (i.e. etching rate decreased). To obtain a constant etching rate and makes copper continue to dissolve from the metal surface, cuprous chloride should be returned back or regenerated to cupric chloride again. This can be accomplished by providing an oxidizing agent that oxidizes cuprous ions $Cu^{+1}$ to cupric ions $Cu^{+2}$. Many oxidizing agents can be used for this purpose, commonly used includes chlorine or air, sodium chlorate ($NaClO_3$), or hydrogen peroxide ($H_2O_2$). Regeneration process by oxygen was done chemically according to the reaction:

$$2Cu^{+} + O + 2H^{+} \rightarrow 2Cu^{++} + H_2O \qquad (2)$$

Reaction (2) consumes hydrogen ion, so that, hydrogen ions should by supplied to the reaction. Addition of hydrochloric acid (HCl) in excess amount to the reaction vessel was suggested to be a good source for $H^+$ ions and chloride balance was maintained. Also, it removes any traces of copper oxide from the surface of copper metal being etched (Chemcut Corp., 2002). It is clear that the original solution volume grows up during the regeneration process in this way. To overcome this problem, one should remove a portion of the etchant from time to time to keep a fixed reaction volume (P. Adaikkalam *et al*, 2002). The overall reaction of the regeneration process is:

$$2HCl + 2CuCl + O \rightarrow 2CuCl_2 + H_2O \qquad (3)$$

In this study, copper from single-sided boards was etched with cupric chloride and the effected parameters on the average etching rate were studied. Regeneration of the solution was done by continuous injection of air to the etching cell.

## EXPERIMENTAL WORK

### The Etching Cell

Etching of copper from single-sided boards with cupric chloride solution was accomplished in a cell designed to meet the necessary requirements needed to study the parameters affecting etching process.

The cell shown in **Fig**. **3** was made from a glass material with dimensions of 27 cm height × 19 cm width × 3.5 cm depth, filled with 1 liter of cupric chloride etchant during each run. It holds an electrical heater used to maintain the solution at the desired temperature fixed by a contact thermometer within ±0.5°C. At the bottom of the cell, an air distributor was installed enabling air bubbles to spread along the cell. The air was injected to the cell at a fixed flow rate of 0.5 liter/min. This flow rate was selected to be the maximum flow rate allowable to prevent the solution from spilling out of the cell. Air function as a source of oxygen required to regenerate the etchant and as an agitator.

Average etching rate was recorded as a function of etching time, etchant density, free acid concentration, and temperature. Etching was monitored by visual inspection of a 2 x 4 cm circuit board sample hanged at the center of the

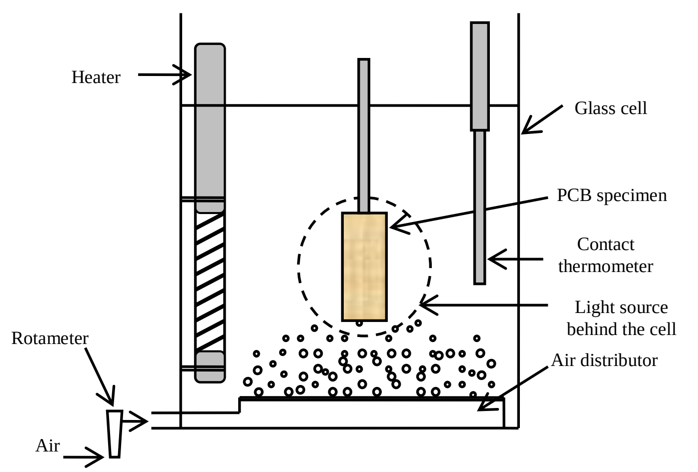


Fig. 3 Etching cell

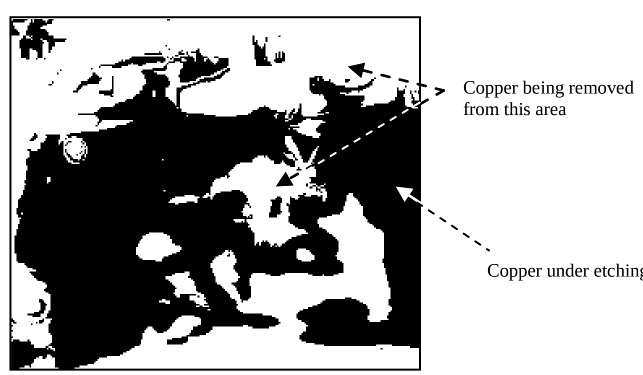


Fig. 4 Typical circuit board sample under etching

cell below the etchant surface level by about 4 cm. Samples are cleaned and polished well to obtain a scratch-free surface before dipping into the etching solution. Because the etchant become darker as its density increases, light source was installed behind the cell enabling best view of sample etching details instead of sample monitoring outside the cell from time to time.

The term '*average etching rate*' was used in this study because etching of the sample is not uniform. In other word not all the copper removed evenly from the sample sheet at the same time as shown in **Fig. 4**. Instead, pits start to appear (white area) and spread in all directions until the copper (black area) was removed completely. At this point, time was recorded and etching rate was calculated from the equation:

$$\text{Average Etching Rate} = \frac{\text{Copper Thickness}}{\text{Total Etching Time}} \quad (4)$$

Solution specific gravity was adjusted between each run after etchant was completely regenerated to its original state by a hydrometer. Leaving the solution about half-hour under air bubbling was considered to be sufficient time to return back the solution nearly to its initial state.

Free acid concentration was measured and adjusted using 37% hydrochloric acid of 1.19 specific gravity. Measurement of the free acid concentration was done by titration with NaOH solution. The amount of acid required to adjust the etchant can be calculated from:

$$y = \frac{x(a-b)}{(c-a)} \quad (5)$$

where y is the volume of acid required to adjust the etchant to the acid concentration required concentration *a*, *x* is the etchant volume (i.e. 1000 ml), *b* is the measured acid concentration by titration, and *c* is the concentration of the hydrochloric acid being added.

Note that the addition of HCl should be the last step in solution adjustment process because small amount of HCl is needed usually to bring the solution up to the desired acid concentration without changing the specific gravity of the solution appreciatory.

## RESULTS AND DISCUSSION

### Effect of Etching Temperature

In general, increasing the temperature tends to increase the etching rate as shown in **Figs. 5-9**. It is desired usually to select a temperature range which should give a relatively acceptable etching rate for practical purposes. Temperatures below 40°C takes long etching times (i.e. low etching rate) with low HCl fumes and above 55°C, etching rate increases many times but causes too much HCl fumes to start also. Under air regenerated cupric chloride etchant, it is observed that temperature range between 45°C and 55°C is the suitable working range depending on the air flow rate because oxygen solubility decreases with increasing temperature (i.e. to work at elevated temperature range to obtain higher etching rates, one should distribute much more bubbles - in the maximum allowable flow - to maximize the rate of solubility of oxygen to the maximum one).

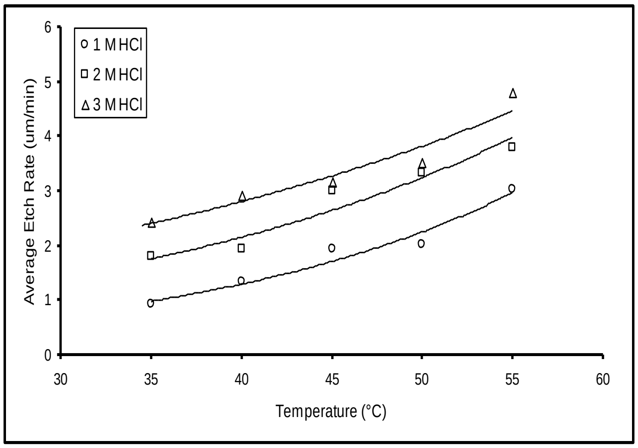


Fig. 5 Average etching rate versus etchant temp. at different free acid conc. and 1.1 sp.gr.

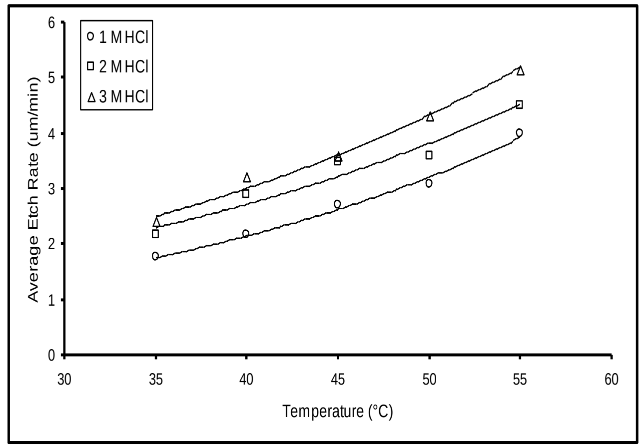


Fig. 6 Average etching rate versus etchant temp. at different free acid conc. and 1.2 sp.gr.

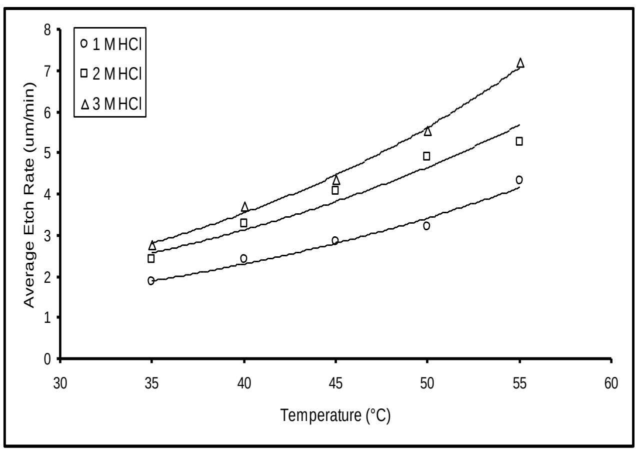


Fig. 7 Average etching rate versus etchant temp. at different free acid conc. and 1.3 sp.gr.

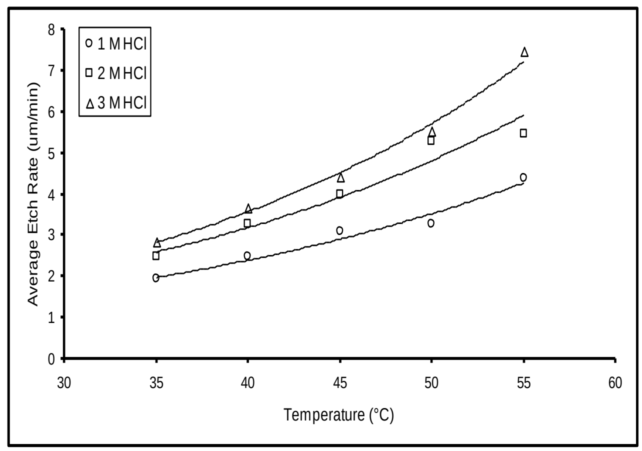


Fig. 8 Average etching rate versus etchant temp. at different free acid conc. and 1.4 sp.gr.

## Effect of Etchant Specific Gravity

As copper continue to dissolve and water evaporates, specific gravity of the etchant will increase also and the etchant become a dense solution. At some point, this will cause average etching rate to slow down because the movement of cuprous ions away from the copper surface become more difficult and may initiates sludges to be formed.

**Figs. 10-14** shows the effect of etchant specific gravity change on average etching rate at different temperatures. It is clear that maximum and nearly constant etching rate occurs between specific gravity of 1.3 and 1.4 as it does not change significantly within this range. Average etching rate decreased below specific gravity of 1.3 and above

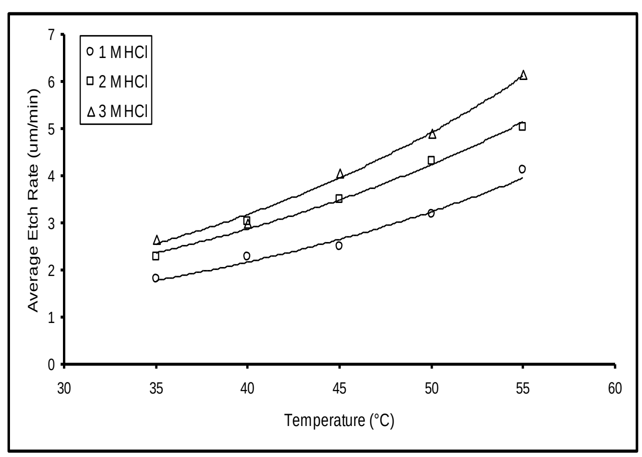


Fig. 9 Average etching rate versus etchant temp. at different free acid conc. and 1.5 sp.gr.

1.4. So that, it is desired to control the specific gravity within this range.

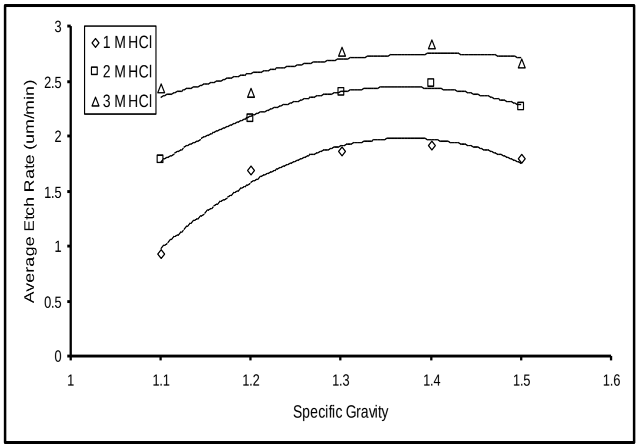


Fig. 10 Etchant specific gravity versus average etching rate at different free acid conc. and 35°C

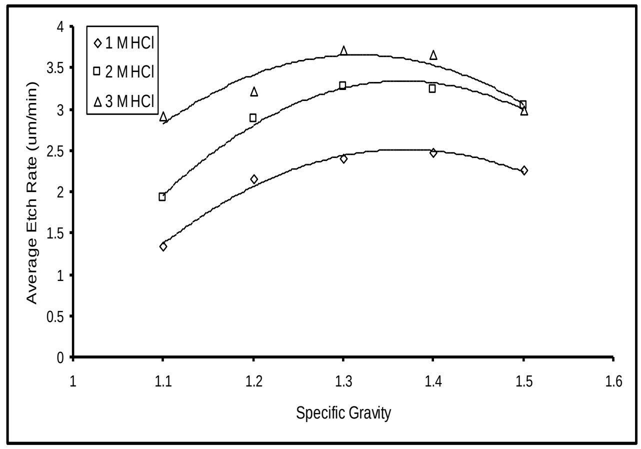


Fig. 11 Etchant specific gravity versus average etching rate at different free acid conc. and 40°C

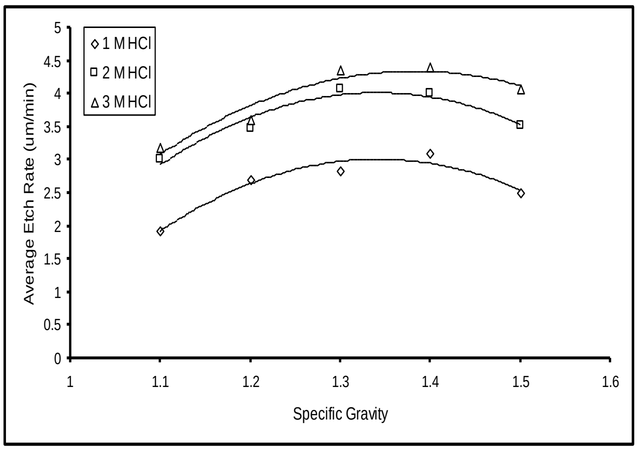


Fig. 12 Etchant specific gravity versus average etching rate at different free acid conc. and 45°C

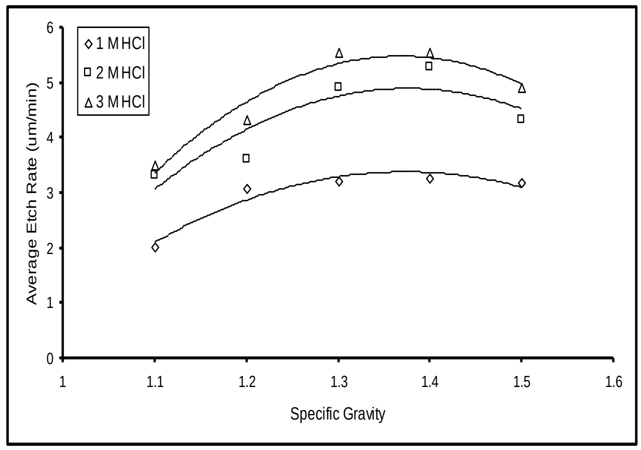


Fig. 13 Etchant specific gravity versus average etching rate at different free acid conc. and 50°C

## Effect of Etchant Free Acid Concentration

From the previous figures (**Figs. 5-14**), it is clear that increasing the free acid concentration in the solution is proportional with the average etching rate. Low etching rate were observed at 1 M HCl with low fuming in all temperature range studied, at 2 and 3M HCl, higher etching rates were obtained but the rate of fuming increases also especially at elevated temperatures when 3 M HCl were used. So that, the selection of HCl concentration should be contributed with the working temperature and the allowable limit of fuming. The best operating free HCl level was suggested to be between 2 and 3 M HCl.

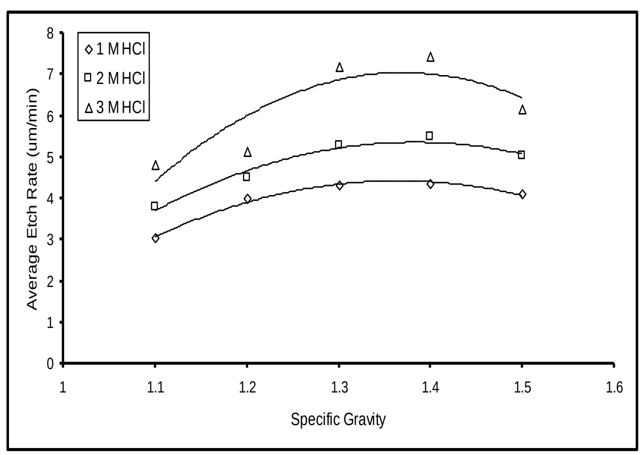


Fig. 14 Etchant specific gravity versus average etching rate at different free acid conc. and 55°C

## CONCLUSIONS

- Single-sided circuit boards can be etched with different etchants but cupric chloride is the most suitable one even for large production lines.
- Cupric chloride can be regenerated using many oxidants even oxygen from air and the parameters affecting etching rates should be contributed together in order to maximize the etching rate.
- It is found that controlling temperature within the range of 45-55°C, etchant specific gravity of 1.3-1.4, and free acid concentration of 1.3-1.4 M would provide the best etching results.

## NOMENCLATURE

*a* Free acid required concentration, M
*b* Measured free acid concentration, M
*c* Acid concentration being added, M
*x* Etchant total volume, ml
*y* Etchant volume required to adjust the etchant to the desired level, ml

## REFERENCES


- Chemcut Corporation., Technical document: *Process Guidelines for Cupric Chloride Etching*, (2002), http://www.chemcut.net, Aug 2009.
- Clyde F. Coombs, Jr, *Printed Circuits Handbook*, 6$^{th}$ edition, McGraw-Hill Companies, 2008.
- O. Cakir, A. Yardimeden, T. Ozben, *Chemical Machining*, Archives of Materials Science and Engineering, Vol. 28, Issue 8 (2007), pp. 499-502.
- O. Cakir, *Copper Etching and Regeneration of Waste Etchant*, Journal of Material Processing Technology, 175 (2006), pp. 63-68.
- O. Cakir, *Photochemical Machining of Engineering Materials*, Archives of Materials Science, Vol. 28 No. 1-4 (2007), pp. 15-19.
- P. Adaikkalam, G. N. Srinivasan, and K. V. Venkateswaran, *The electrochemical Recycling of Printed-Wiring-Board Etchants*. JOM, June (2002).
- Stephen D. Kasten, *Electronic Prototype Construction*, Howard W. Sam & Co., Inc, 1983.
- WECC Global PCB Production Report for 2006, 2007, and 2008, http://www.hkpca.org, Jan 2009.
- Xingsheng Liu, *Processing and Reliability Assessment of Solder Joint Interconnection for Power Chips*, PhD dissertation in Material Engineering and Science, Virginia Polytechnic Institute and State University, 2001.

# FREQUENCY DOMAIN EQUALIZATION TECHNIQUES FOR MULTICODE DS-CDMA IN FREQUENCY SELECTIVE RAYLEIGH FADING CHANNEL

Asst., Prof. Maha George Zia and Msc. Eng. Sameer Akram Dawood
Electrical Engineering Department-College of Engineering, Al-Mustansiriya University

**ABSTRACT**

Orthogonal multicode direct sequence code division multiple access (DS-CDMA) has the flexibility in offering high data rate services. However, in a frequency-selective fading channel, the bit error rate (BER) performance is severely degraded since the orthogonality among spreading codes is partially lost. In this paper, frequency-domain equalization (FDE) and space antenna diversity combining are applied to orthogonal multicode DS-CDMA in order to restore the code orthogonality and improve the BER performance of the system. Two methods of FDE are considered, the first method based on fast Fourier transform (FFT), while the second method based on circulant matrices. Moreover, a channel interleaving method, called chip interleaving is used to improve the performance of multicode DS-CDMA system.

**KEYWORDS: Multicode Ds-Cdma, Frequency Domain Equalization.**

**الخلاصة:**

تعدد الشفرات المتعامدة لنظام تقسيم الشفرات متعدد المداخل ذي المتتابعة المباشرة (DS-CDMA) يعطي مرونة في خدمات نقل البيانات بسرعة عالية. مع ذلك في قناة الخفوت الترددية الاختيارية فان اداء النظام سيقل بشدة وذلك لان التعامد بين شفرات النشر سيفقد جزئيا. في هذا البحث، معادلة مجال التردد (FDE) مع تنوع الهوائيات المكانية ستطبق على نظام (DS-CDMA) متعدد الشفرات المتعامدة وذلك لاستعادة التعامد بين الشفرات وبالتالي تحسين اداء النظام. طريقيتين من طرق معادلة مجال التردد ستعتمد في هذا البحث، الطريقة الاولى تعتمد على تحويل فورير السريع (FFT) بينما الطريقة الثانية تعتمد على طريقة تدوير المصفوفات (circulant matrices) . بالاضافة الى ذلك سيتم استخدام طريقة لبعثرة القناة تدعى بعثرة الشريحة (Chip Interleaving) لتحسين اداء نظام (DS-CDMA) متعدد الشفرات المتعامدة.

## INTRODUCTION

In direct sequence code division multiple access (DS-CDMA), one way to achieve high speed data transmission is to use orthogonal multicode multiplexing. However, frequency selective multipath fading encountered in a broadband wireless communication system severely degrades the bit error rate (BER) performance of multicode DS-CDMA, (T. Itagaki etal, 2004). An effective way to improve the BER performance is to apply frequency-domain equalization (FDE) to multicode DS-CDMA signal reception, (F. Adachi etal, 2003).

Frequency domain equalization (FDE) is an effective technique for improving the single carrier (SC) transmission performance in a frequency selective fading channel, (D. Falconer etal, 2002). Minimum mean square error (MMSE)-FDE based on fast Fourier transform (FFT) was applied to multicode DS-CDMA to obtain a good BER performance similar to that of multi carrier code division multiple access (MC-CDMA), (F. Adachi etal, 2003 and F. Adachi etal, 2005). The distinctive point of this technique is the use of Cyclic Prefix (CP), in order to prevent degradation of transmission characteristics caused by multipath interference, which become more apparent during broadband transmission. CP copies multiple data symbols at the end of a frame to the head part of a frame. Moreover, the equalization is performed on a block of data at a time and the operations on this block involve fast Fourier transform (FFT), (D. Falconer etal, 2002).

Space antenna diversity technique can be used to improve the system performance in a fading channel. Instead of transmitting and receiving the desired signal through one channel, several copies of the desired signal are obtained through different channels, (H. Hourani, 2004-2005).

Chip interleaving is a form of channel interleaver that exploits the spreading process in DS-CDMA and thus improves the BER performance in a frequency selective fading channel. Chip interleaver scrambles the chips and transforms the transmission channel into highly time selective or highly memoryless channel, (D. Garg etal, 2002 and D. Garg etal, 2005).

In this paper, two additional FDE techniques are used; maximum ratio combining (MRC-FDE) and zero forcing (ZF-FDE). Moreover, MMSE-FDE (based on FFT) which was applied in (F. Adachi etal, 2003), will be used too. All the above FDE techniques are applied to multicode DS-CDMA with their performance are compared by simulation.

Finally, two methods of FDE techniques based on FFT and circulant matrices are illustrated. Since FDE based on FFT consumes less time compared with circulant matrices method, it will be used in this work.

Remainder of this paper is organized as follows. Section 2, presents the transmission system model for a multicode DS-CDMA using FDE and antenna diversity combining. MMSE-FDE, MRC-FDE and ZF-FDE based on FFT and circulant matrices methods are presented. Moreover, chip interleaver is presented in this section. In section 3, the BER performance of the system in 3-paths frequency selective Rayleigh fading channel is evaluated by computer simulation. Finally, section 4, offers some conclusions.

## - MULTICODE DS-CDMA WITH FDE AND ANTENNA DIVERSITY

### Transmission System Model

Transmission system model for multicode DS-CDMA using FDE and antenna diversity combining is illustrated in Fig.(1). At the transmitter, the data modulated symbol sequence is serial-to-parallel (S/P) converted into U parallel data streams {$d_i(t)$; i=0~U-1} which are then spread using U orthogonal spreading sequences {$c_i(t)$; i=0~U-1} having a spreading factor of *SF*. The Resultant U chip sequences are summed to form the orthogonal multicode DS-CDMA signal, which then divided into blocks of $N_c$ chips each and then, the last $N_g$ chips of each block is copied as a cyclic prefix and inserted into the guard interval (GI) at the beginning of each block to form a frame of ($N_c$+$N_g$) chips. Figure (2) illustrates the frame structure, (T. Itagaki etal, 2004 and K. Takeda etal, 2004).

The GI-inserted chip sequence is transmitted over a frequency-selective fading channel and is received by $N_r$ diversity antennas at the receiver. After the removal of GI, the received chip sequence on each antenna is decomposed by $N_c$-point FFT into $N_c$ subcarrier components. Then, joint FDE and antenna diversity combining is carried out. Finally, inverse FFT (IFFT) is applied to obtain the equalized and diversity combined time-domain chip sequence for multicode despreading and parallel-to-serial (P/S) converted for data demodulation , (T. Itagaki etal, 2004 and K. Takeda etal, 2004).

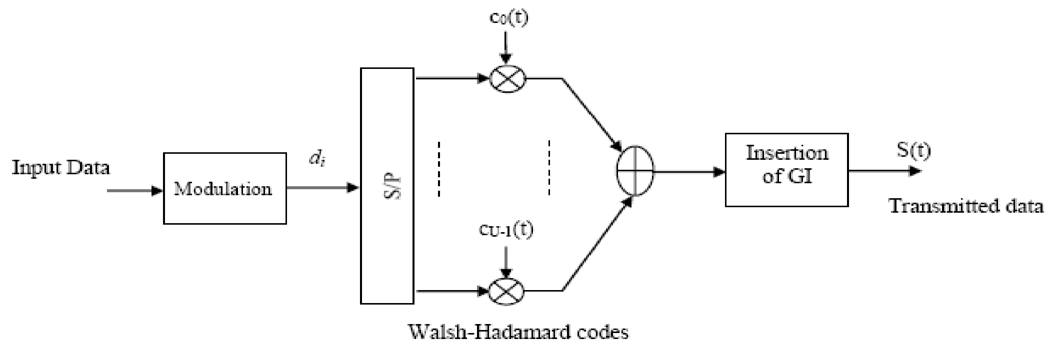


**(a) Transmitter**

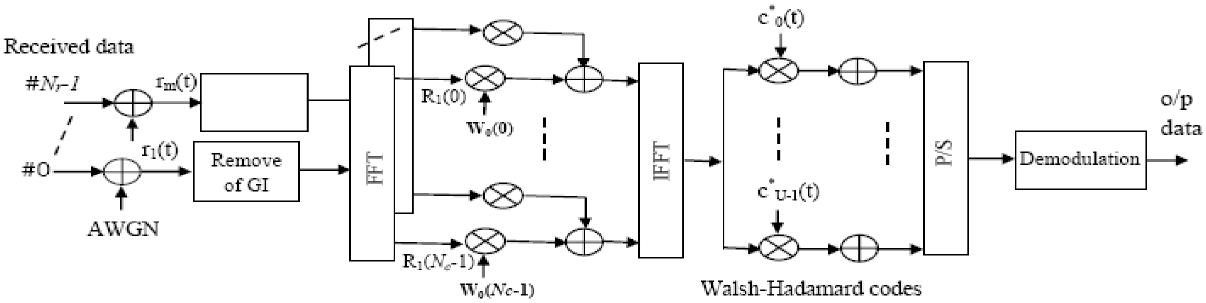


**(b) Receiver**

**Fig. (1)** Transmission system model for multicode DS-CDMA with Joint FDE and antenna diversity combining.

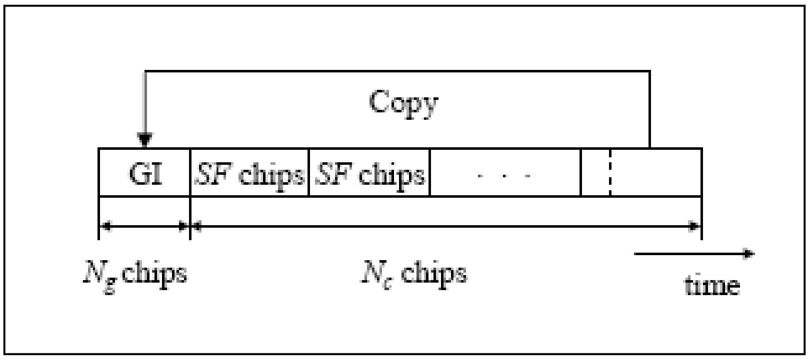


**Fig.(2)** Frame structure.

**Received Signal**

The propagation channel is assumed to be a frequency-selective fading channel having $L$ discrete paths, each subjected to independent fading, where the time delay of the $l$th path ($l = 0 \sim L-1$) is assumed to be $\tau_l$. The chip sequence $\{r_m(t);\ m=0\sim N_r-1,\ t= -N_g\sim N_c-1\}$ received on the $m$th antenna can be represented as (T. Itagaki etal, 2004 and K. Takeda etal, 2004):

$$r_m(t) = \sum_{l=0}^{L-1} h_{m,l}\, s(t-\tau_l) + n_m(t), \qquad (1)$$

where, $h_{m,l}$ is the complex path gain of the $l$th path experienced at the $m$-th antenna and , s(t) is the transmitted chip sequence ($t = -N_g \sim N_c - 1$), and $n_m(t)$ is the additive white Gaussian noise (AWGN).

After removal of GI from the received chip sequence $\{r_m(t)\}$, $N_c$-point FFT is applied to decompose $\{r_m(t);\ t = 0 \sim N_c-1\}$ into $N_c$ subcarrier components $\{R_m(k);\ k=0\sim N_c-1\}$. The $k$th subcarrier component $R_m(k)$ can be written as (T. Itagaki etal, 2004 and K. Takeda etal, 2004):

$$R_m(k) = H_m(k)S(k) + n_m(k), \qquad (2)$$

Where, $S(k)$, $H_m(k)$ and $n_m(k)$ are the $k$th subcarrier components of the transmitted $N_c$-chip signal sequence $\{s(t);\ t=0 \sim N_c-1\}$, the channel gain and noise component due to the AWGN, respectively. They are given by (T. Itagaki etal, 2004 and K. Takeda etal, 2004):

$$\begin{cases} S(k) = \sum_{t=o}^{N_c-1} s(t)\exp(-j2\pi k\frac{t}{N_c}) \\ H_m(k) = \sum_{l=o}^{L-1} h_{m,l}\exp(-j2\pi k\frac{\tau_l}{N_c}), \\ n_m(k) = \sum_{t=o}^{N_c-1} n_m(t)\exp(-j2\pi k\frac{t}{N_c}) \end{cases} \qquad (3)$$

Then, joint one-tap FDE and antenna diversity combining is carried out to obtain (T. Itagaki etal, 2004 and K. Takeda etal, 2004):

$$R\square_m(k) = \sum_{m=0}^{N_r-1} R_m(k)\, W_m(k), \tag{4}$$

where $W_m(k)$ is the equalization weight. MMSE equalization, MRC equalization and ZF equalization are used in this work.

Two methods of FDE are considered in this work to calculate the equalization weight; the first method is based on FFT (T. Itagaki etal, 2004 and K. Takeda etal, 2004), while the second method is based on circulant matrices (Y. YANG, 2003).

## 2.2.1 FDE Based on FFT

FDE based on FFT is much faster than FDE based on circulant matrices. The frequency domain MMSE equalization weight $W_m(k)$ for kth subcarrier is given by, (F. Adachi etal, 2003):

$$W_m(k) = \frac{H_m^*(k)}{\sum_{m=0}^{Nr-1}\left|H_m(k)\right|^2 + \left[\frac{U}{SF}\left(\frac{E_s}{N_o}\right)\right]^{-1}} \tag{5}$$

where, $(E_s/N_o)$ is the average received signal energy per symbol to-single-sided power spectrum density of AWGN process ratio and * denotes complex conjugation.

In this work, the below two FDE methods, (T. Itagaki etal, 2004 and K. Takeda etal, 2004) are used in addition to MMSE-FDE, (F. Adachi etal, 2003).

$$W_m(k) = \begin{cases} H_m^*(k) & \text{, MRC-FDE} \\[2ex] \dfrac{H_m^*(k)}{\sum_{m=0}^{Nr-1}\left|H_m(k)\right|^2} & \text{, ZF-FDE} \end{cases} \tag{6}$$

**FDE Based on Circulant Matrices**

Let h = [ $h(0)$, $h(1)$, …..$h(L$-1) ] is the equivalent discrete time channel impulse response (CIR). The $N \times N$ channel matrix H is circulant with its $(k,l)$th entry given by $h((k\text{-}l) \bmod N)$; or looks like (Y. YANG, 2003):

$$\mathrm{H} = \begin{bmatrix} h(0) & 0 & \cdots & h(L\text{-}1) & \cdots & h(1) \\ h(1) & h(0) & \cdots & 0 & & \vdots \\ \vdots & h(1) & & & & h(L\text{-}1) \\ h(L\text{-}1) & \vdots & & h(0) & & 0 \\ \vdots & h(L\text{-}1) & & \vdots & & \vdots \\ 0 & \cdots & \cdots & h(L\text{-}2) & \cdots & h(0) \end{bmatrix} \tag{7}$$

Since H is a circulant matrix, it can be expressed in term of its eigenvalues and associated eigenvectors, i.e., eigen-decomposition, as follows (Y. YANG, 2003):

$$\mathrm{H} = \mathrm{F}_N^H \, \Lambda \, \mathrm{F}_N \tag{8}$$

where, $\mathrm{F}_N$ is the orthonormal discrete Fourier transform (DFT) matrix whose $(k,l)$th entry is given by $\mathrm{F}_{k,l} = N^{-1/2} \exp(-j2\pi kl/N)$, where $0 \le k,l \le N$-1; and $\Lambda$ is a diagonal matrix with its $(k,k)$ element equal to the $k$th DFT coefficient of the channel impulse response, i.e., $\Lambda_{k,k} = \sum_{n=0}^{N-1} h(n) \exp(-j2\pi nk/N)$. It is also noteworthy that the $N \times N$ matrix $\mathrm{F}_N$ is unitary, i.e., $\mathrm{F}_N^{-1} = \mathrm{F}_N^H$. Here, the superscript $H$ denotes complex conjugate transpose. The diagonal of $\Lambda$ contains uniformly sampled samples of channel frequency response (Y. YANG, 2003).

After discarding CP at the receiver, the received time domain block is transformed to frequency domain by means of $N$-point DFT operations. Then, based on the eigen-decomposition property of circulant matrix H, the input-output relationship can be described as (Y. YANG, 2003):

$$R(i) = \mathrm{F}_N \, \mathrm{r(i)} = \mathrm{F}_N \, \mathrm{F}_N^H \Lambda \, \mathrm{F}_N \, \mathrm{s(i)} + \mathrm{F}_N \, \mathrm{n(i)}$$

$$= \Lambda \, \mathrm{S}(k) + n(\mathrm{k}) \tag{9}$$

where, s(i), and n(i) are the ith transmitted block and corresponding noise vector, both of them of size $N$.

The coefficients of FDE based on circulant matrices are given by (Y. YANG, 2003):

$$W(k) = \begin{cases} \Lambda^H (\Lambda \Lambda^H + \frac{1}{SNR} I_N)^{-1}, & \text{MMSE-FDE} \\ \Lambda^H, & \text{MRC-FDE} \\ \frac{1}{\Lambda}, & \text{ZF-FDE} \end{cases} \quad (10)$$

where, SNR is a signal-to-noise ratio.

**Chip Interleaver**

Chip interleaver is a channel interleaving method used for DS-CDMA mobile radio. Chip interleaver scrambles the chips associated with a data symbols so that the channel gains experienced by neighboring chips are highly uncorrelated. By doing so, the resultant transmission channel can be transformed into highly time-selective or highly memoryless channel, (D. Garg etal, 2002 and D. Garg etal, 2005).

The proposed chip interleaver interleaves the chip sequence obtained after spreading. Figure (3) illustrates the chip interleaver structure, (D. Garg etal, 2002). It is a block interleaver with columns equal to the number of chips to be transmitted ($N_c$) and rows equal to $N_R$. The chip sequence to be transmitted is written column-wise and read row-wise. At the receiver, the received chip sequence is written and read in an opposite manner in the chip de-interleaver before despreading. The number of rows in chip interleaver is chosen to be larger than $SF$, which is given by, (D. Garg etal, 2005):

$$N_R = \frac{SF * a}{N_c} \quad (11)$$

where, $N_R$ is the number of rows in chip interleaver and $a$ is the number of data in each substream.

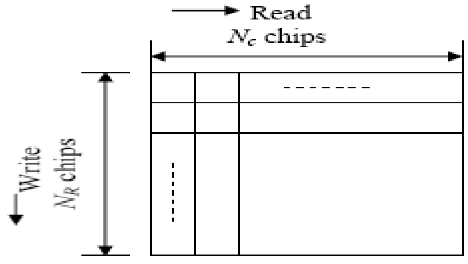


**Fig.(3)** Chip Interleaver Structure.

## - COMPUTER SIMULATION

The parameters that have been used in simulation are listed in Table (1). This system is software implemented with MATLAB 7.0 technical programming language.

**Table 1** Simulation Parameters.

| Parameter | Value |
|---|---|
| Data rate | 3MHz |
| No. of transmitted bits | 100000 |
| Modulation type | QPSK |
| Spreading code type | Walsh code |
| Spreading Factor | *SF*=4, 8, 16, 32 |
| No. of parallel codes | U=4 |
| No. of FFT points | $N_c$ =256 |
| Cyclic prefix interval | $N_g$=32 (chips) |
| fading channel model | Rayleigh fading channel (Jakes model) |
| Doppler Frequency | $f_d$=10 Hz |
| No. of channel paths | L=3 |
| No. of receiver antennas | $N_r$=1, 2, 4 |
| Frequency-Domain Equalization Types | MMSE-FDE, MRC-FDE, ZF-FDE |
| SNR | (0,2,…,22) dB |

## BER Performance Comparison of Multicode DS-CDMA with MMSE-FDE Based on FFT and Circulant Matrices Methods:

Figure (4) shows the BER performance versus SNR of multicode DS-CDMA system with MMSE-FDE using FFT method and circulant matrices method, in three paths Rayleigh fading channel, for *SF*=4 and 16. It can be seen that the FFT method gives better BER performance than circulant matrices method. Moreover, FDE based on FFT is much faster than FDE based on circulant matrices.

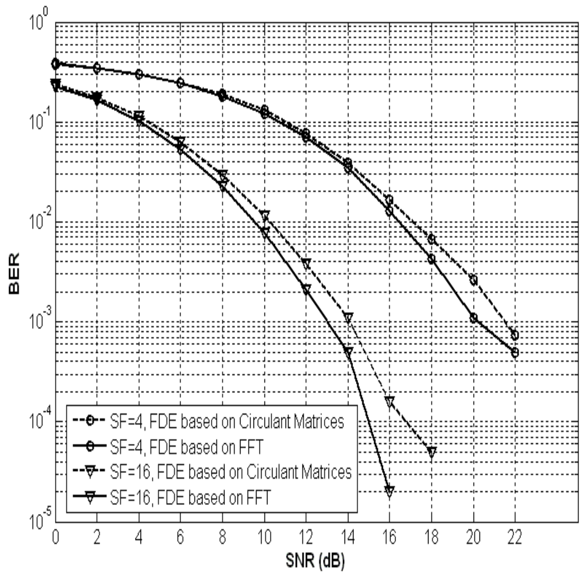


**Fig.(4)** BER performance of multicode DS-CDMA with MMSE-FDE based on FFT and Circulant Matrices methods in 3-paths Rayleigh fading channel.

Since FDE based on FFT method achieves better BER performance. Hence, in the following results, only this method is used.

**BER Performance Comparison of Multicode DS-CDMA with MMSE-FDE, MRC-FDE and ZF-FDE Techniques:**

The BER performances versus SNR of multicode DS-CDMA system using different values of spreading factor (*SF*), with joint MMSE-FDE, MRC-FDE, and ZF-FDE in three paths Rayleigh fading channel are illustrated in Figs.5(a), 5(b), and 5(c), respectively.

The BER performance is improved when *SF* is increased for all types of FDE. The MMSE equalization always achieves better BER performance as compared to MRC and ZF equalization. The MRC equalization achieves poor performance (BER floor) for *SF*=4, due to the larger ICI (intercode interference) produced by the enhanced frequency-selectivity, but when *SF*=8, 16, and 32, the MRC equalization achieves almost the same BER performance as MMSE equalization since the ICI can be sufficiently suppressed during the despreading process. The ZF equalization achieves good performance at high *SF* and at high SNR values only, because the ZF equalization leads to noise enhancement.

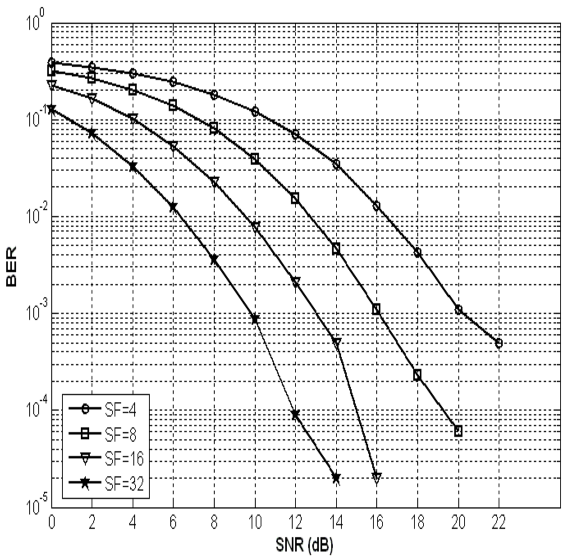


(a) Multicode DS-CDMA with MMSE-FDE

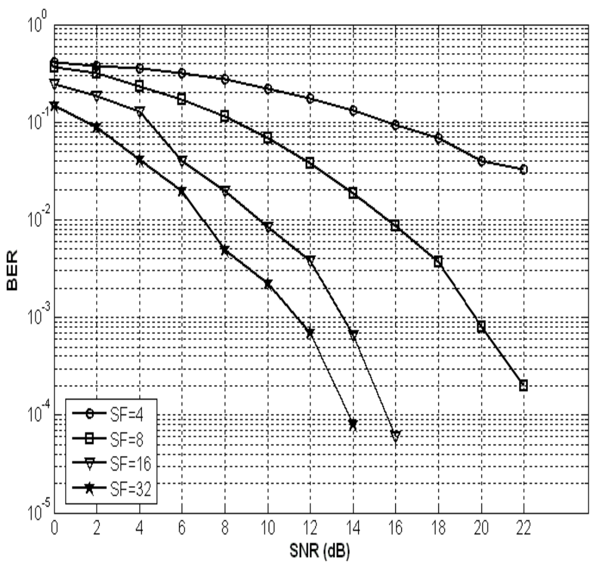


(b) Multicode DS-CDMA with MRC-FDE

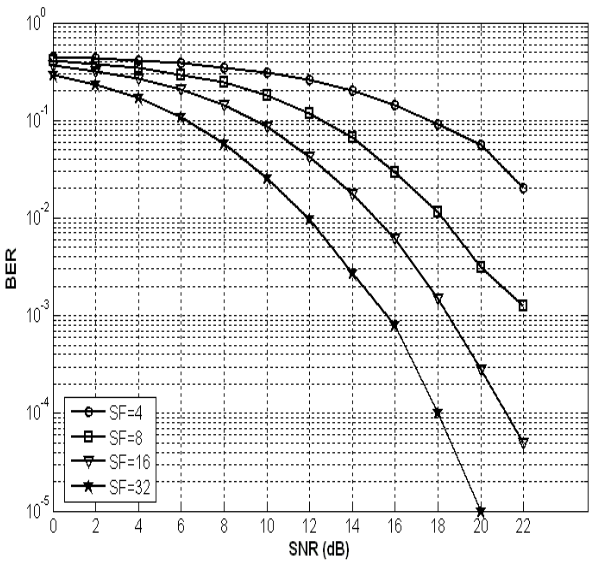


(c) Multicode DS-CDMA with ZF-FDE

**Fig.(5)** BER performances of multicode DS-CDMA using MMSE-FDE, MRC-FDE and ZF-FDE techniques.

## Error Rate Performance of Multicode DS-CDMA with FDE and Fading Rate as a Parameter:

Figure (6) illustrates the BER performance versus SNR of multicode DS-CDMA system in 3-paths Rayleigh fading channel using *SF*=16, and fading rate ($f_d$*$T_{blk}$) as parameter, where $f_d$=10 Hz and 200 Hz. $T_{blk}$= (($N_c$+$N_g$)*$T_c$), here $T_c$ is chip duration. Joint MMSE-FDE, MRC-FDE, and ZF-FDE are used.

In this work, block fading is assumed, where the path gains stay constant over one frame duration. For *SF*=16 and $f_d$*$T_{blk}$=4.8e-4, the BER performance is better than $f_d$*$T_{blk}$=9.6e-3, because as $f_d$ is increased (fast fading), the path gains of the channel do not stay constant during one frame duration. The MMSE equalization still achieves better BER performance as compared with MRC and ZF equalizations.

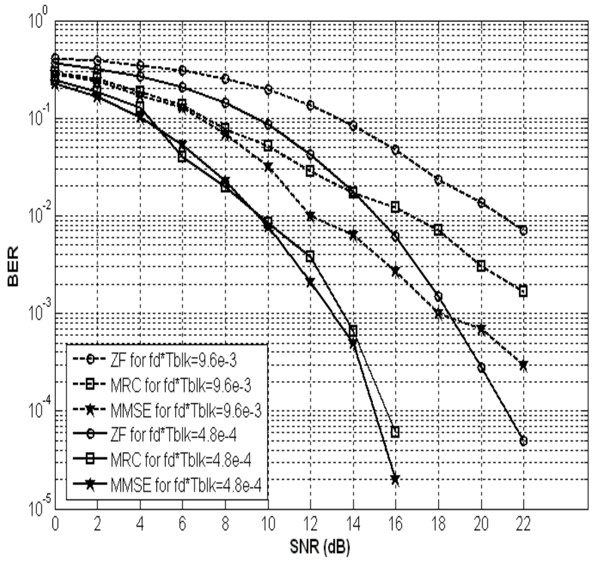


**Fig.(6)** BER performance of multicode DS-CDMA with frequency domain equalizers and fading rate as a parameter ($f_d$=10 & 200 Hz).

Since the MMSE equalization always achieves better BER performance. Hence, in the following results, only MMSE equalization is used.

**The Effect of Chip Interleaver on the Performance of Multicode DS-CDMA with MMSE-FDE:**

Figure (7) shows the BER performance versus SNR of multicode DS-CDMA system using chip interleaver with MMSE-FDE in three paths Rayleigh fading channel, for *SF*=4 and 8. With chip interleaving, the BER performance improves as *SF* increases, when *SF*=4 (8), about 1dB (2dB) improvement is seen in the SNR required for a BER=$10^{-3}$.

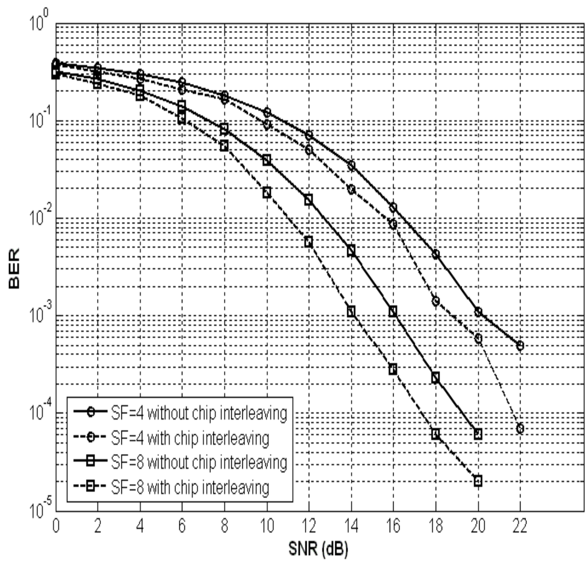


**Fig.(7)** BER performance of multicode DS-CDMA with MMSE-FDE and chip interleaving in 3-paths Rayleigh fading channel.

**- Error Rate Performance of Multicode DS-CDMA with MMSE-FDE and Space Antenna Diversity:**

Figure (8) shows the BER performance versus SNR of multicode DS-CDMA system with MMSE-FDE and space antenna diversity ($N_r$=1,2, and 4) in three paths Rayleigh fading channel for *SF*=4.

It can be clearly seen that the use of antenna diversity combining is always beneficial, where as the number of branches ($N_r$) is increased, the BER decreases.

It can be seen from Fig.(8) that when BER=$10^{-3}$, there is about (2.4)dB and (4)dB improvement for $N_r$=2 and $N_r$=4, respectively.

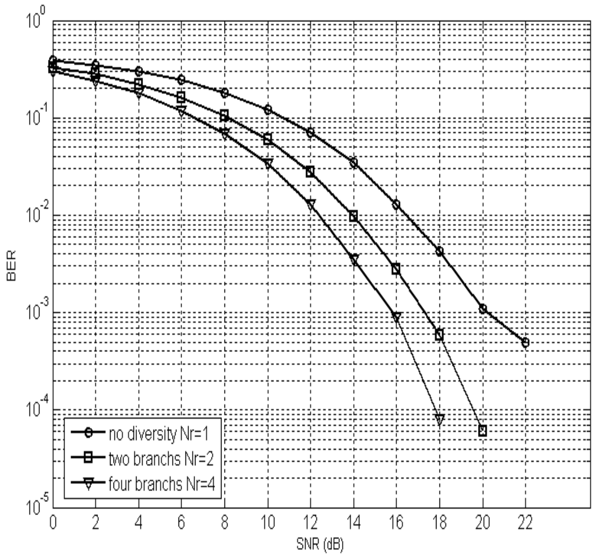


**Fig.(8)** BER performance of multicode DS-CDMA with MMSE-FDE and space antenna diversity in 3-paths Rayleigh fading channel.

**The Effect of Changing the Number of Codes and Spreading Factors on the Performance of Multicode DS-CDMA with MMSE-FDE:**

Figure (9) shows the BER performance versus SNR of multicode DS-CDMA system using different number of parallel codes and spreading factors with joint MMSE-FDE in three paths Rayleigh fading channel.

When the value of U/*SF* (which represents intercode interference (ICI)) becomes smaller, the effect of ICI becomes less and less and thus, the achievable BER performance improves. A mathematically extreme case is when (U/*SF*)→ 0 (i.e., ICI is neglected) (K. Takeda etal, 2004).

It can be clearly seen from Fig.(9) that when the amount of ICI is the same for multicode transmission, the BER performance is improved as *SF* is increased.

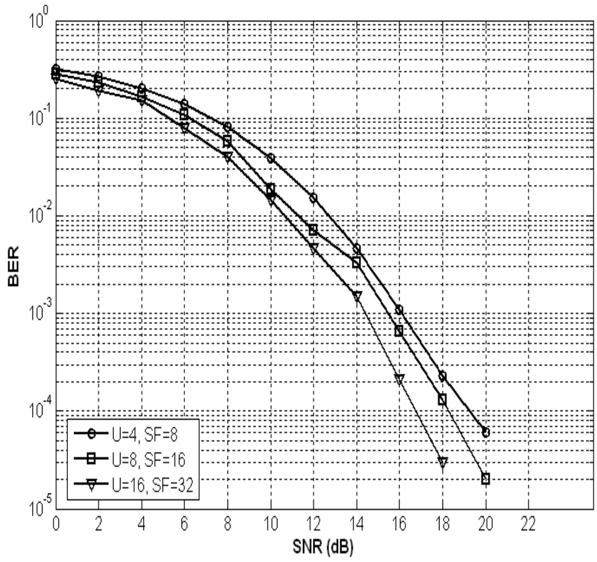


**Fig.(9)** Performance of multicode DS-CDMA with MMSE-FDE in 3-paths Rayleigh fading channel with different codes and spreading factors as a parameter.

## - CONCLUSIONS

In this paper, joint frequency-domain equalization and antenna diversity combining was presented for improving the orthogonal multicode DS-CDMA signal transmission performance in a frequency-selective Rayleigh fading channel and the achievable BER performance was evaluated by computer simulation. It was found that the FDE based on FFT method gives better BER performance than circulant matrices method. Moreover, FDE based on FFT consumes less time and therefore, it is much faster than FDE based on circulant matrices. The BER performance using MMSE, MRC and ZF equalization were compared and the MMSE equalization gives the best BER performance. Also, it was found that as the spreading factor increases, the equalization schemes improve the BER performance since the ICI produced by the frequency-selectivity can be effectively suppressed during the despreading process.

Chip interleaver was also introduced to exploit the time selectivity of the channel in multicode DS-CDMA system with MMSE-FDE. It was shown by computer simulations that the chip interleaving improved the BER performance as *SF* is increased. Finally, space antenna diversity was presented in this paper to improve the BER performance of DS-CDMA with MMSE-FDE. It was shown that the use of antenna diversity is powerful to improve the BER performance, where as the number of branches is increased, the BER performance decreases and the complexity of the system becomes expensive.

## REFERENCES


- D. Falconer, S.L. Ariyavisitakul, A. Benyamin-Seeyar, and B. Eidson, “Frequency Domain Equalization for Single-Carrier Broadband Wireless Systems”, White paper
- http://www.sce.carleton.ca./ bbw/papers/Ariyavisita kul.pdf., 2002

- D. Falconer, S. L. Ariyavisitakul, A. Benyamin-Seeyar, and B. Edison, “Frequency Domain Equalization for Single-Carrier Broadband Wireless Systems,” IEEE Communication Magazine, vol.40, no.4, pp.58-66, April 2002.

- D. Garg, and F. Adachi, “Performance of DS-CDMA with Chip Interleaving and Frequency Domain Equalization in a Fading Channel,” IEE Proc. Commun., vol.152, no.6, pp.757-764, Dec. 2005.

- D. Garg, and F. Adachi, “Chip Interleaved Turbo Codes for DS-CDMA in a Rayleigh Fading Channel with Diversity Reception,” IEE Electron, Lett., vol.38, no.13, pp.642-644, June 2002.

- F. Adachi, T. Sao, and T. Itagaki, “Performance of Multicode DS-CDMA using Frequency Domain Equalization in Frequency-Selective Fading Channel,” Electronic Letter, vol.39, no.2, pp.239-241, Jan. 2003.

- F. Adachi, D. Garg, S. Takaoka, and K. Takeda, “Broadband CDMA Techniques,” IEEE Wireless Communication, vol.12, no.2, pp.8-18, April 2005.

- H. Hourani, "An Overview of Diversity Techniques in Wireless Communication Systems", Postgraduate Course in Radio Communications (2004/2005), Helsinki University of Technology.
- www.comlab.hut.fi/opetus/ 333/2004_2005_slides/Diversity_text.pdf.

- K. Takeda, and F. Adachi, “Bit Error Rate Analysis of DS-CDMA with Joint Frequency Domain Equalization and Antenna Diversity Combining,” IEICE Trans. Commun., vol. E87-B, no.10, pp.2991-3002, Oct. 2004.

- T. Itagaki, and F. Adachi, “Jiont Frequency-Domain Equalization and Antenna Diversity Combining for Orthognal Multicode DS-CDMA Signal Transmissions in a Frequency-Selective Fading Channel,” IEICE Trans. Commun., vol. E87-B, no.7, pp.1954-1963, July 2004.

- Y. YANG, "Frequency-Domain Equalization for Space-Time Block Coded Transmissions over Frequency-Selective Fading Channels", Msc. thesis in Electrical and Computer Engineering National University of Singapore, 2003.